

AD-A111 405 ADVISORY GROUP FOR AEROSPACE RESEARCH AND DEVELOPMENT--ETC F/6 22/3
SPACECRAFT POINTING AND POSITION CONTROL.(U)

NOV 81 P P BROEK, S Z SZIRMAY

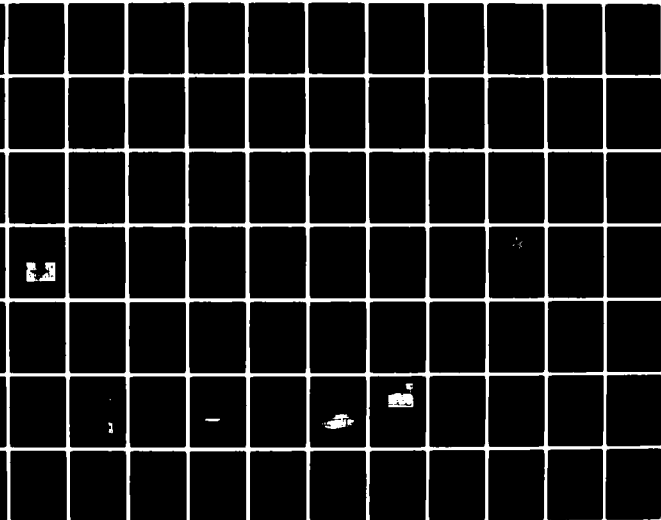
AGARD-AG-260

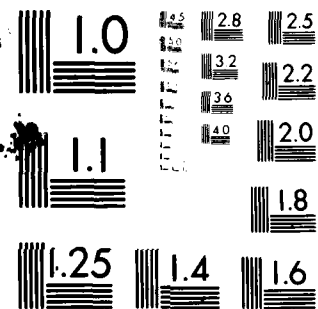
UNCLASSIFIED

NL

Fig 3

Fig 3





MICROCOPY RESOLUTION TEST CHART
NATIONAL BUREAU OF STANDARDS-1963-A

1

AGARD-AG-260

AGARD-AG-260

ADA111405

ADVISORY BOARD FOR AERONAUTICAL RESEARCH & DEVELOPMENT

AGARDograph No. 260

Spacecraft Pointing and Position Control

DTIC
ELECTE
S FEB 26 1982 D
A

This document has been approved
for public release and sale; its
distribution is unlimited.

FILE COPY

DISTRIBUTION AND AVAILABILITY
ON BACK COVER

82 02 26 098

NORTH ATLANTIC TREATY ORGANIZATION
ADVISORY GROUP FOR AEROSPACE RESEARCH AND DEVELOPMENT
(ORGANISATION DU TRAITE DE L'ATLANTIQUE NORD)

AGARDograph No.260
SPACECRAFT POINTING AND POSITION CONTROL

Edited by

P.Ph. van den Broek
Department of Aerospace Engineering
Delft University of Technology
Delft, The Netherlands

Co-editor

Dr S.Z.Szirmay
Guidance and Control Section
Jet Propulsion Laboratory
Pasadena, Cal., USA



Author	
Title	
Source	
Section/	
Availability Codes	
Ordering and/or	
Accession	

A

This AGARDograph was prepared at the request of the Guidance and Control Panel of AGARD.

THE MISSION OF AGARD

The mission of AGARD is to bring together the leading personalities of the NATO nations in the fields of science and technology relating to aerospace for the following purposes:

- Exchanging of scientific and technical information;
- Continuously stimulating advances in the aerospace sciences relevant to strengthening the common defence posture;
- Improving the co-operation among member nations in aerospace research and development;
- Providing scientific and technical advice and assistance to the North Atlantic Military Committee in the field of aerospace research and development;
- Rendering scientific and technical assistance, as requested, to other NATO bodies and to member nations in connection with research and development problems in the aerospace field;
- Providing assistance to member nations for the purpose of increasing their scientific and technical potential;
- Recommending effective ways for the member nations to use their research and development capabilities for the common benefit of the NATO community.

The highest authority within AGARD is the National Delegates Board consisting of officially appointed senior representatives from each member nation. The mission of AGARD is carried out through the Panels which are composed of experts appointed by the National Delegates, the Consultant and Exchange Programme and the Aerospace Applications Studies Programme. The results of AGARD work are reported to the member nations and the NATO Authorities through the AGARD series of publications of which this is one.

Participation in AGARD activities is by invitation only and is normally limited to citizens of the NATO nations.

The content of this publication has been reproduced directly from material supplied by AGARD or the authors.

Published November 1981

Copyright © AGARD 1981
All Rights Reserved

ISBN 92-835-1408-4



*Printed by Technical Editing and Reproduction Ltd
Harford House, 7-9 Charlotte St, London, W1P 1HD*

PREFACE

The missions of most application satellites require that the payload is pointed to the earth during the satellites active lifetime. In many cases also the position of the satellite in its orbit has to be maintained within given limits. The pointing of the payload and the position control of spacecraft are the topics of the papers presented in this AGARDograph. The control problems will become more complex for large spacecraft to be launched in the coming decades, due to the flexibility of the structure. This subject is also discussed in this AGARDograph.

This publication has been divided into three parts; the first one deals with attitude and pointing control.

Attitude control has been applied to spacecraft in some form since the first satellites were placed in orbit. Most satellites carried a payload that required a prescribed orientation and as the payload was fixed to the satellite structure, the orientation of the entire satellite had to be controlled somehow.

Initially passive attitude stabilization was applied. Such stabilization methods use natural torques acting on the satellite, such as magnetic or gravitational torques or inertial effects, to maintain the satellite's orientation. From these spin stabilization has been applied very frequently. If a satellite rotates about its principal axis with the largest moment of inertia, this axis maintains its orientation in inertial space due to the gyroscopic stiffness. Advantages of this type of stabilization are its relative simplicity and its reliability; a disadvantage is the impossibility to change the attitude at will.

Somewhat later active attitude control systems were applied, consisting of attitude sensors, controllers and actuators. Due to the mechanical and electronic components in the system it is less reliable than a passive system, at least in the sense that its lifetime is limited, but it offers the possibility of very high pointing accuracy. Different forms of active attitude control have been applied in scientific satellites. The experiments carried by such satellites require in general a high pointing accuracy but the required active lifetime may be relatively short, in the order of one year.

Application satellites such as communication, and meteorological satellites, require both a relatively high pointing accuracy and a long active lifetime, in the order of 5 to 10 years. The same demands are posed by the payload on board of interplanetary spacecraft, in particular those launched for the exploration of the outer planets. A system that meets these requirements is a combination of a passive stabilization system, viz. spin stabilization, and an active control loop, realized in satellites using momentum wheels and dual spin spacecraft.

In case of attitude control using a momentum wheel the satellite structure is kept in a fixed orientation using the gyroscopic stiffness of a relatively small fast spinning momentum wheel. This type of control is particularly suitable for communication satellites equipped with large solar panels. These panels have to be directed to the sun so that the satellite has to be stabilized about all three axes. Paper 1 of this AGARDograph deals with various aspects of momentum wheels.

The lifetime of such a satellite may be limited due to wear off of the bearings of the momentum wheel. This effect may be eliminated by application of bearings without mechanical contact. An example of such a bearing is a magnetic bearing. However, as such bearings are more elastic than conventional ball bearings, some unwanted relative motion between the wheel and the satellite may be possible. Problems associated with this phenomenon are discussed in paper 2.

In case of dual spin stabilization the main structure of the satellite is rotating, just like a simple spin stabilized satellite. Only a small part of the satellite, the platform carrying the optical observation equipment or a communication antenna is kept stationary. The satellite is rotating at a relatively low speed so that bearing problems are reduced, whereas a large attitude stability is obtained due to the large moment of inertia of the rotating body. Paper 3 deals with the determination of the attitude of an interplanetary spacecraft from observations made by star sensors mounted on the rotating part of such a spacecraft.

Thus far it has been assumed that the payload is rigidly connected to the spacecraft or to an attitude stabilized platform, so that the pointing requirements for the payload determines the pointing requirements for the entire spacecraft. The requirements for the attitude stabilization of the spacecraft may be eased if the payload is mounted to the main structure, such that some controlled relative motion is possible. In that case the payload, such as an antenna of a communication satellite, may be pointed independently from the attitude stabilization of the main satellite. Such antenna control may also be used if two or more antennae on one satellite are to be pointed to different parts of the earth surface. A device for this type of control is described in paper 4.

The second part of this AGARDograph deals with topics on determination and control of the position of a spacecraft.

Orbit determination has always been an important subject in the exploration and the exploitation of space. Usually a spacecraft is not continuously in view of a ground station, so that communication with the spacecraft is limited to relatively short periods of time. To make full use of these periods it is necessary to predict the time at which a satellite will pass over a groundstation, and this requires knowledge about the orbit of the spacecraft. For many satellites a relation exists between the orbit and the mission. If the satellite's mission is to observe certain celestial radiation sources such observations can only be made when the source is not obscured by the earth. If the satellite is not in contact with a groundstation, the experiments have to be preprogrammed and this requires also knowledge about the satellite's orbit. The accuracy of the orbital parameters needed in the given examples is relatively modest. If satellites are used for navigational purposes on the earth surface, e.g. for the position determination of ships or aircraft, the accuracy requirements are considerably higher. In the past satellites have been used in this way, yielding position fixes with an accuracy of the order of one thousandmeters. However, in the next decade

the Global Position System GPS-NAVSTAR will become operational, providing fixes with an accuracy of the order of ten meters in three dimensions. To enable this accuracy the orbits of the satellites concerned have to be very well defined. A procedure that may be used for such an orbit determination is presented in paper 5.

For many satellite missions it is sufficient to determine the position of a spacecraft at certain instances of time, without the necessity to control or to correct the position. However, for an important class of application satellites, e.g. communication satellites and some meteorological satellites, it is necessary that the satellite maintains a fixed position with respect to the earth. Such a fixed position may be obtained by inserting the satellite in a circular equatorial orbit at such an altitude, that the orbital period is equal to the revolution time of the earth. However, even if the satellite has been inserted in a perfect geostationary orbit initially, this orbit will not be maintained over a longer period of time. Due to disturbing effects, caused by the sun and the moon the orbit will not be maintained over a longer period of time. Due to disturbing effects, caused by the sun and the moon the orbit tends to be tilted with respect to the equatorial plane, and due to non-homogeneity of the earth gravitational field the satellite will tend to drift in its orbital plane. These effects and the velocity changes necessary to maintain the satellite's position are discussed in paper 6.

The disturbing effects on the orbit of geostationary satellite are relatively weak and the required accuracy of the satellite's position is still so modest, that the orbital corrections may be applied at relatively large time intervals. The position of the spacecraft is monitored by a groundstation and when the deviation reaches some given value, an orbit correction is performed under control of the groundstation. However, when the required station keeping accuracy increases, the time interval between the corrections may become relatively short, resulting in an increased workload for the groundstation. Then it may be worthwhile to equip the satellite itself with an on-board station keeping system. Such a system is described in paper 7.

Thus far the orbit control has been discussed separately from the attitude control. However, in a communication satellite both the orbit and the attitude have to be controlled, be it, that attitude control is a continuously ongoing activity, and orbit control is performed at separate time. In a satellite the electronics for both control activities are usually combined. An example of the hardware for an attitude and orbit control system for a communication satellite is described in paper 8. In autonomous station keeping the position of the spacecraft may be determined from angle measurements to the earth, the sun and preselected stars, whereas pointing the payload (e.g. the communication antenna) may be accomplished using a different set of sensors, such as horizon sensors, measuring the direction of the earth horizon. In contrast to this in paper 9 a procedure for attitude and orbit control is described in which for both control loops an integrated set of angle sensors is used.

The third part of this AGARDograph deals with effects of flexibility of large spacecraft on the pointing control. It is anticipated that in the coming decades large structures will be placed in orbit for communication, research, manufacturing and defense purposes. The dimensions of such spacecraft will be of the order of tens of meters or larger. Nevertheless the total mass will be limited to reduce the number of launches, needed to place the structure in orbit. Consequently large spacecraft will be very flexible and the resulting flexible modes may interfere with the attitude stabilization and control.

A larger spacecraft may be composed of a number of separate rigid bodies, that are connected by a more or less flexible structure. Such a modular structured spacecraft may be modeled using discrete masses connected by hinges. The control of such a space platform is discussed in paper 10. The performance of the attitude control system of such a platform may be affected by the flexible modes but the deformations of the structure need not affect the performance of the platform as such. The performance of other large space structures, such as a large space telescope or large antenna systems, depends very much on the deformations of the structure. Pointing control does not only include control of the attitude of the spacecraft, as a rigid body, but also the deformations of the structure may very well need to be kept within certain narrow limits. This type of spacecraft control is the subject of the next three papers. Paper 11 presents a survey of techniques, that may be applied for the dynamic control of large spacecraft.

Paper 12 gives a detailed discussion of the modeling of large spacecraft and the synthesis of the control system. The discussion is illustrated with an example, being the control of a complex optical spacecraft. In these papers a general approach to the control problem is given. In contrast to this, paper 13 deals with the application of a particular device for the attitude and structural mode control.

A powerful tool in spacecraft control system development is computer simulation. For this the dynamical properties of the spacecraft and the components of the control system are modeled into mathematical models and the motion of this model is computed using a digital computer. In such simulations the parameters in the equations of the control system may be changed easily, so that a flexible simulation setup is available. However, a drawback is that only known properties of the components can be modeled and ignored dynamical phenomena may impair the performance of an actual hardware system. Therefore simulations, which include hardware components of the spacecraft control system may provide very useful additional information. In the last paper of this AGARDograph problems, associated with the hardware simulation of control systems, both for rigid and for flexible spacecraft, are discussed.

The editor wishes to thank all authors for their efforts. Special recognition should go to Dr. Stephen Z. Szirmay of the Jet Propulsion Laboratory for his assistance in organizing the contributions from the United States. The assistance of the executive staff of the AGARD Guidance and Control Panel was a great help in the process of preparation of this publication.

Ir. Pieter Ph. van den Broek.

CONTENTS

	Page
PREFACE by P.Ph. van den Broek	iii
	Reference
 <u>PART 1 – ATTITUDE CONTROL AND INSTRUMENT POINTING</u>	
ATTITUDE CONTROL OF GEOSTATIONARY SATELLITES WITH DOUBLE GIMBALLED MOMENTUM WHEELS by G.Schulz and Th.Lange	1
ANALYSIS AND EXPERIMENTAL VERIFICATION OF THE NUTATION OF A SATELLITE EQUIPPED WITH MAGNETIC BEARING MOMENTUM WHEELS by C.Rouyer, G.Heimboldt and Th.Lange	2
AUTONOMOUS ATTITUDE DETERMINATION FROM STAR DATA FOR A DUAL-SPIN PLANETARY SPACECRAFT by E.C.Wong and J.Y.Lai	3
SOFA: SYSTEME D'ORIENTATION FINE D'ANTENNE by B.Hubert and P.Brunet	4
 <u>PART 2 – ORBIT DETERMINATION AND CONTROL</u>	
FACTORIZATION METHODS FOR PRECISION SATELLITE ORBIT DETERMINATION by G.J.Bierman, L.A.Campbell and W.A.Feess	5
GEOSTATIONARY COMMUNICATION SATELLITE CONTROL by L.Flook and J.J.Pocha	6
AUTONOMOUS STATION KEEPING OF GEOSTATIONARY SATELLITES by M.C.Eckstein and A.Leibold	7
DIGITAL ATTITUDE AND ORBIT CONTROL ELECTRONICS FOR LONG-LIFE COMMUNICATION SATELLITES by M.Wlaka	8
INTEGRATED ORBIT/ATTITUDE DETERMINATION by A.D.Mikelson	9
 <u>PART 3 – FLEXIBLE SATELLITE CONTROL</u>	
A MULTILEVEL CONTROL APPROACH FOR A MODULAR STRUCTURED SPACE PLATFORM by F.D.Chichester and M.T.Borelli	10
DYNAMIC CONTROL OF LARGE SPACECRAFT – A SURVEY OF TECHNIQUES by R.C.Rogers and M.Burton	11
MODELING, CONTROL AND SYSTEM IDENTIFICATION METHODS FOR FLEXIBLE STRUCTURES by N.K.Gupta, M.G.Lyons, J-N.Aubrun and G.Margulies	12
CONTROL OF LARGE SPACE STRUCTURES USING ANNULAR MOMENTUM CONTROL DEVICES (AMCD's) by S.M.Joshi	13
MODERN SIMULATION TECHNIQUES IN SPACECRAFT DYNAMICS by R.Stapf, G.Heimbold and J.Puls	14

ATTITUDE CONTROL OF GEOSTATIONARY SATELLITES WITH DOUBLE GIMBALED MOMENTUM WHEELS

by

G. Schulz, Th. Lange
Deutsche Forschungs- und Versuchsanstalt für
Luft- und Raumfahrt e.V., 8031 Oberpfaffenhofen, F.R.G.

SUMMARY

Conventional control methods are generalized using state vector feedback design procedures. Alternatively, a decoupled control method using a nondiagonal inertia tensor is derived. These are confronted to modern control theory design methods with observer, where especially the insensitivity with respect to variations of the moments of inertia is demonstrated.

SYMBOLS

r, i	: indices for reference, inertial coordinate system
\vec{M}	: torque vector
\vec{H}	: angular momentum vector
$\vec{\omega}$: angular rate vector
ω_0	: earth rate
ω_N	: nutation angular rate
φ, θ, ψ	: satellite angles with respect to reference system
γ_x, γ_z	: gimbal angles about x, z axis
I_x, I_z	: moment of inertia about x, z axis
I_{xz}	: product of inertia with respect to roll/yaw

1. INTRODUCTION

In future attitude control of geostationary satellites will be performed more and more by flywheels. The main advantage is that they allow for storing a large momentum and thus, without any control, only due to the gyroscopic effect, cause a high attitude stability. Contrary to spin stabilization in which, on principle, the same effect is present, here the satellite is continuously directed towards the earth so that no despin of the antenna is necessary. Apart from a high reliability, the flywheels at disposal nowadays have the property of exerting very precisely quantized actuator torques. This is necessary in order to keep the required high accuracy of positioning. For communication satellites it is approx. 0.1° in the roll and pitch axis, and 0.5° in the yaw axis (line of sight satellite - center of earth). This accuracy results from the fact that instead of one single antenna covering the whole range, today there is preferred a system of several antennae with small beams, however with a high degree of efficiency (antenna gain). Due to this tendency, for the future, the accuracy to be required will rise by the factor of two to three.

There are many possibilities how to use flywheels for the attitude control of satellites [1]. The gimbaled flywheel is particularly suitable for geostationary satellites. It has a high nominal momentum in the range of 20 to 100 Nms, which can be varied by approx. $\pm 10\%$ for exerting actuator torques. The flywheel axis is nominally aligned to the pitch axis of the satellite in order to keep it inertially fixed parallel to the orbit normal. In an earth-oriented satellite the roll and yaw axis, are rotating with orbit rate with respect to the inertial system. This fact and the gyroscopic stiffness already mentioned allow for detecting yaw angle errors largely from the roll angle measurement. Thus in the open loop case, an initial yaw error after $1/4$ of orbit rotation (= 6 hours) appears as a roll error. Practically, this is of particular importance, as those sensors that might furnish a continuous yaw information such as star sensors e.g., do not meet the requirements for reliability and cost of application satellites.

Gimballing of the flywheel offers the possibility of total momentum exchange between satellite and flywheel and thus controlling the roll/yaw motion of the satellite. Thus it is possible to control the attitude in all three axes, as long as the maximum gimbal angle and speed range of the flywheel is not exceeded. In this case the operating condition has to be restored in a so-called momentum desaturation maneuver, without changing the attitude of the satellite when doing so. This requires a balancing of the satellite by means of external torques, as for example by thruster pulses. It is only natural that thus the control system becomes more complicated, if the flywheel is gimbaled. But the efficient on-board computers available today enable sufficient reliability of the whole system. The development of fine-resolving stepper motors for the gimbal actuator, furthermore, allows a simple and effective steering by the computer. The known methods can be used for the controller design as the behaviour of the satellite with flywheel, at least during normal operation mode in consideration here, can be described by means of linearized equations. In this report now the methods already known through the respective litera-

ture will be compared to alternative solutions which have been found out, partly, by means of the modern control theory. This will, however, not be treated exhaustively, since here the satellite is assumed to be a rigid body. The results shown in the following might, however, serve as a preliminary study for investigating the control problem of a satellite with flexible appendages.

2. MOTION OF A GEOSTATIONARY SATELLITE WITH GIMBALED FLYWHEEL ("DOUBLE GIMBALED MOMENTUM WHEEL")

2.1 LINEARIZED EQUATIONS OF MOTION

As already mentioned, a geostationary satellite has to be aligned with respect to an orbit reference system. The relative orientation of the coordinate systems is shown in Fig. 2.1.

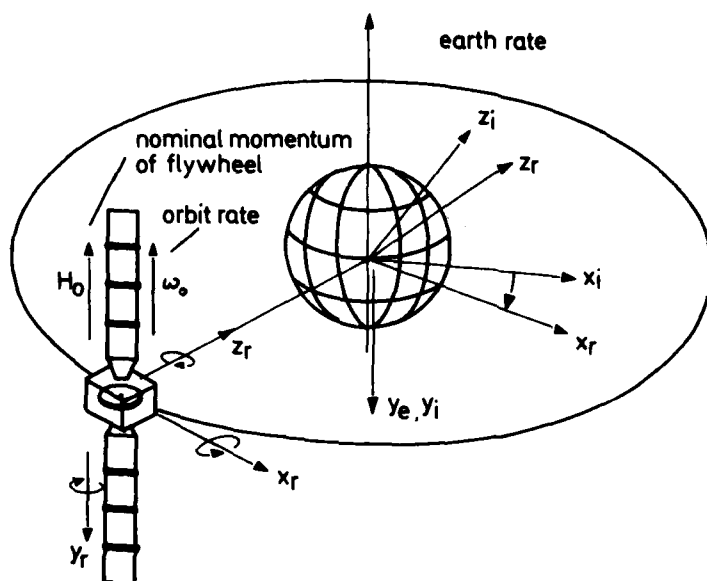


Fig. 2.1 Coordinate System for Geostationary Satellites.

The index i denotes the inertial reference system, from which follows the orbit reference system (index r) by means of a rotation about the y_i -axis with the orbit rate ω_0 . The satellite reference system is then achieved by a small angle rotation, denoted by ϕ and ψ .

The equation of motion of the satellite with a flywheel follows from the law of conservation of momentum. In the orbit reference coordinate system it computes as:

$$(2.1) \quad \dot{\mathbf{H}}_r = \frac{d}{dt} (\mathbf{H}_r) + \boldsymbol{\omega}_{i,r} \times \mathbf{H}_r$$

where

$\boldsymbol{\omega}_{i,r}$ = angular velocity vector of the reference system with respect to the inertial system

\mathbf{H}_r = momentum vector, given in the reference system

\mathbf{M}_r = vector of the external torque, again in the coordinates of the reference system.

The total momentum is composed of that of the satellite itself and that of the flywheel. Taking into consideration that the flywheel with respect to the satellite can be deflected by the gimbal angles γ_x in the roll and γ_z in the yaw axis, and that the satellite attitude in the reference system, in general, is described by the attitude angles ϕ , θ , ψ , the momentum vector in notation of components is:

$$(2.2) \quad \begin{aligned} H_{rx} &= I_x \dot{\phi} + (\psi + \gamma_z)H \\ H_{ry} &= I_y (\dot{\theta} - \omega_0) - H \\ H_{rz} &= I_z \dot{\psi} - (\phi + \gamma_x)H \end{aligned}$$

where I_x , I_y , I_z denote principle moments of inertia of the satellite.

For simplicity it has been assumed that the principal axes of the satellite coincide with the satellite reference coordinate system. Furthermore, second order terms were neglected. According to Fig. 2.1 the following is valid for the angular momentum vector:

$$(2.3) \quad \vec{d}_{i,r} = \begin{bmatrix} 0 \\ -\omega_0 \\ 0 \end{bmatrix}$$

Thus, by inserting the equations 2.2 and 2.3 into the equation 2.1, neglecting again second order terms, we get:

$$(2.4) \quad \begin{aligned} M_{rx} &= I_x \ddot{\phi} + H(\dot{\psi} + \dot{\gamma}_z) + \omega_0 H (\phi + \gamma_x) \\ M_{ry} &= I_y \ddot{\theta} - \dot{H} \\ M_{rz} &= I_z \ddot{\psi} - H(\dot{\phi} + \dot{\gamma}_x) + \omega_0 H (\psi + \gamma_z) \end{aligned}$$

As large deviations of the flywheel angular momentum H from its nominal value are not allowed, the second equation of the equation system 2.4 which describes the pitch motion of the satellite, can be regarded as decoupled from the other two. However, controlling of this subsystem does not cause any problems and will not be treated any further in the following.

2.2 PHYSICAL INTERPRETATION OF THE CONTROL PROBLEM

In order to examine the eigenfrequencies, the reduced equation system 2.4 shall be subjected, first of all, to a Laplace-transformation:

$$(2.5) \quad \begin{bmatrix} M_x \\ M_z \end{bmatrix} = \begin{bmatrix} I_x s^2 + \omega_0 H & H \cdot s \\ -H \cdot s & I_z s^2 + \omega_0 H \end{bmatrix} \begin{bmatrix} \phi \\ \psi \end{bmatrix} + \begin{bmatrix} \omega_0 H & H \cdot s \\ -H \cdot s & \omega_0 H \end{bmatrix} \begin{bmatrix} \gamma_x \\ \gamma_z \end{bmatrix}$$

The characteristic equation for this system is:

$$(2.6) \quad s^4 + s^2 \left(\frac{H^2}{I_x \cdot I_z} + \omega_0 H \frac{I_x + I_z}{I_x \cdot I_z} \right) + \frac{(\omega_0 H)^2}{I_x \cdot I_z} = 0$$

For geostationary satellites the orbit frequency is equal to the earth rate and thus essentially smaller than the nutation frequency of the satellite. Under this condition we get just these two frequencies for the solution of the characteristic equation:

$$s_{1,2} = \pm j \frac{H}{\sqrt{I_x I_z}} ; s_{3,4} \approx \pm j \omega_0$$

Thus the system according to equation 2.5 can be split in a short term - and a long term portion. In normalized form it can be described as follows:

$$(2.7) \quad \begin{bmatrix} M_x^* \\ M_z^* \end{bmatrix} = \begin{bmatrix} 1 & \frac{s}{\omega_0} \\ \frac{-s}{\omega_0} & 1 \end{bmatrix} \left\{ \begin{bmatrix} 1 & \frac{-s}{\omega_3} \\ \frac{s}{\omega_1} & 1 \end{bmatrix} \begin{bmatrix} \phi \\ \psi \end{bmatrix} + \begin{bmatrix} \gamma_x \\ \gamma_z \end{bmatrix} \right\}$$

where

$$\begin{aligned} \omega_1 &= \frac{H}{I_x} & M_x^* &= \frac{M_x}{\omega_0 H} \\ \omega_3 &= \frac{H}{I_z} & M_z^* &= \frac{M_z}{\omega_0 H} \end{aligned}$$

This can be visualized in a very simple block diagram (Fig. 2.2).

It can be realized that by means of the gimbal angles γ_x and γ_z , at most, the nutation motion can be damped, which is characterized by the frequencies ω_1^2 , ω_3^2 , i.e. by the nutation frequency $\omega_n = \sqrt{\omega_1^2 + \omega_3^2}$. On the other hand, a motion stimulated by the orbit frequency ω_0 in principle is preserved. However, there can be found a control law for the gimbal angles γ_x , γ_z in such a way that the satellite angles ϕ and ψ always remain zero. This is obviously only possible if they are controlled by means of the undamped oscillation of the frequency ω_0 .

From the physical point of view this is easy to see, because according to the law of conservation of momentum the total angular momentum of the system can only be changed by external torques. A change of the gimbal angles can, however, only influence the distribution of the momentum portions on each subassembly. In this sense, the satellite is a

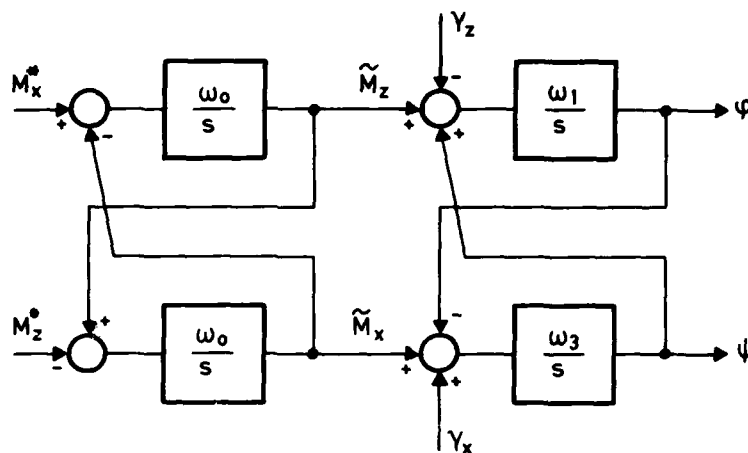


Fig. 2.2 Block Diagram for the State Vector Representation of the System Satellite + Double Gimbaled Momentum Wheel.

subassembly from which the angular momentum caused by external torques has to be removed. Due to the control of the gimbals already mentioned, it completely passes into the flywheel which is to be regarded as the second subassembly.

The behaviour of the system and thus the controller design is essentially determined by the kind of the external torques M_x^* , M_z^* resp. Even if no torques are present, a stimulation with frequency ω_0 according to Fig. 2.2 can occur and that because of the initial conditions. These are not zero, if the momentum vector does not coincide with the orbit normal. In consequence of the kinematic coupling through the orbit rate, the momentum vector traces a cone in the orbit-fixed reference system, the symmetry axis of which coincides with the orbit normal. Fig. 2.3 shows a projection of a point fixed to the momentum vector onto the orbit plane. Thus a misalignment of the momentum vector here appears as a circle about the origin. The angular denominations ϕ , ψ , put in brackets, signify a deflection of the momentum vector with respect to its nominal alignment parallel to the orbit normal.

If an external torque acts on the satellite, the motion of the momentum vector can be found out from equation 2.7, if the nutation dynamics are eliminated (long term behaviour):

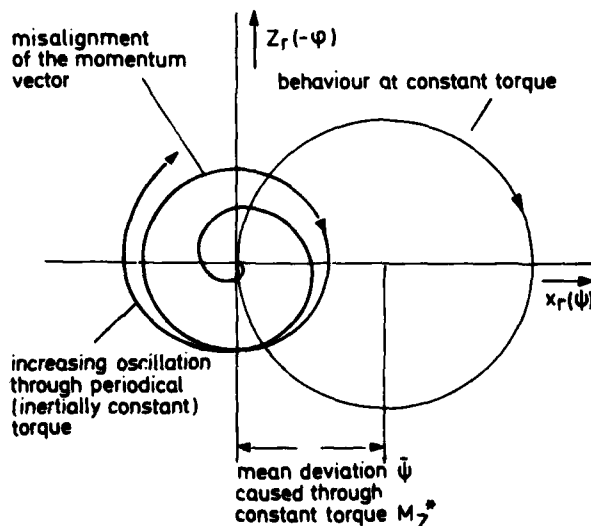


Fig. 2.3 Motion of the Momentum Vector at External Torques, shown as Projection in the Orbit Plane.

$$(2.8) \quad \begin{bmatrix} M_x^* \\ M_z^* \end{bmatrix} = \begin{bmatrix} 1 & \frac{s}{\omega_0} \\ -\frac{s}{\omega_0} & 1 \end{bmatrix} \begin{bmatrix} \phi \\ \psi \end{bmatrix}$$

If this torque referred to the reference system is constant, there is again obtained a circle, the centre of which is shifted with respect to the origin by the amount of M_z^* . In the representation of Fig. 2.3, the nominal alignment was taken as initial condition for this case. For a component M_z^* a mean deviation $\bar{\psi}_r$ is obtained which can be found out from equation 2.4 by cancelling the derivatives with respect to time.

$$(2.9) \quad \bar{\psi}_r = \frac{M_z}{\omega_0 H} = M_z^*$$

This portion can obviously not be observed for the attitude control without yaw angle determination. Because from equation 2.4 follows, too, that only the yaw angular rate is coupled into the roll motion from which the yaw motion has to be estimated. The error $\bar{\psi}_r$ thus can only be kept within boundaries by the proper choice of the nominal momentum H . Then, however, it is possible to counteract the effect of constant torques only by an exchange of momentum over a gimbal angle control without having to initiate a momentum desaturation maneuver.

This is different for the inertially constant torques. They are coming about through the influence of the solar pressure upon the solar panels of the satellite and they represent the largest part of the disturbance torque. Inertially, they produce a constant precession of the momentum vector which appears in the orbit-fixed reference system as an increasing coning motion. The same result is obtained from equation 2.8, if it is taken into consideration that the inertially constant torque in the reference system appears as a torque being periodic with the orbit frequency. This acts on an undamped system being tuned to the same frequency resulting in an unstable behaviour. This fact requires a momentum desaturation at regular intervals, that is always in that case, when the gimbals have reached their maximum deflection.

The starting point for these considerations was, that the short-period nutation motion of the satellite is damped, so that only the long-period oscillations are present. The satellite thus is controlled, i.e. the "subassembly" satellite is free of momentum, whereas the "subassembly" flywheel possesses the total momentum. Therefore here the direction of the momentum vector can be equated with that of the flywheel axis, whereas the pitch axis of the satellite remains inertially fixed parallel to the orbit normal.

For the description of the nutation motion and thus the behaviour of the uncontrolled satellite, we consider the system response after a pulse stimulation caused by an external torque, as for example a thruster pulse. Independent on the fact whether the system is controlled or not, the momentum vector has to precess during the pulse duration according to Fig. 2.3, and that, on principle, on a circle as it is a torque being constant in the reference system. At a short pulse duration, the pertinent short arc of a circle can be approximated by a straight line. Now, of course, the momentum axis does no longer coincide with the flywheel axis. On the contrary, it performs a nutation motion. If this is essentially slower than the pulse it can be described as a circular motion which only begins after the ending of the pulse. The radius of the circle follows from the additional momentum which comes about through the torque pulse. This fact is illustrated in Fig. 2.4 in the state vector representation.

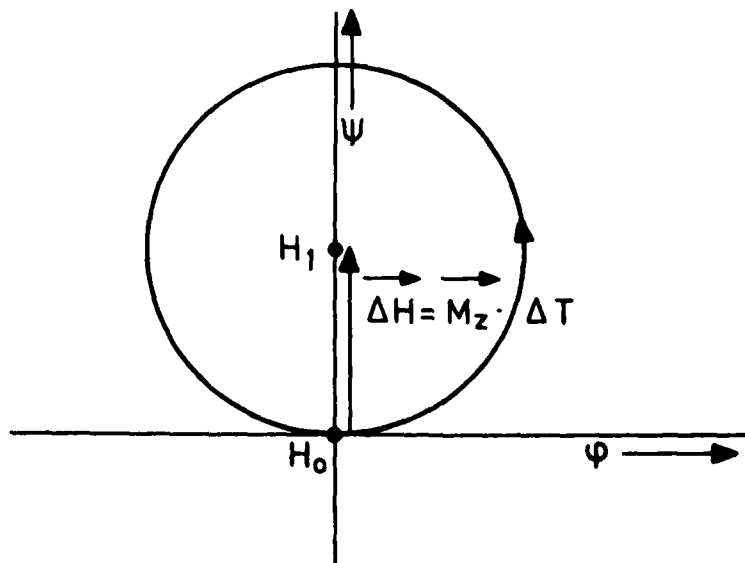


Fig. 2.4 Behaviour of the System after an External Torque Pulse.

Another nutation motion arises when stimulating the system by an internal torque, as for example after deflection of a gimbal angle by an angular increment ΔY through the stepper motor. Although the angular change does not happen infinitely fast, this may be presumed approximately, because of the large inertia of the total system. Hence follows that in the first instant only the flywheel- (spin-) axis having a common initial attitude with the satellite pitch axis and the momentum axis can move. As an internal torque is concerned, the total momentum vector remains inertially fixed. After completion of the gimbal step, satellite and flywheel are again rigidly connected with one another. They perform a common nutation motion in which the cone produced by the flywheel axis has as symmetry axis the total momentum vector, as the momentum component of the subassembly satellite in y-direction is negligible as against that of the subassembly flywheel.

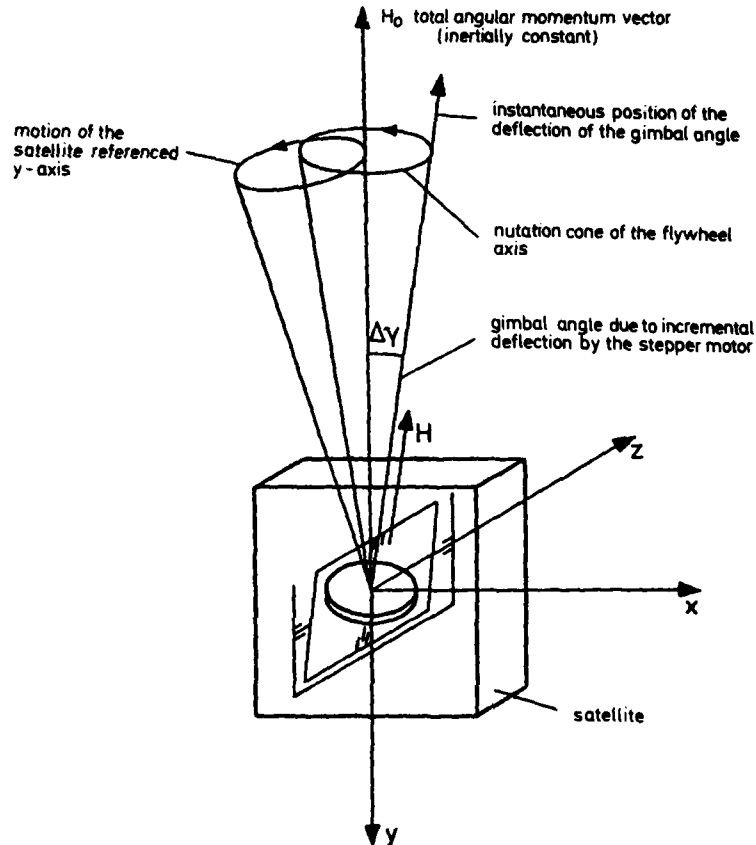


Fig. 2.5 Behaviour of the Satellite after Incremental Deflection of the Gimbal Angle by the Stepper Motor.

3. REQUIREMENTS WITH RESPECT TO THE CONTROL SYSTEM

Dependent on the respective mission, the special demands on the control system are, of course, very different. There are, however, some common points of view being valid for all systems. Thus, as already mentioned, operating without yaw angle measuring shall on principle be possible, generally during the largest part of the mission. If, however, maneuvers shall be performed such as e.g. the momentum - or gimbal angle desaturation, then - because of the disturbances arising - the execution will be timed until a yaw reference e.g. through solar sensors will be available.

By way of contrast, we start in this report, on principle, from a lacking of a yaw reference even in critical maneuvers. The execution can take place at any time and can be optimized according to the respective demands.

In this context there are higher demands for the controller with regard to its disturbance behaviour; but it must also be designed to a sufficient command control behaviour. In this case the disturbance behaviour i.e. the insensitivity of the orientation of the satellite with respect to external disturbance torques, remains the decisive criterion.

We can distinguish here between short term - and long term disturbance. Long term disturbances are caused by external torques and that above all by the solar pressure affecting the solar panels. The effect of this disturbance torque on the satellite has already been discussed at length. It leads to a momentum desaturation having to take place at regular intervals. By choosing the nominal momentum and the gimbal angular range, a trade-off has to be found determining the time interval in such a way that the mean attitude accuracy is not inadmissibly affected by too frequent desaturation maneuvers. Contrary to the quasi-stationary long term disturbances, short term disturbances have as

a result a dynamic transient behaviour of the system. They can be brought about by meteor impacts or by thruster control pulses as they are e.g. required for the gimbal angle desaturation. The shifting of the solar generator also brings about pulsed disturbances, because this happens by means of stepper motors. This torque, however, affects in the first place the pitch axis, the control of which is not so much of interest here. Apart from minimizing the control error amplitude, also short damping time constants shall be obtained. For communication satellites with a moment of inertia in the range of 1000 kgm^2 this means a time constant of approx. 20 - 30 seconds. But this only refers to the roll angle. The yaw angle is less critical as long as it is equivalent approximately to a rotation about the antenna beam axis. This is an essential precondition for the fact that it is possible to get along without yaw reference. Because after damping of the nutation a yaw angle error only appears over the weak kinematic coupling with the orbit rate in the roll angle, which in the open loop case leads to the exchange of errors already described, after $1/4$ of the orbit rotation. A fast yaw angle control thus would result in a very large gain factor. This is, however, avoided in most cases because of the high disturbance sensitivity involved.

During normal operation usually certain attitude maneuvers have to be performed requiring a respective command control behaviour. This is e.g. necessary in regular intervals for the calibration of the antennae of TV-Sat [2]. Similarly, the same is valid here, that has been said with regard to the dynamic transient behaviour at short term disturbances. However, in these maneuvers very large amplitudes of the yaw angle are possible, if the maneuvers are performed without yaw information at all. The same applies to the external torques by thruster pulses. In order to avoid this effect, coupling of the roll and yaw motion should be as small as possible.

Apart from these design criteria for the controller derived from the mission requirements, there is another point of view to be taken into consideration. It was already mentioned at the beginning that on-board computers will be used more and more in future, because of the complex structure of the controller. In this case a direct digital control system might be advantageous. The application of such procedures to a attitude control system with a Double Gimballed Momentum Wheel has already been studied in one case [3]. It is above all of advantage if sampling time plays a decisive roll for the system dynamics, but also if amplitude quantization decisively influences the behaviour as it happens e.g. by the finite step width of the gimbal stepper motors. There are however stepper motors today, the step width of which comes to only some per cent of the required attitude accuracy of the satellite (e.g. 10 arc sec at $\pm 0.1^\circ$), so that a step sequence can be regarded as a continuous gimbal angle rate. To what extent the choice of the sampling time becomes critical depends, of course, on the system dynamics. If it is essentially determined by the rigid body motion, there will hardly be any difficulties in this respect. Therefore and because of better possibilities for comparison in this report only continuous design procedures will be treated.

4. COMPARISON OF DIFFERENT CONTROL PRINCIPLES

In this part different principles of stabilization by a gimballed flywheel shall be studied. In doing so, in each case we consider the disturbance behaviour at normal operation.

Starting from the equations of motion developed in section 2.1, according to the Laplace-transformed equation 2.5, the following block diagram (Fig. 4.1) can be given for the roll/yaw dynamics decoupled from pitch.

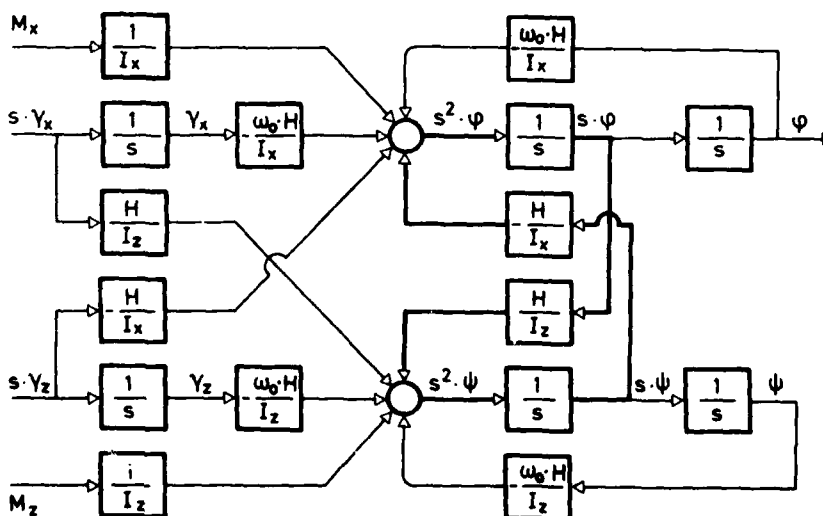


Fig. 4.1 Block diagram roll/yaw loop.

It is favourable for the design of the controller if the system dynamics have minimum order. This is achieved by means of the principle of internal reaction torques between mechanical subassemblies. In this case, the terms dependent on the gimbal angles and their velocities are combined to internal torques, which act as control torques on the satellite.

For demonstration, equation 2.4 first will be shown in vector notation:

$$(4.1) \quad I \begin{bmatrix} \ddot{\phi} \\ \ddot{\psi} \end{bmatrix} + D \begin{bmatrix} \dot{\phi} \\ \dot{\psi} \end{bmatrix} + \omega_o H \begin{bmatrix} \phi \\ \psi \end{bmatrix} + D \begin{bmatrix} \dot{y}_x \\ \dot{y}_z \end{bmatrix} + \omega_o H \begin{bmatrix} y_x \\ y_z \end{bmatrix} = \begin{bmatrix} M_x \\ M_z \end{bmatrix}$$

Here, the following letters are standing for:

$$I = \begin{bmatrix} I_x & 0 \\ 0 & I_z \end{bmatrix} \quad \text{inertia tensor}$$

$$D = \begin{bmatrix} 0 & H \\ -H & 0 \end{bmatrix} \quad \text{gyroscopic coupling matrix}$$

The control torques M_R follow from the actuator dynamics implicitly contained in equation (4.1).

$$(4.2) \quad D \begin{bmatrix} \dot{y}_x \\ \dot{y}_z \end{bmatrix} + \omega_o H \begin{bmatrix} y_x \\ y_z \end{bmatrix} = - \begin{bmatrix} M_{Rx} \\ M_{Rz} \end{bmatrix}$$

Hence, the design for the control torques can be performed in order to get from equation 4.2 the control law for the gimbal angles. The feedback law for the control torques be described by the following equation:

$$(4.3) \quad \begin{bmatrix} M_{Rx} \\ M_{Rz} \end{bmatrix} = K_M \begin{bmatrix} \dot{\phi} \\ \dot{\psi} \\ \phi \\ \psi \end{bmatrix}$$

The desired control law for the gimbal angles has the form:

$$(4.4) \quad \begin{bmatrix} \dot{y}_x \\ \dot{y}_z \end{bmatrix} = K_{R1} \begin{bmatrix} \dot{\phi} \\ \dot{\psi} \\ \phi \\ \psi \end{bmatrix} + K_{R2} \begin{bmatrix} y_x \\ y_z \end{bmatrix}$$

By inserting equation 4.3 and 4.4 into equation 4.2 the following relation is obtained.

$$(4.5) \quad \begin{aligned} K_{R1} &= -D^{-1} K_M \\ K_{R2} &= -D^{-1} \omega_o H = \begin{bmatrix} 0 & \omega_o \\ -\omega_o & 0 \end{bmatrix} \end{aligned}$$

Thus the y -terms in equation 4.1 can be replaced by the control torques M_{Rx} , M_{Rz} further using them for derivation of the feedback matrix K_M , and then determine the feedback matrices K_{R1} , K_{R2} by means of equation 4.5. This reduction proves to be necessary for application of output vector feedback methods (see Section 4.3).

4.1 DISTURBANCE COMPENSATION BY MEANS OF FEEDBACK OF THE ROLL ANGLE AND ITS DERIVATION

The procedures described in the literature by Mork [4] as well as Lyons, Lebsock and Scott [5] utilize the widely apart eigenfrequencies of the satellite dynamics in such a way that by feedback of the roll angle and its derivation

$$(4.6) \quad M_{Rx} = K \phi + K \tau \dot{\phi}$$

they render the roll loop a fast eigendynamic. Hence is valid

$$(4.7) \quad I_x \ddot{\phi} + K \tau \dot{\phi} + K \phi \approx M_x - H \dot{\psi}$$

with the adjustable natural frequency

$$\omega_\phi = \sqrt{\frac{K}{I_x}} \quad (\approx 0.1 \text{ Rad/s resp. } T_\phi \approx 60s \text{ for } K = 10 I_x)$$

and the damping

$$\xi_\phi = \frac{\tau}{2} \sqrt{\frac{K}{I_x}}$$

The coupling disturbance through the yaw speed $\dot{\psi}$ is of minor importance insofar as the yaw loop is made essentially slower by appropriate feedbacks.

$$I_z \ddot{\psi} + k \dot{\psi} + \omega_o H \psi = \Sigma M$$

in which

$$\omega_\psi = \sqrt{\frac{\omega_o H}{I_z}} \quad (\approx 1.9 \cdot 10^{-3} \text{ Rad/s resp. } T_\psi \approx 55 \text{ min})$$

for $H = 50 \text{ Nms}$ and $I_z = 10^3 \text{ kgm}^2$)

Thus the roll/yaw loop is decoupled into a roll loop with *high eigendynamics* and a yaw loop with *low eigendynamics*. If it is intended to increase essentially the eigendynamics of the yaw loop as well, then roll- and yaw motion have to be regarded as coupled motions. If a general feedback is introduced

$$(4.8a) \quad M_{Rx} = k_{x0} \varphi + k_{x1} \dot{\varphi}$$

$$(4.8b) \quad M_{Rz} = k_{z0} \psi + k_{z1} \dot{\psi}$$

the result is the following characteristic equation

$$(4.9) \quad N(s) = (s^2 - \frac{k_{x1} \cdot s + k_{x0} - \omega_o H}{I_x}) (s^2 + \frac{\omega_o H}{I_z}) + \frac{s^2 H^2}{I_x I_z} + (\frac{k_{z0} + k_{z1} \cdot s}{I_x I_z}) s \cdot H$$

$$= s^4 - \frac{k_{x1}}{I_x} s^3 + (\frac{H^2}{I_x I_z} + \frac{k_{z1} H}{I_x I_z} - \frac{k_{x0} - \omega_o H}{I_x} + \frac{\omega_o H}{I_z}) s^2 + (\frac{k_{z0} H}{I_x I_z} - \frac{k_{z1} \omega_o H}{I_x I_z}) s - \frac{\omega_o H}{I_z} (\frac{k_{x0} - \omega_o H}{I_x})$$

The coefficients of the characteristic polynomial and thus the eigenvalues of the system can be prescribed arbitrarily, because each polynomial coefficient can be made dependent from a feedback coefficient k . Then the following is valid:

$$(4.10) \quad N(s) = s^4 + f_1(k_{x1}) s^3 + f_2(k_{z1}) s^2 + f_3(k_{z0}) s + f_4(k_{x0})$$

For a system with two conjugate complex eigenvalues

$$N(s) = (s^2 + 2\epsilon_1 \omega_1 s + \omega_1^2) (s^2 + 2\epsilon_2 \omega_2 s + \omega_2^2)$$

the feedback coefficients are determined as:

$$(4.11) \quad a) \quad k_{x1} = -2(\epsilon_1 \omega_1 + \epsilon_2 \omega_2) \cdot I_x$$

$$b) \quad k_{x0} = \{\omega_1^2 \omega_2^2 - \frac{\omega_o^2 H^2}{I_x I_z}\} \cdot \frac{I_x I_z}{\omega_o H}$$

$$c) \quad k_{z1} = \{\omega_1^2 + \omega_2^2 + 4\epsilon_1 \epsilon_2 \omega_1 \omega_2 + \frac{k_{x0} - \omega_o H}{I_x} - \frac{\omega_o H}{I_z} - \frac{H^2}{I_x I_z}\} \cdot \frac{I_x I_z}{H}$$

$$d) \quad k_{z0} = -\{2\omega_1^2 \epsilon_2 \omega_2 + \omega_2^2 \epsilon_1 \omega_1\} - \frac{k_{z1} \omega_o H}{I_x I_z} \cdot \frac{I_x I_z}{H}$$

The disturbance transfer functions of this controlled system in a general form reads as:

$$(4.12) \quad a) \quad \varphi(s) = \frac{1}{N(s)} \{ (s^2 + \frac{\omega_o H}{I_x}) \frac{M_x}{I_x} - s \frac{H}{I_x} \cdot \frac{M_z}{I_z} \}$$

$$b) \quad \psi(s) = \frac{1}{N(s)} \{ (\frac{k_{z0} + k_{z1} \cdot s}{I_z} + \frac{sH}{I_z}) \frac{M_x}{I_x} + (s^2 - \frac{k_{x1} \cdot s + k_{x0} - \omega_o H}{I_x}) \frac{M_z}{I_z} \}$$

The stationary deviations for a body-fixed constant disturbance torque have the following values:

$$(4.13a) \quad \varphi_{STAT} = \begin{cases} \frac{I_z}{I_x (\omega_o H - k_{x0})} \cdot M_x \\ 0 \cdot M_z \end{cases}$$

$$(4.13b) \quad \psi_{STAT} = \begin{cases} \frac{k_{z0}}{\omega_0 H (\omega_0 H - k_{x0})} \cdot M_x \\ \frac{M_z}{\omega_0 H} \end{cases}$$

Whereas the effect of the disturbance torque M_z on the stationary deviation of the roll angle is zero, the deviation of the yaw angle remains unaffected by the control, at $\psi_{STAT} = M_z / \omega_0 H$. However the deviations are influenced by the feedback because of a disturbance torque M_x . Whereas the roll angle deviation is almost proportional $\frac{1}{k_{x0}}$, the yaw error depends on the ratio k_{z0}/k_{x0} . Large numerical values of k_{x0} reduce the stationary angle errors of the satellite and at the same time increase the bandwidth of the system as is shown in equation 4.11b; because with good approximation $k_{x0} \sim \omega_1^2 \cdot \omega_2^2$.

For the example of a TV-Sat-size satellite [2] with aperiodic damping $E_1 = E_2 = 1$, a period time of $T_1 = T_2 = 5 \text{ min}$ ($\omega_1 = \omega_2 = 2.094 \cdot 10^{-2} \text{ Rad/s}$) was chosen. The result for

$$\begin{aligned} I_x &= 1117,26 \text{ kgm}^2 \\ I_z &= 1309,30 \text{ kgm}^2 \\ H &= 50 \text{ Nms} \end{aligned}$$

were the following feedback coefficients:

$$\begin{aligned} k_{x0} &= -77,32 & k_{z0} &= 2,14 \\ k_{x1} &= -187,25 & k_{z1} &= -1843,9 \end{aligned}$$

For discontinuous disturbance torques $M_x = 10^{-5} \text{ Nm}$ resp. $M_z = 10^{-5} \text{ Nm}$ the result was the transient behaviour shown in Fig. 4.2.

Whereas for a disturbance torque $M_x = 10^{-5} \text{ Nm}$ the stationary deviations remain below 5/1000 degree, due to the control feedback, the yaw angle error shows a value of 0,15 degree at a disturbance torque M_z of the same size. This deviation can only be reduced by a larger momentum of the Double Gimballed Momentum Wheel (see Section 2).

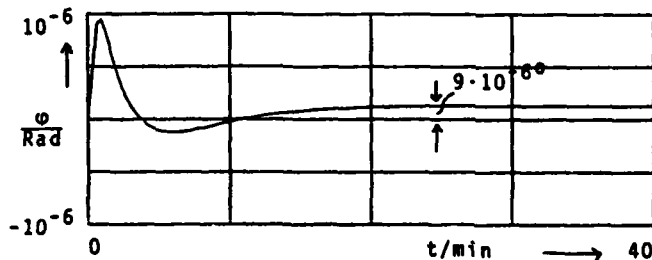


Fig. 4.2a Roll angle $\phi(t)$ for $M_x = 10^{-5} \text{ Nm}$.

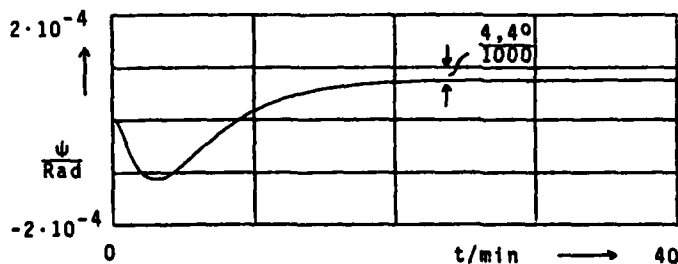


Fig. 4.2b Yaw angle $\psi(t)$ for $M_x = 10^{-5} \text{ Nm}$.

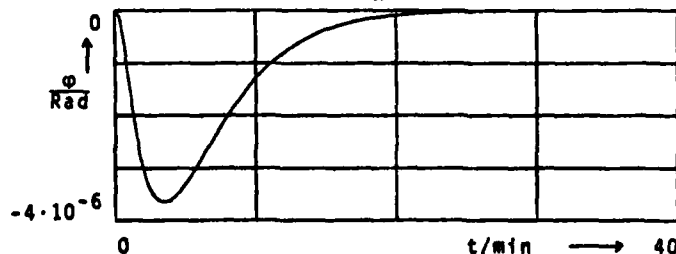


Fig. 4.2c Roll angle $\phi(t)$ for $M_z = 10^{-5} \text{ Nm}$.

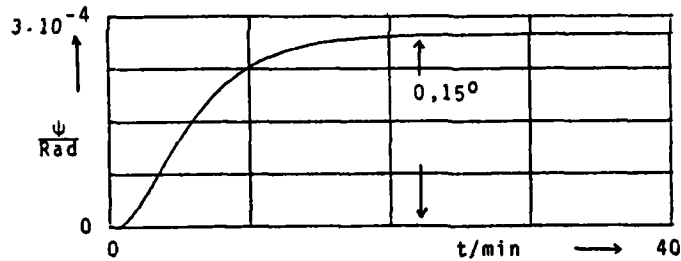


Fig. 4.2d Yaw angle $\psi(t)$ for $M_z = 10^{-5}$ Nm.

4.2 DECOUPLING OF THE YAW- FROM THE ROLL DYNAMICS AT NON-DIAGONAL INERTIA TENSOR

As already explained at length in section 3 it is desirable to keep coupling between the roll- and yaw motion at a minimum so that disturbances of the roll motion do not cause long-periodic yaw oscillations. If the satellite-fixed reference system is no more assumed being at the same time a principal axes system, as it is usual, then even a complete decoupling of the yaw dynamics is possible without impairing the stability through it.

Assuming a deflection of the principal axes system with respect to the reference system about the pitch axis yields a configuration according to Fig. 4.3.

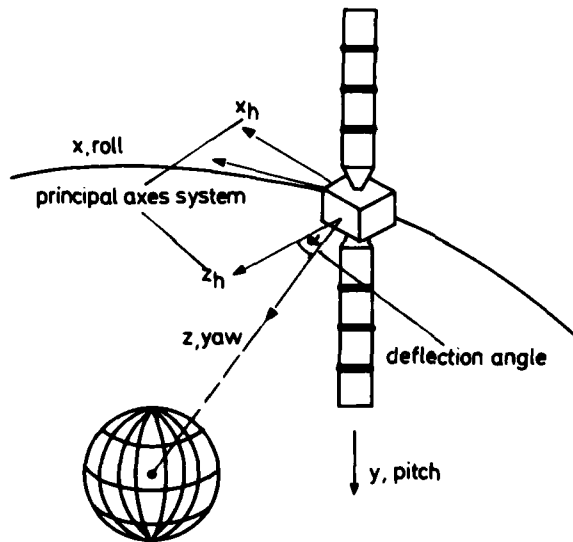


Fig. 4.3 Orientation of the Satellite at non-diagonal Inertia Tensor.

The reference system and thus the measurement- and flywheel gimbal axes, too, show hence a skewing angle with respect to the symmetry axis of the satellite. Thus additional dynamic couplings are introduced which have an effect on the gyroscopic angular rate terms and produce a damping effect, provided the sign of rotation is appropriate.

The equation of motion in matrix notation now reads:

$$(4.4) \quad \begin{bmatrix} \ddot{M}_x \\ \ddot{M}_z \end{bmatrix} = \begin{bmatrix} I_x & -I_{xz} \\ -I_{xz} & I_z \end{bmatrix} \cdot \begin{bmatrix} \ddot{\phi} \\ \ddot{\psi} \end{bmatrix} + \begin{bmatrix} 0 & H \\ -H & 0 \end{bmatrix} \cdot \begin{bmatrix} \dot{\phi} + \dot{\gamma}_x \\ \dot{\psi} + \dot{\gamma}_z \end{bmatrix} + \begin{bmatrix} \omega_o H & 0 \\ 0 & \omega_o H \end{bmatrix} \begin{bmatrix} \phi + \gamma_x \\ \psi + \gamma_z \end{bmatrix}$$

$$\underline{\ddot{M}} = \underline{I} \cdot \underline{\ddot{x}} + \underline{G}(\underline{\dot{x}} + \underline{\dot{\gamma}}) + \underline{P} \cdot (\underline{x} + \underline{\gamma})$$

where

\underline{I} = inertia tensor

\underline{G} = gyroscopic coupling matrix

\underline{P} = stiffness matrix due to the kinematic coupling by the orbit rate.

The vectors are defined as follows:

$$\underline{x} = \begin{bmatrix} \phi \\ \psi \end{bmatrix} \quad \text{state vector (roll-/yaw angle)}$$

$$\underline{y} = \begin{bmatrix} y_x \\ y_z \end{bmatrix} \quad \text{gimbal angle (roll-/yaw gimbal angle)}$$

Equation 4.14 is premultiplied by the inverse inertia tensor.

$$(4.15) \quad \ddot{\underline{x}} + I^{-1} [G \dot{\underline{x}} + P \underline{x} + G \dot{\underline{y}} + P \underline{y}] = I^{-1} \underline{M}$$

This reads in component notation:

$$(4.16a) \quad \ddot{\phi} - \frac{I_{xz}}{N} H \dot{\phi} + \frac{I_z}{N} \omega_o H \phi + \frac{I_z}{N} H \dot{\psi} + \frac{I_{xz}}{N} \omega_o H \psi - \frac{I_{xz}}{N} H \dot{y}_x + \frac{I_z}{N} \omega_o H y_x +$$

$$+ \frac{I_z}{N} H \dot{y}_z + \frac{I_{xz}}{N} \omega_o H y_z = \frac{I_z}{N} M_x + \frac{I_{xz}}{N} M_z$$

$$(4.16b) \quad \ddot{\psi} + \frac{I_{xz}}{N} H \dot{\psi} + \frac{I_x}{N} \omega_o H \psi - \frac{I_x}{N} H \dot{\phi} + \frac{I_{xz}}{N} \omega_o H \phi + \frac{I_{xz}}{N} H \dot{y}_z + \frac{I_x}{N} \omega_o H y_z -$$

$$- \frac{I_x}{N} H \dot{y}_x + \frac{I_{xz}}{N} \omega_o H y_x = \frac{I_{xz}}{N} M_x + \frac{I_x}{N} M_z$$

$$\text{with } N = \det(I) = I_x I_z - I_{xz}^2$$

In case of the product of inertia I_{xz} being positive, the result in the yaw equation is a positive damping term $\frac{I_{xz}}{N} H \dot{\psi}$. In the roll equation it is negative, but the desired dynamics can be easily set as the roll angle is measured. This and also the decoupling of the yaw dynamics is achieved by an appropriate control law for the gimbal angles. It is defined as follows:

$$(4.17) \quad I^{-1} [G \dot{\underline{x}} + P \underline{x} + G \dot{\underline{y}} + P \underline{y}] = D \dot{\underline{x}} + C \underline{x}$$

$$\text{with } D = \begin{bmatrix} d_{11} & d_{12} \\ d_{21} & d_{22} \end{bmatrix} \quad C = \begin{bmatrix} c_{11} & c_{12} \\ c_{21} & c_{22} \end{bmatrix}$$

Through the elements d_{11} , c_{11} the desired roll dynamics are determined:

$$d_{11} = K_1 = 2\zeta_r \omega_r \quad c_{11} = K_0 = \omega_r^2$$

Here ω_r determines the eigenfrequency of the roll loop and ζ_r the damping factor. Decoupling of the yaw motion from roll is accomplished by the following condition:

$$d_{21} = 0 \quad c_{21} = 0$$

The other terms describe the dependence of the system from the yaw angle and can thus not be influenced. They result from equation 4.16

$$d_{12} = \frac{I_z}{N} \cdot H \quad c_{12} = \frac{I_{xz}}{N} \cdot \omega_o H$$

$$d_{22} = \frac{I_{xz}}{N} \cdot H \quad c_{22} = \frac{I_x}{N} \cdot \omega_o H$$

The desired control law has, after solution of equation 4.17, the following form

$$(4.18) \quad G \cdot \dot{\underline{y}} + P \cdot \underline{y} = Q' \cdot \dot{\underline{x}} + Q \cdot \underline{x}$$

$$\text{with} \quad Q' = I D - G$$

$$Q = I C - P$$

After inserting the following relations are the result:

$$(4.19) \quad Q' = \begin{bmatrix} I_x & -I_{xz} \\ -I_{xz} & I_z \end{bmatrix} \cdot \begin{bmatrix} K_1 & \frac{I_{xz}}{N} H \\ 0 & \frac{I_{xz}}{N} \cdot H \end{bmatrix} - \begin{bmatrix} 0 & H \\ -H & 0 \end{bmatrix}$$

$$Q' = \begin{bmatrix} I_x \cdot K_1 & 0 \\ -K_1 I_{xz} + H & 0 \end{bmatrix}$$

$$(4.20) \quad Q = \begin{bmatrix} I_x & -I_{xz} \\ -I_{xz} & I_z \end{bmatrix} \cdot \begin{bmatrix} K_0 & \frac{I_{xz}}{N} \cdot \omega_o H \\ 0 & \frac{I_x}{N} \omega_o H \end{bmatrix} - \begin{bmatrix} \omega_o H & 0 \\ 0 & \omega_o H \end{bmatrix}$$

$$Q = \begin{bmatrix} I_x K_0 - \omega_o H & 0 \\ -I_{xz} K_0 & 0 \end{bmatrix}$$

This result is again inserted in equation 4.18 and yields the final form of the control law:

$$(4.21) \quad \underline{Y} = G^{-1} P \underline{Y} + G^{-1} Q' \dot{\underline{x}} + G^{-1} Q \underline{x}$$

$$\begin{bmatrix} \dot{Y}_x \\ \dot{Y}_z \end{bmatrix} = \begin{bmatrix} 0 & \omega_o \\ -\omega_o & 0 \end{bmatrix} \begin{bmatrix} Y_x \\ Y_z \end{bmatrix} + \begin{bmatrix} (\frac{K_1 I_{xz}}{H} - 1) & \frac{I_{xz} K_0}{H} \\ \frac{I_x K_1}{H} & (\frac{I_x K_0}{H} - \omega_o) \end{bmatrix} \begin{bmatrix} \dot{\phi} \\ \phi \end{bmatrix}$$

A very important criterion for the applicability of this principle is the damping of the yaw loop which is exclusively produced by the product of inertia I_{xz} . It results from the decoupled yaw equation:

$$\ddot{\psi} + \frac{I_{xz}}{N} H \dot{\psi} + \frac{I_x}{N} \omega_o H \psi = 0$$

Thus the following eigenfrequency ω_g and damping factor E_g are obtained

$$(4.22) \quad \omega_g^2 = \frac{I_x}{N} \omega_o H \approx \omega_o \frac{H}{I_z}$$

$$E_g = \frac{1}{2} I_{xz} \sqrt{\frac{H}{N I_x \omega_o}} \approx \frac{1}{2} \frac{I_{xz}}{I_x} \sqrt{\frac{H}{I_z \omega_o}}$$

$$\text{where } N \approx I_x \cdot I_z$$

The necessary rotation angle α between the reference system and the principal axes system (see Fig. 4.3) is of interest now. The transformation relation between the two systems reads:

$$(4.23) \quad I_h = T_R^h \cdot I_r \cdot (T_R^h)^{-1}$$

where

- I_r = inertia tensor in the reference system
- I_h = inertia tensor in the principal axes system
- T_R^h = transformation matrix which transforms the reference system into the principal axes system

$$\text{With } T_R^h = \begin{bmatrix} \cos \alpha & \sin \alpha \\ -\sin \alpha & \cos \alpha \end{bmatrix}$$

the principal axes inertia tensor is obtained as follows:

$$(4.24) \quad I_h = \begin{bmatrix} I_x \cos^2 \alpha - 2I_{xz} \sin \alpha \cos \alpha + I_z \sin^2 \alpha & -(I_x - I_z) \sin \alpha \cos \alpha + I_{xz} (\sin^2 \alpha - \cos^2 \alpha) \\ -(I_x - I_z) \cos \alpha \sin \alpha + I_{xz} (\sin^2 \alpha - \cos^2 \alpha) & I_x \sin^2 \alpha + 2I_{xz} \sin \alpha \cos \alpha + I_z \cos^2 \alpha \end{bmatrix}$$

The principal axes inertia tensor must have a diagonal form. Hence follows:

$$(4.25) \quad (I_x - I_z) \cos \alpha \sin \alpha = I_{xz} (\sin^2 \alpha - \cos^2 \alpha)$$

$$\Rightarrow I_{xz} = \frac{1}{2} (I_z - I_x) \tan(2\alpha)$$

For the numerical estimation of the required rotation angle α the same values for the moments of inertia I_x , I_z and the angular momentum H have to be taken as in section 4.1:

$$I_x = 1117 \text{ kgm}^2 \quad H = 50 \text{ Nms}$$

$$I_z = 1309 \text{ kgm}^2$$

From this the eigenfrequency ω_g is obtained according to equation 4.22

$$\omega_g \approx \sqrt{\omega_o \frac{H}{I_z}} = 1.6665 \cdot 10^{-3} \text{ rad/s}$$

Hence results the required product of inertia

$$I_{xz} \approx 2E I_x \sqrt{\frac{I_z \omega_o}{H}}$$

With $E = \frac{1}{2} \sqrt{2}$ hence follows:

$$I_{xz} \approx 68.95 \text{ kgm}^2$$

According to equation 4.25, the skewing angle of the reference system with respect to the principal axes system is obtained:

$$\alpha = \frac{1}{2} \arctan \frac{2 I_{xz}}{I_z - I_x} = 17.8^\circ$$

From this finally result the principal axes of inertia according to equation 4.24

$$I_{xh} = 1095 \text{ kgm}^2$$

$$I_{zh} = 1331 \text{ kgm}^2$$

These are realistic values corresponding to a satellite of the size of INTELSAT V.

We have, however, to admit, that the moments of inertia are not known very precisely so that a certain safety margin with respect to the choice of the rotation angle is necessary. The higher damping of the yaw dynamic thus obtained is to some extent very advantageous. On the other hand, the inaccurate knowledge of the inertia tensor leads to residual couplings. This has to be taken into consideration particularly in connection with the solar generator. The result of its alignment to the sun is a periodic change of the inertia tensor within 24 hours. The schematic arrangement of the solar generator as it is prevailing today on communication satellites is represented in Fig. 4.4.

The change of the moments of inertia of the total satellite is determined by the rotation angle δ and the moment of inertia of the solar generator about its η -axis. According to [8] the additional terms describing this change read as follows:

$$(4.26) \quad \Delta I_x = I_\eta \cdot \sin^2 \delta$$

$$\Delta I_z = I_\eta \cdot \cos^2 \delta$$

$$\Delta I_{xz} = -I_\eta \cdot \frac{1}{2} \sin 2\delta$$

Assuming that for $\delta = 0$ there is the nominal configuration with the moments of inertia I_{x0} , I_{z0} , I_{xz0} , the following is obtained:

$$(4.27) \quad I_x = I_{x0} + I_\eta \sin^2 \delta$$

$$I_z = I_{z0} - I_\eta (1 - \cos^2 \delta)$$

$$I_{xz} = I_{xz0} - \frac{1}{2} I_\eta \sin 2\delta$$

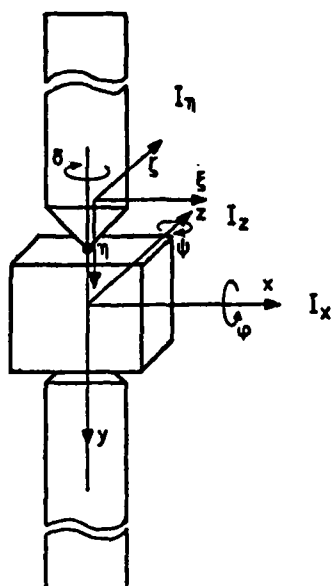


Fig. 4.4 Arrangement of the Solar Generator on Modern Communication Satellites.

According to equation 4.21, the expression for the damping factor of the yaw loop in dependence of the solar panel rotation angle reads:

$$\xi = \frac{\frac{1}{2} \frac{I_{xzo} - \frac{1}{2} I_{\eta} \sin 2\delta}{I_{x0} + I_{\eta} \sin^2 \delta} \sqrt{\frac{H}{[I_{z0} - I_{\eta}(1 - \cos^2 \delta)] \cdot \omega_0}}}{1}$$

The variation of this damping factor is shown in Fig. 4.5, where the following value for the solar generator moment of inertia about the η -axis was assumed:

$$I_{\eta} = 54 \text{ kgm}^2$$

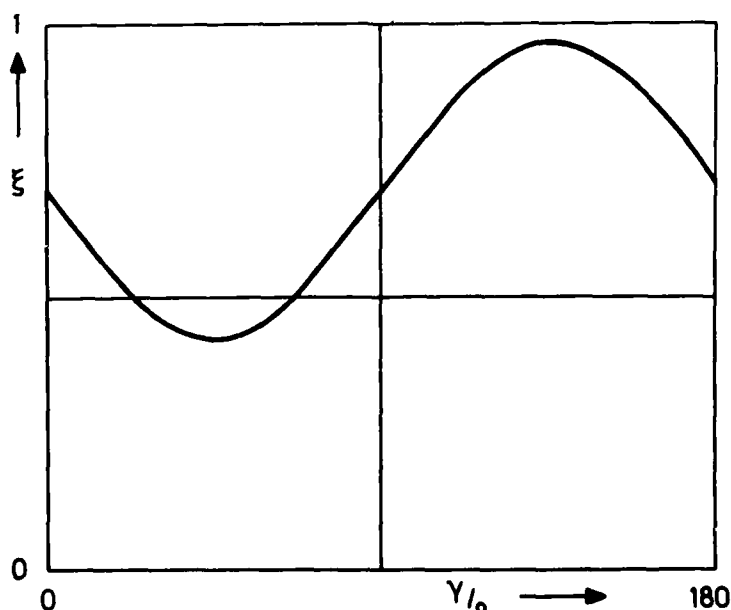


Fig. 4.5 Change of the Damping Factor in Dependence of the Solar Panel Rotation Angle.

By means of the decoupling of the yaw dynamics it is now possible to produce torques by attitude control thrusters affecting only the roll angle. This is important e.g. for desaturation maneuvers. Usually the thruster torques are tuned to the internal torques caused by the gimbal angle desaturation. As however thruster torques are subject to variations, in most cases a superposed control is necessary. In this case it is, of course, of great advantage if the control error only appears in that angle that can be measured.

It is advisable to determine the mounting area of these thrusters referred to the nominal configuration. It results from equation 4.16 regarding that the torque affecting the yaw loop has to disappear:

$$\frac{I_{xzo}}{N} \cdot M_x + \frac{I_{xo}}{N} \cdot M_z = 0$$

Hence follows a skewing angle β of the thrusters

$$\beta = - \arctan \frac{I_{xzo}}{I_{xo}}$$

Now remains to be investigated how the change of the inertia tensor by the rotation of the solar generator affects the coupling in the yaw dynamics. For this reason a computer simulation has been performed where apart from the moments of inertia already mentioned the following data were assumed:

torque produced by the thruster: $M_0 = 10^{-2} \text{ Nm}$

roll dynamics:

$$\omega_r = 0.2 \text{ rad/s}$$

$$\xi_r = \frac{1}{2} \sqrt{2}$$

The result is shown in Fig. 4.6 for different solar panel rotation angles.

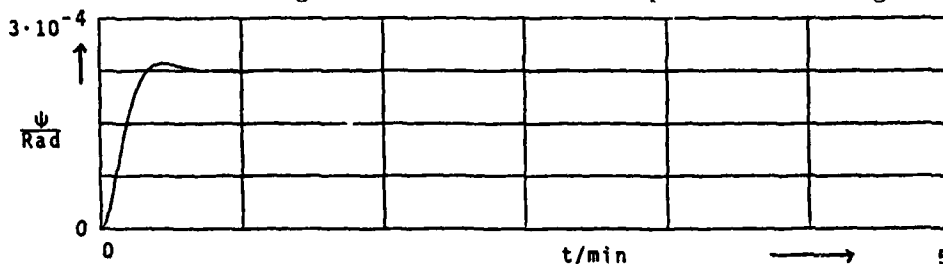


Fig. 4.6a Roll angle due to disturbance torque $M_d = 10^{-2} \text{ Nm}$ (short term).

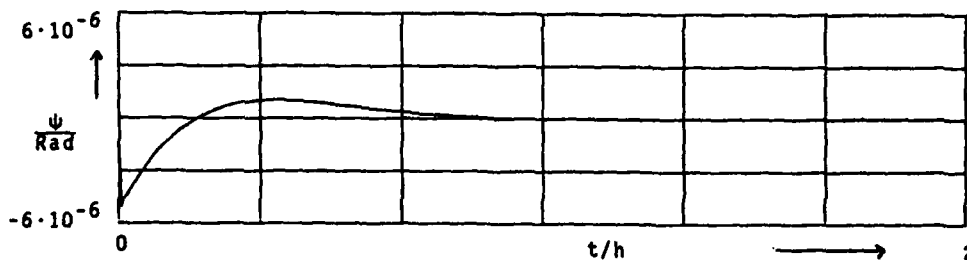


Fig. 4.6b Yaw angle for $\delta = 45^\circ$ (long term).

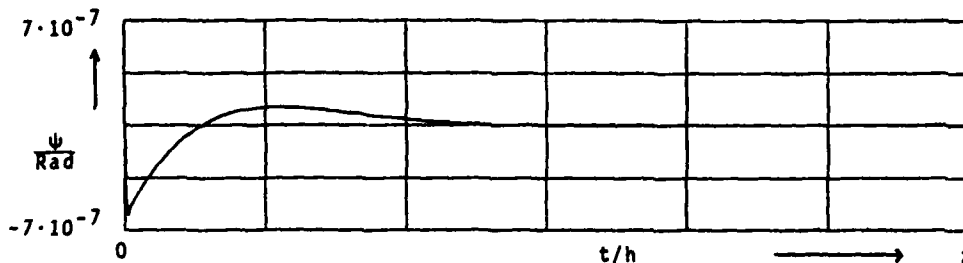


Fig. 4.6c Yaw angle for $\delta = 90^\circ$ (long term).

Disturbance Behaviour in Dependence of the Solar Panel Rotation Angle.

It is remarkable that in all three cases the stationary yaw angle error is zero. An increase of the yaw error only takes place during the relatively short transition time of the roll angle. It becomes the smaller, the shorter this time is. This is valid for all rotation angles δ , as shows the following calculation.

The limiting value is found from the equations 4.16 and 4.21 by setting all derivations of the angles ϕ and ψ equal to zero. In the control law according to equation 4.21 and for the relation of the components of the thruster torques the nominal values for the moments of inertia are inserted.

$$(4.28) \quad \begin{bmatrix} K_O \cdot I_{xO} & 0 \\ -K_O \cdot I_{xzO} & \omega_O H \end{bmatrix} \cdot \begin{bmatrix} \varphi_\infty \\ \psi_\infty \end{bmatrix} = \begin{bmatrix} M_x \\ M_z \end{bmatrix} = \begin{bmatrix} 1 \\ -\frac{I_{xzO}}{I_{xO}} \end{bmatrix} \cdot M_O$$

The limiting value ψ_∞ hence only depends on the nominal values for the moments of inertia. Equation 4.28 yields:

$$\varphi_\infty = \frac{M_O}{K_O \cdot I_{xO}}$$

$$\psi_\infty = \frac{M_O}{K_O \cdot H I_{xO}} (I_{xzO} - \frac{I_{xO} \cdot I_{xzO}}{I_{xO}}) = 0$$

A variation of the moments of inertia has no influence on the stationary limiting value. This can be explained when taking into consideration that the moments of inertia, on principle, only cause dynamic couplings, whereas the limiting value exclusively depends on the stiffness terms effected by kinematic coupling with the orbit rate ω_O and the set gain K_O . The x-component of the disturbance torque, this time, does not cause a yaw angle error due to the decoupling mechanism, but causes a yaw gimbal angle deflection. The mean value of its undamped oscillation with the orbit rate ω_O is due to the component M_z of equation 4.28 shifted by the amount of

$$\Delta \gamma_z = - \frac{M_O}{\omega_O H} \cdot \frac{I_{xzO}}{I_{xO}}$$

This can be verified by inspection of the control law according to equation 4.21. It also corresponds to the condition of the momentum equilibrium according to the law of precession which is explained in detail in section 2. According to it, the motion of the momentum vector is independent of the satellite parameters and the controller, but is only a function of the external torques M , the angular momentum H and the orbit rate ω_O .

In conclusion it should be mentioned that the control concept presented here as a certain analogy to a well known attitude control system, i.e. the so-called WHECON-Attitude Control Concept [6]. There, however, a fixed momentum wheel is concerned and the roll/yaw motion is stabilized by means of attitude control thrusters. These thrusters are skewed by a small angle with respect to the reference system. Thus a "damping" of the eigenfrequency caused by kinematic coupling is obtained. This is not possible when using a gimbaled flywheel, as the damping of the momentum vector precession effected by WHECON cannot be achieved by the internal torques of the flywheel. On the contrary, the undamped eigenfrequency ω_O shows up clearly in the control law. But regarding the satellite as a subassembly according to the principle of internal reaction torques between mechanical subassemblies, the effect is absolutely comparable, even if the physical reasons in both control principles are different according to their nature.

4.3 ATTITUDE CONTROL BY MEANS OF OBSERVERS

Modern communication satellites will be equipped with an on-board computer for data-processing. Thus, the effective use of digital attitude control procedures becomes possible. In the on-board computer, estimation algorithms such as Kalman Filters and state observers can be realised, which reconstruct from the measured roll angle ϕ the yaw angle ψ as well as the derivative of both of them. Of main importance in this section will be the application of state observers.

For the controllable and observable dynamic system

$$(4.29a) \quad \dot{\underline{x}} = A \underline{x} + B \cdot \underline{u}$$

$$(4.29b) \quad \underline{y} = C \underline{x}$$

with the state vector \underline{x} of the order n , the control vector \underline{u} (order m), the measuring vector \underline{y} (order p), the dynamic matrix A (dimension $n \times n$), the input matrix B ($n \times m$) and the measuring matrix C ($p \times n$), the unity observer according to Luenberger [7] has the form

$$(4.30) \quad \dot{\underline{z}} = F \underline{z} + G \underline{y} + D \cdot \underline{u}$$

For $\underline{z} = \hat{\underline{x}}$ hence follows for the estimation error

$$(\underline{x} - \hat{\underline{x}})' = A \underline{x} + B \underline{u} - F \hat{\underline{x}} - G \cdot C \underline{x} - D \cdot \underline{u} = F (\underline{x} - \hat{\underline{x}})$$

as far as

$$(4.31a) \quad F = A - G C$$

and

$$(4.31b) \quad D = B$$

If F and A have different eigenvalues, there exists a unique solution for G and an initial estimation error is damped as follows:

$$(4.32) \quad [\underline{x}(t) - \hat{\underline{x}}(t)] = e^{F \cdot t} [\underline{x}(0) - \hat{\underline{x}}(0)]$$

Usually the eigenvalues of the observer are chosen in such a way that the damping time due to its eigendynamics is shorter than that of the system. In this section, however, the feedback matrix G of the observer shall be calculated in such a way, that the total system is, as far as possible, insensitive to parameter variations.

The rotation of the solar generator as well as the center-of-mass-shift due to the fuel consumption are regarded as the reasons which cause the variations of the system parameters. The fuel consumption is supposed to produce variations of the moments of inertia I_x, I_z of $\pm 20\%$, marked with I_x^+, I_x^- resp. I_z^+, I_z^- . An orbit correction impulse is supposed to be the largest disturbance torque, which generates, because of the misalignment of the orbit correction jet a disturbance torque of 10^{-5} Nm over approx. 60s. The false momentum of $6 \cdot 10^{-2}$ Nms shall result in an initial error of the yaw rate of $4 \cdot 10^{-5}$ rad/s. Furthermore, the initial error of the roll angle shall be 0.05° and that of the yaw angle 0.5° .

For the design of a parameter insensitive controller and observer the Min-Max-Design, described in the appendix in equation (A 11), is inserted, i.e. the following optimization is performed

$$(4.33) \quad \min_{K_G} \{ \max_J J_1 \} \Rightarrow K_{Gopt}$$

$$\text{with} \quad J = \{ (I_{x0}, I_{z0}), (I_x^+, I_z^+), (I_x^-, I_z^-) \}$$

For optimization of K_G , the Lyapunov-equation A.8c has to be solved, which has a unique solution for negative real parts of A . Therefore the actuator dynamics having two poles on the imaginary axis, have to be eliminated from the system equations. This is reasonable, too, because anyway it cannot be influenced by the control. A damping of this partial system would be equal to a shift of the momentum vector in the space which, however, is not possible - as was explained at length in section 2 - because of lacking external torques. Consequently, as mentioned at the beginning of this section, the control coefficients for the control will be optimized with the internal control torques M_{Rx}, M_{Rz} , and by means of equation 4.5 the coefficients for the gimbal angle control will be determined. The system equations considered read in state vector form as:

$$(4.34) \quad \begin{bmatrix} \dot{\phi} \\ \dot{\psi} \\ \dot{\varphi} \\ \dot{\psi} \end{bmatrix} = \begin{bmatrix} -\frac{H}{I_x} & \frac{\omega_0 H}{I_x} \\ \frac{H}{I_z} & -\frac{\omega_0 H}{I_z} \\ 1 & \\ & 1 \end{bmatrix} \begin{bmatrix} \phi \\ \psi \\ \varphi \\ \psi \end{bmatrix} + \begin{bmatrix} \frac{1}{I_x} \\ \\ \\ \frac{1}{I_z} \end{bmatrix} \begin{bmatrix} M_{Rx} \\ \\ M_{Rz} \end{bmatrix}$$

$$\varphi = \begin{bmatrix} \\ \\ 1 \\ \\ \end{bmatrix} \begin{bmatrix} \dot{\phi} \\ \dot{\psi} \\ \phi \\ \psi \end{bmatrix}$$

or abbreviated $\dot{\underline{x}} = A \underline{x} + B \underline{u}$, $\underline{y} = C \cdot \underline{x}$

with the numerical values of the parameters from sections 4.1.

The optimization of the coefficients of controller and observer is bounded as follows:

- (i) The estimated yaw angle is not fed back.
- (ii) Roll motion is decoupled from yaw motion, i.e. variations of the roll angle have no effect on the yaw motion.

The weighting matrices Q and R are chosen in such a way, that for J_0 , which according to equation A.8a and b affects J_1

$$(4.35) \quad J_1 = \max_{\underline{x}_{Go} \leq \underline{x} \leq \underline{x}_{Go}} \frac{J_0}{\underline{x}_{Go}^T \underline{x}_{Go}} = \lambda_{\max}(P)$$

the following is valid:

(4.36)

$$J_0 = \int_0^\infty \left[\left(\frac{\dot{\phi} - \hat{\phi}}{\phi_{\text{Max}}} \right)^2 + \left(\frac{\dot{\psi} - \hat{\psi}}{\psi_{\text{Max}}} \right)^2 + \left(\frac{\phi - \hat{\phi}}{\phi_{\text{Max}}} \right)^2 + \left(\frac{\psi - \hat{\psi}}{\psi_{\text{Max}}} \right)^2 \right. \\ \left. + 10 \left(\frac{\phi}{\phi_{\text{Max}}} \right)^2 + \left(\frac{M_{Rx}}{M_{Rx\text{Max}}} \right)^2 + \left(\frac{M_{Rz}}{M_{Rz\text{Max}}} \right)^2 \right. \\ \left. + \left(\frac{U_{B1}}{U_{B1\text{Max}}} \right)^2 + \left(\frac{U_{B2}}{U_{B2\text{Max}}} \right)^2 + \left(\frac{U_{B3}}{U_{B3\text{Max}}} \right)^2 + \left(\frac{U_{B4}}{U_{B4\text{Max}}} \right)^2 \right] dt$$

Here the individual terms were normalized with respect to their maximum amplitudes. Optimization of the controller and observer coefficients lead to the following result:

(4.37)

$$\begin{bmatrix} M_{Rx} \\ M_{Rz} \end{bmatrix} = \begin{bmatrix} -165.7 & 38.50 & -21.28 & 0 \\ -50 & -36.93 & 0 & 0 \end{bmatrix} \begin{bmatrix} \hat{\phi} \\ \hat{\psi} \\ \phi \\ \psi \end{bmatrix}$$

$$G = \begin{bmatrix} 11.63 \\ -9.55 \\ 3.00 \\ -43.98 \end{bmatrix}$$

The conversion to the gimbal angle control, according to equation 4.5, leads to the following relation:

(4.38)

$$\begin{bmatrix} \dot{y}_x \\ \dot{y}_z \end{bmatrix} = \begin{bmatrix} -1 & -0.7386 & 0 & 0 \\ 3.314 & -0.7701 & 0.4256 & 0 \end{bmatrix} \begin{bmatrix} \hat{\phi} \\ \hat{\psi} \\ \phi \\ \psi \end{bmatrix} + \begin{bmatrix} 0 & 7.28 \cdot 10^{-5} \\ -7.28 \cdot 10^{-5} & 0 \end{bmatrix} \begin{bmatrix} y_x \\ y_z \end{bmatrix}$$

Figures 4.7 and 4.8 show the transient behaviour of the motion of a satellite with nominal moments of inertia I_{x0} , I_{z0} based on the initial conditions assumed in the section 4.3.

Short term behaviour

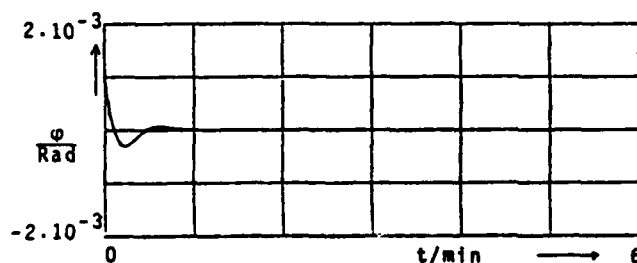


Fig. 4.7a Roll angle.

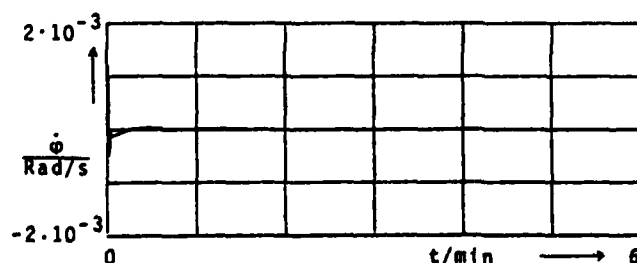


Fig. 4.7b Roll rate.

Long term behaviour

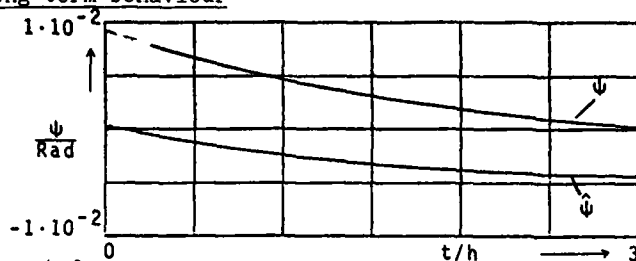


Fig. 4.8a Yaw angle.

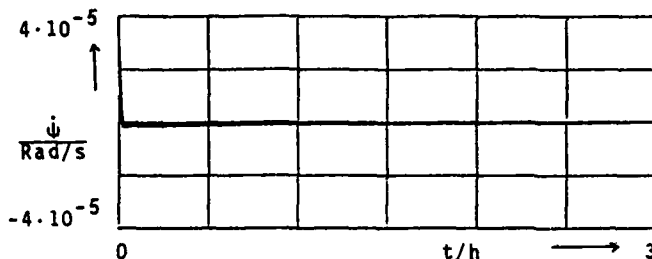


Fig. 4.8b Yaw rate.

The roll angle, after one minute, damps down to zero. The yaw loop is, however, considerably slower with a transient time of approx. 3 h. As the estimated yaw angle is not fed back, the large yaw angle estimation error does not disturb the roll dynamic.

The transient behaviour for the satellite with the same controller, but moments of inertia by 20% larger, is represented in Fig. 4.9.

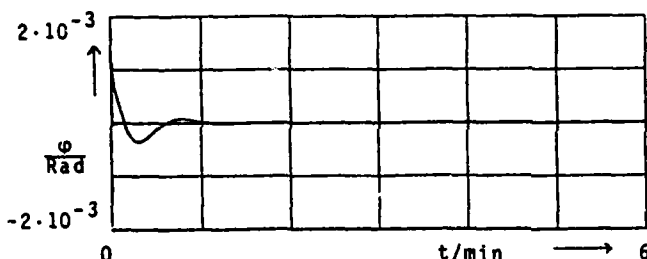


Fig. 4.9a Roll angle (short term).

As shown by Fig. 4.9a and b the increase of the moments of inertia has almost no influence on the transient behaviour.

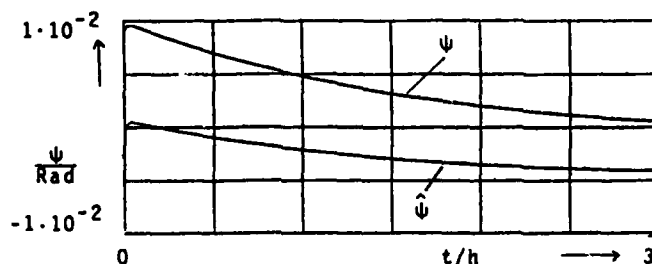


Fig. 4.9b Yaw angle (long term).

Fig. 4.10a and b show roll and yaw angles at moments of inertia being by 20% smaller. There is no essential effect on the transient behaviour, either.

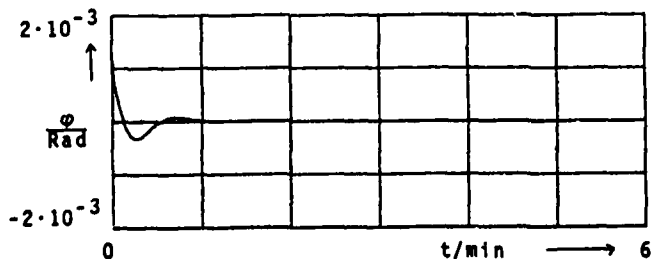


Fig. 4.10a Roll angle (short term).

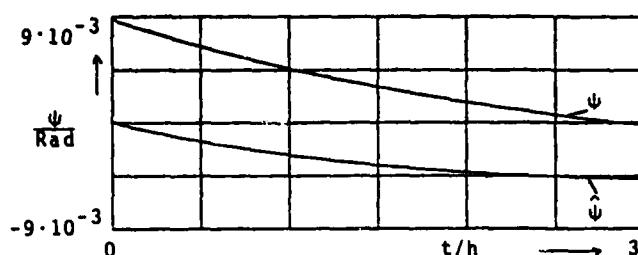


Fig. 4.10b Yaw angle (long term).

The eigenvalues of the controlled nominal system with state vector feedback are

$$\begin{aligned}\lambda_{1,2} &= -7.41 \cdot 10^{-2} \pm j \cdot 0.116 \\ \lambda_3 &= -7.81 \cdot 10^{-2} \\ \lambda_4 &= -9.89 \cdot 10^{-5} \\ \lambda_{5,6} &= \pm j \cdot 7.28 \cdot 10^{-5}\end{aligned}$$

The observer eigenvalues are at

$$\begin{aligned}\lambda_{1,2} &= -1.48 \pm j \cdot 3.05 \\ \lambda_3 &= -3.74 \cdot 10^{-2} \\ \lambda_4 &= -6.22 \cdot 10^{-5} \\ \lambda_{5,6} &= 0\end{aligned}$$

5. SUMMARY

The design of an attitude controller for a geostationary satellite with flywheel is made easier considerably by taking advantage of the physical relations. This enabled Mork [4] as well as Scott [5] to find simple and at the same time effective control systems, which in general can well meet all requirements of application satellites. In this report it has been shown, how to generalize these results, obtained rather empirically, by means of design procedures for state vector feedback.

Taking advantage of the physical relations however, can also lead to modified system dynamics which - compared to the general case - can have principal advantages. This has been demonstrated that a total decoupling of the yaw dynamics is possible if the inertia tensor is non-diagonal. The reaction to external torques produced by thrusters only affects the roll dynamics and thus is much better controllable.

These more conventional procedures from the point of view of control theory, were compared to the design method with observer. In this case it is possible to make the system very insensitive to parameter variations by applying optimization procedures. The expense seems to be very large for rigid satellites, but the additional dynamics of flexible appendages, which are only known rather inaccurately, would justify this design method at least in critical phases of operation.

6. REFERENCES

- [1] BOERSMA, G. Preparatory Study of Satellite Attitude Control with Momentum Wheels.
SONNENSCHNEIN, F.J. Nationaal Lucht-en Ruimtevaartlaboratorium, 1972.
NLR TR 72148 U.
- [2] MBB et. al. TV-SAT.
Interim Study Presentation.
BMFT, Bonn 21.6.1978.
- [3] HIRZINGER, G. Direct Digital Attitude Control with a Double Gimbaled Momentum Wheel.
LANGE, TH. VII IFAC Symposium on Automatic Control in Space.
Rottach Egern 1976.

- [4] MORK, H.L. Synthesis and Design of a gimballed Reaction Wheel Attitude Stabilization Package (GRASP).
AIAA, Guidance, Control and Flight Mechanics Conference, Hempstead.
New York, 16. - 18.8.1971.
- [5] LYONS, M.G.
LEBSOCK, K.L.
SCOTT, E.D. Double Gimballed Reaction Wheel Attitude Control System for High Altitude Communication Satellites.
AIAA, Guidance, Control and Flight Mechanics Conference, Hempstead.
New York, 16. - 18.8.1971.
- [6] SCOTT, et. al. Analysis and Design of WHECON, an Attitude Control Concept.
AIAA 2nd Communication Satellite Systems Conference No. 68-461.
- [7] LUENBERGER, D.G. An Introduction to Observers.
IEEE Trans. on Automatic Control, Vol. AC-16, No. 6, December 1971.
- [8] HEIMBOLD, G. Dynamisches Modell eines dreiachsstabilisierten, geostationären Satelliten mit flexiblen Solarzellenträgern im Normalbetrieb.
DFVLR-IB Nr. 552-77/7.
- [9] JAMESON, A. Optimization of Linear Systems of Constrained Configuration.
Int. J. Control, 1970, Vol. 11, No. 3, 409 - 421.
- [10] D'APPOLITO, J.A.
HUTCHINSON, C.E. Low Sensitivity Filters for State Estimation in the Presence of Large Parameter Uncertainties.
IEEE Trans. on Automatic Control, June 1969.

APPENDIX

DESIGN OF CONTROL SYSTEMS OF LOW SENSITIVITY AT LARGE PARAMETER VARIATIONSA.1 SYSTEM MODELLING

Given be the controllable and observable system

$$(A.1a) \quad \dot{\underline{x}} = A \underline{x} + B \underline{u}, \quad \underline{x}(0) = \underline{x}_0$$

$$(A.1b) \quad \underline{y} = C \underline{x}$$

The corresponding state estimator (Kalman-Filter, unity observer) be described as

$$(A.2) \quad \dot{\hat{\underline{x}}} = A \hat{\underline{x}} + G(\underline{y} - C \hat{\underline{x}}) + B \underline{u}, \quad \hat{\underline{x}}(0) = \underline{x}_0$$

The feedback law for total state feedback reads:

$$(A.3) \quad \underline{u} = K \cdot \hat{\underline{x}}$$

Due to the separation principle, the eigenvalues of the controlled system are determined as the eigenvalues of

$$A + B K$$

and

$$A - G C$$

Defining

$$\tilde{\underline{y}} = \underline{y} - C \hat{\underline{x}}$$

$$\underline{u}_B = G \cdot \tilde{\underline{y}}$$

the following system is obtained by means of state vector extension

$$(A.4) \quad \begin{bmatrix} \underline{x} \\ \hat{\underline{x}} \end{bmatrix} = \begin{bmatrix} A & | & - \\ \hline - & | & A \end{bmatrix} \cdot \begin{bmatrix} \underline{x} \\ \hat{\underline{x}} \end{bmatrix} + \begin{bmatrix} B & | & - \\ \hline B & | & I \end{bmatrix} \cdot \begin{bmatrix} \underline{u} \\ \underline{u}_B \end{bmatrix}; \begin{bmatrix} \underline{x}(0) \\ \hat{\underline{x}}(0) \end{bmatrix} = \begin{bmatrix} \underline{x}_0 \\ \underline{x}_0 \end{bmatrix}$$

$$\underline{z} = \begin{bmatrix} \hat{\underline{x}} \\ \tilde{\underline{y}} \end{bmatrix} = \begin{bmatrix} - & | & I \\ \hline C & | & -C \end{bmatrix} \cdot \begin{bmatrix} \underline{x} \\ \hat{\underline{x}} \end{bmatrix}$$

$$\underline{u}_G = \begin{bmatrix} \underline{u} \\ \underline{u}_B \end{bmatrix} = \begin{bmatrix} K & | & - \\ \hline - & | & G \end{bmatrix} \cdot \underline{z}$$

The new measuring vector is \underline{z} and the new control vector is \underline{u}_G .

With the self explaining abbreviations, the system of equation (A.4) reads in vector form:

$$(A.5) \quad \dot{\underline{x}}_G = A_G \underline{x}_G + B_G \cdot \underline{u}_G; \quad \underline{x}_G(0) = \underline{x}_{G0}$$

$$\underline{z} = C_G \underline{x}_G$$

$$\underline{u}_G = K_G \cdot \underline{z}$$

The feedback matrix K_G , to be determined, contains the elements of the gain G of the estimator as well as of the state feedback K . The equations (A.5) represent the standard form of a dynamic system with output vector feedback.

A.2 OPTIMIZATION OF THE OUTPUT VECTOR FEEDBACK FOR GIVEN INITIAL CONDITIONS

For the system of equation A.5 the constant feedback matrix K_G shall be determined in such a way that the following quadratic integral criterion becomes a minimum.

$$(A.6) \quad J_0(K_G) = \int_0^{\infty} \{ \underline{x}_G^T Q \underline{x}_G + \underline{u}_G^T R \underline{u}_G \} dt$$

According to Jameson [4] the cost functional J_0 is calculated as follows:

(A.7) With $\underline{u}_G = K_G \cdot \underline{z} = K_G \cdot C_G \cdot \underline{x}_G$

becomes

$$J_0 = \int_0^{\infty} \underline{x}_G^T \tilde{Q} \underline{x}_G dt$$

with

$$\tilde{Q} = Q + C_G^T K_G^T R K_G C_G$$

Transformation of the functional J_0 leads to

$$J_0 = \text{tr} \left(\left[\int_0^{\infty} \underline{x}_G \underline{x}_G^T dt \right] \cdot \tilde{Q} \right) = \text{tr}(W \cdot \tilde{Q})$$

in which

$$W = \int_0^{\infty} \underline{x}_G \underline{x}_G^T dt$$

is determined as solution of the Lyapunov-equation (A.8)

$$(A.8) \quad \tilde{A} W + W \tilde{A}^T = - \underline{x}_{Go} \underline{x}_{Go}^T$$

with

$$\tilde{A} = A_G + B_G K_G C_G$$

For negative real parts of \tilde{A} there exists a unique solution of A.8 for arbitrary values of \underline{x}_{Go} . The minimum of the cost functional $J_0(K_G)$ is calculated with numerical optimization methods, in which the respective functional value is determined as shown above.

In order to reduce the dependency of the solution K_G from the respective initial value, Jameson [9] recommends instead of criterion A.6 the determination of the worst-case solution

$$J_1(K_G) = \text{Max}_{\underline{x}_{Go}} \frac{J_0}{\underline{x}_{Go}^T \underline{x}_{Go}} = \text{Max}_{\underline{x}_{Go}} \frac{\underline{x}_{Go}^T P \underline{x}_{Go}}{\underline{x}_{Go}^T \underline{x}_{Go}}$$

This is calculated as the maximum eigenvalue λ_{Max} of P

$$\text{Max}_{\underline{x}_{Go}} \frac{J_0}{\underline{x}_{Go}^T \underline{x}_{Go}} = \lambda_{\text{Max}}(P)$$

P being the solution of the following Lyapunov-equation:

$$\tilde{A}^T P + P \tilde{A} = - \tilde{Q}$$

This second Lyapunov-equation can also be used for the calculation of the cost functional J_0 , as

$$J_0(K_G) = \underline{x}_{Go}^T P \underline{x}_{Go} = \text{tr}(W \cdot \tilde{Q})$$

is valid.

A.3 REDUCTION OF SENSITIVITY OF THE SYSTEM FOR LARGE VARIATIONS OF THE SYSTEM PARAMETERS

According to the design of filters of low sensitivity due to d'Appolito and Hutchinson [10], the concept of the Min-Max-Design is applied to the design of state estimators and controllers of low sensitivity. For i different system realizations

$$\{A_G, B_G, C_G\} = \{A_G(1), B_G(1), C_G(1); \dots A_G(i), B_G(i), C_G(i)\}$$

resp. values of the system parameters

$$p = \{p\}; \quad P = \{p(1), \dots p(i)\}$$

which represent the parameter variations, first of all the maximum of the function J_0 is determined over p , and then minimized over K_G

$$(A.9) \quad \text{Min}_{K_G} \{ \text{Max}_p J_0 \} = K_{Gopt}$$

Maximizing J_0 over p , presents itself as selection of the maximal value of J_0 from the i values of J_0 , to be calculated. The subsequent minimization over K_G is performed with numerical optimization procedures.

As far as $\{A_G(1), B_G(1), C_G(1)\}$ resp. $p(1)$ represent the nominal configuration of the system, the corresponding functional value $J_{NOM}(K_G)$ can be used for normalization so that

$$(A.10) \quad \min_{K_G} \left\{ \max_p \frac{|J_0 - J_{NOM}|}{J_{NOM}} \right\} \Rightarrow K_{Gop}$$

is to be optimized.

By means of the system modelling proposed under A.1, the observer again G for a given state controller K as well as the controller feedback K for given G , or both together can be designed as insensitive with respect to the system parameters. As the system state x , contains the system state x as well as the estimated \hat{x} , the quadratic control error or the quadratic estimation error can be weighted separately by means of Q . The size of the feedback matrices G and K is indirectly influenced by the weighting matrix R .

Instead of J_0 also the criterion J_1 , given in section A.2, can be used for the reduction of the sensitivity, as well as other criteria J_i that need not be quadratic integral criteria.

For the application of the cost criterion $J_1(K_G)$ (equation A.8b) for the design of a controller, insensitive with respect to parameter variations the corresponding Min-Max criterion reads

$$(A.11) \quad \min_{K_G} \left\{ \max_p J_1 \right\} = \min_{K_G} \left\{ \max_p \lambda_{\max}(P) \right\} \Rightarrow K_{Gopt}$$

This criterion is used in section 4.3 for the design of a parameter insensitive controller and observer.

ANALYSIS AND EXPERIMENTAL VERIFICATION OF THE NUTATION OF A SATELLITE EQUIPPED WITH MAGNETIC BEARING MOMENTUM WHEELS

by

C. Rouyer

G. Heimbolt and Th. Lange

Head of Satellites Programmes Group
S.N.I. Aérospatiale
B.P.2 - 78130 Les Mureaux, France

and Deutsche Forschungs und Versuchsanstalt
für Luft und Raumfahrt
Oberpfaffenhofen - 8031 Wessling, F.R.G.

1. INTRODUCTION

The problem of the nutation divergence of a 3-axis stabilized satellite equipped with hydrodynamic bearings momentum wheels has recently made anxious some specialists of satellite attitude control.

The magnetic bearing momentum wheels, having a relatively low transverse rigidity and dissipating energy in the rotor (due to eddy currents), are likely to present an inconvenience of the same nature, if not of the same magnitude.

The purpose of this paper is to give a physical explanation of the phenomenon, to present the results of some tests carried out on an air-bearing table, and to show that the order of magnitude of the time constant of this divergence is so long that the phenomenon cannot be detected on a satellite of the Intelsat size.

2. NOMENCLATURE

x, y, z	Galilean reference axes
X, Y, Z	Reference axes of the stator of the wheel supposed to be the main axes of the satellite
\vec{z}	Axis of the bearings of the wheel
\vec{j}	Rotor axis
I	Transverse moment of inertia of the rotor
α, β	Tilt angles of the rotor axis with respect to the planes XZ and YZ (fig.3)
ϵ	Tilt angle of the rotor axis ($\epsilon = \sqrt{\alpha^2 + \beta^2}$)
Γ_K	Restoring torque
Γ_a	Damping torque
η	Damping coefficient related to a tilt rate
η_R	Damping coefficient related to the rotation of the rotor
ω_R	Rotor rotation rate
θ, φ, ψ	Euler angles defining $X Y Z$ with respect to $x y z$ (fig.6)
A	Transverse momentum of inertia of the satellite ($I_x = I_y = A$)
\vec{H}_R	Kinetic momentum of the rotor
\vec{H}_S	Kinetic momentum of the structure of the satellite
\vec{H}_T	$= \vec{H}_R + \vec{H}_S$
ω_o	Pulsation of the nutation of the satellite
ω_1	Pulsation of the precession of the rotor
ω_2	Pulsation of the nutation of the rotor
T_o	Time constant of the nutation of the satellite

3. DYNAMIC ANALYSIS

3.1 Magnetic Bearing Wheels Description

Many types of magnetic bearing principles can be conceived, depending on the sign of the magnetic forces (attractive or repulsive) and on the number of axes with an active stabilization control loop. Aerospatiale have chosen to develop the type characterized by :

- attractive magnetic forces
- one active axis.

Such a wheel consists of :

- one central part including the magnetic suspension and the driving motor ;
- one rotor, the technology of which depends on the specific maximum speed.

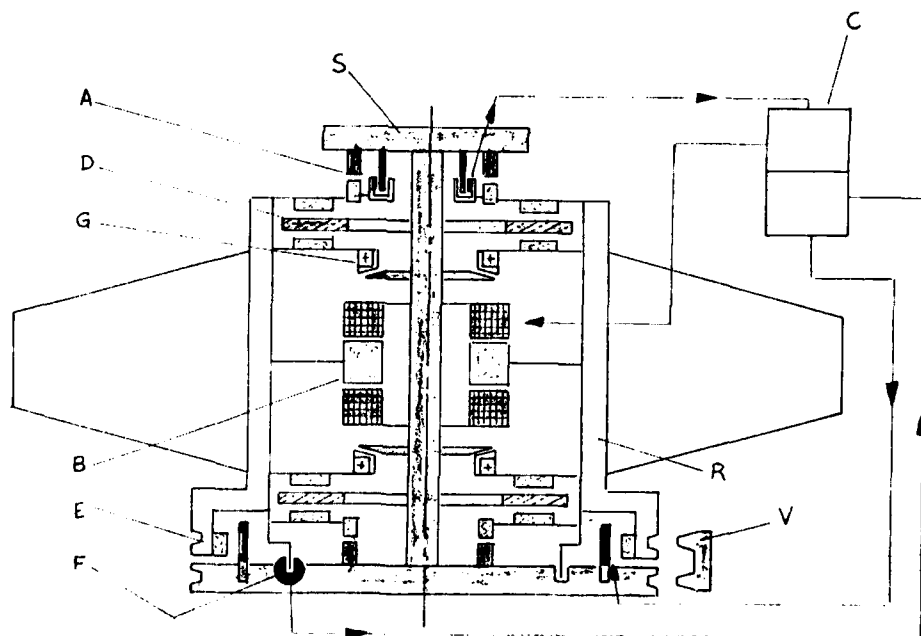
Figure 1 shows a schematic section of the Aerospatiale magnetic bearing momentum wheel.

Passive centering rings (reference A on fig.1) create a radial restoring force when the axis of the rotor does not coincide with the stator axis.

The axial attraction of the magnetic rings of the stator and of the rotor creates an axial instability. The axial stability is achieved thanks to an electronic control loop (C) actuating an electromagnet (B). The error signal is generated by a speed detection which minimizes the power consumption.

A complementary passive damping device (D), consisting of copper discs in which eddy currents are induced when the rotor tilts with respect to the stator, allows an easy crossing of the critical frequency when the rotor accelerates.

An electronic commutation motor (E) completes the assembly. In case of a temporary power supply failure, this motor can operate as a generator capable of supplying power to the axial control loop during more than 80 minutes.



- | | |
|----------------------------------|----------------------------------------|
| A. Centering magnets | F. Electronic commutation of the motor |
| B. Axial Control Loop Actuator | G. Safety ball bearings |
| C. Control Loop Electronics | R. Rotor |
| D. Transverse Oscillation Damper | S. Stator |
| E. Motor | V. Clamping mechanism |

Fig.1

3.2 Torques applied to the rotor

3.2.1 Restoring torque

When the rotor axis tilts by an angle α with respect to the stator axis, the magnetic bearings apply to the rotor a restoring torque given by the formula

$$\Gamma_K = K \alpha \quad (1)$$

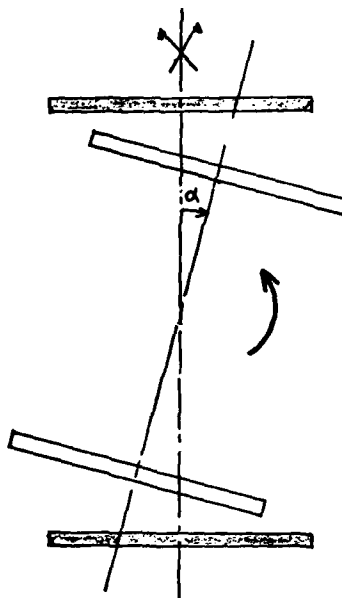


Fig. 2

3.2.2 Damping torques

When the rotor moves with respect to the stator, eddy currents are induced in both of them. As a result, under the influence of the magnetic field of the permanent magnets of the bearings, forces develop on each bearing which result in pure torques when we consider the complete assembly.

We have, however, to distinguish between the torques generated by a tilt around the transverse axes, and those generated by the rotation around the revolution axis (O Z).

a) torque due to a tilt around the transverse axes

Conventional signs :

- | | |
|----------|------------------------------------------------|
| X Y Z | stator axes |
| P | plane perpendicular to OZ |
| Z | intersection of P and \vec{OZ} |
| J | intersection of P with the rotor axis |
| α | tilt angle (rotor/stator), rotation around O X |
| β | tilt angle (rotor/stator), rotation around O Y |
- (fig.3 shows positive values of α and β)

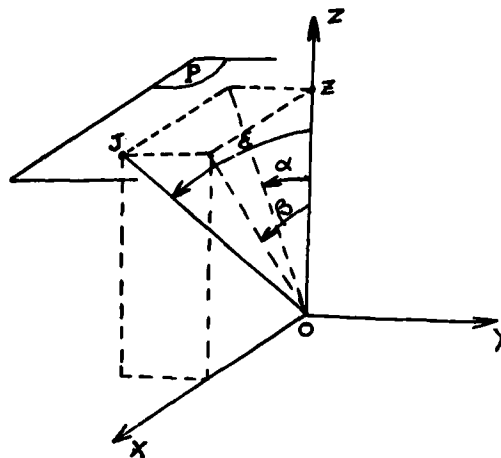


Fig. 3

Let us consider a rotation around O X resulting in a tilt angle α

According to Lenz's law, a damping torque is generated, proportional to $\dot{\alpha} =$

$$\Gamma_a = -\eta \dot{\alpha} \quad (2)$$

where η is a damping coefficient

A similar damping torque is generated by a tilt around O Y :

$$\Gamma_a = -\eta \dot{\beta} \quad (3)$$

b) torque due to a rotation around O Z

Let us consider a disc rotating in a magnetic field presenting a revolution symmetry, the disc center being off-set by an angle α with respect to the axis of the magnetic field (see fig. 4 using the same conventional signs as in fig. 3, plane P being the plane of the rotating disc).

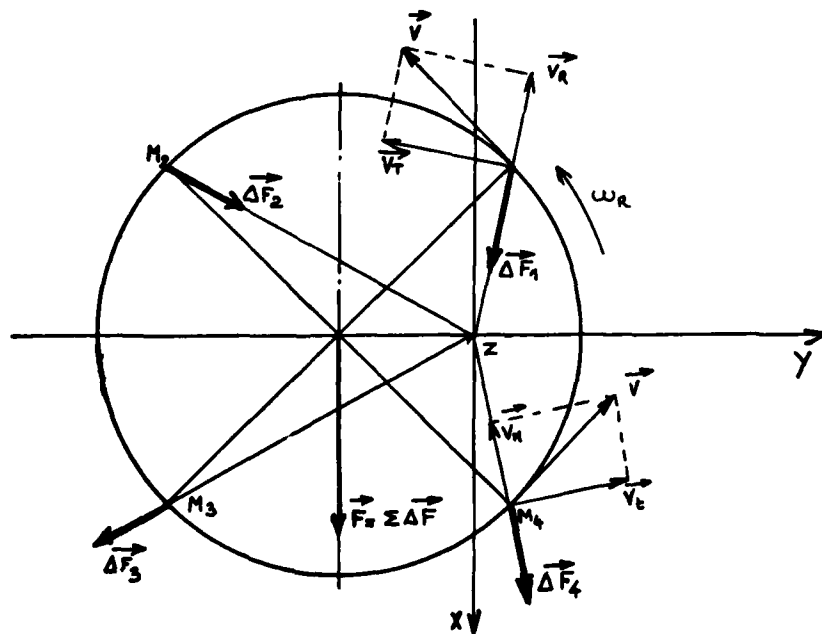


Fig. 4

Due to the off-sat angle α , each radius of the disc sweeps a non uniform magnetic field : this develops eddy currents in the disc, resulting in braking forces according to Lenz's law.

Let us suppose that α is the consequence of a rotation around O X (J on Z Y) and let us consider 4 points ; M_1, M_2, M_3 and M_4 of the disc, M_1 and M_3 on the one hand, M_2 and M_4 on the other hand, respectively symetric with respect to the point J, center of the disc.

Due to the eddy currents generated in the disc, an elementary force is applied on each of these points, colinear with the gradient of the induction flux Φ

The elementary force in M is thus colinear with MZ, since $\vec{\text{grad}} \Phi$ is radial with respect to Z

This is shown in fig. 4 where we consider the components V_t (tangential) and V_r (radial) of the speed vector \vec{V} of M_1 with respect to the field lines. It is obvious that V_t will not induce any eddy current and that Lenz's law will react only against V_r .

When we consider the point M_1 , a similar reasoning shows that $|\Delta \vec{F}_1| = |\Delta \vec{F}_3|$ but that $|\Delta \vec{F}_1|$ aims towards Z while $|\Delta \vec{F}_3|$ aims towards the opposite direction ! The same would apply for any other couple of points symetric with respect to the Y axis, such as M_2 and M_4 . In consequence, the resultant force of all the elementary forces applied to the set of points of the disc is parallel to the X axis. When α is small, we can assume that this resultant is proportional to α and to the spin rate $\omega_R =$

$$\begin{aligned} F_x &= \lambda \omega_R \\ F_y &= 0 \end{aligned} \quad (4)$$

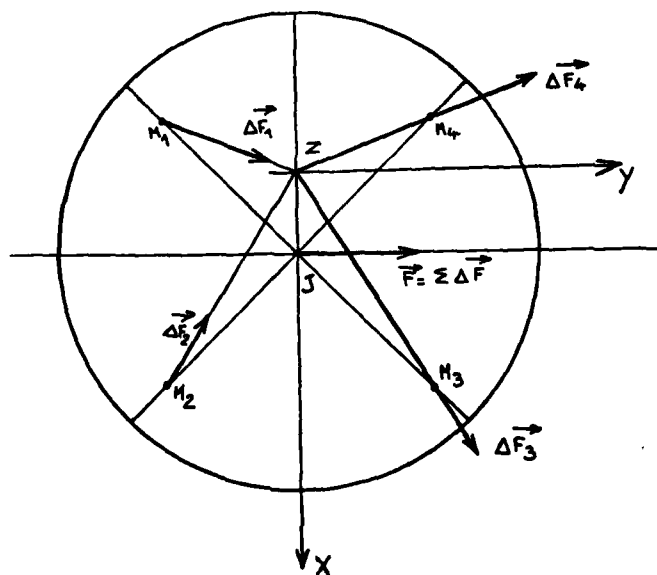
where λ is a coefficient of proportionality. Considering the complete rotor assembly, these forces result in a torque :

$$\Gamma_y = \eta_R \omega_R \alpha \quad (5)$$

where η_R is equal to λ multiplied by the lever arm between the upper and lower parts of the rotor.

In a similar way, a tilt around Y could result in a torque around O X =

$$\Gamma_x = \eta_R \omega_R \beta \quad (6)$$



$$\vec{F} \begin{cases} F_x = 0 \\ F_y = \lambda \omega_R \beta \end{cases} \rightarrow \vec{F} \begin{cases} \Gamma_x = -\eta_R \omega_R \beta \\ \Gamma_y = 0 \end{cases}$$

Fig. 5

3.3. Mathematical Analysis

3.3.1 Reference axes

Let $x y z$ be the Galilean reference axes and $X Y Z$ the stator reference axes.

The orientation of $X Y Z$ with respect to $x y z$ is defined by the angles as shown on fig. 6

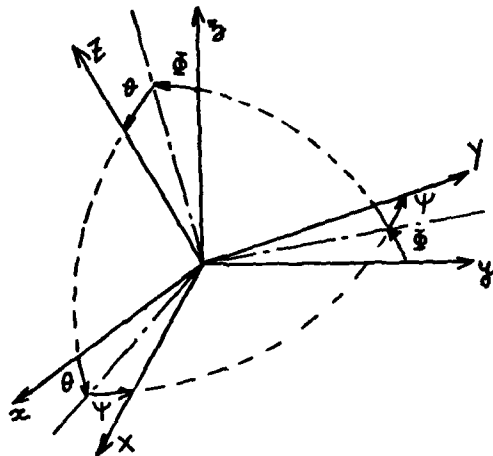


Fig. 6

The rotor axis (J) is still defined, with respect to $X Y Z$, by angles α and β

The 5 angles $\alpha, \beta, \theta, \phi$ and ψ are supposed to be small.

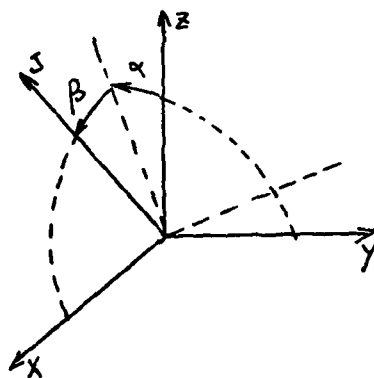


Fig. 7

3.3.2 Torques coordinates

The results of § 2.2 are summarized in the table below

Coordinate on	Torque on the rotor	Torque on the satellite
<u>O X</u>		
restoring	$- K \alpha$	$+ K \alpha$
damping	$- \eta \dot{\alpha}$ $- \eta_R \omega_R \beta$	$+ \eta \dot{\alpha}$ $+ \eta_R \omega_R \beta$
<u>O Y</u>		
restoring	$- K \beta$	$+ K \beta$
damping	$- \eta \dot{\beta}$ $+ \eta_R \omega_R \alpha$	$+ \eta \dot{\beta}$ $- \eta_R \omega_R \alpha$

Note : the damping terms $\eta \dot{\alpha}$ and $\eta \dot{\beta}$ are related to an energy dissipation in the rotor and in the stator. The terms $\eta_R \omega_R \alpha$ and $\eta_R \omega_R \beta$ are related to an energy dissipation in the rotor only

3.3.3 Equations

The equations of the satellite tilting motion, without external torques, can be written as follows, compiling the torques listed in § 3.3.2 :

$$\begin{array}{l} \text{rotor/satellite} \\ \text{interaction} \end{array} \quad \begin{cases} A \ddot{\phi} = K \alpha + \eta \dot{\alpha} + \eta_R \omega_R \beta \\ A \ddot{\theta} = K \beta + \eta \dot{\beta} - \eta_R \omega_R \alpha \end{cases} \quad (7)$$

$$\begin{array}{l} \text{rotor + satellite} \\ \text{assembly} \end{array} \quad \begin{cases} A \ddot{\phi} + I (\ddot{\phi} + \ddot{\alpha}) + H_R (\dot{\theta} + \dot{\beta}) = 0 \\ A \ddot{\theta} + I (\ddot{\theta} + \ddot{\beta}) - H_R (\dot{\phi} + \dot{\alpha}) = 0 \end{cases} \quad (8)$$

where H_R is the kinetic momentum of the rotor, the amplitude of which is supposed to be constant

(Note : it is assumed that the attitude control of the satellite around the Z axis is such that it keeps a fixed direction of the transverse axes with very small rotation rates $\dot{\theta}$ and $\dot{\psi}$. Consequently, the coupling terms (B-C) $\dot{\phi} \dot{\psi}$ and (C-B) $\dot{\theta} \dot{\psi}$ can be neglected).

The characteristic equation of this system of 4 equations is :

$$\begin{aligned} & p^6 \times (A^2 I^2) + p^5 \times (2 A^2 I \eta) \\ & + p^4 \times A^2 (\eta^2 + H_R^2 + 2 I K) - A I H_R \eta_R \omega_R \\ & + p^3 \times (2 A H_R^2 \eta + 2 A^2 H_R \eta_R \omega_R - A I H_R \eta_R \omega_R + 2 A^2 \eta K) \\ & + p^2 \times A^2 (K^2 + \eta_R^2 \omega_R^2) + 2 A H_R^2 K + H_R^2 \eta^2 \\ & + p \times (2 \eta K H_R^2) \\ & + p^0 \times (H_R^2 (K^2 + \eta_R^2 \omega_R^2)) \\ & = 0 \end{aligned} \quad (9)$$

3.3.4 Natural frequencies

Keeping only the main terms, this equation can be simplified as follows :

$$\begin{aligned}
 & p^6 \times (A^2 I^2) \\
 & + p^5 \times (2 A^2 I \eta) \\
 & + p^4 \times (A^2 H_R^2) \\
 & + p^3 \times 2 (A H_R^2 \eta + A^2 \eta K + A^2 H_R \eta_R \omega_R) \\
 & + p^2 \times (A^2 K^2) \\
 & + p \times (2 \eta K H_R^2) \\
 & + p^0 \times (H_R^2 K^2) \\
 & = 0
 \end{aligned}
 \begin{array}{l}
 \text{Rotor} \\
 \text{Nutation} \\
 \\
 \text{Rotor} \\
 \text{Precession} \\
 \\
 \text{Satellite} \\
 \text{Nutation}
 \end{array}
 \quad (10)$$

Assuming that there is no coupling between these 3 modes (their frequencies being quite different), their pulsations can be estimated by the formulae :

$$- \text{ satellite nutation} \quad \omega_0 = \frac{H_R}{A} \quad (11)$$

$$- \text{ rotor precession} \quad \omega_1 = \frac{K}{H_R} \quad (12)$$

$$- \text{ rotor nutation} \quad \omega_2 = \frac{H_R}{I} \quad (13)$$

Orders of magnitude :

$$\begin{array}{ll}
 A & = 4000 \text{ Kg} \times \text{m}^2 \\
 I & = 7 \times 10^{-2} \text{ Kg} \times \text{m}^2 \\
 H_R & = 50 \text{ Nms} \\
 \omega_R & = 850 \text{ rad/s} \\
 K & = 1000 \text{ Nm/rd}
 \end{array}
 \quad
 \begin{array}{l}
 \omega_0 \neq 1,25 \times 10^{-2} \text{ rad/s} \\
 \omega_1 \neq 20 \text{ rad/s} \\
 \omega_2 \neq 714 \text{ rad/s}
 \end{array}$$

identifying the coefficient of the above equation to those of :

$$(p^2 + 2 a_0 p + \omega_0^2) (p^2 + 2 a_1 p + \omega_1^2) (p^2 + 2 a_2 p + \omega_2^2)$$

we can calculate the damping ratio of each mode

$$\xi_i = \frac{a_i}{\omega_i}$$

For the satellite nutation mode we find :

$$\xi_0 = - \frac{H_R^2 \eta_R \omega_R}{K^2} \quad (14)$$

This damping ratio is negative, indicating a divergence of this mode

The time constant of this divergence is

$$T_0 = \frac{1}{|\omega_0 \xi_0|}$$

$$T_0 = \frac{A^2 K^2}{H_R^3 \eta_R \omega_R} \quad (15)$$

The damping ratio of the other two modes are positive, indicating a convergence of these modes :

$$\zeta_1 = \frac{\eta}{H_R} + \frac{\eta_R \omega_R}{K}$$

$$\zeta_2 = \frac{\eta}{H_R}$$

3.4 Physical analysis of the nutation divergence

a) the global kinetic momentum of the satellite can be split into two parts :

$$\vec{H}_T = \vec{H}_R + \vec{H}_S \quad (16)$$

(relative momentum of the rotor with respect to the stator) (momentum of the satellite structure with respect to the galilean reference)

As a first approach, we can consider that :

$$|\vec{H}_S| \ll |\vec{H}_R|$$

$$|\vec{H}_K| \ll |\vec{H}_R|$$

$$\vec{H}_S \perp \vec{H}_R$$

Neglecting the perturbation torques, \vec{H}_T is constant :

$$\frac{d\vec{H}_T}{dt} = 0 \Rightarrow \frac{d\vec{H}_S}{dt} = - \frac{d\vec{H}_R}{dt} \quad (17)$$

In a pseudo steady state, $|\vec{H}_R|$ and $|\vec{H}_S|$ can be considered as constant :

$$\frac{d\vec{H}_R}{dt} = \vec{\omega}_0 \wedge \vec{H}_R \Rightarrow \left| \frac{d\vec{H}_R}{dt} \right| = \omega_0 H_R \gamma \quad (18)$$

$$\frac{d\vec{H}_S}{dt} = \vec{\omega}_0 \wedge \vec{H}_S \Rightarrow \left| \frac{d\vec{H}_S}{dt} \right| = \omega_0 H_S \quad (19)$$

where ω_0 represents the nutation of the satellite ($\vec{\omega}_0$ is colinear with \vec{H}_T) and γ represents the angle between \vec{H}_K and \vec{H}_T

Combining (17), (18) and (19) we obtain the relationship :

$$H_S = \gamma H_R \quad (20)$$

b) The rotor is submitted to a torque $\vec{\Gamma}_R$ which is the resultant of :

- the restoring torque $K\varepsilon$ ($\vec{\Gamma}_K$)
- the damping torque $\eta_R \omega_R \varepsilon$ ($\vec{\Gamma}_a$, perpendicular to $\vec{\Gamma}_K$)
- the damping torque $\eta \dot{\varepsilon}$, colinear with $\vec{\Gamma}_K$, but much smaller, and which can be neglected.

$$\vec{\Gamma}_R = \vec{\Gamma}_K + \vec{\Gamma}_a \Rightarrow |\vec{\Gamma}_R| = \sqrt{K^2 + \eta_R^2 \omega_R^2} \varepsilon$$

$$|\vec{\Gamma}_R| \neq K\varepsilon \quad (21)$$

Since $\vec{\Gamma}_R = \frac{d\vec{H}_R}{dt}$, and comparing with (18) we obtain a relationship between ε and γ

$$\varepsilon = \frac{\omega_0 \gamma H_R}{K} = \frac{H_K^2}{AK} \gamma \quad (22)$$

The satellite is submitted to the torque $\vec{\Gamma}_S$

$$\vec{\Gamma}_S = -\vec{\Gamma}_R = \frac{d\vec{H}_S}{dt} = - \frac{d\vec{H}_R}{dt} \quad (23)$$

c) These torques are shown in fig. 8 where the vectors are projected :

- on the one hand, in a plane perpendicular to OZ
- on the other hand, in the plane (\vec{X}, \vec{Z}) .

Equations (19) and (23) show that \vec{H}_S is perpendicular to \vec{r}_S .

knowing K, η_R, ω_R and A which are characteristic data of the wheel and of the satellite, and ϵ being given, the triangle (H_R, Z, H_T) can be drawn without any ambiguity. This triangle keeps a constant shape as long as we consider that we are in a steady state and that we do not take into account the other two modes of the rotor (precession and nutation) which are decoupled from the nutation of the satellite which we are considering.

If we consider two positions of this triangle during one nutation period of the satellite which is 3-axis stabilized (see fig. 8) where the axes X and Y keep a constant direction), it appears that the relative motion of the rotor with respect to the stator is a rotation $\vec{\omega}_{rel}$ around OZ with the same rate as the nutation rate of the satellite, ω_o .

$$|\vec{\omega}_{rel}| = \omega_o$$

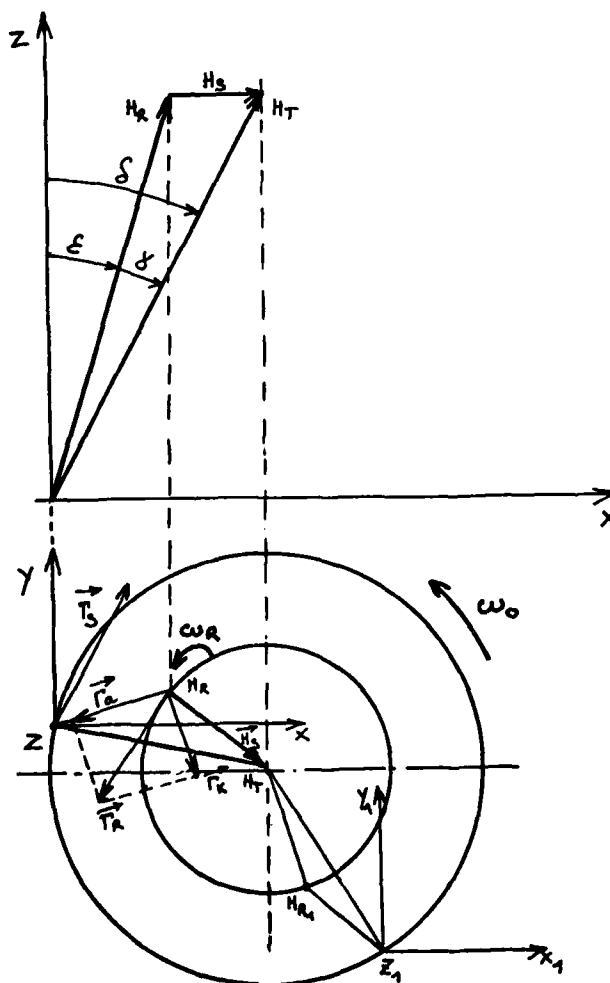


Fig. 8

- d) Let us calculate the power dissipated by the relative motion of the rotor with respect to the stator. This power is related to the damping torque \vec{T}_a and to the relative rotation rate $\vec{\omega}_{rel}$ by the relationship :

$$P_a = \vec{T}_a \cdot \vec{\omega}_{rel} = T_a \omega_o \epsilon > 0 \quad (24)$$

This shows that the mode is divergent since $P_a > 0$

$$P_a = T_a \omega_o \epsilon = \eta_R \omega_R \epsilon^2 \omega_o$$

$$P_a = \eta_R \omega_R \frac{H_R^5 \gamma^2}{A^3 K^2} \quad (25)$$

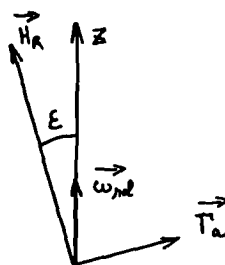


Fig. 9

- e) Let us calculate now the energy related to the nutation of the satellite :

$$E = \frac{1}{2} \left[A (p^2 + q^2) + Cr^2 \right] \quad (26)$$

where :

A = transverse momentum of inertia

C = axial momentum of inertia

p, q, r = coordinates of the rotation vector of the satellite with respect to X Y Z

r = 0 (the satellite is 3-axis stabilized)

$$p^2 + q^2 = \omega_o^2 \delta^2 \text{ (see fig. 10)} \quad (27)$$

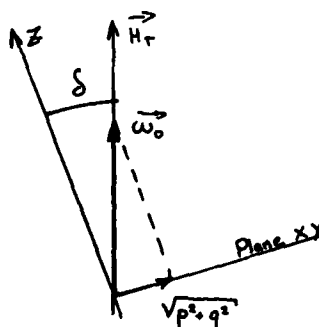


Fig. 10

Referring to fig. 8 and taking into account that $\varepsilon \ll \gamma$ (equation 22 $\rightarrow \varepsilon < \gamma/1000$) it appears that $\delta \approx \gamma$

$$p^2 + q^2 \approx \omega_o^2 \gamma^2 \quad (28)$$

$$E = \frac{1}{2} A \omega_o^2 \gamma^2 = \frac{1}{2} \frac{H^2 \gamma^2}{A} \quad (29)$$

f) On the other hand we have :

$$P_a = \frac{dE}{dt} = \frac{H^2 \gamma}{A} \frac{d\gamma}{dt} \quad (30)$$

Assuming $\gamma = \gamma_o \exp(-t/T_o)$, we have :

$$\frac{d\gamma}{dt} = -\frac{\gamma}{T_o} \quad (31)$$

$$P_a = -\frac{H^2 \gamma^2}{A T_o} = -\frac{2 E}{T_o} \quad (\text{see equation 26})$$

$$T_o = \frac{2 E}{P_a} \quad (32)$$

Combining with equation (25), we obtain :

$$T_o = \frac{H^2 \gamma^2}{A} \frac{A^3}{\eta_R \omega_R H_R^5 \gamma^2} \quad (33)$$

$$T_o = \frac{A^2 K^2}{\eta_R \omega_R H_R^3} \quad (34)$$

which confirms the equation 15 of § 3.3.3.

3.5 Order of magnitude of the time constant of the nutation of the satellite

When the satellite is fixed and the wheel not rotating, the equation of the tilting motion of the rotor can be simplified as follows :

$$I \ddot{\varepsilon} + \eta \dot{\varepsilon} + K = 0$$

where I is the transverse momentum of inertia of the rotor of the wheel.

The damping ratio ζ_R is related to η by the relationship

$$\eta = 2 \zeta_R \sqrt{KI}$$

Tests results obtained on available wheels show that :

$$0.01 < \zeta_R < 0.03$$

Assuming :

$$K = 1000 \text{ Nm/rad}$$

$$I = 12 \times 10^{-3} \text{ Kg.m}^2$$

we have :

$$0.17 < \eta_R < 0.51 \text{ (Nm/rad/s)}$$

On the other hand, the Aerospatiale wheels are designed such that the energy dissipated in the rotor is minimized :

$$\eta_R \approx 0.02 \eta \rightarrow 3.4 \times 10^{-3} < \eta_R < 0.01 \text{ (Nm/rad/s)}$$

Assuming $A = 4000 \text{ Kg} \times \text{m}^2$ and $\omega_R = 830 \text{ rad/s}$, we can calculate :

$$15.4 \times 10^6 \text{ s} < T_o < 45 \times 10^6 \text{ s}$$

$$182 \text{ days} < T_o < 546 \text{ days}$$

This time constant is quite long, and the nutation of the satellite will never be perceived.

4. AIR BEARING TESTS

The Aerospatiale magnetic bearing momentum wheel RCPM50 was subjected to dynamic tests on an air bearing platform performed at the DFVLR in Oberpfaffenhofen, Germany. Due to the very low friction torques produced by an air bearing, the platform and thus the payload mounted on it, is free to move about its center of mass with very low damping. Therefore this test facility allows the experimental verification of the small nutation divergence effect produced by the flywheel.

It is quite obvious, that in order to identify the respective parameters, one has to know very exactly the properties of the measurement system. Therefore a large amount of time must be spent in preparing the test. To begin with, in the following paragraph, a short description of the test set up will be given.

4.1 Test Set up

To reduce aerodynamic losses the wheel has to be operated under low pressure. For this purpose a special vacuum chamber was constructed at the DFVLR, which for reasons of weight reduction was manufactured from aluminium. By carefully sealing the chamber, the wheel could be tested for several hours without exceeding the specified pressure level of $4 \cdot 10^{-2}$ mbar.

The platform, where the wheel with vacuum chamber, electronic boxes and pack of NiCd batteries were mounted, is shown in Fig. 11. Its basic configuration was adopted from the test specifications developed by DFVLR and MBB for the INTELSAT V attitude control system. There the moment of inertia ratio pitch vs. transverse axes was required to be less than unity. For this purpose large booms were attached to the platform in vertical direction. The bearing itself is of the monoflow type (3). It consists of a steel ball underneath the platform and the spherical counterpart mounted on a ground-fixed pedestal. By pumping highly pressurized air into the central inlet hole, an air cushion is generated between ball and bearing supporting the whole platform.

For initial excitation of the platform motion, an integrated system of cold gas jet thrusters was used. The gas supply, a set of air pressure bottles, is arranged underneath the mounting surface of the platform in a configuration, so that the center of mass shift due to gas unloading and thus gravity-induced disturbance torques are nearly zero.

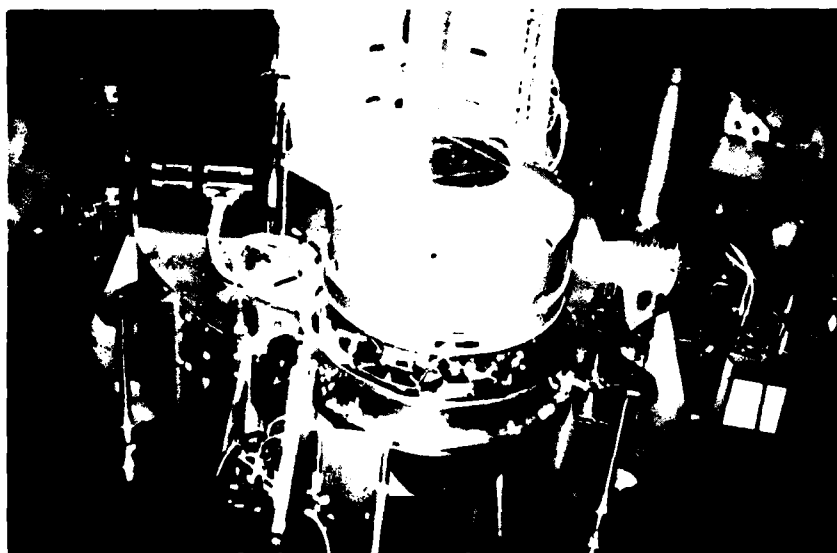


Fig.11 Air bearing platform

As no telemetry system was available, the data transfer to the ground had to be done via flexible wires. They were fixed very near to the center of rotation of the platform, to keep spring restraint and damping forces to a minimum. In this way the damping influence of the wires could no more be detected when comparing the pendulous motion of the platform with and without them.

The attitude measurement of the platform had to be very accurate, as only small oscillation amplitudes are permitted. This is due to the restraint forces of the flexible wires and the bending of the platform itself. Therefore high resolution optical sensors have been utilized, which operate according to the collimator principle, where the photocathode of a multiplier system is arranged in the focussing plane of the optical system. They were fixed to the ground on special pedestals and focussed on platform-fixed mirrors.

The testing equipment comprised various data acquisition devices, which are shown in the block diagram Fig. 12. The data to be evaluated are wheel speed, relative motion of the wheel and the platform oscillation. Wheel speed can be derived from the commutator pulses of the motor by a frequency counter.

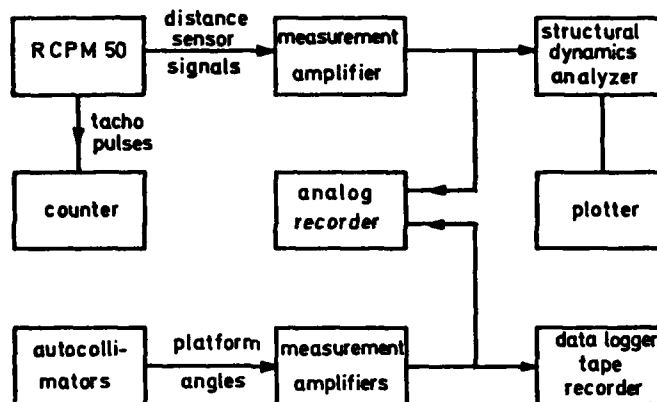


Fig. 12 Block diagram of data acquisition

The relative wheel motion was indicated by a distance sensor especially provided for test purposes. It was mounted opposite to the lower part of the wheel. As only one sensor was installed, a separation of translational from tilt motion was not directly possible. Additionally, due to residual balancing errors of the wheel, the sensor signal also contained speed information. But the different components could be identified as the pertaining frequency bands were clearly different.

On-line data handling was provided by a structural dynamics analyzer and was used for the investigation of the relative wheel motion. Due to reasons mentioned below it was evaluated separately by the so-called fixed base tests which will not be described in detail here.

For the very low frequency platform oscillation, an off-line evaluation of the measurement data was preferred. The data were comprehended by a data logger and registered on a magnetic tape recorder. The evaluation was performed on a digital computer, where a fast Fourier analysis program was utilized completed by special damping evaluation procedures.

4.2 Calibration Procedures

As the effects to be detected are very small, adequate calibration of the whole test facility was necessary. To begin with, the wheel axis and the attitude sensors were accurately aligned, parallel to a reference system, by means of optical instruments.

Secondly, the platform center of mass had to be shifted towards the center of rotation to minimize gravity-induced disturbance torques. For balancing the platform, a torquing closed loop was used, consisting of coils attached to the fixed frame in front of permanent magnets mounted on the platform. A correct balance is obtained when the current in the coils which is necessary to keep the platform horizontal is equal to zero. But this method allows only for balancing in the horizontal plane. In the vertical direction this is not necessary. It is sufficient to have a pendulous restraint torque yielding a platform precessional frequency well below the platform nutation ("gyrostat") frequency. The ratio of these frequencies was adjusted to be at least 15, referring to the total range of wheel speeds to be commanded.

This turned out to be an advantage, since with a pendulous restraint torque the platform motion is less sensitive to balancing errors. Another aspect is the effect of orbital rate simulation generated by the pendulous torque. It allows a scaled simulation with the true ratio of satellite nutation with respect to orbital rate thus ensuring realistic simulation conditions (2).

In addition to these static adjustment procedures, dynamic coupling effects also have to be considered. These effects are introduced, if the principal moment of inertia axes are not coincident with the reference axes. As for an axis distortion about the vertical (pitch) axis, it does not affect the results, since only frequency and damping of the platform oscillation are of interest. It is different, if the vertical axis is not a principal axis of inertia, since during the tests, the platform remained caged about that axis preventing it from drifting out of the field of view of the optical sensors. Thus any residual dynamic coupling into pitch axis would cause a portion of the nutational energy to be dissipated in the caging loop.

The calibration of this effect is performed with wheel running, while the pitch caging loop contains only a proportional feed-back thus being completely undamped (Fig. 13).

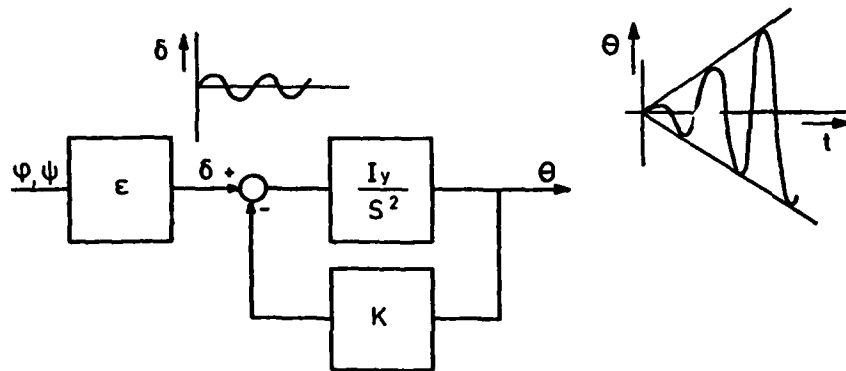


Fig. 13 Block diagram dynamic calibration

The feedback gain, K , is defined such that the caging loop is in resonance with the platform nutation frequency. If a dynamic coupling from roll (ϕ) and yaw (ψ) into the pitch axis, denoted by ϵ , is present, the pitch angle θ will start to oscillate with increasing amplitude. The envelope of this motion is a ramp, the slope of which depends directly on the coupling factor ϵ . The phase relations allow a direct association to the respective transverse axis being coupled with pitch. The sensitivity of this balancing method is limited by the disturbance torque influence, which makes the identification of the ramp slope impossible, if the dynamic coupling is too weak. The experimental results indicate that the cross-product of inertia to be identified is less than 1%, relative to the maximum moment of inertia. This seemed sufficient since residual damping introduced by this coupling is equivalent to a time constant of 20 hours, which is much greater than the contribution of the air damping effect being discussed in the next paragraph.

4.3 Measurement Results

During the tests with the oscillating air bearing platform, no wheel precession could be detected. Therefore, the relative motion of the rotor was investigated separately (refer to paragraph 4.1). By the determination of the eigenvalues from the time record of the platform attitude angles (platform nutation and precession) a mathematical model of the system could be verified. It turned out, that, due to the limited moment of inertia of the platform, coupling terms between the oscillation modes as described in chapter 3 had to be taken into account to some degree. In addition, air damping in the laboratory had to be included in the analysis. Thus the basic equations for a parameter identification have to be modified to the following form

$$\omega_o = \frac{H_R}{A} \left(1 - \frac{H_R^2}{A \cdot K} \right) \quad (35a)$$

$$\zeta_o = \frac{\eta_R \omega_R^4 J_R^3}{A^2 \cdot \bar{K}^2} - \frac{d_a}{A} = \frac{R}{A} \frac{R}{K^2} - \frac{d_a}{A} \quad (35b)$$

where $\bar{K} = K + 2 \frac{H_R^2}{A}$

and J_R = rotor moment of inertia about the rotor axis

d_a = air damping coefficient

$$\omega_o \zeta_o = \frac{1}{T_o} = \text{"damping" (divergence-) eigenvalue}$$

From equation (35b) it is clear that although the platform nutation is damped by the atmospheric environment, this damping effect decreases with increasing energy losses in the rotating parts of the wheel (first part of Eq. 35b). Therefore a parameter identification of either parameter is possible from this relation. Similarly in Eq. 35a, we have an increasing nutation frequency with increasing wheel speed, which on the other hand is influenced by a decreasing term due to the finite stiffness K of the wheel. Thus, this relation can be used to identify the parameters A and K . It should be noted that the items describing the platform characteristics, i.e. the moment of inertia A and the air damping coefficient d_a , had been identified additionally in a preliminary test where the wheel was not running and just the pendulous motion of the platform was observed.

For example, the platform response in roll with $H_R = 35$ Nms and $H_R = 51$ Nms is shown in Fig. 14. Two oscillations are clearly to be identified. In addition to the nutation there is a nearly undamped platform precession with a relatively long period resulting from the shift center of mass vs. center of rotation. Concerning the parameter identification from the measured frequencies, it can be shown that for weakly coupled oscillation modes a decoupled frequency can be computed by simply subtracting the precessional from the nutation frequency (1). At least this is true to the degree of measurement accuracy, if the respective frequencies are about one order of magnitude apart from each other. This was fulfilled as shown in Fig. 15, where the result of the Fast Fourier Transformation of the platform roll angle is presented, the wheel angular momentum being 51 Nms. The plot in Fig. 16 confirms, that the pitch axis is almost completely decoupled from roll/yaw and that there is practically no energy flow into the pitch axis caging loop. Anyhow from Fig. 14 it can be seen that the platform nutation is damped, but for an angular momentum of 51 Nms obviously the air damping and the divergence effect due to rotor losses are nearly equal.

The evaluation results are shown in the next two graphs. In Fig. 17, a curve fit to the measured frequencies is shown yielding a least square fit confidence level of very

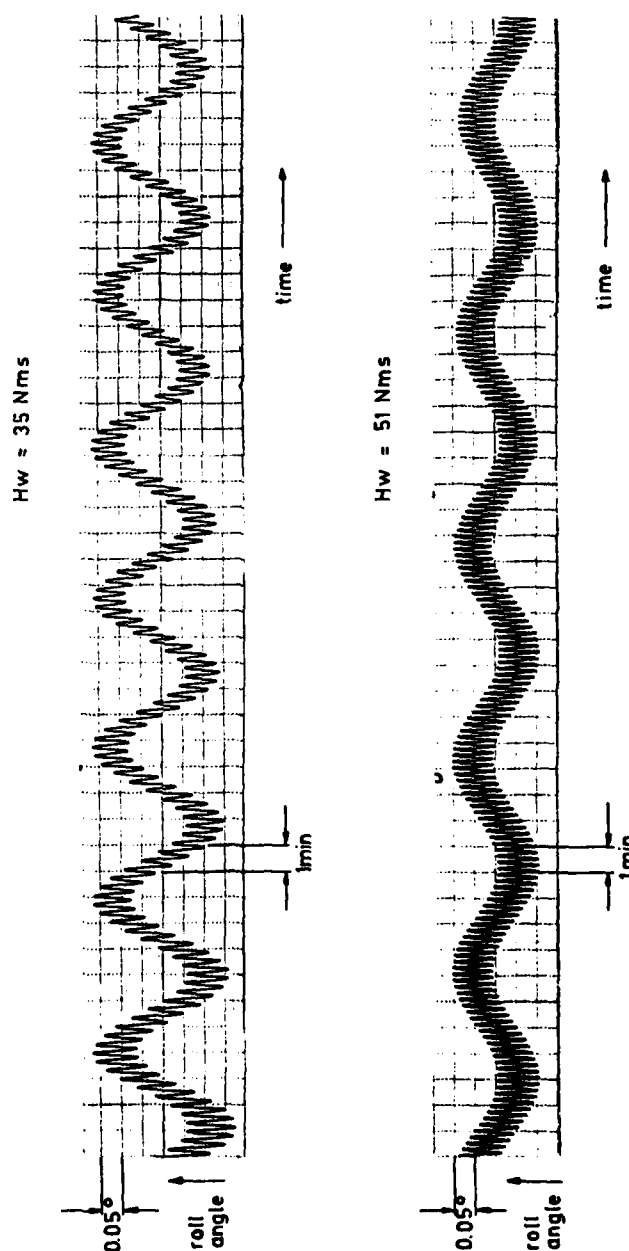


Fig. 14

Air bearing table response, roll axis

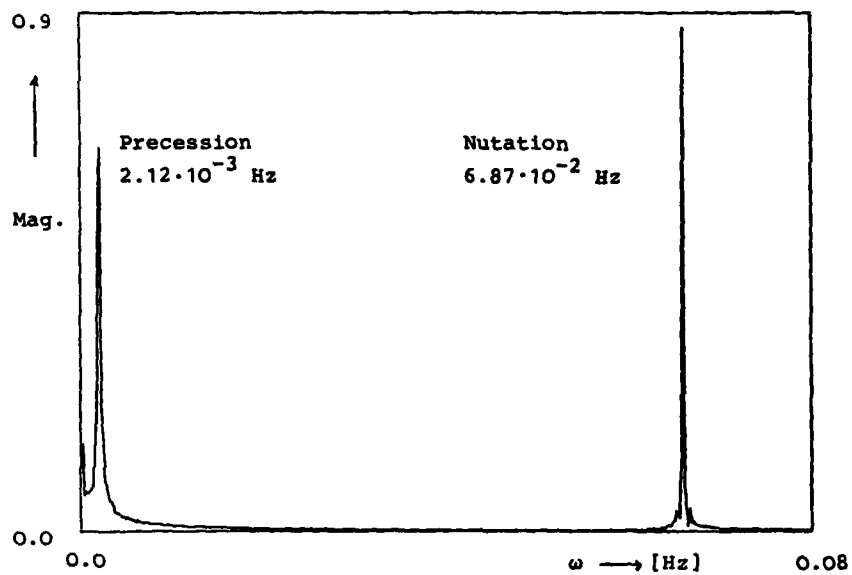


Fig. 15 Linear spectrum, roll axis $H_w = 51$ Nms, $= 1.9 \cdot 10^{-4}$ Hz.

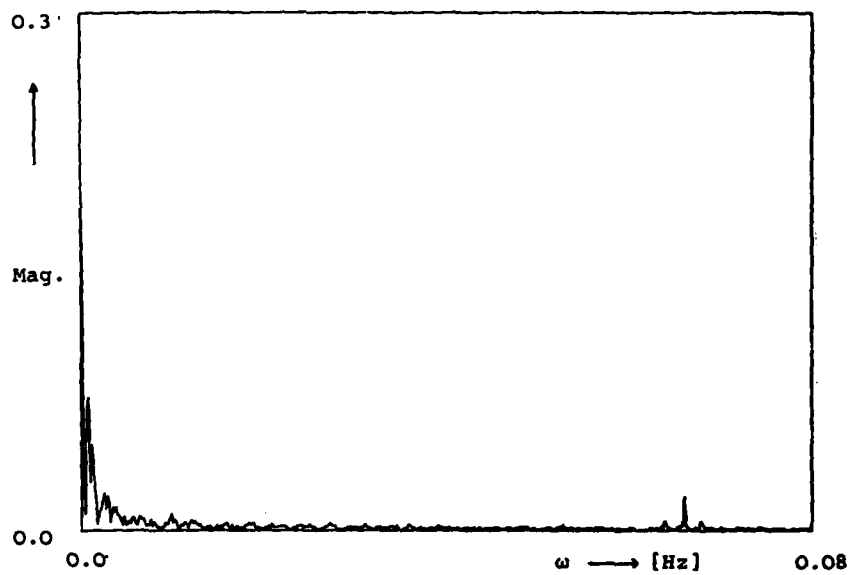


Fig. 16 Linear spectrum, pitch axis $H_w = 51$ Nms, $= 1.9 \cdot 10^{-4}$ Hz.

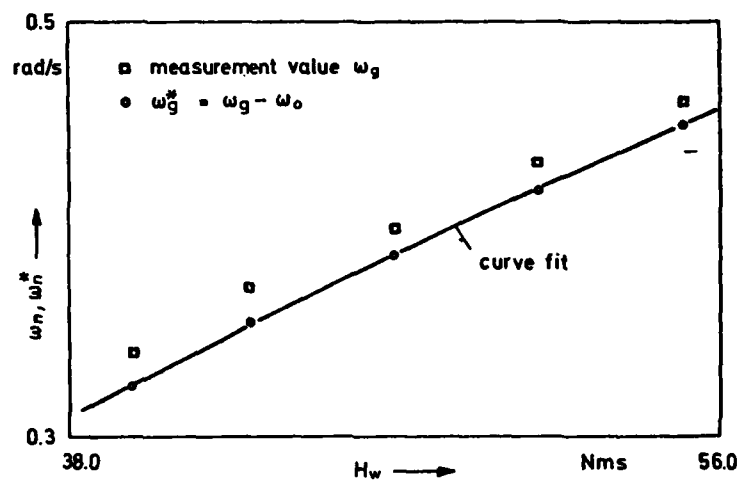


Fig. 17 Test results, air bearing table nutation frequency

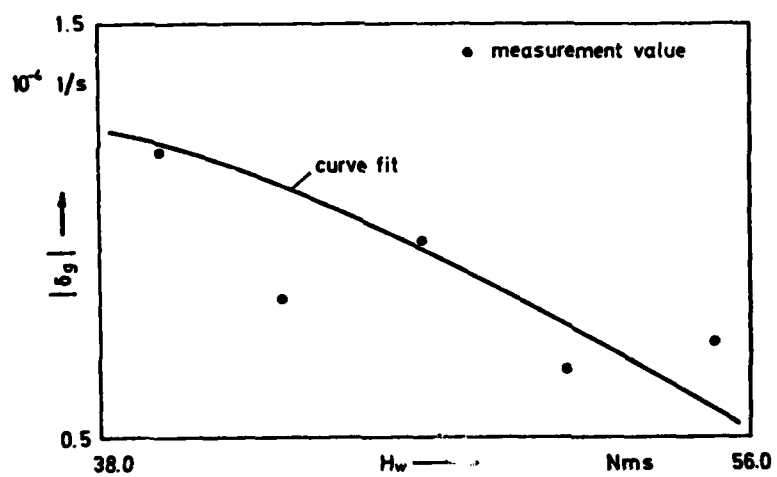


Fig. 18 Test results, air bearing nutation damping

nearly 1.0. The parameters, which have been extracted are :

$$A = 118.9 \text{ kgm}^2$$

$$K = 901.3 \text{ Nm/rad}$$

The damping factor evaluation was as to be expected not quite as good. The result is plotted in Fig. 18 ; the pertaining confidence level was 0.66. The parameter identification yields :

$$\eta_R = 0.7 \cdot 10^{-2} \text{ Nms}$$

$$d_a = 1.7 \cdot 10^{-2} \text{ Nms}$$

In any case, the value of η_R appeared to be comparable to that being extracted from the fixed base tests, which naturally is also the case for the stiffness parameter K. Thus, according to the parameter values identified, we may extrapolate according to Eq. 35, what the time constant would be for an INTELSAT-size modern telecommunication satellite. Assuming a transverse moment of inertia of 4000 kgm² and nominal wheel speed equivalent to H = 50 Nms, the divergence time constant would be 150 days, which is in the order of the approximative estimation from chapter 3.5.

5. CONCLUSIONS

The dynamic analysis revealed that, due to eddy current losses in the rotor, restoring forces lagging behind the spin axis deflection are generated. By physical analysis, it was shown that these forces generate an instable satellite nutation motion. The approximative estimation of the pertaining divergence time constant, referring to a satellite of the INTELSAT size, shows that this effect is so small, that it can hardly be detected. The results from the analysis have been confirmed by an experimental verification on an air bearing platform.

Literature

- (1) HEIMBOLD G. Final Report
LANGE Th. Test on the Magnetic Bearing Momentum Wheel.
RCPM 50 Manufactured by AEROSPATIALE, France
DFVLR, Oberpfaffenhofen, Germany, 1980.
- (2) LANGE Th. Luftlagersimulation des Kreiselkompassseffektes
bei einem Satelliten-Lageregelungssystem mit
Schwungrad.
Oberpfaffenhofen, DFVLR-IB
552/76-23.
- (3) ROELKER A. Der Satellitenbewegungssimulator in der DFVLR
Oberpfaffenhofen.
DLR-Mitt. 69-20
- (4) LAURY L. Comportement dynamique d'un satellite équipé
MALLE J. d'une roue cinétique à paliers magnétiques
CHARRON M. AEROSPATIALE Report (MU/ESS 33028/76).
- (5) BURELLO M. Essais dynamiques d'une roue cinétique à
TORRES M. paliers magnétiques.
CNES Report (79/CT/PRT/SST/SS/014).
- (6) LACOMBE J.L. Study of OTS 2 in flight behaviour nutation
interaction with momentum wheel.
MATRA Note (30/1357).
- (7) COCHET J.P. La roue cinétique pour la stabilisation des véhicules
BURELLO M. de Telecommunications futurs.
TORRES M. CNES-DGT-TDF
Colloque International - Toulouse (France) 5-9 Mars 1979.

AUTONOMOUS ATTITUDE DETERMINATION FROM STAR DATA FOR A DUAL-SPIN PLANETARY SPACECRAFT

by
Edward C. Wong and John Y. Lai
Members of Technical Staff
Jet Propulsion Laboratory
California Institute of Technology
4800 Oak Grove Drive
Pasadena, California 91109

SUMMARY

An entirely autonomous attitude determination algorithm for a dual-spin planetary spacecraft has been developed. A batch mode process which identifies three reference stars within a rotor-mounted star scanner's field-of-view based on the criteria of intensity and geometry is established. The sequential mode which continuously tracks the reference stars provides star transit times and estimates of rotor's spin rate. A least-squares estimator is formulated which sequentially determines the spacecraft's attitude from successive star crossings by minimizing the error in the star and scanner slit normal orthogonality. This spacecraft attitude also provides intermittent updates for the gyro propagated inertial attitude of the despun science platform. Simulation results are presented, showing successful star identification and attitude convergence in the presence of nutation and star transit time uncertainty.

1. INTRODUCTION

The concept of a star-mapping technique onboard a spin-stabilized vehicle for attitude determination has been designed and successfully implemented in various earth-orbiting satellites [Ref. 1-4]. It involves a star scanner mounted on the rotating section of the spacecraft for data collection. The algorithms for determining the attitude are basically star identification and attitude estimation using the techniques such as direct match, angular separation, phase match and discrete attitude variation [Ref. 5]. Their applications depend on the scanner design, output data format, computing capability and a priori attitude information. However, the essential function is to associate the observed data to stars recorded in a star catalog. From the scanner observations which relate the spacecraft reference frame to the star positions in inertial space, the spacecraft attitude can be evaluated. The attitude estimator takes on a variety of forms from a simple deterministic approach to a complicated stochastic minimization algorithm with multidimensional spacecraft dynamic model. The choice depends on the required accuracy as well as the available computing capability. The concerted operations of these two processes can determine the spacecraft attitude in any orientations with little or no a priori attitude information.

Due to the complexity of these algorithms, the star-mapping techniques have been applied mostly to earth orbiting satellites where ground communication support is available. In an earlier application for the Project Scanner, manual sorting of star transit time pairs is required. Other systems such as the Application Technology Satellite (ATS-C), Orbiting Solar Observatory (OSO), and the NASA Multimission Modular Spacecraft (MMS) use a wide variety of instruments, reticle designs and attitude determination software implementation where limited ground base support is still necessary. The Pioneer mission to Venus employed an extensive star-mapping and attitude determination (AD) algorithm using the sun and two stars as celestial reference. However, the entire processing is performed on ground using onboard sensor telemetry. The estimated attitude is then uplinked to the spacecraft for attitude control.

For outerplanetary missions, autonomous onboard AD is required because of mission complexity and communication time delay. One innovative feature of such AD system is the capability to determine the absolute spacecraft attitude with respect to a fixed celestial-referenced frame by onboard processors without explicit prior attitude knowledge and ground support. Such design concept has been realized in the development of a spacecraft for the NASA's Galileo (GGL) mission to Jupiter. The spacecraft configuration is shown in Fig. 1. It consists of a spinning section (rotor) that carries a high gain antenna for earth communication, two radioisotope thermoelectric generators (RTGs) for power supply and a magnetometer boom for measurement of magnetic fields. The spacecraft also consists of a despun section (stator) and an articulated scan platform that provide celestial pointing for the science instruments. The spacecraft's inertial attitude is determined by a V-slit star scanner mounted on the rotor. Accurate pointing is aided by a pair of gyros located on the scan platform.

The paper is organized as follows: in Section 2, the overall attitude determination functional interfaces are described. The sensor hardware typically used for celestial pointing are reviewed in Section 3. The batch and sequential star identification algorithms are described in Section 4 and formulation of the attitude estimator is presented in Section 5. Scan platform attitude propagation and update procedures are described in Section 6. In-flight calibration procedures are outlined in Section 7. Section 8 presents the computer simulation results of the attitude determination scheme only from star scanner data. Conclusions are given in Section 9.

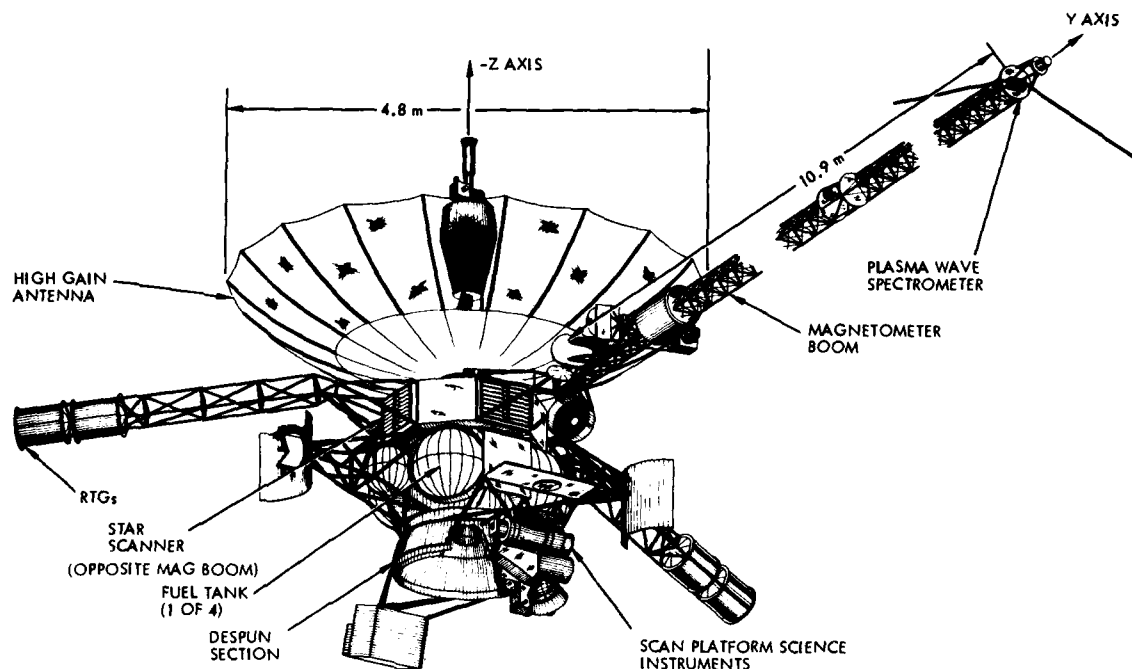


Figure 1. Galileo Spacecraft (Deployed Configuration)

2. ATTITUDE DETERMINATION FUNCTIONAL OVERVIEW

The star scanner generated data are processed by two distinct onboard algorithms to provide the spacecraft attitude in inertial coordinates, such as the Earth Mean Equatorial system of 1950 (EME50). These algorithms are the Star Identification Algorithm (SID) and the Attitude Estimator (AE).

Two modes of the SID algorithm: batch and sequential, are designed to operate in sequence. Two revolutions of star data are required before the batch mode processing can be initiated. The batch SID operates on the data to identify three reference stars through correlation of their angular separations and intensities with data in a star catalog. Coarse spin rate estimate, provided by the acquisition sun sensor, can be refined from the periodic pattern of the star data recorded in the two revolutions. The sequential SID is for continuous tracking of the three reference stars defined in the batch mode. It operates on the principle of prediction and confirmation. A time range of the star crossing event is predicted, and the data within the predicted range is processed to confirm the occurrence of the star.

Spacecraft attitude information is needed for real-time onboard control algorithms such as high gain antenna pointing, scan platform pointing, and initializing command turns. The purpose of the AE is to sequentially determine the spacecraft attitude and angular momentum vector (H) in the inertial space from the data of each star transit.

The scan platform's inertial attitude specified in quaternions is propagated by a gyro integrator algorithm from the gyro's incremental position outputs. The propagated attitude contains drift due to the inherent truncation and roundoff errors in the quaternion integration routine. Hence, an onboard algorithm is required to update the inertial referenced platform quaternions from star data.

The AD system of the Galileo spacecraft is depicted by the functional block diagram in Fig. 2. For attitude re-acquisition after spacecraft maneuvers, the autonomous AD procedures are initiated starting from the batch mode SID to acquire a new set of three stars. The time sequence of the AD execution is shown in Fig. 3. For the Galileo spacecraft, the total time for initial attitude acquisition takes approximately 4-8 minutes. The relative difficulties in interpreting the star data increase as the spacecraft motion deviates from pure spin. Combination of nutation and wobble effects will degrade the performance of the SID and the AE. Consequently, the attitude determination algorithms are executed only after these adverse dynamical effects have been damped or controlled.

3. SENSORS

Rotor mounted star scanner (Fig. 4) is widely employed as celestial sensing element for spin stabilized spacecraft. Examples are BBRC CS-20 and Bendix GLL Star Scanner Assembly. It consists of a set of refractive optics which project the star field images onto a V-slit reticle (Fig. 5). One of the slits, known as the clock slit, will provide the clock positions of the stars detected in the spacecraft body frame. It is, in general,

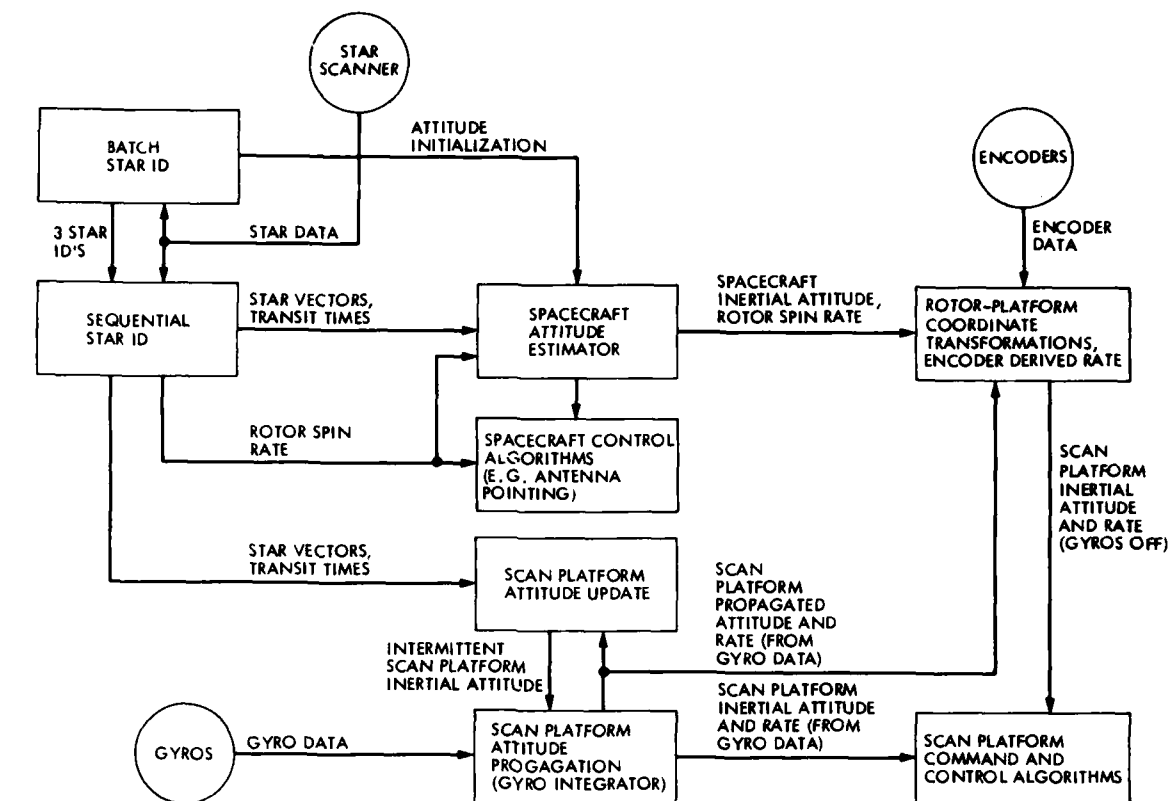


Figure 2. Block Diagram of Attitude Determination from Star Data

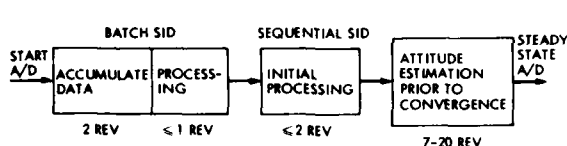


Figure 3. Sequence of Attitude Initialization

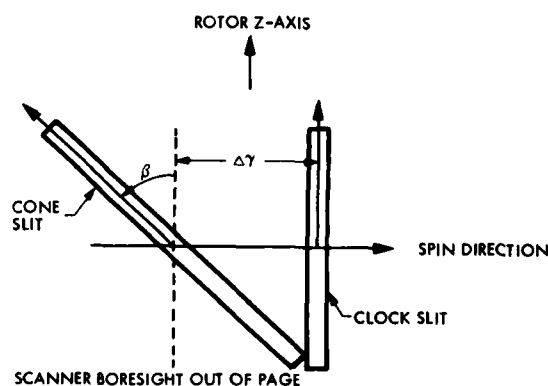


Figure 5. Star Scanner Slit Configuration

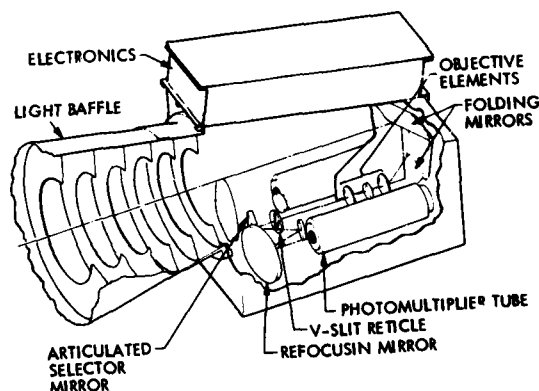


Figure 4. Beadix GLL Star Scanner Assembly

aligned tangentially to the meridian of a celestial sphere with the poles along the spin axis. The other, termed the cone slit, is slanted with respect to the former to provide the cone positions of the stars. A coincidence pulse pair is generated whenever a star is scanned through the V-slit detector. The magnitudes as well as the time of crossings corresponding to a reference clock are recorded for processing. The time difference between pulses of a pair indicates the star cone angle while the relative clock angle

between any two stars can be evaluated from the difference between the two clock slit transit times. These computations require that spin rate information be available. In general, spin rate can be determined based on the repetitive star pattern over several revolutions. Frequently, an a priori estimate of spin rate for initialization comes from a different sensor, e.g. sun sensor or gyro. A sun sensor may operate inefficiently for rate determination when the spacecraft -- sun line is within 5° from the spin axis. This may often be true for outerplanetary missions when the high gain antenna boresight

which lies along the spin axis is aimed towards the Earth for communication. However, for a dual-spin spacecraft, encoders can be used in conjunction with stator-mounted gyros for spin rate determination by measuring the relative clock position between the rotor and stator and the stator rate as sensed by the gyros.

4. STAR IDENTIFICATION

There are two modes involved in the SID algorithm: batch and sequential. The batch mode is executed when there is no a priori attitude information available. From two revolutions of recorded data, a coarse attitude can be evaluated along with a spin rate estimate. Three reference stars are also defined based on various criteria for subsequent tracking by the sequential mode. The sequential mode will then continuously track the defined stars by confirming their occurrences within the time window predicted. However, it can also be initiated independently to track three ground selected reference stars within the scanner FOV (Field-of-View).

4.1 Batch Star Identification

The batch SID identifies three reference stars by comparing the data to a star catalog. A nominal set containing about 200 stars which are within the detecting capability of the scanner should provide enough candidates for tracking at any attitude. Three major operations are performed by this algorithm, namely, star pair selection, spin rate determination and star matching.

(a) Star Pair Selection

Star data containing magnitudes and transit times information for both clock and cone slits are recorded sequentially in a stack register according to their time order of detection. A procedure based on magnitudes and elevation angles is commenced for pairing two star pulses corresponding to the clock and cone slit transits. To determine if two consecutive pulses ($i, i+1$) are recorded from the same star, a relative intensity check is executed which is defined by the following inequalities,

$$\begin{aligned} \alpha I_{AVG} &\leq I_i \leq \frac{1}{\alpha} I_{AVG} \\ \alpha I_{AVG} &\leq I_{i+1} \leq \frac{1}{\alpha} I_{AVG} \\ I_{AVG} &= (I_i + I_{i+1})/2 \\ \alpha &< 1 \end{aligned}$$

where I denotes the pulse intensity and α is the relative intensity measurement accuracy. If both intensities are within bounds, an elevation angle test is performed. From the transit time difference between pulses, the star elevation angle E_i relative to the rotating body of spacecraft can be evaluated as

$$\begin{aligned} E_i &= \tan^{-1} \{ k_1 \sin [\omega(t_{i+1} - t_i)] - k_2 \cos [\omega(t_{i+1} - t_i)] \} \\ k_1 &= \frac{\cos(\Delta r)}{\tan \beta} \\ k_2 &= \frac{\sin(\Delta r)}{\tan \beta} \end{aligned}$$

where k_1, k_2 are constants determined from the scanner mounting configuration, [Ref. 6]. ω is the spin rate and t_i, t_{i+1} are pulse transit times, Δr and β are angles as shown in Fig. 5. The angle computed should be within the scanner cone FOV. However, when there is a large initial spin rate uncertainty, the FOV criterion should be increased accordingly to avoid deleting any valid star pair. If both tests are satisfied, the two pulses are assumed to be a valid star pair by assigning a confidence index J of 1, otherwise, an index of 0 is assigned. An ideal sequence of J should contain only alternating 1s and 0s. However, there can be ambiguous situations when more than two pulses of equivalent magnitudes are grouped together, thereby, satisfying both tests. To select the more probable pairs, magnitude differences between two consecutive pulses within the group are evaluated. The pair with a smaller magnitude difference when compared to the following pair will be chosen. The confidence indices for such pairs are reduced to ensure a lower probability for being chosen as star matching candidates. The index is computed as

$$J = A(1 - e_1/e_2) \quad \text{for } e_1 \leq e_2 \quad \text{and} \quad A < 1$$

where

$$\begin{aligned} e_1 &= |I_i - I_{i-1}| \\ e_2 &= |I_i - I_{i+1}| \end{aligned}$$

If $e_1 > e_2$, proceed to check I_i, I_{i+1}, I_{i+2} with e_1 and e_2 redefined accordingly. To choose unambiguous bright stars which are not close to the edge of the scanner FOV, each possible pair with $J \neq 0$ is assigned a point rating P as follows

$$P = C \times J \times (1 - M/7)$$

where

$$C = \begin{cases} C_1 & \text{if } |E| < \text{FOV} - 1^\circ \\ C_2 & \text{otherwise} \end{cases}$$

and

$$C_1 > C_2$$

M is the averaged magnitudes of the pair computed as

$$M = -2.5 \log_{10} (I_{\text{AVG}}/IR)$$

where IR is a reference intensity greater than the brightest star recorded.

(b) Spin Rate Determination

Spin rate is determined from the periodic pattern of the stars in terms of magnitudes and elevation angles. Magnitudes recorded for the same star over two revolutions should be within the relative intensity measurement accuracy, or

$$\alpha I_i \leq I_k \leq \frac{1}{\alpha} I_i$$

The difference in elevation angle should be within the limit of residual nutation and wobble angle of θ_e as

$$|E_i - E_k| \leq \theta_e$$

Each pair (i) is checked against all other pairs (k) following it according to the two criteria. When both tests are satisfied, the difference in clock slit transit Δ_k is recorded where $k = 1, 2, \dots, N$ for some N . Let m_k be the number of times that Δ_k satisfies the criterion

$$|\Delta_k - \Delta_n| < \Delta t \quad k, n = 1, 2, \dots, N \quad k \neq n \quad (4.1)$$

The Δt limit should reflect the maximum variation in spin rate between revolutions and the clock measurement accuracy of the scanner. Let m_{max} be the maximum value of m_k , $1 \leq k \leq N$, the Δ 's that correspond to m_{max} are averaged to determine the spin rate. With the improved spin rate, the procedures given in section (4a) are repeated for one revolution of data. After the points P have been evaluated, the top four pairs are chosen as matching candidates for comparison with the star catalog.

(c) Star Matching

The four candidates are compared to a star catalog based on the absolute magnitude and angular separation test. For the i -th candidate, a magnitude compatible star set (i) is defined with its elements satisfying the constraint

$$r I_{im} \leq I_{kc} \leq \frac{1}{r} I_{im}$$

$$r < 1$$

where I_{im} is the measured magnitude of the i -th pair and I_{kc} is the cataloged magnitude of the k -th star and r is the absolute magnitude measurement accuracy of the scanner. The angular separation between two candidates (i,j) is computed as

$$X_{ij} = \cos^{-1} (\underline{SB}_i \cdot \underline{SB}_j)$$

where \underline{SB} is the measured star vector expressed in the spacecraft body frame and evaluated from the clock and cone angle measurements. Similarly, the angular separation for any two stars (k, l) corresponding to the compatible set (i,j) respectively is computed as

$$X_{kl} = \cos^{-1} (\underline{SC}_k \cdot \underline{SC}_l)$$

where \underline{SC} is the star vector expressed in EME50 from the catalog. The difference between these two angles

$$e_x = |X_{ij} - X_{kl}|$$

is then checked to ascertain if it is less than the criterion Δ_x given as

$$\Delta_x = 2 \times \eta \times \sin(2\epsilon/3) + 2 \times \phi \times \sin(\epsilon/2) + v$$

where ξ is the clock angle separation between star i and j , η is the nutation angle, ϕ is the wobble angle and v is the measurement uncertainty introduced by the scanner [Ref. 6]. All possible combinations of the elements in the four sets are tested for angle compatibility while a point rating scheme is evaluated to determine the best matching combination. It is computed as

$$\text{POINT} = \sum_{i=1}^4 (P_i \times D_i) \{TR + 1\}$$

where D is the number of pair matches for the i -th star and TR is the number of triangle matches for the combination. The matching combination with the maximum rating is considered to be the correct identification if there is at least one triangle match. From the matching combination, three stars which establish a triangle with the lowest distribution index λ are chosen as references. The index is defined as

$$\lambda = |(S_1 \cdot S_2)(S_2 \cdot S_3)(S_3 \cdot S_1)| \quad 0 \leq \lambda < 1 \quad (4.2)$$

to ensure large angular separations among the stars for improved performance of the AD estimator.

4.2 Sequential Star Identification

The sequential mode can only search for the three defined reference stars based on the concept of prediction and confirmation. A time window is predicted within which a particular star is expected to be observed. All pulses within the window are checked for magnitude and elevation angle compatibility with the expected star to confirm its occurrence. This operation is performed sequentially in real time. When a star is confirmed, the transit time information is routed to the AD estimator for attitude update. If confirmation cannot be achieved, the next star will be considered. Two stages of operation are involved: search phase and output phase.

(a) Search Phase

Since the sequential SID is designed to allow initialization independent of the batch SID, timing synchronization between the actual star transit and the algorithm is required for prediction. To locate the $i = 1$ reference star, all recorded pulses will be checked until two consecutive ones which satisfy the absolute and relative magnitude tests as well as the elevation angle check are detected. The range of occurrence of the next star j is then predicted as follows

$$t_{\text{INITIAL}} = t_{ic} + (\theta_{ij} - e)/\omega$$

$$t_{\text{FINAL}} = t_{\text{INITIAL}} + \Delta t_j + (2e/\omega)$$

where t_{ic} is the star i clock slit transit time, θ_{ij} is the relative clock angle between star i and j , Δt_j is the transit time difference between slits for star j (evaluated from the elevation angle), and e is a tolerance on both bounds. Absolute/relative magnitude and elevation angle checks are performed for all pulses within the bounds. Upon confirmation of all three reference stars, the search phase is considered to be completed and will proceed to the output phase.

(b) Output Phase

Similar procedure of time range prediction and star pulses confirmation is executed. For each confirmed star, the clock/cone slit transit times as well as the star vector are sent to the AE. To account for the gradual drift in the H vector, the elevation angle and the relative clock angle for each confirmed star are updated for the next prediction. In addition, spin rate is evaluated at the end of each revolution by averaging the clock slit time differences between revolutions for all the confirmed stars.

4.3 Noise Consideration

The star scanner detector, whether it is built based on CCD or photo-multiplier tube (PMT) technology, is very susceptible to radiation noise. Radiation environment is sometimes encountered in orbiting missions to outer planets (e.g. Jupiter). The noise is introduced in the form of false pulses in the data stream. Consequently, the sequential SID should allow interleaving of other pulses between the reference star pulse pair when performing magnitude and elevation angle test within the time window. Due to high radiation background, the sensitivity of the scanner will be reduced thereby lowering the star detection probability. In such situations, failure to confirm a reference star can occur frequently. When there is no confirmed star for several revolutions, the time range prediction may not be accurate because of the invalid constant spin rate assumption over this period. Under such circumstances, an alternative approach can be taken based on gyro information. Assuming that the gyros are turned on during this period, thereby providing the rotor attitude and spin rate in inertial space. The transformation E_{TR} from rotor EME50 can thus be obtained at any specified t_g . The next reference star vector can be expressed in the rotor coordinate as

$$[S_{Rx} \ S_{Ry} \ S_{Rz}]^T = [E_{TR}]^T S_E$$

from which the star clock angle ϕ in the rotor coordinate is evaluated as

$$\phi = \tan^{-1} (S_{Ry}/S_{Rx})$$

and $[.]^T$ denotes a matrix transpose. Rotor spin rate ω can be measured by the gyros and encoders for time range prediction which is given as

$$t_{\text{INITIAL}} = t_s + (\phi - e)/\omega$$

$$t_{\text{FINAL}} = t_{\text{INITIAL}} + \Delta t_j + (2e/\omega)$$

for the j -th reference star. All testing procedures will then remain the same. With the reduced scanner sensitivity, the magnitudes of any star detected may deviate from the true value larger than anticipated. To compensate for intensity variations, a function relating the measured intensity with the true star intensity and background is required. Background information is a measure of radiation level as monitored by the scanner. An empirical model is given as

$$I_c = K \ln(1 + I_o / [(1 - \zeta)K - B])$$

where B is the background intensity, I_o is the measured intensity of a star, ζ is a scanner constant, K is the scanner saturation level and I_c is the true star intensity. Based on such a model, recorded intensities should be adjusted prior to the magnitude tests for more accurate result. If the scanner threshold is adjustable, it is recommended to set the level high enough to be able to just detect the dimmest reference star. Subsequently, the number of noise pulse will be reduced to the minimum while the scanner is still sensitive to detect the entire reference star set.

5. SPACECRAFT ATTITUDE ESTIMATOR

The attitude estimator (AE) for the Galileo spacecraft is designed to sequentially process the star scanner measurements and determine spacecraft's attitude and angular momentum vector in EME50. The AE formulation uses the least-squares method to determine the attitude which satisfies the necessary condition of star and slit normal orthogonality. Nutation and wobble are initially considered in the dynamical modeling. However, with the presence of a passive nutation damper and an onboard wobble control algorithm, nutation and wobble can be assumed negligible during steady state operations. Consequently, the model can be simplified to a pure spin case.

5.1 Formulation of the Dynamical Model

A spacecraft inertial coordinate frame A established by three orthonormal vectors

$$A = [a_1, a_2, a_3]$$

is first defined with a_3 aligned with the estimated angular momentum vector H , and a_1 lying in the plane defined by H and the line-of-sight (LOS) of the "first" reference star. A is also called the attitude matrix of the spacecraft.

The basic concept in the model formulation is that when a star falls in the scanner slit FOV, the star vector S is orthogonal to a vector n normal to the scanner slit. The star vector is defined in E (EME50), and the slit normal is defined in rotor coordinates R . If the slit orientation and the star transit times are exactly known, then at each star crossing, the necessary condition of orthogonality holds:

$$S \cdot n_j = 0 \quad j = \begin{cases} 1 & \text{clock slit} \\ 2 & \text{cone slit} \end{cases} \quad (5.1)$$

However, due to the presence of spacecraft modeling errors, transit time resolutions and measurement noise, errors would exist in the orthogonality defined by

$$e_j = S \cdot n_j \neq 0 \quad j = 1, 2 \quad (5.2)$$

To carry out the above dot-product operation, both S and n are expressed in the same coordinate frame (A), i.e.

$$S_B = A^T S_E \quad (5.3)$$

and

$$n_B = [I + e_{\eta} x][I + e_{\phi} x] \begin{cases} [\omega(t_1 - t_0)]_3^T n_{1R} & \text{clock slit crossing} \\ [\omega(t_2 - t_0)]_3^T n_{2R} & \text{cone slit crossing} \end{cases} \quad (5.4)$$

where $[e_i]$ denotes a rotation about the i -th axis by an angle θ , $t_1(t_2)$ is the clock (cone) transit time, and n_{1R} and n_{2R} are the slit normals in R which are constant vectors for known slit mounting orientations after in-flight misalignments calibration.

Furthermore,

$$e_n = [\delta t]_3 \begin{bmatrix} n_x \\ n_y \\ 0 \end{bmatrix}; \quad e_\phi = [\omega t]_3 \begin{bmatrix} \phi_x \\ \phi_y \\ 0 \end{bmatrix}$$

where δ is the precession rate, and the x, y components of nutation angle n_x, n_y and wobble angle ϕ_x, ϕ_y are assumed small. I is an identity matrix. The notation ex is a matrix cross-product operator defined as

$$ex = \begin{bmatrix} 0 & -e_3 & e_2 \\ e_3 & 0 & -e_1 \\ -e_2 & e_1 & 0 \end{bmatrix}, \quad \text{for } e = \begin{bmatrix} e_1 \\ e_2 \\ e_3 \end{bmatrix}$$

For some special modes of spacecraft maneuver (e.g., all-spin mode) when wobble and, perhaps, nutation become significant, the vector $[n_x, n_y, \phi_x, \phi_y]$ can be simultaneously estimated together with the attitude error by utilizing equation (5.4).

In the sequel, we will assume that the spacecraft attitude is generally estimated when all the spacecraft dynamical excitations and nutation are essentially damped out and wobble is controlled. Then the errors contributed by both nutation and wobble can be assumed small. Typically, onboard memory size and execution time margins are major concerns in the design of spacecraft control algorithms, and it is deemed appropriate to assume a pure-spin model for the AE formulation. Consequently, the slit normal in the absence of nutation and wobble is given by

$$n_A = \begin{cases} [\omega(t_1 - t_0)]_3^T n_{1R} & \text{clock slit crossing} \\ [\omega(t_2 - t_0)]_3^T n_{2R} & \text{cone slit crossing} \end{cases} \quad (5.5)$$

The objective is then to determine the spacecraft coordinate frame A such that the error in (5.2) for both slit crossings are minimized.

5.2 Attitude Estimator Algorithm

At each star crossing time k , the sequential SID provides the star vector $S(k)$, and the transit times $t_1(k)$ and $t_2(k)$. Given the last estimate $A(k-1)$, our objective is to determine $A(k)$. Let γ be the desired angular rotation about the axes of $A(k-1)$ to assume a new $A(k)$. By small angle approximation, (5.2) can be formulated as

$$[I - \gamma X] \underline{S}(k) \cdot \underline{n}_j(k) = v_j(k), \quad j = 1, 2 \quad (5.6)$$

where $S(k)$ and $\underline{n}_j(k)$ are expressed in the $A(k-1)$ coordinates, and $v_j(k)$ is the associated error in the orthogonality due to measurement noise. Rearranging (5.6) one can obtain the equation

$$\underline{S}(k) \cdot \underline{n}_j(k) = (\underline{S}(k) \times \underline{n}_j(k)) \cdot \underline{\gamma}(k) + v_j(k), \quad j = 1, 2 \quad (5.7)$$

A coordinate system $L = (L_1, L_2, L_3)$ is defined with the star vector aligned with L_1 and L_2 aligned with the clock slit normal at transit. This enables simple expressions of the sensitive axes ($h_i = S \times n_i$, $i = 1, 2$) orientations to be defined in the L_2 - L_3 plane (Fig. 6). As the change in the actual attitude between the two transits $t_1(k)$ and $t_2(k)$ is small, the attitude update can be performed immediately after the cone slit transit, using both clock and cone transit information. With $h_i(k)$ and $\underline{\gamma}(k)$ expressed in L_2L_3 coordinates, (5.7) can be written as

$$\underline{\epsilon} = H(k) \underline{\gamma}(k) + \underline{v}(k) \quad (5.8)$$

where

$$\underline{\epsilon} = \begin{bmatrix} S \cdot n_1 \\ S \cdot n_2 \end{bmatrix}, \quad H \triangleq \begin{bmatrix} (S \times n_1)^T \\ (S \times n_2)^T \end{bmatrix} \triangleq \begin{bmatrix} h_1^T \\ h_2^T \end{bmatrix}, \quad \underline{v} = \begin{bmatrix} v_1 \\ v_2 \end{bmatrix}$$

For $90^\circ > \beta > 0$, H is a nonsingular matrix. The least-squares estimate of the error rotation $\underline{\gamma}$ in (5.8) is

$$\underline{\gamma}(k) = H^{-1} \underline{\epsilon}(k) \quad (5.9)$$

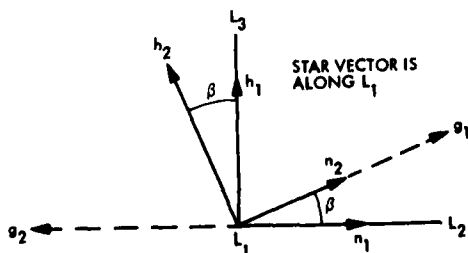


Figure 6. Star-Normals Coordinate Frame (L)

At each star crossing k , (5.8) is given by

$$\underline{\varepsilon}(k) = \begin{bmatrix} 0 & 1 \\ -\sin\beta & \cos\beta \end{bmatrix} \underline{\gamma}(k) + \underline{v}(k), \quad \beta \neq 0 \quad (5.10)$$

(5.10) is solved to give

$$\underline{\gamma}(k) = [\underline{g}_1 \quad \underline{g}_2] \underline{\varepsilon}(k) \triangleq \begin{bmatrix} \cot\beta & -\frac{1}{\sin\beta} \\ 1 & 0 \end{bmatrix} \underline{\varepsilon}(k)$$

in the L2-L3 plane. Furthermore, $\underline{g}_1, \underline{g}_2$ can also be expressed in terms of \underline{n}_1 and \underline{n}_2 . From Fig. 6

$$\underline{g}_1 = \frac{1}{\sin\beta} \underline{n}_2, \quad \underline{g}_2 = \frac{-1}{\sin\beta} \underline{n}_1$$

Then, with $\underline{n}_1, \underline{n}_2$ defined in $A(k-1)$, $\underline{\gamma}(k)$ can be expressed in the $A(k-1)$ frame by

$$\underline{\gamma}(k) = (\varepsilon_1(k)\underline{n}_2(k) - \varepsilon_2(k)\underline{n}_1(k))/\sin\beta \quad (5.11)$$

Although we have derived a desired rotation about the coordinates of $A(k-1)$ to assume a new $A(k)$, it is desirable, for better noise tolerance, that the actual attitude update is controlled by different estimator gains $K(k)$ depending on whether the spacecraft is in the transient or steady state. The actual rotation angle is specified as:

$$\underline{\rho}(k) = K(k) \underline{\gamma}(k) \quad (5.1)$$

At transient state, fast reduction in the attitude error is desirable and hence full gain on star information is used. Such a gain, however, weighs equally on the true attitude error as much as on the effect of noise. At steady state, the gain is reduced to a minimum magnitude (e.g. comparable to the size of jittering), so that sporadic, high frequency noise can be adequately filtered out.

The estimator gain $K(k)$ can be set at

$$K(k) = \begin{cases} 1 & k \leq k_0 & \text{transient state} \\ \frac{k_0}{2k} + K_{\min} & k > k_0 & \text{steady state} \end{cases} \quad k = 1, 2, 3, \dots$$

where k is a slit crossing counter (six per revolution), and is reset to zero whenever an external torque is applied to the spacecraft (e.g. thruster firings). k_0 can be chosen based on the distribution of the three identified stars $S_i, i = 1, 3$ in the inertial space. In a deterministic sense, the estimation error $e(k)$ can be reduced by $e(k) = \lambda e(k-1)$ per revolution in the transient state, where λ , defined in (4.2), is a star distribution index indicating the degree of orthogonality in the reference stars distribution. Since the spacecraft is initialized by the batch SID with an error in the order of one degree, λ vs. k_0 is computed to be

λ	0.014	0.12	0.24	0.34	0.49	0.59	0.63	0.75	0.8
k_0	3	6	9	12	18	24	27	45	54

where $k_0 = 3\tau$, and τ is the number of revolutions required to reduce the error from 17.45 mrad to below 0.3 mrad. From the above relation, k_0 can be assigned a value onboard each time λ is computed from three identified stars.

For computational efficiency, the Galileo onboard attitude estimation is done using quaternions as follows:

$$\underline{q}(k) = \cos\Omega \underline{q}(k-1) + \frac{\sin\Omega}{2\Omega} \begin{bmatrix} -(\underline{\rho} \times) & \underline{\rho} \\ \dots & \dots \\ \underline{\rho}^T & 0 \end{bmatrix} \underline{q}(k-1) \quad (5.1)$$

$$\Omega^2 \triangleq \frac{1}{4} (\underline{\rho}(k) \cdot \underline{\rho}(k)) \text{ for the interval } [k-1, k].$$

5.3 Attitude Estimator Initialization

An estimated A coordinate frame defined in EME50 can be computed from the orientations and the scanner clock/cone measurements of any two identified stars for initializing the attitude estimator. For two unit star vectors \underline{S}_1 and \underline{S}_2 of known orientations, an

orthonormal coordinate system $D = [d_1, d_2, d_3]$ can be defined as:

$$d_2 = S_1, d_3 = \frac{S_2 \times S_1}{|S_2 \times S_1|}, d_1 = d_2 \times d_3$$

Since S_1, S_2 in E (EME50) are readily available from the star catalog, $[d_1, d_2, d_3]$ can be defined in E which is equivalent to a transformation matrix from D to E or ETD . Furthermore, S_1, S_2 can be expressed in the spacecraft body coordinate frame from the scanner clock and cone angular measurements of the star transits, and $[d_1, d_2, d_3]$ in A , or ATD , is thus available. Subsequently, an estimate of the A coordinate frame, equivalent to a transformation matrix from A to E , or ETA , is given by $ETD[ATD]^T$. Note that the third column of ETA corresponds to the attitude of the spin axis, and hence an estimate of the angular momentum vector in EME50. For Galileo, this procedure provides an initial estimate of the spacecraft body coordinate frame with error of about one degree per axis.

6. SCAN PLATFORM ATTITUDE PROPAGATION AND UPDATE

Accurate determination of the attitude and rate of the platform coordinate system with respect to inertial space is essential for high precision platform pointing and slewing. For the Galileo spacecraft, the sensors are a pair of rate integrating gyros mounted on the platform. The gyro outputs are used by an integration algorithm onboard to propagate the scan platform attitude and rotational rate. Absolute inertial attitude information is computed using star scanner data for intermittent update of the propagated platform attitude.

6.1 Platform Attitude Propagation

The scan platform attitude relative to the inertial space is specified by quaternions q , and can be obtained by numerically integrating the quaternion differential equation:

$$\dot{q}(t) = \frac{1}{2} \Lambda(t) q(t), \quad \Lambda(t) \triangleq \begin{bmatrix} \frac{\omega \times}{- \omega^T} & \frac{\omega}{0} \end{bmatrix}$$

Since $\Lambda(t)$ is time varying, a closed form solution is not readily available, and a series method is used for the solution design. A fourth order algorithm [Ref. 7] is chosen for Galileo after performing a tradeoff study among algorithm complexity, truncation and roundoff errors for 32-bit floating point arithmetic:

$$q_j = \begin{bmatrix} 0 \\ 0 \\ 0 \\ 1 \end{bmatrix} + \frac{1}{2} \theta_j + \frac{1}{8} \theta_j^2 + \frac{1}{48} (\theta_j^3 + \theta_{j-1} \theta_j - \theta_j \theta_{j-1}) + \frac{1}{384} (\theta_j^4 + 4(\theta_j(\theta_{j-2} - 2\theta_{j-1}) - (\theta_{j-2} - 2\theta_{j-1})\theta_j)) q_{j-1} \quad (6.1)$$

where θ_j is the gyro incremental position vector

$$\theta \triangleq \begin{bmatrix} \theta \\ 0 \end{bmatrix}$$

at its sampling time j . For Galileo, the gyro sampling interval is 44 4/9 msec.

6.2 Platform Attitude Update

Since the gyro outputs provide incremental positions, the algorithm in (6.1) only propagates the attitude with respect to an initialized platform attitude. For prolonged periods of time, this propagated attitude may be drifted away significantly from the true attitude due mainly to the inherent truncation and roundoff errors in the integrator algorithm. In the case of Galileo spacecraft, star scanner information is used to intermittently update the platform's absolute inertial attitude. The main differences between platform attitude update and the AE are as follows:

1. The star vectors S and slit normals n are expressed in the platform coordinates via the spin bearing assembly and articulated scan subsystem's encoders, using synchronized star crossing data, encoder data and gyro readouts.
2. The AE determines the 'A' coordinates, which is basically an inertially stationary coordinate frame within the periods when no external torque is applied to the spacecraft. For the AE, rapid attitude convergence from a large initial error is of prime importance. On the other hand, the scan platform attitude updating procedure is designed for small error corrections (such as due to integrator algorithm drift) in the steady state. For Galileo, the gyro integrator algorithm drifts in the order of 0.4 mrad per hour (3σ).

The error in \underline{n} is reflected by the error function

$$V = \frac{1}{2} \sum_{j=1}^2 (\underline{S} \cdot \underline{n}_j)^2 \quad (6.2)$$

and can be minimized by rotating \underline{n} according to the kinematics

$$\dot{\underline{n}}_j = \underline{\mu} \times \underline{n}_j \quad j = 1, 2$$

This minimization can be achieved by choosing $\underline{\mu}$ such that \dot{V} , given by

$$\dot{V} = \sum_{j=1}^2 (\underline{n}_j \cdot \underline{S})(\dot{\underline{n}}_j \cdot \underline{S}) = \sum_{j=1}^2 \underline{\mu} (\underline{n}_j \cdot \underline{S})(\underline{S} \times \underline{n}_j) \quad (6.3)$$

remains nonpositive. The identity $(\underline{\mu} \times \underline{n}) \cdot \underline{S} = \underline{\mu} \cdot (\underline{n} \times \underline{S})$ is used in (6.3). $\dot{V} \leq 0$ always holds if we choose

$$\underline{\mu}(k) = \underline{S}(k) \times (\epsilon_1(k) \underline{n}_1(k) + \epsilon_2(k) \underline{n}_2(k)) \quad (6.4)$$

for each k , where $\epsilon_j = \underline{n}_j \cdot \underline{S}$, $j = 1, 2$, which constitutes to the desired coordinate rotation of

$$\underline{p}(k) = G \underline{\mu}(k), \quad 0 < G \leq 1 \quad (6.5)$$

for each star crossing pair, [Ref. 8] (6.5) can be directly applied to the quaternion updating equation (5.12), in which $q(k-1)$ is the latest propagated platform quaternion just prior to the star update.

7. IN-FLIGHT CALIBRATION

The exact orientations of the slit normal vectors \underline{n}_i in the rotor coordinate system are essential for the AD accuracy. Due to mounting misalignments and other systematic errors, ground calibration of the scanner from in-flight data is thus required. The basic equation representing the slit crossing by a star is given as

$$\underline{S}_E^T \underline{E}_{TR} \underline{n}_i = 0 \quad i = \begin{cases} 1 & \text{clock slit} \\ 2 & \text{cone slit} \end{cases} \quad (7.1)$$

The actual slit normal defined in the rotor coordinate can be modeled as

$$\underline{n}_i = (I - [e_i \times]) \underline{n}_i^* \quad (7.2)$$

where \underline{n}_i^* is the known nominal and e_i the slit misalignment error vector. The transformation \underline{E}_{TR} can be determined from gyros which are appropriately calibrated and initialized. On substituting (7.2) to (7.1), an observation model can be defined

$$y_i = \underline{S}_E^T \underline{E}_{TR} \underline{n}_i^* = H e_i + v$$

where

$$H = - \underline{S}_E^T \underline{E}_{TR} [\underline{n}_i^* \times]$$

At each star crossing, the transit time and the star vector are telemetered along with gyro information for attitude reconstruction. The transformation \underline{E}_{TR} is evaluated at the time of star crossing for defining the observables y_i and the observation matrix H . A standard sequential Kalman estimator can be applied for error estimation with e_i assumed time invariant. The equations are as follows;

$$\begin{aligned} e(k+1) &= e(k) + K(k+1)[y(k+1) - H(k+1) e(k)] \\ K(k+1) &= P(k)H(k+1)[H(k+1)P(k)H^T(k+1) + R(k+1)]^{-1} \\ P(k+1) &= [I - K(k+1)H(k+1)]P(k)[I - K(k+1)H^T(k+1)]^T + K(k+1)P(k+1)K^T(k+1) \end{aligned}$$

Simulation studies indicate that convergence can be achieved in 18 star measurements with residual error of less than 0.05 mrad [Ref. 9]. The error estimates are then uplinked to the onboard AE for improved attitude determination.

8. SIMULATION

For performance evaluation, the star scanner data was simulated using a three-body spacecraft model. The star field observed was defined by the input attitude and nutation angle based on a 200 stars catalog. The data was generated for 60 revolutions at twenty inertial pointing directions along a nominal Galileo trajectory. A sample of such data for 4 revolutions is shown in Fig. 7. Successful identifications were achieved in all cases by the batch SID while the sequential SID could track the three

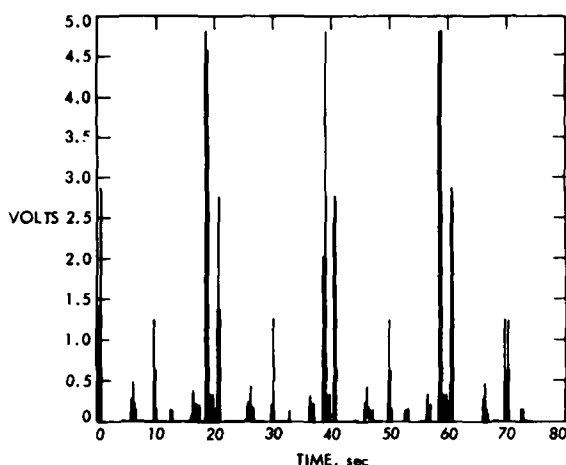


Figure 7. Star Scanner Pulse Sequence

Fig. 9, a noise-free case is shown. A simulation with transit time noise of $\sigma = 0.5$ msec and nutation of 0.5 mrad is shown in Fig. 10. Figure 11 depicts large uncertainty in the transit times ($\sigma = 1.3$ msec) and high nutation of 2 mrad.

Table 1. Star ID Simulation Parameters

PARAMETERS	DESCRIPTIONS	VALUES
α_r	RELATIVE INTENSITY CRITERION	0.871
ω	ROTOR SPIN RATE	0.33 mrad/sec
k_1	SCANNER MOUNTING CONFIG CONSTANT	1.245
k_2	SCANNER MOUNTING CONFIG CONSTANT	1.089
A	CONFIDENCE INDEX COMPUTATIONAL CONSTANT	0.7
c_1	POINT COMPUTATIONAL CONSTANT	100
c_2	POINT COMPUTATIONAL CONSTANT	65
FOV	FIELD-OF-VIEW	$\pm 5^\circ$
θ_e	RESIDUAL NUTATION AND WOBBLE	0.5°
Δt	SPIN RATE VARIATION CRITERION	8 msec
α_a	ABSOLUTE INTENSITY CRITERION	0.795
η	NUTATION ANGLE	0.5°
ϕ	WOBBLE ANGLE	0.006°
ν	SCANNER ANGLE MEASUREMENT UNCERTAINTY	0.25°
e	TIME RANGE PREDICTION TOLERANCE	5°
K	SATURATION LEVEL	6.5×10^6
ζ	SCANNER CONSTANT	0.00775
IR	REFERENCE INTENSITY	1.5×10^4

reference stars during subsequent revolutions. The processing time is approximately 30 seconds on UNIVAC 1108 for the batch with uncertainty of 0.1 mrad/sec in spin rate. The processing time of the sequential SID for each prediction and confirmation is small (in order of msec). Values of the various parameters employed in the simulation are given in Table 1.

The AE was simulated and tested with various orientations of the H-vector in EME50. Table 2 shows the corresponding star distribution index, the initial and final errors, and the number of star crossings prior to attitude convergence for each test case. Transit time noise of $\sigma = 0.5$ and 1.3 msec and nutation angles up to 2 mrad were tested. Figure 8 depicts the various transitions to the steady state gains from the transient state gain depending on different values of λ . Several test cases with $H = [1 \ 0 \ 0]^T$ are depicted in Figs. 9-11, showing the quaternions update vector ρ the error function $V = \epsilon \cdot \epsilon$, and the estimation error in H versus star observations by both slits (3 per rev.). In

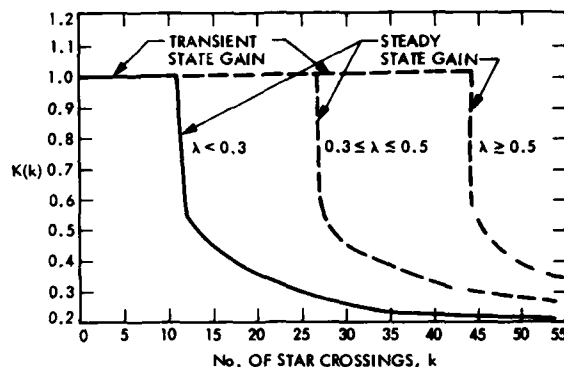


Figure 8. Estimator Gains

Table 2. Spacecraft Inertial Attitude (A) Estimation

H Attitude in EME50	Star Distribution Index	Initial Error per Axis (mrad)	Final Error per Axis (mrad)	Number of Star Crossings Prior to Convergence
$\begin{bmatrix} 1 \\ 0 \\ 0 \end{bmatrix}$	0.03	21	0.42	26
$\begin{bmatrix} 0 \\ 1 \\ 0 \end{bmatrix}$	0.68	15	0.37	60
$\begin{bmatrix} 0 \\ 0 \\ 1 \end{bmatrix}$	0.02	10	0.35	24
$\begin{bmatrix} 0.1710 \\ 0.2962 \\ 0.9397 \end{bmatrix}$	0.21	17	0.45	38
$\begin{bmatrix} -0.5 \\ -0.5 \\ 0.7071 \end{bmatrix}$	0.16	35	0.27	37

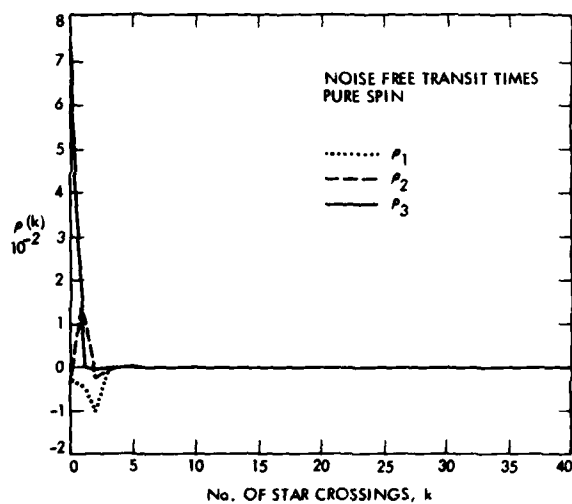


Figure 9(a). Attitude Update Parameter

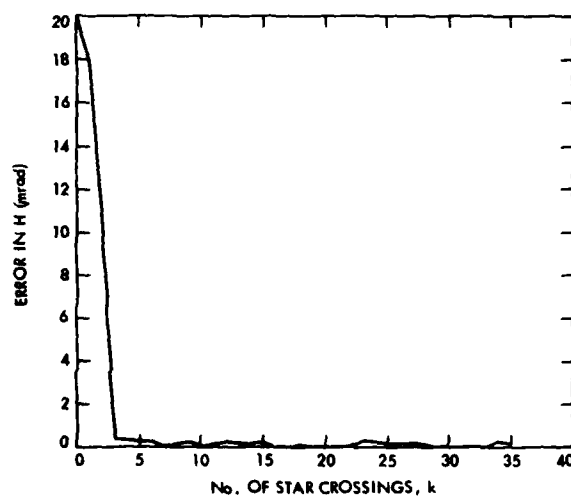


Figure 9(c). Angular Momentum Attitude Error

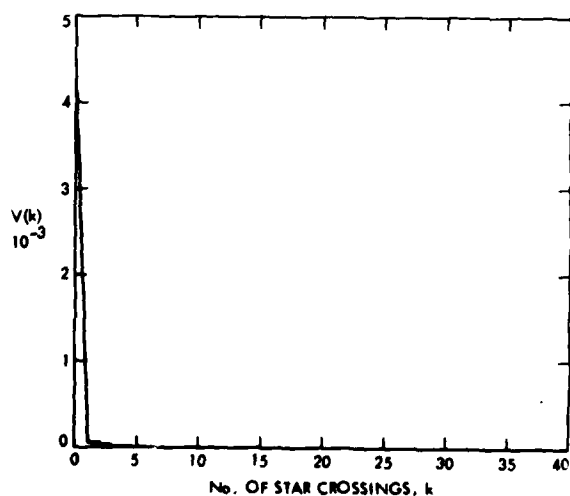


Figure 9(b). Error Function

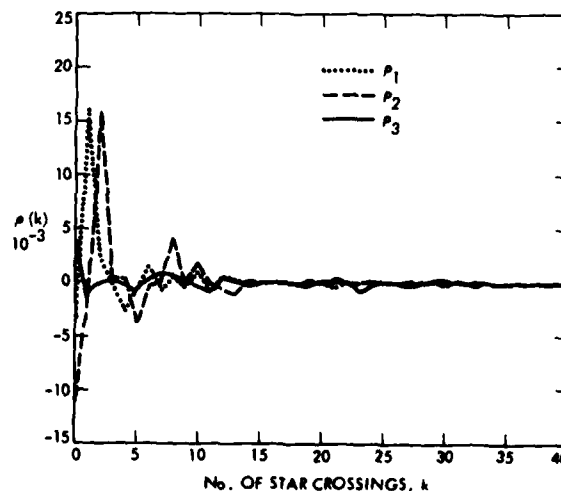


Figure 10(a). Attitude Update Parameter

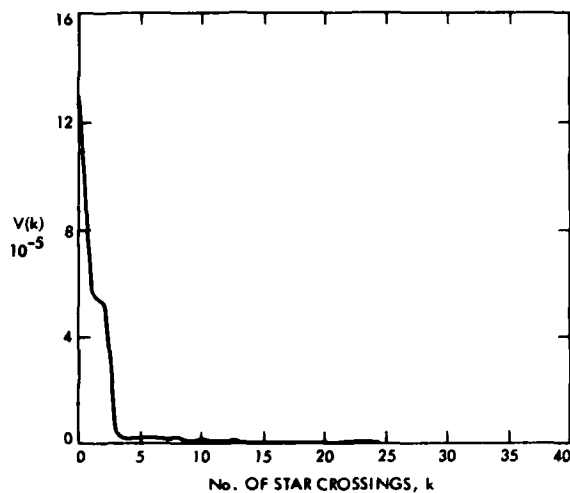


Figure 10(b). Error Function

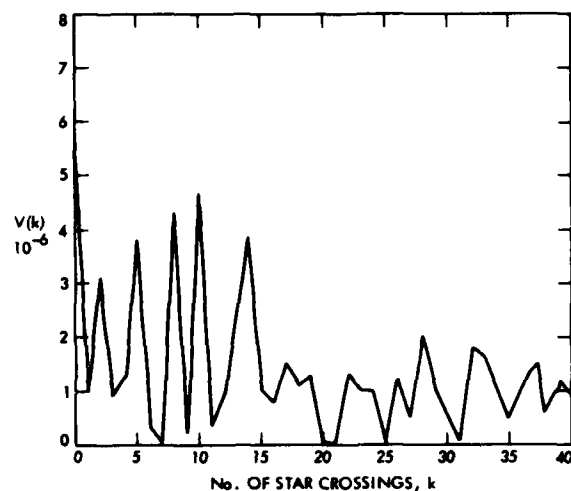


Figure 11(b). Error Function

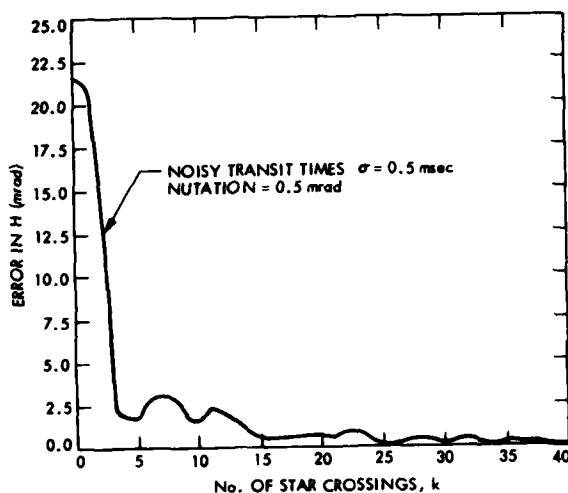


Figure 10(c). Angular Momentum Attitude Error

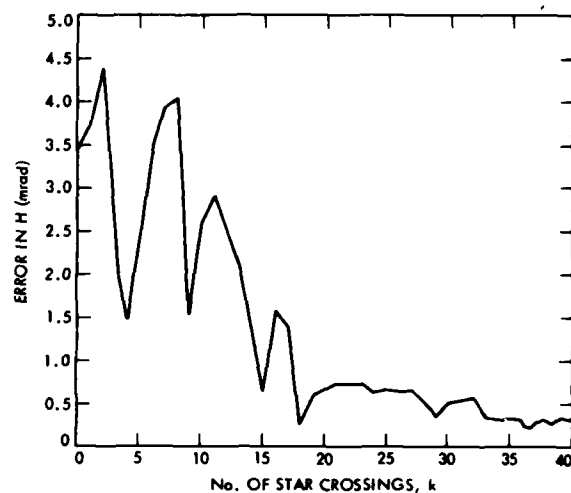


Figure 11(c). Angular Momentum Attitude Error

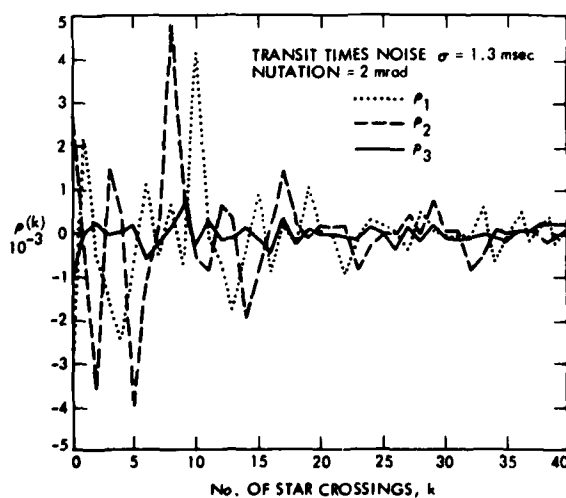


Figure 11(a). Attitude Update Parameter

Depending on the value of λ computed each time a set of star was identified, k_0 was assigned a value as follows:

$$k_0 = \begin{cases} 12 & (4 \text{ rev}) & \lambda < 0.3 \\ 27 & (9 \text{ rev}) & 0.3 \leq \lambda < 0.5 \\ 54 & (18 \text{ rev}) & \lambda \geq 0.5 \end{cases}$$

where the values of k_0 relative to λ as shown in section 5.2 are slightly increased to account for noise disturbance. Convergence in H error to below 0.5 mrad was achieved in all test cases, including initial errors as large as 10° .

IX CONCLUSIONS

An entirely autonomous star-referenced attitude determination system for a dual-spin planetary spacecraft has been presented. The design concept is realized in the design of the Galileo spacecraft for its mission to Jupiter. Two algorithms pertaining to this system are the star identification and attitude estimator algorithms. The star identification algorithms define three reference stars for continuous tracking. Then the star transit

times are input to the attitude estimator to establish the spacecraft attitude within an accuracy of 0.5 mrad (3 σ). A procedure for determining the attitude of the scan platform is also presented. Simulation results show that attitude determination from star data are successful for all inertial pointing directions along a nominal Galileo mission trajectory.

REFERENCES

1. Walsh, T.M. and Hinton, D.E., "Development and Application of a Star Mapping Technique to the Attitude Determination of the Spin-Stabilized Project Scanner Spacecraft," Proceedings of the Symposium on Spacecraft Attitude Determination, The Aerospace Corp., El Segundo, CA, Oct. 1969, pp. 207.
2. Mackison, D.L., Gutshall, R.L., and Volpe, F., "Star Scanner Attitude Determination for the OSO-7 Spacecraft," J. of Spacecraft & Rockets, Vol. 10, No. 4, April 1973.
3. Grosch, C.B., LaBonte, A.E. and Vanelli, B.D., "The SCNS Attitude Determination Experiment on ATS-III," Proceedings of the Symposium on Spacecraft Attitude Determination, J. of Astro. Sciences, Vol. 15, No. 3, Sept. 1977.
5. Wertz, J.R., Editor, Spacecraft Attitude Determination and Control, D. Reidel Publishing Co., Dordrecht, Holland, 1978.
6. Wong, E.C., and Lai, J.Y., "Attitude Determination of Galileo Spacecraft from Star Data," AIAA Guidance and Control Conference, 80-1732-CP, Denver, Mass., Aug. 1980.
7. O'Conner, B., and Comick, D., "Attitude Determination Algorithm for A Strapdown IMU," The Bendix Corp., Teterboro, N.J., 1976.
8. Wong, E.C., and Breckenridge, W.G., "Inertial Attitude Determination for a Dual-Spin Planetary Spacecraft," AIAA Guidance and Control Conference, Albuquerque, N.M., Aug. 1981.
9. Lai, J.Y., and Hayati, S., "Simultaneous In-Flight Calibrations of the Galileo Science Platform and Attitude Control Subsystems," AIAA Guidance and Control Conference, Albuquerque, N.M., Aug. 1981.
10. Murrell, J.W., "Precision Attitude Determination for Multimission Spacecraft," AIAA Guidance and Control Conference, Palo Alto, CA, Aug. 1978.
11. Beck, J.V., and Arnold, K.L., "Parameter Estimation in Engineering and Science," John Wiley & Sons, New York, 1977.

SOFA : SYSTEME D'ORIENTATION FINE D'ANTENNE

(an antenna fine pointing mechanism)

Bernard HUBERT and Pierre BRUNET

Société Nationale Industrielle Aérospatiale
CANNES, FRANCE**ABSTRACT :**

AEROSPATIALE's SOFA is a device designed for the highly accurate, 2-axis pointing of antenna or any feature installed on a spacecraft.

The SOFA system, now pending an AEROSPATIALE patent, is particularly suited to the transmit-and-receive antennae of Television Satellites. It is one of the requisites for a Radio-Frequency type deviation detector.

The major characteristic of this system is complete freedom from friction and wear-out, resulting in numerous advantages, such as outstanding precision, virtually endless service life, high simplicity and reliability.

The sizing method is described and performances are analysed. The results from analogue simulations are presented.

A functional model of the electrical and mechanical parts has been built and subjected to on-ground tests using a 2-axis platform simulating the spacecraft's motions. The results obtained are thoroughly in keeping with the predictions and simulations. A qualification model is under test. Various possible applications of the SOFA system are mentioned.

1. INTRODUCTION

Telecommunication satellites as a rule and television satellites in particular require increasingly fine antenna pointing accuracies. Despite increased sophistication, the conventional means do not meet the present demands. As a matter of fact the earth sensor kinetic wheel assembly, even with one or 2 degrees of freedom does not meet safe accuracy values of 0.1° or 0.05° .

Furthermore the overall pointing budget has to take into account the misalignments and thermal deflections.

Certain improvements have been made to the late projects: increase of the number of Earth Sensors, location of the Sensors on the tower supporting the antenna feed reflector reorientation device for misalignment compensation.

However, these changes are not sufficient. On the contrary the adoption of a radio frequency sensor, whose major advantage is the use of a radio electrical path very close to that of the useful beam, is a decisive improvement in pointing accuracy.

This sensor may be used to control the overall satellite's attitude. That configuration ensures the excellent accuracy for the Antenna used in receiving the Beacon's signal.

Alternatively, this sensor may be used to pilot only the beam delivered by the Antenna receiving the RF Beacon signal. The latter concept ensures the best accuracy in pointing the transmit Antenna and fair accuracy in pointing a receive antenna other than the transmit antenna.

In this case, the orientation mechanism is interlaid between the antenna's reflector and the spacecraft's structure, with the source remaining in a fixed position on the spacecraft, e.g. on a tower. The reflector position is then continuously adjusted to nullify the error signal delivered by the RF Sensor.

The beam is permanently orientated towards the on-ground Beacon through an independent control loop whilst the satellite itself is stabilised by conventional means with regard to earth centre.

The antenna fine pointing system, the so called SOFA developed by AEROSPATIALE CANNES is the subject of the description herein after which also covers the efforts conducted to demonstrate the performances of the system.

An application has been filed for a patent to cover such system.

2. SPECIFICATIONS AND CONSTRAINTS

The specifications adopted are suited to utilisation for the transmit antenna of the French TV Satellite.

The main data to be considered in the conceptual design and sizing of the pointing system may be summarised as below :

- satellite's in orbit weight : 1,000 Kg
- thruster's torque : 10 Nm
- inertiae : $I_x = I_z = 25,000 \text{ m}^2 \text{ Kg}$
 $I_y = 900 \text{ m}^2 \text{ Kg}$
- solar panels' rotation by 0.15° steps
- solar panels' torsion inertia = $50 \text{ m}^2 \text{ Kg}$
- solar panels' minimal oscillation period = 3 sec
- satellite stabilisation accuracy = 0.3°
- maximal perturbation torque in orbit corrections : 0.8 Nm
 (misalignment of thrusters and dissymetry of thrusts).

The most stringent typical perturbation effects to be considered in beam pointing are under the following conditions :

- a spacecraft oscillation, period 24 hours, amplitude 0.3°
- 0.05 Nm torque steps on the reflector during station keeping
- spacecraft body oscillation at a period of 3 sec and an amplitude of 0.02°
- the signal from the radio frequency sensor is assumed to be affected by a random noise, density $2.8 \cdot 10^{-4} \text{ }^\circ/\text{Hz}^{1/2}$ within the 0 - 15 Hz band, say a of $1.1 \cdot 10^{-3}$ degrees (1σ).
- the 10 Kg elliptic reflector whose inertiae are 5 and 9 $\text{m}^2 \text{ Kg}$

The beam pointing error added to the sensor error is required to stay below 0.01 degree (1σ).

Taking into account the amplifications, the adopted vibration level specifications are:

- 40 g on the longitudinal axis
- 30 g on the transverse axis

with the reflector's C. of G. 15 cm above the mechanism's axis.

The temperature limits selected are $-120^\circ + 80^\circ \text{ C}$.

3. DESCRIPTION OF THE MECHANISM

3.1 General presentation

The system developed by AEROSPATIALE Cannes, the SOFA (système d'orientation fine d'Antenne) is an antenna fine pointing device absolutely free from friction or any source of wearout and having infinite resolution.

The principle is illustrated in figure 1. Two plates, the lower one mounted on the spacecraft and the upper one clamped to the reflector, are linked by a deformable element, the central spring, acting as a ball joint.

The forces required to orientate the reflector are provided by 4 circumferentially located linear motors.

The mechanical system furthermore includes :

- travel stops
- a locking device for launch phase
- an electromagnetic temporary locking device

A control loop electronics drives the current into the coils depending on the sensor's error signal. Each of the above element is detailed hereinafter.

3.2 The spring

The spring utilised is a beryllium copper cylinder having superimposed and alternated series of 120° spaced slits (figure 2).

The properties of such deformable system are well fitted to the problem :

- the bending stiffness (0.1 Nm/degree) selected is a fairly small one to reduce the permanent electrical consumption,
- the other motions are not damped but they remain very small even when in resonance excited by the thrusters,
- the spring's stresses and fatigue during in orbit operations are quite negligible.

3.3 The motors

Each motor consists of a magnetic circuit with permanent magnets which is attached to the reflector clamped platform and a flat coil attached to the spacecraft mounted platform (fig. 3).

Interaction between current running through the coil and magnetic field generates a force according to Laplace's law:

$$\vec{F} = 2 l n \vec{I} \wedge \vec{B}$$

which is proportional to the current value.

Only one motor is used on each axis while the opposite motors are used for redundancy.

Each coil counts 800 turns for 45 ohms, stop piece limit deflection to $\pm 1.5^\circ$ in the present configuration, which permits to compensate a beam deflection of approximatively $\pm 3^\circ$.

For example a 35 mA current is necessary to rotate the reflector by 0.5° (approx 1° for the beam) which amounts to 55 m W.

3.4 Locking device for launch

Of course this hinged device has to be secured to carry the reflector throughout launch. The device chosen is an adaptation of the system previously qualified for the retraction of solar arrays. Three 120° spaced feet are tilted to bottom on the 3 stops which motion compresses the spring by 4 mm (figure 1).

The assembly is locked by a kevlar cable, the tension of which provides overall assembly prestress.

Tension is applied through a deformable lever that has tension regulating action whenever deflections are felt.

At the time of in orbit deployment a pyro cutter releases the system. Each contact foot is returned by a spring that frees the stops as well as the reflector supporting plate, which takes up its nominal operation position after expansion of the central spring.

3.5 Temporary locking

A temporary locking device can be incorporated to restrain the two platforms into zero position.

This system consists of an electromagnetically driven flip-flop locking device. Two similar 90° spaced devices are used. Their distance to centre is 10 cm. With the spring as the third attach point, restraint is thoroughly ensured. This system would be used only in the event of failure of the on-ground RF Beacon, which would only be temporary, or in the event of dual failure of the RF Sensor and on-board SOFA system.

4. PERFORMANCE ANALYSIS

4.1 Environment analysis

A mathematical model was established for the purposes of system analysis.

The two axis are decoupled.

On one axis the transfer function may be expressed as :

$$\mathcal{E}(p) = \frac{\theta(p) \left[\left(\frac{A}{2} - B \right) p^2 + \frac{K}{2} \right] + G F(p) \tilde{\mathcal{E}} + \Gamma_R}{\frac{1}{2} (A p^2 + K) - G F(p)}$$

where p is Laplace's variable

$\varepsilon(p)$: pointing error

$\theta(p)$: spacecraft rotation

G : static gain of the loop

$F(p)$: control law

$\tilde{\varepsilon}$: sensor noise

Γ_R : perturbation torque on reflector

A and B are inertia of the system

K : spring's constant

The transfer function is illustrated by the diagram in figure 4.

An integral control loop was integrated to the control law $F(p)$ to avoid occurrence of an error in presence of a torque Γ_R during orbit controls, whence:

$$F(p) = \frac{1 + \zeta p}{1 + 2\frac{\zeta}{\omega_1}p + \frac{p^2}{\omega_1^2}} + \frac{K}{p}$$

Examination of the roots of the characteristic equation and of the various transfer functions has led to a compromise between all 3 types of perturbations phenomena which are:

- spacecraft motions
- reflector torques
- sensor noise

The effects of which disturbances may be summarised as follows:

- error induced by a torque Γ_R is in reverse ratio to gain: $\varepsilon \approx 0.8 \frac{\Gamma_R}{G}$
- error due to spacecraft oscillation is of the form $\varepsilon = \theta \left(\frac{F}{F_1}\right)^2$ thereby in reverse ratio to the gain

with F being the oscillation frequency

$$\text{and } F_1 \approx \frac{1}{2\pi} \sqrt{\frac{K}{B}}$$

- error due to noise is given by $\varepsilon(1\sigma) = D_0 (6F_1)^{1/2}$

where: D_0 is the spectral density of sensor noise in $^\circ/\sqrt{\text{Hz}}$, $(6F_1)$ is the equivalent band pass of the system.
This error is proportional to the 4th root of gain.

These variations are illustrated in figure 5. The parameters selected for the case analysed are as follows:

- a 200 Nm/rad gain for the $9 \text{ m}^2/\text{Kg}$ inertial axes and a 111 Nm/rad gain for the $5 \text{ m}^2/\text{Kg}$ inertial axis.
- the filter is identical for the 2 axes:

$\omega_1 = 39 \text{ rd/sec}$	$\zeta = 0.85$
$\zeta = 0.26 \text{ sec}$	$K = 1.5 \text{ sec}^{-1}$

2 Pointing accuracy

With the selected adjustment the expected errors are as follows:

- noise leads to $2 \cdot 10^{-3}$ degree depointing (3σ) within the 0 - 6 Hz band over the 2 axes, which leads to a power consumption of 0.03 W per axis

- the spacecraft's daily oscillations are quite negligible
- the effect of solar panel's rotation steps gives $4 \cdot 10^{-3}$ degree in the East-West direction
- the 0.05 Nm torque which may occur during station keeping shows 1 sec peaks at the beginning and at the end of each manoeuvre which peaks have an amplitude of :
 - . 1.10^{-2} degree around the 9 m^2 Kg inertial axis, which is due to the longitude corrections
 - . $1.8 \cdot 10^{-2}$ degree around the lesser inertiae axis, which is due to the inclination correction manoeuvres
- such other sources of error as the roll or pitch desaturations give errors less than 1.10^{-3} degree.

In brief, apart from the peaks observed at start and end of station-keeping manoeuvre (duration 1 sec, amplitude less than $1.8 \cdot 10^{-2}$ degree 3σ), the error induced by the SOFA is at 3σ less than $3 \cdot 10^{-3}$ degrees in the North South direction and $5 \cdot 10^{-3}$ degrees in the East West direction. The sensor's noise effect is included in the above values.

The beam's global pointing budget is obtained by adding the constant and daily errors from the RF sensor itself.

4.3 Analogue simulations

The mathematical model was simulated on an analogue computer and many simulations were performed with provided checking of the selected setting and verification that the variation of parameters, particularly of the filter's setting was not critical.

The findings are that the performances obtained are absolutely compliant with predictions.

The spacecraft body's oscillations are indeed reduced to the extent nominally predicted (see figure 6).

Figure 8 shows the effects of a torque on the reflector and of sensor noise as well as the effect of integral control.

A 0.05 Nm torque gives peaks of 1.10^{-2} degrees (duration 1 sec) and the $2.5 \cdot 10^{-3}$ degrees (3σ) noise gives a pointing error of $1.5 \cdot 10^{-3}$ degrees (3σ).

The model has been used to study certain transient phenomena.

The simulations provided knowledge of the effect of thrusters' impulses at variable periods with the error staying below 10^{-3} degrees (see figure 7). Acquisition from maximum deviation (reflector tilted by 1.5°), taking into account a sensor signal peak-clipped at 0.4° has been analysed.

The system is still convergent and acquisition is performed in 20 sec.

Even with substantial noise the driving current for the motors can be filtered and is a fair measurement of SOFA rotation apart from the transient phenomena. Finally as the system's equivalent bandpass is 1 Hz, the antenna's structural modes should necessarily be greater than 5 Hz to ensure good frequency decoupling.

4.4 Description of the electronic

To qualify the antenna pointing mechanism under as good as "real like" conditions a functional development model of the driving electronic was designed and developed by AE-ROSPATIALE Cannes.

This model is electrically typical of the actual unit as planned today but with the absence of redundancy (only 1 North South and East West control loop instead of 2).

As shown in the synopsis attached hereto (figure 9), the model is made up of 3 parts, namely :

- solar cells adaptation : amplification of signals delivered by the solar cells (simulation of RF Sensor) by $0.1 \text{ V}/^\circ$ to $20 \text{ V}/^\circ$ (the predictional output level for the RF sensor).
- This part will not exist on the actual unit.

- North South control loop : comprises the following circuits :

- . summators of the N S error signal with a preset bias voltage (purposeful depointing of the beam)
- . filter
- . integrator (provides integral feedback of control loop)
- . current amplifier (gain $G = 0.25 \text{ A/V}$), (the charge presented by the motor is $45 \text{ Ohms} \pm 40\%$; a voltage command is impossible due to this dispersion).

- East West control loop : same as here above

The model here built proved thoroughly satisfactory permitting the successful performance of many design and development tests on the antenna pointing mechanism.

5. FUNCTIONAL TESTS

A functional development model was built from the motors spring and driving electronic, see figure 10.

The test set up utilised suggests the operational conditions :

- the mechanism is installed on a table with 2 degrees of freedom providing simulation of the spacecraft roll and pitch motions (see figure 11)
- the reflector is simulated by the inertia of a rectangular metal frame
- the radio frequency sensor is simulated by an optical system : the picture of a flood light is shaped after reflection on a mirror (which is fixed to the moving part) at the centre of 4 photo electric cells.

The noise and stability of the error signals are better than $0.5 \cdot 10^{-3}$ degree.

Figure 12 shows the principle of sensor simulation.

With this set-up the different sorts of perturbations were tested in quite realistic conditions, namely :

- torque on reflector (figure 8)
- spacecraft's oscillations at various frequencies;
- satellite depointing
- noise on the sensor signal (figure 8)
- acquisition with great initial depointing.

The results obtained provide adequate verification of the shape of responses and the values obtained by both the analytical study and the analogue simulations (figure 8).

The consistency of all above results is a verification of the mathematical model and demonstrates that the parameters of the control loop law have indeed been mastered.

6. RELIABILITY

The electronic is designed for pointing the beam to a particular angular distance from the beacon.

To improve reliability such presetting is performed on board prior to launch but there is a register that enables refinement of such setting and corrections of the misalignments or zero errors.

The electronic and motors are fully redundanted and no cross-coupling is needed between those elements owing to the high reliability.

The reliability of the electronic parts calculated with quality (E2) components over 7 years is 0.995.

The reliability figure for the largely over-dimensioned mechanical part is 0.9996 and undergoes no degradation over time as the spring is the only element that is stressed after pointing mechanism release, with the very high reliability of 0.99999.

7. STATUS OF DEVELOPMENT

The model was utilised in very numerous tests for 1 year.

A qualification model was built with no change made to the functional elements i-e spring and motors. The locking system is an adaptation of some already qualified systems.

The qualification tests are under way to completion.

Adaptation to a given mission can be done smoothly with minor changes to essential elements.

Adaptations are in progress for different applications, particularly a model including position sensors that enable a reflector to be locked to a given position or to the position of a first reflector, itself locked by control loop to an RF sensor as described herein.

8. CONCLUSION

The SOFA described here is a system that permits to solve, under optimal conditions the problem of fine antenna pointing.

The SOFA offers numerous advantages, namely :

- very high pointing accuracy = 1.10^{-2} degrees (3σ) to be added to RF sensor's accuracy on beam pointing even during orbit controls
- small weight (4 Kg including electronic) and power consumption (less than 1 W)
- very high reliability and virtually endless service life of the frictionless, free from wear mechanical part
- small outline dimensions and easy accommodations by all configurations
- small height minimising the effects of defocusing

Using the SOFA leads to very significant relaxation of the system constraints, as the SOFA:

- puts up with simplified stabilization of spacecraft body
- allows great relaxation of the alignment and thermal deflection requirements on the various constituents of the Antenna and on the sensors.

Thus the SOFA system largely simplifies satellite attitude control as well as all alignment and stability constraints of structures .

Several applications are possible :

- a) antenna fitted with a SOFA and an RF sensor ensures both transmit and receive functions or transmission alone, as the receive antenna requires no accurate pointing
- b) an antenna fitted with a SOFA and an RF sensor plus another antenna also equipped with a SOFA reproducing the evolutions of the first one. This set up corrects all attitude control errors.
- c) the SOFA's electronic is designed to permit orientation of an antenna beam's axis on a different direction from that defined by the RF sensor's on-ground beacon. This variable offset is telecommanded.

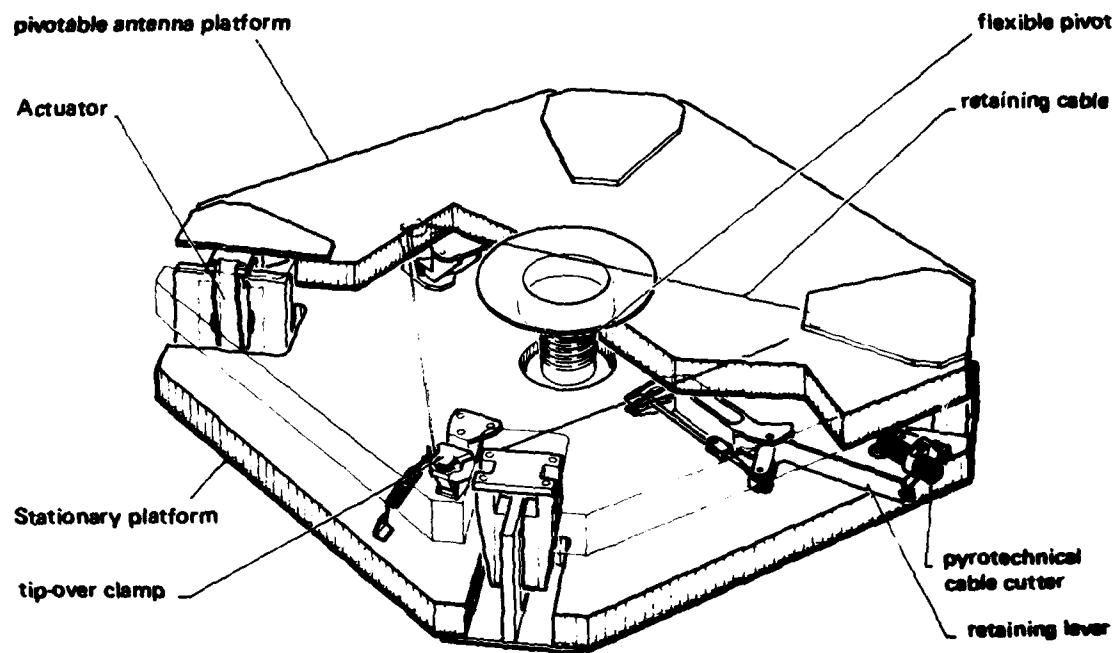


FIG. 1 - S.O.F.A. DEVICE

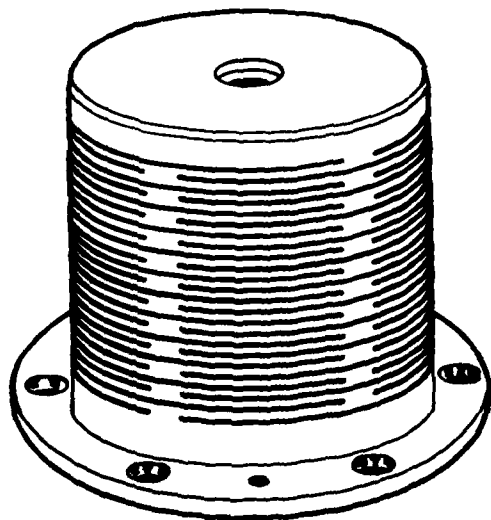


FIG. 2 - FLEXIBLE PIVOT

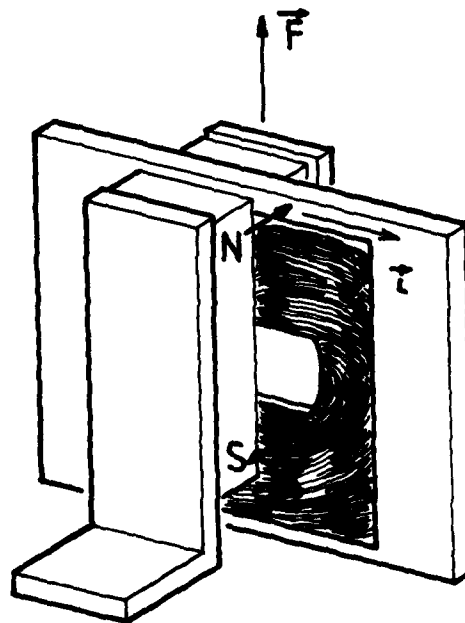


FIG. 3 - ACTUATOR PRINCIPLE

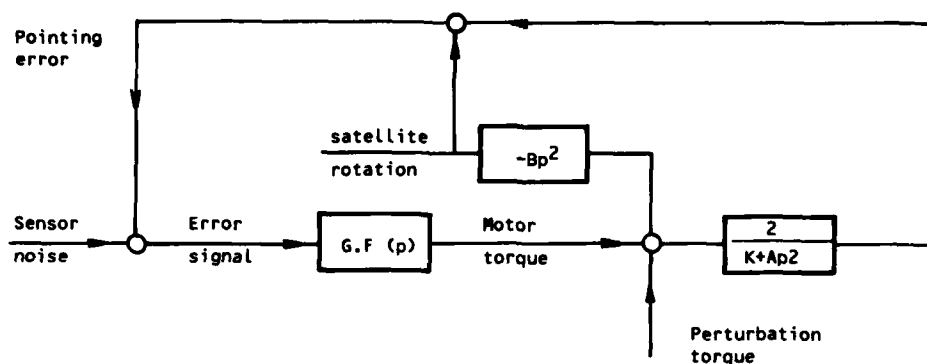


FIG. 4 - FUNCTIONAL BLOCK-DIAGRAM

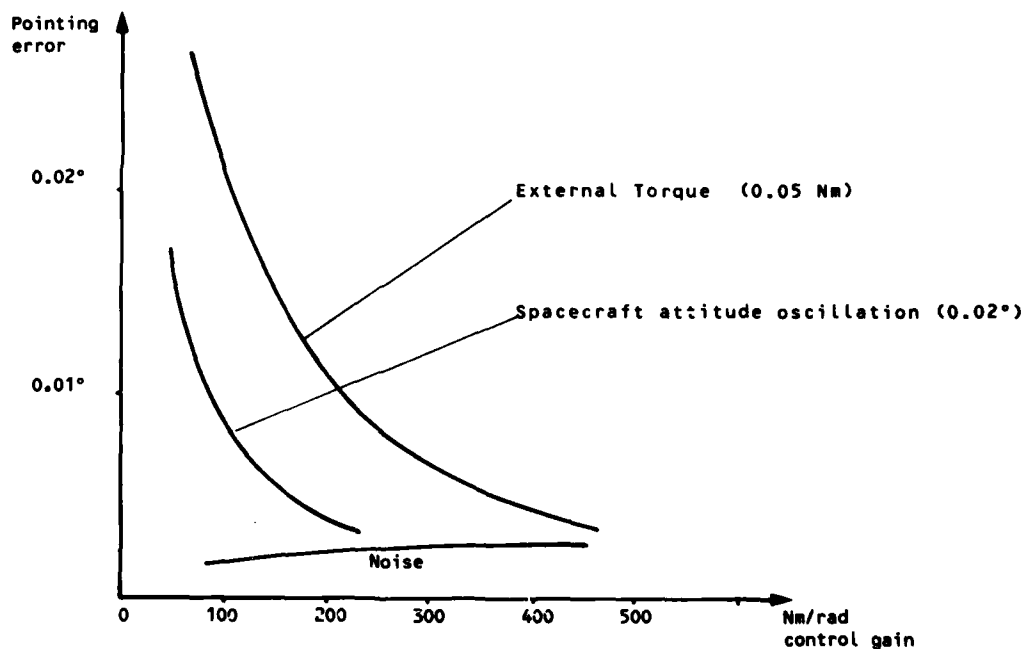


FIG. 5 - CONTROL LOOP ADJUSTMENT

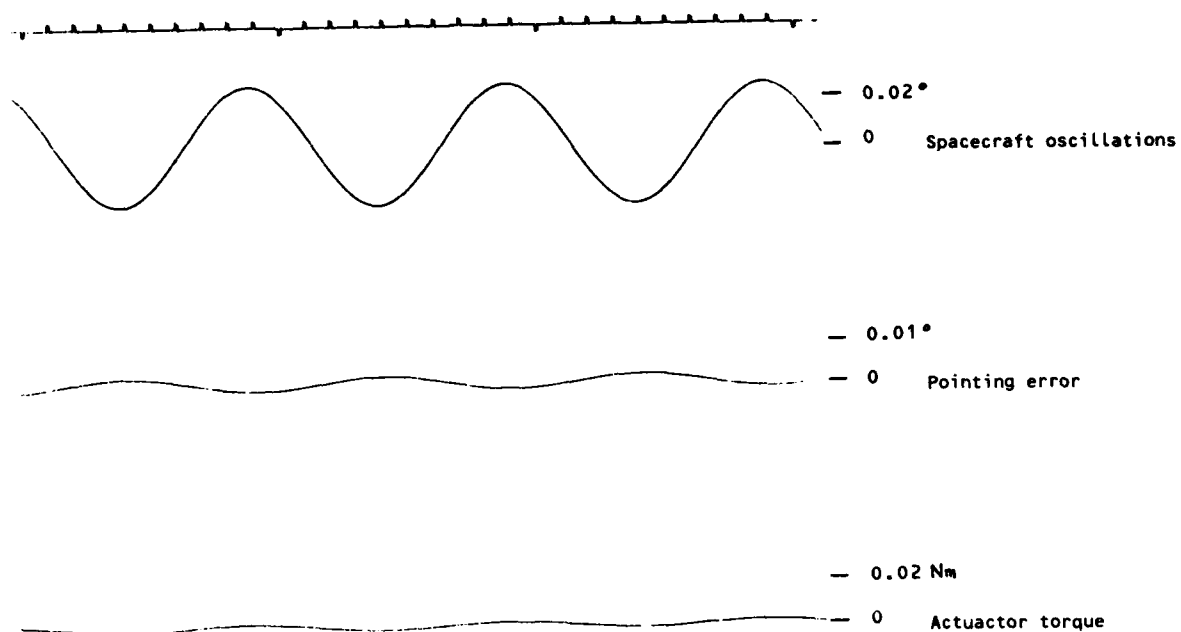


FIG. 6 - SPACECRAFT OSCILLATIONS EFFECT

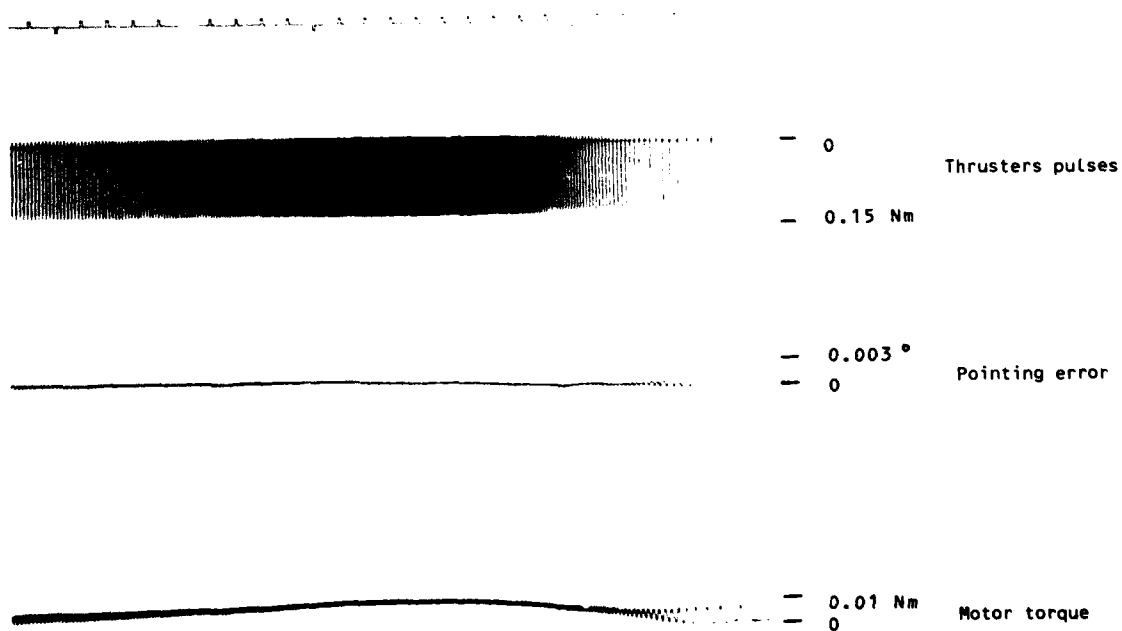
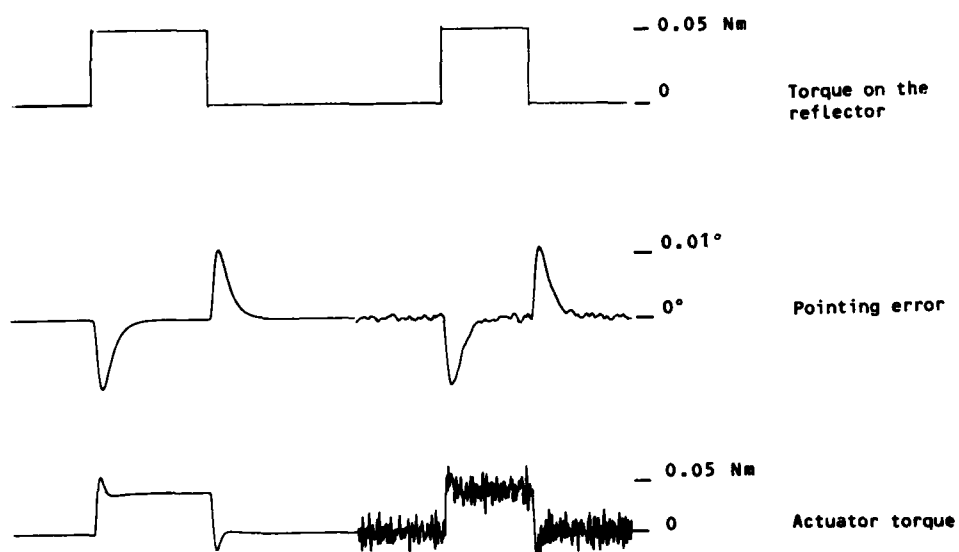
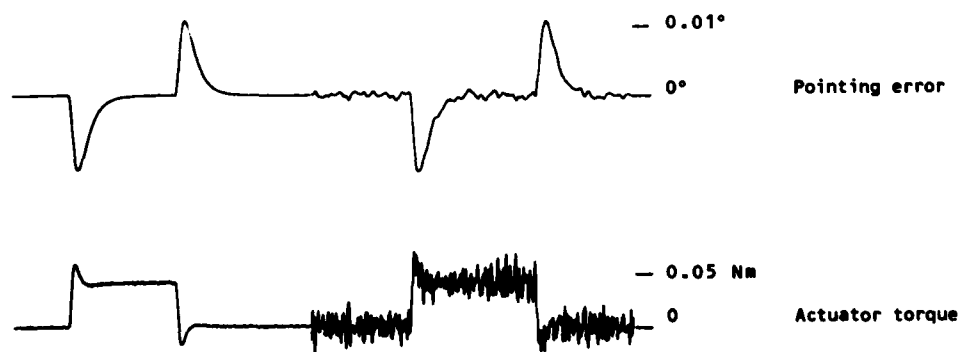


FIG. 7 - THRUSTER PULSES TRAIN EFFECT



Simulation results



Test results

FIG. 8 - SIMULATION AND TEST RESULTS

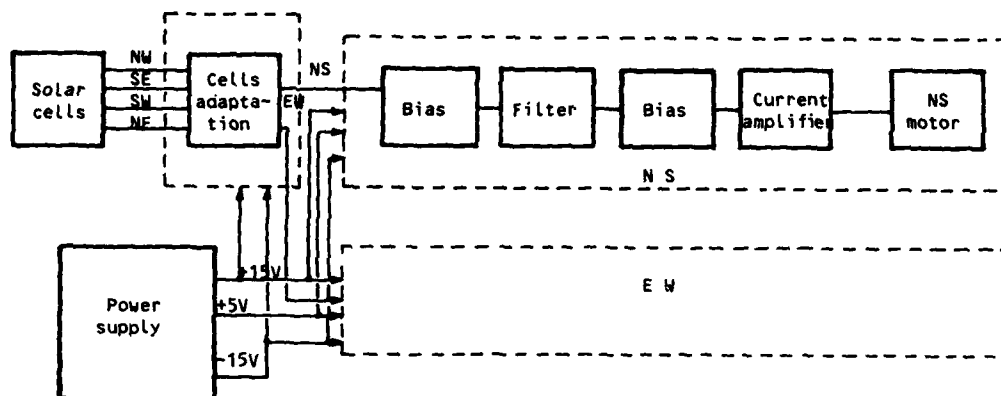


FIG. 9 - ELECTRONICS FUNCTIONAL BLOCK-DIAGRAM



FIG. 10 - S.O.F.A. BREADBOARD MODEL

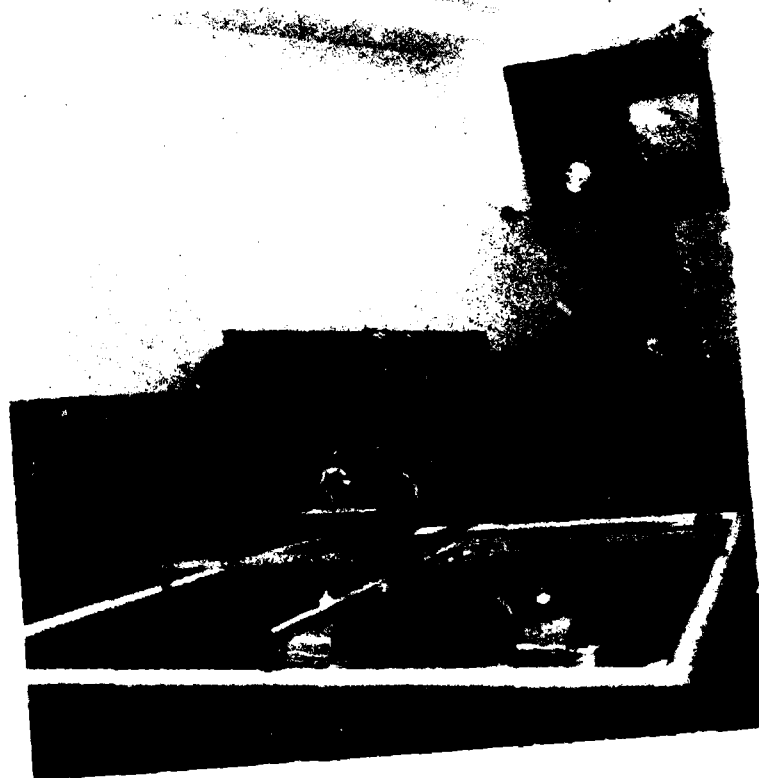


FIG. 11 - DYNAMICAL TEST FACILITIES

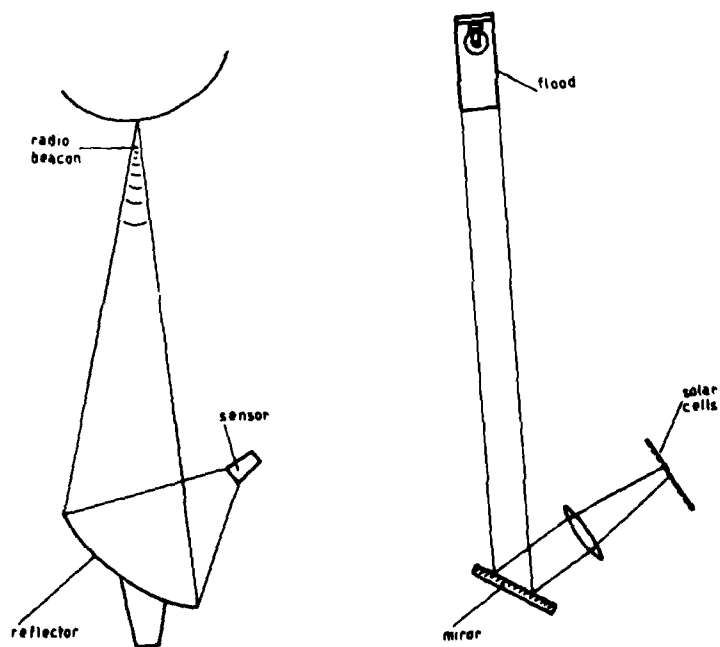


FIG. 12 - R.F. SENSOR OPTICAL SIMULATOR

Factorization Methods for Precision Satellite Orbit Determination

G. J. Bierman,
Consultant to The
Aerospace Corporation
President, Factorized
Estimation Applications, Inc.

L. A. Campbell,
Member of the Technical Staff
The Aerospace Corporation

W. A. Feess,
Sr. Engineering Specialist
The Aerospace Corporation

Summary

This paper documents state-of-the-art square root information filtering and smoothing technology that has been incorporated into the Aerospace TRACE orbital analysis program. Topics include (1) a pseudo-epoch state batch-sequential filter formulation, (2) techniques for inclusion of Markov process noise models, (3) a variable dimension filter structure that accommodates state vectors of large size, and (4) inclusion of a GPS second-order Markov clock model within the framework of the square root information filter/smoothing formulation. Planned evaluation of filter/smoothing performance in a GPS context is also discussed. The filter/smoothing is to be used for post-flight orbit determination, covariance analysis, navigation system performance monitoring, and to generate reference "best estimate" orbits.

Introduction

Our primary goal in this paper is to paint a representative picture of the use of state-of-the-art techniques for precision satellite orbit determination. Rather than present a survey, we elect to focus on our installation of a square root information filter/smoothing into a large orbital analysis program, TRACE, and to illustrate the ideas involved using the Global Positioning System of navigation satellites. We use these specific examples in order to clarify the relation of the mathematical formalism underlying the filter to its intended applications. No numerical results or actual cases are presented. We have assumed some familiarity on the part of the reader with linear estimation theory, but have tried to respond to the needs and tastes of those of our audience who are not specialists in filter theory, and have omitted many of the mathematical details that are available in other publications.

The Global Positioning System (GPS) was designed to provide accurate location and time information to many different classes of users through the use of a constellation of navigation satellites called Navstars. Phase I of GPS got underway in 1974, and the first Navstars were launched in 1978. At the time of this writing, there are six Navstars aloft in 12 hour orbits. Each Navstar carries a precision clock (oscillator) onboard. Pseudo-range and delta pseudo-range data from the Navstars are collected at a number of monitor stations. For precise definitions of pseudo-range, delta pseudo-range and other GPS terms and for a general introduction to the GPS system, see the papers collected in [1]. The data are obtained by comparing satellite clocks with monitor station clocks and measuring transit times. The collected data are transmitted to the Master Control Station, which uses a square root covariance (Kalman) filter, involving a large state vector, to estimate the satellite ephemerides and clock offsets for the Navstars and monitor stations. Predicted Navstar ephemerides and clock offsets are transmitted (uploaded) to the Navstars at regular intervals. A GPS user receives transmissions from those Navstars in view, which enable it to make pseudo-range and delta pseudo-range measurements and to retrieve the uploaded navigation information. Using the predicted Navstar ephemerides and clock offsets, in conjunction with corrected measurements, a user can determine its own position, velocity, and time (clock offset), if enough Navstars (four in the absence of other information) are in view. Navigation accuracy is heavily dependent on relative satellite geometry and Navstar clock accuracy.

TRACE is an orbital analysis program developed at Aerospace. The principal functions which TRACE addresses are ephemeris prediction, simulated data generation, orbit determination, and covariance analysis, see [3]. TRACE has extensive modeling capabilities, with sophisticated geopotential models allowing for high order spherical harmonics and embedded point masses, several built in atmosphere models, outgassing and other thrust models, solar radiation pressure effects, planetary perturbations, orbit adjusts, five basic timekeeping systems, four basic reference coordinate systems, and certain non earth-centered (e.g. lunar) and powered flight capabilities. Analytic models can be used for orbit propagation, but the standard method is integration of the equations of motion and the variational equations for parameter partial derivatives using a Cartesian coordinate system and a high precision numerical integrator. Our principal concerns are orbit and parameter determination and covariance analysis. In 1979, Aerospace began the installation in TRACE of a square root information filter and smoother, which uses techniques developed by one of us (Bierman) and suggested by his prior orbit determination experience at the Jet Propulsion Laboratory. This is where our story begins.

There are limits to the accuracy with which data can be collected. A high precision orbit determination program takes this measurement noise into account and determines an orbit that provides a "best fit" to the collected data. To produce accurate answers, such

programs have depended, in the main, on precise numerical integration and sophisticated deterministic models of orbital dynamics and planetary geography (including, for example, the effects of solar radiation pressure on orbits and pole wander on geography). As complex as the models may be, they cannot be perfect. Consequently, model errors are often ascribed to process noise, which lumps together both unmodeled and truly random perturbations. Stringent accuracy requirements, such as those imposed by GPS, necessitate models with many states and accurate stochastic modeling of certain key parameters (e.g. GPS clock phase, frequency and aging terms). After a study of various recursive stochastic filter formulations, Aerospace chose a batch-sequential, square root information filter with an associated U-D covariance factorized smoother, see [4], [5]. Key features of the implementation include

An estimation algorithm with an established reputation for numerical stability. The algorithm (SRIF) is an efficient and flexible extension of the weighted least-squares estimator that makes maximal use of numerically stable orthogonal transformations, see [6], [4].

A pseudo-epoch state vector formulation, [5], reduces the amount of computation required and effectively uses epoch state partials. This dovetails with previous TRACE software, which generated epoch state partials for use in batch mode weighted least squares fitting.

Pass dependent parameters, which allow for handling of problems with an unusually large number of parameters, [7]. The U-D covariance factorized smoother for pass dependent parameters is currently unique to TRACE.

Colored process noise, in particular second-order Markov models (developed for use as models of GPS clocks). The models and algorithms used generalize the first order case, presented in [4] and [5].

The remainder of this paper is organized as follows: Section 1 presents the mathematical algorithms used. The use of data equations and orthogonal transformations is emphasized. A review of the square root information filter in the white noise case is included, both for completeness and to clarify subsequent discussions of colored noise and smoothing. This section assumes some familiarity with linear estimation theory, Kalman filters, etc. Section 2 concerns proposed applications of the SRIF filter/smoothing to some GPS problems and planned tests of filter/smoothing performance in a GPS context. Section 3 compares alternative approaches to the orbit estimation problem to the SRIF approach and considers, in a speculative vein, the general directions that forthcoming developments in high precision orbit determination are likely to take.

Equations are numbered consecutively within each subsection. Equations with more than one part carry a distinguishing letter. Equation 6a of subsection 0 of Section 1 is referred to as (6a) in subsection 1.0, as (0.6a) in other subsections of Section 1, and as (1.0.6a) when referenced in other sections.

1. Mathematical Formulation of the Estimation Algorithms

1.0 Data Equations, Orthogonal Transformations, and Filter Updating

References [4] and [5] treat the square root information filter (SRIF) in considerable detail, and here we only review the basic ideas and techniques. When dealing with linear unbiased minimum variance estimation problems the key information is contained in the state estimate \hat{x} and the estimation error covariance \hat{P} . This is, of course, the fundamental idea of the Kalman filter. Let R be any square root of the information matrix \hat{P}^{-1} , i.e. $\hat{R}\hat{R}^T = \hat{P}^{-1}$. If \hat{z} is defined to be $\hat{R}\hat{x}$, then, assuming Gaussian noise, the definition of \hat{P} as the estimation error covariance shows that $v = \hat{R}x - \hat{z}$ is a zero-mean Gaussian random vector with unit covariance, which we write as $v \in N(0, I)$. In the SRIF formulation, we replace the pair (\hat{P}, \hat{x}) by the equivalent data equation

$$\hat{R}x = \hat{z} + v, \quad v \in N(0, I) \quad (1a)$$

The pair (\hat{P}, \hat{x}) can be recovered from this data equation, since \hat{x} must equal $\hat{R}^{-1}\hat{z}$ for an unbiased estimator and, as can be seen by a simple computation, \hat{P} is then $\hat{R}^{-1}\hat{R}^{-T}$. For simplicity of notation we write $a \sim b$ to mean $a = b + v$, $v \in N(0, I)$ so that (1a) becomes

$$\hat{R}x \sim \hat{z} \quad (1b)$$

The data equation concept arises naturally from least-squares analysis and the minimization of quadratic performance functionals. The key idea in the square root information filter is to exploit the freedom of choice in the selection of the square root information matrix \hat{R} by using premultiplication by orthogonal transformations to generate more useful data equation representations.

We will need the following properties of orthogonal transformations ($T^{-1} = T^T$).

(a) Given a matrix A , there is an easily computed (Householder) orthogonal transformation T , such that the product TA has zeroes below the first element in its first column.

(b) The product of orthogonal transformations (matrices) is orthogonal.

(c) Given a matrix A , there is an orthogonal transformation (matrix) T_A such

that $T_A A$ has zeroes below the main diagonal. $T_A A$ is then a (not necessarily square) upper triangular matrix. This fact follows from (a) and (b) by induction on the size of A . Crucial to the intended SRIF applications is the fact that one can construct the triangularized result $T_A A$ without explicit construction or storage of the orthogonal transformation matrix T_A .

(d) If $v \in N(0, I)$ then $Tv \in N(0, I)$ for any orthogonal transformation T . Thus $a \sim b$ if, and only if, $Ta \sim Tb$.

(e) If T is orthogonal, then matrices A and TA have the same rank. Most importantly, as discussed in [6], the computed product TA is relatively insensitive to roundoff errors. Thus premultiplication by orthogonal transformations is numerically rank preserving.

These facts about orthogonal transformations are used to construct the measurement and time update algorithms for the SRIF as follows:

Measurement Updating

Given a priori information about the state vector x , in the form of a data equation $Rx \sim u$, and linear measurements $z = Ax + v$, assumed normalized ($v \in N(0, I)$) then

$$\begin{bmatrix} R \\ A \end{bmatrix} x \sim \begin{bmatrix} u \\ z \end{bmatrix} \quad (2)$$

Now, by property (c), the array $\begin{bmatrix} R \\ A \end{bmatrix}$ can be triangularized by an orthogonal transformation T , say

$$T \begin{bmatrix} R \\ A \end{bmatrix} = \begin{bmatrix} \hat{R} \\ 0 \end{bmatrix} \quad (3)$$

where \hat{R} is upper triangular. Applying T to both sides of (2) produces

$$\begin{bmatrix} \hat{R} \\ 0 \end{bmatrix} x \sim \begin{bmatrix} \hat{z} \\ e \end{bmatrix}, \text{ where } T \begin{bmatrix} u \\ z \end{bmatrix} = \begin{bmatrix} \hat{z} \\ e \end{bmatrix} \quad (4)$$

and the data equation $\hat{R}x \sim \hat{z}$ represents the combined information, a priori plus measurements, about x . By property (e), if the original problem is overdetermined and of full rank, then the minimum variance unbiased estimate \hat{x} of x can be computed as $\hat{x} = \hat{R}^{-1} \hat{z}$.

Let $\| \cdot \|$ denote euclidean norm. Since T is norm preserving $\|e\| = \min_x \left\| \begin{bmatrix} \hat{R} \\ 0 \end{bmatrix} x - \begin{bmatrix} \hat{z} \\ e \end{bmatrix} \right\|$
 $= \min_x \left\| \begin{bmatrix} R \\ A \end{bmatrix} x - \begin{bmatrix} u \\ z \end{bmatrix} \right\|$. Thus $\|e\|$ is a post-update measure of the residual least-squares error.

Time Updating

Consider a discrete time dynamic model of the form

$$x_{j+1} = \phi_j x_j + \Gamma w_j \quad (5)$$

where ϕ_j is nonsingular, $\Gamma = (\Gamma_1, \dots, \Gamma_{nw})$ and w is a discrete time white sequence of zero-mean random vectors with uncorrelated components $w_i(i)$, $i=1, \dots, nw$. Thus $E(w_i w_j^T) = 0$ if $j \neq i$ and $Q_i = E(w_i w_i^T)$ is a positive definite diagonal matrix. For purposes of algorithm development, decompose the dynamic model (5) as the product of a deterministic update

$$x_{j+1}^{(D)} = \phi_j x_j \quad (6a)$$

and nw successive single component stochastic updates

$$x_{i+1}^{(D)} = x_i^{(D)} + \Gamma_i w_j(i) \quad (6b)$$

where $i = 1, \dots, nw$ and the variables $x_i^{(D)}$ are defined by (6b) and the relations $x_1^{(D)} = x_{j+1}^{(D)}$. From (5), it follows that $x_{j+1} = x_{1+nw}^{(D)}$.

The point of this decomposition is that it makes more transparent the component SRIF data equation steps. Starting with $\hat{R}_j x_j \sim \hat{z}_j$, construct a data equation for $x_{j+1}^{(D)}$

$$R_{j+1}^{(D)} x_{j+1}^{(D)} \sim \hat{z}_j \quad (\text{where } R_{j+1}^{(D)} = R_j \phi_j^{-1}) \quad (7)$$

The single component stochastic updates are carried out by considering an augmented state vector and an associated data equation

$$\begin{bmatrix} r_w^{(j,i)} & 0 \\ -R^{(i)} \Gamma_i & R^{(i)} \end{bmatrix} \begin{bmatrix} w_j(i) \\ x'_{i+1} \end{bmatrix} \sim \begin{bmatrix} 0 \\ z'_i \end{bmatrix} \quad (8)$$

where $r_w^{(j,i)} w_j(i) \sim 0$ is a data equation for the noise component $w_j(i)$ and, for $i = 1$ $R^{(1)} = R_{i+1}^{(D)}$ and $z'_1 = \hat{z}_1$. This data equation is then partially triangularized by premultiplying by an elementary orthogonal transformation, cf. property (a), to obtain the equivalent data equation

$$\begin{bmatrix} s_w^{*(i)} & s_{wx}^{*(i)} \\ 0 & R^{(i+1)} \end{bmatrix} \begin{bmatrix} w_j(i) \\ x'_{i+1} \end{bmatrix} \sim \begin{bmatrix} z_i^* \\ z'_{i+1} \end{bmatrix} \quad (9)$$

which serves to define $R^{(i+1)}$ and z'_{i+1} . The lower portion, $R^{(i+1)} x'_{i+1} \sim z'_{i+1}$, is a valid data equation for x'_{i+1} and is used as input to the next step. The $i+1$ terminal value of this process, $(R^{(1+n)}, z'_{1+n})$, is a square root information array for x_{j+1} . The top row in (9) embodies information concerning the noise and its relation to the system state. It is saved for later use in computing smoothed estimates, [4], [5]. As far as the filter estimate \hat{x}_{i+1} is concerned, the top row can be simply "thrown away" because the partially triangular structure isolates the noise variable $w_j(i)$ from the filter state x_{i+1} , and neither the estimate \hat{x}_{i+1} nor its associated error covariance are affected by the top row. This theme - augment the state vector, (partially) triangularize, save data for the smoother, and reduce the state vector size in preparation for the next filter step - occurs again and again. Section 1.5 on smoothing discusses how the saved data are used to generate smoothed estimates.

The SRIF implementation in TRACE involves a number of refinements to the basic filtering process represented by the above algorithm for measurement and time updating. These refinements are described individually in the following sections.

1.1 Treatment of Biases and First-Order Markov Colored Noise

Considerable gains in processing efficiency (in both the filter and the smoother) can be realized by partitioning and rearranging the state vector in the discrete time model (0.5). In the TRACE implementation the dynamic model takes the form

$$\begin{bmatrix} p \\ f \\ x \\ y \end{bmatrix}_{j+1} = \begin{bmatrix} M & 0 & 0 & 0 \\ 0 & 1 & 0 & 0 \\ \phi_{xp} & \phi_{xf} & \phi_x & 0 \\ 0 & 0 & 0 & 1 \end{bmatrix}_j \begin{bmatrix} p \\ f \\ x \\ y \end{bmatrix}_j + \begin{bmatrix} w_j \\ 0 \\ 0 \\ 0 \end{bmatrix} \quad (1)$$

where

- p = process noise states (the only states to which process noise is explicitly added)
- f = force states (which may influence the dynamic states through ϕ_{xf})
- x = dynamic states (nonsingular transitions, ϕ_x ; possibly influenced by the p and f variables)
- y = bias parameters (trivial dynamics; affect measurements only)

In (1) the added process noise w_j is a white noise sequence of random vectors, whose components may be correlated. The fact that M is not further specified, and may be singular, allows for a good deal of generality. A single component, say s , of p may satisfy an equation of the form

$$s_{j+1} = m s_j + w_j^s \quad (2)$$

extracted from (1), where m may, in general, depend on j . Situations of special interest are $m = 1$, in which case s is a random walk parameter, and $m = 0$, in which case s is a white noise parameter. When $0 < m < 1$, we call s a first-order Markov colored noise parameter. Such parameters are used for modeling drag, solar radiation pressure, slowly varying gyro drifts, range and doppler drifting measurement biases, nongravitational forces, etc.

The colored noise time updating algorithm, described in [4] and [5], is arranged to handle the full range of m values, in particular $m = 0$, which corresponds to a transition matrix singularity. The point to note is that in the SRIF algorithm only the deterministic portion of the time update requires a nonsingular transition matrix (cf. equations (0.7) and (0.8)). In the TRACE implementation the transition matrix for the dynamic states is a matrix of partials obtained by the integration of variational

equations and is always nonsingular.

Process noise is effectively added to the dynamic states because they are coupled to the process noise states through the matrix ϕ_{xp} . The dynamic states are usually simply vehicle position and velocity, and process noise is not added directly to these states because they are modeled as continuous processes. Force states, f , and bias parameters, y , differ only in that bias parameters do not dynamically affect any other states and appear only in the measurements. This allows bias parameters to be treated as force states, if desired, by defining appropriate columns of zeros in ϕ_{xf} .

The arrangement of states given here was chosen for computational efficiency of the time update. Just as in 1.0, the time update can be decomposed into a deterministic update followed by stochastic updates. If M is diagonal, these stochastic updates take the form of n_p successive single component stochastic updates, where n_p is the number of process noise states. If the n_y bias parameter states are placed at the bottom of the list, neither the deterministic update nor the stochastic parameter updates will affect the bottom n_y rows of the equations involved. For the stochastic parameter updates, the minimum number of columns that must be triangularized is the depth of the parameter (i.e. its location) in the parameter list. Placing the process noise parameters at the top of the list thus minimizes the computational effort.

1.2 Second-Order Markov Models

The matrix of the discrete time dynamic model (1.1) need not be diagonal. Here we describe a two state (clock phase and clock frequency) model intended to be used for GPS clocks. This model has been implemented in TRACE (but simpler models are also available pending testing and evaluation). It is based on a continuous time model of the form

$$\frac{d}{dt} \begin{bmatrix} cp \\ cf \end{bmatrix} = \begin{bmatrix} 0 & 1 \\ 0 & -1/\tau \end{bmatrix} \begin{bmatrix} cp \\ cf \end{bmatrix} + \begin{bmatrix} \xi_1 \\ \xi_2 \end{bmatrix} \quad (1)$$

where ξ_i , $i = 1, 2$ are continuous time zero mean white noise processes with intensity matrix $\text{Diag}(q_p, q_f) \delta(t-t')$, see [8]. An analytic solution to (1) gives the discrete time results

$$\begin{bmatrix} cp \\ cf \end{bmatrix}_{j+1} = \begin{bmatrix} 1 & a \\ 0 & b \end{bmatrix} \begin{bmatrix} cp \\ cf \end{bmatrix}_j + \begin{bmatrix} B_1 & B_2 \\ 0 & B_3 \end{bmatrix} \begin{bmatrix} w_1 \\ w_2 \end{bmatrix} \quad (2)$$

where the w vector is $N(0, I)$ and

$$\begin{aligned} b &= \exp(-Dt/\tau) \\ Dt &= t_{j+1} - t_j \\ a &= \tau(1-b) \end{aligned} \quad (3)$$

and the matrix B is an upper triangular Cholesky factor of the system response covariance matrix

$$\begin{bmatrix} B_1 & B_2 \\ 0 & B_3 \end{bmatrix} \begin{bmatrix} B_1 & B_2 \\ 0 & B_3 \end{bmatrix}^T = \int_{t_j}^{t_{j+1}} \phi(t_{j+1} - s) \begin{bmatrix} q_p & 0 \\ 0 & q_f \end{bmatrix} \phi^T(t_{j+1} - s) ds \quad (4)$$

where

$$\phi(t) = \begin{bmatrix} 1 & a(t) \\ 0 & b(t) \end{bmatrix}$$

with $a(t)$ and $b(t)$ defined as in (3), using t instead of Dt .

Note that cf is a first-order Markov colored noise parameter. Because the use of a second-order Markov model in this form is so far unique to TRACE, we present the clock model time update, published here for the first time, in somewhat greater detail than we have used heretofore. Since the basic idea in the SRIF time updates is to factor the transformation described by the dynamic model into a product of simpler transformations, attention is restricted to the case where the transformation involved is that described by (2) for the clock states, and reduces to the identity for all other states (since the clock states are dynamically decoupled from the other states, the time updates for the other states can be done before or after the clock state update). Assume, then, that the dynamic model is of the form

$$\begin{bmatrix} x \\ cp \\ cf \end{bmatrix}_{j+1} = \begin{bmatrix} I & 0 & 0 \\ 0 & 1 & a \\ 0 & 0 & b \end{bmatrix} \begin{bmatrix} x \\ cp \\ cf \end{bmatrix}_j + \begin{bmatrix} 0 & 0 \\ B_1 & B_2 \\ 0 & B_3 \end{bmatrix} \begin{bmatrix} w_1 \\ w_2 \end{bmatrix} \quad (6)$$

where x now represents all the other states, and assume that we have a data equation

$$\begin{bmatrix} R_x & R_{xp} & R_{xf} \\ 0 & R_p & R_{pf} \\ 0 & R_{fp} & R_f \end{bmatrix} \begin{bmatrix} x \\ cp \\ cf \end{bmatrix}_j \sim \begin{bmatrix} z_x \\ z_p \\ z_f \end{bmatrix} \quad (7)$$

in partially triangular form. The task is to find a comparable data equation for the states at time t_{j+1} . Write out the model (6) as a system of equations

$$x_{j+1} = x_j \quad (8a)$$

$$cp_{j+1} = cp_j + a(cf_j) + B_1 w_1 + B_2 w_2 \quad (8b)$$

$$cf_{j+1} = b(cf_j) + B_3 w_2 \quad (8c)$$

and introduce the variables

$$\bar{cp} = cp_j + a(cf_j) \quad (9a)$$

$$\bar{\bar{cp}} = \bar{cp} + B_2 w_2 \quad (9b)$$

Clearly

$$cp_{j+1} = \bar{\bar{cp}} + B_1 w_1 \quad (10)$$

The utility of this decomposition of the cp update becomes clearly when (9a) and (9b) are substituted into the data equation (7), yielding

$$\begin{bmatrix} R_x & R_{xp} & (R_{xf} - aR_{xp}) \\ 0 & R_p & (R_{pf} - aR_p) \\ 0 & R_{fp} & (R_f - aR_{fp}) \end{bmatrix} \begin{bmatrix} x_{j+1} \\ \bar{cp} \\ cf_j \end{bmatrix} \sim \begin{bmatrix} z_x \\ z_p \\ z_f \end{bmatrix} \quad (11a)$$

and

$$\begin{bmatrix} 1 & 0 & 0 & 0 \\ -B_2 R_{xp} & R_x & R_{xp} & (R_{xf} - aR_{xp}) \\ -B_2 R_p & 0 & R_p & (R_{pf} - aR_p) \\ -B_2 R_{fp} & 0 & R_{fp} & (R_f - aR_{fp}) \end{bmatrix} \begin{bmatrix} w_2 \\ x_{j+1} \\ \bar{\bar{cp}} \\ cf_j \end{bmatrix} \sim \begin{bmatrix} 0 \\ z_x \\ z_p \\ z_f \end{bmatrix} \quad (11b)$$

The top row of (11b) merely states that $w_2 \in N(0,1)$. The key substitution step now is to use the relation (8c) to eliminate w_2 and to introduce cf_{j+1} . Namely, use

$$w_2 = [cf_{j+1} - b(cf_j)] / B_3 \quad (12)$$

to eliminate w_2 from each row of data equation (11b), obtaining an equivalent data equation involving x_{j+1} , $\bar{\bar{cp}}$, cf_{j+1} and cf_j . Reorder the resulting equations to obtain a data equation of the form

$$\left[\begin{array}{c|c} -b/B_3 & 0 \ 0 \ 1/B_3 \\ \hline V & R' \end{array} \right] \begin{bmatrix} cf_j \\ x_{j+1} \\ \bar{\bar{cp}} \\ cf_{j+1} \end{bmatrix} \sim \begin{bmatrix} 0 \\ z' \end{bmatrix} \quad (13)$$

While the development appears complicated (so much so that we do not explicitly write out the terms V , R' and z'), these manipulations, involving basically elementary column operations, require relatively little code when implemented on a computer. The next step is to premultiply (13) by an orthogonal transformation that partially triangularizes it, obtaining

$$\begin{bmatrix} s^* \\ \hline 0 & R'' \end{bmatrix} \begin{bmatrix} cf_j \\ \hline x_{j+1} \\ \bar{c}_p \\ cf_{j+1} \end{bmatrix} \sim \begin{bmatrix} z^* \\ \hline z'' \end{bmatrix} \quad (14)$$

The top row (s^* , z^*) is stored away for later use in smoothing and the square root information array (R'' , z'') is retained for use by the filter. The final step is to use the standard procedure for single component first-order Markov parameter stochastic updates to obtain a data equation for x_{j+1} , $c_{p,j+1}$ and cf_{j+1} from the given one for x_{j+1} , \bar{c}_p and cf_{j+1} , using the relation (10).

When B_0 is zero, that is, when there is no white noise cross correlation, the algorithm just described reduces to a deterministic update followed by two single component stochastic updates. This second-order model updating algorithm is thus a generalization of the first-order colored noise update, and shares with it the property of being well defined and numerically stable even when the process noise states transition matrix is singular. The algorithm is readily modified to handle higher order models.

A point worth emphasizing is that the update outlined here actually takes on a simpler appearance when described in terms of the assignment and array indexing statements of computer code and turns out to involve only a modest amount of computation. This is typical of SRIF algorithms.

1.3 Addition and Deletion of Parameters

There are over one hundred different types of parameters available to a TRACE user. Even if only a few different types of parameters are used, the total parameter set can be quite large when there are a number of different ground stations and satellites involved.

The basic storage required for an orbit determination/covariance analysis program is roughly proportional to the square of the number of parameters used. This limits the number of parameters that may be used in a given run. For TRACE this basic limit has been arbitrarily set at 100 parameters.

Our square root information filter formulation provides a means for evading the restriction on the total number of parameters. By means of the orthogonal transformation triangularization techniques that are central to the SRIF, it is possible to dynamically add and delete parameters. Even though the parameter set at any one point in time cannot contain more than 100 parameters, the total number of parameters used in a run can be quite large. The following is an outline of the technique used.

The total parameter set for a SRIF run is divided into two subsets, called common parameters and disposable parameters. The total timespan under consideration is divided into arcs, which are adjacent subintervals specified by the program inputs. Each arc may contain many time steps of the underlying discrete time dynamic model. The disposable parameters are labeled with pass identifiers and pass dependent start/stop times (not necessarily coincident with arc boundaries) are supplied. When arc boundaries are crossed, disposable parameters are added to or deleted from the current state vector. Common parameters cannot be eliminated and must appear in the state vector in each arc. The convention used in TRACE is that disposable parameters cannot be process noise parameters and must be dynamically decoupled from the vehicle states. In terms of the discrete time dynamic model (1.1) they must be bias parameters, and we may take the common parameters to be the p , f , and x vectors of (1.1) and the disposable parameters to be the y vector. These restrictions, which could be relaxed somewhat, cover the class of problems encountered in TRACE applications.

Let the state vector be partitioned as

$$\begin{bmatrix} x \\ y \end{bmatrix} \quad (1)$$

where x now represents all the common parameters and y represents the current set of disposable (bias) parameters. At an arc boundary a new set of disposable parameters y' is introduced, where y and y' may share some states. If

$$\begin{bmatrix} R_x & R_{xy} \\ R_{yx} & R_y \end{bmatrix} \begin{bmatrix} x \\ y \end{bmatrix} \sim \begin{bmatrix} z_x \\ z_y \end{bmatrix} \quad (2)$$

is the data equation obtained at the end of the arc, then the following steps are taken in the transition to the new arc. First, the data equation columns are permuted so that in the resulting equation the parameters to be deleted head the parameter list. This equation is then triangularized to yield

$$\begin{bmatrix} * & * & * \\ 0 & R'_x & R'_{xr} \\ 0 & 0 & R'_{xr} \end{bmatrix} \begin{bmatrix} y_{del} \\ x \\ y_{ret} \end{bmatrix} \sim \begin{bmatrix} * \\ z'_x \\ z'_{ret} \end{bmatrix} \quad (3)$$

Here y_{del} , y_{ret} represent the sets of parameters to be deleted and retained, respectively. The top row, denoted by asterisks, is saved for later smoothing. To the bottom two rows, which form a data equation for x and y_{ret} , is added the a priori information concerning the newly introduced disposable states, y_{add} , resulting in the data equation

$$\begin{bmatrix} R'_x & R'_{xr} & 0 \\ 0 & R'_r & 0 \\ 0 & 0 & R'_a \end{bmatrix} \begin{bmatrix} x \\ y_{ret} \\ y_{add} \end{bmatrix} \sim \begin{bmatrix} z'_x \\ z'_{ret} \\ z'_{add} \end{bmatrix} \quad (4)$$

A priori standard deviations and values for the newly introduced disposable parameters are supplied by user input. Equation (4) is a data equation for x and y' , where y' , the set of disposable parameters for the new arc, consists of y_{ret} followed by y_{add} .

1.4 Pseudo-Epoch State Variables

In the discrete time dynamic model (1.1) the dynamic states, x , are current time states. Restrict attention to the case of a single vehicle and assume that x consists of earth centered inertial (ECI) position and velocity for the vehicle (center of mass). Most conventional orbit determination procedures solve for initial conditions (usually called "epoch states") rather than current time states and compute measurement partials with respect to epoch states. A large investment in computer code is tied up in the routines that calculate the measurement partials. Both to avoid the extensive rewriting of code that would be required to use current time states directly and because the resulting simpler dynamic model affords greater computational efficiency, the TRACE implementation of the SRIF uses a pseudo-epoch state formulation of the discrete time dynamic model and the measurement model. This formulation is briefly described here. Full details can be found in [4] and [5]. In estimating pseudo-epoch states, the filter operates in batch-sequential mode, generating pseudo-epoch state estimates at time t_j based on data with measurement times up to, but not including, t_{j+1} .

The filter only provides estimates of the states at discrete time points, but one can define an estimated continuous trajectory, consistent with the choice of a piecewise constant process noise model, by

$$\hat{x}(t) = \phi_x(t, t_j) \hat{x}_j + \phi_{xp}(t, t_j) \hat{p}_j + \phi_{xf}(t, t_j) \hat{f}_j \quad (1)$$

for $t_j \leq t < t_{j+1}$, where $\phi_x(t, t_j)$, $\phi_{xp}(t, t_j)$, and $\phi_{xf}(t, t_j)$ are transition matrices (actually matrices of partials, since the problem is linearized) relating the vehicle states at time t to parameter values at time t_j . Call \hat{x}_0 an equivalent pseudo-epoch state estimate, if it produces the same estimated trajectory

$$\hat{x}(t) = \phi_x(t, t_0) \hat{x}_0 + \phi_{xp}(t, t_j) \hat{p}_j + \phi_{xf}(t, t_0) \hat{f}_j \quad (2)$$

Note that in this equation t_j has been replaced by t_0 (the initial or epoch time) in all but the term corresponding to the process noise states. The term "pseudo-epoch" is used because the relation (2) between $\hat{x}(t)$ and \hat{x}_0 depends on the current estimate of the process noise states p . Thus \hat{x}_0 is not, in general, an estimate of the epoch state $x(t_0)$, and is meaningful only through (2). When there are no process noise states, the pseudo-epoch state \hat{x}_0 is independent of j and does reduce to the epoch state, $x(t_0)$.

The fundamental transition relation $\phi(t, t_0) = \phi(t, t_j) \phi(t_j, t_0)$ gives rise to the "chain rule"

$$\phi_{xf}(t, t_0) = \phi_x(t, t_j) \phi_{xf}(t_j, t_0) + \phi_{xf}(t, t_j) \quad (3)$$

Equating the right hand sides of (1) and (2) one obtains the relation

$$\hat{x}_0 = \phi_x^{-1}(t_j, t_0) (\hat{x}_j - \phi_{xf}(t_j, t_0) \hat{f}_j) \quad (4)$$

This relation with " $\hat{\cdot}$ " removed, is used to define the pseudo-epoch states. The dynamic model (1.1), reexpressed in terms of these pseudo-epoch states, becomes simply

$$\begin{bmatrix} p \\ f \\ x_0 \\ y \end{bmatrix}_{j+1} = \begin{bmatrix} M & 0 & 0 & 0 \\ 0 & I & 0 & 0 \\ VP & 0 & I & 0 \\ 0 & 0 & 0 & I \end{bmatrix}_j \begin{bmatrix} p \\ f \\ x_0 \\ y \end{bmatrix}_j + \begin{bmatrix} w_j \\ 0 \\ 0 \\ 0 \end{bmatrix} \quad (5)$$

where

$$VP_j = \phi_x^{-1}(t_{j+1}, t_0) \phi_{xp}(t_{j+1}, t_0) - \phi_x^{-1}(t_j, t_0) \phi_{xp}(t_j, t_0) \quad (6)$$

This dynamic model enjoys both advantages claimed

- it is computationally simpler than (1.1): the transition matrix is more sparse and more highly structured than that of (1.1).
- it makes effective use of epoch state partials: equation (6) expresses the terms of the transition matrix for the pseudo-epoch states entirely in terms of epoch state rather than current time partials and requires only the inversion of small (6x6) matrices.

The only measurement partials that need to be corrected in order to account for the fact that pseudo-epoch states are being used are the measurement partials for the process noise states. To see this, let

$$z(t) = A_p p(t) + A_f f + A_x x(t) + A_y y + v, \quad v \in N(0, I) \quad (7)$$

be the (linear and normalized) measurement model for a measurement at time t (between t_j and t_{j+1}) expressed in terms of measurement partials with respect to current time states and let

$$z(t) = A_p^0 p(t_0) + A_f^0 f + A_x^0 x(t_0) + A_y y + v, \quad v \in N(0, I) \quad (8)$$

be the corresponding measurement model using epoch states. The epoch state measurement partials can be expressed in terms of the current time measurement partials using the chain rule for partial derivatives. They are computed without knowledge of the process noise states transition matrices M_j (i.e. assuming $M_j = I$). To obtain the measurement model in terms of pseudo-epoch states, set $p(t)$ equal to p_j (piecewise constant process noise) and substitute (2) (with " \wedge " s removed) into (7). Collect terms to obtain

$$z(t) = A_p' p_j + A_f' f + A_x' x_0 + A_y' y + v, \quad v \in N(0, I) \quad (9)$$

Comparison of terms shows that

$$\begin{aligned} A_f' &= A_f^0 \\ A_x' &= A_x^0 \\ A_y' &= A_y \end{aligned} \quad (10)$$

and that

$$A_p' = A_p + A_x \phi_{xp}(t, t_j) \quad (11)$$

Since

$$A_p^0 = A_p + A_x \phi_{xp}(t, t_0) \quad (12)$$

(11) can be expressed as

$$A_p' = A_p^0 + A_x \phi_{xp}(t, t_j) - A_x \phi_{xp}(t, t_0) \quad (13)$$

Algebraic manipulation, using

$$A_x^0 = A_x \phi_x(t, t_0) \quad (14)$$

and the chain rule, shows that

$$A_p' = A_p^0 - A_x^0 (\phi_x^{-1}(t_j, t_0) \phi_{xp}(t_j, t_0)) \quad (15)$$

Relation (15) represents the only adjustment that must be made to the epoch state measurement partials. The correction term factor

$$\phi_x^{-1}(t_j, t_0) \phi_{xp}(t_j, t_0) \quad (16)$$

is calculated only once per time step, regardless of the number of measurements in the time step, and is used both in the calculation of VP_j (Equation (6)) and to adjust the measurement partials (Equation (15)).

1.5 Smoothing

Reference [5] contains a complete description of the square root information smoother (SRIS) as it is applied to the orbit determination problem. Here we focus primarily on the computation of smoothed estimates, with only a few remarks on the

computation of smoothed covariances. Smoothed estimates are optimal (minimum variance) unbiased linear estimates that are based on a priori model knowledge and measurements that encompass the entire time span of interest. In contrast, filter estimates¹ are based on only part of the data.

The smoothed estimates are generated in a two pass procedure. The first pass (operating in reverse time order) uses the stored smoothing coefficients to generate pseudo-epoch smoothed estimates. The second pass uses equation (4.2) to generate current time smoothed estimates from the pseudo-epoch smoothed estimates. The operation of the second pass is straightforward, so we discuss only the first (backward) pass.

There are two basic steps in the operation of the filter: measurement updates and what we call model updates. The latter category includes deterministic updates, single component stochastic updates, clock model updates, and addition and deletion of parameters at the ends of arcs. In a measurement update the square root information array for the filter state vector is updated so as to incorporate the information provided by the measurements. In a model update the current filter state vector actually changes, that is, we start with a square root information array for the current filter state vector and consider a new filter state vector (of possibly different length) which bears a mathematical relation to the previous (no longer current) filter state vector. The nature of the mathematical relationship is determined by the model, including its stochastic aspects. For instance, in a single component stochastic update (Section 1.0), one typically augments the state vector (by a single component), deduces the square root information array for the augmented state vector, reorders the states and triangularizes the resulting data equation, then saves a row of smoothing coefficients before reducing the size of the state vector again. Here the change in size of the filter state vector is of transitory nature. A deterministic update, in contrast, is a simple linear transformation and does not involve any augmented state vectors nor any saving of smoothing coefficients.

Suppose that

$$\begin{bmatrix} s_1 & s_2 \\ 0 & R \end{bmatrix} \begin{bmatrix} x_{del} \\ x_{ret} \end{bmatrix} \sim \begin{bmatrix} z_d \\ z_r \end{bmatrix} \quad (1)$$

is a data equation generated at a point where the states x_{del} are to be deleted from the current filter state and the states x_{ret} are to comprise the new filter state. The smoothing data (s_1, s_2, z_d) are saved^{ret} at this point. Suppose we were to leave the states x_{del} in the filter state vector. Consider the effect of performing a measurement update^{del} (Section 1.0) corresponding to the (linear normalized) measurement model

$$z = Ax_{ret} + v, \quad v \in N(0, I) \quad (2)$$

We form the data equation

$$\begin{bmatrix} s_1 & s_2 \\ 0 & R \\ 0 & A \end{bmatrix} \begin{bmatrix} x_{del} \\ x_{ret} \end{bmatrix} \sim \begin{bmatrix} z_d \\ z_r \\ z \end{bmatrix} \quad (3)$$

and partially triangularize by premultiplication by an orthogonal transformation to obtain a data equation

$$\begin{bmatrix} s_1 & s_2 \\ 0 & R' \end{bmatrix} \begin{bmatrix} x_{del} \\ x_{ret} \end{bmatrix} \sim \begin{bmatrix} z_d \\ z_r' \end{bmatrix} \quad (4)$$

which incorporates the knowledge gained from the observations, (2). The fact that the matrix of measurement partials (bottom row of (3)) has zeros in the columns corresponding to the x_{del} states, together with certain properties of the Householder Transform guarantees that the smoothing data array (s_1, s_2, z_d) is left unchanged (depending on the specifics of the Householder code implementation, one might have various rows with sign changes, but that does not affect the significance of the equations). Since measurement updates do not affect the relation between deleted variables and current variables, we can, conceptually, consider a gigantic data equation, growing in time, for all the states that have appeared in the current state vector at one time or another

¹ Our batch-sequential filter formulation produces pseudo-epoch state estimates at time t_j based on data with measurement times up to, but not including, t_{j+1} (see 1.4). In the modern estimation literature, [2] the usual convention is that filter estimates at time t are based on all the data occurring at times up to and including t .

$$\begin{bmatrix}
 s_{11} & s_{12} & & & & & \\
 & s_{21} & s_{23} & & & & \\
 & & \ddots & \ddots & \ddots & & \\
 & & & s_{*} & s_{**} & & \\
 & & & & R & &
 \end{bmatrix}
 \begin{bmatrix}
 x_{d1} \\
 x_{d2} \\
 \vdots \\
 x_{d*} \\
 x
 \end{bmatrix}
 \sim
 \begin{bmatrix}
 z_{d1} \\
 z_{d2} \\
 \vdots \\
 z_{d*} \\
 z
 \end{bmatrix}
 \quad (5)$$

(zeros not shown)

At the end of the filtering process we have a banded data equation for all these states which incorporates the information corresponding to all the measurements. The significance of this banded structure is that each row of the above matrix only involves two sets of variables. This large triangular system of equations can thus be solved by back substitution, with a solution vector of small effective size, since only two sets of variables need be handled in any one step. The state estimates obtained are clearly based on all the measurement information and model knowledge, i.e. they are the smoothed estimates.

The actual computation of smoothed pseudo-epoch state estimates does not proceed in exactly the fashion outlined above. First of all, the equations for all the states are not considered simultaneously, as depicted schematically in (5). Rather, starting with the filter solution at the terminal time (the solution to $Rx \sim z$ in (5)), one obtains recursively the smoothed estimates of the filter state vector at the various time points by "reversing" the steps in the model updates corresponding to a change in the current filter state vector, i.e.

- applying the inverse linear transformation to reverse a deterministic update
- solving an equation such as (1) to obtain a smoothed estimate x_{del}^* for deleted states from a smoothed estimate x_{ret}^* for the retained states
- dropping components of the smoothed estimate where the state vector was augmented in the filtering process
- applying the inverse permutation to the smoothed estimate components to reverse a permutation of the filter state vector

Furthermore, when covariances for the smoothed estimates are calculated it proves to be convenient and efficient to compute separately estimates of the bias parameters and "bias-free" estimates of the common parameters (see 1.3 for definitions of bias and common parameters). "Bias-free" estimates of the common parameters are estimates of the common parameters computed within an arc by ignoring the bias parameters, i.e. by using only the (logically anterior but temporally posterior) bias free covariance and estimates derived at arc change and the portions of the smoothing array related only to the common parameters. Estimates of the pseudo-epoch states are obtained by combining the bias-free common parameter estimates and the bias parameter estimates using a sensitivity matrix which expresses the influence of the bias parameter estimates on the pseudo-epoch common state estimates. In this approach separate recursion relations are used for the U-D factors of the bias-free smoothed estimate covariance matrix, the U-D factors of the bias parameter smoothed estimate covariance matrix, and the smoothed estimate sensitivity matrix. The advantage of this approach is that the U-D factors of the bias parameter covariance matrix change only when a transition to another arc occurs.

The choice of a U-D factorized covariance propagation scheme for the smoothed estimates over a scheme involving the use of data equations for the smoothed estimates is based primarily on considerations of efficiency. For single component stochastic updates (involving a single row of smoothing coefficients) the covariance update for the smoothed estimate covariance is a simple rank two update and there are attractive algorithms, [9] available for carrying these out for the U-D factors.

2. Applications to Global Positioning System Orbit Estimation

2.0 Current Areas of TRACE Application

TRACE has been used extensively in support of many space programs for post-flight orbit determination as well as error analysis, i.e. projections of orbit determination and prediction capabilities. For the Global Positioning System (GPS) the support activities, which have called for the use of TRACE include

- generation of test data for use in end-around checks (in which the simulated data is processed by the system components and the results obtained are compared with "known" truth - see [10])
- validation of the accuracy of orbit determination and prediction by the operational system (by comparing operational results with orbits obtained by post-flight estimation based on extensive data spans)
- modeling studies (in particular, a number of studies of alternative solar pressure models)

- system parameter determination (comparison of system data-base values with values obtained by TRACE, studies of the effects on orbit determination of variation of assumed measurement noise and process noise² levels)
- post-flight investigation of orbital parameter discontinuities caused by, e.g. space vehicle (SV) momentum dumps
- diagnosis of clock anomalies (spontaneous changes in clock model parameters or stochastic behavior)

2.1 GPS Measurement Description

In GPS the term pseudo-range has been adopted for the measurement obtained from the computed signal transit time determined from onboard and ground station clock readings. The use of this term reflects the fact that the measurement is a function of the clock offsets as well as the actual range. Both pseudo-range (from code tracking) and delta pseudo-range (doppler data from carrier tracking) measurements are available (see [1] for details). Raw measurements are edited and corrected for tropospheric delays, ionospheric delays, transit time of the signal, satellite lever arm (displacement of satellite transmitting electrical center with respect to satellite center of mass), and the periodic relativistic effects. The measurements are also "smoothed"; in the current context, smoothing means only that raw measurements are combined into a single measurement covering a time span much greater than that between the raw measurements and time-tagged with an appropriate interior time point of the smoothing interval.

2.2 Current SV Orbit and Clock Determination Procedures

Before the installation of the SRIF, TRACE orbit determination capability was limited to batch and sequential batch modes in which constant or segmented constant parameters were estimated using a priori covariances for the parameters and a weighted least-squares fit to the data (obtained using a standard "normal equations" approach). Segmented parameters are, essentially, multiple copies of a single parameter with each copy "valid" during a different time interval. Thus one could, for example, estimate a separate solar pressure force parameter for each pass of a Navstar over a ground station or for each day. The use of segmented parameters and of a deweighting capability available in the sequential batch mode were the tools used to study the effects of process noise.

Because of the nature of the stochastic behavior of oscillator driven clocks, pseudo-range data could not be effectively processed using TRACE in the batch mode (where the clock model is treated as a deterministic, lumped parameter process, i.e. epoch phase, frequency, and aging are the sum of constant states and arbitrarily selectable pass dependent parameters). Indeed, attempts to fit pseudo-range data in the batch mode resulted in a significant aliasing of estimated ephemeris states³ due to random clock phase errors. However, the GPS atomic clock frequency stochastic behavior can be regarded as a white noise process over smoothing intervals of 900 seconds (the current GPS nominal data smoothing interval). This empirically determined aspect of the clock frequency behavior holds, in fact, for smoothing intervals much larger than 900 seconds. Consequently, delta pseudo-range can be adequately modeled as a white noise process in the measurement model for batch processing. Up to now only delta pseudo-range measurements have been used in the post-flight orbit determination process - the process in which a Best Fit Ephemeris (BFE) is produced. Because only delta pseudo-range data is used in producing the BFE, SV clock offsets (which depend critically on phase information) are not estimated. Using orbits derived in this way and the fully corrected pseudo-range data obtained from the Vandenberg tracking station (which acts as the ground station carrying the reference clock for the system), the individual SV clock offsets with respect to the defined reference clock are estimated by attributing residual errors (differences between the fully corrected pseudo-range data and the range computed from the BFE) to SV clock errors. These estimates constitute a Best Fit Clock (BFC) file. Together the BFE and BFC are called a Best Fit Ephemeris/Clock. Dissemination of the BFE/C to a variety of agencies has been an ongoing Aerospace function. The BFE/C has also served as a diagnostic tool to evaluate and study the operational real-time system.

2.3 Tests of the SRIF/SRIS Algorithms

The inclusion of SRIF/SRIS algorithms adds a new dimension to the analytic capabilities of TRACE. Because these algorithms can deal with stochastic processes in both the force model and the measurement model, pseudo-range data can be used directly in the estimation process. Thus, maximum (optimal) use can be made of available data in various modeling and validation efforts.

Tests of the new capabilities (and of the assertions made above) are being conducted by one of us (Feess). First, a test case using simulated data is being evaluated. The test data for this case are the same as those generated for the GPS Phase I Ephemeris End-

² Investigated by using deweighting and segmented bias parameters.

³ In simulated data cases, batch mode fits using pseudo-range data only performed noticeably more poorly in recovering the (known) ephemeris than did batch mode fits in which delta pseudo-range data was included and pseudo-range data was deweighted.

Around Check, [10]. Secondly, a number of tests are planned which will use real data obtained from the operational GPS system. In addition to independent evaluation of the results (based on the criteria outlined below), the results will be compared with BFE/Cs (discussed in 2.2).

In the simulated data case, a data base model is perturbed to obtain a "real" world model. Both the data base model and the perturbations to it are described in [11]. Perturbations consist of changes in the number and magnitude of geopotential coefficients, changes to the solar radiation pressure reflectivity coefficients, tracking station survey locations, earth spin axis, polar motion, and deterministic clock model parameters. As described in [11], TRACE is then used to generate perfect measurements based on this "real" world model. Noise is added to these measurements based on stochastic models of receiver measurement noise, tropospheric delay variation, ionospheric correction from dual frequency measurement processing, and random clock oscillator variations (for the latter the models described in [12] are used).

The simulated data case has the advantage that the "truth" is known (i.e. the orbit used to generate the data). Thus direct comparisons of the estimation results and the "truth" can be made and used to assess the quality of the estimation. The value of the conclusions drawn depends on the realism of the simulated data case. In view of the random character of the perturbations to the data base model and the stochastic components of the generated data, a number of cases (10 are planned) will be run to ensure statistical significance of the results.

In the real data cases, truth (i.e. the actual orbit) is not known. Consequently, measures of the quality of the estimation based only on the estimates themselves must be devised. The measures used in evaluating the real data cases are

- are measurement residuals consistent with the assumed stochastic model?
- are corrections to states based on measurements consistent with state estimation covariance matrices?
- do predictions of the orbit based on estimated parameters agree well with the results of batch fits to the data subsequently obtained during the predict period?

The tests outlined here are not intended to serve purely as a means of validating the implementation of the SRIF/SRIS algorithms in TRACE. On the contrary, it is expected that they will provide useful insight into the operation of the GPS operational (square root covariance Kalman) filter, and by allowing for the simultaneous estimation of ephemeris and clock states, will lead to a simplification of the task of generating reference orbits for use in studies of the GPS system.

2.4 Future Capabilities

Error analysis, i.e. the study of the effects on estimation error covariances of unmodeled or mismodeled parameters and incorrect statistical assumptions, plays an important role in the study of systems such as GPS, where there is an abundance of parameters affecting the ultimate results (e.g. the user's estimate of his position). It is particularly important when possible modifications to the system design are being considered. As described in [4], the SRIF/SRIS algorithms lend themselves easily to such error analysis. TRACE has significant error analysis capabilities in batch mode. Corresponding capabilities in the SRIF/SRIS mode of operation have not yet been implemented, but the required effort is not large. It may be confidently predicted that they will find immediate application as soon as installed. Analysis of large numbers of "consider" parameters (unestimated parameters) can be taken into account in computing estimation error covariances. This capability can increase the accuracy of the estimation error covariances and can be used to identify the most sensitive parameters so that the (limited state) operational GPS filter can be "fine-tuned".

3. A Look at the Estimation Algorithms in a Larger Framework

3.0 Comparison with Other Estimation Techniques

The SRIF pseudo-epoch state filter has been successfully applied in a number of significant cases, [13] - [16]. In regard to computational efficiency, we note that none of the researchers in the cases cited above have expressed dissatisfaction with the computational costs of the estimation algorithm, though such costs are, of course, always a matter of concern.

Among alternative estimation techniques are the conventional weighted least-squares techniques based on the solution of the normal equations

$$(A^T W A) x_{1s} = A^T W z \quad (1)$$

and variants of that approach involving various "deweighting" schemes, limited memory (fading memory and moving window) filters, the inclusion of "segmented" parameters to account for drag or other stochastic effects, or combinations of all of these. In the hands of a clever and experienced engineering staff, these and other ad hoc techniques yield acceptable results and are not to be dismissed. The SRIF orthogonal transformation techniques are, however, numerically more reliable than techniques based on the solution

of the normal equations, see e.g. [9], and this additional reliability is purchased at a relatively low computational cost, [17]. Further, the implementation of the more sophisticated stochastic models, such as Markov models, in the least-squares algorithms is generally expensive and tends to require skills bordering on artistry. A propos of least-squares techniques, it should be noted that mathematical equivalents of these (including their variants) are special cases of the SRIF algorithms.

Another alternative to the SRIF is the Kalman filter, which recursively computes estimates and estimate error covariances. For problems involving large numbers of measurements the Kalman filter can be far more costly than the SRIF; [17] contains arithmetic operation counts that demonstrate this point. It is now well established, [9] that covariance update formulas for Kalman filters are numerically unreliable, and that the U-D factorized covariance updates described in [5] and [9] have far superior (indeed excellent) numerical characteristics. Comparison of U-D factorized Kalman filters⁴ with the SRIF in orbit determination problems has shown them to be of comparable accuracy and except in extreme cases they incur comparable computational costs. These two algebraically equivalent approaches are developed in parallel in [4], and for orbit determination problems there seems to be little reason to favor one approach over the other.

The U-D factorized covariance smoothing algorithm developed in [5] operates from coefficient arrays generated during the operation of the SRIF. For the typical orbit determination problem (many measurements and a relatively small number of process noise variables) this smoother is more efficient than its competitors: the Rauch-Tung-Streifel (RTS) Kalman filter based backward pass smoother, the Kaminski-Bierman square root information smoother (SRIS), the modified Bryson-Frazier adjoint variable smoother, the Mayne-Fraser two filter bi-directional smoother, and the covariance formulated SRIS. For descriptions of these algorithms the reader may consult [4] and the references cited therein. The principal reason for its efficiency is the compact nature of the smoothing coefficient arrays that are generated by the SRIF. It is numerically reliable, being based on rank two updates of U-D factors, and does not call for the calculation of differences of covariance matrices (as do e.g. the RTS and modified Bryson-Frazier smoothers).

3.1 Prospects for the Future

Ever more precise measurement hardware and increasing computing capacity are clearly impacting the areas of high precision orbit determination and control. Because of competition for limited manpower resources, it will be more difficult in the future to find skilled and experienced staff for operational systems and staffing costs will rise. Together these factors provide impetus to develop reliable, easy to use software and processing techniques that require less in the way of technical judgment from the user. The thought is to automate operations wherever possible, and to design systems that can be operated and maintained by technicians rather than technical specialists. Such automation would represent a considerable advance over current practice.

It seems likely that numerically reliable orthogonal transformation techniques and related square root algorithms will be more commonly used both for estimation and for control and guidance. The state of the art is such that key mathematical functions can be standardized so that they can be applied in a variety of situations by selection of readily understandable parameters. In particular, it should not be necessary to require senior navigation engineers to devote their energies to the development of ad hoc strategies whose function is mainly to numerically stabilize a Kalman filter or batch processor.

Large scale integration techniques in chip fabrication are bringing down computational costs and new developments in computer architecture, such as the use of array processors and distributed processing, are increasing computational speeds. With lower costs and higher speeds, we expect to see more use of the current generation of adaptive estimation and identification techniques. Currently, the choice of stochastic parameter characteristics (σ -ing levels, etc.) is still something of a "black art". The use of adaptive techniques should require far less in the way of intuition and judgment from the user. We also expect to see on-site processing (in parallel) of multi-station tracking data using algorithms currently thought to be too slow or too complex.

Because of the very high data rates (say 100-1000 Hz) involved in raw data processing, there is currently an emphasis in this area on the use of simplistic algorithms that avoid the use of the Kalman filter. One exciting development that we expect to see in the near future is the fabrication of special purpose chips designed to handle such applications.

Automated navigation capabilities, eventually space-based, are among the applications we expect to see arise from the developments foreshadowed above. In [18] some preliminary results regarding automated (ground-based) navigation are discussed. U-D covariance factors are used in the navigation processing, which is applied to Galileo Jupiter encounter data.

⁴ There are square root covariance algorithms which propagate a square root of (rather than the U-D factors of) the covariance matrix. These involve slightly more arithmetic than the U-D algorithms with no attendant accuracy benefits, so they will not be further discussed.

More users will turn to the generation of smoothed estimates (as opposed to filter estimates) when process noise models are involved. The problem of smoothing has until now generally been thought to be a more difficult, complicated and expensive problem than the filtering problem. Experience shows, however, that generation of smoothed estimates is far simpler than the initial construction of filter estimates. Furthermore, the generation of smoothed covariances, see [5], is comparable to operating only part of the filter process (the time update portion). For certain applications, e.g. those involving maneuvering vehicles, smoothed estimates (from, say, a fixed lag smoother) often give results that are much improved over those that would be obtained from a simple filter. The relative simplicity and efficiency of the smoother algorithms briefly touched on in this paper makes it likely that they will be popular in those applications in which smoothed estimates offer a significant advantage in accuracy over filter estimates.

Finally, we venture a few remarks on the durability of the algorithms discussed in this paper. The SRIF process noise filter was applied at JPL to the Mariner 10, [13]. A more flexible SRIF formulation, corresponding to what we describe (it included a predecessor smoothing algorithm) was applied to the 1975 Viking Mars exploration, [14]. This same filter/smoother has been employed in the current Voyager missions. The point of these highlights is that, although we expect to see modifications evolve (such as the pass parameter feature and the higher order Markov models discussed in Section 1 and 2), our feeling is that the SRIF/U-D factorized smoother will play a useful role in spacecraft navigation for years to come.

In closing this section, we note that a soon to be published new result of investigations by one of us (Bierman) of the smoothing algorithms mentioned here shows that one can obtain the smoothing algorithm results directly from the output of a U-D factorized Kalman filter. The idea of having a U-D filter/smoother is clearly very attractive.

3.2 Concluding Remarks

We have described a particular implementation of the SRIF, one which we feel is flexible and well suited to the types of orbit estimation problems discussed here. SRIF is not the only way - the choice of SRIF over a U-D factorized filter was based primarily on the advantages of batch-sequential processing for large numbers of measurements. The SRIF is efficient and it is based on numerically sound procedures that have been extensively analyzed and accepted by the numerical analysis community. Furthermore, the methods used in the SRIF (data equations and orthogonal transformations) are simple and elegant. It is our belief that these factors will lead to an increasing popularity for the SRIF.

Bibliography

1. "Global Positioning System - papers published in Navigation", Reprinted by the Institute of Navigation, Washington, D.C. Copyright 1980, The Institute of Navigation. International Standard Book No. 0-426406-003.
2. Meditch, J. S., "Stochastic Optimal Linear Estimation and Control", McGraw Hill, 1969.
3. Mercer, R. J., Prislun, R. H., Walker, D. C., "TRACE 66 Trajectory Analysis and Orbit Determination Program. Volume 1: General Program Objectives, Description and Summary", The Aerospace Corporation TOR-0059(9320)-1, Volume 1, 15 August 1971 (also appears as Air Force Report No. SAMSO TOR-71-191, Volume 1).
4. Bierman, G. J., "Factorization Methods for Discrete Sequential Estimation", Academic Press, 1977.
5. Bierman, G. J., "Square-Root Information Filtering and Smoothing for Precision Orbit Determination", in - Mathematical Programming Study - Numerical Techniques in System Engineering, R. J. Wets Ed., to appear.
6. Hansen, R. J., Lawson, C. L., "Solving Least-Squares Problems", Prentice-Hall, 1974.
7. Bierman, G. J., "An Application of the Square-Root Information Filter to Large-Scale Linear Interconnected Systems", IEEE Trans. Auto. Control, Vol. AC-22, No. 6, December, 1977, pp. 989-991.
8. Damoulakis, J. N., Upadhyay, T. N., "Sequential Piecewise Recursive Filter for GPS Low-Dynamics Navigation", IEEE Trans. on Aerospace and Electronic Systems, Vol. AES-16, July 1980, No. 4, pp. 481-490.
9. Bierman, G. J., Thornton, C. L., "UDU^T Covariance Factorization for Kalman Filtering", in Control and Dynamic Systems, Vol. XVI C. E. Leondes Ed., Academic Press, 1980, pp. 177-248.
10. Feess, W. A., Harkins, M.D., Murch, W. G., Schaibly, J. H., "Simulated and Projected Performance of the Navstar GPS Control Segment" in NAVSTAR Global Positioning System (GPS), AIAA Guidance and Control Conference, San Diego, California, August 16-18, 1976. American Institute of Aeronautics and Astronautics, 1290 Avenue of the Americas, N.Y.
11. Conrad, D. A., "Data Base for GPS Ephemeris End-Around Check", The Aerospace Corporation TOR-0079(4473-04)-3, April 1979.

12. Meditch, J. S., "Clock Error Models for Simulation and Estimation", The Aerospace Corporation TOR-0076(6474-01)-2, 1976.
13. Christensen, C. S., "Performance of the Square-Root Information Filter for Navigation of the Mariner 10 Spacecraft", Jet Propulsion Laboratory Technical Memorandum 33-757, January 1976.
14. Acton, C. H., Breckenridge, W. G., Campbell, J. K., Christensen, C. S., Donegan, A. J., Jerath, N., Mottinger, N. A., Rinker, G. C., Rourke, K. H., Winn, F. B., "The Determination of the Interplanetary Orbits of Vikings 1 and 2", AIAA-77-71, AIAA 15th Aerospace Sciences Meeting, Los Angeles, January 1977.
15. Campbell, J. K., Mandel, S., Morahito, L. A., Reidel, J. E., Rinker, G. C., Synnott, S. P., "Voyager 1 and Voyager 2 Jupiter Encounter Orbit Determination", AIAA-80-0241, AIAA 18th Aerospace Science Meeting, January 1980.
16. Bierman, G. J., Hamata, N. E., Mohan, S. N., Stavert, L. R., "Seasat Orbit Refinement for Altimetry Application", J. Astronomical Sciences, Vol. XXVIII, No. 4, Oct-Dec, 1980, pp. 405-417.
17. Bierman, G. J., "A Comparison of Discrete Linear Filtering Algorithms", IEEE Trans. Aero. Elect. Systems AES-9, No. 1, pp. 28-37.
18. Bon, B. B., D'Amasio, L. A., Downing, G. P., Frauenholz, R. B., Klumpp, A. R., McReynold, S. R., "Automated Optical Navigation with Application to Galileo", AIAA/AAS Astrodynamics Conf., August 11-13, 1980, Danvers, Mass.

Acknowledgement

The work covered in this paper was performed under Air Force Contract No. F04701-80-C-0081.

GEOSTATIONARY COMMUNICATION SATELLITE CONTROL

L. Flook
Chief Dynamics Engineer
British Aerospace Dynamics Group
Space and Communications Division
Site B, Gunnels Wood Road,
Stevenage, Hertfordshire SG1 2AS
United Kingdom.

J.J. Pocha
Section Leader
British Aerospace Dynamics Group
Space and Communications Division
Site B, Gunnels Wood Road,
Stevenage, Hertfordshire SG1 2AS
United Kingdom.

SUMMARY

The requirements for the control of the position and attitude of geostationary communications satellites are examined and some of the principle system parameters and options available are outlined. A number of current systems are compared and the principal limitations of their performance are discussed. The overall communication system trends are indicated and the effect of these upon the design of both attitude and position control is indicated.

1. INTRODUCTION

In order to receive the uplink signal and transmit the downlink signal to a prescribed area on the ground a communications satellite in geostationary orbit must be controlled in both position and attitude.

The accuracy of positioning required is dictated principally by the uplink antenna beamwidth which for large ground stations is a fraction of a degree. The satellite is therefore typically controlled to $\pm 0.1^\circ$ in both latitude and longitude in order to remove the necessity for a tracking system on the ground antenna. A change in the orbital position of the order indicated changes the antenna pointing direction by a quantifiable but generally negligible amount.

The accuracy with which the downlink beam must be pointed is dictated by the beamwidth and is generally established to be 10% of the beamwidth. The precise level is influenced by the effect of pointing errors on the overall system performance and by the cost and complexity of achievement of desired accuracy.

Early designs employed spin stabilised cylindrical configurations where the power level is limited by the available surface area of the body upon which the solar cells are mounted. The requirement to provide for more cost effective high capacity satellite systems has resulted over the past two decades in changes to the beam coverage from full earth to narrow multiple spot beam systems and higher satellite power. This has in turn resulted in increasing emphasis being placed upon the use of 3-axis stabilised systems employing deployable solar arrays. Such systems are not as highly constrained by the available launch vehicle payload volume. The emphasis in this paper is therefore directed toward such systems and to the on-orbit operation of such systems.

The attitude control system invariably utilises propulsion equipment in conjunction with the orbit control system and the total system is generally referred to as an Attitude and Orbit Control System (AOCS). The paper first discusses the problem of position control or station keeping, followed by consideration of attitude control.

2. Station-Keeping2.1 Perturbations

A spacecraft in geostationary orbit changes its position with respect to an Earth-fixed frame of reference due to the action of a number of perturbations. The word "perturbation" is used to signify forces other than those due to the gravitational potential of a homogeneous spherical Earth. The effect of the perturbations is to cause the spacecraft to drift away from its nominal station. The congestion of the geostationary orbit and the use of higher frequencies leads to requirements for tighter longitude and latitude limits to avoid inter-satellite radio-frequency interference. A dead zone of $\pm 0.1^\circ$ latitude and longitude is typical of present generation spacecraft such as Intelsat IV and V, OTS, ECS, MARECS, etc.

The perturbations causing spacecraft drift can, to good accuracy, be separated into those causing longitude drift, and those causing latitude drift, and separate manoeuvres can be devised to counteract the drift in each direction. The perturbations causing the satellite to drift in longitude arise from the ellipticity of the Earth's equatorial cross-section (expressed mathematically by the J_{22} harmonic of the Earth's gravitational potential), and the effect of solar radiation pressure on the satellite surfaces.

The former causes a change in the orbit semi-major axis, which results in a longitude drift-rate; while the latter causes the orbit to become eccentric, which results in a diurnal variation in the spacecraft's longitude (this diurnal variation is also known as libration). The perturbations causing the spacecraft to drift in latitude are due to the gravitational attraction of the Sun and Moon. These perturbations cause the geostationary orbit pole (the vector normal to the orbit plane and in the direction of its angular momentum) to move in the general direction of the vernal equinox, thereby causing a change in orbit inclination and ascending node position. Diurnal latitude variation results from a non-zero inclination of the spacecraft's orbit, and the spacecraft describes a figure-of-eight relative to an Earth-bound observer (the axis of the figure-of-eight being in the North-South direction). It can be seen, therefore, that control of longitude drift implies control over the orbit's semi-major axis and eccentricity (and, for completeness, argument of perigee), while control of the latitude drift implies control over the orbit's inclination and ascending node position. In order to appreciate the impact of station-keeping requirements upon spacecraft design it is important to assess the correction requirements of the perturbations outlined above. A simplified general approach is adopted to highlight the most important results. As the counteraction of the perturbations involves manoeuvring, which imparts velocity increments to the spacecraft, the significance of the perturbations will be expressed in terms of the velocity increment (ΔV) needed to counteract them.

AD-A111 405

ADVISORY GROUP FOR AEROSPACE RESEARCH AND DEVELOPMENT--ETC F/6 22/3
SPACECRAFT POINTING AND POSITION CONTROL, (U)

NOV 61 P P BROEK, S Z SZIRMAY

AGARD-AG-260

UNCLASSIFIED

NL

2-3

2-3

2-3

2-3

2-3

2-3

2-3

2-3

2-3

2-3

2-3

2-3

2-3

2-3

2-3

2-3

2-3

2-3

2-3

2-3

2-3

2-3

2-3

2-3

2-3

2-3

2-3

2-3

2-3

2-3

2-3

2-3

2-3

2-3

2-3

2-3

2-3

2-3

2-3

2-3

2-3

2-3

2-3

2-3

2-3

2-3

2-3

2-3

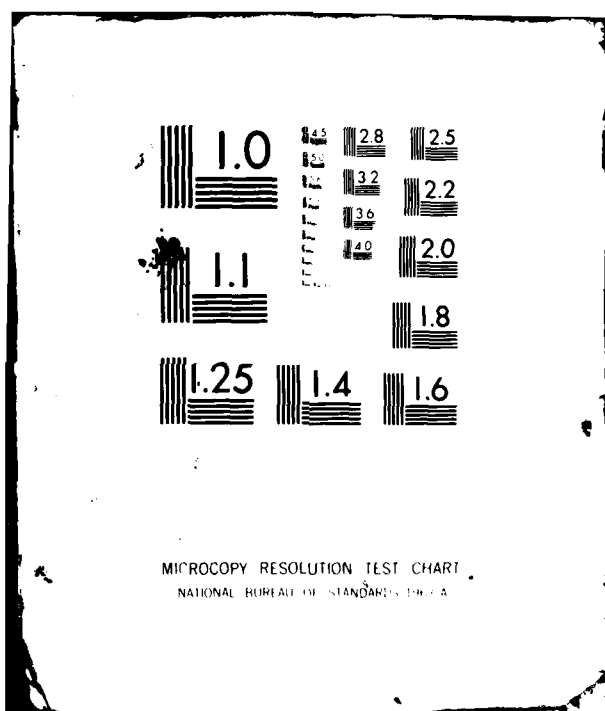
2-3

2-3

2-3

2-3

2-3



The longitude drift acceleration imposed upon a spacecraft by the J_{22} perturbation could be about $0.00197^\circ/\text{day}^2$. (Owing to the nature of this perturbation its value is dependent upon the spacecraft's nominal on-station longitude. The value given above corresponds to a peak in the perturbation variation with longitude). For a station-keeping manoeuvre cycle time of about 28 days (typical of a large number of such spacecraft) this results in the requirement of an initial drift rate of $0.028^\circ/\text{day}$ in order to remain within a $\pm 0.1^\circ$ deadband. The resulting manoeuvre applies to the spacecraft a velocity increment of 0.16 m/s . Over the period of a year the ΔV requirement is about 2.1 m/s .

The longitude drift imposed upon a spacecraft by solar radiation pressure depends upon the area-to-mass ratio of the spacecraft. For spacecraft of the recent past and present, the area-to-mass ratio has been of the order of $0.03 \text{ m}^2/\text{kg}$. This results in a manoeuvre requirement of the same order as that required to correct for the J_{22} perturbations - about 2 m/s per year.

The inclination drift arising from luni-solar gravitational perturbations depends upon the phasing of the Sun and Moon orbits relative to the geosynchronous orbit, but varies between 0.76° and 0.95° per year. The velocity impulse to correct this drift therefore varies from about 41 m/s to 51 m/s per year.

The results for the three different perturbation sources is summarised in Table 1. Since the ΔV required from the manoeuvres is directly related to the amount of propellant the spacecraft must carry, it becomes obvious at once that correcting latitude drift imposes a fuel penalty upon the spacecraft an order of magnitude greater than that imposed by the correction of longitude drift.

For a fairly typical spacecraft with a latitude deadband of $\pm 0.1^\circ$ and a 7-year lifetime, the hydrazine propellant mass required for latitude drift control (also known as North-South station-keeping) amounts to about 75 kg (for a spacecraft with a mass on-station of 520 kgs). The corresponding fuel mass requirement for correction of J_{22} and solar pressure effects (also known as East-West station-keeping) is only about 3.5 kg . North-South station-keeping, therefore, has a much greater impact upon spacecraft design than East-West station-keeping.

2.2

North-South Station Keeping

The large fuel penalty imposed by North-South station-keeping has led to an investigation of the ways in which the design impact can be minimised. Briefly, three alternatives are open to the designer.

The first consists of accepting the fuel penalty as the most cost-effective solution for the particular satellite under consideration. A large number of satellites currently in use adopt this approach, and carry about $70\text{--}80 \text{ kg}$ of monopropellant hydrazine for North-South station-keeping alone. The manoeuvre size is large and, typically, imparts to the spacecraft a ΔV of 3.5 m/s . This has a direct impact upon the attitude control system of the spacecraft, which has to maintain pointing accuracy in the face of the resulting jet misalignment and plume impingement disturbance torques. This can require the inclusion of control hardware (and software) dedicated to the station-keeping phases of the mission. North-South station-keeping, therefore, increases the control system design complexity in addition to imposing a fuel penalty.

The adverse interaction with the control system is likely to become more severe on future satellites with larger solar arrays which are both flexible and more susceptible to interference with the propulsion system thruster plume. Plume impingement disturbance torques have resulted in a revision of the North-South station-keeping manoeuvre strategy for the Orbital Test Satellite (OTS). An originally planned single manoeuvre has been broken into several stages, with periods of attitude control system adjustment (momentum wheel dumping) between the stages.

The second alternative is to relax the latitude deadband in order to reduce, or eliminate altogether, the North-South station-keeping requirement. If latitude limits of $\pm 3.0^\circ$ were allowed it is possible, in certain cases, to avoid North-South station-keeping altogether. Such a strategy does, however, require the accurate placement of the geosynchronous orbit pole in inertial space at the start of the mission. This complicates the transfer orbit phase of the mission and somewhat narrows the launch window, but results in a very worthwhile payload mass gain. Generally, wide-beam communications coverage allows the latitude limits to be relaxed. Such a strategy has been adopted by the ESA Maritime Communications Satellite (MARECS).

The third alternative is to use a highly efficient propulsion system. Currently available chemical propulsion systems have specific impulses in the range of about 200 secs to 400 secs , while those suitable for satellite use have specific impulses in the range 200 secs to 300 secs . An order of magnitude increase in specific impulse is available from electromagnetic thrusters or ion engines.

They have to date had limited use, but they must be regarded as strong candidates for long duration missions (lifetime ≥ 10 years) requiring North-South station-keeping. Experimental packages have already been flown. The use of ion engines requires a very short station-keeping cycle time (1 or 2 days instead of several weeks) owing to the very low thrust level available from them (typically 0.01N). Though this enables very accurate station-keeping, it is operationally inconvenient and imposes a high workload on the satellite control station. Another problem is that the exhaust plume causes contamination of the surfaces upon which it impinges. Contamination of the solar array leads to a drop in available power, requiring a larger array to compensate for the loss. This results directly in a mass penalty. Integration of the ion engines in the satellite is made difficult due to the bulk of the packages, and the requirement to carry redundant systems. The ion engines, though fuel efficient, consume a considerable amount of electrical power which would make their use during an eclipse undesirable. Such considerations have hitherto limited the use of electric propulsion. However, for long lifetime satellites, the mass gain resulting from their use becomes significant and the future could well see an increase in their use.

2.3 Station-Keeping Strategies

Currently station-keeping is carried out in an open-loop mode. The ground station tracks the satellite and evaluates the time and magnitude of the next manoeuvre. The appropriate commands are sent to the satellite which then executes the manoeuvres as instructed. The ground station then tracks the satellite to verify the correct execution of the manoeuvre and computes the time and manoeuvre details of the next cycle, and so on.

If the station-keeping cycle is of the order of weeks this results in an acceptable workload for the ground station. As the North-South manoeuvres are so much larger than East-West ones, any thrust misalignment errors during the former will couple into the latter. To avoid a consequent fuel penalty the North-South manoeuvres are interleaved with the East-West ones and any cross-coupling corrected by the subsequent East-West manoeuvre.

It is usually a requirement that the specified deadzone be maintained to a certain probability level. This recognises that manoeuvres will be non-nominal owing to errors in orbit determination, thruster alignment and thruster performance. OTS, for example, was required to be controlled to within a deadzone of $\pm 0.1^\circ$ in latitude and longitude to a probability of 99%. The strategy derived therefore, took into account the likelihood of adverse dispersion impacts on a stochastic basis. Frequently there is a requirement on the minimum cycle time. This requires the strategy to be designed such that even if dispersions occur (to a specified probability level) so as to reduce the cycle time, the latter is not lower than the specified value.

Various manoeuvre implementation strategies are available. For East-West station-keeping, when the perturbations are small, it is possible to maintain the deadband with a single-burn strategy. This implies that a single burn is used per cycle. With such a strategy the J_{22} and solar pressure perturbations are compensated together by sizing the burn for the former and timing the burn for the latter. Operationally, this is very convenient and has been implemented on OTS. When the perturbations are larger, multi-burn strategies become necessary.

Two-burn strategies implement the burns approximately 12 hours apart to correct for both the J_{22} and solar pressure perturbations. A characteristic of this strategy is that the fuel used for the manoeuvres is the larger of that required for the J_{22} and solar pressure perturbations separately. The strategy is, therefore, fuel-efficient.

In order to minimise fuel usage, the station-keeping strategies correct only for the satellite's secular drift, and the short period perturbations, being of second order, are allowed for separately within the deadband. The deadband within which the satellite is actually controlled - the control deadband - is therefore somewhat smaller than the specified deadband. An understanding of this is particularly important for North-South station-keeping, where the fuel requirement, already high, could easily be doubled if the short-period motions were required to be counteracted. There is therefore a lower limit on the deadband within which the spacecraft can be maintained. In practice, tracking and execution errors provide a limitation that is reached before that of second-order short-period perturbations. As an experiment, OTS has been kept within North-South deadband limits of $\pm 0.05^\circ$ latitude. A much higher accuracy would impose requirements on tracking accuracy that would be difficult and expensive to meet.

3. ATTITUDE CONTROL

3.1 Current Systems

Spin stabilisation, where the total satellite or a major portion of the satellite is spun to provide an angular momentum sufficient to produce short term stabilisation, has been employed on a large number of satellites. INTELSAT 4 (Figure 1) employed spin-stabilisation in what is termed a dual-spin configuration. A major portion of the satellite - the solar array drum - is spun while the communication subsystem including antennas is pointed toward the Earth. The despun portion of the satellite is provided with a damper having a time constant chosen to provide overall stability. The power of such satellites is limited by the size of the fixed solar array mounted on the surface of the spinning drum which can be accommodated within the launch vehicle.

Most current communication satellites overcome such limitations by the use of three axis stabilisation. The most common configuration adopted is a central equipment body from which solar arrays are deployed in a symmetrical manner (Figure 2). A symmetrical configuration is adopted in order to minimise the solar radiation pressure disturbance torque, the principal naturally occurring disturbance torque in geostationary orbit. The solar arrays are rotated once per day to follow the sun.

The Earth provides the most suitable reference in two axes and most current systems employ a two axis infra-red horizon sensor to provide sensing of pitch and roll attitude (Figure 3). The problem of sensing attitude on the yaw axis is influenced by the choice of stabilisation concept.

The simplest concept employs a fixed momentum wheel with momentum vector aligned along the pitch axis. The interchange of roll and yaw axes each quarter orbit results in a roll/yaw coupling which may be utilised to produce a bounded yaw error. Such a system operates satisfactorily in the presence of naturally occurring disturbance torques. During station-keeping manoeuvres a significantly higher level of disturbance torque is applied to the satellite and an active loop is used to limit the yaw error. Sensing may be performed using gyros, sun sensors or star sensors. The use of sun sensors constrains the time at which station keeping can be performed as no yaw information is available near mid-day. As North-South station-keeping is most efficiently performed near the orbit ascending or descending node a suitable strategy minimising the increase in propellant must be devised. Star sensing is an expensive and complex option which has not generally been used. The other loops may also be modified during station-keeping manoeuvres to enable them to maintain pointing in the presence of the higher disturbance torques.

Three basic control concepts have been employed (Figure 3).

- Fixed momentum wheel
- Reaction wheels
- Gimballed momentum wheel

The first of these concepts has been briefly discussed. The wheel is operated as a reaction wheel in the pitch axis. It is the simplest of the three concepts and is utilised on a number of British Aerospace satellites including OTS, ECS and MARECS.

The second concept employs three reaction wheels in basic form and provides an independent control loop on each axis. In this case yaw sensing must be performed at all times. Provided that a suitable level of reliability can be achieved, gyros updated with sun sensor information provides a satisfactory scheme.

The third concept can be implemented using a single or double gimbal. The gimbal torquers are used to rotate the momentum vector and provide a reaction torque as directed by the roll and yaw control loops. The pitch loop operates on the wheel speed in a reaction wheel mode as in the first concept. The system may also be implemented by use of two or more fixed momentum wheels aligned along different axes where the rotation of the net momentum vector is achieved by varying the relative speed of the wheels.

All the concepts become 'saturated', that is reach the limits of wheel speed or gimbal position, and a non-conservative device such as a gas-jet is used to return the system to a state from which it is capable of absorbing additional angular momentum. Most current systems employ a hydrazine gas jet system for this purpose and for station-keeping. The control loop pointing error is sensor limited.

The accuracy to which the beam centre is required to be is dependent upon the beam width. All the systems discussed are capable of achieving accuracy of the order of $\pm 0.2^\circ$ in pitch and roll and of the order of $\pm 0.5^\circ$ in the yaw axis. They are therefore capable of being used with systems having a beamwidth of the order of 2° . Some limited improvement to these figures can be achieved by careful design and alignment. The problem of improvement is illustrated by reference to Table 2. The allocation to the control system is significantly smaller than the overall error and thus a large overall improvement requires a number of improvements to be made.

The boresight error is calculated assuming that the antenna is pointed at the subsatellite point, and that the roll and pitch errors are independent and are normally distributed. When the antenna is directed toward some other ground position, the method of adding the component errors is calculated by reference to the orbital geometry.

4. FUTURE TRENDS AND REQUIREMENTS

A study of the evolution of communications satellites indicates that they will increase in number, increase in capacity and be required to achieve higher reliability. The first trend will lead to a crowding of the geostationary orbit, the second to larger satellites, and the third to longer design lifetimes. All three trends will have a direct impact upon the station-keeping requirements. In addition there is a trend toward the use of higher frequencies in order to increase the system capacity. This will lead to narrower beams and increased pointing accuracy requirements.

The use of higher frequencies will lead to a progressive tightening of the East-West deadband in order to minimise ground station complexity, and radio-frequency interference with closely spaced neighbouring satellites. Tighter deadbands require a greater ΔV for station-keeping, and higher tracking accuracies. The former will provide the impetus for more efficient propulsion systems, while the latter could result in novel tracking techniques, such as laser tracking or satellite-to-satellite tracking. One means of overcoming the congestion is to use spacecraft in 24-hour orbits of non-zero inclination. This could double or treble the orbit capacity but would require a family of satellites and fairly complex ground stations. The station-keeping requirements would also be quite severe, with inclination maintenance imposing up to a 10-20% penalty in fuel compared to the zero-inclination orbit. A family of satellites, typically 4 to 8, would provide two virtual satellites at latitudes of approximately $\pm 15^\circ$.

Correct phasing of communications handover between the satellites could provide unbroken service with the advantages of better geometrical configuration for communications to moderate-to-high latitudes (i.e. N. America and Europe), more cost-effective provision of spare satellites, and avoidance of communications drop-outs due to Sun blinding of ground station receive antennae. The station-keeping requirements to maintain inclination and phasing could be severe.

The increase in communications power will lead to larger satellites through larger solar arrays and antennae. The trend for an increasing spacecraft area-to-mass ratio is already well established. This will lead to the dominance of solar pressure perturbations over those related to J_{22} , and will result in an increase in the East-West station-keeping fuel requirement. Furthermore, the large structures will be relatively more flexible than present day satellites and will require careful design of the control system if the pointing accuracy is to be maintained during periods of manoeuvring.

The increase in spacecraft reliability will lead to satellite lifetimes substantially greater than those of present generation spacecraft. This characteristic, coupled with a requirement for North-South station-keeping within a small deadband, will point to the use of higher efficiency propulsion systems, possibly electric propulsion. These in turn will lead to manoeuvres being required every few days or so. Though this would to some extent alleviate the severity of structure-control system interaction, the frequency of the manoeuvres would impose a high workload on the ground station controlling the satellite. The obvious answer to this problem is to use a closed-loop station-keeping system fully autonomous within the spacecraft.

The feasibility of the autonomous station-keeping has already been established, and an experimental implementation has been flown. The concept consists of determining the satellite's orbit on-board the satellite using appropriate sensors, and an ephemeris model stored in a satellite-borne computer. Based upon a knowledge of the satellite's orbit and position, simple algorithms evaluate the time and magnitude of station-keeping manoeuvres. These manoeuvres are then initiated automatically. The system has been shown to be suitable for implementation in conjunction with electric propulsion systems.

Other possible future developments include a very large structure in geostationary orbit capable of being used as a "hanger" upon which to mount a variety of communications payloads providing a variety of services. This would reduce the congestion in the orbit and the risk of collisions. The station-keeping of one large composite satellite would replace the station-keeping of individual satellites bringing a reduction in ground station workload.

Other concepts include satellite clusters with station-keeping being carried out on the master satellite alone, the other satellites maintaining position with respect to the master automatically using on-board radar.

A summary pictorial representation of the impact of Comsat evolution upon the station-keeping requirements is shown in Figure 4.

The effect of these trends upon the pointing requirements is illustrated in Figure 5.

The concept of radio frequency sensing, that is sensing the position of a radio frequency beacon located near the centre of the main beam ground pattern, provides a large improvement in sensor accuracy. If the sensor signal is derived from a radio frequency feed within the antenna being controlled then the alignment errors may be more easily controlled and reduced.

The use of larger spacecraft with multiple antennas leads to consideration of the use of antenna pointing mechanisms. These can be used to remove fixed errors which are present and in the case of more complex beam patterns adjust the position of the beam so that the optimum position is achieved.

The introduction of inter-satellite links to increase the capacity of systems where more than one satellite is operating within a single communication system again requires a more complex controller to ensure that the pointing requirements of both the inter-satellite link and the satellite to ground link are met without adverse effect of one upon the other.

First generation communication satellite designs employing spin stabilisation have been largely replaced by second generation systems employing three axis stabilisation and currently being designed and deployed. The station keeping requirements have not changed significantly during the developments from first to second generation.

Future systems will require a number of developments in both station-keeping and pointing if the potential improvement in system performance is to be achieved.

Perturbation	Compensating ΔV (m/s)/year	Hydrazine Mass (kg)
J ₂₂	2.1)
Solar Pressure	2.0) 3.5
Luni-Solar	51.0) 75

TABLE 1 STATION KEEPING PROPELLANT MASS

Axis Error Source	Roll	Pitch	Yaw	Error Type
Antenna				
(i) RF alignment	0.02	0.02	0.002	A
(ii) Hysteresis	0.02	0.02	0.003	A
(iii) Thermal	0.05	0.05	0.01	B
IRES				
(i) Null	0.01	0.01	-	A
(ii) Thermal etc.	0.03	0.03	-	B
Alignment				
(i) Wheel/IRES/ Antenna	0.03	0.03	0.04	A
(ii) Thermal	-	-	0.04	B
(iii) AOCS Loops	0.05	0.05	0.3	C
RSS A	0.042	0.042	0.04	A constant errors
RSS B	0.058	0.058	0.041	B Cyclic at orbit rate
RSS C	0.05	0.05	0.3	C Higher frequency
A + B + C	0.15	0.15	0.381	
Boresight error = 0.171°				

TABLE 2 A TYPICAL CURRENT POINTING SYSTEM ERROR BUDGET



FIGURE 1 INTELSAT 4

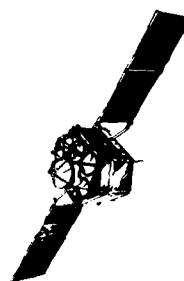


FIGURE 2 ORBITAL TEST SATELLITE (OTS)

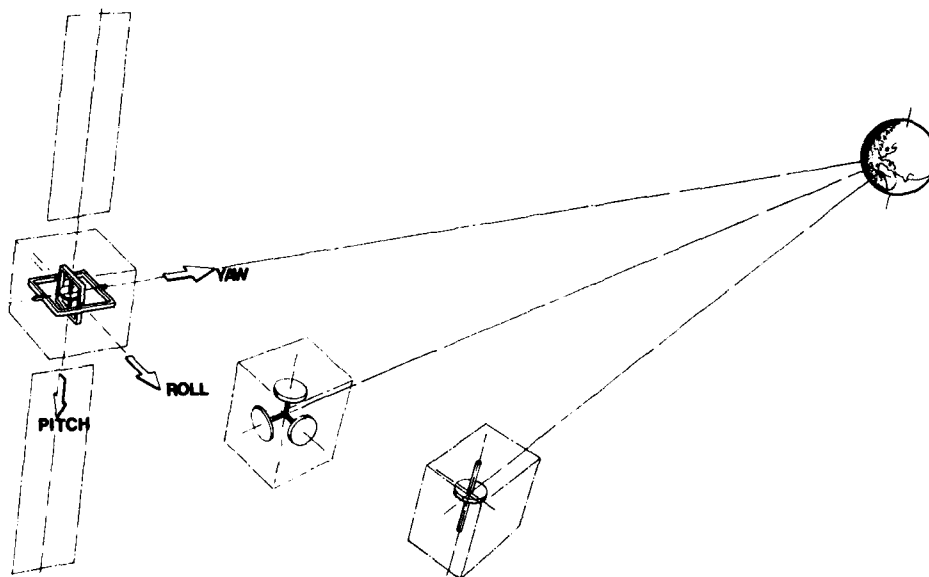
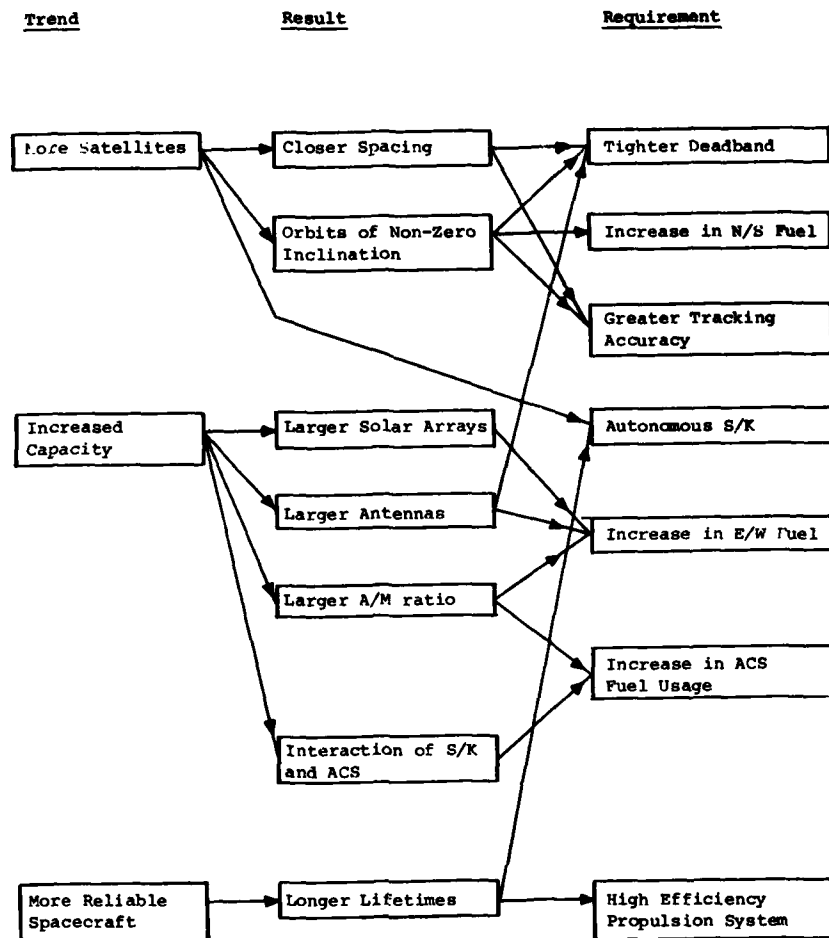


FIGURE 3 CONTROL SYSTEM CONCEPTS



Impact of Comsat Evolution on S-K Requirements

Figure 4

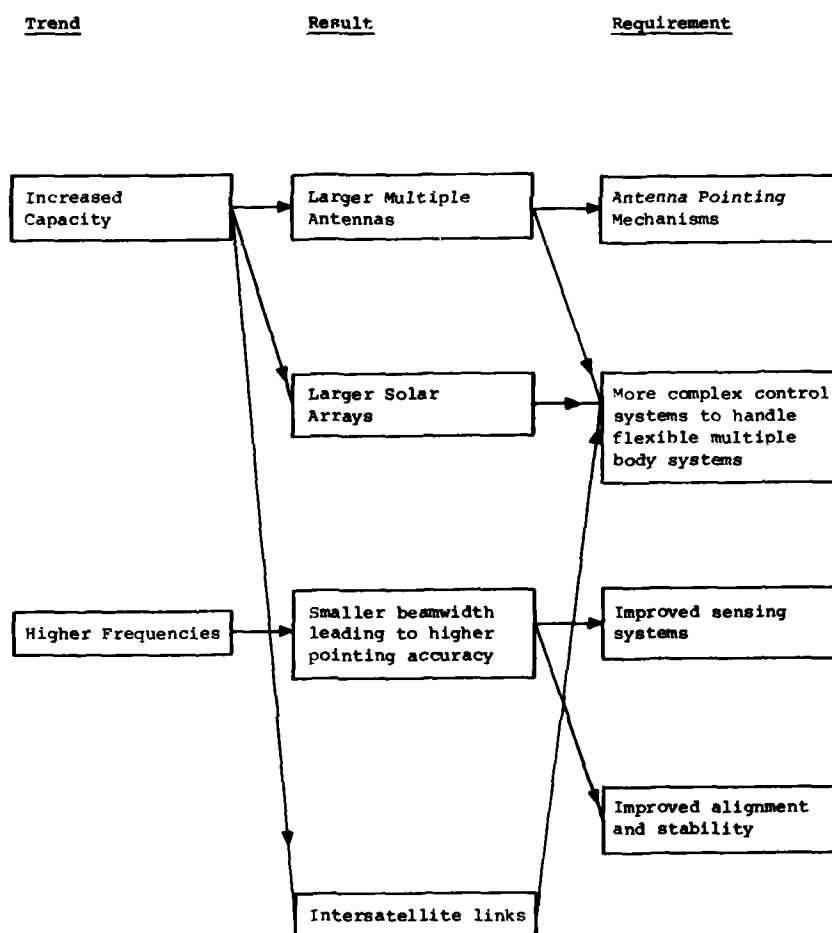


FIGURE 5 IMPACT OF COMSAT EVOLUTION ON COMSAT POINTING REQUIREMENTS

AUTONOMOUS STATION KEEPING OF GEOSTATIONARY SATELLITES

by

M.C. Eckstein, A. Leibold
Deutsche Forschungs- und Versuchsanstalt für
Luft- und Raumfahrt e.V., 8031 Oberpfaffenhofen, F.R.G.

SUMMARY

The increasing ground operational complexity of controlling the orbits of future 3-axis stabilized geostationary satellites, introduced by more stringent station keeping accuracy requirements over long mission times, suggests the consideration of autonomous orbit control. A self-contained on-board navigation system consisting of an Earth sensor, several sun sensors, a Polaris sensor and an on-board clock is investigated. An epoch element filter along with a reasonably simple orbit model is used to evaluate the navigational information from the sensor data. The orbit corrections are performed by low thrust electric propulsion according to an optimal strategy. The feasibility and performance of the autonomous system is demonstrated by computer simulation of a one year station keeping period for a large 1000 kg geostationary satellite at 19° West. All computations relevant to the station keeping system are carried out in single precision in order to simulate the reduced on-board processor capacity.

1. INTRODUCTION

Once a satellite has been injected into a geostationary orbit, it tends to drift away from its prescribed position because of

- injection errors entailing an angular velocity slightly different from that of the Earth's rotation and
- perturbation effects due to the triaxiality of the geopotential (resulting in a longitude drift), lunisolar gravitation (mainly disturbing the orbital plane) and solar radiation pressure (primarily changing the orbit eccentricity). Hence the orbit has to be corrected artificially from time to time in order to keep the satellite within given tolerance limits around its nominal geostationary position.

Existing Geostationary Satellites are controlled from the ground, i.e. tracking stations and ground computer facilities as well as telemetry/telecommand systems are required to determine the orbit, to compute the necessary manoeuvre parameters and to transmit the corresponding manoeuvre commands by radio link to the satellite. On board the satellite a ranging transponder is needed.

The increase of ground operational workload associated with more stringent accuracy requirements and long durations of future geostationary missions has initiated investigations of autonomous station keeping systems as an alternative to ground based orbit control. An autonomous station keeping system must be capable of performing the measurements for orbit determination (OD), the manoeuvres for orbit correction (OC), and the necessary computations automatically on board the satellite. Various degrees of autonomy can be considered. Fully autonomous OD would be completely independent of any ground support, whereas semi-autonomous concepts could include the use of beacons on the ground, existing relay satellites or the Global Positioning System (GPS). Similarly, the OC may demand automatic corrections of all 6 orbital elements, or less than 6 elements if, for instance, only the longitude motion is controlled.

The subject of autonomous station keeping and related topics have first been studied already nearly 20 years ago. Good general surveys, covering the 1960's are given by Gansler⁽¹⁾ and Braga-Illa⁽²⁾. Further valuable review papers were published by Gura et al⁽³⁾ and Brogan and LeMay⁽⁴⁾ at the begin of the 1970's. A very recent and clear assessment of the present systems technology state achieved up to 1979 is provided by Lowrie⁽⁵⁾.

In 1968 the US Air Force began to investigate the potential of on-board autonomous spacecraft navigation: experimental, autonomous systems controlling the mean orbit longitude of the spin-stabilized geostationary satellite LES-6 (1968) to an accuracy of 2° and of the 3-axis stabilized satellites LES-8,9 (1975) to an accuracy of 0.02° were tested and qualified^(5,6,7); several pulsed plasma thrusters, two sun transit sensors, an Earth horizon sensor, a solar ephemeris synthesizer and a simple hardware algorithm were used. Primarily for low orbiting spacecraft an on-board autonomous and a semi-autonomous navigation concept was developed also on behalf of the US Air Force: a Lunar/Star Space Sextant^(5,8) providing 250 m position accuracy after 1 day tracking, and a Passive Ranging Interferometer System⁽⁸⁾ with the capability of precise angle tracking of, and pseudo ranging to known radio stars achieving an accuracy of 450 ft after 1 revolution with signals from 3 radar stations.

Parallel to these activities autonomous navigation systems, primarily for low orbiting satellites using landmarks^(5,9,10), Navstar GPS^(11,12,13,14,15) were investigated by space research institutions.

A more recent study on in-plane and out-of-plane autonomous station keeping of future communication satellites was supported by ESA (16). Optical sensors for Earth, sun and Polaris provide the navigational information. The OD concept involves the satellite attitude. OC can be accomplished by a high or low thrust propulsion system. Autonomous station keeping is demonstrated for 5 days.

The present paper follows a slightly different approach using an attitude-independent orbit determination concept and an optimal orbit correction strategy especially designed for low thrust propulsion. The fully autonomous system is based on present or near future technology hardware. Assuming a 3-axis stabilized satellite, the measurements of an Earth sensor, several sun sensors and a Polaris sensor are taken in regular time intervals to compute the angles subtended by the Earth-sun and Earth-Polaris directions. These navigation angles do not depend on the attitude of the satellite and contain only orbit information. The navigational data are evaluated by an *epoch element filter* which combines the advantages of Batch Least Squares Estimators (insensitive with respect to system- and measurement model errors; accurate estimation which guarantees reliable orbit prediction; good numerical stability) with the benefits of Sequential Filter Algorithms (recursive and on-line data processing). For *filter stabilization* a Nonadaptive Stabilization Method is used.

Orbit correction manoeuvres have to be carried out by a suitable propulsion system. The advanced state of development of ion thrusters (17) and the considerable fuel savings (18) to be expected especially for the long mission duration and heavy weight of future satellites, justify a concept which provides *electric propulsion* for autonomous station keeping. The low thrust level necessitates the development of a correction strategy which is basically different from the conventional ones to be found in the literature (19,20,21). In contrast to the commonly applied "waiting strategy" which provides orbit corrections only when the satellite is going to exceed certain tolerance limits, a "precaution strategy" is required: the total correction, to be carried out during a specified time interval, is pre-computed and distributed on several correction manoeuvres, each of them small enough to be within the capability of the low thrust propulsion system. Whereas the "waiting strategy" minimizes the frequency of manoeuvres, which is desirable from a ground operational point of view, the fuel optimization in the "precaution strategy" leads to a maximum number of thrusts (22). The width of the tolerance window is only partially used, leaving the remainder as a safety zone. The latter is particularly useful for autonomous station keeping because of the limited navigational data accuracy, orbit model deficiencies and thrust execution errors. On the other hand, the arguments favouring infrequent thrusts are no longer important in case of autonomous operations.

As it is difficult to judge the described autonomous station keeping system theoretically, it has to be tested by computer simulation with respect to feasibility and performance. Hence the controlled motion of a geostationary satellite is simulated with realistic assumptions on the various error sources and on-board processor accuracy.

2. STATION KEEPING HARDWARE COMPONENTS

A brief survey of available on-board equipment and a discussion on its qualification for autonomous station keeping can be found in the recent ESA-study (16). Similar considerations lead to the conclusion that fully autonomous *OP* requires the following hardware components:

- 1 Earth sensor
- 4 sun sensors
- 1 Polaris sensor
- 1 on-board clock.

The *OC* can be carried out by means of a propulsion system consisting of at least

- 4 ion thrusters.

The necessary *computations* have to be performed by

- an on-board processor.

2.1 SENSORS

Most of the sensors mentioned, with the exception of the Polaris sensor, are standard on present day geostationary satellites. The main characteristics for a few examples are shown in Table 1.

	Earth-Sensor	Sun-Sensor	Polaris-Sensor
Mass [kg]	2.5	1	5
Field of View	$\pm 12^\circ / \pm 14^\circ$	$\pm 64^\circ / \pm 64^\circ$	$\pm 8^\circ / \pm 8^\circ$
Noise	± 0.0073	± 0.004	± 0.0008
Bias	$0.02 \text{ } \therefore \text{ } 0.03$		0.003
RMSE	$0.021 \text{ } \therefore \text{ } 0.031$	0.015	0.0031
Manufacturer	OFFICINE GALILEO OTS IR Earth Sensor (IRES)	ADCOLE 20910 (digital)	BALL BROTHERS CT-411

Table 1 Potential Sensors for an Autonomous Station Keeping System.

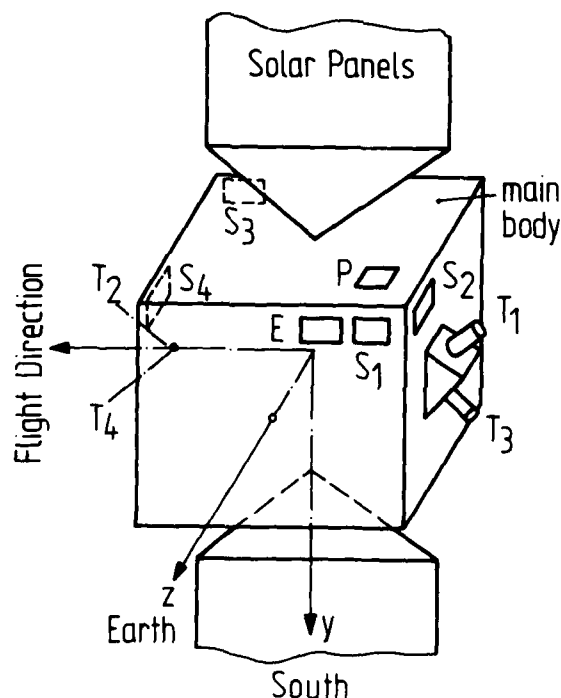


Fig. 1 Sensor (E,P,S_i) and Thruster (T_i) Arrangement.

2.1.1 SENSOR CONFIGURATION AND MEASUREMENTS

It will be assumed that the satellite is 3-axis stabilized with the x-axis nominally pointing east, the y-axis south and the z-axis towards the Earth's centre (Fig. 1). In order to cover all possible sun directions, the 4 sun sensors S₁ ... S₄ are to be mounted on the side walls of the satellite. Earth sensor E, Polaris sensor P, and the sun sensors S₁, S₂ should be mounted close together so as to reduce the effects of alignment errors and thermal effects. The calibration between the various sensors and with respect to the satellite coordinate system is alleviated by putting the Earth sensor E and the sun sensor S₁ on a common platform. Each Sensor measures 2 of the 3 direction cosines of the observed object in a sensor dedicated coordinate system. The transformation of the sensor outputs to the satellite fixed coordinate system is rather simple for the specific sensor arrangement shown in Fig. 1.

The Earth sensor measures the unit vector components (X_E, Y_E) , the Polaris sensor (X_P, Z_P) and the 4 Sun sensors (X_{S1}, Y_{S1}) , (Y_{S2}, Z_{S2}) , (X_{S3}, Y_{S3}) , (Y_{S4}, Z_{S4}) in the satellite system. Hence the unit vectors in the directions to the Earth, Polaris and Sun are given by

$$\begin{aligned} \underline{U}_E &= \begin{bmatrix} X_E \\ Y_E \\ \sqrt{1-X_E^2-Y_E^2} \end{bmatrix} ; & \underline{U}_P &= \begin{bmatrix} X_P \\ -\sqrt{1-X_P^2-Z_P^2} \\ Z_P \end{bmatrix} ; \\ \underline{U}_S &= \begin{bmatrix} X_{S1} \\ Y_{S1} \\ \sqrt{1-X_{S1}^2-Y_{S1}^2} \end{bmatrix} = \begin{bmatrix} -\sqrt{1-Y_{S2}^2-Z_{S2}^2} \\ Y_{S2} \\ Z_{S2} \end{bmatrix} = \begin{bmatrix} X_{S3} \\ Y_{S3} \\ -\sqrt{1-X_{S3}^2-Y_{S3}^2} \end{bmatrix} \\ &= \begin{bmatrix} \sqrt{1-Y_{S4}^2-Z_{S4}^2} \\ Y_{S4} \\ Z_{S4} \end{bmatrix} . \end{aligned} \quad (1)$$

2.1.1 NAVIGATION ANGLES

The unit vectors \underline{U}_E , \underline{U}_P and \underline{U}_S depend on the attitude because they refer to a satellite fixed coordinate system. However, if \underline{U}_E and \underline{U}_S are measured simultaneously, one can compute the attitude-independent angle α between the Earth- and Sun direction by

$$\alpha = \arccos \frac{|\underline{U}_E \cdot \underline{U}_S|}{|\underline{U}_E| |\underline{U}_S|}, \quad 0 < \alpha < \pi \quad (2)$$

similarly one obtains the angle β between the Earth and Polaris directions

$$\beta = \arccos (\underline{U}_E \cdot \underline{U}_P), \quad 0 < \beta < \pi \quad (3)$$

The simple expression (3) is sufficient for accurate evaluation of β because $\beta \sim \frac{\pi}{2}$. The sun direction \underline{U}_S can be taken from the output of any of the 4 Sun sensors. In general, only one sensor will see the sun at a time, although there is some visibility overlap because of the $\pm 64^\circ$ field of view of the sun sensors. In these cases the smaller pair of measured sensor coordinates is to be preferred.

Since α and β contain exclusively orbit information, they will be used as navigation angles. The attitude can influence α and β only if

- the directions \underline{U}_E and \underline{U}_S or \underline{U}_E and \underline{U}_P are not measured simultaneously and the attitude varies between the measurements, or
- the sensors are used beyond their nominal measuring range where the errors are relatively large.

The first error source can largely be eliminated by interpolation between a series of measurements of both contributing sensors, the second by discarding navigational data collected during very non-nominal attitude phases.

2.1.3 MEASUREMENT ERRORS

Random Errors

The random errors in α and β can be considered as a sum of errors due to discretization (uniformly distributed errors), due to errors caused by short term temperature variations within a particular sensor and/or within the satellite structure changing in particular the phase angles between the Earth sensor and the different sun sensors. According to the central limit theorem zero-mean normal distribution will be assumed for the random errors in α and β .

Information on sensor accuracy is rather limited. In general, the manufactures give an overall value of the angular error from which a rough estimate of the variance of α may be obtained by assuming the directions of both Earth and Sun to be close to the sensor axes. Then the variances of the sensor outputs are added geometrically as

$$\sigma_\alpha^2 \sim \left. \begin{array}{l} \sigma_{XE}^2 + \sigma_{XS}^2 \\ \sigma_{XE}^2 + \sigma_{ZS}^2 \end{array} \right\} \text{ for sun sensors } \left\{ \begin{array}{l} 1 \text{ and } 3 \\ 2 \text{ and } 4 \end{array} \right\} \quad (4)$$

Similarly one obtains for the variance of β

$$\sigma_{\beta}^2 = \sigma_{YE}^2 + \sigma_{ZP}^2 \quad (5)$$

Systematic Errors

The measurements X, Y, Z of each sensor may be additionally corrupted by constant and/or periodic systematic errors due to long term temperature variations with a period of ~1 day, caused by periodic heating and cooling of different parts of the satellite structure facing the sun or the opposite direction. Periodic errors in α and β are also produced through residual mounting errors which can not be eliminated by pre-flight or in-flight calibrations. Due to lack of reliable experimental data on most of the systematic errors only the residual mounting errors are included in the navigational data simulation, resulting in systematic shifts of α and β .

2.2 THRUSTERS

A system of 4 Ion thrusters is assumed to be used for both North-South (NS) and East-West (EW) corrections. *Typical* characteristics are listed in Table 2.

Type:	ION-Thruster
Thrust level:	10 mN
Fuel:	HG
Specific Impuls:	31000 Ns/kg
Mass:	9 kg
Power Requ.:	375 W
Manufacturer:	MBB - RIT 10

Table 2 Characteristics of the Adopted Propulsion System.

2.2.1 THRUSTER CONFIGURATION

In order to avoid contamination of the solar paddels, the thrusters are mounted on the east- and west walls of the satellite body, inclined by $+45^\circ$ with respect to the satellite equator (Fig. 1). Hence the individual thrust directions of the 4 thrusters are nominally NE, NW, SW, SE with no component in the direction towards the Earth. Accelerations in the main directions North, East, South and West can be generated by operating two thrusters simultaneously. Although this results in a 30% efficiency loss, the fuel mass savings of an electric propulsion system with respect to chemical propulsion is still considerable. Slightly better efficiency could be achieved by a steeper inclination up to the admissible limit of $+55^\circ$ with respect to the satellite equator because the major velocity increments are needed in the North-South directions. However, the configuration of $\pm 45^\circ$ inclined thrusters has been chosen here for the sake of simplicity.

2.2.2 THRUST ERRORS

Very little is known about errors in thrust level and directions of Ion thrusters. Hence several values of random and systematic errors up to $\pm 3\%$ in thrust level and $\pm 3^\circ$ in the thrust directions were assumed in the station keeping simulation.

2.3 ON BOARD CLOCK

The accuracy of the on-board clock should be compatible with the sensor accuracy. A crystal-controlled clock of accuracy 10^{-8} to 10^{-9} is sufficient.

2.4 ON BOARD PROCESSOR

The processor will be used for other purposes besides the autonomous station keeping. Word length, core store, speed will therefore be determined by the overall requirements. Those for station keeping are not yet defined. Most likely a 16-bit machine (partly re-programmable in-flight) with single and double length arithmetic available should be ade-

quate. This confidence is justified by the fact that all algorithms relevant for station keeping were successfully tested in single precision without any numerical problems. Implicit scaling by proper orbit and measurement modeling and the use of a robust OD algorithm are additional supporting factors.

3. ORBIT AND MEASUREMENT MODELING

Orbit generators will be needed

- for the OD algorithm in order to compute residuals between measured and predicted quantities
- for the OC algorithm in order to consider future orbit variations
- for the station keeping simulation in order to produce realistic satellite motion and measurement data.

In the first two cases the orbit model must be rather simple even at the cost of reduced accuracy so as to fit the limited capability of the on-board processor. Considerably higher accuracy is required in the third case in combination with a long term prediction capability because the simulations extend over several hundreds of revolutions. Hence analytical perturbation models with different degrees of complexity are selected for the 3 tasks (23). In addition to the natural perturbations due to the triaxiality of the geopotential, luni-solar gravitation and solar radiation pressure, the thrust effects also have to be modeled.

3.1 GEOSTATIONARY ELEMENTS

As the classical set of Keplerian elements $(a, e, i, \omega, \Omega, M)$ is inappropriate for geostationary orbits because the angular quantities are undefined for zero eccentricity and inclination, a different set of "Geostationary Elements" (D, h, l, p, q, λ) is introduced (24). They are related to the classical ones as follows:

$$\begin{aligned} D &= (n - n_E)/n_E, \text{ where } n = \mu^{1/2} a^{-3/2} \\ h &= e \sin(\Omega + \omega) \\ l &= e \cos(\Omega + \omega) \\ p &= \sin \frac{i}{2} \sin \Omega \\ q &= \sin \frac{i}{2} \cos \Omega \\ \lambda &= M + \Omega + \omega - L. \end{aligned} \quad (6)$$

In Eq. (6) n_E is the Earth's angular velocity of rotation and L the station right ascension, whereas μ is the geocentric gravitational constant. The geostationary elements are non-dimensional and vanish in case of an undisturbed, exact geostationary orbit. The element D is a normalized drift rate, λ the mean off-station longitude, whereas (h, l) and (p, q) essentially represent the eccentricity and inclination vectors.

The perturbations expressed in these elements do not contain any singularities for circular and equatorial orbits (24). For abbreviation the geostationary elements in the above order will also be denoted by the vector

$$\underline{E} = (D, h, l, p, q, \lambda)^T \quad (7)$$

All the components of \underline{E} are small and can be treated as first order quantities for a satellite orbit controlled within a small geostationary tolerance window. This fact ensures well conditioned matrices in the orbit determination algorithm without the need of scaling. In case of unperturbed Keplerian motion the element vector \underline{E} is constant with the exception of the last component, λ , which is a linear function of time. In the presence of perturbations all 6 components of \underline{E} are time dependent according to the variational equations (25). Hence the variation of \underline{E} is governed by the equation

$$\dot{\underline{E}} = \dot{\Phi} \underline{E} + \dot{\Psi} \underline{a} \quad (8)$$

$$\text{with } \dot{\Phi} = \begin{pmatrix} 0 & 0 & 0 & 0 & 0 & 0 \\ 0 & 0 & 0 & 0 & 0 & 0 \\ 0 & 0 & 0 & 0 & 0 & 0 \\ 0 & 0 & 0 & 0 & 0 & 0 \\ 0 & 0 & 0 & 0 & 0 & 0 \\ n_E & 0 & 0 & 0 & 0 & 0 \end{pmatrix} \quad (9)$$

$$\dot{\psi} = \frac{1}{V} \begin{pmatrix} 0 & -3 & 0 \\ -\cos L & 2\sin L & 0 \\ \sin L & 2\cos L & 0 \\ 0 & 0 & \frac{1}{2} \sin L \\ 0 & 0 & \frac{1}{2} \cos L \\ -2 & 0 & 0 \end{pmatrix} \quad (10)$$

The acceleration vector

$$\underline{a} = (a_R, a_T, a_N)^T \quad (11)$$

consisting of components in radial, tangential and normal direction with respect to the orbital motion is due to any non-Keplerian forces acting on the satellite. The first term in Eq. (8) represents the Keplerian mean motion which affects only the off-station mean longitude, whereas the second term exclusively describes the perturbation effects. In Eq. (10), $V = 3.07$ km/s is the geostationary orbit velocity. The rather simple form of the variational equations is obtained by neglecting all terms proportional to squares or higher powers of the geostationary elements, as it is justified for a nearly geostationary orbit.

3.2 NATURAL PERTURBATIONS

Since a geostationary satellite maintains its position relative to the geopotential, the contribution of triaxiality to the acceleration vector \underline{a} is constant. The contributions from luni-solar gravitation and solar radiation pressure repeat with daily, monthly and yearly periods. Hence the second term on the right hand side of Eq. (8) can be represented by a triple Fourier Series. The integration of Eq. (8) yields the result (23)

$$\underline{E}(t) = \Phi(t, t_0) \underline{E}_0 + \underline{c}(t-t_0) + \frac{1}{2} \ddot{\underline{c}}(t-t_0)^2 + \Delta \underline{E}_{LP}(t) + \Delta \underline{E}_{SP}(t) \quad (12)$$

with the abbreviations

$$\Phi(t-t_0) = \begin{bmatrix} 1 & 0 & 0 & 0 & 0 & 0 \\ 0 & & & & & \\ 0 & & & & & \\ 0 & & & I_{5 \times 5} & & \\ 0 & & & & & \\ n_E(t-t_0) & & & & & \end{bmatrix}_{6 \times 6} \quad (13)$$

\underline{E}_0 for the epoch mean element vector,

\underline{c} for the secular perturbation rates of the orbital element vector,

$$\Delta \underline{E}_{LP}(t) = \sum_{m=M}^M \sum_{s=-S}^S [\underline{A}_{oms} \cos(mL_e + sL_\odot) + \underline{B}_{oms} \sin(mL_e + sL_\odot)] \quad (14)$$

for the long periodic perturbations and

$$\Delta \underline{E}_{SP}(t) = \sum_{n=0}^N \sum_{m=M}^M \sum_{s=S}^S [\underline{A}_{nms} \cos(nL + mL_e + sL_\odot) + \underline{B}_{nms} \sin(nL + mL_e + sL_\odot)] \quad (15)$$

for short periodic perturbations at time t .

$L_e = L_e(t)$ = mean longitude of the moon,

$L_\odot = L_\odot(t)$ = mean longitude of the sun.

The coefficients A_{nms} , E_{nms} vary slowly with time because of variations of the Moon's orbit. This effect can be modeled with sufficient accuracy by a 2-degree polynomial as

$$\begin{aligned} A_{nms} &= \sum_{j=0}^2 A_{nmsj} d^j \\ E_{nms} &= \sum_{j=0}^2 E_{nmsj} d^j \end{aligned} \quad (16)$$

where d is the number of days elapsed since a fixed epoch date. The coefficients can be calculated ⁽²³⁾ from the geographic station longitude, satellite mass and cross section area for a time interval ≤ 2 years specified by 2 dates.

3.3 THRUST EFFECTS

The orbit corrections for a satellite with a tolerance window of about $+0.1^\circ$ can be considered as differential corrections. Thus, for their computation the variational equations (10) can be used again. The effect of finite thrusts, constant between t_{x1} and t_{x2} , on the orbital elements at time t is obtained by integration of (8) and summation over all thrust phases. The result is

$$\Delta E_{TH}(t) = \sum_{x=1}^K \Psi_x(t) \underline{a}_x \quad (17)$$

$$\Psi_x(t) = \frac{1}{\sqrt{n_E}} \begin{bmatrix} 0 & -3\Delta L_x & 0 \\ -2\cos L_x \sin \frac{1}{2} \Delta L_x & 4 \sin L_x \sin \frac{1}{2} \Delta L_x & 0 \\ 2 \sin L_x \sin \frac{1}{2} \Delta L_x & 4 \cos L_x \sin \frac{1}{2} \Delta L_x & 0 \\ 0 & 0 & \sin L_x \sin \frac{1}{2} \Delta L_x \\ 0 & 0 & \cos L_x \sin \frac{1}{2} \Delta L_x \\ -2\Delta L_x & -3\Delta L_x (L - L_x) & 0 \end{bmatrix} \quad (18)$$

where

K = number of predetermined thrusts,

\underline{a}_x = acceleration vector of x^{th} thrust,

$L = L_0 + n_E(t - t_0),$ (19)

$L_x = L_0 + n_E[\frac{1}{2}(t_{x1} + t_{x2}) - t_0]$ (20)

$\Delta L_x = \begin{cases} 0 & \text{if } t \leq t_{x1} \\ n_E(t - t_{x1}) & \text{if } t_{x1} < t < t_{x2} \\ n_E(t_{x2} - t_{x1}) & \text{if } t \geq t_{x2} \end{cases}$ (21)

t_{x1}, t_{x2} = switch-on and switch-off times of x^{th} thrust,

L_0 = station right ascension at epoch t_0 .

Eqs. (17) - (21) are obtained under the assumption that the acceleration is constant during each thrust period. The switch times and the acceleration vectors have to be known for all thrusts occurring in the time interval (t_0, t) . They are precomputed by the orbit correction algorithm described in section 6.

3.4 MEASUREMENT MODEL

The navigation angles α and β are determined by the position vectors \underline{x} , \underline{x}_1 and \underline{x}_2 of the satellite, the sun and Polaris, respectively, in the equinoctial system with the origin at the Earth's centre. Introducing the measurement vector

$$\underline{y} = (y_1, y_2)^T = (\alpha, \beta)^T \quad (22)$$

one obtains

$$\cos y_i = -\underline{x} \cdot (\underline{x}_i - \underline{x}) / (r \Delta_i) = -\underline{x} \cdot \underline{x}_i / (r \Delta_i) + r / \Delta_i \quad (23)$$

with

$$r = |\underline{x}|, \quad \Delta_i = |\underline{x}_i - \underline{x}|. \quad (24)$$

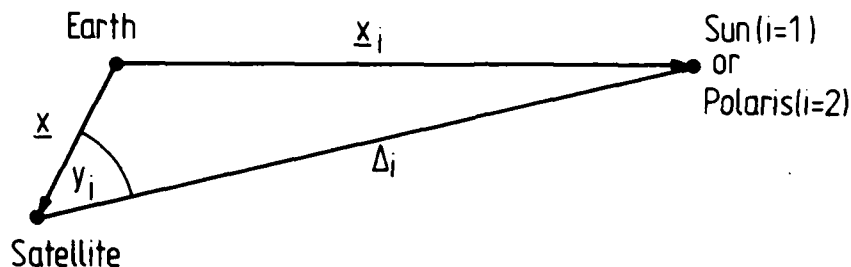


Fig. 2 Definition of Navigation angles $(y_1, y_2) = (\alpha, \beta)$.

The position vector \underline{x} can be expressed in terms of the geostationary elements as

$$\underline{x} = r \begin{pmatrix} \cos(L+\lambda) - 1(1-\cos 2L) + h \sin 2L \\ \sin(L+\lambda) - h(1+\cos 2L) + h \sin 2L \\ -2p \cos L + 2q \sin L \end{pmatrix} \quad (25)$$

whereby squares and higher powers of the geostationary elements are neglected.

If \underline{y}_{ST} is introduced as the measurement vector which would be observed from the nominal geostationary satellite position $\underline{x}_{ST} = r_{ST}(\cos L, \sin L, 0)^T$ one obtains from Eqs. (23) and (25)

$$\cos y_i = \cos y_{STi} + \sum_{n=0}^2 (a_{in} \cos nL + b_{in} \sin nL) \quad i = 1, 2 \quad (26)$$

with the coefficients

$$a_{i0} = (h \sin \alpha_i + 1 \cos \alpha_i) \cos \delta_i \quad (27)$$

$$a_{i1} = -\lambda \sin \alpha_i \cos \delta_i - 2p \sin \delta_i \quad (28)$$

$$b_{i1} = \lambda \cos \alpha_i \cos \delta_i - 2q \sin \delta_i$$

$$a_{i2} = (h \sin \alpha_i - 1 \cos \alpha_i) \cos \delta_i \quad (29)$$

$$b_{i2} = -(h \cos \alpha_i + 1 \sin \alpha_i) \cos \delta_i$$

where (α_1, δ_1) and (α_2, δ_2) are the right ascension and declination of the Sun and Polaris, respectively.

It is interesting to note that the eccentricity vector $(1, h)$ can be determined from Eqs. (29) after evaluating, for instance, a_{12} and b_{12} from observations of only one navigation angle y_1 . Measurements from Earth and Sun sensors are preferable because $\cos \delta_1 \approx 1$ whereas $\cos \delta_2 \ll 1$. However, the remaining elements occur only in Eqs. (28) defining a_{i1} and b_{i1} . They can be determined only if, at least, 2 navigation angles y_1 and y_2 are observed, in order to provide 4 independent equations for λ, p, q .

The choice of Sun ($\delta_1 \leq 23.5^\circ$) and Polaris ($\delta_2 = 89^\circ$) as measurement sources is justified by Eqs. (28) which then becomes a well conditioned system yielding good separation between inclination effects (p, q) and longitude drift behaviour (λ).

Expansion of the left hand side of Eq. (26)

$$\cos y_i = \cos y_{STi} - (y_i - y_{STi}) \sin y_{STi} + \dots \quad (30)$$

yields a linear relationship between geostationary elements and the measurements

$$\underline{y}(t) = \underline{y}_{ST}(t) + H(t) \underline{E}(t) \quad (31)$$

with the measurement matrix

$$H(t) = \begin{bmatrix} H_1 \\ H_2 \end{bmatrix} \quad (32)$$

where

$$H_i = - \frac{1}{\sin y_{STi}} \begin{bmatrix} 0 \\ [\sin \alpha_i + \sin(\alpha_i - 2L)] \cos \delta_i \\ [\cos \alpha_i - \cos(\alpha_i - 2L)] \cos \delta_i \\ 2 \cos L \sin \delta_i \\ \sin(\alpha_i - L) \cos \delta_i \end{bmatrix}^T \quad i = 1, 2 \quad (33)$$

Note that the measurement matrix $H(t)$ does not depend on \underline{E} . The right ascensions and declinations α_i, δ_i are known functions of time or constant in case of Polaris. The neglected terms containing squares and higher powers of the geostationary elements contribute only few arcseconds to the navigation angles which is well below any measurement error.

4. ORBIT DETERMINATION

A station keeping system, autonomous in measurement data acquisition and data processing, requires a careful match of the orbit model (dynamic system) and the estimation algorithm: complex models and sophisticated estimation algorithms lead to high computer storage requirements and long computation times, respectively; however, simple models usually cause either poor orbit determination accuracy or divergence of the estimation algorithm. The following properties are desirable for an on-board station keeping system:

- 1) The orbit model used in the orbit determination algorithm should be simple but consistent with the moderate sensor accuracies.
- 2) The algorithm should be sufficiently robust to tolerate a simple measurement model as well as temporary sensor and thruster failures.
- 3) Numerical stability on a limited word length on-board processor.
- 4) Sufficient accuracy for reliable orbit prediction as required for the orbit correction strategy.
- 5) Low sensitivity with respect to model and measurement error statistics.
- 6) Recursive and sequential data processing which eliminates data storing.

In the literature primarily two methods are applied to satellite OD problems:

- **Batch Estimator Algorithms** such as the Weighted Least Squares (WLQ) Method, often modified to include also a-priori information on the orbital elements, evaluating the tracking data. This classical and widely used method in ground station OD lacks particularly the property 6) in which one is interested for onboard OD.
- **Sequential Estimator Algorithms** such as the Extended Kalman Filter (EKF) frequently used in satellite on-board navigation problems. To avoid filter divergence due to modeling errors in the dynamic system, measurement equations as well as in the process and measurement noise statistics, nonadaptive (26) and adaptive (structural (27) and statistically (28) adaptive) methods are applied to modify the filter. To guarantee numerical filter stability on a word length limited on-board processor, "covariance matrix square root" (29) and "square root-free" (30) algorithms have been proposed with the same computational

efficiency and accuracy reached by the EKF in double precision on a large scale computer (³¹). In this investigation none of these methods is used. It is assumed that the outlined sequential algorithms will probably either have divergence problems under the conditions (1), (2) and (5) or will be still too complex. An EPOCH MEAN ELEMENT FILTER processing also a-priori information was developed. Ideas from the Least Squares Method and of the Kalman Filter are used.

4.1 MODEL SIMPLIFICATION

The expression (12) for the natural Perturbations is rather complex and not well suited for the orbit determination algorithm. Fortunately, the *short periodic perturbations* ΔE_{SP} are very small. Their effects in longitude are of the order of 0.005 and much less in latitude which is well below measurement accuracy. Additionally, the OD procedure to be described in section 5 largely eliminates short periodic effects because they are averaged over one revolution. Hence, they may be omitted in the orbit model for both the orbit determination and orbit correction phases.

The *long periodic perturbations* ΔE_{LP} are considerably larger (up to some hundredths of a degree in longitude) than the short periodic ones, but their variation during a few days is also very small. Hence, if the measurements extend over one or a few days only, the omission of ΔE_{LP} in the OD model results essentially in a offset $\Delta E_{LP}(t_0)$ to the estimated epoch mean elements \underline{E}_0 , i.e. instead of \underline{E}_0 , the set

$$\underline{\tilde{E}}_0 = \underline{E}_0 + \Delta E_{LP}(t_0) \quad (34)$$

is obtained.

Since the orbital element vector has to be computed for each measurement time, a simple orbit model is very essential. Therefore, the long periodic effects ΔE_{LP} are also neglected in the OD method described in the sequel. The resulting values \underline{E}_0 can be corrected to obtain $\underline{\tilde{E}}_0$ whenever necessary because ΔE_{LP} is a known function of time t . These considerations lead to the following simplified orbit (system) model

$$\underline{E}_j = \Phi_{j,0} \underline{E}_0 + c(t_j - t_0) + \frac{1}{2} \ddot{c}(t_j - t_0)^2 + \sum_{\kappa=1}^K \Psi_{\kappa,j} a_{\kappa} + \tilde{n}_j \quad (35)$$

where the subscript j refers to values at time t_j . The 4-th term on the right hand side is the contribution by the thrusts according to Eq. (17) and the last term

$$\tilde{n}_j = \int_{t_0}^{t_j} G(\tau) \Phi(\tau, t_0) \underline{w}(\tau) d\tau + \Delta E_{LP} + \Delta E_{SP} \quad (36)$$

is added to include various error effects; it accounts for errors in the systems equations due to modeling errors of both the natural perturbations as well as of the thrust, due to numerical errors because of truncation, round-off errors and process noise. In Eq. (36) $G(\tau)$ is a transformation matrix and $\underline{w}(\tau)$ is non-zero mean white noise. Since Φ , c and $\Psi_{\kappa,j}$ do not depend on \underline{E}_0 , the partial derivatives can easily be obtained from Eq. (35) as

$$\frac{\partial \underline{E}_j}{\partial \underline{E}_0} = \Phi_{j,0} \quad \frac{\partial \underline{E}_j}{\partial a_{\kappa}} = \Psi_{\kappa,j} \quad (37)$$

4.2 MEASUREMENT MODEL FOR ORBIT DETERMINATION

The measurement model is taken from Eq. (31) supplemented by systematic and random errors:

$$\underline{y}_j = \underline{y}_{STj} + H_j \underline{E}_j + \underline{m}_j + \underline{v}_j \quad (38)$$

$$\text{where } \underline{m}_j + \underline{v}_j \sim N(\underline{m}_j, R_j) \quad (39)$$

The partial derivatives with respect to the osculating elements are

$$\frac{\partial \underline{y}_j}{\partial \underline{E}_j} = H_j \quad (40)$$

4.3 EPOCH MEAN ELEMENT FILTER

The algorithm basically consists of an estimation (measurement updating) cycle and a prediction (time updating) cycle: within the estimation cycle the a-priori known epoch mean element information is combined with the information obtained from a Least Square Fit over a block of measurements by elementary statistical principles; in the prediction cycle the estimated epoch mean elements are propagated to the begin of a new block of data to be fit in the next estimation cycle.

Combining system equation (35) and measurement equation (38) one obtains the navigation angles $z_j(\underline{E}_0) = y_j(\underline{E}_j(\underline{E}_0))$ at time t_j as a function of the epoch mean elements \underline{E}_0 :

$$\begin{aligned} z_j(\underline{E}_0) = & \underline{y}_{STj} + H_j \Phi_j \underline{E}_0 + H_j c(t_j - t_0) + \frac{1}{2} H_j \dot{\Phi} c(t_j - t_0)^2 + H_j \sum_{k=1}^K \Psi_{kj} \underline{a}_k \\ & + H_j \tilde{n}_j + \underline{m}_j + \underline{v}_j \end{aligned} \quad (41)$$

Eq. (41) will be used to estimate the epoch mean elements \underline{E}_0 from the measured angles z_j , whereas the \underline{a}_k are treated as *consider parameters* only. Since the vector

$$\underline{f}_j = \underline{y}_{STj} + H_j c(t_j - t_0) + \frac{1}{2} H_j \dot{\Phi} c(t_j - t_0)^2 + H_j \sum_{k=1}^K \Psi_{kj} \underline{a}_k \quad (42)$$

does not depend on \underline{E}_0 , it is a known function of time. The following additional abbreviations are introduced for simplification:

$$\underline{A}_j = H_j \Phi_{j,0}; \quad \underline{n}_j = H_j \tilde{n}_j + \underline{m}_j + \underline{v}_j \quad (43)$$

4.3.1 SEQUENTIAL WEIGHTED LEAST SQUARES WITHIN A BLOCK OF DATA

For the derivation and justification of the filter equations for the estimation cycle the following aspects of the physical problem must be outlined:

- i) The major deviations between and modeled navigation angles occurring during an OD arc are due to systematic and random sensor errors. They are assumed of about equal size. Compared to these effects those from the neglected long- or short-periodic perturbations are small or introduce a known offset (bias) in the estimates, respectively. Of minor importance are also the thrust errors during one OD arc.
- ii) Six epoch elements are to be estimated:
 - The "in-plane" elements: D (driftrate); $\Delta\lambda$ (mean off-station longitude); h, l (eccentricity components). Contributions to their estimation come mainly from the navigation angle Earth/satellite/sun.
 - The "out-of-plane" elements p, q (inclination vector components) are preferably estimated by the navigation angle Earth/satellite/Polaris.

With (i) and (ii) it seems justifiable to use as weight for the navigational data the reciprocal of the associated mean square errors or variances only. The filter equations are summarized in the subsequent table:

Measurement Model	$\underline{z}_j = \underline{A}_j \underline{E}_0 + \underline{f}_j + \underline{n}_j \quad (44)$ $\underline{A}_j, \underline{f}_j, \underline{n}_j \text{ as defined in (43); (42); (36); (39)}$
A-priori Statistics	$\underline{n}_j \text{ "system noise"}$ $\underline{m}_j + \underline{v}_j \sim N(\underline{m}_j, R_j) \text{ non-zero mean measurement white noise sequence}$ $\underline{m}_j = (m_{1j} \ m_{2j})^T; R_j = \begin{pmatrix} R_{1j} & 0 \\ 0 & R_{2j} \end{pmatrix} \quad (45)$
Initial Conditions	
Estimate	\underline{E}_{00}
A-priori Covariance Matrix	\underline{P}_0

(46)

At Time t_j within Block k	
Measurement Weighting Matrix	$W_j = \begin{bmatrix} W_{1j} & 0 \\ 0 & W_{2j} \end{bmatrix} \quad (47)$ $W_{\ell j} = (m_{\ell j}^2 + R_{\ell j})^{-1}$
Intermediate Estimate for Element Corrections (stored in 2x6 matrix)	$\Delta \hat{\mathbf{e}}_j = \Delta \hat{\mathbf{e}}_{j-1} + K_j T_j \quad (48)$ <p>with $\Delta \hat{\mathbf{e}}_0 = \mathbf{0}$</p>
Gain	$K_j = N_{j-1}^{-1} A_j^T [W_j^{-1} + A_j N_{j-1}^{-1} A_j^T]^{-1} \quad (49)$
Inverse of the Normal Matrix	$N_j^{-1} = M_j N_{j-1}^{-1} M_j^T + K_j W_j^{-1} K_j^T \quad (50)$ <p>where $M_j = I - K_j A_j$ and $N_0^{-1} = \bar{P}_0$</p>
Modified Residual Error	$T_j = \begin{bmatrix} t_{1j} & 0 \\ 0 & t_{2j} \end{bmatrix} \quad (51)$ $t_j = z_j - f_j - A_j \Delta \hat{\mathbf{e}}_{j-1} u$ $u = (1 \ 1)^T$
Covariance Matrices Corresponding to 1 st and 2 nd Column of Δ_j	$\bar{P}_{\ell j} = M_j \bar{P}_{\ell j-1} M_j^T + K_{\ell j} R_{\ell j} K_{\ell j}^T \quad (52)$ <p>with $\bar{P}_{\ell 0} = 0$</p>
At End t_n of Block k	
Final Estimates and A-posteriori Covariance Matrix	$\hat{\mathbf{e}}_{an} = \bar{\mathbf{e}}_{ao} + \Delta \bar{\mathbf{e}}_n \quad (53)$ $\hat{P}_n = \bar{P}_n + N_n^{-1} \bar{P}_0^{-1} N_n^{-1}$ $\Delta \bar{\mathbf{e}}_n = \Delta \hat{\mathbf{e}}_n S_{k,n}$ $\bar{P}_n = \bar{P}_1 S_{1,n}^2 + \bar{P}_2 S_{2,n}^2$ <p>Matrix S_k is used for filter stabilization and is here not further specified. P^{-1} is obtained by Cholesky Decomposition (52). Inversion of \bar{P}_0 can be avoided for the stable filter ($S_k \approx I$) and if (47) is replaced by $W_{\ell j} = R_{\ell j}^{-1}$ which is justified by ii) of this section.</p>

Table 3 Filter Equations for the Estimation (Measurement Updating) Cycle.

4.3.2 TRANSITION TO THE NEXT BLOCK

To propagate the obtained estimate from epoch t_k of data block k to epoch t_{k+1} of the next data block $k+1$ the orbit model (35) assuming nominal thrust is used whereby \dot{h}_j is neglected.

To obtain the a-priori element estimate variance for the new block $k+1$ the a-posteriori covariance from block k is time-propagated using $\Phi_{k,k+1}$ in the familiar way. To take account of the neglected natural perturbations and thrust error effects (to be expected during block $k+1$) on the estimates, a "noise matrix" Q is added, constructed from the terms which are in the average neglected during each OD arc.

Element Propagation from Epoch t_k of Block k to $k+1$	$\bar{E}_{\square 0} = \Phi_{k+1,k} \hat{E}_{\square 0} + c(t_{k+1} - t_k) + \frac{1}{2} \ddot{c} (t_{k+1} - t_k)^2 + \sum_{n=1}^K \Psi_{n,k+1} a_{0n} \quad (54)$
Covariance Matrix Propagation	$\bar{P}_0 = \Phi_{k+1,k} \hat{P}_n \Phi_{k+1,k}^T + Q \quad (55)$
"Noise" Matrix	$Q = \begin{bmatrix} \sigma_1^2 & 0 \\ 0 & \sigma_6^2 \end{bmatrix} \quad (56)$ <p>where</p> $\sigma_1^2 = \frac{1}{L-1} \sum_{\ell=1}^L \left[\frac{1}{n} \sum_{j=1}^n \tilde{n}_j \right]_{\ell} + \Psi_{\Pi,n} a_N (\Delta_{\psi}^2 \sigma_{\psi}^2) a_N^T \Psi_{\Pi,n}^T \quad (57)$ <p>$\sigma_2, \dots, \sigma_6$ are similarly constructed;</p> <p>L = number of OD arcs per year, and</p> <p>n = number of measurements collected during an OD arc;</p> <p>Ψ_{Π} is the second column of Ψ_n from Equ. (18);</p> <p>a_N = the acceleration and</p> <p>$(\Delta_{\psi}^2 + \sigma_{\psi}^2)$ is the mean square error in the thrust direction during the daily inclination corrections.</p>

Table 4 Prediction (Time Updating) Cycle.

4.3.3 NONADAPTIVE FILTER STABILIZATION

The neglected natural long-and short-periodic perturbations as well as the thrust error effects may not be perfectly compensated by Q defined in (57). To prevent filter divergence its structure is modified in order to change the element corrections properly depending on the behaviour of the mean residuals averaged over a data block. The technique applied is derived from the method described in Ref. 26 and outlined in Table 5.

Matrix of the Means of the Residuals in Block k	$\bar{M}_k = \begin{bmatrix} \bar{r}_1 & 0 \\ 0 & \bar{r}_2 \end{bmatrix} \quad (58)$ <p>where $\bar{r}_1 = \frac{1}{n} \sum_{j=1}^n z_j - \bar{f}_j - A_j \bar{E}_{\square 0}$</p>
Matrix of the Means of the Residuals from the m last Blocks	$\bar{M}_k = \frac{1}{m} [\bar{M}_{k-1} m - \bar{M}_{k-m} + \bar{M}_k] \quad (59)$ <p>$k > m$ already assumed</p>
Matrix with Normalizing Factors	$\tilde{M} = \begin{bmatrix} \frac{1}{\bar{r}_1} & 0 \\ 0 & \frac{1}{\bar{r}_2} \end{bmatrix} \quad (60)$ <p>\tilde{r}_{ℓ} = Navigation Angle + Root Mean Square Error = $\sqrt{v_{m\ell}^2 + R_{\ell}}$</p>

Matrix to Modify Element Corrections within Block k	$S_k = I + Q_k = \begin{bmatrix} S_{1k} & 0 \\ 0 & S_{2k} \end{bmatrix} \quad (61)$ <p>where</p> $Q_k = \frac{m-1}{m} Q_{k-1} + \frac{1}{m} Q'_k$
Auxiliary Matrices	$C_k = \bar{M}_k \bar{M}_k = \begin{bmatrix} c_{11} & 0 \\ 0 & c_{22} \end{bmatrix}$ $G_k = \bar{M}_k \bar{M} = \begin{bmatrix} g_{11} & 0 \\ 0 & g_{22} \end{bmatrix} \quad (62)$ $Q'_k = \begin{bmatrix} q'_{11} & 0 \\ 0 & q'_{22} \end{bmatrix}$ <p>where</p> $q'_{\ell\ell} = \begin{cases} g_{\ell\ell} & \text{if } c_{\ell\ell} > 0 \\ 0 & \text{elsewhere} \end{cases}$

Table 5 Modification Matrix S_k for Filter Stabilization.

5. ORBIT CORRECTION

The triaxiality of the geopotential, luni-solar gravitational influence and solar radiation pressure perturb the geostationary orbit with the effect that the satellite will sooner or later exceed the prescribed tolerance window. Hence the orbit has to be corrected once in a while by artificial accelerations produced by the on-board propulsion system. As it was pointed out earlier, an electric propulsion system is preferred for station keeping because of considerable savings of fuel weight. A simple concept of an electric propulsion system is shown in Fig. 1. Assuming three-axis-stabilization, ⁴ ion thrusters can generate thrusts in directions which are inclined against the North-South axis in order to avoid contamination of the solar paddles. Each thruster produces about 10^{-2} N thrust resulting in 10^{-8} km/s² acceleration for a 1000 kg satellite. This is only little more than the acceleration by natural perturbations. The tolerance window of future geostationary missions will be of the order of $\pm 0.1^\circ$ in longitude and latitude. Hence the orbit correction strategy for station keeping must be based on a very low thrust and narrow tolerances of the orbital elements.

5.1 CONSEQUENCES OF LOW THRUST PROPULSION

Conventional station keeping generally applies a "waiting strategy", i.e. corrections are carried out only when the satellite is going to exceed the tolerance window. Such a strategy minimizes the number of necessary manoeuvres which is desirable from the ground operations point of view. The magnitude of the corrections corresponds to the size of the tolerance window.

However, this waiting strategy cannot be applied in case of electric propulsion because the low thrust level limits the magnitude of the orbit corrections attainable by a single thrust. For instance, a pair of thrusters of the aforementioned electric propulsion system produces about 0.3 m/s velocity increment in 6 hours of burning time which should not be exceeded for efficiency reasons. This is far below the 11 m/s required for an inclination correction of 0.2° associated with the aforementioned tolerance window of $\pm 0.1^\circ$ in latitude.

Hence one has to apply a different strategy which provides more frequent corrections of smaller size. In fact, the maximum number of two thrusts daily should be chosen at least for the out-of-plane corrections in order to reduce efficiency losses associated with non-impulsive burns. In contrast to the waiting strategy this may be called a "precaution strategy" because it prevents the orbit from exceeding the range of corrections attainable by a single low thrust manoeuvre.

5.2 CORRECTION CYCLES

The switch times of the thrusters have to be derived from the necessary orbit corrections which in turn depend on the present orbit obtained from orbit determination and on the future variations according to the orbit model used for prediction. Furthermore, the solution should minimize the fuel consumption which is proportional to the total velocity increment. If orbit determination, orbit prediction and thrust execution were free of errors, the switch times of the thrusters could be determined in advance for the entire mission. However, the errors of orbit prediction limit the time period for which a reliable thrust program can be defined. Hence the mission is split in a sequence of correction cycles, each of them short enough to permit a reliable determination of the switch times. The latter are then based on the observed orbit at the start and an orbit correction to be achieved within each cycle.

There is also a lower bound on the cycle duration. If the cycles are very short, the corresponding corrections are quite small and may become of the same order of magnitude as the errors in the determination of the initial orbit. Hence the computed switch times are strongly influenced by orbit determination errors, which introduces a risk of wasting fuel for correcting non-existent effects that are simulated by orbit determination errors. This risk is reduced if a longer cycle duration is selected, with the effect that the orbit correction associated with one cycle is considerably larger than the initial orbit errors.

The optimal cycle duration is very difficult to derive theoretically but can be found by realistic simulation of the entire station keeping process. In the following, a duration of 1 or 2 weeks will be assumed.

The corrections of the orbital elements to be achieved at the end of each correction cycle have to be defined by a long term strategy which minimizes the total velocity increment needed for the entire mission. This requires the solution of an optimization problem involving the long term behaviour of the orbit perturbations. Once the element corrections are obtained for a specific cycle, the switch times are found from the solution of a short term optimization problem.

5.3 LONG TERM STRATEGY

5.3.1 MODEL SIMPLIFICATION

As in the case of orbit determination, the orbit model described by Eq. (12) must be simplified for on-board computation of the corrections but still contain the major perturbation effects. For this reason all short periodic perturbations are neglected here. Their effects can be considered globally by a slight reduction of the tolerance window. Of the remaining perturbations the secular contribution and the major long periodic terms have to be included. Numerical evaluation of the amplitudes of the periodic terms obtained by perturbation theory (23), shows that only the contributions ΔE_0 by solar radiation pressure are significant and have to be compensated by corrections.

Hence the OC strategy is based on an element vector

$$\underline{E}_0(t) = \Phi(t, t_0) \hat{\underline{E}}_0 + \underline{c}(t-t_0) + \frac{1}{2} \ddot{\underline{c}}(t-t_0)^2 + \Delta \underline{E}_0(t) + \Delta \underline{E}_{TH}(t) \quad (63)$$

In Eq. (63) the epoch mean elements $\hat{\underline{E}}_0$ are estimates from orbit determination corrected by Eq. (34). The corrections $\Delta \underline{E}_{TH}$ have to be determined so as to keep $\underline{E}_0(t)$ within prescribed limits which correspond to the given tolerance window.

5.3.2 CORRECTION OF SECULAR EFFECTS

For the compensation of secular perturbations the corrections $\Delta \underline{E}_{TH}$ are derived from the condition that a given target orbit has to be reached by the end of each cycle. If t_A is the start time and T the duration of the cycle, one obtains from Eq. (63) without the periodic terms $\Delta \underline{E}_0(t)$

$$\Delta \underline{E}_{TH} = \underline{E}_{0ST} - \Phi(t_A + T, t_A) \hat{\underline{E}}_0(t_A) - \underline{c}T - \frac{1}{2} \ddot{\underline{c}}T^2 \quad (64)$$

The target elements are defined as

$$\underline{E}_{0ST} = (-c_6/n_E, 0, 0, 0, 0, 0)^T \quad (65)$$

with a non-zero drift rate in order to compensate the secular perturbation rate c_6 of the longitude. In the absence of any errors the estimated initial orbits $\hat{\underline{E}}_0(t_A)$ are identical to the target orbit \underline{E}_{0ST} (if only secular perturbations are considered) and the corrections $\Delta \underline{E}_{TH}$ will be the same for all cycles if T is not changed during the mission. As the fuel consumption is proportional to the sum of correction magnitudes, this is an optimal stra-

$$T_\varphi = \varphi/n_0 \quad (66)$$

where φ is defined by the initial eccentricity vector and the mentioned tangent as shown in Fig. 3, and n_0 is the mean motion of the sun. If T_φ is greater than the cycle duration T , only part of the correction is carried out, observing the requirement that E is always inside the tolerance circle. On the other hand, if $T_\varphi < T$, the point E_1 should be reached by the end of the cycle, where E_1 can be determined from the angle $\varphi_T = n_0 T$ by the condition that $\underline{E}_0 \underline{E}_T$ is parallel to \underline{OE}_1 . The formulae for computing the correction $\Delta \underline{e}_{TH}$ are derived in Ref. 33 and summarized below

$$\Delta \underline{e}_{TH} = \begin{cases} -\delta \underline{e} - y(\underline{e}_0 - \underline{e}_r) & \varphi > \varphi_T \\ \left(\frac{r}{R}-1\right) \begin{pmatrix} \cos \varphi_T & -\sin \varphi_T \\ \sin \varphi_T & \cos \varphi_T \end{pmatrix} (\underline{e}_0 - \underline{e}_c) - \underline{e}_c, & \varphi < \varphi_T, \end{cases} \quad (67)$$

where

$$\left. \begin{aligned} \underline{e}_r &= \frac{r}{|\underline{e}_c|^2} \begin{pmatrix} r-R & \sqrt{|\underline{e}_c|^2 - (R-r)^2} \\ -\sqrt{|\underline{e}_c|^2 - (R-r)^2} & r-R \end{pmatrix} \underline{e}_c \\ \varphi &= \arccos \left(\frac{\underline{e}_r (\underline{e}_0 - \underline{e}_c)}{rR} \right), \quad \varphi_T = n_0 T \\ \delta \underline{e} &= \begin{pmatrix} 1-\cos \varphi_T & \sin \varphi_T \\ -\sin \varphi_T & 1-\cos \varphi_T \end{pmatrix} (\underline{e}_0 - \underline{e}_c) \\ y &= \frac{\delta \underline{e} \cdot \underline{e}_r}{(\underline{e}_r - \underline{e}_0) \underline{e}_r} \end{aligned} \right\} \quad (68)$$

The vectors \underline{e}_0 and \underline{e}_c are the initial eccentricity \underline{OE}_0 and the position vector \underline{OE}_c of the centre of the drift circle.

In Case II (Fig. 4) the optimal strategy is to shift the drift circle completely into the tolerance circle, by corrections along the connection line between the two centres, observing the condition $|\underline{e}| < r$. The resulting expression for each cycle is

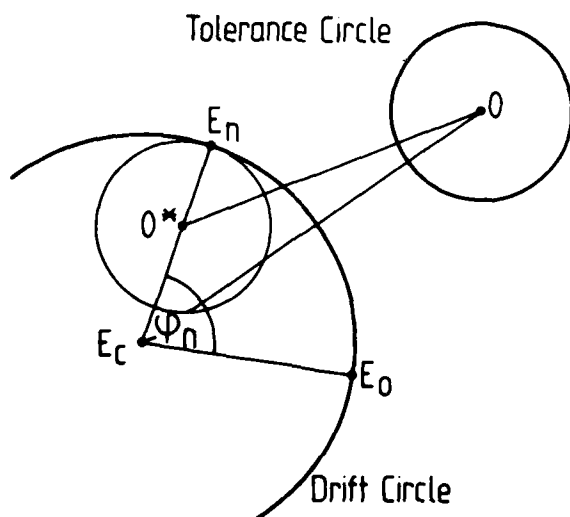


Fig. 5 Optimal correction in Case III. The total correction is a relative shift of the circles such that the tolerance circle touches the drift circle from inside in a point E_n which is reached by the eccentricity after n cycles. The number n is to be chosen as small as possible, observing that the magnitude of the correction per cycle is limited because of the low thrust.

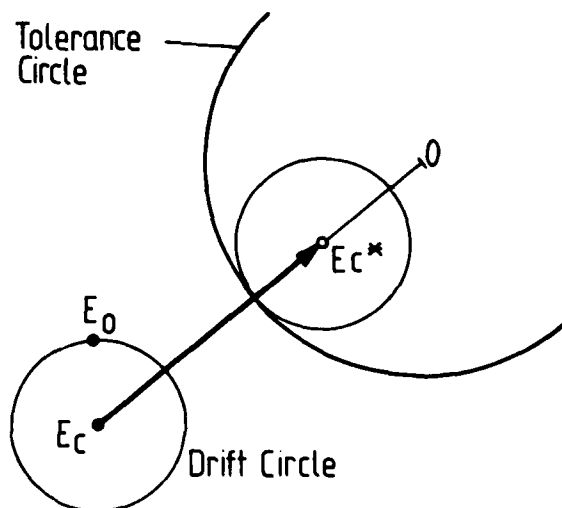


Fig. 6 Optimal strategy for frequent corrections in Case IV. The drift circle should be moved into the tolerance circle as fast as possible, which results in a total correction $\underline{E}_c \underline{E}_c^*$.

$$\Delta e_{TH} = \begin{cases} -e_c [1 - (R \cos \psi + \sqrt{r^2 - R^2 \sin^2 \psi}) / |e_c|] & \text{if } |e_c| > r - R \\ 0 & \text{otherwise} \end{cases} \quad (69)$$

where

$$\left. \begin{aligned} \psi &= \psi_0 + \delta\psi \\ \psi_0 &= \arctan \frac{\sqrt{4r^2 |e_c|^2 - (R^2 - r^2 - |e_c|^2)}}{R^2 - r^2 + |e_c|^2} \\ \delta\psi &= \frac{\pi - \psi_0}{\pi - \varphi_0} \varphi_T \\ \varphi_0 &= \arccos \frac{e_c (e_c - e_0)}{|e_c| R} \\ \varphi_T &= Tn_0 \end{aligned} \right\} \quad (70)$$

In Case III the eccentricity is initially outside the tolerance circle (Fig. 5), and it should be moved as fast as possible to a position E_n on that circle such that fuel optimal corrections are possible afterwards. While the eccentricity completes the angle φ_n from E_0 to E_n on the drift circle, the two circles should approach each other such that the tolerance circle touches the drift circle from inside in the point E_n . Then the correction vector Δe_{TH} for a single cycle is obtained from the relation $\vec{O}^* \vec{O} = \vec{O}^* \vec{E}_c + \vec{E}_c \vec{O}$ or, using the previous definitions

$$n \Delta e_{TH} = -e_c - \frac{R-r}{R} \begin{pmatrix} \cos \varphi_n & -\sin \varphi_n \\ \sin \varphi_n & \cos \varphi_n \end{pmatrix} (e_0 - e_c), \quad (71)$$

$$\varphi_n = n \varphi_T, \quad (72)$$

where n is the number of cycles necessary to achieve the total correction. If Δe_{max} is the largest possible correction per cycle this number is obtained by iteration from the inequality

$$n \Delta e_{max} \geq |n \Delta e_{TH}| \geq (n-1) e_{max}. \quad (73)$$

In Case IV the drift circle should be shifted into the tolerance circle as fast as possible, i.e., in a direction opposite to $e_c = \vec{OE}_0$ (Fig. 6). If n cycles are necessary, the shift Δe_{TH} is obtained from

$$n \Delta e_{TH} = \vec{E}_c \vec{E}_c^* = -e_c + \frac{e_c}{|e_c|} (r-R), \quad (74)$$

where n is again defined by (73).

5.4 CALCULATION OF SWITCH TIMES

Once the corrections of the orbital elements for a specific correction cycle have been found by the long term strategy, the switch times for each thruster can be obtained by an inverse application of Eq. (17) to (21) which describe the orbit changes as a function of the switch times.

The problem is reduced to the solution of Eq. (17) for the L_s and ΔL_s where the left hand side is replaced by the known $\Delta e_{TH}(T, \underline{a}_s)$, with the additional requirement that the fuel is minimized, i.e.

$$\sum_{k=1}^K |a_k| \Delta L_k = \text{Min}. \quad (75)$$

Evidently this problem

- is non-linear,
- yields solutions only if $K \geq 3$,

- is expected to yield multiple solutions because the unknowns appear in trigonometric functions,
- may be split in two parts, one containing the 4th and 5th, the other containing the remaining rows and columns of the Matrix Ψ_K ,
- is further simplified because the propulsion system does not generate radial components, hence $a_{Rk} = 0$.

Splitting the matrix Ψ_K in two parts allows the well known separation of North-South and East-West station keeping if the propulsion system is properly designed to produce acceleration vectors a_k with only one component different from zero. The electric propulsion system mentioned here fulfills this requirement nominally. It should be noted, however, that any deviations due to inherent thrust execution errors introduce a coupling of North-South and East-West correction which deteriorates the station keeping accuracy.

5.4.1 NORTH/SOUTH CORRECTIONS

In order to achieve prescribed corrections ($\Delta p, \Delta q$) to the geostationary elements p and q , the pairs (T_1, T_2) or (T_3, T_4) of thrusters (Fig. 1) have to be operated. The switch times are obtained from the solution of the following optimization problem with respect to the unknowns L_k and ΔL_k :

$$\sum_{k=1}^{K_N} a_{Nk} \sin L_k \sin \frac{1}{2} \Delta L_k = V_{nE} \Delta p, \quad \sum_{k=1}^{K_N} a_{Nk} \cos L_k \sin \frac{1}{2} \Delta L_k = V_{nE} \Delta q, \quad (76)$$

$$\sum_{k=1}^{K_N} |a_{Nk}| \Delta L_k = n_E \Delta V_N = \text{Min}. \quad (77)$$

The constraints (76) are obtained from Eqs. (17) and the cost function (77) to be minimized is proportional to the velocity increment ΔV_N due to the N/S-corrections. The acceleration components are of equal magnitude

$$a_{Nk} = \pm a_N, \quad a_N > 0, \quad k = 1, \dots, K_N. \quad (78)$$

For a given number of thrusts K_N the optimal solution is

$$\left. \begin{aligned} L_k &= L_N + k\pi \\ \Delta L_k &= 2 \arcsin \frac{V_{nE}}{K_N a_N} \sqrt{\Delta p^2 + \Delta q^2} \end{aligned} \right\} \quad k = 1, 2, \dots, K_N, \quad (79)$$

where

$$\sin L_N = \frac{+\Delta p}{\sqrt{\Delta p^2 + \Delta q^2}}, \quad \cos L_N = \frac{+\Delta q}{\sqrt{\Delta p^2 + \Delta q^2}}. \quad (80)$$

The velocity increment

$$V_N = \frac{2K_N a_N}{n_E} \arcsin \frac{V_{nE}}{K_N a_N} \sqrt{\Delta p^2 + \Delta q^2} \quad (81)$$

decreases with increasing K_N . Hence the number of thrusts should be chosen as large as possible under the constraint that all thrusts must happen within the correction cycle, i.e., the inequalities

$$L_A \leq L_1 - \frac{1}{2} \Delta L_1 \leq L_A + \pi, \quad L_E \geq L_{K_N} + \frac{1}{2} \Delta L_{K_N} \geq L_E - \pi \quad (82)$$

must be satisfied, where L_A and L_E are the station longitude at the start and at the end of the cycle. The conditions (82) may be used to determine K_N . As ΔL_1 and ΔL_{K_N} depend on K_N according to Eqs. (79), an iteration procedure is indicated.

Once the number K_N of thrusts has been found, the unknowns L_k and ΔL_k , as well as the velocity increment ΔV_N can be computed from Eqs. (79) - (81). The sign in Eq. (80) has to be chosen so as to satisfy the condition (82) for the first thrust. The switch times are obtained as

$$\left. \begin{aligned} t_{\kappa 1} &= t_A + \frac{1}{n_E} (L_{\kappa} - \frac{1}{2} \Delta L_{\kappa} - L_A) \\ t_{\kappa 2} &= t_A + \frac{1}{n_E} (L_{\kappa} + \frac{1}{2} \Delta L_{\kappa} - L_A) \end{aligned} \right\} \kappa = 1, 2, \dots, K_N, \quad (83)$$

where t_A is the cycle starting time.

5.4.2 EAST/WEST CORRECTIONS

The calculation of the switch times for E/W thrusts requires the solution of the system

$$\begin{aligned} \sum_{\kappa=1}^{K_T} a_{T\kappa} \Delta L_{\kappa} &= -\frac{1}{3} V n_E \Delta D, & \sum_{\kappa=1}^{K_T} a_{T\kappa} \sin L_{\kappa} \sin \frac{1}{2} \Delta L_{\kappa} &= \frac{1}{4} V n_E \Delta h, \\ \sum_{\kappa=1}^{K_T} a_{T\kappa} \cos L_{\kappa} \sin \frac{1}{2} \Delta L_{\kappa} &= \frac{1}{4} V n_E \Delta \ell, & \sum_{\kappa=1}^{K_T} a_{T\kappa} (L_E - L_{\kappa}) \Delta L_{\kappa} &= -\frac{1}{3} V n_E \Delta \lambda \end{aligned} \quad (84)$$

with respect to the L_{κ} and ΔL_{κ} under the condition that the velocity increment ΔV_T due to E/W-corrections is minimized:

$$\sum_{\kappa=1}^{K_T} |a_{T\kappa}| \Delta L_{\kappa} = n_E \Delta V_T = \text{Min}. \quad (85)$$

The constraints (84) are obtained from Eqs. (17) with $a_{R\kappa} = 0$ because the propulsion system produces no radial thrusts. For the tangential components one has

$$a_{T\kappa} = \pm a_T, \quad a_T > 0, \quad \kappa = 1, \dots, K_T. \quad (86)$$

Solutions of the system (84) exist only if $K_T \geq 2$. As in the North-South case, the number K_T of thrusts should be taken as large as possible.

However, this leads to a complex problem which does not admit a simple analytical solution. Considering the fact that East-West station keeping requires only a small fraction (~ 5%) of the velocity increment needed for the North-South component, one concludes that the thrust arcs ΔL_{κ} will be quite short even for small K_T , which justifies the following simplifications without a significant loss of performance:

$$K_T = 3 \quad (87)$$

$$\sin \frac{1}{2} \Delta L_{\kappa} \approx \frac{1}{2} \Delta L_{\kappa}, \quad \kappa = 1, 2, 3. \quad (88)$$

Although $K_T = 2$ would be sufficient to obtain solutions L_{κ} and ΔL_{κ} satisfying Eqs. (84), the existence of a solution cannot be guaranteed. Furthermore, there would be no freedom for fuel minimization. For instance, if the eccentricity correction ($\Delta \ell, \Delta h$) is dominant, fuel minimization is achieved only if the eccentricity vector changes due to the thrusts are in the same direction, which requires that

$$L_{\kappa} = L_T + m_{\kappa} \pi, \quad m_{\kappa} = \text{integer number}. \quad (89)$$

Eq. (89) can, in general, not be satisfied if $K_T = 2$. On the other hand, if $K_T = 3$, the enlarged number of unknowns $L_{\kappa}, \Delta L_{\kappa}$ allows to introduce the condition (89) *a priori* in addition to (84).

The extended system yields a 3-parameter family of solutions which can be examined with respect to their velocity increments. The switch times are then computed from the solution with the smallest velocity increment.

Using normalized velocity increments

$$v_{\kappa} = \frac{a_{T\kappa}}{V n_E} \Delta L_{\kappa}, \quad \kappa = 1, 2, 3 \quad (90)$$

the equations

$$\sin L_T = \frac{\Delta h}{\sqrt{\Delta h^2 + \Delta \ell^2}}, \quad \cos L_T = \frac{\Delta \ell}{\sqrt{\Delta h^2 + \Delta \ell^2}} \quad (91)$$

and the following linear system of equations can be derived from Eqs. (84) to (89):

$$\begin{pmatrix} 1 & 1 & 1 \\ (-1)^{m_1} & (-1)^{m_2} & (-1)^{m_3} \\ m_1 & m_2 & m_3 \end{pmatrix} \begin{pmatrix} v_1 \\ v_2 \\ v_3 \end{pmatrix} = \begin{pmatrix} -\frac{1}{3} \Delta D \\ \frac{1}{2} \sqrt{\Delta h^2 - \Delta \ell^2} \\ \frac{1}{3\pi} [\Delta \lambda - (L_E - L_T) \Delta D] \end{pmatrix} \quad (92)$$

Eq. (92) yields a 3-parameter family of solutions for all combinations m_1, m_2, m_3 associated with a non-vanishing determinant of the matrix on the left side. This condition is equivalent to

$$\left| \sum_{k=1}^3 (-1)^{m_k} \right| < 3. \quad (93)$$

The 3-parameter family of solutions is further restricted to values of L_k within the longitude interval imposed by the limits of the correction cycle. The condition

$$\frac{1}{\pi} (L_A + \frac{1}{2} \Delta L_1 - L_T) < m_1 < m_2 < m_3 < \frac{1}{\pi} (L_E - \frac{1}{2} \Delta L_3 - L_T) \quad (94)$$

admits only thrusts during the correction cycle and eliminates the possibility that the same thrusts occur twice with interchanged subscripts.

After rejecting all combinations of the m_k which do not satisfy the conditions (93) and (94), the solutions v_k and the associated velocity increments

$$\Delta V_T = V \sum_{k=1}^3 |v_k| \quad (95)$$

are computed and used to select the fuel optimal solution.

If several solutions need the same velocity increment, additional criteria have to be applied. For instance, it may be advantageous to carry out the correction manoeuvres in the early part of the cycle, which means that among fuel optimal solutions the one with the smallest m_k should be preferred.

Once the m_k and v_k are known, the switch times can easily be computed by (89) - (91) and (83).

6. STATION KEEPING SIMULATION

6.1 SIMULATION PROGRAM AND INPUT DATA

The orbit determination and orbit correction algorithms were tested by a closed loop simulation of the satellite motion and measurement data on an Amdahl 470 V/6. The satellite motion was simulated by means of the model described in section 3 without simplifications, considering all secular and periodic perturbations with amplitudes greater than 10^{-5} . The nominal thrusts were superimposed by errors. Systematic thrust execution errors Δa for the magnitude and $\Delta \psi$, $\Delta \phi$ for the direction, constant during the whole test period, and errors δa , $\delta \psi$, $\delta \phi$ constant during one orbit determination arc, but random for different arcs, were assumed. The simulated navigational data were corrupted by systematic sensor misalignment errors and random noise. The true motion and measurements are computed in double precision whereas all computations relevant to the station keeping systems were performed in single precision. The investigations cover a period of 384 days, identical to 369 OD arcs, each arc 25h long. The sampling rate was 1 pair of navigational angles per hour (corresponding to a step size of 15° in orbit longitude). By the arc length of 25h instead of 24h a small asymmetry in the measurement distribution was intentionally introduced. The orbit model for the OD and OC was strongly simplified as indicated in the preceding chapters. Additionally, small biases were added to the coefficients for the secular perturbations to be used in the OD process.

The orbit correction algorithm was based on a 10 day correction cycle duration. It includes emergency updates of the switch times if one of the limits: 0.0004 for the eccentricity, ± 0.0046 for the off-station mean longitude and 0.91 for the inclination is exceeded during a cycle.

Simulated Period: 1983/1/1-1984/1/20		Elements of Matrix Q:	
Satellite Data		$Q_{11} = 1.5157 \cdot 10^{-13},$ $Q_{22} = 1.3465 \cdot 10^{-10},$ $Q_{33} = 0.6679 \cdot 10^{-10},$ $Q_{44} = 0.9888 \cdot 10^{-10},$ $Q_{55} = 1.8970 \cdot 10^{-10},$ $Q_{66} = 7.4381 \cdot 10^{-10},$ $Q_{ij} = 0; i \neq j;$	
Cross Sectional Area F_x	= 44 m ² ,	Estimated Parameters: D, h, ℓ , p, q, λ_0 .	
Satellite Mass M	= 1058 kg,		
Reflectivity Coefficient K	= 1.2;		
Orbit Data (Initial Values):		Orbit Correction	
D	= $-7.67 \cdot 10^{-5},$	Correction Cycle Time T = 10 days.	
h	= $-2.29 \cdot 10^{-4},$	Electric Propulsion Thrust Level: 10 mN;	
ℓ	= $4.89 \cdot 10^{-5},$	Single Thrust Duration ≤ 6 hours;	
p	= $2.64 \cdot 10^{-5},$	Maximum Number of North-South Thrusts,	
q	= $1.70 \cdot 10^{-5},$	3 Tangential Thrusts per Cycle;	
λ_0	= $6.86 \cdot 10^{-5},$	Eccentricity Tolerance Circle r = 0.00025.	
L_0	= 190W		
Orbit Determination:			
Measurement of Navigation			
Angles $\alpha, \beta,$			
Orbit Determination Arc,			
Block Length DT = 25h,			
Sampling Time dt = 1h.			

Table 7 Input Data for the Autonomous Station Keeping Simulation.

Measurement Bias		Measurement Noise		Systematic Thrust Error			Random Thrust Error			Annual Velocity Increment (m/s)		Violations in X % of the time
m ₁	m ₂	$\sqrt{R_1}$	$\sqrt{R_2}$	$\Delta\alpha$	$\Delta\psi$	$\Delta\phi$	$\sigma_{\Delta\alpha}$	$\sigma_{\Delta\psi}$	$\sigma_{\Delta\phi}$	N/S	E/W	
0°010	0°005	0°035	0°010	3%	3°	3°	0%	0°	0°			100
				1%	1°	1°	1%	1°	1°	66.5	8.6	3
				1%	0°5	0°5	1%	1°	1°	66.2	6.7	1.5
				0%	0°	0°	3%	3°	3°	67.2	8.8	0
0°015	0°010	0°035	0°010		0°25	0°25	1%	1°	1°	66.3	4.7	0
0°020					0°30	0°30				66.5	4.8	0.3
				1%	0°25	0°25				66.5	6.7	0.3
					0°20	0°20				66.5	6.1	0
0°035					0°10	0°20				65.7	4.7	0.3
		0%	0°00	0°00	66.7	4.7	0.3					

Table 8 Station Keeping Simulation for Various Measurement Biases m_1 and N/S Thrust Direction Errors $\Delta\psi$, $\Delta\phi$ in yaw and roll.

The simulation was started with the input data given in Table 7 and carried out for various combinations of errors as shown in Table 8 in order to investigate their influence on the station keeping performance.

6.2 DISCUSSION OF RESULTS

It turns out that measurement noise (R_1, R_2) and random errors ($\sigma_{\Delta\alpha}, \sigma_{\Delta\psi}, \sigma_{\Delta\phi}$) of thrust magnitude and direction are of minor importance for the station keeping process. This is also true for systematic errors m_2 of the Earth/Satellite/Polaris angle β and the thrust magnitude bias $\Delta\alpha$. On the other hand, the key roles are played by the systematic measurement error m_1 of the Earth/Satellite/Sun angle α caused by sensor misalignment and the thrust misalignment $\Delta\psi, \Delta\phi$ during the N/S corrections. A systematic angular error $\Delta\psi$ around the yaw axis entails an undesired tangential acceleration component which strongly influences the E/W motion. The effects of various combinations of m_1 and $\Delta\psi$ are shown in Table 8.

In columns 11 and 12 the annual velocity increments for N/S and E/W corrections are listed. These numbers are by 40% larger than the ideal values because the thrusters are inclined by 45° against the optimal thrust directions in order to avoid solar panel contamination (Fig. 1).

The last column shows the percentage of violations of the E/W-tolerance window. The comparison of line 1 and 4 as well as Fig. 7 and Fig. 8 show that the (unestimated) errors $\Delta\psi, \Delta\phi$, constant during all N/S-corrections of the station keeping period, are critical, whereas the corresponding errors $\delta\psi, \delta\phi$, random from arc to arc, are not serious. For $\Delta\psi = \Delta\phi = 3^\circ$ the satellite will leave the tolerance window rather quickly, for $\Delta\psi = \Delta\phi = 1^\circ$ violations

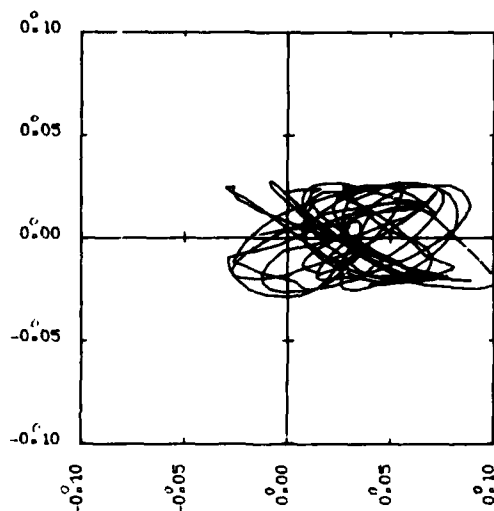


Fig. 9 True Position within Tolerance Window for Controlled Satellite
- $m_1 = 0.035^\circ$ Bias on Earth/Satellite/Sun-Angles.

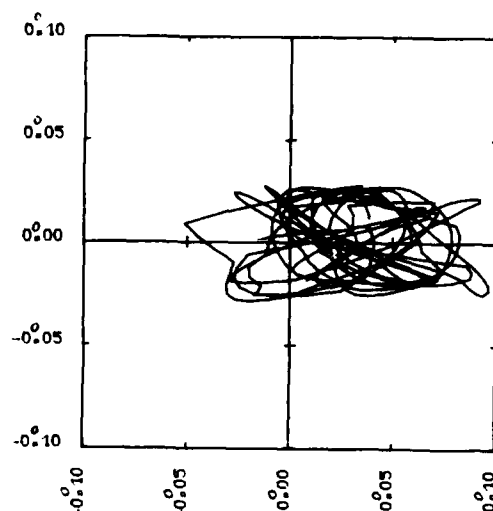


Fig. 10 True Position within Tolerance Window for Controlled Satellite
Assuming $m_1 = 0.02^\circ$ and $\Delta a = 1\%$
 $\Delta\psi, \Delta\phi = 0.2^\circ$ as Residual Errors.

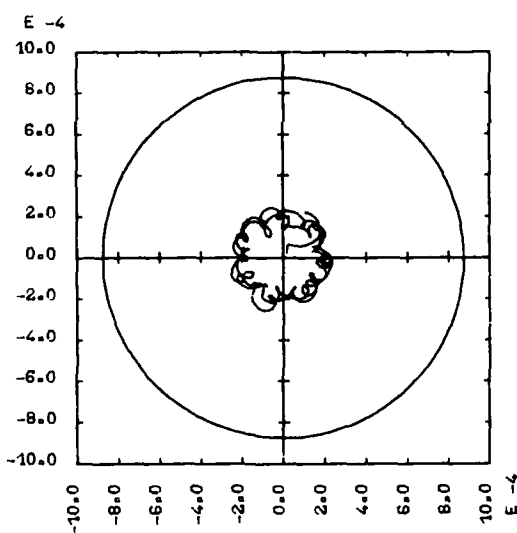


Fig. 11 Inclination Vector (p, q) for Controlled Satellite.

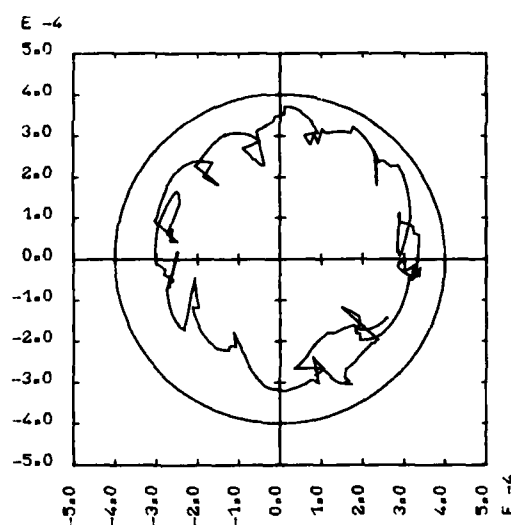


Fig. 12 Eccentricity Vector (l, h) for Controlled Satellite.

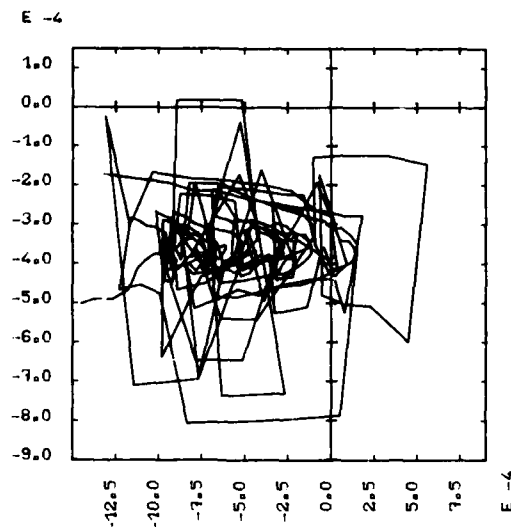


Fig. 13 Driftrate (D) Versus Epoch Mean Longitude (λ_0) for Controlled Satellite.

7. IMPACT ON GROUND SYSTEMS

Station keeping within a narrow tolerance window for a future geostationary satellite with large solar panels will be troublesome. Even assuming a geostationary position favourable wrt the geopotential, the drift rate and the - at least - partial correction of the orbit eccentricity requires in the average 1 correction per week preceded by 1±2 days tracking and orbit determination period. Future geostationary satellites will most likely be equipped with an electric propulsion system for the inclination corrections. Due to its low thrust level, at least every 2 days (maybe each day) a N/S-station keeping manoeuvre has to be performed. Again orbit determination has to be done periodically (every 10 days) to design and schedule the manoeuvre. This workload burdens the ground station during the whole 7 to 10 years satellite life time. At least to some degree these manoeuvres must be automatized. Substantial reductions in the requirements of repetitive tracking, orbit determination and in the workload associated with frequent orbit corrections can be obtained with an on-board autonomous station keeping system with the consequence of lower operating costs on ground.

On the other hand, it is obvious that ground stations will still be needed even in case of fully autonomous satellites.

Assuming an autonomous system as described in the preceding chapter III to IV the following tasks only would remain with the ground station:

- i) during the first few months:
 - Conventional station keeping by ground station tracking, orbit determination and manoeuvre execution via telecommand;
 - Calibration of on-board sensors and sensor configuration;
 - Calibration of thrusters and thruster configuration;
- ii) Within particular time intervals:
 - Updating of the numerical values of the orbit model parameters every 2 years by on-board computer reprogramming;
 - Clock synchronization in appropriate time intervals according to guaranteed clock accuracy;
- iii) Periodic monitoring tasks and emergency duties:

this may involve orbit determination based on telemetry sensor data, orbit correction- and manoeuvre parameter computation on ground and manoeuvre execution commands by radio link to override the commands of the on-board system in order to reposition the satellite in case of attitude loss or unwanted violation of the tolerance window.

8. CONCLUSIONS

A simulation of a one year period of controlled satellite motion indicated that accuracies of about 0.1 are feasible for the described autonomous station keeping system. Most of the assumed hardware components are presently available and in use for satellite attitude control, the others are in an advanced state of development.

The simulation revealed two critical error sources, one being a residual bias in the Earth-satellite-sun angle caused by sensor misalignment, the other being a systematic North-South thrust axis misalignment error. The former cannot be observed on-board and introduces a longitude bias $\Delta\lambda$ into the station keeping process. The only way to eliminate this error is by calibration with ground observations. The latter introduces an uncontrolled bias in the satellite drift rate, entailing violations of the admissible longitude tolerance. This error should therefore be estimated to an accuracy better than ± 0.2 and taken in account in the orbit correction algorithm.

Since the orbit determination - and correction algorithms were tested in single precision, no serious difficulties are expected to arise from limited word length of on-board processors. In case of numerical problems on the on-board computer the OD algorithms can be modified using square root-free techniques similar to those which achieve numerical stability for the Kalman Filter.

During the initial station keeping phase, the necessary in-flight sensor- and thruster-calibrations have to be performed by qualified personnel of the ground station. Exchange of a few program modules for the orbit model every 2 years are periodic ground station tasks, and possibly clock synchronization activities every 4 to 8 weeks. Finally, the ground station must monitor the spacecraft periodically and has emergency duties.

Further investigations of the autonomous station keeping system will include on-board processor implementation, laboratory demonstrations as well as weight-, power-, reliability- and emergency-considerations.

9. ACKNOWLEDGEMENTS

The authors wish to acknowledge the significant contributions of Dr. F. Hechler, on the sensor error effects and the optimization of the long term correction strategy. The work of Ms. S. Angermeier for producing the computer graphs and the untiring efforts of Mrs. Ch. Schmitz in typing the manuscript are gratefully appreciated.

10. REFERENCES

- [1] Gansler, J.S. "Space Navigation", TNB General Precision Aerospace 8, 1st Quarter 1965.
- [2] Braga-Illa, A.A. "The Future of Self-Contained Control of Synchronous Orbits", AIAA paper 70.479. AIAA 3rd Communication Satellite Systems Conference, Los Angeles, California, April 6-8, 1970.
- [3] Gura, I.A. et al "Configuration Studies for Autonomous Satellite Navigation", Aerospace Corporation, TR-0059 (67 84)-1, May 1971.
- [4] Brogan, W.L. and LeMay, J.L. "Autonomous Satellite Navigation - An Historical Summary and Current Status", Joint Automatic Control Conference, 14th, Columbus, Ohio, June 20-22, 1973.
- [5] Lowrie, J.W. "Autonomous Navigation Systems Technology Assessment" 79-0056, 17th Aerospace Science Meeting, New Orleans, La., Jan 15-17, 1979.
- [6] Automatic Orbit Control of the Experimental Satellite LES-6, M.I.T. Tech. Ref. 469, 10th July 1969.
- [7] Srivastava, S. "Flight Results of LES-8 Autonomous Station Keeping System". Lincoln Lab., Mass., Inst. of Techn., Lexington TN-1978-8.
- [8] Greenleaf, G.L. et al "On-Board Spacecraft Navigation Techniques", VII. IFAC Symposium on Automatic Control in Space, Rottach-Egern (FRG), May 17-21, 1976, Volume 2.
- [9] Paulson, D.C. "Autonomous Navigation Technology" Phase 1A; Final Report, March 1975.
- [10] Fuchs, A.J. et al "Orbit and Attitude State Recoveries from Landmark Data", AAS/AIAA Astrodynamics Specialist Conference, Nassau, Bahamas, July 28-30, 1975, Paper No. AAS75-058.
- [11] Jordan, J.F. and Fuchs, A.J. "Autonomy in Space Navigation", Astronautics & Aeronautics, May 1979.
- [12] Fuch, A.J. et al "Autonomous Satellite Navigation with the Global Positioning System", AAS/AIAA Astrodynamics Conference, Jackson Hole, Wy, Sept. 77.

- [13] Kruczynski, L. "Global Positioning System Navigation Algorithms", Applied Mechanics Research Lab., Dept. of Aerospace Engineering and Engineering Mechanics, University of Texas at Austin, Rep. No. AMRL 1078, May 1978.
- [14] Dunham, J.B. and Wooden, W.H. "Simulation of Autonomous Satellite Navigation With the Global Positioning System", AIAA Paper 78-1429, Palo Alto, Calif., Aug. 1978.
- [15] Tapley, B.D. "A Study of Autonomous Satellite Navigation Methods Using the Global Positioning Satellite System", Final Report, NASA-CR-162635, April 1980.
- [16] Vendy, . and Plummer, D. "Autonomous Station Keeping of Geostationary Satellites", in "Automatic Control in Space", Proceedings of the 8th Symposium, Oxford, England, July 2-6, 1979.
- [17] Bassner, H. et al "Development Status and Application of the Electric Propulsion System RIT-10 used for Station Keeping". XXXth IAF Congress, Munich, 16-23 Sept. 1979, Paper 79-07.
- [18] Selke, W. "Einsatz von elektrischen Steuertriebwerken in Nachrichtensatelliten", Raumfahrtforschung Heft 6, 1973.
- [19] Balsam, R. and Anzel, B. "A simplified approach for correction of perturbation on a stationary orbit", T. of Spacecraft 6, No. 7, 805-811, 1969.
- [20] Metzger, R. "Stationkeeping for Symphonie", XXVth IAF Congress, Amsterdam, 74-019, 1974.
- [21] Martinez, T.T. "Optimal orbit control for station keeping within the multi-satellite support system (MSSS)", Proc. AOCSS Conference, Noordwijk, ESA-SP-128, 1977.
- [22] Eckstein, M. "Positionshaltung Geostationärer Satelliten mit elektrischen Triebwerken", DGLR, Walter Hohmann Symposium Raumflugmechanik, Köln, 12. und 13. März 1980, DGLR 80-009.
- [23] Eckstein, M.C. "Ein Verfahren zur Herstellung analytischer Bahnmodelle für geostationäre Satelliten", DFVLR-FB 79-16, 1979.
- [24] Eckstein, M.C. "Optimal Station Keeping by Electric Propulsion with Thrust Operation Constraints", Cel. Mech. 21, p. 129-147, 1980.
- [25] Brouwer, D. and Clemence, G.M. "Methods of Celestial Mechanics", p. 301, Academic Press, New York and London, 1961.
- [26] Torroglosa, V. "Filtering Theory Applied to Orbit Determination", Goddard Space Flight Center, Report S-582-73-379, December 1973.
- [27] Kenneth, A.M. "Dynamical Model Compensation for Near-Earth Satellite Orbit Determination", AIAA Journal, Vol. 13, No. 3, March 1975.
- [28] Jazwinski, A.H. and Hipkins, C. "J-Adaptive Estimation with Estimated Noise Statistics", Goddard Space Flight Center, Contr. No. NAS 5-22144, June 1974.
- [29] Tapley, B.C. and Peters, G. "A Triangular Covariance Factorization for Sequential Filtering Algorithms", AIAA/AAS Astrodynamics Conference, Palo Alto, California, August 1978.
- [30] Thornton, C.L. "Triangular Covariance Factorizations for Kalman Filtering", Tech. Memo 33-798, Jet Propulsion Laboratory, Pasadena, California, Oct. 1976.
- [31] Bierman, G.J. and Thornton, C.L. "Numerical Comparison of Discrete Kalman Filter Algorithms: Orbit Determination Case Study", Automatica, February 1977.
- [32] Fadeeva, V.N. "Computational Methods of Linear Algebra", Dover Publ., New York, N.Y., pp. 81-84.
- [33] Eckstein, M. and Hechler, F. "Station Acquisition and Station Keeping with Low-Thrust Systems", ESA International Symposium Spacecraft Flight Dynamics, Paper 5.4, May 1981.

DIGITAL ATTITUDE AND ORBIT CONTROL ELECTRONICS FOR LONG-LIFE COMMUNICATION SATELLITES

by

Michael Wlaka

Dornier System GmbH
7990 Friedrichshafen, FRG

SUMMARY

For the new generation of large three-axes stabilized communication satellites now under design, digital data handling electronics is being applied in different areas. The requirement for performing complicated control algorithms for attitude and orbit control (AOC) and the desire to use standardized on-board electronics has led to a modular, microprocessor based data handling system being developed. It consists of a 16 bit-processor, a memory block and various input/output modules.

Special features of the system with respect to space applications are low weight, small volume and low power consumption. This is achieved by using multilayer boards and flat-pack CMOS chips.

The stringent reliability requirements for long-life satellites has led to a high degree of redundancy and cross-strapping capability within the system.

LIST OF ABBREVIATIONS

ADC: analog to digital converter	MSI: medium scale integration
APM: antenna pointing mechanism	MW: momentum wheel
AOCS: attitude and orbit control system	PROM: programmable read only memory
BAPTA: bearing and power transfer assembly	RAM: random access memory
CMOS: complementary metal oxid semiconductor	SSI: small scale integration
DMA: direct memory access	TC: telecommand
DW: data-way	TM: telemetry
MPX: multiplexer	UPS: unified propulsion system
	WD: watch dog

1. INTRODUCTION

Spacecraft and payloads have become progressively larger and more sophisticated. This tendency has been accompanied by two other trends towards higher requirements for the subsystem performance and the standardization of subsystem components. Many of the enhanced subsystem or payload performance requirements result directly or indirectly in higher requirements for attitude and orbit accuracy. In spite of larger spacecrafts and higher efficiency minimum cost per transmission channel will be the primary design goal.

Significant examples for subsystem or payload requirements which induce also requirements for attitude and orbit control are:

- o more precise antenna pointing and stationkeeping due to limitation of coverage area with max. EIRP.
- o larger solar arrays to fulfill higher power demands, these larger arrays cause dynamic oscillations with very low eigenfrequencies.
- o more effective propulsion systems like electrothermal hydrazine, bipropellant propulsion or ion thrust systems, to save mass reduction of the performance capability.

All these system requirements have a large impact on the design of attitude and orbit control electronics. Higher pointing accuracy demands a higher accuracy for the control algorithm computation. The use of new equipment as gyro packages, radio frequency sensor, antenna pointing mechanism etc. introduces new more sophisticated operation modes.

In particular flexibility for adaptation of future trends must be guaranteed in order to ensure compatibility with new equipment to be introduced as soon as it has reached the required reliability and qualification level.

The control electronics concept described hereafter is based on this design philosophy, making use of space qualified equipment.

2. SYSTEM CONCEPT

Many ways have been sought to simplify the method of interconnecting the different sensors and actuators with the control electronics. The application of digital technology provides several improvements to the system design and for the capability of on-board operations.

The potential advantages of digital techniques in attitude and orbit control system for operational use are:

- o adequate precision and range of computing power including sophisticated algorithms
- o more efficient use of modern control theory as there are optimization, estimation and adaptive control
- o techniques for Kalman filtering for more accurate attitude and rate determination
- o stability of the encoded data
- o wider range and automation of mode selection
- o multiplexing of data channels

The modular on-board data processing system for attitude and orbit control is based on a 16-bit concept. It consists of a central data processor which performs arithmetic and logical operations and controls the data transfer via a 16-bit parallel and bidirectional data bus to the different peripheral modules. The essential characteristics of the data processor, MUDAS DP 430-R are given in Tab. 1. (MUDAS = Modular Universal Data and Acquisition and Processing System).

Technology	CMOS (SSI, MSI)
Organization	16 bit word length
Hardware register	16 x 16 bit
Instruction set	70 instructions
Execution time (clock 1 MHz)	Branch 4,5 - 6 μ s Add/Sub 6 μ s I/O transfer 7,5 μ s Multiply 21 μ s Divide 37,5 μ s
Program interrupt	4 flags, 1 external condition 3 external alarm request lines
Data transfer rate	module transfer 130 K words/sec. Direct Memory Access 300 K words/sec.
Memory (RAM, PROM)	64 K addressable
Power consumption (processor)	0,8 W

Tab. 1.: Essential Characteristics of the MUDAS-Data Processor DP 430-R.

Most of the system components like sensors, actuators, or telemetry and telecommand units are adapted to the data bus by standard modules. The interface to sun sensors may be realized by digital inputs or analog to digital converters respectively. Gyro outputs will require a counter module or a digital input module. For time correlation and proper sequencing a real time clock will be required. To operate actuators like thrusters, momentum wheels and drive mechanism for solar generators or antenna pointing, digital outputs, digital to analog converters as well as special type modules will be necessary.

Components located far from the data processing unit can be connected to the parallel data bus by serial data lines via the serial interface module of the data processing system.

A typical configuration of the modular data processing system is shown in Fig. 1. Fig. 2 shows the hardware implementation of such a system in flight standard

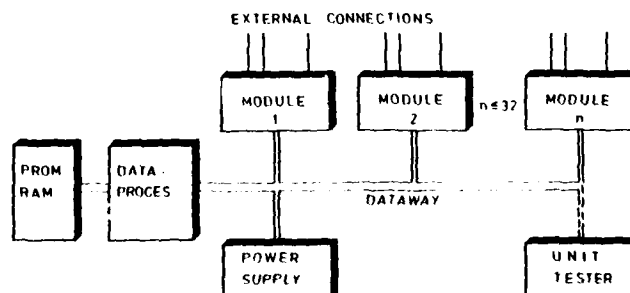


Fig. 1.: System Configuration with a Data Processor

3. REDUNDANCY CONCEPT

A redundancy data processing system is necessary to meet the high reliability requirements which arise from the envisaged lifetime of 10 years for the coming generation of communication satellites.

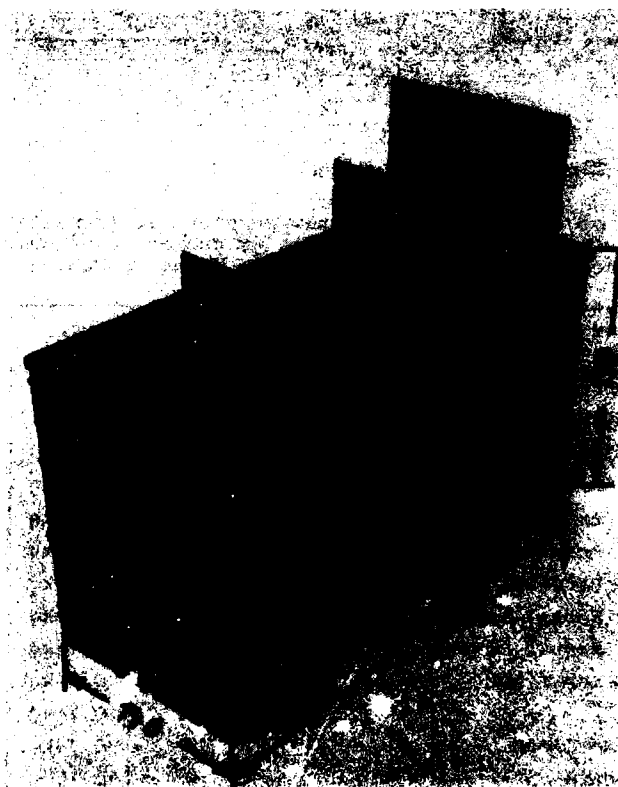


Fig. 2.: MUDAS-R Processing Unit

An analysis of a data processing system which meets the reliability requirements for an operational lifetime of 10 years resulted in a system design with the processor and the memory in four-fold redundancy, Fig. 3 shows the block-diagram of this system.

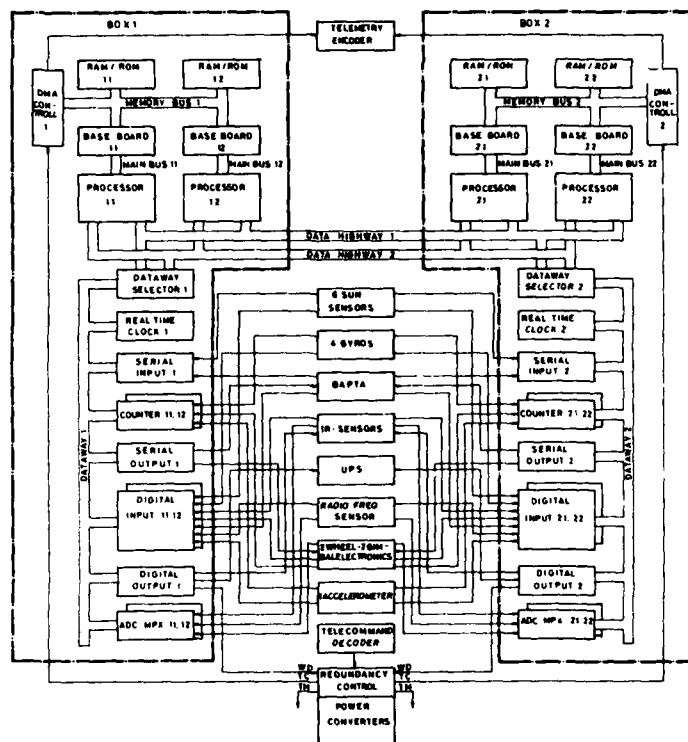


Fig. 3.: AOCS Electronics Block-Diagram

Besides the advantage of rapid adaption to new mission requirements and changes, the modular system allows the easy implementation of redundant configurations. A mass and power balance for this configuration is given in Tab. 2.

No.	COMPONENT	UNITS	TOTAL MASS	TOTAL MASS (+)
1	Data Processor	4	0,96kg	0,8 W
2	Memory (2k RAM, 4k PROM)	4	0,30kg	0,8 W
3	Base Board	4	0,36kg	0,1 W
4	Dataway Selector	2	0,18kg	0,2 W
5	DMA Controller	2	0,14kg	0,1 W
6	Digital Parallel Output	2	0,14kg	0,1 W
7	Digital Parallel Input	4	0,24kg	0,2 W
8	Digital Serial Input	2	0,14kg	0,1 W
9	Digital Serial Output	2	0,14kg	0,1 W
10	Multiplexer & ADC	2	0,14kg	1,6 W
11	Counter	2	0,14kg	0,1 W
12	Real Time Clock	2	0,14kg	0,1 W
13	Motherboard	2	0,15kg	-
14	Standardbox (incl. connectors and harness)	2	3,60kg	-
	Grand Total		7,27kg	4,3 W

(+) redundant parts are switched off

Tab. 2.: Mass and Power Balance of AOCS Electronics

The four-fold redundant system according to Fig. 3 can be operated in different modes:

- o only one processor with associated memory and one dataway are in operation, while the other components stand in cold redundancy
- o two processors work in parallel on different data-highways. In this mode a higher processing capacity is provided during normal operation. In case of failure one processor can keep the AOCs in a safe mode while the other can run test sequences for failure detection.
- o two processors and two data ways with attached I/O modules run in parallel sharing the different attitude control tasks. Synchronization can be achieved by software or by means of a common external clock.

Switching of redundant elements is in general a complicated task. It includes activities such as; detection of error, initiating of a system's safe mode, identification of error and isolation of the failed element.

In the described system a "watch dog" circuit is the major element of system monitoring. It checks a frequent status signal delivered by the processor system in operation.

Two conditions have to be fulfilled to give a positive status signal: a processor self-test routine has to give a positive output and one significant attitude sensor signal must not exceed the nominal range. In case of a default of the status signal the watch dog circuit, as part of a redundancy control electronics, initiates a system reconfiguration.

A possible strategy for switching of redundancies is given by a flow chart in Fig.4.

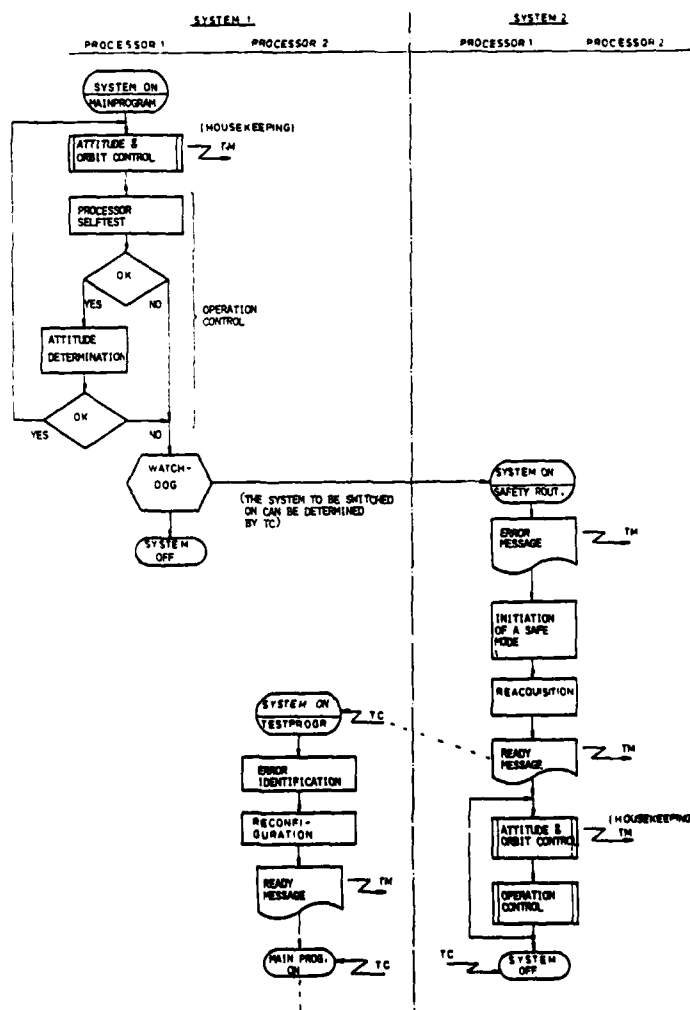


Fig. 4.: Redundancy Switching Strategy

In case of a failure all AOCs components will be switched over to the redundant one. This will be done by switching the power supply of the different components. This first step will be performed automatically without ground interference to keep the time of a malfunction as short as possible.

Further activities as starting of test routines for failure identification and system reconfiguration will be initiated by ground station via telecommand.

A fully automatic system results in more effort for on-board hardware and software and bears a higher risk. For communication satellites fulltime groundstation coverage can be assumed so that the outlined strategy will be feasible.

4. SOFTWARE CONCEPT

Software is a vital part of the modular data processing system. The flexibility of the concept depends on software as much as on hardware. The mission specific requirements are implemented by software rather than by hardware.

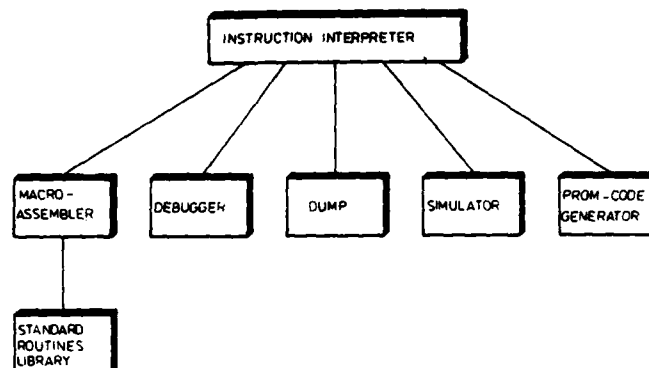


Fig. 5.: Structure of the Software Development System

Therefore much care has been taken to provide versatile system software and useful software development aids. A survey of the existing software is given in Fig. 5. The different software aids are:

- o Crossassembler written in Fortran IV which can be run on host computers. It includes a versatile macropreprocessor which allows the user to define macro-instructions by himself. A computer configuration for software development is shown in Fig. 6
- o Simulator program, which simulates all processor functions. With this aid the user's program will be tested logically before implementation on the dataprocessor.
- o PROM-code generator, as an extension to the simulator program. It generates the paper tape necessary for programming the processor's PROM.
- o Dump and debugger program, lists the contents of all registers and used RAM elements. In addition it provides the possibilities of modifying these data and defining breakpoints within the user's program.
- o Standard routines library.
- o Processor resident operating system for attached teletype and unit tester. Several editor functions such as program input, program listing, modification of instructions etc. ease the system integration.

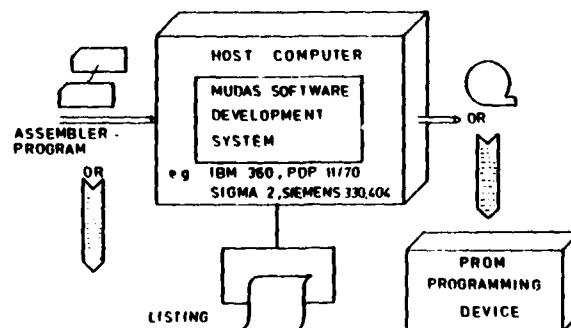


Fig.6.: Computer Configuration for Software Development

Normally the user's program e.g. the attitude control algorithms, are written in assembler language. This is reasonable for programs up to a few thousand instructions. For more complicated programs the programming effort becomes so great that the use of a high order programming language becomes necessary.

Therefore the described data processing system provides the possibility of writing programs in PEARL (Process and Experiment Automation Realtime Language). PEARL is a highly sophisticated language which is ideally suited for realtime applications in the field of automatic control.

5. APPLICATION

The described modular data processing system has found several applications in space projects such as the Spacelab Instrument Pointing System (IPS) and the Microwave Remote Sensing Experiment (MRSE).

The modularity in hardware in connection with the existing software proved to be very useful for cost and time efficient development, manufacturing and integration of on-board attitude control and data handling systems.

6. REFERENCES

- /1/ Attitude and Orbit Control Systems for Long-Life Communication Satellites; by H. Bittner, M. Wlaka, H.-D. Zago; AIAA Paper No. 78-1264
- /2/ A Microcomputer based system for on-board attitude control applications, by R. Gunzenhauser, M. Wlaka, H.-D. Zago; British Interplanetary Society, Conference on Computer Techniques for Satellite Control and Data Processing Appleton Laboratory, Slough, England, Oct. 1977.

7. ACKNOWLEDGEMENT

The work presented in this paper was sponsored by the German Federal Ministry for Research and Technology, represented by DFVLR-BPT. The author is solely responsible for the contents of the paper.

INTEGRATED ORBIT/ATTITUDE DETERMINATION

A. Dale Mikelson
Space Sextant Program Manager
Martin Marietta Aerospace
Post Office Box 179
Denver, Colorado 80201

SUMMARY

The Space Sextant - Autonomous Navigation Attitude Reference System (SS-ANARS) being developed by Martin Marietta Aerospace for the USAF is a spacecraft subsystem that has the integrated capability of on-board orbit determination with on-board attitude determination. An instrument, called the Space Sextant, is a gimballed-two telescope included angle measurement device that is driven by an on-board computer to measure the angles between celestial bodies, as seen from a spacecraft, to an accuracy of 1 arc second.

Orbit determination with the system is achieved by measuring the included angles between brighter stars and the limbs of the moon and earth, and processing these angle measurements through a Kalman filter with an on-board digital computer. Spacecraft position accuracy from 800 to 1200 feet is determined for any earth orbit.

Attitude determination relative to the celestial sphere is determined with the same device to an accuracy of less than 1 arc second by measuring the included angles between the brighter stars and a reference platform consisting of a mirror and a Porro prism.

The SS-ANARS has been under development since its inception in 1973 and has progressed through critical technology development, a proof of concept model, a laboratory model and a flight demonstration system. This flight demonstration system is to be flown as a sortie payload on the Space Transportation System (Space Shuttle) to prove its autonomous-integrated orbit and attitude determination capabilities.

A. ORBIT DETERMINATION MEASUREMENTS

Navigation or position determination with the aid of celestial observations has been practiced by our ancestors for centuries. The vast roving of our oceans by the Norsemen must have necessitated use of celestial observations even though their techniques were not recorded for us to study. Recent investigations into the navigation techniques of the Polynesians show that they have, for generations, plied the Pacific in their outriggers using the stars, sun and moon as part of their navigation information, passing their art to their descendants by word of mouth and life long training, leaving no written record of their techniques.

Marine navigators began using devices such as the quadrant or astrolabe as early as 500 AD to determine their latitude. More sophisticated devices using mirrors and lenses, called quadrants, octants and sextants, came in use about 1730 and were designed to measure angles to the sun or stars with respect to the local plumb bob or visible horizon.

However, few of these early navigators had any way of determining their longitude, thus requiring that they travel north or south to the latitude of their destination and then east or west until they arrived, days maybe weeks, different than planned. Not until 1760 was a good timepiece called a chronometer developed allowing determination of longitude. Total earth relative navigation with a sextant and a timepiece has been in use only approximately 200 years.

Navigation in space by making angle measurements to celestial bodies with a device called a sextant differs from navigation on earth in that the spacecraft's radius from the earth's center is not known and precise measurements to the earth's horizon or to its center is difficult because of the earth's atmosphere. The next most apparent body to which angle measurements can be made is then, our moon. It is specifically this body, our nearest celestial neighbor that the SS-ANARS relies upon for its primary navigation measurements.

The simple concept of navigation with a lunar-star space sextant is depicted in Figure 1. It is apparent that if: 1) the sextant can precisely determine the angles between the stars and the moons

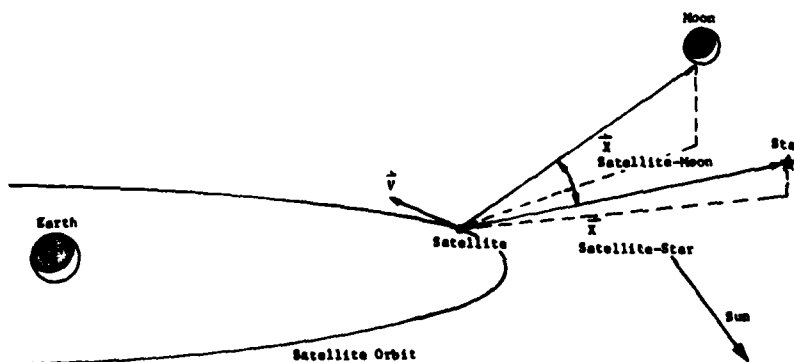


FIGURE 1 Space Sextant Navigation Concept

center of mass; 2) the stars directions are precisely known; 3) the moon's ephemeris is precisely known; and 4) International Atomic Time (IAT) is known, then it should be possible to determine the spacecraft's position in space. However, since the spacecraft's radius to the earth's center is not known, observations to the moon from one position in space does not provide a unique solution of spacecraft position.

An angle measured between a star at virtually infinite distance and an object such as the moon at a finite distance, places the navigator somewhere on the surface of a cone with the cone apex at the position of the object and the cone axis in the direction of the star (Figure 2). A second measurement to another star and the same nearby object establishes a line of position which places the navigator somewhere along the intersection of the two cones (where the second ambiguous intersection is obviated by the navigator's approximate knowledge of his position). No further position information is possible solely on the basis of additional star to moon measurements except for the inevitable refinement of the original line of position. However, because the spacecraft and the moon move relative to one another, new lines of position are continually obtained. Old lines of position can be in effect projected forward in time in a highly predictable manner by virtue of the dynamical laws that govern the motion of the spacecraft.

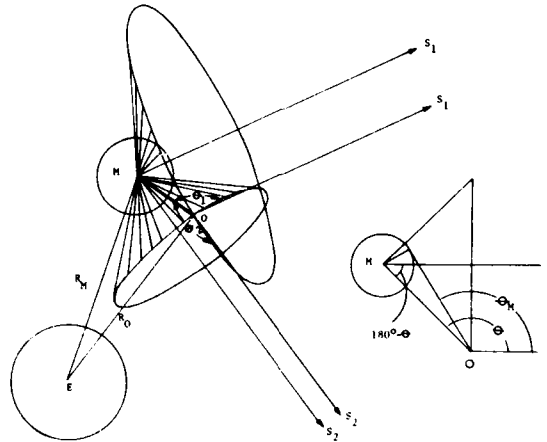


FIGURE 2 Navigation Principle Using Two-Star Measurements

Correlating the moon to star included angle measurements with time to result in a continuous on-board orbit determination of a spacecraft can be achieved with a Kalman-recursive filter being executed in a spaceborne computer.

However, because spacecraft motion relative to the moon is required to refine the line of position to a series of lines intersected by a dynamical model, the time duration from beginning of measurements until precise position estimates are known may be a matter of many hours. The SS-ANARS could also use earth limb to star angle measurements thus establishing a second line of position. This line intersects the first as defined by the moon and stars, thus allowing a complete position fix in as short a period of time as is necessary to complete these measurements.

B. CONCEPTS OF INCLUDED ANGLE MEASUREMENT AND ATTITUDE DETERMINATION

The orbit determination accuracy of a space sextant system is proportional to the accuracy to which the included angle between the stars and the limb of the earth or moon can be determined. The SS-ANARS included angle measurement concept is quite simple, although somewhat complex to implement, and consists of two optical trackers gimbaled on a common axis with a measurement head to determine the angles between the optical centerlines of each tracker. The fundamental concept of operation of the measurement device is depicted in Figure 3.

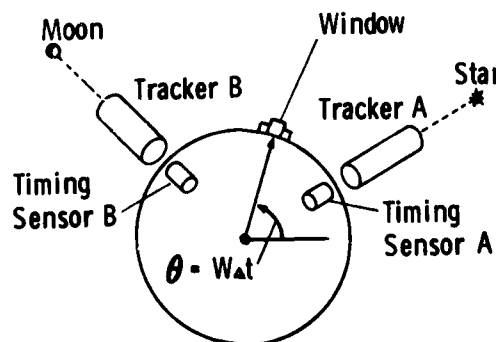


FIGURE 3 Wheel Angle Measurement Concept

Assume that each tracker is aligned to its respective target and visualize a very narrow window that is rotating through an arc with a constant angular velocity W . As the window passes through the optical axis of tracker A, the timing sensor sees an impulse of light (t_1). As the window continues in its arc, it will pass through the optical axis of tracker B, at which instant timing sensor B sees an impulse (t_2). The included angle is $\theta = W(t_2 - t_1)$.

A cross sectional drawing of such an included angle measurement head mounted on two stacked outer gimbals is shown in Figure 4. The two rays required for operation are shown and called the tracker ray and the timing pulse ray. The tracking ray enters the telescope at 1) (both telescopes pointing downward in the figure), reflects off the primary mirror 2), the secondary mirror, 3) and finally to the tracking detector, 4) where pointing error signals are developed. These error signals are used to drive the gimbals to maintain orientation in the measurement plane and to maintain lock onto the celestial object.

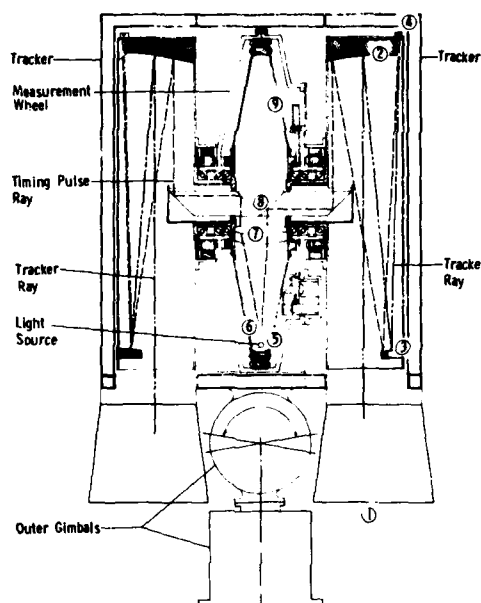


FIGURE 4 Cross Section of Space Sextant

The timing ray originates from an internal light source 5) emerges from a slit, 6) and is collimated, 7) before being split into two branches by the prism assembly which diverts half of the energy into each telescope. The prism, 8) is coaxial with the wheel and rotates with it. At one instant in each revolution of the wheel the timing ray is exactly parallel to optical axis of one of the telescopes and impinges on the detector at that instant thus creating the required timing pulse. The time that this occurs depends upon the relative orientation of the telescope to the wheel, and the time difference depends upon the relative orientation of the two telescopes. The timing pulse from each sensor is used to start and stop a digital counter that counts a precision clock. The corresponding binary number represents the properly scaled scalar angle between the two telescopes optical axes.

The factor allowing the accuracy achievable by this design is in the precise integration of the angle rotated by the wheel as a point on it moves from the axis of one telescope to that of the other. This is achieved with a phase-locked loop and self compensation for radial runout and encoder disk systematic errors.

Since such a design is a celestial body tracking system and since it measures the included angles between celestial bodies, it is ideally suited for incorporation into a system that does both orbit determination and celestial attitude determination. By the mere addition of a platform reference mirror and a precision three axis gyro package, the integrated concepts shown in Figure 5 arose.

Implementation of this concept was achieved by replacing the stacked gimbals with a ring gimbal and addition of the attitude reference platform consisting of a reference platform mirror, a Porro prism assembly, and a strapdown gyro package, and a stray light and thermal control system. Direct optical correlation of sextant measurements to the reference mirror was achieved by incorporation of a light source in the telescopes and allowing one telescope to autocollimate off of the mirror while the other is tracking a star. This angle (the angle between the perpendicular to the mirror and the direction of the star) is called an Elevation measurement. The perpendicular attitude is determined by making included angle measurements between two or more stars and the reference mirror.

The Porro prism was added to allow an Azimuth Measurement of the mirror with respect to the celestial sphere. A Porro prism has the unique property that light impinging on the prism perpendicular to the prism apex is reflected back perpendicular to the apex of the prism. Thus by implementing the sextant to allow single axis autocollimate off a Porro prism assembly while the other telescope is

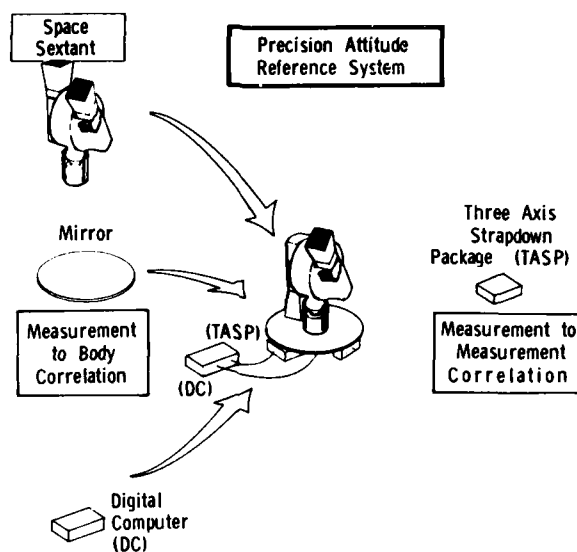


FIGURE 5 Concept for an Integrated Orbit/Attitude Device

tracking a star, a direct measurement of mirror azimuth with respect the celestial sphere is also achieved with one device.

Figures 6 and 7 depict the elevation and azimuth measurements, respectively. The strap down gyro package is used only to allow correlation of one measurement to the next utilizing a Kalman recursive filter in the on-board computer.

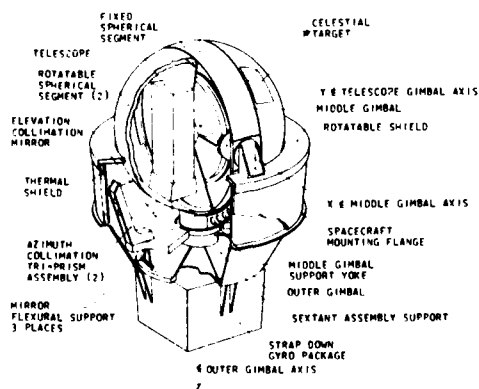


FIGURE 6 Sextant Collimation Off Mirror - Elevation Measurement

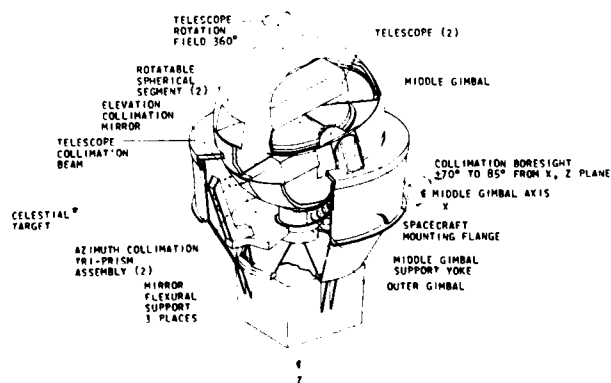


FIGURE 7 Sextant Collimation Off Porro Prisms - Azimuth Measurement

C. EXPECTED SS-ANARS PERFORMANCE

The expected performance of the SS-ANARS has been extensively evaluated by two types of analysis; covariance sensitivity analysis and non-linear Monte Carlo simulation. Orbits studies included those in Table 1.

TABLE 1 TEST CASE ORBITS

ORBIT	PERIOD HOUR	APOGEE N.MI.	ECCENTRICITY	INCLINATION DEG.
A	12	24,850	.73	63.4
B	24	22,760	0	0
C	12	14,350	0	63
D	124	68,000	0	90
E	272	115,000	0	90

The system's attitude determination performance was found to be independent of orbit parameters since the attitude measurements are in no way correlated with altitude, velocity, or direction of the vehicle with respect to the earth. The covariance analyses results to be presented was verified with non-linear Monte Carlo simulation of both navigation and attitude reference for orbit A. The principal parameters that affect the Space Sextant performance are included angle measurement noise and the time needed to slew, acquire and read the measurement (measurement interval). The secondary error sources are gyro drift in attitude determination and uncertainties in moon position and lunar/earth limb terrain height in navigation.

ORBIT DETERMINATION

The performance sensitivity to measurement noise for Orbit A is shown in Figure 8. The measurement noise consists of the uncompensated random component of the included angle error and is representative of a composite of the true electromechanical sensor noise as well as the gaussian uncertainties in the calibrated systematic sensor errors, such as tracker to tracker bias, telescope to planet limb bias, and telescope to star bias.

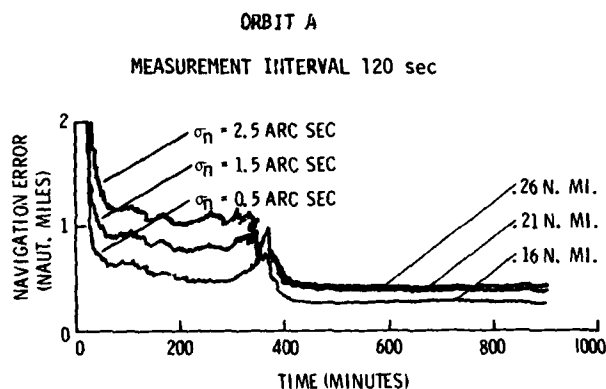


FIGURE 8 Navigation Sensitivity to Measurement Noise

The time to converge from initial position uncertainty (30 n.mi.) at apogee to steady state accuracy was found to be independent of measurement noise. The position error reduces to less than 1 nautical mile in less than 25 measurements. It then remains nearly constant until the satellite passes through perigee where it drops to a smaller steady state value. Since the system was initialized at apogee, the final convergence occurs at approximately 6 hours.

The measurement interval was found to have an effect on the performance. Figure 9 shows the growth in the navigation error with measurement interval. The nominal measurement interval was 120 seconds for this study to reflect a combined navigation-attitude reference system performance. It is noted that navigation measurements could approach a 30 second measurement interval.

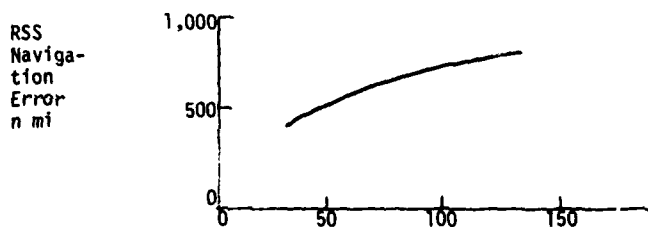


FIGURE 9 Navigation Sensitivity to Measurement Interval (Δt_m)

The above error values were taken at 1500 minutes which is after two complete orbits. The position error at 10 hours of Figure 8 for the 120 second measurement interval was 1000 feet.

The performance profiles for orbits B, C, D, and E are shown in Figure 10. The basic profile is the same for all orbits; rapidly converging to 1 nautical mile error and then more slowly to an ever decreasing steady state value. The higher orbits take longer to converge to precision accuracy because their angular motion with respect to the moon (or earth) is less. In theory and as shown by simulation, the steady state performance should be independent of the orbit.

Covariance Analysis

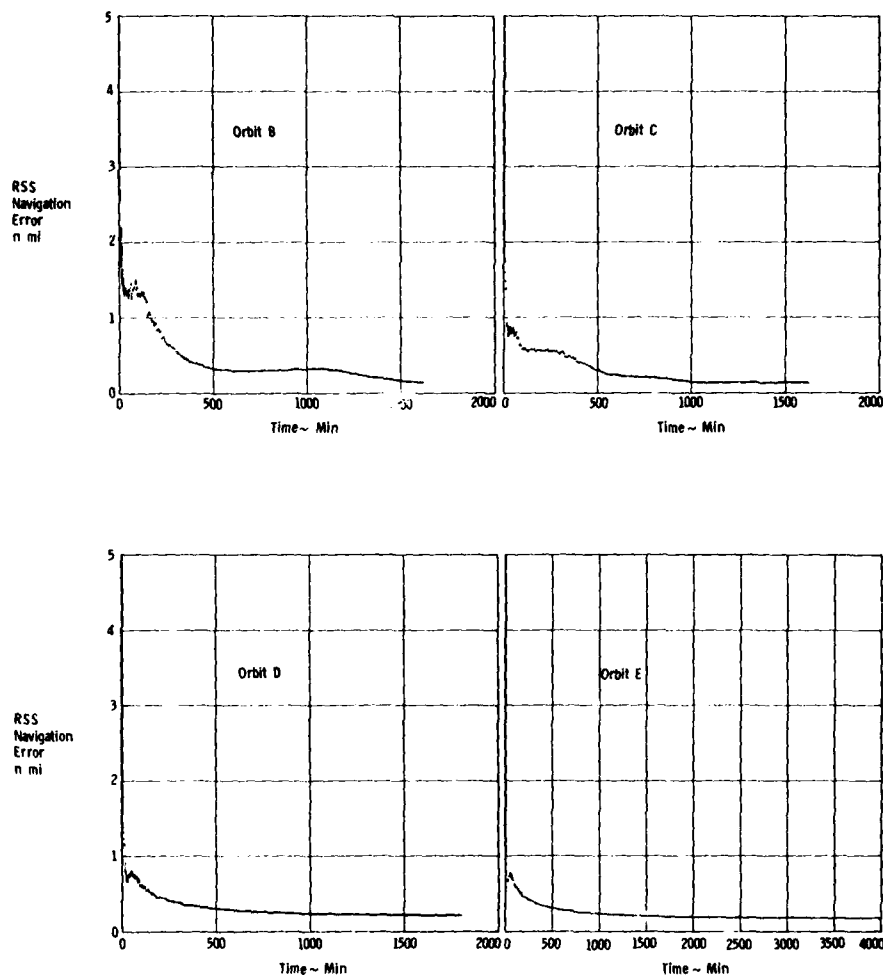


FIGURE 10 Navigation Accuracy in Orbit B, Orbit C, Orbit D and Orbit E

Theory shows that the inclusion of earth-star observations significantly reduces convergence time and provides continuous navigation during moon occultation by either the earth or sun. Figure 11 dramatically corroborates theory and shows the difference between processing all lunar measurements, all earth measurements and two ratios of moon-earth measurements. It is obvious that earth-star measurements, when mixed with moon-star measurements, decrease the time for convergence.

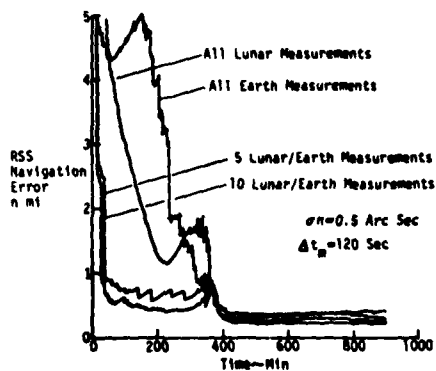


FIGURE 11 Influence of Earth Measurement on Navigation Performance

The earth's limb uncertainty, which was estimated to be 1 nautical mile, is greater than the moon's limb uncertainty of 1700 ft. Figure 12 shows the performance sensitivity to the earth limb uncertainty for the nominal sequencing of an earth observation for each lunar observation. The curve is nearly flat; accurate lunar observations are the dominant factor in steady state performance.

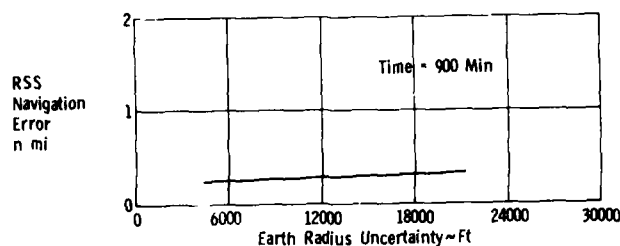


FIGURE 12 Navigation Sensitivity to Earth Limb Uncertainty

The rigorous non-linear Monte Carlo simulations validated the covariance analysis. The cumulative standard deviation curves are shown with corresponding covariance analysis results for the three parametric measurement noise levels in Figure 13. The agreement validates the covariance analyses.

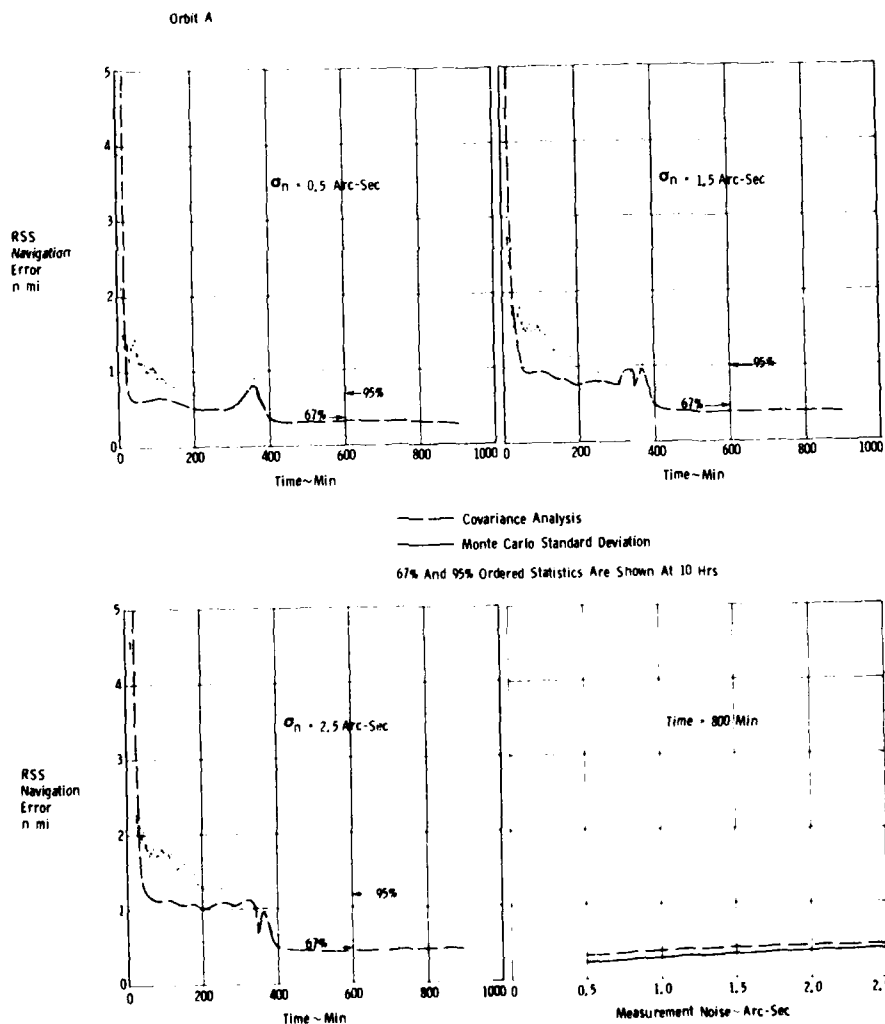


FIGURE 13 Navigation Accuracy Comparisons - Covariance Analysis vs. Monte Carlo Simulations

ATTITUDE DETERMINATION

The error sources that most effect the attitude determination accuracy of the SS-ANARS were found to be, as expected, the included angle measurement accuracy (measurement noise - σ_n), measurement interval ($\Delta t_m = 20$ sec) and non-compensable long term gyro drift. Figure 14 shows the ANARS systems sensitivity to measurement noise (σ_n) as well as a comparison of the covariance analysis results to Monte Carlo simulations. Also, the rate of convergence of attitude determination errors to steady state values was not significantly effected by measurement noise (σ_n).

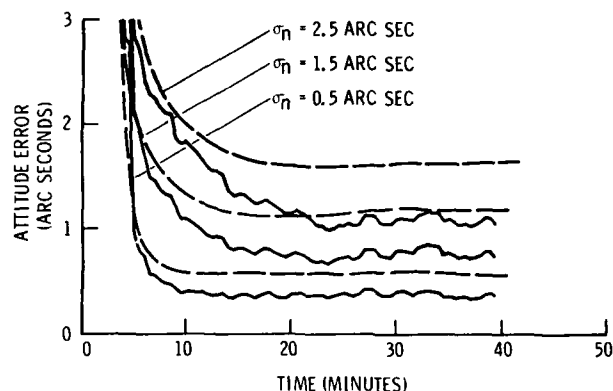


FIGURE 14 Attitude Determination Sensitivity to Measurement Noise

Figure 15 shows system sensitivity to measurement interval and Figure 16 shows system sensitivity to non-compensable gyro drift.

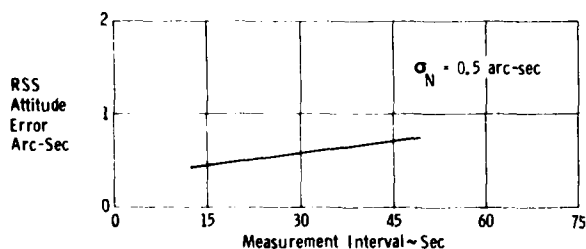


FIGURE 15 Attitude Determination Sensitivity to Measurement Interval (Δt_m)

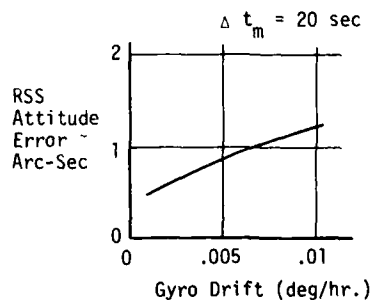


FIGURE 16 Attitude Determination Sensitivity to Gyro Drift

The results of the ANARS system performance studies are summarized in Figure 17 as a function of the included measurement accuracy (measurement noise - σ_n). In conclusion, if the SS-ANARS can be designed to: 1) measure included angles to an accuracy of 0.5 arc sec; 2) make measurements as often as each 30 sec; and 3) have non-compensable gyro drifts of no more than 0.001°/hour it will determine its own orbit to within 600 ft. and its attitude to 0.4 arc seconds.

The next section describes the results of laboratory model tests showing that the SS-ANARS should have a measurement noise approaching 0.5 arc seconds.

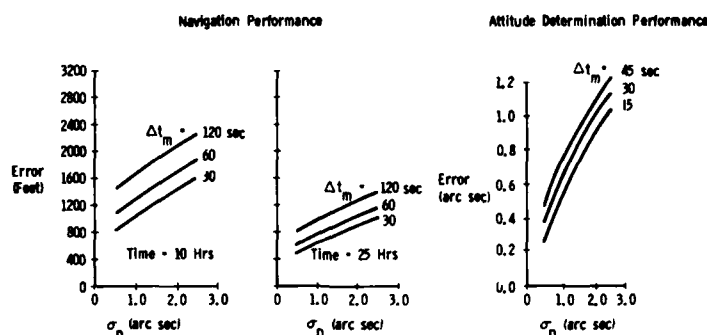


FIGURE 17 SS-ANARS System Performance Summary

D. PROOF OF CONCEPT AND DEVELOPMENT TESTS

ERROR MODELS

To provide quantitative values and yield confidence in the conceptual design, a system model was developed that incorporated the dominant error sources. This model provided time solutions of the modeled servo state equations in conjunction with the support electronics, yielding time histories of sextant induced measurement errors. These errors were averaged over a one second measurement interval to produce "single measurement" error values. The standard deviation of a sample set was then calculated to yield the sextant's measuring capability of 0.56 arc sec (1σ).

A "self-calibration" scheme for on-orbit sensor calibration has also been developed. This technique was predicated on a fundamental design feature that permits either telescope to track a star (or the moon's limb). By measuring the angular separation between two known stars, the systematic tracker to tracker bias errors may be solved for and compensated for in the on-board computer. The uncertainty in this calibration was statistically averaged with the composite sensor noise to yield an overall random measurement error of approximately 0.6 arc second.

RESEARCH MODEL

An engineering model of the Space Sextant has been developed and tested to demonstrate the included angle measurement accuracy of the current design. This research model was developed primarily to demonstrate "proof of principle", and to obtain a laboratory verification of the inplane measurement noise predicted by the theoretical model previously described. This model (Figure 18) employed a single gimbal for in-plane measurement, contained several expedients made necessary by cost and schedule constraints, and consequently departed in many important respects from the ideal instrument design. However, despite these known deficiencies this suboptimal device was capable of 0.65 (1σ) arc-sec random noise, thus amply fulfilling its anticipated performance (Figure 19).

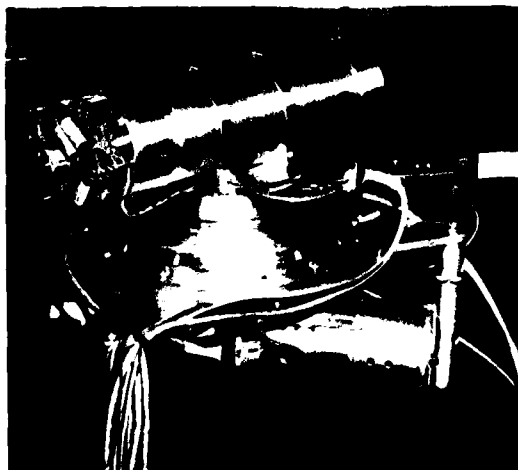


FIGURE 18 Sextant Research Model

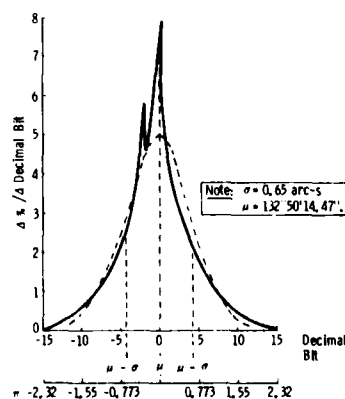


FIGURE 19 Measurement Repeatability

LABORATORY DEMONSTRATION MODEL

The favorable research model results prompted construction of a Laboratory Demonstration model, containing all the functional equivalents of a flight article, Figure 20, excluding the thermal control system. The four degree of freedom device was controlled by a PRIME 300 minicomputer and demonstrated search, acquisition, and capture of stellar, lunar and autocollimation targets followed by statistical processing of the included angle measurement data.

The testing facility, Figure 20, was a thermally controlled positive pressure test cell, with a six ton granite optical slab. On the slab were two American Optical Company star signal simulators, one 12 inch aperture off axis parabolic mirror used for lunar limb simulation, and two Wild T-3 theodolites to provide the angular references for Sextant data comparison.

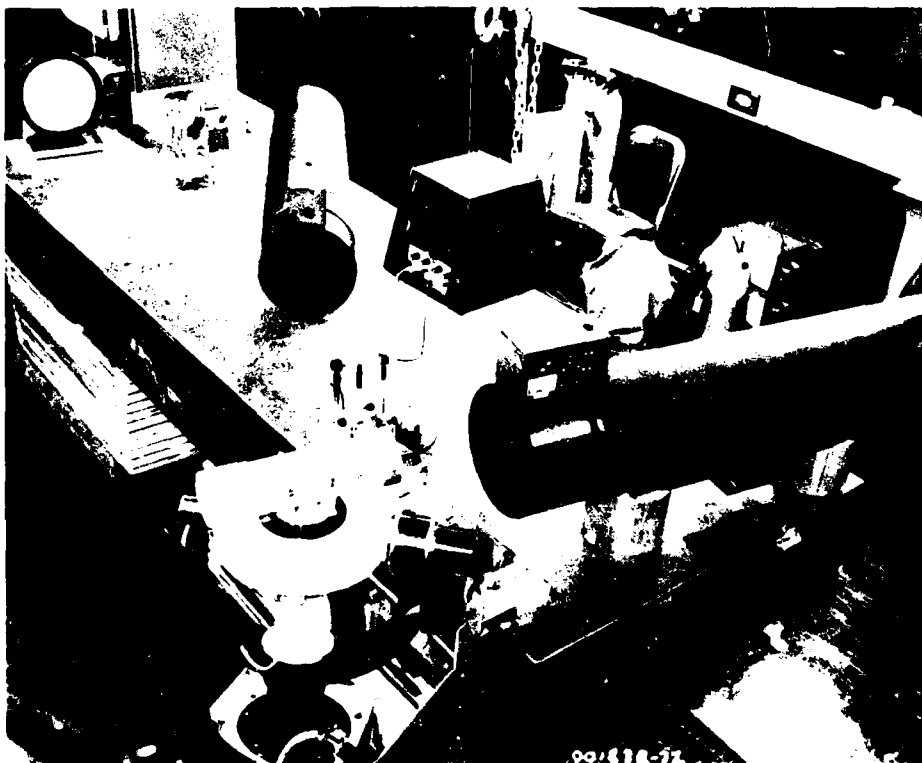


FIGURE 20 Laboratory Model & Test Facility

Test results demonstrated a measurement accuracy of less than 1 arc-sec after compensation for sextant biases and systematic errors and test fixture thermal distortions. Very satisfactory slewing, raster scan for acquisition with the coarse detectors and hand-over and to the fine detectors was demonstrated for both the simulated stars and the lunar limb. Thus, the functional performance of the system was demonstrated as well as showing that a single detector can be used for both star tracking and lunar limb tracking. Limited Testing also showed little system sensitivity to base motions and temperature sensitivity. The autocollimation features for the attitude determination measurements of autocollimation off a reference mirror and off a Porro prism were also demonstrated.

E. ORBITAL DEMONSTRATION IN SYSTEM DESIGN

The orbital demonstration system design of the SS-ANARS is comprised of three packages (Figure 21): 1) the Computation and Storage Package (CSP); the Support Electronics Package (SEP); and the Sensor Package (SP). The on-orbit demonstration of autonomous orbit determination and attitude determination is to be performed flying as a sortie payload on an early STS (Space Shuttle) flight. Figure 22 presents an artist's cutaway of the flight demonstration sextant.

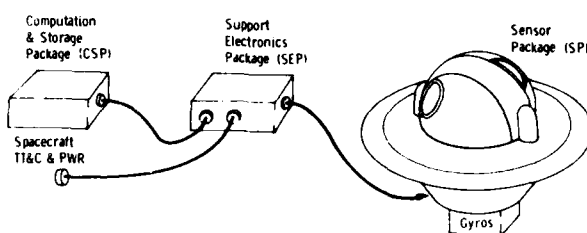


FIGURE 21 Orbital Demonstration Configuration

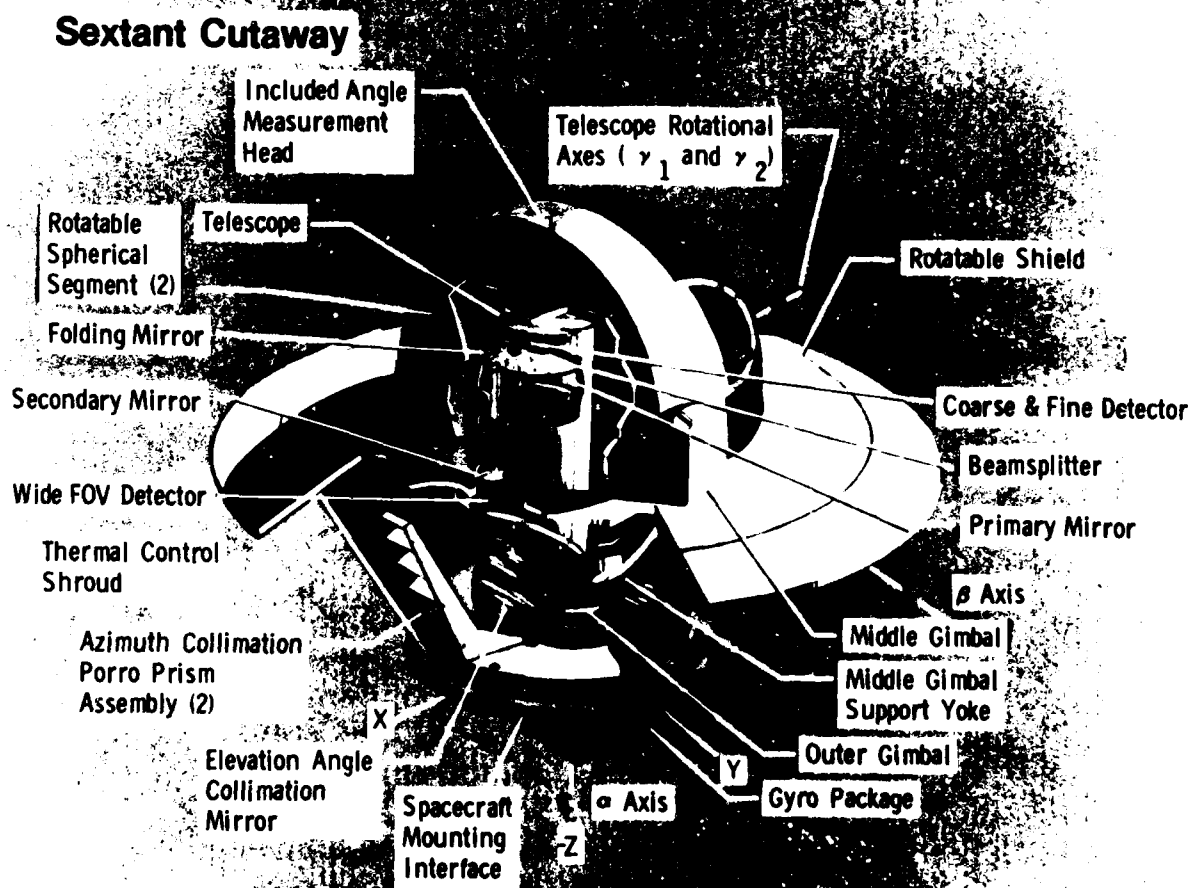


FIGURE 22 Flight Demonstration Sextant Cutaway

The outer and middle gimbals are used for positioning the measurement head into the plane of measurement and controlling crossplane motion in both telescopes after target lock. A base plate supports these two gimbals, a gyro package, a reference collimation mirror and two Porro prism assemblies.

The gyro package contains two, two degree of freedom, unheated ball bearing gyros with expected on-orbit performance of 0.01 degrees per hour considering random noise, alignment and scale factor and bias thermal sensitivities. As the reference mirror and Porro prisms provide the attitude reference triad, dynamic short term alignment stability of the optical elements to the gyro package was designed to be 0.003 degrees per hour.

The outer and middle gimbals contain class seven wet lubricated bearings. Gimbal torque is provided by brushless, two phase, DC torquers with position feedback obtained from multispeed resolvers. Signal and power feedthrough is effected by slipring assemblies.

A casted yoke supports the middle gimbal and provides, in conjunction with the bearings, 30 arc seconds long term stability of the outer/middle gimbal orthogonality.

The Sensor Package's Thermal Control System is a cold biased system consisting of the Thermal Control Shroud, rotatable shield, and rotatable spherical segments utilizing heaters and proportional controllers to maintain operating temperatures within limits.

The telescopes are off-axis Cassegrains consisting of an $f/7$ quarter wave parabolic primary mirror, a beam splitter-hyperbolic secondary mirror, a folding mirror, a beam splitter pellicle and two hybrid electronics detector assemblies. The wide Field Of View (FOV) detector assembly is behind the secondary mirror and has a 4 deg. FOV. The coarse and fine FOV detector is at the focal plane of the Cassegrain system with a coarse FOV of 6 arc min. Autocollimation is achieved via an infrared light source placed at the Cassegrain's focal plane below the pellicle. The telescope focal length is 60 inches resulting in an eight arc second star image size on the fine detector elements. The telescope sunshades are a dual internal baffle design providing stray light attenuation of 260 db. Figure 23 shows how the three target types (star image or returned autocollimation light source, lunar limb, and slit image timing light) are focused relative to the coarse/fine FOV detector.

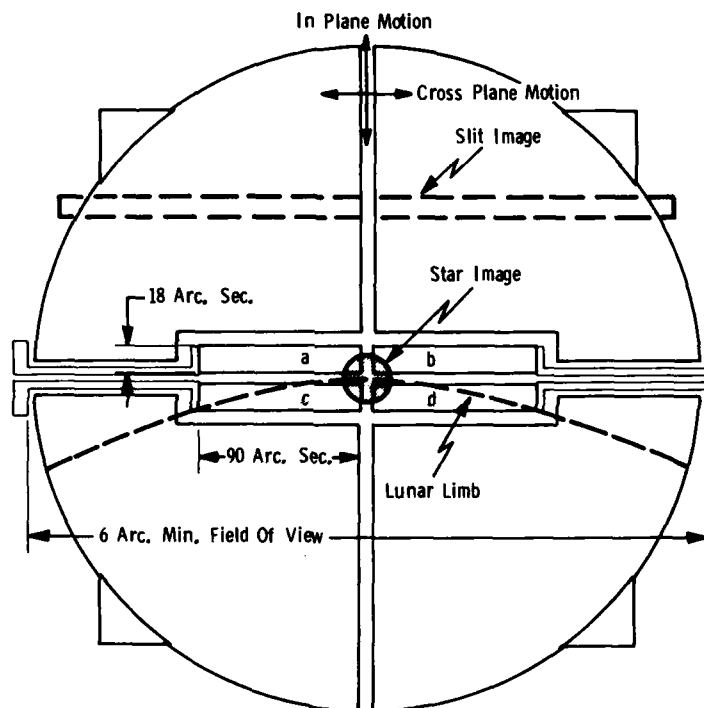


FIGURE 23 Coarse/Fine FOV Detector & Focused Images

The two critical developments of the program: the wheel bearing assembly and the hybrid electronic detector assemblies have proven to be very adequate. Figures 24 and 25 show these critical assemblies. Figure 26 shows the flight demonstration system sensor package assembled up to thermal shroud installation. The Computation and Storage Package (Digital Computer) and the Support Electronics package have completed qualification testing and system testing has progressed through slew and star image acquisition. Preliminary data analysis indicate that system performance should be as good or better than expected resulting in a system with included angle measurement errors of less than 1 arc second (1σ). Flight software design is complete utilizing less than 30 thousand 16 bit words of memory. The flight demonstration ANARS will complete qualification testing in 1981. Upon completion of flight demonstration on the STS it is anticipated that a long life, single package version of the space sextant system will be developed for operational usage on advanced space systems.



FIGURE 24 Wheel Bearing Assembly

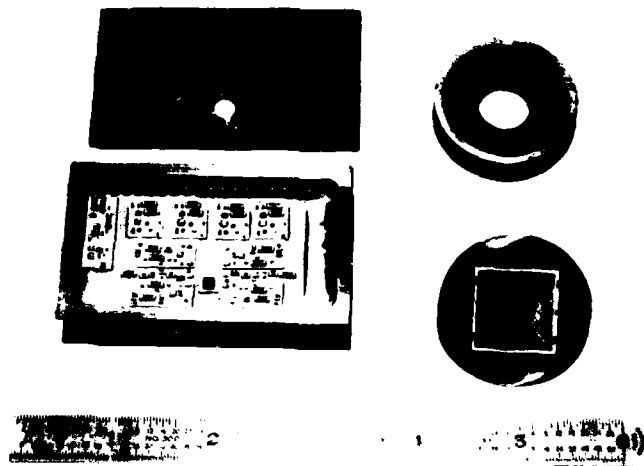


FIGURE 25 Hybrid Electronics Detector Assemblies



FIGURE 26 Partially Assembled Sextant

A MULTILEVEL CONTROL APPROACH FOR A MODULAR STRUCTURED SPACE PLATFORM

by

F. D. Chichester
The Bendix Corporation
Guidance Systems Division
Teterboro, New Jersey 07608

and

M. T. Borelli
NASA Marshall Space Flight Center
Systems Dynamics Laboratory
Huntsville, Alabama 35812

SUMMARY

A three-axis mathematical representation of a modular assembled space platform consisting of interconnected discrete masses, including a deployable truss module, was derived for digital computer simulation. The platform attitude control system was developed to provide multilevel control utilizing the Gauss-Seidel second level formulation along with an extended form of linear quadratic regulator techniques. The objectives of the multilevel control are to decouple the space platform's spatial axes and to accommodate the modification of the platform's configuration for each of the decoupled axes.

1. INTRODUCTION

The successful first flight of the Space Shuttle has presented the world scientific and technical communities with a new era for opportunities in both research and applications. The Space Shuttle will be used to place in Earth orbit many large payloads, some of which include the Space Telescope, Advanced X-Ray Astrophysics Facility, 25 kW Power System, and Science and Applications Space Platforms (SASP). A second order SASP, as shown in Figure 1, is a moderately large spacecraft that will require more than one Space Shuttle flight for its complete assembly. Some of the elements used for the SASP are Earth assembled modules and others are deployable on orbit. A typical deployable truss module under current development is shown in Figure 2. The truss module will be used for connecting Earth-assembled modules and also serve as a mounting base for experimental packages.

The control requirements for a space platform to be assembled on-orbit present some unique problems. The initial problem is how to control the platform during the assembly phase, i.e., in its partially completed state with relatively large changes in mass, moments of inertia, structural dynamics characteristics, etc., occurring as each module is added to the platform. Also, for the platform to be really versatile, it must be adaptable to varying geometry to meet different mission objectives over its extended lifetime. A natural consequence of the modular nature of the SASP would be a modular designed control system that would not require complete redesign each time a module is removed from, added to, or rearranged on the platform. A control system that embodies potential capabilities to fulfill the necessary requirements for the SASP is currently under development and can be described as a multilevel multivariable system. The control system utilizes a combination of Gauss-Seidel multilevel control and an extended form of linear quadratic regulator (LQR) techniques to accomplish two objectives. The first is to decouple the spacecraft spatial axes and thereby reduce the dimensionality of the control problem. The second is to accommodate the modification of the platform's configuration for each of the decoupled axes. Both objectives are achievable by the inherent characteristics of the multilevel techniques that decompose the control problem into two-level hierarchy of subproblems. Each first-level subproblem is treated in this paper as a two point boundary value problem using LQR techniques, and the second-level subproblem is the coordination of solutions of first-level subproblems.

2. PLATFORM MODELING

The basic module for the SASP is the 25 kW Power System (PS) spacecraft. For this study the flexible body PS was modeled using five discrete masses consisting of a central body and four masses representing the solar arrays as shown in a topological diagram of Figure 3. The radiator panel and antenna were not included in the model. Appropriate hinge constants were selected to interconnect the masses that would provide the characteristic low-frequency dynamic response expected from very flexible solar arrays. The deployable truss connected to the PS central body is represented by four masses numbered six through nine in Figure 3. Attached to the end of the truss is a rigid module or a second spacecraft represented by a single mass. Actuators and sensors for attitude control of the platform will be located in the PS central body and can also be in the second spacecraft.

The rotational dynamics of the ten body three-axis space platform of Figure 3 were developed primarily by utilizing the augmented body techniques of Hooker and Margulies (1) and extended by Cornell (2)(3) and Lipski (4)(5). These techniques were recently applied

to a five-body three-axis model of the Power System spacecraft by Chichester (6). The procedure can be outlined in ten steps as follows:

- 1) Approximate the assembly of vehicles with rigid bodies interconnected by a spring-hinge suspension.
- 2) List symmetry conditions that may apply to elements of the model.
- 3) Determine the vector locating the center of mass of each rigid body with respect to its barycenter.
- 4) Determine the vectors locating each adjacent hinge with respect to the barycenter of each rigid body.
- 5) Derive augmented moment of inertia matrix equivalent to the effective moment of inertia of each rigid body in the model with respect to its barycenter.
- 6) Write the effective torque balance about each barycenter with rigid body angular rates, $\underline{\omega}_i$, as vector state variables.
- 7) Express the equations resulting from 6) in vector-matrix form.
- 8) Invert the coefficient matrix of $\dot{\underline{\omega}}$ in the model of 7) to obtain the state variable rigid body angular rate model.
- 9) Express time rate of change of relative Euler angles in terms of rigid body angular rates to obtain the state variable Euler angle model.
- 10) Aggregate the state variable Euler angle model with the state variable rigid body angular rate model to obtain the state variable rotational dynamics model.

3. STATE VARIABLE ROTATIONAL DYNAMICS MODEL

The linearized rigid body angular rate equations and the linearized Euler angle rate equations may be combined into a state variable rotational dynamics model of the following form.

$$\begin{aligned}\dot{\underline{\omega}} &= GLC_s \underline{\omega} + GLK_s \hat{\underline{\alpha}} + G\underline{u} \\ \dot{\hat{\underline{\alpha}}} &= K\underline{\omega}\end{aligned}\quad (1)$$

where: $\underline{\omega}$ = rigid body angular rate vector

$\hat{\underline{\alpha}}$ = Euler angles

\underline{u} = actuator torques

and the definitions of the matrices G , L , K , C_s and K_s are given in the appendix.

If these vectors and matrices are expanded in terms of their scalar components and elements, respectively, they may be rearranged in such a way that scalars associated with a specific axis of the model are grouped into the same subvector. Each coefficient matrix appearing in the resulting state variable model may be written in the following form:

$$\dot{\underline{x}}_j = \sum_{k=1}^3 (A_{jk} \underline{x}_k + B_{jk} \underline{u}_k) \quad j = 1, 2, 3 \quad k = 1, 2, 3 \quad (2)$$

where:

$$\begin{aligned}\underline{x}_k &= (\underline{\omega}_k^T, \underline{\alpha}_k^T)^T \\ A_{jk} &= \begin{bmatrix} \hat{G}_{jk} L_k C_{sk} & \hat{G}_{jk} L_k K_{sk} \\ K_{jk} & [0] \end{bmatrix} \quad B_{jk} = \begin{bmatrix} \hat{G}_{jk} \\ [0] \end{bmatrix} \quad [0] = 10 \times 10 \text{ zero matrix} \\ \underline{\omega}_1 &= (\omega_{1x}, \omega_{2x}, \dots, \omega_{10x})^T \quad \underline{\omega}_2 = (\omega_{1y}, \omega_{2y}, \dots, \omega_{10y})^T \\ \underline{\omega}_3 &= (\omega_{1z}, \omega_{2z}, \dots, \omega_{10z})^T \\ \underline{u}_k \quad (k = 1, 2, 3) &\text{ has scalar expansion of the same form as } \underline{\omega}_k\end{aligned}$$

$$\underline{a}_1 = (\phi_1, \Delta\phi_{12}, \Delta\phi_{13}, \Delta\phi_{24}, \Delta\phi_{35}, \Delta\phi_{16}, \Delta\phi_{67}, \Delta\phi_{78}, \Delta\phi_{89}, \Delta\phi_{9,10})^T$$

$$\underline{a}_2 = (\theta_1, \Delta\theta_{12}, \Delta\theta_{13}, \dots, \Delta\theta_{9,10})^T$$

$$\underline{a}_3 = (\psi_1, \Delta\psi_{12}, \Delta\psi_{13}, \dots, \Delta\psi_{9,10})^T$$

Using the definitions of matrices G, L, K, C_g, and K_g as given in the appendix, L_k is a 10 x 9 matrix of the same form as the 10 x 9 partitioned matrix L, with "1" in the place of each submatrix "I" and "0" in place of each submatrix "[0]". K_{g1} is a 9 x 10 matrix of the same form as the 9 x 10 partitioned matrix, K_g with "k12x" in the place of each 3 x 3 submatrix "K12" and similar substitutions for the remaining submatrices. C_{g1} is a 9 x 10 matrix similarly developed from the 9 x 10 partitioned matrix C_g. The matrices K_{g2} are similarly expanded with the subscript, y, in the place of x as are the submatrices K_{g3} and C_{g3} with the subscript, z, in the place of x, K_{jk} = [0] for k ≠ j. For k = j, it is a 10 x 10 matrix of the same form as the partitioned matrix K, with "1" in the place of each "I" and "0" in the place of each "[0]".

4. MULTILEVEL STATE VARIABLE MODEL

The subscripts appearing in the state variable rotational dynamics model, equation (2), correspond to the axes of the model. The matrix coefficients, A_{jk} and B_{jk}, represent interaxial coupling with k ≠ j. This model may be recast into multilevel form by decomposing it into a series of submodels. Decomposition temporarily suppresses the interaxial coupling in the overall model producing three single axis submodels and a coordination submodel. It is effected by writing the following coordination equations which constitute the coordination subproblem.

$$\underline{a}_j = \sum_{\substack{k=1 \\ k \neq j}}^3 (A_{jk} \underline{d}_j^k + B_{jk} \underline{s}_j^k) \quad j = 1, 2, 3 \quad (3)$$

$$\underline{d}_j^k = \underline{x}_k \quad \underline{s}_j^k = \underline{u}_k \quad k \neq j = 1, 2, 3 \quad (4)$$

Equation set (4) is in the form of Gauss-Seidel coordination as presented in Wismer (7).

Substitution of equation sets (3) and (4) into the state variable rotational dynamics model of equation (2) yields three submodels of the following form.

$$\dot{\underline{x}}_j = A_{jj} \underline{x}_j + B_{jj} \underline{u}_j + \underline{a}_j(t) \quad j = 1, 2, 3 \quad (5)$$

The four submodels developed in this section may be assembled into the two level hierarchy shown in Figure 4.

Corresponding to the decomposed state variable equations of this model, a decomposed performance index and a decomposed Hamiltonian are constructed.

4.1 Decomposed Performance Index and Hamiltonian

The decomposed performance index for the application of optimal attitude control to this vehicle may be written as follows:

$$J = \sum_{j=1}^3 \int_{t_0}^{t_f} P_j dt \quad (6)$$

where:

$$P_j = \frac{1}{2} (\underline{x}_j - \underline{x}_{jd})^T Q_j (\underline{x}_j - \underline{x}_{jd}) + \frac{1}{2} \underline{u}_j^T W_{ju} \underline{u}_j \quad \underline{x}_{jd} = \text{prespecified desired value of } \underline{x}_j$$

Q_j = positive definite state variable error weighting coefficient matrix

W_{ju} = positive definite control energy weighting coefficient matrix

The corresponding decomposed Hamiltonian expressing the energy state of the system is written as follows.

$$H = \sum_{j=1}^3 H_j \quad (7)$$

where:

$$H_j = P_j + \lambda_j^T \left[A_{jj}x_j + B_{jj}u_j + \sum_{\substack{k=1 \\ k \neq j}}^3 (A_{jk}d_j^k + B_{jk}s_j^k) \right] + \sum_{\substack{k=1 \\ k \neq j}}^3 (\rho_j^k)^T (x_j - d_k^j) + (\nu_j^k)^T (u_j - s_k^j) \quad (8)$$

λ_j = jth vector costate variable (Lagrange multiplier)

d_j^k, s_j^k, ρ_j^k , and ν_j^k = Gauss-Seidel type vector coordination variables

4.2 Costate Equations

The costate equations result from application of the following necessary condition for minimization of the decomposed Hamiltonian:

$$\dot{\lambda}_j = - \frac{\partial H}{\partial x_j} = - A_{jj}^T \lambda_j - Q_j (x_j - x_{jd}) + b_j(t) \quad (9)$$

where:

$$b_j(t) = - \sum_{\substack{k=1 \\ k \neq j}}^3 \rho_j^k \quad \lambda_j(t_f) = 0 \text{ (final boundary conditions)} \quad (10)$$

4.3 Control Equations

The control equations result from application of the following necessary condition for minimization of the Hamiltonian:

$$\frac{\partial H}{\partial u_j} = 0 + u_j = - W_{ju}^{-1} (B_{jj}^T \lambda_j + \sum_{\substack{k=1 \\ k \neq j}}^3 \nu_j^k) \quad (11)$$

4.4 Combination of jth State, Control, and Costate Equations Into The jth TPBV Subproblem

Substitution of the jth control equation into the jth state equation yields a new state equation in terms of x_j and λ_j . Association of the jth costate equation with the equation representing the combination of the state equation and the control equation results in the jth two-point boundary value (TPBV) subproblem.

$$\dot{x}_j = A_{jj}x_j + R_j\lambda_j + \hat{a}_j(t) \quad \dot{\lambda}_j = - Q_jx_j - A_{jj}^T\lambda_j + \hat{b}_j(t) \quad (12)$$

where:

$$\hat{a}_j(t) = \sum_{\substack{k=1 \\ k \neq j}}^3 (A_{jk}d_j^k + B_{jk}s_j^k - B_{jj}\nu_j^k) \quad \hat{b}_j(t) = Q_jx_{jd} - \sum_{\substack{k=1 \\ k \neq j}}^3 \rho_j^k \quad R_j = -B_{jj}W_{ju}^{-1}B_{jj}^T$$

$$x_j(t_0) = x_{j0} \text{ (initial boundary conditions)}$$

$$\lambda_j(t_f) = 0 \text{ (final boundary conditions)}$$

Solution of the subproblems requires an extension of the LQR techniques to reflect the presence of the additional terms on the right hand side of the corresponding TPBV subproblems. This extension, which was presented in Chichester (8), begins with generalizing the assumed form of λ in terms of x to the following,

$$\lambda(t) = K(t)x(t) + m(t) \quad (13)$$

where $K(t)$ and $m(t)$ are a time variable matrix and vector, respectively, to be determined. The assumed form of λ results in the generation of two simultaneous Riccati type equations to be solved for $K(t)$ and $m(t)$. Substitution of these solutions into equation (13) yields the feedback control to minimize the performance index at time t_f . It should be noted that the corresponding solutions to the TPBV subproblems are obtained subject to the value of the coordination variables d_j^k, s_j^k, ρ_j^k and ν_j^k .

4.5 Assembly of Coordination Equations Into the Coordination Subproblem

The remaining necessary conditions for minimization of the Hamiltonian result in additional coordination equations to be satisfied.

$$\begin{aligned} \frac{\partial H_j}{\partial \underline{p}_j} = 0 \rightarrow \underline{d}_j^k &= \underline{x}_j & \frac{\partial H_j}{\partial \underline{v}_j} = 0 \rightarrow \underline{s}_j^k &= \underline{u}_j \\ \frac{\partial H}{\partial \underline{d}_j} = 0 \rightarrow \underline{p}_j^k &= A_{kj}^T \underline{\lambda}_k & \frac{\partial H}{\partial \underline{s}_j} = 0 \rightarrow \underline{v}_j^k &= B_{kj}^T \underline{\lambda}_k \end{aligned} \quad (14)$$

The top two of the above coordination equations are associated with the state equations while the bottom two are associated with the costate equations. All of the coordination equations are assembled into an overall coordination subproblem. Inputs for this coordination subproblem are state vectors, \underline{x}_j , control vectors, \underline{u}_j , and costate vectors, $\underline{\lambda}_k$, obtained as solutions of the j th and k th TPBV subproblems, respectively.

4.6 Construction of the Subproblem Hierarchy

The original problem of generating the optimal attitude control contours for the prototype flexible space vehicle has been transformed into a series of interrelated subproblems to be solved. Due to these interconnections it is evident that these subproblems can be assembled into a hierarchy with the coordination subproblem at its apex. This hierarchy is depicted in Figure 4. Solution of the overall optimal attitude control problem is attained by iteration between the levels of the hierarchy. The modification of the space platform's configuration by adding or removing modules is treated at the first level subproblem as presented in Chichester (8).

5. CONCLUSION

A three axis state variable model of the rotational dynamics of a space platform, consisting of a typical flexible space vehicle connected to another space vehicle by a deployable truss, was developed utilizing augmented body techniques. The equations of the model were then linearized and recast into state variable form. The scalar equations of this model were rearranged by grouping them according to axis to attain a higher degree of block diagonalization in the coefficient matrices of the model. The resulting model consisted of three submodels with light coupling between them. The coupling between the axes of this model is light because of the symmetry of the platform, however, with an asymmetric configuration the axis cross coupling will be much stronger. Platform models with stronger coupling will be investigated in the future.

A combination of Gauss-Seidel multilevel and an extended form of LQR attitude control techniques was applied to the three coupled submodels. This approach reduced the original three dimensional attitude control problem to a set of single loop control subproblems with coordination of their solutions accomplished in a coordination subproblem. The attitude control problem was thus recast into a hierarchical form. Iteration between the subproblems, required to solve the overall attitude control problem in this form, appears to afford adaptive capabilities in the controlled system.

REFERENCES

1. Hooker, W. W. and G. Margulies, "The Dynamical Equations for an n-Body Satellite," Journal of the Astronautical Sciences, Vol. XII, No. 4, Winter, 1965, pp. 123-128.
2. Cornell, G. A., "Derivation of the Equations of Motion of the Space Base Configurations I through XII," Bendix Research Laboratories Internal Memorandum, November 3, 1977.
3. Cornell, G. A., "Space Base Mathematical Model," Bendix Research Laboratories Internal Memorandum, December 14, 1977.
4. Lipski, D. B., "Linearized Five Body Space Base Simulation Model," Bendix Research Laboratories Internal Memorandum, April 23, 1979.
5. Lipski, D. B., "Discrete Coordinate Modeling of Flexible Bodies," Bendix Engineering Development Center Internal Memorandum, January 12, 1981.
6. Chichester, F. D., "Development of a Three Axis Gauss-Seidel Multilevel Rotational Model of a Flexible Space Vehicle, "Proceedings of the Twelfth Annual Pittsburgh Conference of Modeling and Simulation, April 1981, University of Pittsburgh, Pittsburgh, Pennsylvania
7. Wismer, D. A., "Optimal Control of Distributed Parameter Systems Using Multilevel Techniques," Ph.D. dissertation, University of California, Los Angeles, California, 1966.
8. Chichester, F. D., "Application of Gauss-Seidel Multilevel Control to a Single Axis Torsional Model," Proceedings of the Space Transportation System Symposium, 1980 SAE Aerospace Congress and Exposition, October 1980, Los Angeles Convention Center, Los Angeles, California.

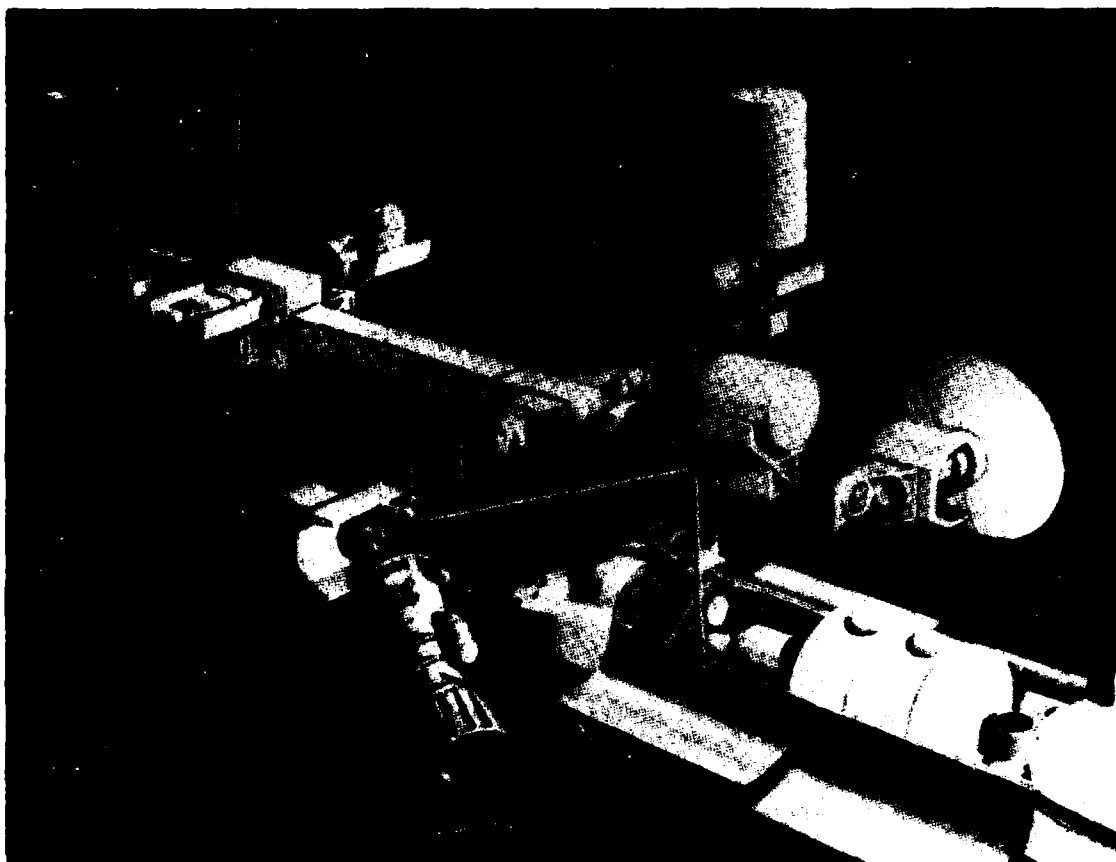


Figure 1. Second Order Science and Applications Space Platform

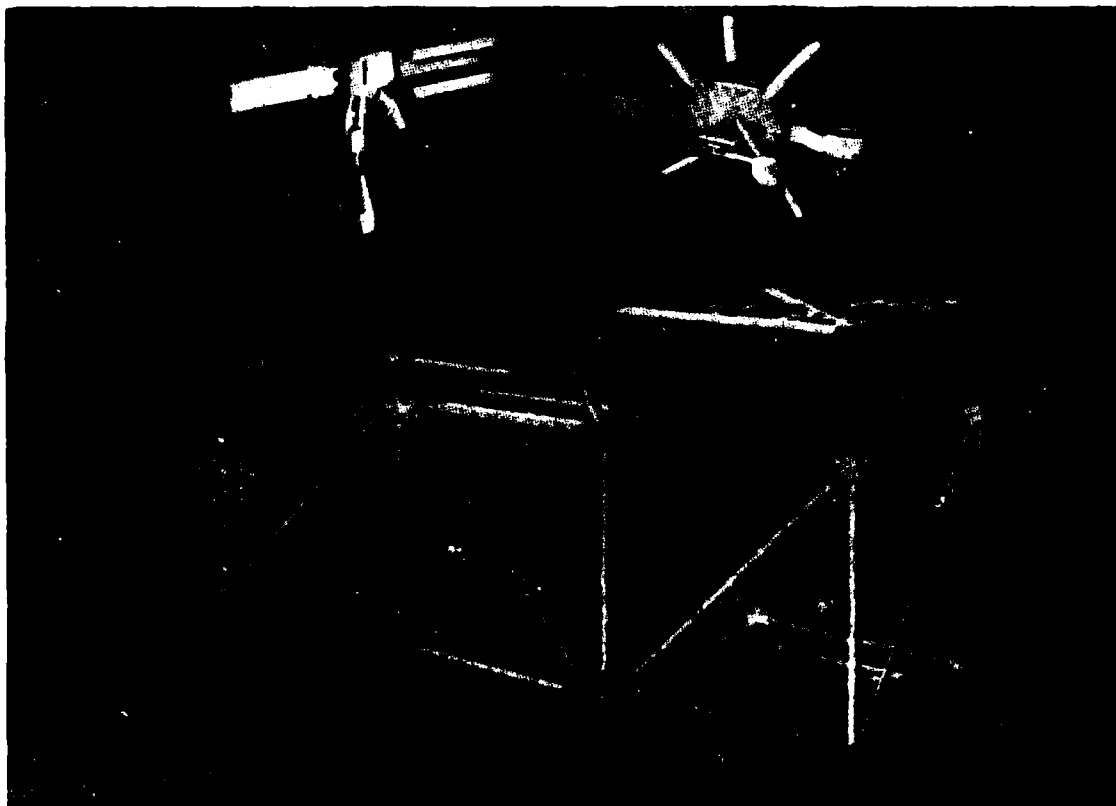


Figure 2. Deployable Truss Module

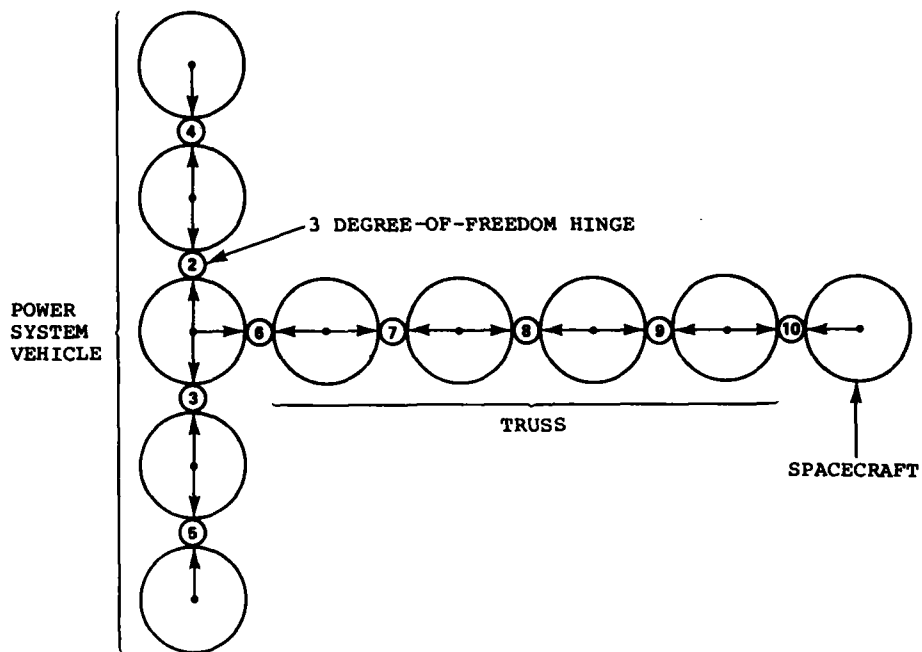


Figure 3. Topological Diagram of Discrete Mass Model of Truss Interconnecting Two Space Vehicles

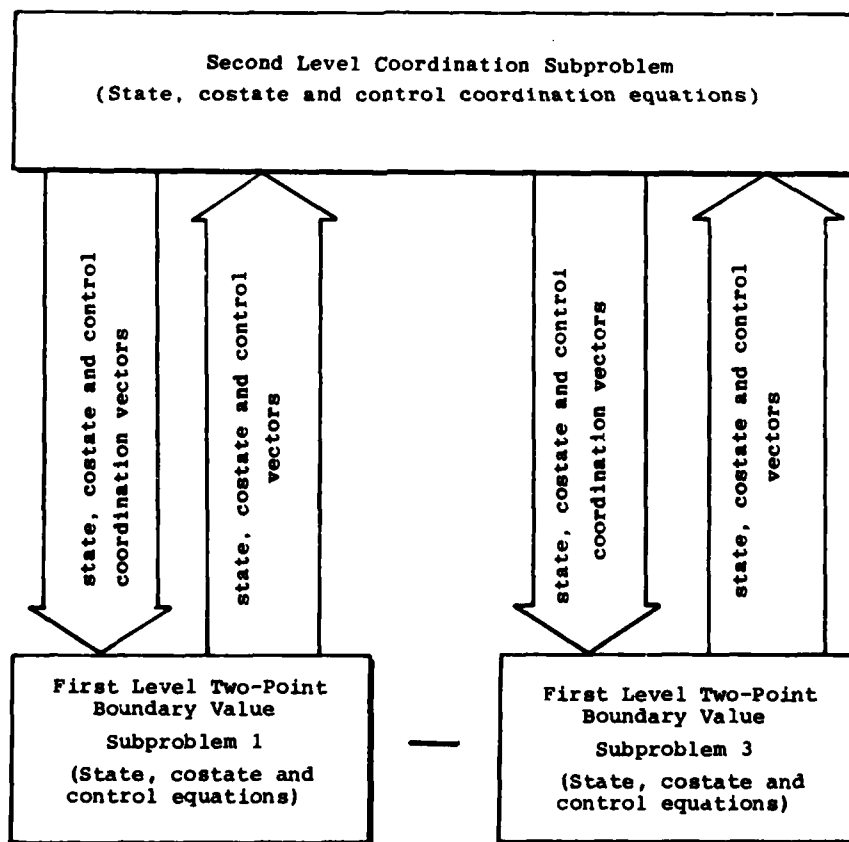


Figure 4. Subproblem Hierarchy for Combined Multilevel and LQR Attitude Control of Ten Body Model

APPENDIX

Definitions for matrices appearing in the state variable rotational dynamics model, Eq. (1).

$$G = \begin{bmatrix} g_{11} & \cdots & g_{1,30} \\ \vdots & \ddots & \vdots \\ g_{30,1} & \cdots & g_{30,30} \end{bmatrix} = A^{-1} \quad \hat{G} = \begin{bmatrix} \hat{G}_{11} & \hat{G}_{12} & \hat{G}_{13} \\ \hat{G}_{21} & \hat{G}_{22} & \hat{G}_{23} \\ \hat{G}_{31} & \hat{G}_{32} & \hat{G}_{33} \end{bmatrix}$$

$$\hat{G}_{1k}^T = [q_{1k}, q_{4k}, q_{7k}, \dots, q_{28k}]$$

$$\hat{G}_{2k}^T = [g_{2k}, g_{5k}, g_{8k}, \dots, g_{29k}]$$

$$\hat{G}_{3k}^T = [q_{3k}, q_{6k}, q_{9k}, \dots, q_{30k}]$$

$$\mathbf{g}_{j1}^T = (g_{j1}, g_{j4}, g_{j7}, \dots, g_{j28})$$

$$\mathbf{g}_{j2}^T = (g_{j2}, g_{j5}, g_{j8}, \dots, g_{j29})$$

$$\underline{g}_{j3}^T = (g_{j3}, g_{j6}, g_{j9}, \dots, g_{j30})$$

SUSPENSION MATRIX

$$L = \begin{bmatrix} -I & -I & [0] & [0] & -I & [0] & [0] & [0] & [0] \\ I & [0] & -I & [0] & [0] & [0] & [0] & [0] & [0] \\ [0] & I & [0] & -I & [0] & [0] & [0] & [0] & [0] \\ [0] & [0] & I & [0] & [0] & [0] & [0] & [0] & [0] \\ [0] & [0] & [0] & I & [0] & [0] & [0] & [0] & [0] \\ [0] & [0] & [0] & [0] & I & -I & [0] & [0] & [0] \\ [0] & [0] & [0] & [0] & [0] & I & -I & [0] & [0] \\ [0] & [0] & [0] & [0] & [0] & [0] & I & -I & [0] \\ [0] & [0] & [0] & [0] & [0] & [0] & [0] & I & -I \\ [0] & [0] & [0] & [0] & [0] & [0] & [0] & [0] & I \end{bmatrix}$$

$$I = \begin{bmatrix} 1 & 0 & 0 \\ 0 & 1 & 0 \\ 0 & 0 & 1 \end{bmatrix} \quad [0] = \begin{bmatrix} 0 & 0 & 0 \\ 0 & 0 & 0 \\ 0 & 0 & 0 \end{bmatrix}$$

SPRING CONSTANT MATRIX

[illegible]

DAMPING COEFFICIENT MATRIX

[illegible]

TRANSFORMATION MATRIX

[illegible]

DYNAMIC CONTROL OF LARGE SPACECRAFT - A SURVEY OF TECHNIQUES

R.C. Rogers
Dynamics Engineer
British Aerospace Dynamics Group
Space and Communications Division
Site B, Gunnels Wood Road,
Stevenage, Hertfordshire SG1 2AS
United Kingdom.

M. Burton
Assistant Group Leader
British Aerospace Dynamics Group
Space and Communications Division
Site B, Gunnels Wood Road,
Stevenage, Hertfordshire SG1 2AS
United Kingdom.

SUMMARY

A number of techniques for the dynamic control of large spacecraft are discussed. The main problems identified are the high order of the system and model accuracy.

One basic approach is to design a controller for a low order model obtained by truncating modes from the system model. This may lead to instability problems due to interaction with unmodelled modes. A number of techniques are discussed which aim to avoid or overcome these problems.

An alternative approach to controller design aims at ensuring stability in the presence of modelling errors and truncated modes. In the simplest case this involves direct output feedback. A technique which enables a dynamic approach to be used is also discussed although it uses rate measurement and can therefore only be applied to vibration control.

A brief comparison of the various control approaches applied to the control of a large platform is presented.

1. INTRODUCTION

With the introduction of the Space Transportation System the construction of large space structures for use in communications, scientific and solar power applications will become feasible. In order to minimize the mass of these structures they will be flexible and control systems capable of controlling their vibration will be necessary. In this paper the nature of this control problem is discussed, a number of approaches are described and their relative merits assessed.

2. THE CONTROL PROBLEM

In general the space structures under consideration will have the usual modes of rotation and translation of a rigid spacecraft, together with an infinite number of modes corresponding to flexure of the structure. In order to obtain mathematical models of the systems, techniques such as finite element analysis will be needed. Techniques are available for the construction of models consisting of interconnected elastic bodies.

Consider a large flexible space structure provided either with a number of actuators applying a torque and sensors measuring angular position, or, alternatively, with actuators applying a force to the structure and sensors measuring linear displacement. The structure dynamics may be represented by the generalized wave equation

$$m(r)\rho_{tt}(r,t) + 2\zeta L\rho_t(r,t) + L^2\rho(r,t) = \sum_{i=1}^m \alpha_i(r)u_i \quad (2.1)$$

where $\rho(r,t)$ represents the displacement from the equilibrium position at point r of the structure in response to the applied force distribution due to the inputs u_1, \dots, u_m to the actuators. $m(r)$ is the mass density of the structure as a function of position r . L is a symmetric, non negative, time invariant differential operator. ζ is a non negative real number representing the damping coefficient of the structure. Here it is assumed the damping is constant throughout the structure. Typically ζ will be very small.

Consider $m(r) = 1$ by scaling $\rho(r,t)$ as necessary. Then the operator L has distinct eigenvalues $\lambda_i, i=1, \dots, \infty$ and orthogonal eigenfunctions $\phi_i(r)$. This enables a transformation to be made by defining x_i so that

$$\rho(r,t) = \sum_{i=1}^{\infty} x_i \phi_i(r) \quad (2.2)$$

$$\ddot{x}(t) + 2\zeta\Omega\dot{x}(t) + \Omega^2 x(t) = Ru(t) \quad (\Omega \text{ diagonal}) \quad (2.3)$$

and the measurements, $y_i, i=1, \dots, p$ are given by

$$y = Sx.$$

For practical purposes only a finite number of modes need be considered since very high frequency modes will have negligible effects. Ω, R, S will then be matrices and will be available, for example, by finite element analysis. Because of the special properties of mechanical structures and the types of actuators and sensors used, $S = \nu R^T$ ($\nu > 0$) if actuators and sensors are colocated.

This system may be written in standard state space form as follows:

$$\dot{v} = \begin{bmatrix} 0 & I \\ -\Omega^2 & 2\zeta\Omega \end{bmatrix} v + \begin{bmatrix} 0 \\ R \end{bmatrix} u \quad (2.4)$$

$$y = [S \ 0] v \quad (y \text{ is the position vector at actuator locations})$$

$$v = \begin{bmatrix} x \\ \dot{x} \end{bmatrix}$$

The model derived by finite element analysis is likely to be too large for direct use in controller design, and so lower order models are needed. Certain modes are selected as being particularly important and the remainder ('residual' modes) truncated by deleting the appropriate rows and columns of the system matrices. If x_N corresponds to retained modes and x_R to residual modes, with

$$v_N = \begin{bmatrix} x_N \\ \dot{x}_N \end{bmatrix}, \quad v_R = \begin{bmatrix} x_R \\ \dot{x}_R \end{bmatrix}, \quad y = \begin{bmatrix} C_N & C_R \end{bmatrix} \begin{bmatrix} v_N \\ v_R \end{bmatrix}$$

the system may be written

$$\frac{d}{dt} \begin{bmatrix} v_N \\ v_R \end{bmatrix} = \begin{bmatrix} A_N & 0 \\ 0 & A_R \end{bmatrix} \begin{bmatrix} v_N \\ v_R \end{bmatrix} + \begin{bmatrix} B_N \\ B_R \end{bmatrix} u \quad (2.5)$$

If an observer is used to reconstruct v_N from the measurements y neglecting the residual modes, the estimate is given by

$$\frac{d}{dt} \hat{v}_N = A_N \hat{v}_N + B_N u + K(y - C_N \hat{v}_N) \quad (2.6)$$

If this is used to control the system using feedback $u = -G\hat{v}_N$ it follows that

$$\frac{d}{dt} \begin{bmatrix} v_N \\ v_R \\ e \end{bmatrix} = \begin{bmatrix} A_N - B_N G & 0 & -B_N G \\ -B_R G & A_R & -B_R G \\ 0 & K C_R & A_N - K C_N \end{bmatrix} \begin{bmatrix} v_N \\ v_R \\ e \end{bmatrix} \quad (2.7)$$

$$y = C_N \hat{v}_N + C_R v_R$$

The effect of the residual modes on the system depends on their coupling with the retained modes in the control model and the observer modes. This depends on the terms $-B_R G$ and $K C_R$ in the second row and column respectively.

In [1] a sufficient condition is given for the stability of this system in terms of the matrix $K C_R$ and the stability margin (slowest decay rate) of the system without this coupling term. This interaction of the residual modes and the modelled system is known as spillover, and is the fundamental problem which occurs when designing controllers using truncated models. It is particularly important in the case of large space structures which have low inherent damping, since the residual modes can easily become unstable.

A number of authors have discussed the problem of selecting modes for retention in a control model [2,3,4,5,6]. An interesting concept is the model completeness index of [2]. This indicates the effect of truncation by considering the proportion of structure momentum interaction corresponding to the modelled modes. The index tends to unity as the number of modes is made large.

3. CONTROLLER DESIGN APPROACHES

Three control objectives may be considered.

- reduction of structure vibration
- attitude control of part of the structure (e.g. pointing an antenna)
- shape control of the structure.

The shape control problem, applicable for example to large antennas, is the most difficult case, likely to lead to large numbers of actuators and sensors. Vibration and attitude control are of most interest here. A number of approaches to attitude control using a truncated control model are described and these could also be applied to vibration control. Also direct output feedback and a related approach are considered, which aim primarily at vibration control of the whole structure but which might be adapted with suitable actuator placement to attitude control.

Many physical constraints on system design involve hardware availability and precision. Actuators and sensors here are assumed to be perfectly linear devices giving immediate response. In practice this will not be the case, and there may also be restrictions on device locations such as requiring a particular field of view.

Approaches to control system design are now described and some aspects of their performance in the context of large platform control are summarized in Table 1.

3.1 Model Truncation

This is simply the implementation of a controller designed for the truncated control model. Consider system (2.7) where additional terms are included to represent disturbances and observation noise, so that

$$\frac{d}{dt} \begin{bmatrix} v_N \\ v_R \\ e \end{bmatrix} = \begin{bmatrix} A_N - B_N G & 0 & -B_N G \\ -B_R G & A_R & -B_R G \\ 0 & K C_R & A_N - K C_N \end{bmatrix} \begin{bmatrix} v_N \\ v_R \\ e \end{bmatrix} + \begin{bmatrix} D_N W \\ D_R W \\ K n \end{bmatrix}, \quad y = C_N v_N + C_R v_R + n \quad (3.1.1)$$

One approach is to determine feedback matrix G by optimum control theory to minimize an appropriate cost function of form

$$\lim_{t \rightarrow \infty} E (v_N^T Q_N v_N + u^T R_u u)$$

where E is the mathematical expectation and t time, the residual modes being neglected. K is selected as the steady state Kalman gain for the truncated system, assuming whiteness of the noise processes.

This approach takes no account of the spillover problem and so is likely to lead to an unstable system. Other approaches modify this design to avoid spillover, or provide techniques to overcome instability when this initial design is evaluated.

3.2 Equilibrium Enforcing Optimal Control (Sesak)

This approach, alternatively known as the Singular Perturbation method is described in [7]. The controller is of form (2.6) but with the feedback gain G chosen in a manner which reduces the excitation of residual modes. This requires the designer to have knowledge of these modes and in practice there will be further residuals not known to him. The aim of the approach is to constrain the residual state v_R to be constant (effectively preventing excitation of residual modes). From (2.5) this means

$$\dot{v}_R = A_R v_R + B_R u = 0$$

$$\text{so } v_R = -A_R^{-1} B_R u$$

(3.2.1)

This expression is used to eliminate v_R from an optimal control cost function. Suppose this is

$$J = \int_0^\infty (v_N^T Q_N v_N + v_R^T Q_R v_R + u^T R_u u) dt \quad (3.2.2)$$

where Q_N , Q_R and R_u are constant positive semidefinite matrices (R_u positive definite). Substituting for v_R gives

$$J_1 = \int_0^\infty (v_N^T Q_N v_N + u^T [R_u + B_R^T (A_R^{-1})^T Q_R (A_R^{-1}) B_R] u) dt \quad (3.2.3)$$

This approach provides a systematic way for reducing spillover to a number of residual modes by a suitable choice of Q_R , assumed diagonal. This is chosen to give the best control consistent with spillover limitations.

It has been shown that this technique is sensitive to errors in the control model parameters and an approach which aims to overcome this is proposed. The state vector is augmented by v_S consisting of the partial derivatives of v_N with respect to uncertain parameters in the control model. The previous ideas are then applied to constrain to zero

$$\frac{d}{dt} \begin{bmatrix} v_R \\ v_S \end{bmatrix}$$

By choosing suitable values of coefficient matrices Q_R , Q_S in the cost function a compromise is made between performance, spillover reduction and robustness.

3.3

Balas's Cancellation Technique

A basic control system is designed using the truncated control model as in Section (3.1). Consider the system (2.5) with v_N 2N-dimensional, v_R 2R-dimensional, u m-dimensional and y p-dimensional. The technique modifies the control law and observer equation (2.6) in order to eliminate excitation of the remainder of the system by a number of selected residual modes. These are chosen following evaluation of the basic control approach based on truncation (see 3.1) in order to overcome stability problems. This technique is described in [8].

A maximum of P/2 residuals may be selected. The technique involves an additional control term based on the innovations process

$$H_N(y - C_N \hat{v}_N)$$

and a modification to the input term of the observer dynamics.

The input term to the system (2.5) becomes

$$u = -G_N \hat{v}_N + H_N(y - C_N \hat{v}_N) \quad (3.3.1)$$

and the observer equation (2.6) becomes

$$\frac{d}{dt} \hat{v}_N = A_N \hat{v}_N + B_N u + K(y - C_N \hat{v}_N) + T_Q B_Q u \quad (3.3.2)$$

where A_Q , B_Q , C_Q are formed by taking rows and columns of A_R , B_R , C_R corresponding to the Q modes from which spillover is to be cancelled, and T_Q is the solution of

$$(A_N - K C_N) T_Q - T_Q A_Q + K C_Q = 0 \quad (T_Q \text{ is } 2N \times 2Q) \quad (3.3.3)$$

$$\text{Let } C_E = C_Q - C_N T_Q, \quad C_E^\# = (C_E^T C_E)^{-1} C_E^T \quad (3.3.4)$$

$$\text{Then } H_N = G T_Q C_E^\# \quad (3.3.5)$$

The overall system matrix now becomes, for state

$$\begin{bmatrix} v_N \\ v_Q \\ v_\beta \\ e \end{bmatrix} \quad e = \hat{v}_N - v_N - T_Q v_Q \quad (3.3.6)$$

$$\begin{bmatrix} A_N - B_N G & 0 & B_N H_N C_\beta & -B_N G - B_N H_N C_N \\ -B_Q G & A_Q & B_Q H_N C_\beta & -B_Q G - B_Q H_N C_N \\ -B_\beta G & 0 & B_\beta H_N C_\beta & -B_\beta G - B_\beta H_N C_N \\ 0 & 0 & K C_\beta & A_N - K C_N \end{bmatrix}$$

Therefore there is no excitation of other modes due to the cancelled modes corresponding to A_Q , though the cancelled modes will still be excited. Note here the cancelled and residual modes have been separated for convenience. There is no restriction over which residual modes are chosen for cancellation.

The system (A_N, B_N, C_N) is assumed controllable and observable. Then the following conditions are sufficient for the existence of a unique solution to (3.3.3).

- (i) $A_N - K C_N$ and A_Q have no common poles
- (ii) $2Q \leq \text{rank}(C_E) \leq P \leq 2R$ (note: C_E is P by 2Q)

In fact $2Q \leq \text{rank}(C_E)$ is necessary and implies both position and rate measurements must be available (i.e. at least Q position and Q rate measurements). If only position measurements are available the rank of C_E can be no greater than Q.

Since this technique is based on cancellation of terms due to normal and innovations feedback, and uses the parameter values of the control model and cancelled modes in a complicated design procedure, there may be parameter sensitivity problems.

3.4 Additional Direct Output Feedback

In this approach rate output feedback is used to stabilise the system designed using the approach in Section 3.1, which may suffer from spillover problems. In the system (2.5) where the actuators and sensors are assumed to be colocated the control law is changed to

$$u = -G_N \dot{y} + F \dot{y} \quad (3.4.1)$$

Because of the property $S = \mu R^T$ in (2.4)

$$\dot{y} = \mu \begin{bmatrix} B_N \\ B_R \end{bmatrix}^T \begin{bmatrix} v_N \\ v_R \end{bmatrix}, \mu > 1$$

Therefore the system becomes

$$\frac{d}{dt} \begin{bmatrix} v_N \\ v_R \end{bmatrix} = \begin{bmatrix} A_N & 0 \\ 0 & A_R \end{bmatrix} \begin{bmatrix} v_N \\ v_R \end{bmatrix} + \mu \begin{bmatrix} B_N \\ B_R \end{bmatrix} F \begin{bmatrix} B_N \\ B_R \end{bmatrix}^T \begin{bmatrix} v_N \\ v_R \end{bmatrix} - \begin{bmatrix} B_N \\ B_R \end{bmatrix} G_N^T \quad (3.4.2)$$

If F is chosen negative semidefinite (for example $F = -kI$, $k > 0$) the contribution of the direct output feedback to the system matrix

$$\mu \begin{bmatrix} B_N \\ B_R \end{bmatrix} F \begin{bmatrix} B_N \\ B_R \end{bmatrix}^T$$

is negative semidefinite. This form of F implies energy absorption at the actuator locations.

This approach is only immediately applicable to systems with colocated actuators and rate sensors.

Several studies have used this technique in controller design [9,10]. An alternative approach is to apply the direct output feedback before designing the 'optimal' controller for the reduced order model.

3.5 Pure Direct Output Feedback

A number of papers [11,12,13] consider the use of direct output feedback alone for the control of large space structures. Some of these consider the use of passive devices. When active devices are used it is important to consider the effect of phase lags in the actuators and sensors on the high frequency modes. These are not included here.

The approach taken here is to apply local position (angular or linear) feedback to establish attitude control and then apply rate feedback to damp the vibrations. The system following the application of local position feedback may be written in the form (mode shapes and frequencies will in general be different to those in (2.5))

$$\frac{d}{dt} \begin{bmatrix} \omega_1 x_1 \\ \omega_N x_N \\ \dot{x}_1 \\ \dot{x}_N \end{bmatrix} = \begin{bmatrix} 0 & \Omega \\ -\Omega & D \end{bmatrix} \begin{bmatrix} \omega_1 x_1 \\ \omega_N x_N \\ \dot{x}_1 \\ \dot{x}_N \end{bmatrix} + B_u u; y = C \begin{bmatrix} x_1 \\ x_N \end{bmatrix} \quad (3.5.1)$$

where $B = \begin{bmatrix} 0 \\ R \end{bmatrix}$, $C = \mu R^T$, $\Omega = \text{diag}(\omega_1, \dots, \omega_N)$, D negative

semidefinite.

For the cost function

$$\int_0^\infty (\sigma \dot{y}^T \dot{y} + u^T u) dt, \quad \sigma > 0$$

the optimal control law obtained from the (steady state) Ricatti equation is, taking $D = 0$ (no inherent damping)

$$u = -(\sqrt{G}/\mu)\dot{y}$$

This motivates the use of local rate feedback to minimize vibration at the actuator/sensor locations. Similarly, control laws of the form

$$u = -M\dot{y}$$

may be motivated for positive semidefinite M .

If the overall feedback for the system (2.5) is

$$u = -(J_1 y + J_2 \dot{y}) \quad (3.5.2)$$

with J_1 and J_2 both positive semidefinite symmetric matrices stability is assured since the effect of J_1 is equivalent to the attachment of passive devices (springs at the actuator locations) and the effect of rate feedback is to remove energy from the system.

As reported in [11] there is a limit to the amount of rate feedback which can be usefully applied for vibration control. High gains will result in low amplitude vibrations at the actuators but the mode shapes will change so that the structure vibrates between the actuators. In the extreme case the actuator locations will be stationary and the vibrations elsewhere will have only inherent structure damping. For some intermediate feedback gains the overall vibrations can be minimized.

3.6

Robust Controllers

The possibility of designing controllers with the general structure of section 3.1 but having guaranteed robustness properties is discussed in [14]. The approach discussed here is a special case of these controllers, and is a development of the pure direct output feedback approach. The rate feedback, instead of being direct uses an estimated rate value. This is derived from an observer which includes only a subset of the system modes. These would generally be chosen as low frequency modes. The idea is to avoid - or reduce - the problem of direct output feedback, where control of the modes is achieved only at the actuator locations as gain increases. A suitable choice of observer gain assures system stability. This corresponds to state estimation in the presence of sensor noise and disturbances due to actuator noise, with rate measurements. That is the effect of spillover is considered as sensor and actuator noise. This controller makes the structure well behaved before the application of direct output position feedback for attitude control.

Consider the system with no feedback expressed in form (3.5.1). Instead of the control law $u = -\alpha\dot{y}$ in this case $u = -\alpha\hat{\dot{y}}$ where

$$\hat{\dot{y}} = \mu \bar{R}^T \begin{bmatrix} \hat{\dot{x}}_1 \\ \hat{\dot{x}} \end{bmatrix}, \quad n < N \quad (3.6.1)$$

The observer is

$$\frac{d}{dt} \begin{bmatrix} \hat{v} \\ \hat{w} \end{bmatrix} = \begin{bmatrix} 0 & \bar{\Omega} \\ -\bar{\Omega} & \bar{D} \end{bmatrix} \begin{bmatrix} \hat{v} \\ \hat{w} \end{bmatrix} + \beta^2 \bar{B}(y - \hat{y}) + \bar{B}u \quad (3.6.2)$$

and the observer state is

$$\begin{bmatrix} \hat{x}_1 \bar{\omega}_1 \\ \hat{x}_n \bar{\omega}_n \\ \hat{x}_1 \\ \hat{x}_n \end{bmatrix}$$

$\bar{\Omega}$, \bar{D} , \bar{B} , \bar{R} represent the truncated versions of Ω , D , B , R , and may include modelling errors.

$$\text{Writing } v = \begin{bmatrix} x_{1\omega_1} \\ x_{N\omega_N} \\ \dot{x}_1 \\ \dot{x}_N \end{bmatrix}, \text{ then } \frac{d}{dt} \begin{bmatrix} v \\ \frac{\sqrt{\beta}}{\beta} v \end{bmatrix} = M \begin{bmatrix} v \\ \frac{\sqrt{\beta}}{\beta} v \end{bmatrix} \quad (3.6.3)$$

The system matrix M may be decomposed into negative semidefinite and skew Hermitian components from which it may be concluded there are no eigenvalues with strictly positive real parts. This provides a robustness result for the controller.

In order to implement this approach with system (2.5) the feedback law is

$$u = -(J_1 y + J_2 \dot{y})$$

where y is generated by an observer of the form

$$\frac{d}{dt} \hat{v} = \begin{bmatrix} 0 & \bar{\Omega} \\ -\bar{\Omega} & \bar{D} \end{bmatrix} \hat{v} + \beta^2 \bar{B}(\dot{\hat{y}} - \hat{y}) + \bar{B}u \quad (3.6.4)$$

J_1 is positive semidefinite and J_2 diagonal (this could be relaxed) positive semidefinite.

With position feedback included in this form stability is no longer assured. However, if a high level of rate feedback is used to establish vibration control it should be possible to close position feedback loops without difficulty. An alternative is to remove the $-J_1 y$ component of the position feedback in the observer by adjusting the parameter matrices $\bar{\Omega}$, \bar{B} . This is an attractive approach in that it does assure stability, but it would probably require a more complicated procedure for design in order to obtain suitable values for the matrices.

3.7

'Forgetting Factor' in Observer

As a tentative approach to stabilizing the basic controller of Section 3.1 the matrix A_N in the observer equation (2.6) could be replaced by $A_N - \sigma I$ for small $\sigma > 0$. This corresponds to making the observer 'forget' the information presented to it in an exponential manner with time. The possible advantage of this technique, compared to the similar approach of additional direct output feedback is that the observer states are all available, so the technique may be used with non collocated actuators and sensors.

TABLE 1

Comparison of Controllers for Large Platform Control

	Advantages	Disadvantages
1. Model Truncation	Applicable to a wide range of control objectives	Liable to instability due to spillover
2. Equilibrium Enforcing Optimal Control	Reduced spillover problems	Possible parameter sensitivity
3. Cancellation Technique	Overcomes spillover from selected modes	Possible parameter sensitivity. May be difficult to apply with non colocated actuators and sensors
4. Additional Direct Output Feedback	Predictable performance	Requires colocated actuators and rate sensors
5. Pure direct output feedback	Robust to parameter errors	Limited control objectives. Requires actuators and sensors to be colocated and suitably placed
6. Robust Controller (as in Section 3.6)	Robust to parameter errors. Improved control compared to approach 5 by concentrating on most important modes.	As for approach 5
7. Forgetting Factor in observer	Applicable to non colocated actuators and sensors case.	Appears to distort control model and observer pole patterns excessively.

4. CONCLUSIONS

The approaches to the control of flexible spacecraft considered in this paper fall into two categories:

- Controllers based on truncated system models
- Controllers based on output feedback having robustness properties

Each of these has limitations. The first category is sensitive to parameter value errors and spillover effects. It may also be difficult to obtain a sufficiently accurate model for design of a controller of this type. The second category of controller is less sensitive to parameter errors, and remains stable at least for idealized actuators and sensors. However, control performance is somewhat limited, particularly since only rate measurements may be used. This precludes direct application to attitude control, though once the system has been made stable a further control loop could be added for this purpose.

The use of additional output rate feedback to overcome stability problems following application of a controller designed for a truncated model is widely discussed in the literature and appears to work well. An outstanding problem is to coordinate the design of the original controller with the output feedback. The Robust Controller also appears to give good results. The particular case discussed in this paper combines the direct output feedback approach and a truncated model of the system used in a controller. The equilibrium enforcing optimal control technique provides a systematic approach to selecting optimal control cost function control cost coefficients in order to reduce spillover. Since this coefficient is often chosen in an arbitrary way this technique should be helpful. Finally, in a practical design problem it may be possible to combine features of several approaches to achieve the desired features.

REFERENCES

1. M.J. Balas, Direct Output Feedback Control of Large Space Structures, J. Astronautical Sciences, Vol. 27 No. 2, April-June 1979, pp157-180.
2. P.C. Hughes, Modal Identities for Elastic Bodies with Applications to Vehicle Dynamics and Control, J. Applied Mechanics, March 1980.
3. P. Likins, Y. Ohkami, C. Wang, Appendage Modal Coordinate Truncation Criteria in Hybrid Coordinate Dynamic Analysis, J. Spacecraft, Vol 13 No. 10, October 1976, pp611-617.
4. P.C. Hughes, R.E. Skelton, Modal Truncation for Flexible Spacecraft, Joint Automatic Control Conference, Denver, Colorado, 1979.
5. R.E. Skelton, P.C. Hughes, Flexible Spacecraft Model Reduction and Control Design by Modal Cost Reduction, 2nd Conference on the Dynamics and Control of Large Flexible Spacecraft, Blacksberg, Virginia, 1979.
6. Y. Ohkami, Commutativity of Inversion and Truncation Operations in Modal Analysis for Flexible Large Spacecraft, 2nd Conference on the Dynamics and Control of Large Flexible Spacecraft, Blacksberg, Virginia, 1979.
7. J.R. Sesak, Control of Large Space Structures via Singular Perturbation Optimal Control, AIAA Conference on Large Space Platforms: Future Needs and Capabilities, Los Angeles, California, Sept. 1978 Paper 78-1690.
8. M.J. Balas, Enhanced Modal Control of Flexible Structures via Innovations Feedthrough, 2nd Symposium on Dynamics and Control of Large Flexible Spacecraft, Blacksberg, Virginia, 1979.
9. D.C. Herrick, J. Canavin, R. Strunce, An Experimental Investigation of Modern Modal Control, 17th Aerospace Sciences Meeting, January 1979, AIAA paper 79-0199.
10. M.J. Balas, Direct Velocity Feedback Control of Large Space Structures, J. Guidance and Control, Vol 2 No.3, May-June 1979, pp252-253.
11. T.C. Henderson, J.R. Canavin, Damping Augmentation for Large Space Structures, Structures, Structural Dynamics and Materials Conference, Bethesda Md, April 3-5, 1978, AIAA paper 78-490.
12. J.N. Aubrun, Theory of the Control of Structures by Low Authority Controllers, AIAA Conference on Large Space Platforms: Future Needs and Capabilities, Los Angeles, California, 1978, AIAA paper 78-1689.
13. J.R. Canavin, The Control of Spacecraft Vibrations using Multivariable Output Feedback, AIAA and American Astronautical Society Astrodynamics Conference, Palo Alto, California, 1978. AIAA paper 78-1419.
14. R.J. Benhabib, R.P. Iwens, R.L. Jackson, Stability of Distributed Control for Large Flexible Structures using Positivity Concepts, AIAA Guidance and Control Conference, Boulder California, 1979. AIAA paper 79-1780.

MODELING, CONTROL AND SYSTEM IDENTIFICATION METHODS FOR FLEXIBLE STRUCTURES

by

N. K. Gupta and M. G. Lyons
Integrated Systems, Inc.
151 University Avenue, Suite 400
Palo Alto, CA 94304

and

J-N. Aubrun and G. Margulies
Lockheed Palo Alto Research Laboratory
3251 Hanover Street
Palo Alto, CA 94304

SUMMARY

Modeling, control design and system identification techniques to synthesize feedback control laws for large space structures are discussed. The theoretical background is covered. Techniques are applied to a mathematical model with complexity comparable to that of real flexible spacecraft. The paper includes a tutorial description of the problem and summarizes recent developments. The discussion is oriented towards the control design engineer.

1. INTRODUCTION

Deployment of large space structures for communications, space defense, power generation, manufacturing, and research has become a major objective of space mission planners for the mid-1980's and beyond. These systems typically combine large size with extremely rigorous pointing and surface figure error requirements. There is a clear desire to achieve diffraction limited performance with large apertures and the most stringent requirements are posed by antennas operating above 10 GHz and large optical systems. Boresight jitter stabilization well below 1 μ rad and dynamic surface figure error near one twentieth of a wavelength are necessary to realize the performance capability of these large systems.

Coupled to these ultra-high performance requirements are the obvious needs to minimize spacecraft mass and construction and launch costs. High system mass may entail multiple launches and on-orbit assembly, greatly increasing system cost. In addition, structural design and materials limitations may, in many cases, make high performance unreachable with any mass in a passive system. For these missions the need to create control-configured spacecraft is clear. Our ability to conceptualize space systems, to select structural materials, and to build mechanisms for on-orbit construction and deployment has now far outstripped our demonstrated ability to control the resulting structures. Stability augmentation and its integration with flight control systems, now a well-established discipline for high-performance aircraft, must be invoked if current system concepts are to be realized. The objective of this paper is to discuss recent research results in stability augmentation for flexible spacecraft in the context of system requirements, modeling, controls synthesis, and system identification.

Control requirements for large space structures may be broadly divided into three categories: (1) attitude control in the presence of structural bending, (2) transient vibration suppression (usually required during maneuvering), and (3) suppression of steady-state vibration propagation due to on-board disturbance sources. Stability augmentation and flight control system configurations are dictated by mission-dependent mixes of these objectives. Passive structural damping can, in some cases, provide the desired performance or enhance active system performance. Such passive methods, however, have unpredictable performance characteristics, address only a small subset of the main control objectives, and in some cases can degrade system performance (see Section 4). Control requirements are an essential ingredient in proper modeling, synthesis, and evaluation activities as illustrated later in the paper.

The paper is organized into five main sections: modeling (Section 2), controls synthesis (Section 3), a complex spacecraft example (Section 4), computational considerations (Section 5), and system identification (Section 6). Hardware aspects including actuator/sensor developments, digital processor development and brassboard demonstrations constitute an adequate basis for separate papers [1,2]. These issues are not discussed here.

The subject of flexible spacecraft modeling, discussed in Section 2, has received much attention in the recent literature and the reader is directed to several references. Modeling methods are restricted to those essential for closed-loop structural control, including synthesis and performance evaluation. The role of data-base management and interfaced structural modeling and controls synthesis software is addressed both in Section 2 and later in Section 5 on numerical methods. Order-reduction of these models, necessary for controls synthesis, is addressed early in Section 3 (Controls Design), including an example, which examines modal convergence properties for a simple beam.

A two-level controls synthesis approach is developed in the remainder of Section 3. A more complete description of the methodology may be found in Ref. 3. High-authority control exploiting specific knowledge of spacecraft dynamics is combined with low-authority colocated sensor/actuator systems to control spillover and to satisfy robustness requirements. Synthesis methods using frequency-shaped quadratic costs and the basic low-authority formulas are given with a limited discussion of robustness properties as discussed previously in Refs. 4 and 5.

A non-trivial spacecraft example of a representative optical space structure, using a 120-state evaluation model, is treated in Section 4. This example illustrates both procedural techniques in synthesis and evaluation, and potential payoffs for the stability augmentation approach discussed earlier. Numerical details of the computations are discussed in Section 5.

To complete the paper, some general requirements and characteristics of system identification methods, applicable to closed-loop systems, are discussed. Traditional modal testing methods, for open-loop structures, have been found to be generally inadequate to evaluate closed-loop structural dynamics behavior. Various methods including maximum likelihood and instrumental variables are discussed. The summary and conclusions provide a status report on accomplishments and important research objectives to be addressed in the near term.

2. MODELING OF FLEXIBLE SPACECRAFT

A central issue in the active control of space structures is the development of "correct" mathematical models for the open- and closed-loop dynamical plants. While a great deal of controversy has been recently generated over finite-element methods and their assorted pitfalls, programs such as NASTRAN and SPAR are nevertheless the primary current tools for generating dynamical models of conceptual spacecraft whose structure cannot be idealized by simple models of beams, plates, and beams with lumped masses.

Finite-element structural programs generally provide the control designers with a set of modal frequencies ω_n and a set of mode shapes (eigenvectors) ϕ_n corresponding to appropriate boundary values*. These eigenvectors are given in discretized form, i.e., a set of modal displacements in the x, y, and z directions at each nodal station. In some cases, modal rotations ϕ_x, ϕ_y, ϕ_z are also required. In addition, coordinates and a "map" of the structure's nodes must be provided to allow the reconstruction of physical displacements in terms of their modal expansions.

The important point here is that, for any nontrivial flexible satellite configuration, the volume of information is so large that the data handling must remain entirely within the computer and its mass-storage facilities. Development of this data base, in a form usable by control synthesis software, is a fundamental necessity for the synthesis and evaluation of complex controls which require modal truncation, actuator/sensor location and type changes, and evaluation of system performance for parameter and system order changes. Preparation of a structure for controls is a major part of the overall effort required to develop structural control systems.

2.1 State-Space Models

As an example, consider the dynamic equations of a structure, which are linear for small displacements and are written as

$$M\ddot{\delta} + K\dot{\delta} = f, \quad (2.1)$$

where δ is a column vector obtained by "stacking" the components of the displacements at all nodes, f is a similar vector of (control) forces applied at those nodes, and M and K are generalized mass and stiffness matrices of appropriate dimensions. The usual procedure [6] is then to diagonalize (2.1) by solving the eigenproblem:

$$M^{-1}K\phi = \phi \begin{bmatrix} -\omega_1^2 & & \\ & \ddots & \\ & & -\omega_n^2 \end{bmatrix}, \quad (2.2)$$

where ϕ is the matrix whose columns ϕ_n are the mode shapes corresponding to the modal cyclic frequencies ω_n (i.e., eigenvalues of $M^{-1}K$). Because of reciprocity properties, K and M are symmetric matrices (M is a diagonal for lumped-mass models if δ is the vector of displacement at lumped-mass locations). It is known that there exists then a normalization of ϕ (whose columns are only determined up to a multiplicative constant by Eq. (2.2)) such that $\phi^T M \phi = I$, and hence, from Eq. (2.2),

$$\phi^T K \phi = \begin{bmatrix} -\omega_1^2 & & \\ & \ddots & \\ & & -\omega_n^2 \end{bmatrix}. \quad (2.3)$$

*For single-body monolithic spacecraft considerations, free-free modes are appropriate. For gimbaled multi-body structures, see discussion at the end of this subsection.

Using then the basic modal transformation $\delta = \phi q$ (where q is a vector of modal amplitudes), Eq. (2.1) is thereby transformed into the classical modal equations

$$\ddot{q} + \begin{bmatrix} -\omega_n^2 & \\ & \ddots \end{bmatrix} q = \phi^T f. \quad (2.4)$$

In general, forces are applied only at a few nodal points of the structure, via specific actuators, and there are linear relations between the set of command inputs, represented by some vector u , and the vector f or control forces, such as:

$$f = \mathcal{A} u.$$

In the same way, sensor measurements may be stacked in a vector y which is linearly related to the position and rates of the nodal points, i.e.,

$$y = \mathcal{R} \begin{bmatrix} \dot{x} \\ x \end{bmatrix} = \mathcal{R} \begin{bmatrix} \phi & 0 \\ 0 & \phi \end{bmatrix} \begin{bmatrix} \dot{q} \\ q \end{bmatrix}$$

Defining the modal state vector as

$$x \triangleq \begin{bmatrix} \dot{q} \\ q \end{bmatrix}, \quad (2.5)$$

the equations describing the dynamics of the spacecraft can be finally written in the usually first-order form:

$$\begin{aligned} \dot{x} &= Fx + Gu, \\ y &= Hx, \end{aligned} \quad (2.6)$$

where

$$F \triangleq \begin{bmatrix} -2\zeta_n\omega_n & -\omega_n^2 \\ I & 0 \end{bmatrix}, \quad G \triangleq \begin{bmatrix} \phi^T \mathcal{A} \\ 0 \end{bmatrix} \quad \text{and} \quad H = \mathcal{R} \begin{bmatrix} \phi \\ \phi \end{bmatrix}. \quad (2.7)$$

The diagonal elements $-2\zeta_n\omega_n$ are added in the F matrix to represent the (usually small) natural modal damping. The F matrix is the state-space form of the (open-loop) dynamics matrix and now has complex eigenvalues and eigenvectors. The calculation of the matrices F , G and H from the structural data and the actuator/sensor definitions usually requires a direct handling and processing of the data by digital computers since hand calculations become rapidly prohibitive for large systems. The introduction of actuator or sensor dynamics may further complicate the construction of these matrices. Nevertheless, Eqs. (2.6), along with the definitions (2.5) and (2.7) constitute the basic model for preliminary control design.

2.2 Structural Transfer Functions

Although modern control synthesis methods are principally formulated in the time domain, frequency-domain methods provide a useful complement, especially when steady-state responses are sought. In particular, combinations of frequency-domain performance criteria with time-domain synthesis methods, discussed in Section 3, can produce control designs which are accurately realized in hardware. Using Eq. (2.3) (with an added term for modal damping) one may easily obtain the open-loop modal amplitude transfer functions:

$$(q_n/f_i) = \frac{\phi_{in}}{(j\omega_n^2 + 2j\zeta_n\omega_n - \omega_n^2)}, \quad (2.8)$$

where f_i is the force acting on the i th degree of freedom and $j = \sqrt{-1}$. The linear relations between x and q , y and x and f and u make it easy to compute the other transfer functions of interest, e.g., x_k/u_i and y_e/u_i .

2.3 Nonlinear Models

For single-body monolithic structures, the fine-pointing attitude dynamics are subsumed in the rotational rigid body modes included in the modal matrix ϕ . When only small motions of a space structure are being considered, the conventional linear structural dynamics analyses (NASTRAN and SPAR) are adequate, and the rigid-body modes are formally

handled together with the elastic modes, even though the actuators necessary to control them will be different, in general, from those used to control elastic vibrations. When larger attitude angles need to be considered, and angular rates remain small, the linear equations (2.6) are still applicable provided that the rigid body modes are now given in terms of three attitude angles which then constitute the first three modal coordinates. The displacements δ_i are then interpreted as the linear deformations of the structure with respect to the rotated frame. This procedure removes the kinematic nonlinearities resulting from the linear stretching of the structure under the classical rigid-body modes. However, for large angular rates, nonlinear dynamic effects have to be modeled, even though structural deformations can still be represented by linear equations.

For multi-body configurations, such as spacecraft with gimballed power equipment sections, the dynamics become highly nontrivial. The field of multi-body dynamics was pioneered in the late sixties when, based on the earlier work of Hooker and Margulies [7,8], the first N-body attitude dynamics computer software was developed. A number of subsequent extended programs were written in the next few years, and these are documented in Ref. 9. These N-body programs provide a hybrid synthesis of large-angle nonlinear multi-rigid-body dynamics with the modal representation of linear elastic deformations used in structural mechanics. More recent models, based on T. R. Kane's formulation [10], have been developed for monolithic structures containing stored momentum [11]. However, while those dynamic models and associated computer programs are very useful for evaluation purposes, the associated nonlinear control synthesis problem is still extremely difficult to tackle and will not be discussed in this paper.

3. CONTROL DESIGN FOR LARGE SPACE STRUCTURES

Problems associated with vibration control and accurate pointing of large flexible vehicles are quite different than those posed by traditional rigid spacecraft even if they have flexible appendages. Differences in control requirements and constraints and in synthesis and evaluation methodologies are now addressed in the context of the flight control system design.

Control design is principally driven by spacecraft dynamic characteristics, performance considerations, on-board or environmental disturbances, and sensor/actuator availability. The special features of large flexible spacecraft in these four categories are summarized below.

1. There are an infinite number of elastic modes, usually with low natural damping, and the controller bandwidth extends over a significant number of these modes (Fig. 3-1). This last feature is the defining characteristic of a large space structure.
2. Flexible modes interact not only with the attitude controller but contribute directly to the deformation geometry of the structure which itself may require accurate control. Performance criteria must then be precisely formulated or the control problem is ill-posed.
3. A variety of disturbances may excite the structure and degrade its performance. Again, the formulation of the control problem will be strongly affected by the type of the disturbances and their spatial and spectral characteristics.
4. Most of the actuators and sensors currently envisioned for large space structures have only been studied theoretically. Ground experiments in active vibration control and hardware development are just beginning and it is safe to state that there is no available flight-qualified hardware. The control designer must therefore rely on believable extrapolations of available data.

The major problems encountered in the control design of large flexible spacecraft are directly due to the first three characteristics. The truly infinite-dimensional character of the structure has to be approximated by a finite-dimensional model. A good structural analysis usually generates modal models with a large number of modes which provide a

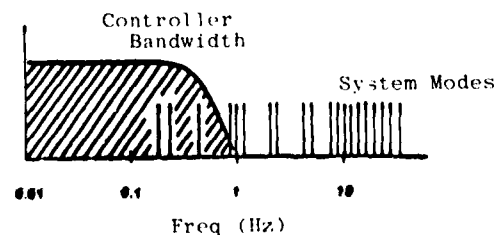


Fig. 3-1. Flexible structure mode location and controller bandwidth.

reasonable representation of the spacecraft. However, such models have two fundamental drawbacks: (1) their size is much beyond the computational capability of current control synthesis methods, and (2) the higher-frequency modes of a structural model are known only imprecisely. Indeed, modes are usually accurate in the low-frequency part of the total spectrum. They depart more and more from the actual spacecraft modes as frequency increases and can only be used in a qualitative manner in the design process. Thus, the control design must be based on a reduced-order model containing only selected low-frequency modes. This is not, by itself, a major limitation since low-frequency modes are those usually requiring most control because of their longer settling times and larger contribution to performance degradation. Nevertheless, the control design approach must properly handle the poorly known higher-frequency modes by not destabilizing them while controlling the low-frequency modes. Indeed, no matter where the controller roll-off frequency is situated, the infinite nature of the modal spectrum implies that there will be modes within and beyond the roll-off region. It has been shown [12] that destabilization is likely and almost certain to occur in the roll-off region, a situation which can only worsen for closely packed modes and low natural damping. This so-called "spillover" phenomenon is one of the most crucial problems faced by the control designer.

The high-order model is used with advantage to evaluate both spillover and the total performance of the controller, since it is this model which reflects the effects of the unmodeled modes. Finally, on-board implementation considerations may require even further reductions of the controller order with minimum degradation of closed-loop performance.

To summarize, large space structure control design usually requires three models:

1. Evaluation model (large order; e.g., 40 or more modes),
2. Control synthesis model (reduced order; e.g., 10-20 modes), and
3. Reduced-controller model (simplified controller; e.g., less than 10 modes).

Correspondingly, the overall control-design procedure includes three major steps:

1. Model reduction.— Development of reduced models for control synthesis, which essentially represent accurately the low-frequency behavior while approximating the impact of high-frequency modes on low-frequency response.
2. Control design.— Selection of actuator and sensor types and locations and of the controller structure for control synthesis.
3. Controller simplification.— Reduction of the controller obtained in the previous step to simplify implementation, and in some cases, to improve robustness.

Finally, steps 2 and 3 must be validated by checking the controller against the large evaluation model, so that spillover effects and performance of the total system may be assessed. These steps may have to be performed iteratively.

3.1 Model Reduction

Model reduction is a process by which the order of the dynamical system is reduced, for a fixed number of actuator inputs and sensor outputs. The traditional structural mechanics approach first approximates the infinite-dimensional nature of the real structure by a large, but finite, number of degrees-of-freedom representation. This approximation may be based on a direct physical interpretation in terms of lumped-masses and inter-connecting springs or on the improved "consistent mass matrix" method. Several methods can be used to further reduce the degrees of freedom, and correspondingly, the number of nodal points in the representation of the structure. Most of the techniques used in dynamics and control, however, focus on modal-coordinate reduction. Reducing the number of modes is usually done by modal truncation, whereby modes above a chosen frequency or in an intermediate frequency range are simply discarded. For large space structures control, the frequency criterion is not sufficient in general, and more sophisticated criteria need to be used, resulting in selective deletion of modes. In more general methods, the reduction involves a dimension-reducing coordinate transformation in which the individual meaning of the modes is no longer apparent [13].

In general, the requirements for model reduction for active control of large space structures must include the following:

1. The reduced model should be suitable for control design and synthesis. It should incorporate all features critical for the selection of a feedback structure and control gains.
2. The reduced model should accurately incorporate actuator effectiveness, sensor measurements and disturbance distribution [ref. 3].
3. The dynamical characteristics of interest in the structure should be represented in the reduced model.

3.1.1 Modal Representations and General Considerations

Consider a high-order large space structure model with $N \times 1$ state vector x , $q \times 1$ control vector u and $p \times 1$ output vector y :

$$\dot{x} = Fx + Gu, \quad (3.1)$$

$$y = Hx + Du. \quad (3.2)$$

The transfer function between y and u is

$$y(s) = [H(sI - F)^{-1}G + D] u(s) \\ \triangleq T(s) u(s). \quad (3.3)$$

The transfer function may be expanded about the N poles of the system. Because of the particular form of Eqs. (3.1) and (3.2), the number of zeros does not exceed the number of poles, and the expansion takes the general form:

$$T(s) = R_0 + \frac{R_1}{(s-\lambda_1)} + \frac{R_2}{(s-\lambda_2)} + \dots + \frac{R_N}{(s-\lambda_N)}, \quad (3.4)$$

where the R 's represent constant coefficient matrices. For any input-output pair (k, l) the transfer function may also be written as a ratio of zeros and poles:

$$T_{kl}(s) = \frac{g(s-z_1)(s-z_2) \dots (s-z_M)}{(s-\lambda_1)(s-\lambda_2) \dots (s-\lambda_N)}, \quad (3.5)$$

where the scalar g and the zero's z_i depend upon the choice of k and l . In most representations, the number of zeros is less than or equal to the number of poles.

If the model is to be reduced to n states, the number of poles will drop to n . Criteria have to be developed to determine the set of poles which may be dropped, along with the corresponding set of modes. These criteria must consider the following:

1. Any mode which is uncontrollable and undisturbable or unobservable can be dropped. Either of these conditions corresponds to a zero residue or a perfect pole-zero cancellation in all transfer functions.
2. Controllable modes should not necessarily be discarded even if they are nondisturbable and add nothing to the cost functional, since they may be excited by the control actuators.
3. Highly controllable modes in the bandwidth of interest should be retained even if they are not disturbable or observable. Similarly, highly observable modes should be retained for robustness reasons.
4. Proper mode ordering based on cost analysis [13] should include the above factors in addition to performance considerations.

For very small feedback gains, the rate at which the poles migrate depends upon the residues. High-gain, closed-loop behavior is described more accurately by open-loop poles and zeros. Therefore, an ideal reduced-order model should maintain the residues of the retained poles and zeros in the spectrum of interest. Unfortunately, both zeros and residues cannot be preserved simultaneously. The attempt, in reduced-order modeling methods, is to maintain either poles or zeros or provide approximations to both of them.

3.1.2 Retention of Residues

The procedure for retaining residues is implemented as follows. Let F , G , H and D be in modal form and assume that the first n modes are retained. The state equations are then written as

$$\begin{bmatrix} \dot{x}_1 \\ \dot{x}_2 \end{bmatrix} = \begin{bmatrix} F_{11} & 0 \\ 0 & F_{22} \end{bmatrix} \begin{bmatrix} x_1 \\ x_2 \end{bmatrix} + \begin{bmatrix} G_1 \\ G_2 \end{bmatrix} u, \quad (3.6)$$

$$y = [H_1 \mid H_2] \begin{bmatrix} x_1 \\ x_2 \end{bmatrix} + Du. \quad (3.7)$$

Let the average frequency of the retained modes be ω_a . The state x_2 is approximated by

$$x_2 = \text{Re}[(j\omega_a I - F_{22})^{-1} G_2] u, \quad (3.8)$$

where $\text{Re}(\cdot)$ represents the real part of (\cdot) . The real part is selected because it is not feasible to match the imaginary part of the approximation using a reduced model with real coefficients. Therefore, the reduced model is approximated by

$$\begin{aligned} \dot{x}_1 &= F_{11}x_1 + G_1 u, \\ y &= H_1 x_1 + [D + \text{Re}[(j\omega_a I - F_{22})^{-1} G_2]] u. \end{aligned} \quad (3.9)$$

In order to match the dc gain of the reduced model to that of the high-order model, ω_a may be set to zero. Most approximations match only the dc gain because for zero ω_a , the right-hand side of Eq. (3.8) is real. The problem of not being able to match the complex component in Eq. (3.8) then disappears.

3.1.3 Retention of Zeros

To retain the first m zeros and n poles about the average frequency, ω_a . The transfer function of Eq. (3.5) is simplified to

$$T_{kl}(s) = \frac{g(j\omega_a - z_{m+1}) \dots (j\omega_a - z_M)}{(j\omega_a - \lambda_{n+1}) \dots (j\omega_a - \lambda_N)} \frac{(s - z_1) \dots (s - z_m)}{(s - \lambda_1) \dots (s - \lambda_n)}. \quad (3.10)$$

The first term is approximated by a real gain. Each input-output transfer function is simplified as in Eq. (3.10). These simplified transfer functions are reconverted into a state-variable description.

The computation time requirements to obtain reduced-order models which retain zeros are very high. Poles and residues of high-order models are determined much more easily than zeros. This model-reduction procedure, therefore, has never been used for large space structures applications.

Table 3-1 shows the partitioning of the infinite series representing the exact transfer function for the case of a general undamped structure. The ϕ_i 's are the mode shapes at the location where the displacement-to-force ratio is measured (or rotation-to-torque, etc.). The number of modes to be controlled is n_c , the number of modes retained in the model of the structure is n_r .

In the straight truncation case one has $n_r = n_c$, and a substantial error is committed in representing the zeros of the system, leading to erroneous control design. The expanded truncation uses a larger model, but still a significant error may remain. The "rounded" transfer function approximates the remainder of the infinite series by a constant bias term. (For these terms, s is indeed much less than the ω_i 's, hence the approximation.)

Because all these approximations depend on the convergence of the series, there are open questions regarding the use of other kinds of mode shape functions which may improve convergence. For instance, mode shape derivatives (used to express rotation and torque properties) converge much slower than the usual displacement modes when free-free modes are

Table 3-1. Modal Partitioning and Approximate Transfer Functions

	MODES	TO BE CONTROLLED	RETAINED IN MODEL	NOT RETAINED IN MODEL
Transfer Function		$s \geq \omega_1$	$s \leq \omega_1$	$s \ll \omega_1$
Exact	$T_c(s) =$	$\sum_{i=1}^{n_c} \frac{\phi_i^2}{\omega_i^2 + s^2}$	$+ \sum_{n_c+1}^{n_r} \frac{\phi_i^2}{\omega_i^2 + s^2}$	$+ \sum_{n_r+1}^{\infty} \frac{\phi_i^2}{\omega_i^2 + s^2}$
Total Truncation	$T_d(s, n_c) =$	$\sum_{i=1}^{n_c} \frac{\phi_i^2}{\omega_i^2 + s^2}$		
Expanded Truncation	$T_d(s, n_r) =$	$\sum_{i=1}^{n_c} \frac{\phi_i^2}{\omega_i^2 + s^2}$	$+ \sum_{n_c+1}^{n_r} \frac{\phi_i^2}{\omega_i^2 + s^2}$	
Rounded	$T_d^R(s, n_r) =$	$\sum_{i=1}^{n_c} \frac{\phi_i^2}{\omega_i^2 + s^2}$	$+ \sum_{n_c+1}^{n_r} \frac{\phi_i^2}{\omega_i^2 + s^2}$	$+ \sum_{n_r+1}^{\infty} \frac{\phi_i^2}{\omega_i^2}$

used. However, using mode shapes which reflect better the boundary conditions imposed by a torquer may drastically improve convergence.

3.1.4 Mode Selection Criteria

Mode selection may be formally based on modal cost analysis methods developed by Skelton [13]. An ad hoc approach involving modal controllability, observability and disturbance is often more physically motivated and can sometimes be related to modal cost. In addition, reduced models are preferably chosen to represent the low-frequency region because: (1) actuators and sensors have finite bandwidth, (2) the model is known more accurately only at low frequencies, and (3) the resulting control law can be implemented adequately with a lower sampling rate than if high-frequency modes are retained (digital processor requirements are simplified).

3.1.5 Example

Mode selection methods must ultimately address the inadequacy of (finite) modal representations under boundary conditions imposed by closed-loop control. A simple beam example is shown. Here, two methods are used to compute plant transfer functions. The first provides a discrete (modal) approximation, equivalent to a finite-element representation; the second yields exact transfer functions from the partial differential equations. The two methods are now discussed in more detail.

The first method converts the partial differential equations (PDE's) and associated boundary conditions into an infinite set of ordinary differential equations (ODE's). A small subset of these ODE's is then chosen as a model, and this is strictly equivalent to the finite-element approach, except that a finite set of modes is obtained analytically and not via a numerical eigensystem decomposition.

The second method starts with the same PDE's but does not expand the solution into modes. Rather, it obtains directly an exact analytical transfer function which can be used in classical control theory, or in the more elaborate distributed optimal control theory.

Since approximate transfer functions can also be obtained from modal expansion of the first method, comparisons can be made between finite-element representations (identical to the first method) and the exact model (second method). The particular problem of a free-free beam was treated using these two approaches and analytical expressions obtained for the continuous and discrete (modal) transfer functions are shown in Fig. 3-2. Two types of transfer function appear in Fig. 3-2, i.e., displacement/force and rotation/torque at one end. All symbols are defined in Fig. 3-2. The discrete transfer function $T_d(s;n)$ is a function of the number n of modes retained in the series expansion.

Figure 3-3 shows a graphical comparison of the exact rotation-to-torque transfer function $T_c(s)$ (obtained from the continuous model) and the truncated (discrete) transfer functions $T_d(s;n)$ when 7 terms or 20 terms are retained, i.e., the beam is modeled by one rigid-body mode and either 6 or 19 structural modes. The graph clearly shows the error in the zero-crossings, while the other parts of the curves are in excellent agreement. Because the zeros of the open-loop system play an important part in the closed-loop

<p>ρ: BEAM DENSITY A: CROSS-SECTIONAL AREA E: YOUNG'S MODULUS I: CROSS-SECTIONAL INERTIA l: BEAM LENGTH</p>	<p>S: LAPLACE TRANSFORM VARIABLE $\beta^4 \equiv -l^4 \rho A s^2 / EI$</p>	<p>y: BEAM DEFLECTION AT ONE END θ: BEAM SLOPE AT THAT END f: FORCE APPLIED TO BEAM AT THAT END τ: TORQUE APPLIED TO BEAM AT THAT END</p>
-----------------------------------------------------------------------------------------------------------------------------------------------------------------------------------------------------	---------------------------------------------------------------------------------------------------------	----------------------------------------------------------------------------------------------------------------------------------------------------------------------------------------------------------------------

(DEF.)	$\left\{ \begin{array}{l} T(\beta) \equiv y(s, l) / f(s, l) \\ T'(\beta) \equiv \theta(s, l) / \tau(s, l) \end{array} \right.$	$\left\{ \begin{array}{l} \text{(CONTINUOUS OR DISCRETE)} \\ \text{(CONTINUOUS OR DISCRETE)} \end{array} \right.$
--------	--------------------------------------------------------------------------------------------------------------------------------	-------------------------------------------------------------------------------------------------------------------

TRANSLATION/FORCE	$\left\{ \begin{array}{l} T_c(\beta) = \frac{3}{EI\beta^3} \frac{\sin \beta \cosh \beta - \cos \beta \sinh \beta}{1 - \cosh \beta \cos \beta} \\ T_d(\beta;n) = \frac{4l^3}{EI} \left[\frac{1}{\beta^4} + \sum_{i=1}^n \frac{1}{\beta_i^4 - \beta_i^4} \right] \end{array} \right.$	$\left\{ \begin{array}{l} \text{(CONTINUOUS)} \\ \text{(DISCRETE)} \end{array} \right.$
ROTATION/TORQUE	$\left\{ \begin{array}{l} T_c'(\beta) = \frac{l}{EI\beta} \frac{\sin \beta \cosh \beta + \cos \beta \sinh \beta}{1 - \cosh \beta \cos \beta} \\ T_d'(\beta;n) = \frac{4l}{EI} \left[\frac{3}{\beta^4} + \sum_{i=1}^n \frac{\beta_i^2}{\beta_i^4 - \beta_i^4} \left(\frac{\cos \beta_i - \cos \beta_i}{\sin \beta_i - \sin \beta_i} \right) \right] \end{array} \right.$	$\left\{ \begin{array}{l} \text{(CONTINUOUS)} \\ \text{(DISCRETE)} \end{array} \right.$

Fig. 3-2. Continuous and discrete open-loop transfer functions for beam (I)

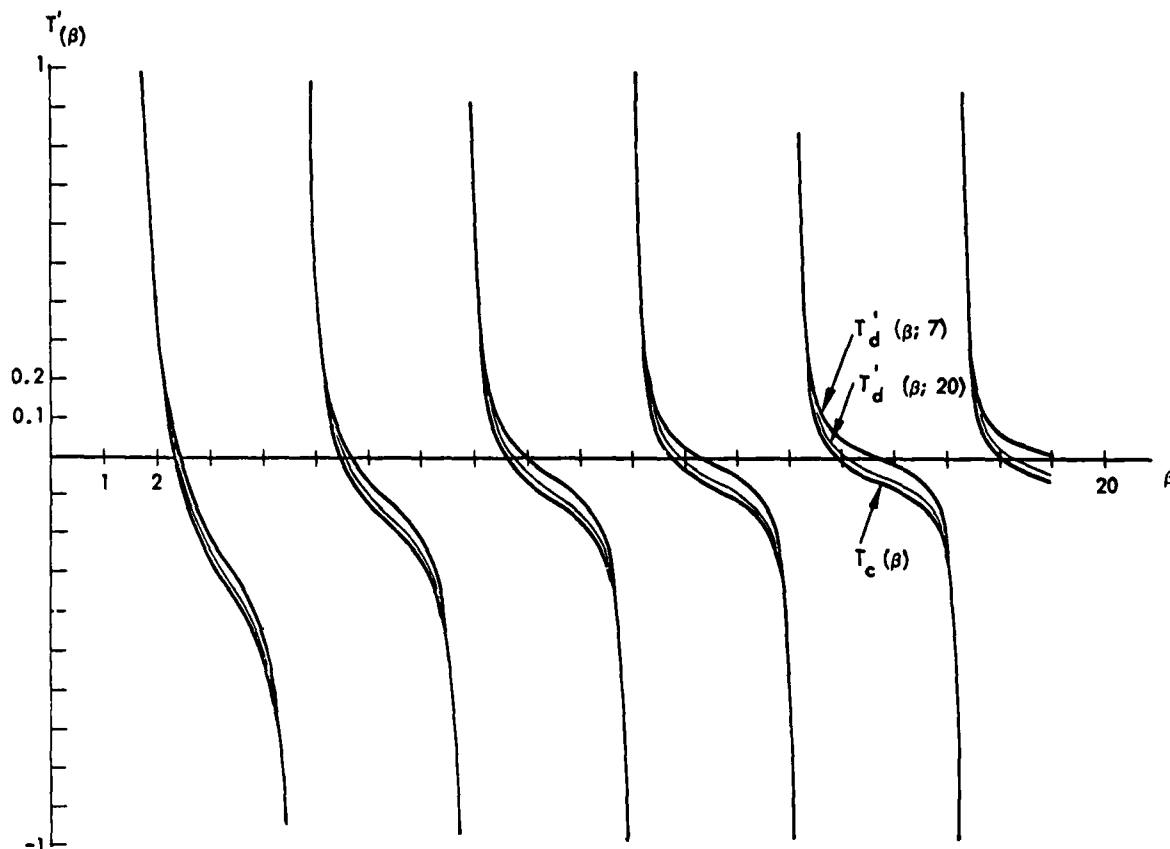


Fig. 3-3. Continuous and discrete open-loop transfer functions for beam (II)

system, their insensitivity to modal truncation is of prime importance to the control design. Zero crossing errors can be reduced by increasing the number n of modeled modes, but a satisfactory result will require a very large value for n . These curves indicate that a much better approximation could be obtained by adding a constant bias term (negative in this case) to the discrete transfer function.

3.2 Design of Controllers

Design of feedback control laws for large space structures is dictated by the following considerations:

1. Model.— Because of modeling accuracy as well as computational considerations, the model is of low order. The neglected modes have low damping and can be unstable if not properly considered in control design.
2. Sensors and actuators.— Though structures have significant response up to infinite frequency, physical actuators/sensors have finite bandwidth. In addition, actuators and sensors have dead zones, hysteresis and nonlinearities; their type and placement may be restricted in actual structures.
3. Model uncertainties.— The behavior of structures is known only approximately at high frequency. Therefore, control design cannot depend on the behavior of high-frequency modes.

To address these issues and to provide adequate robustness, a two-level control-design approach, previously discussed in Ref. 4, is now described in more detail.

The two-level approach consists of a wide-band, low-authority control (LAC) and a narrow-band, high-authority control (HAC). HAC provides high damping or mode-shape adjustment in a selected number of modes to meet performance requirements. LAC, on the other hand, introduces low damping in a wide range of modes for maximum robustness. Figure 3-4 shows the control-design procedure with integrated LAC and HAC designs.

LAC is usually implemented with colocated sensors and actuators. However, the theory, based on the work of Aubrun, is applicable to multiple actuators/sensors with cross-feedback and possible filters [5].

HAC uses a collection of sensors and actuators not necessarily colocated. Selecting the increase in damping ratio is realized by use of a state estimator filter. A unique frequency-shaped extension of the linear-quadratic-Gaussian (LQG) method has been developed

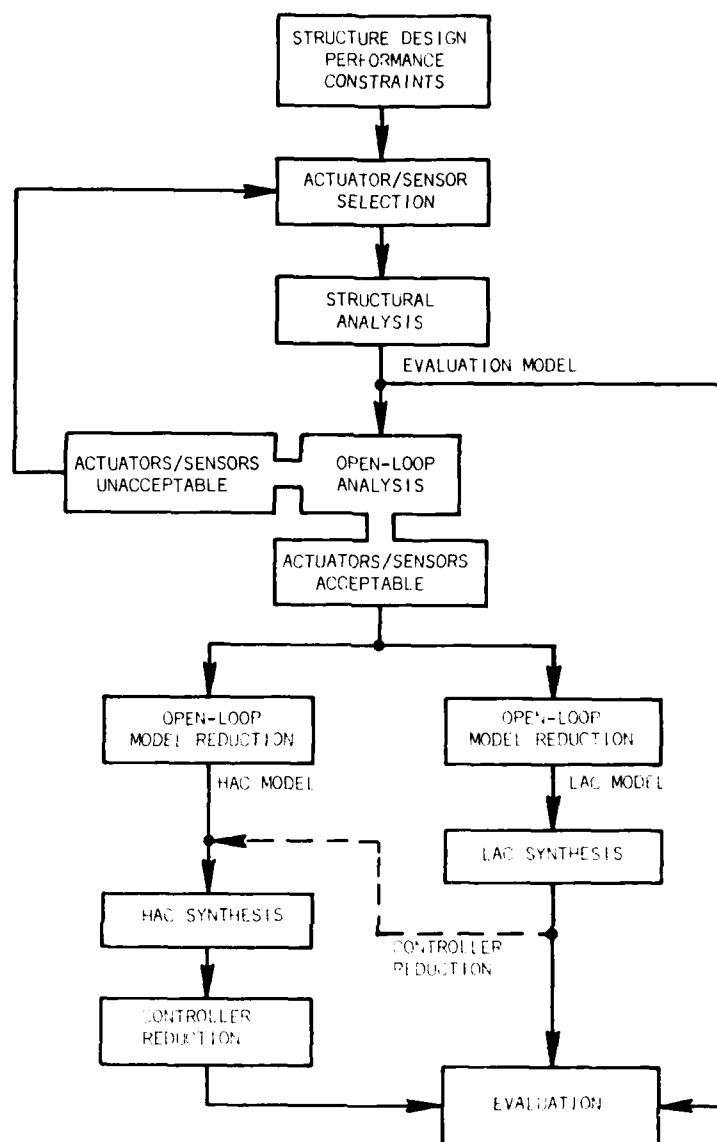


Fig. 3-4. Analytical control-design procedure.

to provide roll-off over desired frequency regions and selected disturbance rejection [15]. HAC may destabilize modes not used in the design. LAC is, therefore, necessary to "clean up" problems created by HAC.

The need to integrate HAC with LAC is shown in Fig. 3-5. HAC is based on models valid over a limited frequency region. It produces large increases in damping ratio and disturbance rejection in the frequency range of interest. The effect of the HAC controller on modes not used in the control design and outside the controller bandwidth may be stabilizing or destabilizing. LAC is designed to provide protection such that adequate damping is provided in the mode most adversely perturbed by HAC. With reference to Fig. 3-5, the LAC moves the entire uncertainty region above the zero level damping ratio.

3.2.1 Low-Authority Control Design

Low-authority control (LAC) systems [16], when applied to structures, are vibration control systems consisting of distributed sensors and actuators with limited damping authority. The control system is allowed to modify only moderately the natural modes and frequencies of the structure. This basic assumption, combined with Jacobi's root perturbation formula, leads to a fundamental LAC formula for predicting algebraically the root shifts produced by introducing an LAC structural control system. Specifically, for an undamped, open-loop structure, the predicted root shift $(d\lambda_n)_p$ is given by

$$(d\lambda_n)_p \approx \frac{1}{2} \sum_{a,r} C_{ar} \phi_{an} \phi_{rn}, \quad (3.11)$$

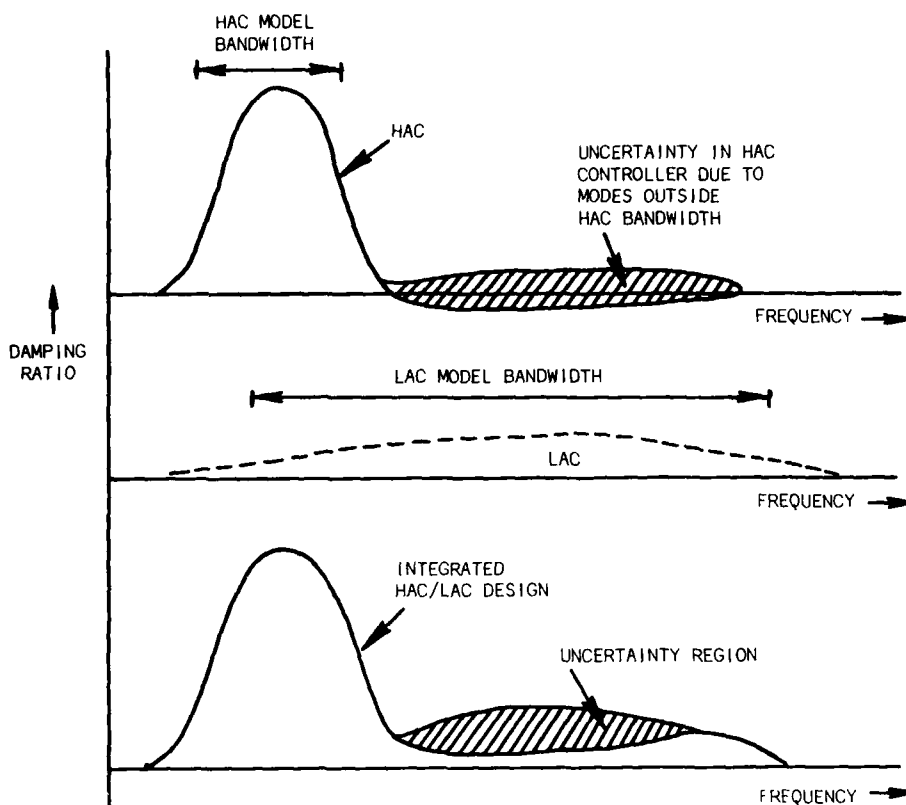


Fig. 3-5. Need to integrate high-authority controller (HAC) and low-authority controller (LAC).

where the coefficient matrix* $C = [C_{ar}]$ is a matrix of (damping) gains, and ϕ_{an} , ϕ_{rn} denote, respectively, the values of the n th mode shape at actuator station a and sensor station r .

Equation (3.11) may also be used to compute the unknown gains C_{ar} if the $d\lambda_n$ are considered to be desired root shifts or, equivalently, desired modal dampings. While an exact "inversion" of Eq. (3.11) does not generally exist, weighted least-squares type solutions can be devised to determine the actuator control gains C_{ar} necessary to produce the required modal damping ratios. This determination of the gains is the synthesis of LAC systems, and is achieved by minimizing the special weighted quadratic cost function

$$J(C) \equiv \sum_n w_n [(d\lambda_n)_P - (d\lambda_n)_D]^2 + \sum_{a,r} C_{ar}^2, \quad (3.12)$$

in which the $(d\lambda_n)_P$ denote the predicted root shifts given by formula (3.11), and the $(d\lambda_n)_D$ denote desired root shifts (i.e., given numbers). In the cost function $J(C)$, the modal weights w_n help specify pole locations, and the term $\sum_{a,r} C_{ar}^2$ improves robustness of the controller.

Since the cost function $J(C)$ is quadratic in $(d\lambda_n)_P$, and hence, in view of Eq. (3.11), also quadratic in the elements of the matrix C , the gains can be obtained algebraically by solving the linear equations

$$\frac{\partial J(C)}{\partial C} = 0 \quad (3.13)$$

for the elements of C . This is an exact algebraic process in which both the modal weights w_n and the desired root shifts (modal dampings) $(d\lambda_n)_D$ play the role of adjustable synthesis parameters, similar to the weights on the control effort and the state error in standard optimal control synthesis procedures.

* This LAC gain matrix will subsequently be denoted by C_L in Section 5 to distinguish it from the high-authority control gain matrix C .

For structures which already have some damping or control systems in which sensor, actuator, or filter dynamics can either be ignored or are already embedded in the plant dynamics, the root perturbation techniques and cost function minimization methods above can similarly be used to synthesize low-authority controls. In this case, the perturbation method proceeds from the state equations

$$\begin{aligned} \text{Dynamics: } \dot{x} &= Fx + Gu, \\ \text{Sensors: } y &= Hx, \\ \text{Controls: } u &= Cy, \end{aligned} \quad (3.14)$$

which result in the closed-loop dynamics

$$\dot{x} = (F + GCH)x. \quad (3.15)$$

For sufficiently small controls C [8], let $GCH \equiv dF$ be considered as a perturbation of F , so that the closed-loop dynamics may now be written as

$$\dot{x} = (F + dF)x. \quad (3.16)$$

Let λ_n denote the n th (complex) root of F , and denote by L_n, R_n , respectively, the corresponding left and right eigenvectors of F , i.e.,

$$\begin{aligned} F^T L_n &= \lambda_n L_n \\ F R_n &= \lambda_n R_n \end{aligned} \quad (3.17)$$

normalized so that $L_n^T R_n = 2$ (this normalization makes Eqs. (3.11) and (3.18) formally compatible).

For small C , let $d\lambda_n$ denote the eigenvalue shift corresponding to dF . Then, as shown in Ref. 16, Jacobi's formula leads to the fundamental root-shift formula:

$$\begin{aligned} d\lambda_n &\approx \frac{1}{2} L_n^T dF R_n \\ &= \frac{1}{2} L_n^T G C H R_n \\ &= \frac{1}{2} (\phi_n^A)^T C \phi_n^R, \end{aligned}$$

hence,

$$d\lambda_n \approx \frac{1}{2} \sum_{a,r} C_{ar} \phi_{an}^A \phi_{rn}^R, \quad (3.18)$$

where $\phi_n^A = G^T L_n$ and $\phi_n^R = H R_n$ are generalized actuator and sensor modes, respectively.

Formula (3.18) is a generalization of formula (3.11) and reduces to Eq. (3.11) when sensors and actuators are complementary (i.e., translation/force, rotation/torque), sensors measure rates, and the structure is undamped.

Robustness of LAC systems.— When sensors and actuators are colocated (i.e., $a=r$), are complementary, and only rate feedback is used, formula (3.11) reduces to

$$d\lambda_n = -\xi_n \omega_n \approx \frac{1}{2} \sum_a C_a \phi_{an}^2, \quad (3.19)$$

which shows that the root shifts are always towards the left of the $j\omega$ -axis if all the gains are negative. This robustness result is obviously based on the assumption that both sensors and actuators have infinite bandwidth, and also that the structure was initially undamped*. Several departures from this idealization occur in the actual practical implementation of the LAC systems. The most severe of these results from the finiteness of the actuators' bandwidths. More precisely, the second-order roll-off introduced by the actuator dynamics will always destabilize an undamped structure. However, when some natural damping is present in the structure, or when a passive damper is mounted in parallel with the actuator, additional active damping can be obtained without destabilizing the structure. The precise statement of this result is given in the following theorem:

LAC Stability Theorem [4]. *Unconditional stability of an LAC system is guaranteed if and only if, for each mode n , the active damping ratio ξ_{cn} is less than a*

*Robustness is that quality of a controller of remaining stable in the presence of parameter variations in the structure and/or control system parameters. For example, the above stability condition (negativity of all the root shifts) is independent of mode shapes and frequencies, and depends only on the negativity of the gains C_a . Any parameter variation in the controller which modifies the values (but not the signs) of the gains will not affect the stability condition.

certain maximum ξ_{cn}^* . This maximum active damping ratio in any of the modes within the bandwidth of an active LAC controller is proportional to the sum of the natural structural damping ξ_{on} and the damping ξ_{pn} introduced by a passive damper mounted in parallel with the actuator. Specifically,

$$\xi_{cn}^* = R_{\max}(\xi_{on} + \xi_{pn}), \quad (3.20)$$

where the value of the proportionality constant R_{\max} is given by:

$$R_{\max} = \min(K + 2\sqrt{K}, \tau_1 \tau_2 / \tau_0^2), \quad (3.21)$$

$$\text{where } K = \tau_1 / \tau_2 + \tau_2 / \tau_1 + 2, \quad (3.22)$$

and where $1/\tau_1, 1/\tau_2$ are the poles of the active damper, and $1/\tau_0$ is the pole of the passive damper.

The proof of this theorem is given in Ref. 4.

3.2.2 High-Authority Control Design

The HAC control design procedure is based on linear-quadratic-Gaussian (LQG) methods. Increased penalties in the LQG cost functional are placed at those frequencies where less response is desired. The concept of frequency-shaped cost functionals has been introduced previously [15]. This section demonstrates the application of these methods to the large space structures problem.

The frequency-shaping methods are useful in several areas of large space structures control. Three principal applications are important: (1) spillover avoidance, (2) disturbance rejection, and (3) state estimation.

Management of spillover.—Spillover in closed-loop control of space structures is managed by injecting minimum control power at the natural frequencies of the unmodeled modes. Procedures for controlling spillover at high-frequencies are discussed, although similar techniques are applicable for other regimes.

The high-frequency spillover may be controlled by modifying the state or the control weighting. The state weighting $A(j\omega)$ may be made a decreasing function of frequency. Three of the possible forms for $A(j\omega)$ are shown in the following:

$$1. \quad A(j\omega) = \frac{1}{\omega^2} A, \quad (3.23)$$

$$2. \quad A(j\omega) = \frac{\omega_0^4}{(\omega_0^2 + \omega^2)^2} A, \quad (3.24)$$

$$3. \quad A(j\omega) = \frac{(\omega_1^2 + \omega^2)^2}{(\omega_0^2 + \omega^2)^2} A, \quad \omega_1 > \omega_0. \quad (3.25)$$

To include the frequency shaping of Eq. (3.23), define additional states \bar{x} as

$$\dot{\bar{x}} = \bar{x}. \quad (3.26)$$

The performance index is then

$$\lim_{T \rightarrow \infty} \frac{1}{T} \int_0^T (\bar{x}^T A \bar{x} + u^T B u) dt, \quad (3.27)$$

and the control law will be of the form

$$u = C_1 \bar{x} + C_2 \dot{\bar{x}}. \quad (3.28)$$

The control gain C_2 will ensure that the high-frequency response is minimized. This formulation resembles integral control. However, the weighting matrices used in the design are different.

Spillover may also be reduced by placing high control weighting at high frequency. Examples of $B(j\omega)$ which reduce high-frequency spillover are as follows:

$$1. \quad B(j\omega) = \frac{(\omega^2 + \omega_0^2)}{\omega_0^2} B, \quad (3.29)$$

$$2. \quad B(j\omega) = \frac{\omega_1^2 + \omega^2}{\omega_0^2 + \omega^2} B, \quad \omega_1 < \omega_0, \quad (3.30)$$

$$3. \quad B(j\omega) = \frac{\omega^4}{[(\omega^2 + \omega_0^2)^2 + 2\omega_0^2\omega^2]} B. \quad (3.31)$$

The frequency-shaped parts of these weightings are reciprocals of the frequency-shaped parts of state weightings. To implement the weighting function of Eq. (3.29), define a vector \bar{u} by

$$\dot{\bar{u}} + \omega_0 \bar{u} = \omega_0 \bar{u}. \quad (3.32)$$

The performance index then takes the form

$$J = \lim_{T \rightarrow \infty} \frac{1}{T} \int_0^T (x^T A x + \bar{u}^T B \bar{u}) dt, \quad (3.33)$$

and the feedback control law will be

$$\dot{\bar{u}} + \omega_0 \bar{u} = \omega_0 \bar{u} = \omega_0 (C_1 x + C_2 u),$$

or

$$\dot{\bar{u}} + \omega_0 (1 - C_2) \bar{u} = \omega_0 C_1 x. \quad (3.34)$$

This control law is shown schematically in Fig. 3-6.

During maneuvers and in other missions, there is often a need to not excite a particular mode at ω_0 . Minimization of spillover at one frequency ω_0 is achieved by:

$$A(j\omega) = (\omega^2 - \omega_0^2)^2, \quad (3.35)$$

or by

$$B(j\omega) = \frac{B}{(\omega^2 - \omega_0^2)^2}. \quad (3.36)$$

Spillover reduction in state estimation.— The discussion will again address the estimation of low-frequency states when the high-frequency modes are not modeled. Extension to other cases is straightforward.

In the linear systems of Eqs. (2.6), a linear transformation can be used to place all errors caused by unmodeled modes into the measurement equations. Note that when high-frequency modes are not modeled in the state equations, measurement errors in the modified system are also at high frequency. Therefore, the lumped modeling error at high frequency represents a high-frequency noise measurement with many peaks.

To derive a filter with desirable high-frequency behavior, consider the optimal estimation as the output of an optimization problem with the following performance index:

$$\bar{J} = \lim_{T \rightarrow \infty} \int_0^T (w^T Q w + v^T R v) dt. \quad (3.37)$$

Again, conversion to the frequency domain gives the following performance index:

$$\bar{J} = \int_{-\infty}^{\infty} (w^* Q(j\omega) w + v^* R(j\omega) v) d\omega. \quad (3.38)$$

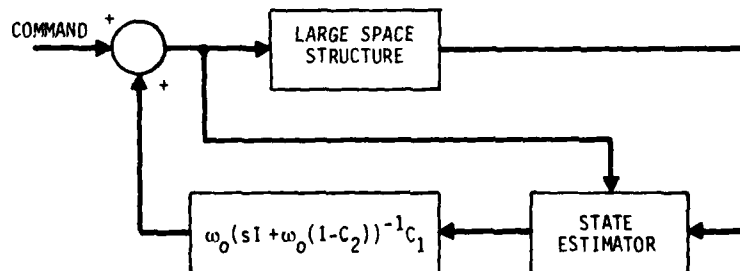


Fig. 3-6. A frequency-shaped controller to reduce high-frequency spillover.

The problem of model invalidity at high frequency is solved by making Q and R functions of frequency.

Since all errors associated with model truncation are incorporated in the measurements, frequency shaping is used only in R . High-frequency measurement spillover is controlled by increasing $R(j\omega)$ at high frequency. For example, choose $R(j\omega)$ as:

$$R(j\omega) = \frac{(\omega^2 + \omega_0^2)}{\omega_0^2} R. \quad (3.39)$$

Defining a new measurement \bar{y} as

$$\frac{\dot{\bar{y}}}{\omega_0} + \omega_0 \bar{y} = \omega_0 y, \quad (3.40)$$

then

$$\bar{y} = H\bar{x} + v, \quad (3.41)$$

where

$$\frac{\dot{\bar{x}}}{\omega_0} + \omega_0 \bar{x} = \omega_0 x. \quad (3.42)$$

and the state estimator is then of the form:

$$\begin{aligned} \dot{\hat{x}} &= F\hat{x} + Gu + K(y - H\hat{x}), \\ \dot{\bar{x}} &= -\omega_0 \bar{x} + \omega_0 \hat{x} + \omega_0 \bar{K}(\bar{y} - H\bar{x}), \\ \dot{\bar{y}} &= -\omega_0 \bar{y} + \omega_0 y. \end{aligned} \quad (3.43)$$

This filter is shown schematically in Fig. 3-7. Note that a standard filter is obtained by setting \bar{K} to zero and $\omega_0/(s+\omega_0)$ to one. In this formulation, filtered measurements are compared with filtered states. The eigenvalues of the closed-loop system are, in general, in the low-frequency region. Low-frequency, closed-loop eigenvalues reduce excitation of high-frequency modes through feedback in the state estimator. The filter shapes may be modified to provide any desired roll-off. The filter, of course, becomes more complex as faster roll-off is obtained. Note also that the transfer function between the estimated state and the measurements has at least two more poles than zeros.

Although this filter has been developed for application to large space structures, it is believed to have a wide applicability in the design of practical state estimators.

Disturbance rejection in large space structures.— Large space structures are often subject to high disturbance levels caused by rotating machines, combustion devices, rotating antennae, and other on-board equipment. In addition, gravity gradients and solar pressure are external disturbance sources. These sources are usually nonwhite. Frequency-shaping methods may be applied to minimize the effect of these disturbances on the structure. Procedures for realizing disturbance rejection are shown in the following.

Consider a cryogenic cooler or control-moment gyro. The primary disturbance produced by these devices is at one frequency (typically the rotational frequency) and possibly its harmonics. Let the disturbance frequency be ω . To minimize the effect of this disturbance on output y , the following term J_1 is included in the performance index:

$$J_1 = \frac{1}{(\omega^2 - \omega_0^2)^2} y^T A_y y. \quad (3.44)$$

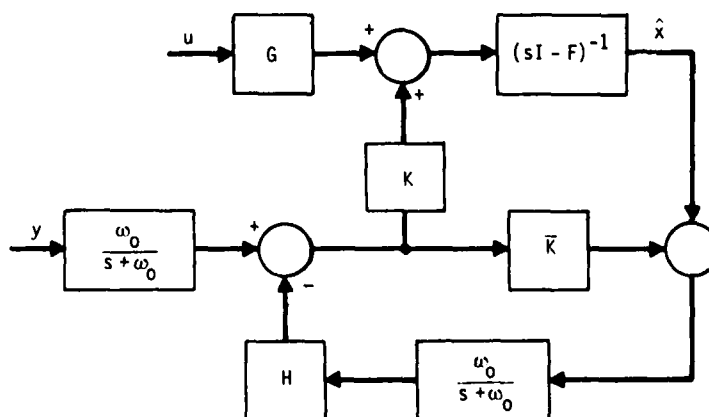


Fig. 3-7. A frequency-shaped filter to reduce high-frequency spillover.

Note that the output penalty goes to infinity at the disturbance frequency. Thus, the impact of disturbance on the output is minimized.

The implementation of this frequency-shaped weighting requires definition of additional states as follows:

$$\dot{\bar{x}} = \begin{bmatrix} 0 & I \\ -\omega^2 I & 0 \end{bmatrix} \bar{x} + \begin{pmatrix} 0 \\ I \end{pmatrix} y . \quad (3.45)$$

The performance index will then take the form

$$J = \lim_{T \rightarrow \infty} \int_0^T (\bar{x}^T A_y \bar{x} + x^T A x + u^T B u) dt , \quad (3.46)$$

and the corresponding control law becomes

$$u = C_1 x + C_2 \bar{x} .$$

The flowchart for this control law is shown in Fig. 3-8.

The control formulation given above may be extended to include disturbance at other frequencies or over a frequency band. In each case, as shown in Fig. 3-8, there is memory in the control portion of the feedback.

Summary.— The application of frequency-shaping methods to large space structures leads to a linear controller with memory. However, the additional states needed to represent frequency-dependent weights increase the controller order. The software needed for these controller designs is similar to that for standard LQG problems.

3.3 Controller Simplification

The frequency-shaped controllers developed in the previous section are of the form

$$x_c = F_c x_c + K y , \quad (3.47)$$

$$u_c = C x_c + D y . \quad (3.48)$$

The controller, therefore, has the same form as the system itself, except that: (1) the roles of input and output are switched, (2) the controller state vector depends on the choice of frequency shaping, and (3) K and C are known exactly (unlike G and H in the design model). Controller simplification is, therefore, similar to model reduction.

All unobservable or uncontrollable modes of the controller should be dropped, since they have no effect on controller performance. In addition, poles with small residues can also be dropped. Note that the residues are physical matrices representing force or moment applied per unit error.

Further selection of modes or states which should be retained in the low-order controller is a difficult problem. One approach is to drop one or two states at a time to determine the set of states which may be eliminated without loss of performance. To minimize computation time, a stepwise search procedure is needed. A modal cost function could be used in the search [13].

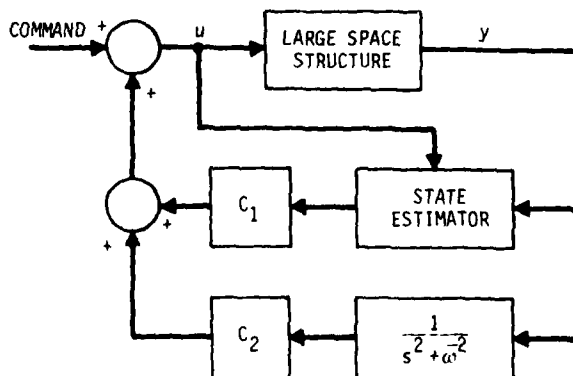


Fig. 3-8. A frequency-shaped controller to eliminate the effect of disturbance at ω on output y

4. APPLICATION TO A COMPLEX OPTICAL SPACECRAFT CONFIGURATION

The illustration and demonstration of control-design methods for large space structures has been, and remains, a difficult problem. The very nature of large space structures precludes the construction of simple textbook examples which illustrate the theory. Control theorists have unfortunately confused this issue often by postulating dynamical plants which are no more than sets of matrices to be immediately processed through a maze of procedures and algorithms developed in theoretical approaches.

Under the Defense Advanced Research Projects Agency sponsored program on Active Control of Space Structures (ACOSS), an important step towards the resolution of this problem was taken by the Charles Stark Draper Laboratory (CSDL). Early in 1980, DARPA commissioned CSDL to develop a (paper) design of a "generic" optical space structure which embodied the essential characteristics needed to illustrate and demonstrate large space structure control-design methodology, implementation, and performance evaluation. The resulting non-trivial spacecraft model, known today as "CSDL Model #2," has been fully documented in Ref. 17. It is available to the dynamics and controls community via a NASTRAN computer tape which contains the entire structural model. References to "CSDL #2" are becoming increasingly more frequent, particularly in view of the fact that this model was also recently chosen by Wright-Patterson Air Force Base as the "test bed" for a program they will sponsor and initiate later this year on the Vibration Control of Space Structures (VCOSS).

4.1 The CSDL #2 Structural Model

The CSDL #2 model [17], shown conceptually in Fig. 4-1, is a wide-angle, three-mirror optical space system, together with a line-of-sight model giving the law of displacement of the image in the focal plane when the structure deforms (see Section 4.2). The assumption is made that the mirror surfaces are simply displaced and maintain their nominal (rigid) shapes. The mirror shapes are off-axis sections of rotationally symmetric coaxial surfaces. Since the intent is to derive a first-order optical model (by neglecting the influence of light redistribution in the image), the asphericity of each mirror is disregarded.

The total structure is approximately 28 m high, weighs about 9,300 kg, and embodies a structural design based on realistic sizes and weights; the corresponding mass distribution is indicated in Fig. 4-1. Principal lumped masses are graphically displayed in Fig. 4-2. As "seen" by the NASTRAN program input, the structure contains many more beams than in the artist's conception of Fig. 4-1. The computer-graphic display shown in Fig. 4-3 represents the actual structural model which was input to the NASTRAN program, together

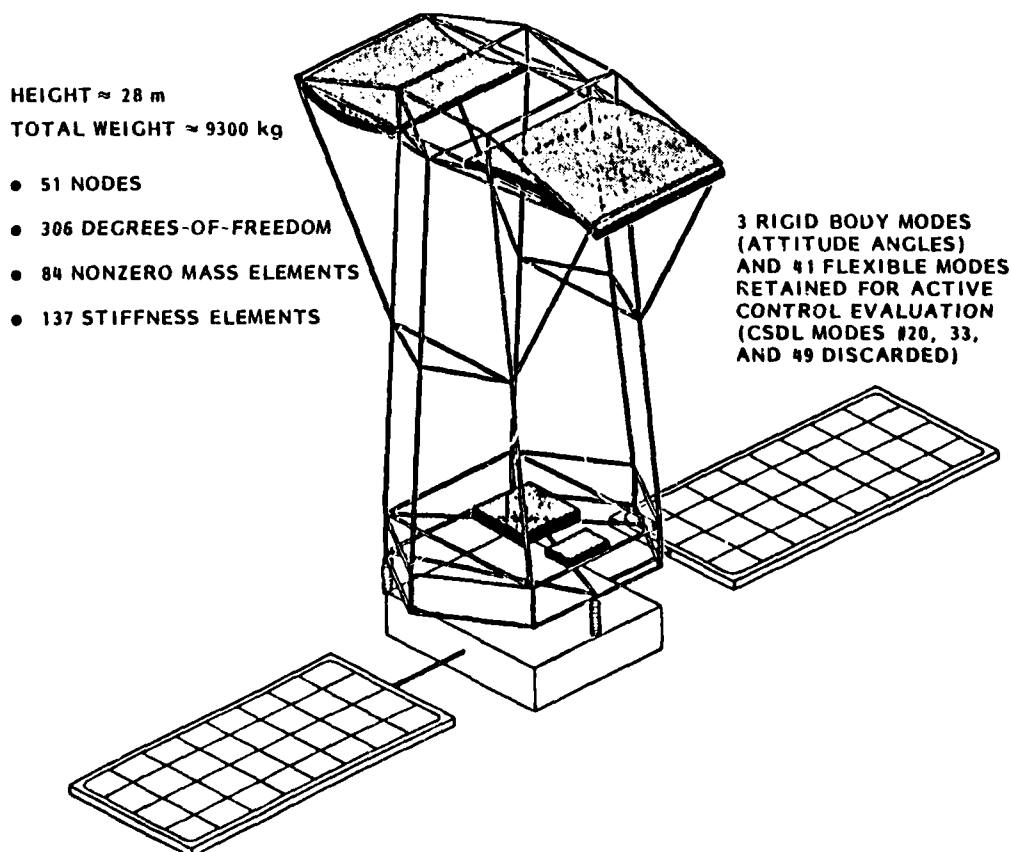


Fig. 4-1. CSDL #2 model (artist's conception)

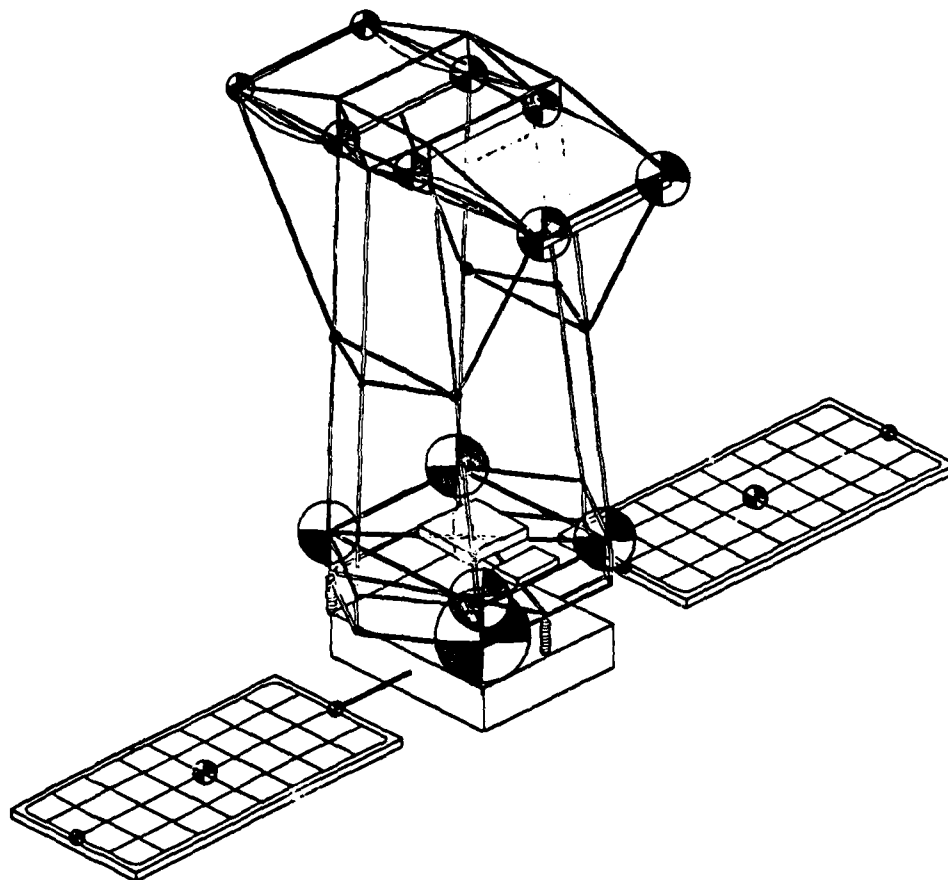


Fig. 4-2. Principal lumped masses in CSDL #2 (masses in relative proportional size).

ACOSS DRAPER MODEL

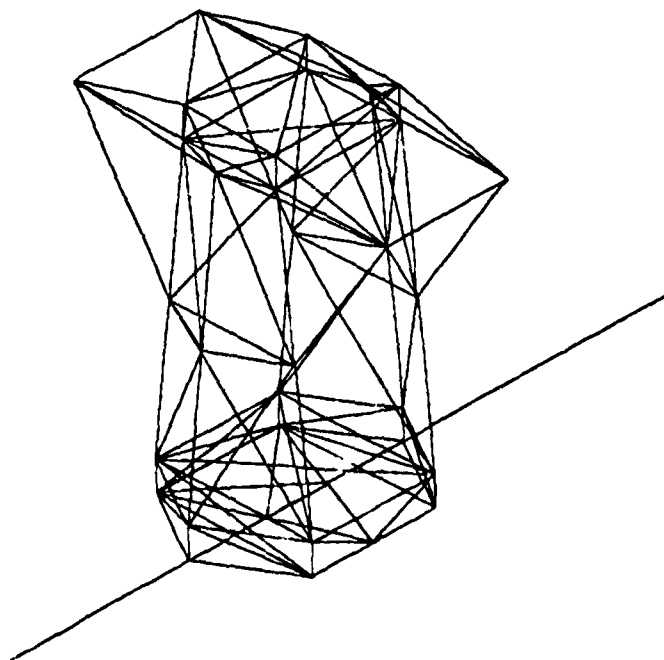


Fig. 4-3. Computer-graphic display of CSDL #2 (all beam elements shown).

AD-A111 405 ADVISORY GROUP FOR AEROSPACE RESEARCH AND DEVELOPMENT--ETC F/6 22/3
SPACECRAFT POINTING AND POSITION CONTROL.(U)

NOV 81 P P BROEK, S Z SZIRNAY

UNCLASSIFIED AGARD-A6-260

NL

3 of 3

AD-A111

AD-A111

AD-A111

AD-A111

AD-A111

AD-A111

AD-A111

AD-A111

AD-A111

AD-A111

AD-A111

AD-A111

AD-A111

AD-A111

AD-A111

AD-A111

AD-A111

AD-A111

AD-A111

AD-A111

AD-A111

AD-A111

AD-A111

AD-A111

AD-A111

AD-A111

AD-A111

AD-A111

AD-A111

AD-A111

AD-A111

AD-A111

AD-A111

AD-A111

AD-A111

AD-A111

AD-A111

AD-A111

AD-A111

AD-A111

AD-A111

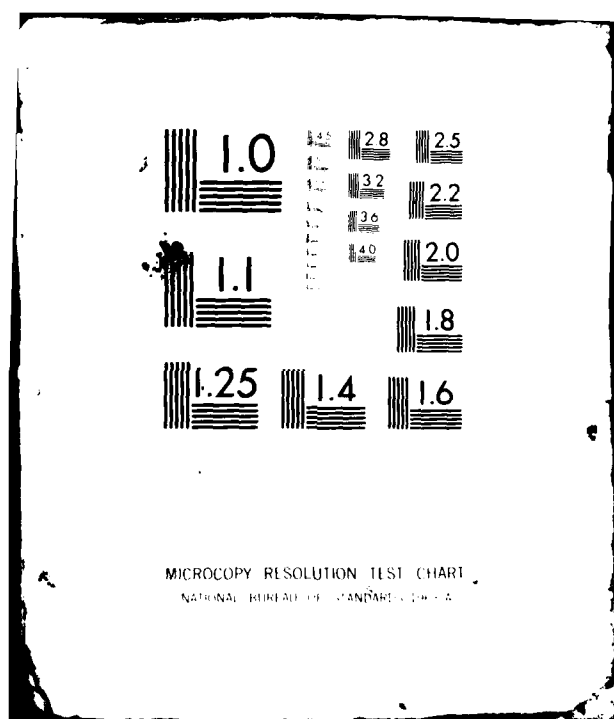
AD-A111

AD-A111

AD-A111

AD-A111

END
DATE
FILMED
3 82
DTIC



with its number of nodes, degrees of freedom, nonzero mass elements and stiffness elements*. The structure is configured as a truss, but it is assumed that all joints allow a full moment connection. Thus, both bending and axial stiffness are included in the model for all structural members.

To complete the structural scenario, two perturbation models were also included in the CSDL #2 design. Combined lumped-mass perturbations and beam stiffness perturbations are obtained by changing the thickness of the 25 cm diameter graphite epoxy hollow tubes used in the metering truss. The locations of these perturbations are shown in Fig. 4-4, and their specific descriptions are given in Tables 4-1 and 4-2, where P_0 denotes the nominal model, and P_2 and P_4 the perturbed models. The latter two models are to be used to evaluate the control laws designed for P_0 and, hence, provide a specific test for control-system robustness. The frequencies of the first 44 flexible modes for P_0 , are given in Section 4.2, Table 4-3.[†] Natural damping was assumed to be 0.1% for all modes.

The disturbance model consists of two sinusoidal forces applied to a point on the upper optical structure and a point on the equipment section below the isolators, as shown in Fig. 4-5. These forces simulate on-board vibrating equipment. It is assumed that they both act simultaneously.

4.2 The CSDL #2 Line-of-Sight Control Problem

To define a control problem for the CSDL #2 configuration, a performance metric is required. This is chosen to be the line-of-sight (LOS) error, i.e., the displacement of the image of a target when the structure deforms under the influence of the two on-board sinusoidal disturbances. The mathematical model giving the displacement law is described

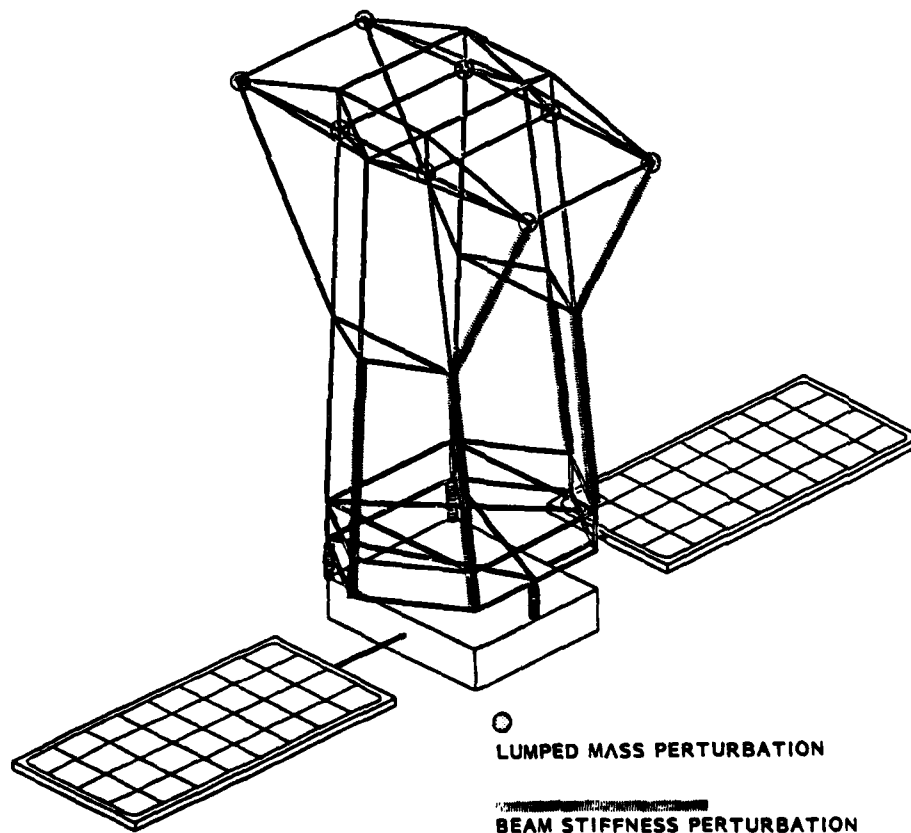


Fig. 4-4. CSDL #2 model perturbation (qualitative).

*Reference 17 incorrectly lists 37 nodes and 117 stiffness elements

[†]These were obtained using SPAR, a large-scale structural dynamics analysis program (available through the COSMIC library) whose detailed numerical procedures, structural reduction, eigen-computations, etc., are implemented differently than in NASTRAN. SPAR was used for comparison purposes, and for the first 68 modes, frequencies varied less than 0.1% compared with NASTRAN. In Table 4-3, modes 1 through 6 represent rigid-body modes.

Table 4-1. Description of member perturbations.

MEMBER NO.	NODE A	NODE B	NOMINAL MODEL P0	PERTURBED MODELS	
				P2	P4
PROPERTY					
76	8	14	400	1	1
80	9	15	400	1	2
81	11	17	400	1	1
85	13	19	400	1	2
99	15	32	400	1	2
101	17	33	400	1	2

PROPERTY 1	PROPERTY 2	PROPERTY 400 (NOMINAL)
25 cm DIA x 0.10 cm ROUND TUBE	25 cm DIA x 0.025 cm ROUND TUBE	25 cm DIA x 0.05 cm ROUND TUBE
$A = 7.823 \times 10^{-4} \text{ m}^2$	$A = 1.962 \times 10^{-4} \text{ m}^2$	$A = 3.919 \times 10^{-4} \text{ m}^2$
$I = 6.063 \times 10^{-6} \text{ m}^4$	$I = 1.539 \times 10^{-6} \text{ m}^4$	$I = 3.0496 \times 10^{-6} \text{ m}^4$
$J = 1.213 \times 10^{-5} \text{ m}^4$	$J = 3.059 \times 10^{-6} \text{ m}^4$	$J = 6.099 \times 10^{-6} \text{ m}^4$

Table 4-2. Description of mass perturbations.

NODE NO.	NOMINAL MODEL P0	PERTURBED MODELS	
		P2	P4
27	375	350	375
28	375	350	375
29	375	350	375
30	375	350	375
32	500	500	550
33	500	500	450
34	250	300	300
35	250	250	200

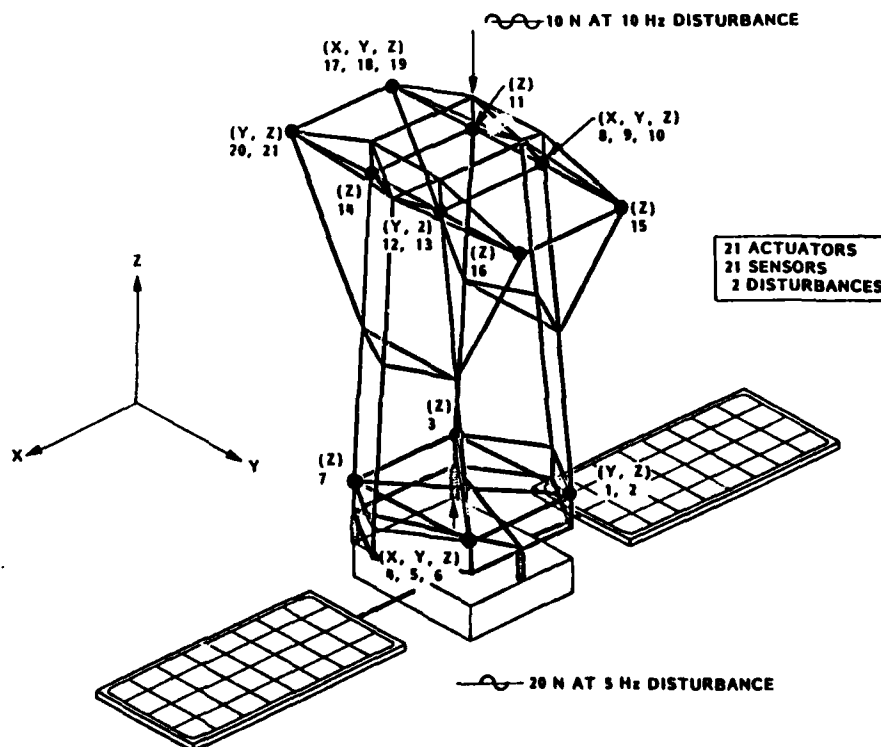


Fig. 4-5. Disturbances and actuator/sensor locations for CSDL #2.

in Ref. 17, wherein it must be assumed that the coordinates x_I, y_I of the image point are chosen to be zero.

The LOS error is a vector with components LOSX and LOSY in the focal plane, and is a function of the transverse defocus (X,Y). The defocus itself is denoted by Z, and together, X, Y, Z are linear functions of the 16 optical variables:

$$X_p, Y_p, X_t, Y_t, X_f, Y_f, Z_p, Z_s, Z_t, Z_f, \theta X_p, \theta Y_p, \theta X_s, \theta Y_s, \theta X_t, \theta Y_t,$$

where the $X_i, Y_i, Z_i, \theta X_i, \theta Y_i$ refer to the translations and rotations in the global X, Y and Z directions of the primary (p), secondary (s), tertiary (t) and focal plane (f). These 16 optical variables are, in turn, linear functions of 21 variables which are X, Y or Z coordinates of 12 particular nodes whose displacements control the geometry of the optical path. These 21 variables are therefore the physical coordinates of LOS and correspond to 21 degrees of freedom of the structure. Indeed, each of these physical coordinates can now be given its modal expansion in terms of the structure's mode shapes, and the resulting transformation:

LOS → OPTICAL VARIABLES → PHYSICAL COORDINATES → MODAL COORDINATES

gives rise to the modal expansion of the LOS. More importantly, it suggests directly that, in order to control the LOS, one should control its physical coordinates where actuators can be placed. And indeed, the control actuators and their locations were chosen to correspond to these 21 degrees of freedom at the 12 particular nodes involved, as shown in Fig. 4-5.

Remarks:

1. This actuator selection procedure is generic in that it can always be implemented whenever an LOS is to be controlled. In other applications, extrema of controllability and/or observability maps can be used.
2. An interesting consequence of the above selection of colocated sensors/actuators is that, in the resulting on-board disturbance-rejection control design, the steady-state behavior of the CSDL #2 spacecraft is not guaranteed to be globally quiescent. However, the 21 actuators keep the 12 nodes (where they are mounted) under sufficient displacement control to guarantee good LOS performance, but do little to control the rest of the structure's vibrational motion since the control system was not designed for that purpose (see Section 4.4).

The performance requirements are specified by the total LOS error defined as the quantity

$$LOS = \sqrt{(LOSX)^2 + (LOSY)^2}.$$

The contribution of each flexible mode to LOS can be calculated as follows. For simplicity, denote by l_α ($\alpha=1$) the quantities $l_1 = LOSX$ and $l_2 = LOSY$. The expression of LOS in terms of its physical coordinates is then of the form

$$\begin{aligned} l_\alpha &= \sum_i l_{\alpha i} x_i \\ &= \sum_n \sum_i l_{\alpha i} \phi_{in} q_n \\ &= \sum_n L_{\alpha n} q_n, \quad (L_{\alpha n} = \sum_i l_{\alpha i} \phi_{in}) \end{aligned} \quad (4.1)$$

in which the modal expansion $x_i = \sum_n \phi_{in} q_n$ was used. The value $S_{\alpha n}$ of $L_{\alpha n} q_n(t)$ represents the contribution of the n th mode to the components of the LOS error. The modal amplitude q_n is obtained from the structural transfer function defined in Eq. (2.8) of Section 2.2, and its maximum is the sum of the amplitudes corresponding to the two sinusoidal disturbance frequencies ω_k ($k=1,2$). Thus:

$$S_{\alpha n} = \max L_{\alpha n} q_n = \sum_{k=1,2} \frac{|L_{\alpha n} \phi_{kn} f_k|}{\sqrt{(\omega_k^2 - \omega_n^2)^2 + 4\zeta_n^2 \omega_k^2 \omega_n^2}}, \quad (4.2)$$

where f_k denotes the magnitude of the k th disturbance. Finally, the contribution of the n th node to the LOS error is defined by

$$S_n = \sqrt{S_{1n}^2 + S_{2n}^2}. \quad (4.3)$$

The control problem is to reduce the LOS error produced by the two steady-state disturbances below a required level. The disturbance magnitudes and the performance tolerances used in this paper were based on preliminary CSDL estimates*, and are as follows:

Upper truss disturbance: 10 N @ 10 Hz
 Lower truss disturbance: 20 N @ 5 Hz
 LOS tolerance: 50×10^{-9} rad
 Defocus tolerance: 25×10^{-6} m } Performance requirements

The LOS open-loop performance of CSDL #2, obtained from Eqs. (4-1) and (2.8) (Section 2.2), is 972 nrad. The axial defocus already meets the requirements, and hence is discarded from further consideration. The LOS error can be broken down into its modal components defined in Eq. (4.3), and are listed in Table 4-3 for the first 44 flexible modes and 3 rigid=body rotational modes.

Table 4-3. System modes and their contributions to the line-of-sight error

MODE NO.	NATURAL FREQ.	MODAL LOS ERROR (n RAD)
4	0.000	98
5	0.000	66
6	0.000	--
7	0.145	41
8	0.263	--
9	0.317	--
10	0.333	7
11	0.443	--
12	0.578	65
13	0.581	12
14	1.22	113
15	1.30	--
16	1.34	175
17	1.72	6
18	1.81	--
19	1.81	--
20	1.88	--
21	2.36	633
22	2.98	365
23	3.17	--
24	3.38	815
25	5.16	--
26	5.26	143
27	7.87	--
28	8.11	67
29	8.35	124
30	8.57	630
31	8.78	1
32	8.80	--
33	11.32	--
34	11.49	45
35	12.72	382
36	13.52	115
37	13.71	334
38	14.16	37
39	15.65	59
40	16.07	35
41	16.52	47
42	16.74	48
43	17.15	87
44	17.82	30
45	19.07	93
46	23.77	3
47	24.41	39
48	25.91	17
49	26.27	--
50	26.36	200

*These were subsequently revised, and in Ref. 17 they have been scaled up by a factor of 20. Since these quantities scale linearly, the control problem remains unchanged.

4.3 Control Design for CSDL #2

Active control is clearly required to meet the LOS requirements. Conventionally, vibration control has been realized by imparting damping to all structural modes, so as to reduce the overall response of the structure. Unfortunately, for steady-state disturbances, structural damping often fails to achieve the expected result and may even worsen the performance. As a test, 30% damping was assumed to be present in all modes. The total LOS error with damping was found to increase from 972 nrad to 1131 nrad. This phenomenon can be explained with reference to Fig. 4-6 which shows the ratios of transfer functions (LOS/disturbance) obtained, respectively, for the assumed 30% and the nominal 0.1% damping ratios. Near the disturbance frequencies, these ratios are larger than 1 in three cases out of four. Similar results are obtained when there are no rigid-body modes (Table 4-4).

The conclusion to be drawn from this example is that damping augmentation does not work in all cases. Its effectiveness depends specifically upon the type of disturbance and the distribution of the modal frequencies in the disturbance spectrum.

The approach which is taken here to solve the CSDL #2 control problem is based on the control-design method of Section 3. A quadratic performance criterion which contains explicitly the effect of the two disturbances is optimized. Thus, the LOS error due to these 5 Hz and 10 Hz disturbances is strongly reduced, while the overall system is stable.

The overall procedure for a disturbance-rejecting controller design is shown in Fig. 4-7. As was stated in Section 4.2, 21 single degree-of-freedom force actuators were selected to control the physical coordinates of the LOS. These actuators are located at the structural nodes shown in Fig. 4-7. Correspondingly, 21 sensors collocated with these actuators and measuring displacement rates are introduced for the low-authority controller (LAC).

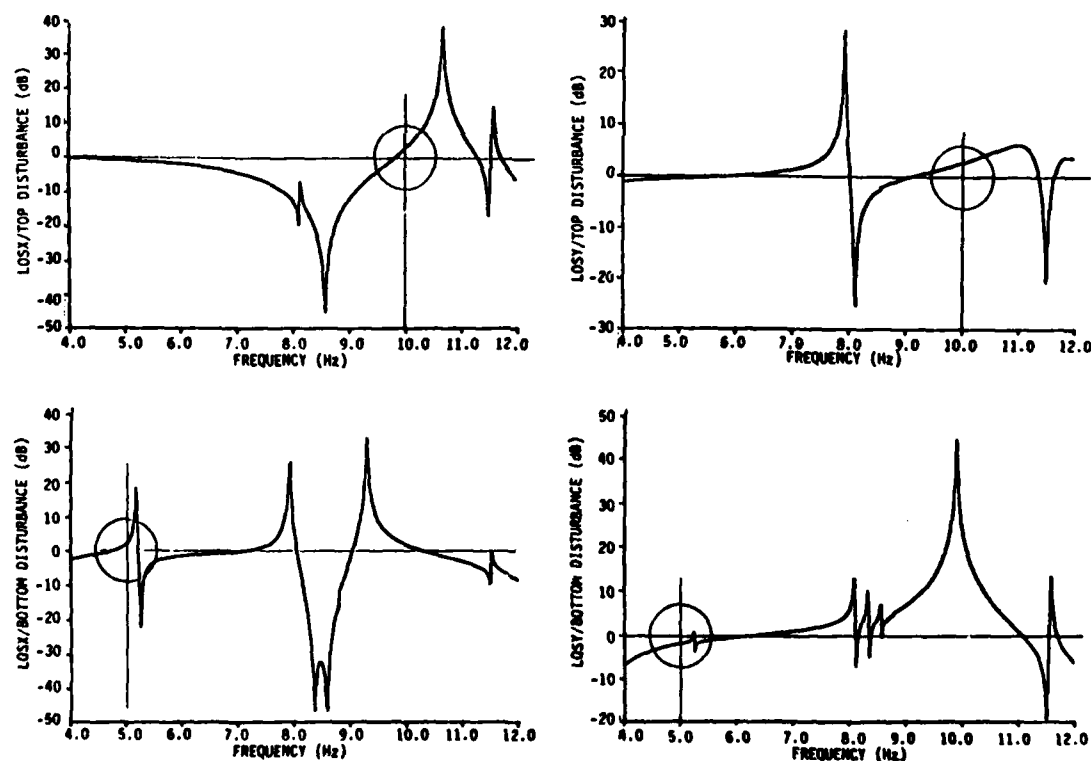


Fig. 4-6. Ratio of LOS-error-to-disturbance transfer functions for damping ratios of 0.3 and 0.001.

Table 4-4. Effect of passive damping on LOS performance.

	WITHOUT CONTROL (n rad)	WITH 30% PASSIVE DAMPING
No Rigid-Body Modes	990	1,180
With Rigid-Body Modes	972	1,131

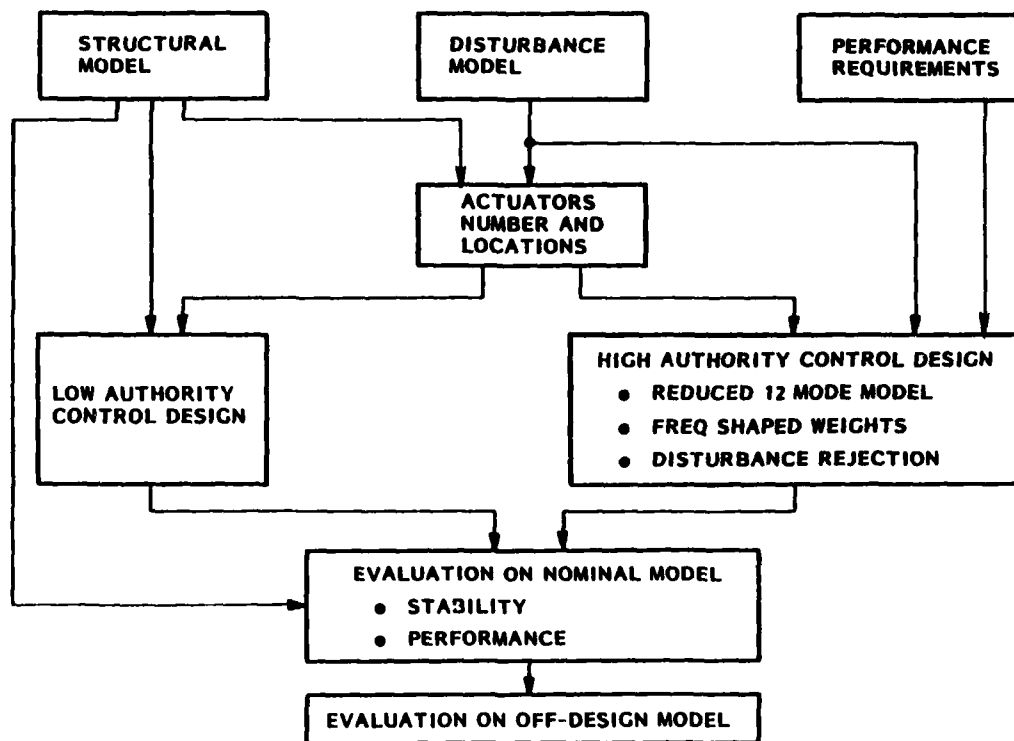


Fig. 4-7. Control design approach for disturbance rejection.

The high-authority controller (HAC) uses only three measurements: the two LOS errors (LOS_x and LOS_y) and the rigid-body angular rotation θ_z . This last measurement is necessary to control the attitude of the spacecraft about the z-axis, which is otherwise not observable through the line of sight. These measurements may be obtained directly by optical means or reconstructed from structural information and kinematics.

Three modes were first discarded (20, 33 and 49) from the initial model because they were neither observable nor controllable. The evaluation model thus contains 3 rigid-body modes and 41 flexible modes. The reduced model was obtained by selecting ten modes with the highest controllability \times observability product and the two most disturbable modes as shown in Table 4-5. This 12-mode model (which includes the 3 rigid-body modes) is used for control design. Since the disturbances occur at the two discrete frequencies (5 and 10 Hz), the following state penalty is used in the design

$$J = T(j\omega)[LOS_x^2 + LOS_y^2] + bu^T u, \quad (4.4)$$

where the frequency-shaping weight is given by

$$T(j\omega) = \frac{4}{(\omega^2 - 100\pi^2)^2} + \frac{10}{(\omega^2 - 400\pi^2)^2}. \quad (4.5)$$

Table 4-5. Mode selection for HAC (12 modes).

ORDERING BASED ON MODAL COST	ORDERING BASED ON CONTROLLABILITY	ORDERING BASED ON OBS/CONTROLLABILITY PRODUCT
24✓	21✓	21✓
21✓	28✓	30✓
30✓	30✓	17✓
22✓	17✓	28✓
16	12✓	4✓
26	11	5✓
29	13✓	6✓
14	4✓	12✓
4		13✓
28✓		7✓
5		

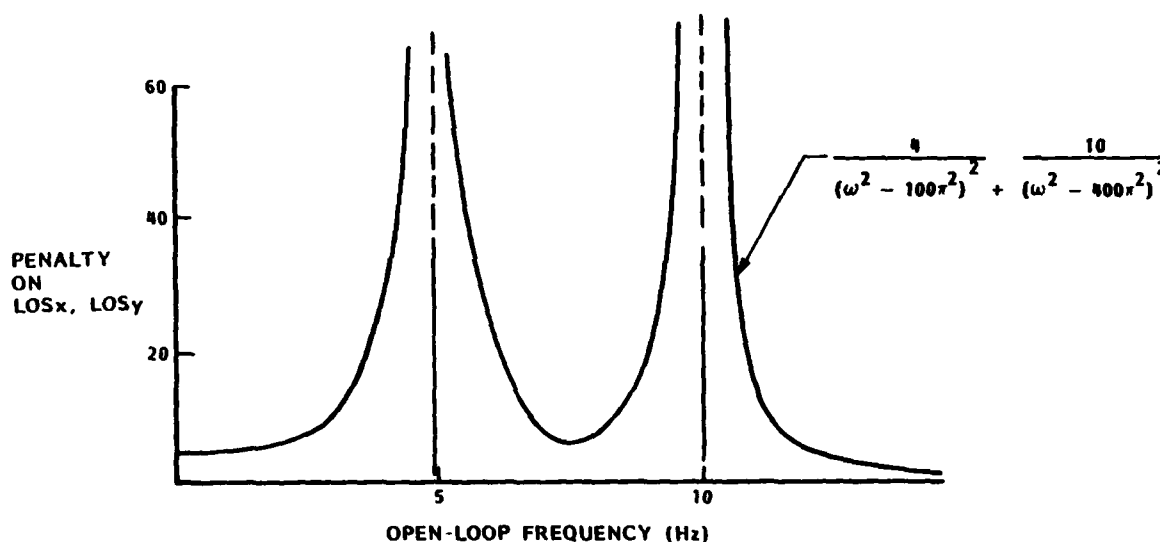
A plot of $T(j\omega)$ as a function of frequency is shown in Fig. 4-8. The control weight b is selected to ensure that the control effort in the closed loop is not excessive.

The 24 states of the reduced model are estimated by a Kalman filter to which the 8 additional states necessary for frequency shaping are appended. The overall structure of the controller/filter is shown in Table 4-6. The measurement vector y is used directly as input to the estimator. In the reduced model, this measurement is approximated by y_o based on a reduced number of states. The quadratic weights used in the design are given in Table 4-7 and the resulting closed-loop filter and controller damping ratios are given in Table 4-8.

The LAC law is designed separately to minimize spillover. The model used for LAC synthesis includes the 12 modes used for HAC plus 10 additional modes chosen outside of the HAC bandwidth on the basis of their controllability. The LAC mode selection is shown in Table 4-9. The LAC control law is defined by the diagonal gain matrix C_L relating the 21 measured velocities at the actuator locations to the corresponding 21 actuator forces. These LAC gains are selected to provide approximately 3% damping in all modes. Because of variation in level of controllability from mode to mode, it is possible to achieve this condition only approximately. Table 4-10 shows the LAC gains.

4.4 Performance Evaluation for CSDL #2

The HAC/LAC controller performance evaluation combines the HAC controller/filter equations (shown in Table 4-6), the LAC control law and the 44-mode evaluation-model equations. The total system is of order 120. The stability is evaluated by complex eigenvalue determination shown in Table 4-11. A significant feature of the design



REQUIRES FOUR ADDITIONAL MODES IN CONTROL DESIGN

Fig. 4-8. Frequency-shaped weights for disturbance rejection.

Table 4-6. Frequency-shaped controller/filter structure.

<u>Reduced model for optimal control synthesis</u>	
$\dot{\hat{x}} = F_O \hat{x} + G_O u + \Gamma_O w$	24-state model (12 modes)
$\dot{\xi} = \Omega \xi + M y_o$	8 frequency-shaping states (2 frequencies)
$z_o = L_O \hat{x}$	3 measurements
<u>Controller</u>	
$u = C_O \hat{x} + C_\xi \xi$	21 controls
<u>Estimator</u>	
$\dot{\hat{x}} = F_O \hat{x} + G_O u + K(z - L_O \hat{x})$	Kalman filter (24 states)
$\dot{\xi} = \Omega \xi + M z$	frequency-shaping states (8 states)
$u = C_O \hat{x} + C_\xi \xi$	control law (21 controls)

Table 4-7. Control and filter weighting used in the design (non zero elements).

STATE PENALTY WEIGHTING							
AS (1, 1) =	1.000-04	AS (2, 2) =	1.000-04	AS (3, 3) =	1.000-04	AS (4, 4) =	1.000-04
AS (5, 5) =	1.000-04	AS (6, 6) =	1.000-04	AS (27,27) =	1.000-03	AS (28,28) =	1.000-03
AS (31,31) =	4.000-02	AS (32,32) =	4.000-02				
CONTROL PENALTY WEIGHTING							
R (1, 1) =	2.000-11	R (1, 2) =	2.000-11	R (1, 3) =	2.000-11	R (1, 4) =	2.000-11
R (1, 5) =	2.000-11	R (1, 6) =	2.000-11	R (1, 7) =	2.000-11	R (1, 8) =	2.000-11
R (1, 9) =	2.000-11	R (1, 10) =	2.000-11	R (1, 11) =	2.000-11	R (1, 12) =	2.000-11
R (1, 13) =	2.000-11	R (1, 14) =	2.000-11	R (1, 15) =	2.000-11	R (1, 16) =	2.000-11
R (1, 17) =	2.000-11	R (1, 18) =	2.000-11	R (1, 19) =	2.000-11	R (1, 20) =	2.000-11
R (1, 21) =	2.000-11						
STATE NOISE DISTRIBUTION USED FOR FILTER DESIGN							
D (1, 1) =	1.000-06	D (3, 2) =	1.000-06	D (5, 3) =	1.000-06	D (7, 4) =	1.000-06
D (9, 5) =	1.000-00	D (11, 6) =	1.000-00	D (13, 7) =	1.000-00	D (15, 8) =	1.000-00
D (17, 9) =	1.000-00	D (19, 10) =	1.000-00	D (21, 11) =	1.000-00	D (23, 12) =	1.000-00
STATE NOISE COVARIANCE							
W (1, 1) =	1.000-01	W (1, 2) =	1.000-01	W (1, 3) =	1.000-01	W (1, 4) =	1.000-04
W (1, 5) =	1.000-04	W (1, 6) =	1.000-04	W (1, 7) =	1.000-04	W (1, 8) =	1.000-04
W (1, 9) =	1.000-04	W (1, 10) =	1.000-04	W (1, 11) =	1.000-04	W (1, 12) =	1.000-04
MEASUREMENT DISTRIBUTION MATRIX							
M (1, 2) =	1.000-00	M (1, 8) =	-2.577-07	M (1, 10) =	7.381-04	M (1, 12) =	2.416-06
M (1, 14) =	2.738-05	M (1, 16) =	2.212-05	M (1, 18) =	1.345-04	M (1, 20) =	5.610-07
M (1, 22) =	-4.273-04	M (1, 24) =	1.867-02	M (2, 4) =	1.000-00	M (2, 8) =	3.254-04
M (2, 10) =	-6.868-06	M (2, 12) =	8.721-04	M (2, 14) =	-2.775-03	M (2, 16) =	1.376-02
M (2, 18) =	2.734-06	M (2, 20) =	-4.542-04	M (2, 22) =	-1.702-03	M (2, 24) =	-1.139-05
M (3, 6) =	1.000-00						
MEASUREMENT NOISE COVARIANCE							
V (1, 1) =	5.000-11	V (1, 2) =	5.000-11	V (1, 3) =	5.000-11		

Table 4-8. Closed-loop high-authority-control (HAC) design.

MODE NO.	OPEN-LOOP FREQ. (Hz)	CLOSED-LOOP CONTROL DAMPING RATIO	STATE ESTIMATOR DAMPING RATIO
4	Rigid Body	0.74	0.70
5	Rigid Body	0.78	0.71
6	Rigid Body	0.78	0.71
7	0.145	0.009	0.247
12	0.578	0.014	0.039
13	0.581	0.012	0.046
17	1.72	0.021	0.017
21	2.36	0.127	0.044
22	2.99	0.001	0.001
24	3.39	0.001	0.001
28	8.118	0.004	0.001
30	8.57	0.046	0.005
FREQ.-	5.0	0.028	
SHAPING	5.0	0.057	
MODES	10.0	0.011	
	10.0	0.036	

Table 4-9. LAC mode selection.

4, 5, 6, 7, 12, 13, 17, 21, 22, 24, 28, 30(12 HAC modes)
34, 35, 37, 39, 41, 43, 44, 45, 46, 50 (10 high-frequency modes)

Table 4-10. LAC gains C_L

ACTUATOR NO.	GAIN N/ms ⁻¹	ACTUATOR NO.	GAIN N/ms ⁻¹
1	-548	12	-43.9
2	-815	13	0.0
3	-9830	14	-3380
4	0.0	15	-7120
5	-458	16	-3850
6	-2380	17	-3450
7	-5470	18	-583
8	-12800	19	0.0
9	-220	20	-94.6
10	-6410	21	-3500
11	-6620		

Table 4-11. Closed-loop poles with HAC/LAC controller.

CLOSED-LOOP MODE	FREQUENCY	DAMPING	CLOSED-LOOP MODE	FREQUENCY	DAMPING
1	0.027865	.715573	32	4.9365	.048290
2	0.032277	.677591	33	5.0330	.048502
3	0.037175	.592291	34	5.1613	.001000
4	0.037728	.847899	35	5.2598	.001000
5	0.042809	.784749	36	6.8506	.079446
6	0.057039	.789423	37	7.8743	.001000
7	0.11387	.521452	38	8.1267	.005536
8	0.15508	.241302	39	8.3553	.001001
9	0.24282	.245263	40	8.4296	.035427
10	0.29085	1.000000	41	8.5404	.100827
11	0.33410	.033916	42	8.7853	.001000
12	0.35873	.027640	43	8.8050	.001000
13	0.53354	1.000000	44	9.9597	.026767
14	0.56785	.215362	45	9.9798	.006723
15	0.57863	.039949	46	11.486	.030355
16	0.58241	.045567	47	12.762	.035712
17	0.58627	.091911	48	13.525	.001016
18	1.2235	.001175	49	13.608	.026854
19	1.3015	.006101	50	14.168	.013692
20	1.3449	.004299	51	14.524	.051410
21	1.7175	.018675	52	14.594	.013809
22	1.7182	.131110	53	15.743	.035748
23	1.8178	.001014	54	16.513	.023005
24	1.8188	.001009	55	16.787	.018722
25	2.2411	.468032	56	17.178	.056485
26	2.3519	.044981	57	19.903	.026593
27	2.9885	.001181	58	23.883	.046616
28	2.9886	.001037	59	24.509	.011362
29	3.1753	.001158	60	26.092	.009018
30	3.3860	.001082	61	26.178	.030306
31	3.3864	.001226			

is that no pole has a lower damping ratio in closed loop than in open loop. The evaluation of the LOS error is obtained by computing the steady-state responses at 5 and 10 Hz using the complex equation:

$$l = H_S(j\omega_k I - F_S)^{-1} \Gamma_S w_k, \quad j \equiv \sqrt{-1}, \quad (4.6)$$

where l is the LOS error vector (whose components have complex amplitudes), w_k is the magnitude of the disturbance at the frequency $\omega_k/2\pi$, and the matrices F_S , Γ_S and H_S correspond to the total closed-loop system defined by the equations

$$\begin{aligned} \dot{x}_S &= F_S x + \Gamma_S w, \\ l &= M_S x. \end{aligned} \quad (4.7)$$

The magnitude of the vector sum of x-axis and y-axis LOS error is found to be 0.013 nrad.

The larger than four-order of magnitude reduction in the LOS error is in striking contrast to the relatively small closed-loop damping ratios, showing that large performance improvements do not necessarily require large increases in damping ratios. This significant result is indeed typical of the application of optimal control. It exemplifies the difference between the colocated LAC system which locally absorbs vibratory energy, and the HAC system which judiciously redistributes it, producing favorable cancellations so as to optimize the performance. However, this latter controller can be much more sensitive to model errors, and this sensitivity may be evaluated on perturbed models.

Evaluation on perturbed models.— The two perturbed models P_2 and P_4 described in Section 4.1 are used to evaluate the previously described HAC/LAC controller. The transfer functions between the x-axis LOS error and the upper-disturbance input are compared in Fig. 4-9 for the nominal and the two perturbed models. There is a significant change in the P_2 transfer function around 10 Hz, where an interchange between modes #30 and #32 occurs. This can be seen in Table 4-12 where the LOS modal contributions are compared for the three models, allowing mode #30 to be tracked through the perturbations P_2 and P_4 .

The controller is stable for perturbed model P_4 . However, stability with P_2 requires only the knowledge of the natural frequency of mode #30 (which had become mode #32 and was no longer properly represented). LOS errors for the three models are compared in Table 4-13. Table 4-14 compares the open-loop performance to the closed-loop LOS errors. The improvement in performance for the perturbed models is of the same order of magnitude as for the nominal models.

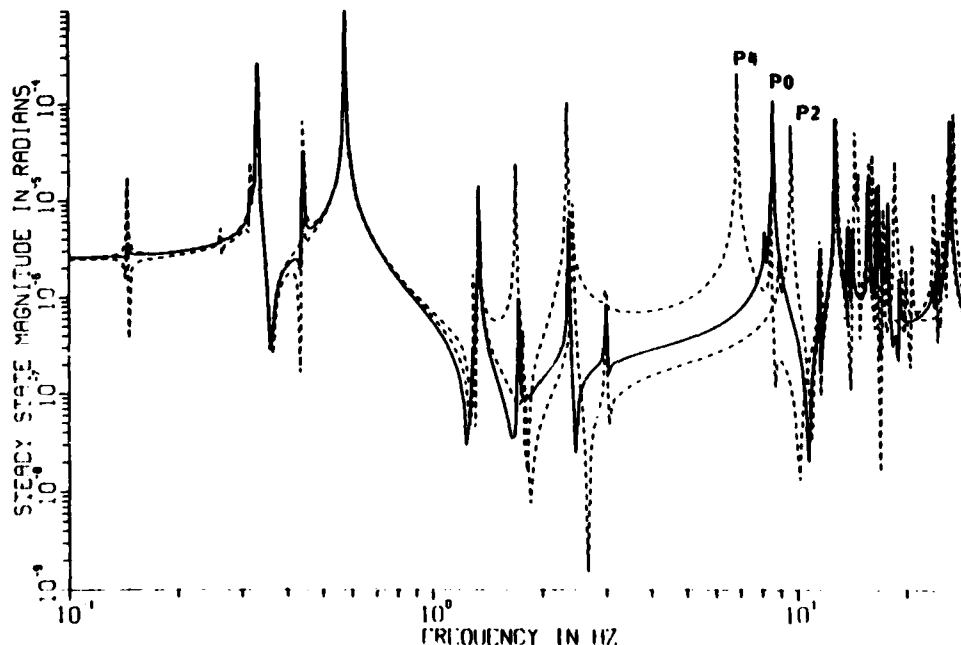


Fig. 4-9. Frequency responses to sinusoidal disturbance of upper support truss, nominal and perturbed models.

Table 4-12. Frequency and LOS observability comparisons — nominal and perturbed models

MODE NO.		OPEN-LOOP FREQ (Hz)			LOS MODAL COMPONENTS ^(*)		
		FOR MODEL			FOR MODEL		
FLEX #	CSDL #	P0	P2	P4	P0	P2	P4
1	7.	.145	.145	.145	.325	.330	.324
2	8.	.263	.262	.263	.214	.202	.218
3	9.	.317	.317	.317	.001	.001	.005
4	10.	.333	.333	.333	.229	.227	.230
5	11.	.443	.443	.443	.006	.001	.023
6	12.	.578	.576	.578	.736	.724	.746
7	13.	.581	.581	.581	.873	.875	.872
8	14.	1.224	1.224	1.224	.236	.213	.244
9	15.	1.300	1.301	1.300	.152	.047	.224
10	16.	1.347	1.347	1.347	.159	.149	.163
11	17.	1.721	1.769	1.695	2.775	2.046	3.096
12	18.	1.818	1.818	1.818	.001	.003	.004
13	19.	1.819	1.819	1.819	.012	.011	.013
14	20.	1.889	1.889	1.889	.001	.001	.001
15	21.	2.364	2.427	2.342	13.757	13.769	13.665
16	22.	2.989	2.989	2.989	.135	.118	.143
17	23.	3.175	3.175	3.175	.261	.275	.268
18	24.	3.386	3.386	3.386	.454	.478	.442
19	25.	5.161	5.161	5.161	.000	.000	.000
20	26.	5.260	5.260	5.260	.034	.027	.042
21	27.	7.874	7.874	7.874	.000	.000	12.721
22	28.	8.118	8.355	7.874	1.756	.064	.000
23	29.	8.355	8.785	8.355	.283	.003	.151
24	30.	8.572	8.805	8.463	18.569	.012	16.419
25	31.	8.785	8.851	8.755	.331	3.713	.020
26	32.	9.005	9.601	8.605	.052	15.290	.027
27	33.	11.221	11.321	11.321	.010	.002	.015
28	34.	11.499	11.571	11.467	2.237	2.834	2.708
29	35.	12.727	12.837	12.697	11.001	11.357	11.079
30	36.	13.525	13.525	13.524	.521	.431	1.027
31	37.	13.716	13.806	13.612	10.141	11.315	10.952
32	38.	14.132	14.230	14.147	7.145	4.350	6.826
33	39.	15.654	16.394	14.417	14.510	10.816	10.270
34	40.	16.075	16.553	14.710	10.523	14.871	7.458
35	41.	16.527	17.200	15.745	7.105	5.481	8.530
36	42.	16.748	18.585	16.571	3.952	15.542	11.527
37	43.	17.157	19.001	16.731	8.405	5.091	13.010
38	44.	17.629	19.351	17.265	3.440	1.096	3.928
39	45.	19.072	20.652	19.337	14.472	6.214	12.617
40	46.	23.773	25.180	23.839	28.120	25.158	25.864
41	47.	24.416	25.208	24.531	38.221	20.782	39.313
42	48.	25.910	25.934	26.043	12.027	34.004	9.150
43	49.	26.272	26.272	26.272	.000	.000	.000
44	50.	26.565	27.004	26.254	17.817	21.654	18.493

$$(*) (LOS)_n = 10^3 \sqrt{(LOSX)_n^2 + (LOS Y)_n^2} \text{ WHERE } (LOSX)_n, (LOS Y)_n \text{ ARE NTH ELEMENTS IN FIRST TWO ROWS OF LOS MATRIX}$$

Table 4-13. LOS error and control efforts for nominal and perturbed models

		NOMINAL MODEL	P ₂	P ₄
LOS _x (nrad)	5 Hz	0.002	0.004	0.001
	10 Hz	0.005	0.007	0.004
LOS _y (nrad)	5 Hz	0.006	0.007	0.005
	10 Hz	0.004	0.004	0.004
Average Control Effort (N)		0.82	0.90	0.69

Table 4-14. Comparison of open-loop and closed-loop LOS errors.

	OPEN LOOP (nrad)	CLOSED LOOP (nrad)	CLOSED LOOP AS A FRACTION OF OPEN LOOP	AVERAGE CONTROL EFFORT (Newtons)
Nominal	972	0.013	13 x 10 ⁻⁶	0.82
P2	1,740	0.016	9.2 x 10 ⁻⁶	0.90
P4	674	0.010	15 x 10 ⁻⁶	0.69

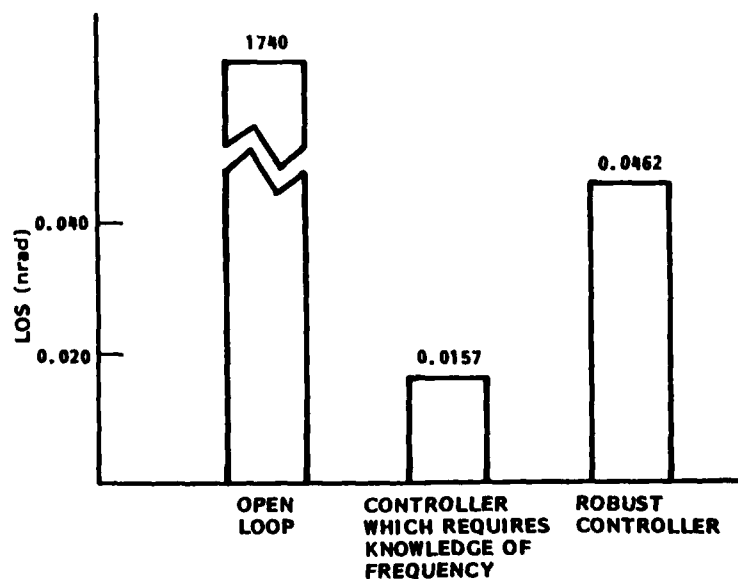
Controller simplification.— Because of the eight additional states required by the implementation of frequency-shaping methods, the modified LQG problem from which control gains are obtained is of order 32. For practical implementation reasons, it may be desirable to reduce this order. The controller is simplified by setting the control and filter gains corresponding to various modes to zero. Table 4-15 shows three simplified controllers (with orders 30, 26, and 20); the simplification does not degrade the LOS error significantly and the control effort is also the same as for the full-order controller.

Table 4-15. Closed-loop controller simplification.

	MODES IN MODEL			
	NOMINAL	1	2	3
	RIGID	✓	✓	✓
	RIGID	✓	✓	✓
MODES	RIGID	✓	✓	✓
	0.145	✓	✓	X
	0.578	✓	✓	X
	0.581	✓	✓	X
	1.72	✓	✓	✓
	2.36	✓	✓	✓
	2.99	✓	X	X
	3.39	✓	X	X
	8.12	X	X	X
	8.57	✓	✓	✓
COST	12.6	12.7	12.7	12.7
CONTROL	0.822	0.822	0.821	0.822
CONTROLLER ORDER	32	30	26	20

Note that when a 20th order controller is designed directly, the closed-loop system is unstable.

Robust controller.— A robust controller may be designed so that knowledge of the natural frequency of mode #30 is not required for stability of perturbed model P_2 . The robust design is obtained by increasing the control penalty and measurement noise covariance by a factor of ten. The robust controller is stable for all models. The closed-loop performance for P_2 degrades from 0.016 nrad to 0.046 nrad (see Fig. 4-10). This result illustrates the usual trade-off between maximum performance and robustness. Slightly relaxing the performance requirement can produce large improvements in system robustness.

Fig. 4-10. A robust controller for P_2 .

5. COMPUTATIONAL ALGORITHMS

Large space structure modeling, control design, and closed-loop evaluation require numerical solutions to high-order matrix problems. Standard digital computer procedures used successfully for small-scale problems are simply not applicable in the large space structure case because of high memory storage requirements and numerical instabilities. In addition, a significant part of the software is devoted to the manipulation and construction of the various large matrices involved in the control syntheses and evaluation procedures. To give an idea of the size and type of the software operations needed for the control of large space structures, an example is given next corresponding to the CSDL #2 problem discussed earlier.

In this previous example: (a) 44 modes are used as the total model for the configuration, (b) two disturbances $w = \begin{bmatrix} w_1 \\ w_2 \end{bmatrix}$ are assumed to be applied, each at a given structural node, and (c) 21 single DOF control actuators are placed on the structure. The state equations then take the form

$$\dot{x} = \begin{matrix} 88 \times 1 \\ 88 \times 88 \end{matrix} x + \begin{matrix} 88 \times 21 \\ 88 \times 21 \end{matrix} u + \begin{matrix} 88 \times 2 \\ 88 \times 2 \end{matrix} w, \quad (5.1)$$

where the matrix dimensions are included. The matrices G and Γ are of the form shown in Eq. (2.7) for the G matrix.

Equation (5.1) represents only the initial formulation of the control problem: a large modal model of a disturbed structure to be controlled by a control vector to be determined. For reasons given in Section 2.4, the controller design is carried out on a reduced-order model. For example, in the CSDL #2 configuration, if 12 modes were deemed as the most important ones for designing a certain type of control, then one needs also the equation:

$$\dot{x}_o = \begin{matrix} 24 \times 1 \\ 24 \times 24 \end{matrix} x_o + \begin{matrix} 24 \times 21 \\ 24 \times 21 \end{matrix} u + \begin{matrix} 24 \times 2 \\ 24 \times 2 \end{matrix} w, \quad (5.2)$$

where now those columns of Φ (appearing in G and Γ) corresponding to the discarded modes have to be crossed out, as well as the corresponding ω_n^2 's in the matrix F given in Eq. (2.7).

Equations (5.1) and (5.2) together are still a very incomplete model for the controls problem: they appear as the first two equations (denoted by "PLANT" and "REDUCED MODEL") in Fig. 5-1 which represents the total system equations for a particular

TOTAL SYSTEM

$$\dot{x} = \begin{matrix} 88 \times 1 \\ 88 \times 88 \end{matrix} x + \begin{matrix} 88 \times 21 \\ 88 \times 21 \end{matrix} u + \begin{matrix} 88 \times 2 \\ 88 \times 2 \end{matrix} w$$

PLANT

$$\dot{x}_o = \begin{matrix} 24 \times 1 \\ 24 \times 24 \end{matrix} x_o + \begin{matrix} 24 \times 21 \\ 24 \times 21 \end{matrix} u + \begin{matrix} 24 \times 2 \\ 24 \times 2 \end{matrix} w$$

REDUCED MODEL

$$\begin{bmatrix} \dot{\hat{x}} \\ \hat{e} \end{bmatrix} = \begin{matrix} 32 \times 32 \\ 32 \times 32 \end{matrix} \begin{bmatrix} \hat{x} \\ \hat{e} \end{bmatrix} + \begin{matrix} 32 \times 21 \\ 32 \times 21 \end{matrix} u + \begin{matrix} 32 \times 11 \\ 32 \times 11 \end{matrix} K_1 \begin{bmatrix} M \\ L \end{bmatrix} \begin{bmatrix} \hat{x} \\ \hat{e} \end{bmatrix}$$

FREQUENCY SHAPED KALMAN FILTER

$$u = \begin{matrix} 21 \times 32 \\ 21 \times 32 \end{matrix} \begin{bmatrix} \hat{x} \\ \hat{e} \end{bmatrix} + \begin{matrix} 21 \times 21 \\ 21 \times 21 \end{matrix} G^T x$$

CONTROL

WHERE:

$$F = \begin{bmatrix} F_o & 0 \\ 0 & 0 \end{bmatrix}, \quad \Omega = \begin{bmatrix} 0 & 0 & 1 & 0 \\ 0 & 0 & 0 & 1 \\ \omega_1^2 & 0 & 0 & 0 \\ 0 & -\omega_2^2 & 0 & 0 \end{bmatrix}, \quad L = \begin{bmatrix} 0 \\ L \\ 0 \\ L \end{bmatrix}, \quad L_o = \begin{bmatrix} 0 \\ L_o \\ 0 \\ L_o \end{bmatrix}, \quad \text{AND} \quad \begin{cases} K_1 = \begin{bmatrix} K & 0 \end{bmatrix} \\ L_1 = \begin{bmatrix} L_1 & 0 \end{bmatrix} \\ M_1 = \begin{bmatrix} M_o & 0 \end{bmatrix} \end{cases}$$

L IS THE LOS MATRIX GIVEN BY $\begin{bmatrix} LOSX \\ LOSY \end{bmatrix} = \begin{bmatrix} L \\ 0 \end{bmatrix} x$. L_o IS THE REDUCED LOS MATRIX GIVEN BY $\begin{bmatrix} LOSX \\ LOSY \end{bmatrix} = \begin{bmatrix} L_o \\ 0 \end{bmatrix} x_o$.

M IS THE MEASUREMENT MATRIX GIVEN BY $\begin{bmatrix} LOSX \\ LOSY \end{bmatrix} = \begin{bmatrix} M \\ 0 \end{bmatrix} x$. M_o IS THE REDUCED MEASUREMENT MATRIX GIVEN BY $\begin{bmatrix} LOSX \\ LOSY \end{bmatrix} = \begin{bmatrix} M_o \\ 0 \end{bmatrix} x_o$.

DISTURBANCE FREQUENCIES: $\omega_1/2\pi = 5 \text{ Hz}$, $\omega_2/2\pi = 10 \text{ Hz}$

Fig. 5-1. Total system equations (CSDL #2 control system).

$$\dot{X} = F_S X + \begin{bmatrix} D \\ - \\ 0 \end{bmatrix} w, \quad (5.3)$$

and to compute the associated transfer functions like those shown in Fig. 4-6. To obtain the closed-loop system performance, this solution X is substituted into the measurement equation (third equation of Fig. 5-3):

$$z = [M \quad 0] X, \quad (5.4)$$

and to obtain the control effort (forces), X is substituted into the control equation (second equation of Fig. 5-3):

$$u = CX + C_L^T X, \quad (5.5)$$

where the two terms on the right-hand side, corresponding to the HAC and LAC control effort, can be evaluated separately.

The three components of z in Eq. (5.4) are LOSX, LOSY, and DEFOCUS. (The quantities $LOS \equiv \sqrt{(LOSX)^2 + (LOSY)^2}$ and DEFOCUS are the performance metrics for the particular CSDL #2 controls problem).

In the above discussion, the path from the original structural concept (e.g., CSDL #2) to the final closed-loop evaluation model (Fig. 5-3) constitutes the dynamics and controls modeling of a controlled flexible spacecraft. Thus, in addition to the considerable expertise required to design and synthesize modern optimal control systems, the extensive "preparation of a structure for controls" process must be included in any generalized modeling capability requirements necessary to address the vibration control technology for flexible spacecraft. Control design involves extensive manipulation of large matrices (e.g., construction, modification, partitioning, aggregation, algebraic operations, complex eigenanalysis, etc.). Furthermore, this must be carried out in a large-scale digital computer by referencing the structural dynamics data tape in such a way that any change in the latter (due to model refinement, design modification, etc.) allows one to repeat the entire process rapidly.

6. IDENTIFICATION OF MODELS FROM TEST DATA

Analytical representations of actual space structures may be inaccurate, even at low frequency, and achievable robustness is limited when fixed gain controllers must exhibit high performance. Thus, the need for open-loop system identification from test data both in ground tests and orbital operations is clear. Open-loop testing using curve-fitting (least-squares) techniques to chirp and sine-dwell generated transfer functions is well established [2]. Measurement of closed-loop system characteristics, i.e., verification of closed-loop performance, is, however, not well developed in laboratory tests. Real-time identification and the entire feasibility of ground-test experiments depend on accurate closed-loop identification methods. This section summarizes some requirements and compares promising techniques which may offer the experimental investigator the tools to enhance the understanding of control-configured spacecraft.

Space structure system identification requirements are driven by the following:

1. need to know poles (modal natural frequency and damping ratio) as well as zeros;
2. low damping ratios of open-loop modes and high damping ratio in selected closed-loop modes;
3. high-order systems;
4. multi-input excitation and multi-sensor measurements;
5. the identified model must be of much lower order than the real system — the identification method must work in the presence of truncated modes; and
6. both system and measurement noise sources are present, in general.

This section considers appropriate model forms, identification algorithms, and a brief numerical example. The section concludes with a comparison of techniques.

6.1 Model Forms

Three models forms can be used for large space structure system identification:

1. transfer function or continuous autoregressive moving average (ARMA),
2. sampled-data transfer function or discrete ARMA, and
3. state variables.

Transfer function.— The qxl input u to pxl output y transfer function is

$$\frac{y(s)}{u(s)} = T(s), \quad (6.1)$$

which may be written as

$$T(s) = \frac{N(s)}{D(s)} \quad (6.2)$$

$$= \sum_{i=1}^n \frac{R_i}{(s + \lambda_i)} \quad (6.3)$$

$N(s)$ is a matrix polynomial and $D(s)$ is a scalar polynomial in s . R_i are pxq matrices and λ_i are the pole locations.

For scalar input and output, the transfer function is also written as

$$T(s) = K \sum_{i=1}^m (s + z_i) / \sum_{i=1}^n (s + \lambda_i), \quad (6.4)$$

where z_i are the zeros and K is the gain. A continuous ARMA form is

$$y^{(n)} + \sum_{i=1}^n \alpha_i y^{(n-i)} = \sum_{i=0}^m B_i u^{(m-i)}, \quad (6.5)$$

where $y^{(j)}$ is the j th derivative of y . Advantages and disadvantages of various transfer-function forms are shown in Table 6-1.

Sampled data transfer function.— This transfer function and ARMA representation is similar to the continuous transfer function except a z -transform is used in place of the s -transform.

Because of very small damping ratios characteristic of large space structures, this transfer function could have poor numerical conditioning except when expressed as a combination of residues/poles or zeros/poles.

State-variable models.— Defining the state vector as x , these models are written as

$$\dot{x} = Fx + Gu, \quad (6.6)$$

$$y = Hx. \quad (6.7)$$

F , G and H can take many forms because the $[F, G, H]$ model has the same input-output behavior as a $[TFT^{-1}, TG, HT^{-1}]$ model if T is a nonsingular matrix. If poles, residues and low-frequency gains are to be identified without any a priori knowledge about the structure of the model, the following representation appears useful (for single-input systems):

Table 6-1. Advantages and disadvantages of various transfer function forms.

REPRESENTATION	ADVANTAGES	DISADVANTAGES
Numerator Polynomial Divided by Denominator Polynomial	<ul style="list-style-type: none"> • Easier nonlinear optimization problem in the identification stage 	<ul style="list-style-type: none"> • Numerical conditioning may not be good • Requires solution of polynomials to determine poles and zeros
Residues and Poles	<ul style="list-style-type: none"> • Directly convertible into state-variable form • Good numerical conditioning • Easier estimation problem 	<ul style="list-style-type: none"> • Complex residues • Difficult to interpret control laws and control structures
Gains, Zeros and Poles	<ul style="list-style-type: none"> • Directly usable in classical control design and interpretations of control laws 	Difficult identification problem
Auto-Regressive Moving Average	Same as the first representation	
Discrete Forms	Easiest estimation problem	Often very poor numerical conditioning

$$F = \begin{bmatrix} B_1 & & & \\ & B_2 & & \\ & & \ddots & \\ & & & B_n \end{bmatrix}, \quad G = \begin{bmatrix} 0 \\ 1 \\ 0 \\ 1 \\ \vdots \\ 0 \\ 1 \end{bmatrix}, \quad (6.8)$$

$$B_i = \begin{bmatrix} 0 & 1 \\ -\omega_i^2 & -2\xi_i\omega_i \end{bmatrix}, \quad (6.9)$$

and H is a general matrix with potentially all nonzero elements. With multi-input systems, the remaining part of matrix G is general and unknown. This representation is also suitable for closed-loop control design.

If physical parameters of a structure are to be determined a more general form must be used.

6.2 Identification Algorithms

Although many identification algorithms exist, four appear particularly applicable in large space structure system identification:

1. least squares,
2. extended Kalman filter,
3. instrumental variables, and
4. maximum likelihood with its simplified forms.

Since the principal objective is control design, both the zeros and poles of the transfer function must be identified.

Least squares.— The measured transfer function $T_m(j\omega)$ is fitted to the parametrized transfer function based on Eqs. (6.1)–(6.5). The cost functional is

$$\int_{-\infty}^{\infty} [T(j\omega) - T_m(j\omega)]^* W(j\omega) [T(j\omega) - T_m(j\omega)] d\omega. \quad (6.10)$$

$W(j\omega)$ is a positive-definite Hermitian weighting matrix. A nonlinear optimization numerical procedure is required to determine the parameters of the transfer function.

Extended Kalman filter.— The extended Kalman filter (EKF) uses a state-variable formulation with parameters modeled as a random function

$$\dot{x} = F(\theta)x + G(\theta)u + w, \quad (6.11)$$

$$y = H(\theta)x + v, \quad (6.12)$$

$$\dot{\theta} = E\theta + \eta, \quad (6.13)$$

where θ is the vector of unknown parameters, and w , v and η are noise sources. A nonlinear system Kalman filter may be developed for state equations (6.11) and (6.13) with measurements given by Eq. (6.12).

Instrumental variables method.— The least-squares method gives biased estimates of parameters when the input measurement is contaminated by noise. The instrumental-variables technique was developed to minimize the bias in estimates [18]. In addition, unlike least-squares, the instrumental-variables method does not require solution to a nonlinear programming problem. The instrumental-variable estimates are, therefore, obtained in a single step. The details of the technique are given in Ref. 18. The concept is now described.

The matrix transfer function is expressed as follows:

$$D(j\omega) y(j\omega) = N(j\omega) u(j\omega) + \text{noise},$$

or

$$y(j\omega) = N(j\omega) u(j\omega) + (I - D(j\omega)) y(j\omega) + \text{noise}.$$

$N(j\omega)$ and $D(j\omega)$ are linear functions of the parameters. Therefore, the large space structure transfer function identification problem may be formulated as $y = X\theta + v$, where y and X are the measured data; θ is the vector of system parameters to be identified, and v is random noise with zero mean. The least-squared-error estimate of θ is

$\hat{\theta}_{LS} = (X^T X)^{-1} X^T y$. If the measurements X and the noise v are uncorrelated, this estimate is accurate. However, if X and v are correlated, the expected value is $E(\hat{\theta}_{LS}) = \theta + (X^T X)^{-1} E(X^T v)$, and the least-squared-error estimate will have a bias. In the presence of noise, least-squared-error techniques do not give useful results. In the instrumental-variables technique, a matrix Z is selected which is not correlated with v . Then the instrumental-variables estimate $\hat{\theta}_{IV} = (Z^T X)^{-1} Z^T y$ has no bias, $E(\hat{\theta}_{IV}) = \theta$. In the present case, the measurements at a past time are used for instrumental variables. The time lag τ between the current measurements and the instrumental variables must be long enough so the current random noise is not correlated with the measurements at τ . Averaging all the data to obtain an input/output relation of the form $y = X\theta$ leads to auto- and cross-correlations. Equivalently, integrals of the spectra can be used in the frequency domain. Note that if the parameter τ is set to zero, the algorithm reduces to a least-squared-error estimate.

Maximum-likelihood method.— The standard maximum-likelihood method [19] has to be extended to accommodate specific problems associated with large space structure model estimation. Four problems must be directly addressed:

1. Lumped-mass models of large space structures approximate a small subset of the infinite modes defining dynamic behavior of a structure. The identification method must treat large modeling errors, which appear as nonwhite and non-Gaussian state and measurement noise.
2. The models are of high order. Including 20 or more modes in a model is not uncommon.
3. The model order must be specified based on control requirements or sensor/disturbance bandwidth, or identified from data.
4. Because of the interest in actively controlled structures, the identification technique must work in both open- and closed-loop.

Table 6-2 shows extensions of the maximum-likelihood method to solve the above problems.

The problem associated with nonwhite noise has made previous applications difficult. Frequency-shaping concepts can help resolve this problem. With reference to state equations (6.6) and (6.7), the state transition and measurement distribution matrices do not change if the inputs, states and outputs are filtered by the same transfer function. Therefore, we may use an equivalent model

$$\begin{aligned} x_c &= Fx_c + Gu_c, & x_c(0) &= x_0, \\ y_c &= Hx_c + \text{noise}, \end{aligned} \quad (6.14)$$

where

$$\begin{aligned} u_c &= T(s)u, \\ y_c &= T(s)y. \end{aligned} \quad (6.15)$$

$T(j\omega)$ should ideally be as shown in Fig. 6-1. Such forms are not realizable because they are not ratios of polynomials. It is important to note that only the variation of gain with frequency, and not the phase angle, is of significant interest. Frequency-shaping methods may also be used to divide the overall problem into a number of smaller problems.

Table 6-2. Maximum-likelihood methods.

DIFFICULTIES	SOLUTIONS
Nonwhite state and measurement noise from truncated modes	Frequency-shaped transformation to eliminate truncated modes
High-order model	Use 2x2 block diagonal form for state transition matrix
Need to know model order	Use higher order model than required; extra modes should have low gains
A priori parameter values are needed in nonlinear optimization	Natural frequency is determined from transfer function or analysis; damping ratio and gains may be set to zero
Closed-loop system operation	Identify closed-loop model with appropriate correction or directly with open-loop model

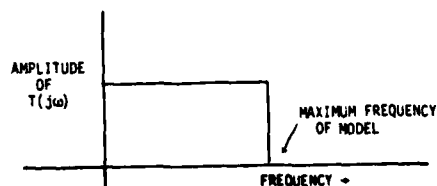


Fig. 6-1. Desired filter transfer function for maximum likelihood estimation

6.3 A Simulation Example

Application of the maximum likelihood method to a five-mode model is now discussed to indicate procedural details.

The open-loop transfer function is shown in Fig. 6-2. A random input, shown in Fig. 6-3, was applied and the response measured with additive noise is shown in Fig. 6-4. The frequency-shaping method is used to estimate a two-mode model valid at low frequency. The standard maximum-likelihood method did not converge with a fourth- or fifth-order model.

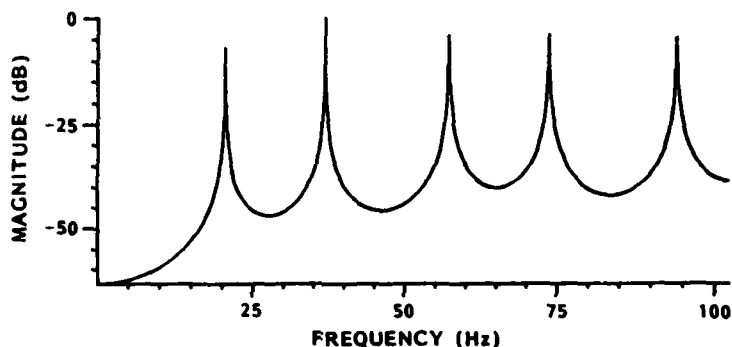


Fig. 6-2. System transfer function.

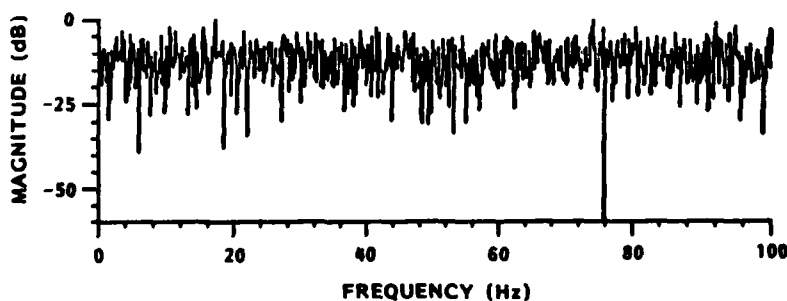


Fig. 6-3. Spectrum of broadband input.

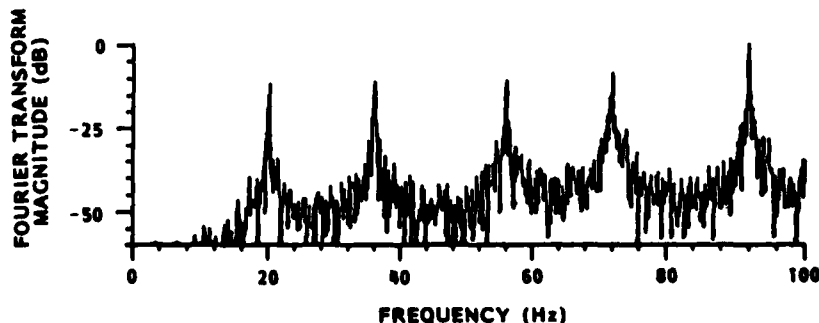


Fig. 6-4. Response of system to white-noise input.

The frequency-shaped weighting penalty in Fig. 6-5 was used to eliminate the effect of high-order truncated modes. This weighting required passing the input and output through a filter with pole-zero locations shown in Fig. 6-6. Spectra of the filtered input and output are shown in Figs. 6-7 and 6-8, respectively. The frequency-shaped maximum-likelihood method converged with the identified transfer function shown in Fig. 6-9. A comparison of simulated and identified poles is shown in Table 6-3.

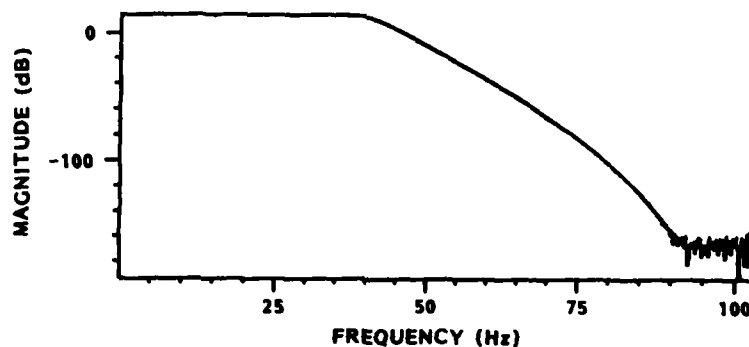


Fig. 6-5. Filter gain used in frequency-shaping method.

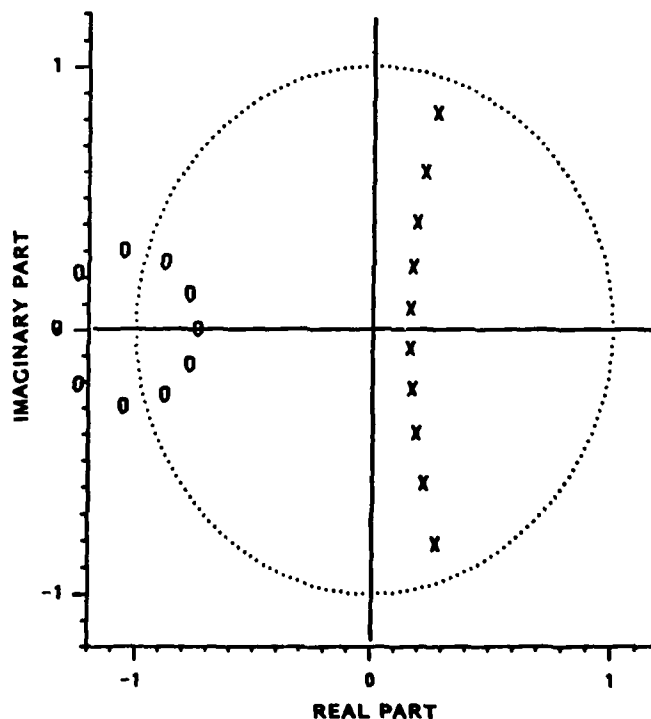


Fig. 6-6. Poles/zeros of filter used to minimize effect of truncated modes.

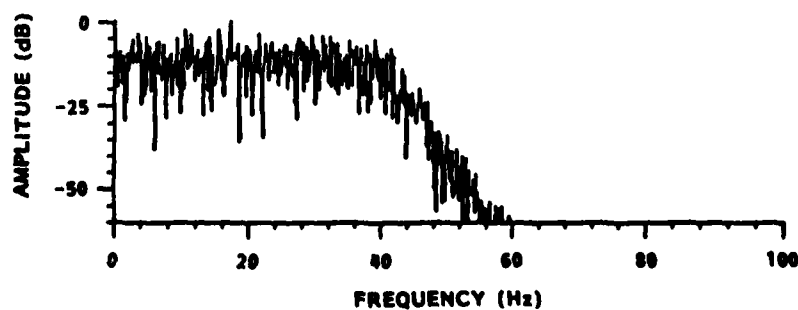


Fig. 6-7. Filtered input.

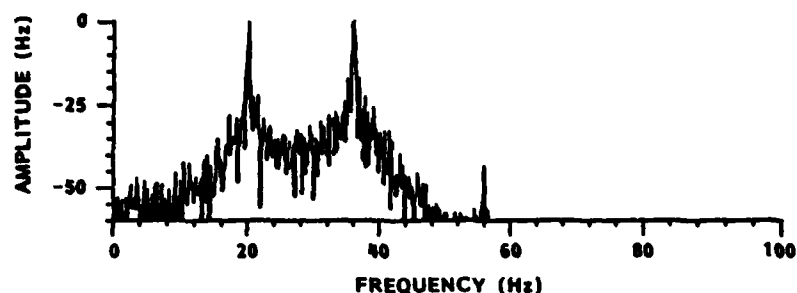


Fig. 6-8. Filtered output.

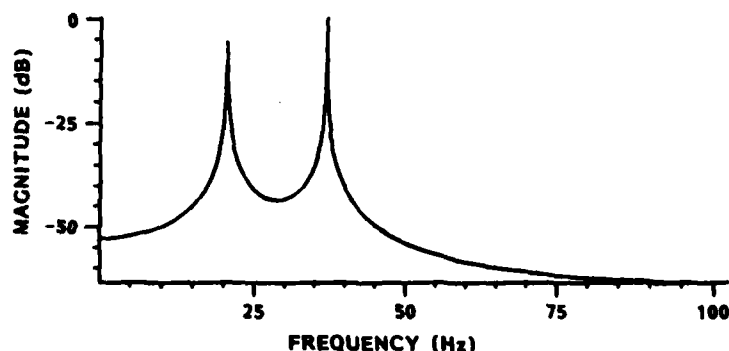


Fig. 6-9. Identified transfer function (fourth-order).

Table 6-3. Comparison of simulated and identified transfer functions.

FREQUENCY		DAMPING RATION	
SIMULATION	IDENTIFIED	SIMULATION	IDENTIFIED
20.5	20.5	0.02	0.04
36.8	36.8	0.04	0.03

6.4 Summary

Table 6-5 summarizes the characteristics of various identification methods. The maximum-likelihood and instrumental-variables methods appear to be two of the most useful approaches.

7. CONCLUSIONS AND SUGGESTIONS FOR RESEARCH

The discussions above have delineated procedural details and the state-of-the-art for controls synthesis and evaluation for large space structures using a hierarchical control methodology. Sequentially, plant-dependent high-authority control laws, highly robust low-authority mechanizations, and, finally, passive actuator damping are used. Each of these techniques is characterized by robustness properties matched to system model uncertainty. Frequency-shaping techniques give the control designer a powerful method to combine classical controls synthesis with multi-input/multi-output LQG techniques to achieve high performance, including disturbance rejection, without exciting unmodeled modes. Low-authority gain synthesis can proceed from a higher-order reduced model using a weighted least-squares formula to achieve desired stability augmentation across a broad range of frequencies. This assures robustness of the high-authority mechanizations. Although these analytical methods are now well developed procedurally and have been implemented in software, further work is needed to assess robustness properties for systems with densely packed modes. More complete performance vs. robustness trades are also required.

Detailed hardware performance studies, now in progress, must consider actuator/sensor hardware dynamics and non-colocation effects on global stability. Although detailed hardware mechanizations are not discussed here, selection and design of actuators and sensors and implementation of these controls on actual structures is non-trivial. A great deal of work remains to be done in this area. In particular, parallel algorithms and architectures for real-time implementation of modern control, estimation, and

Table 6-5. Characteristics of identification methods.

	LEAST SQUARES	EXTENDED KALMAN FILTER	INSTRUMENTAL VARIABLES	MAXIMUM LIKELIHOOD
Formulation	Nonlinear optimization	Riccati equation recursive gain	Linear algebraic equations	Nonlinear optimization
Frequency/Time Domain	Frequency domain	Time domain	Frequency domain	Time domain
Batch/Recursive	Batch	Recursive	Batch	Batch/recursive
Parameters Identified	Poles (zeros and gains)	Elements of F, G and H matrices	Transfer function numerator and denominator polynomial	Elements of F, G and H matrices
Computation Time	Low	High	Low	Medium
Accuracy	Good (poles) Fair (zeros)	Fair (poles) Good (zeros)	Good	Excellent
Stability	Good	Fair	Good	Good

identification techniques must be developed and tested to enhance the credibility of flying reliable high-performance, control-configured spacecraft. Finally, comparison of predicted and actually achieved performance depends on further development and testing of system identification algorithms on closed-loop hardware experiments; flight experiments, the ultimate test of these ideas, must be considered and implemented in the near-term if future high-performance mission concepts are to be realized.

REFERENCES

1. Aubrun, J-N. and J.A. Breakwell, "Experimental Results in Active Structural Control," IEEE Conference on Decision & Control, San Diego, Dec. 1981.
2. Stroud, R.C. et al., "Development Towards Active Control of Space Structures," SAE Paper 801234, Presented at Aerospace Congress and Exposition, Los Angeles, Oct. 1980.
3. "Active Control of Space Structures (ACOSS)," Phase IA Final Report, Prepared by Lockheed Missiles & Space Co., Inc., for the Defense Advanced Research Projects Agency under contract F30602-80-C-0087, Aug. 1981.
4. Aubrun, J-N., N.K. Gupta and M.G. Lyons, "Large Space Structures Control: An Integrated Approach," AIAA Guidance and Control Conference, Boulder, Colorado, Aug. 1979.
5. Aubrun, J-N. and G. Margulies, Low Authority Control Synthesis for Large Space Structures, Contractor Report NAS-14887-Task 11, May 1981.
6. Aubrun, et al., "Stability Augmentation for Flexible Space Structures," IEEE Decision and Control Conference, Hollywood, Florida, Dec. 1979.
7. Hooker, W. and G. Margulies, "The Dynamical Attitude Equations for an N-BODY Satellite," J. Astron. Sci., Vol. XII, pp. 123-128, 1965.
8. Hooker, W., "A Set of r Dynamical Equations for an Arbitrary Satellite Having r Rotational Degrees of Freedom," AIAA J., Vol. 8, No. 7, pp. 1205-1207, 1970.
9. "Dynamics of Spacecraft Structures, Shock and Vibration Computer Programs," SVM-10, The Shock and Vibration Information Center, United State Department of Defense, pp. 48-50, 60-61, 1975.
10. Kane, T.R. and C.F. Wang, "On the Derivation of Equations of Motion," J. Soc. for Ind. & Appl. Math., Vol. 13, No. 2, June 1965, pp. 487-492.
11. Levinson, D.A. and T.R. Kane, "Large Motions of Unrestrained Space Trusses," J. Astronautical Sci., Vol. 28, No. 1, Jan-Mar 1980, pp. 49-88.
12. Balas, M., "Modal Control of Certain Flexible Dynamic Systems," SIAM Journal of Control and Optimization, Vol. 16, 1978, pp. 450-462.
13. Skelton, R.E., "Cost Decomposition of Linear Systems with Application to Model Reduction," International J. of Control, Dec. 1980.
14. Chen, C.T., Introduction to Linear System Theory, Holt, Rinehart and Winston, Inc., New York, 1970.
15. Gupta, N.K., "Frequency-Shaped Cost Functionals: Extensions of Linear-Quadratic-Gaussian Design Methods," AIAA J. of Guid. and Control, Nov./Dec. 1980, pp. 529-535.
16. Aubrun, J-N., "Theory of the Control of Structures by Low-Authority Controllers," AIAA Conf. on Large Space Platforms: Future Needs and Capabilities, Los Angeles, CA, Sep. 1978, Paper No. 78-1689; also in AIAA J. of Guid. & Cont., Vol. 3, No. 5, 1980, pp 444.

17. Strunce, R., et al., "Active Control of Space Structures: Interim Report," Charles Stark Draper Laboratory Report R-1404, Oct. 1980.
18. Johnson, W. and N.K. Gupta, "Instrumental Variables Algorithm for Modal Parameter Identification in Flutter Testing," AIAA Journal, Vol. 16, No. 8, Aug. 1978, pp. 800-806.
19. Gupta, N.K. and R.K. Mehra, "Computational Aspects of Maximum Likelihood Estimation and Reduction of Sensitivity Function Calculations," IEEE Trans. on Auto. Control, Vol. AC-19, No. 6, 1974, pp. 774-783.

CONTROL OF LARGE SPACE STRUCTURES USING ANNULAR MOMENTUM CONTROL DEVICES (AMCD'S)

S. M. Joshi
 O.D.U. Research Foundation
 Mailing Address: Mail Stop 152E
 NASA Langley Research Center
 Hampton, VA 23665, U.S.A.

SUMMARY

A controller design approach for large space structures, which proposes the use of several Annular Momentum Control Devices (AMCD's) for structural damping enhancement, and either torque actuators or AMCD's for primary attitude control, is investigated. The damping enhancement controller makes the system asymptotically stable under certain relatively simple conditions. The closed-loop stability of the system with the primary attitude controller as well as the overall controller is established. It is shown that the same AMCD's can be used for the actuation of the damping enhancement controller and the primary attitude controller. Numerical results are obtained for a finite-element model of a large, thin, completely free, flat aluminum plate.

1. INTRODUCTION

The problem of designing control systems for large space structures (LSS) is a very complex one because of the high order of LSS dynamics, and extremely low inherent energy dissipation (damping). Because of practical considerations, it is necessary to design a reduced-order attitude control system for LSS, with only few structural modes, if any, controlled actively. The stability and performance of the resulting closed-loop system depend heavily on the inherent structural damping--particularly that in the uncontrolled or "residual" modes [1]. Inherent structural damping ratios are often difficult--if not impossible--to predict. Therefore, it is highly desirable to increase the structural damping of LSS using a secondary or damping enhancement controller. Structural parameters such as modal frequencies and mode shapes (i.e., influence coefficients for sensors and actuators) are often not known accurately. Therefore, an ideal controller should be robust; that is, the closed-loop system should be stable regardless of parameter inaccuracies.

Concepts such as direct velocity feedback controllers [2], member dampers [3], and low-authority structural controllers [4] with guaranteed Lyapunov stability, have been proposed in the literature for damping enhancement in LSS. The use of an Annular Momentum Control Device (AMCD) [5] was proposed for damping enhancement in References [6] through [9]. An AMCD, shown in Figure 1, consists of a rotating thin rim, which is suspended in three or more noncontacting electromagnetic actuator stations, and is driven by a non-contacting electromagnetic spin motor. The use of several AMCD's (distributed on the LSS) for damping enhancement was proposed and investigated in References [8] and [9]. Along those lines, the design of secondary controller using several AMCD's is discussed in Section 2 of this paper. As in the previous investigations, it is assumed in this investigation that the AMCD rims are relatively small (≈ 2 m diameter); therefore they are considered to be rigid. Electromagnetic force actuators and position sensors used for AMCD's have very high bandwidths (several hundred Hz), and are assumed to be without phase lag.

A primary attitude control system consisting of torque actuators and attitude and rate sensors is next investigated in Section 3. When the torque actuators are colocated with attitude and rate sensors, the closed loop system is Lyapunov-stable (assuming infinite-bandwidth actuators and sensors). For the noncolocated case, design methods based on linear-quadratic-Gaussian (LQG) control theory can be employed to achieve satisfactory control. The use of the secondary controller causes a significant improvement in the performance. Finally, a method for designing AMCD actuator gains is presented, which permits the use of the same AMCD's for primary and secondary controller actuation. Numerical results are presented in Section 4 in order to demonstrate and evaluate the design methods discussed.

2. SECONDARY CONTROLLER USING AMCD'S

It is assumed that v (>1) AMCD's are distributed on an LSS of mass m_0 , inertia matrix I_0 (two-dimensional), and n_q structural bending modes. The AMCD rims are assumed to be relatively small (≈ 2 m) in diameter; therefore, they can be considered to be rigid. Only X and Y axis rotations and Z-axis translations are considered, which suffices to present the principles. The location of nominal rim center position of the i th AMCD in the LSS coordinates is (x_i, y_i) . m_{ai} , r_i , I_{ai} , l_i (>3) represent the mass, rim radius, transverse-axis rim inertia matrix, and number of actuator stations for the i th AMCD. C_{1i} represents $2 \times l_i$ moment-arm matrix of the AMCD actuator stations, and C_{2i} is a $1 \times l_i$ vector consisting of all unity entries. e_i represents the difference between Z axis displacement of the i th AMCD rim center and rigid-body translation of the corresponding point on the LSS. Let $u_0 = (\phi_0, \theta_0)$ denote LSS attitude vector about the X and Y axes, and $u_{ai} = (\phi_{ai}, \theta_{ai})$ denote rim attitude vector for the i th rim.

The actuator stations are assumed to produce only axial (Z-axis) forces. (Only radial rim centering is accomplished by radial actuator forces and is of no consequence in the present analysis.)

From the basic principles of dynamics the combined AMCD/LSS equations of motion can be written as:

$$A\ddot{x} + B\dot{x} + Cx = Yf \quad (1)$$

$$x = (\alpha_s^T, \alpha_{a_1}^T - \alpha_s^T, \dots, \alpha_{a_v}^T - \alpha_s^T, \epsilon_1, \dots, \epsilon_v, q^T)^T \quad (2)$$

where q denotes the n_q -vector of modal amplitudes of LSS

$$f = (F_1^T, F_2^T, \dots, F_v^T)^T \quad (3)$$

$$F_i = (f_{i1}, f_{i2}, \dots, f_{i n_i})^T \quad i = 1, 2, \dots, v \quad (4)$$

f_{ik} being the axial force at actuator station k of the i th AMCD.

A is a $(n_1 \times n_1)$ symmetric positive definite coefficient matrix (where $n_1 = n_q + 3v + 2$):

$$A = \begin{bmatrix} A_{1(3v+2) \times (3v+2)} & 0 \\ 0 & I_{n_q \times n_q} \end{bmatrix}$$

$$A_1^{-1} = \begin{bmatrix} I_s^{-1} & -I_s^{-1} & \dots & -I_s^{-1} & -I_s^{-1}\zeta_1 & \dots & -I_s^{-1}\zeta_v \\ -I_s^{-1} & I_s^{-1} + I_{a_1}^{-1} & I_s^{-1} & \dots & I_s^{-1} & I_s^{-1}\zeta_1 & \dots & I_s^{-1}\zeta_v \\ -I_s^{-1} & I_s^{-1} & I_s^{-1} + I_{a_2}^{-1} & \dots & I_s^{-1} & I_s^{-1}\zeta_1 & \dots & I_s^{-1}\zeta_v \\ \vdots & \vdots & \vdots & \ddots & \vdots & \vdots & \ddots & \vdots \\ -I_s^{-1} & I_s^{-1} & \dots & I_s^{-1} + I_{a_v}^{-1} & I_s^{-1}\zeta_1 & \dots & I_s^{-1}\zeta_v \\ -\zeta_1^T I_s^{-1} & \zeta_1^T I_s^{-1} & \dots & \zeta_v^T I_s^{-1} & \vdots & \vdots & \vdots & \vdots \\ \vdots & \vdots & \vdots & \vdots & \vdots & \vdots & \vdots & \vdots \\ -\zeta_v^T I_s^{-1} & \zeta_v^T I_s^{-1} & \dots & \zeta_v^T I_s^{-1} & \vdots & \vdots & \vdots & \vdots \end{bmatrix}$$

(5)

where $\zeta = [\zeta_1, \dots, \zeta_v]^T$, $\zeta_i = (y_i, -x_i)$, $M_a = \text{diag. } (m_{a_1}, \dots, m_{a_v})$, and $\{M_s\}_{ij}^{-1} = m_s^{-1}$. (The notation $\text{diag. } ()$ is used to represent diagonal or a block-diagonal matrix.)

$$B = \begin{bmatrix} \sum_{i=1}^v W_i & W_1 & W_2 & \cdots & W_v & 0 & 0 \\ \hline W_1 & W_1 & 0 & & 0 & 0 & 0 \\ \cdot & & W_2 & & \cdot & & \\ \cdot & & & & & & \\ W_v & & & & W_v & & \\ \hline 0 & & & & 0 & 0 & 0 \\ \hline 0 & & & & 0 & 0 & D \end{bmatrix} \quad (6)$$

where $D = D^T \geq 0$ denotes the $n_q \times n_q$ LSS damping matrix.

$$W_i = \begin{bmatrix} 0 & H_i \\ -H_i & 0 \end{bmatrix} \quad (7)$$

H_i being the angular momentum of the i th rim about the Z axis.

$$C = \begin{bmatrix} 0_{(3v+2) \times (3v+2)} & 0 \\ \hline 0 & \Lambda_{n_q \times n_q} \end{bmatrix} \quad (8)$$

Where $\Lambda = \Lambda^T > 0$ is the LSS modal frequency matrix (usually diagonal, with squared modal frequencies as its entries).

$$Y = \begin{bmatrix} 0_{2 \times 2} & 0 & \cdot & \cdot & 0 \\ C_{11} & 0 & \cdot & \cdot & 0 \\ 0 & C_{12} & \cdot & \cdot & 0 \\ \cdot & & & & \\ \cdot & & & & \\ 0 & 0 & \cdot & \cdot & C_{1v} \\ \hline C_{21} & 0 & \cdot & \cdot & 0 \\ 0 & C_{22} & & & 0 \\ \cdot & & & & \\ \cdot & & & & \\ 0 & \cdot & \cdot & \cdot & C_{2v} \\ \hline -\phi_1^T & -\phi_2^T & \cdot & \cdot & -\phi_v^T \end{bmatrix}_{n_1 \times \ell} \quad \Delta = \begin{bmatrix} 0_{2 \times \ell} \\ \hline \eta_{n_2 \times \ell} \end{bmatrix} \quad (9)$$

ϕ_i ($i = 1, 2, \dots, v$) represents $l_i \times n_q$ mode shape matrix for actuator locations of the i th AMCD. $l = \sum_{i=1}^v l_i$, and $n_2 = n_q + 3v$ (\triangleq in Eq. (9) denotes equality by definition).

Let δ_{ik} be the axial centering error at actuator station k of the i th AMCD. The $l \times 1$ centering error vector δ is given by

$$\delta = (\delta_{11}, \dots, \delta_{1l_1}, \dots, \delta_{v1}, \dots, \delta_{vl_v})^T = -\gamma^T x \quad (10)$$

Consider a control law of the type

$$f = K_p \delta + K_r \dot{\delta} \quad (11)$$

where K_p and K_r are real symmetric positive definite $l \times l$ proportional and rate gain matrices.

It was proved in [8] that the closed-loop system given by Eqs. (1) and (11) has at least two zero eigenvalues for all K_p and K_r . The zero eigenvalues correspond to α_s which represents LSS rigid-body attitude. Defining:

$$p = (\alpha_{a_1}^T - \alpha_s^T, \dots, \alpha_{a_v}^T - \alpha_s^T, \epsilon_1, \dots, \epsilon_v, q^T)^T \quad (12)$$

$$\tilde{x} = (p^T, \dot{x}^T)^T = (p^T, \dot{\alpha}_s^T, \dot{p}^T)^T \quad (13)$$

Equation (1) (excluding α_s) can be expressed as:

$$\dot{\tilde{x}} = \tilde{A} \tilde{x} + \tilde{B} f \quad (14)$$

It was proved in Reference [8] that the closed-loop system given by Eqs. (14) and (11) is stable in the sense of Lyapunov if $K_p > 0$ (positive definite) and $K_r \geq 0$ (positive semidefinite), and that it is asymptotically stable if

- (i) $\sum_{i=1}^v H_i \neq 0$, (ii) $K_p > 0$, $K_r > 0$, (iii) $l \geq n_q + 3$, and (iv) $\text{rank}(\gamma) = n_q + 3$.

However, conditions (iii) and (iv) are too restrictive and difficult to satisfy in practice. In order to obtain the least restrictive conditions, it was proved in [9] that the control law of Eq. (11) is optimal with respect to a steady-state, linear quadratic (LQ) regulator performance index. (The philosophy followed was along the lines of [10].) The performance index consists of quadratic penalties on state and control vectors, and also a state-control cross-penalty term. Well-known properties of LQ regulators were subsequently used to obtain the necessary and sufficient conditions for asymptotic stability. These conditions (Theorem 2, Ref. [9]) are somewhat difficult to apply, but can be used to obtain the following simpler sufficient conditions, which are much less restrictive than the sufficient conditions stated above.

Theorem 1. The system of Eq. (14) with control law of Eq. (11) is asymptotically stable if all of the following conditions are satisfied: (i) the LSS structural model is stabilizable, (ii) $\sum_{i=1}^v H_i \neq 0$ and (iii) LSS does not have undamped structural mode at twice the spin frequency of any of the AMCD's.

Proof. The proof is given in [9].

Thus a secondary controller using several AMCD's assures stability of the system regardless of parameter inaccuracies and number of structural modes. The amount of damping enhancement in different modes would be determined by the locations of AMCD's on the LSS. However, if several AMCD's are distributed on the LSS, structural damping of a number of modes should be enhanced. The hardware required for this type of secondary controller is within the reach of the present-day technology [10].

3. PRIMARY ATTITUDE CONTROL SYSTEM

The secondary control system increases modal damping and thus controls shape of the LSS. It also aids in primary controller design by reducing the effect of "spillovers" [11], especially when the primary control actuators and sensors are not colocated. Primary attitude control system design using infinite bandwidth torque actuators and attitude and rate sensors is considered first.

Assuming that primary attitude control is accomplished using σ (>1) two-axis torque actuators distributed on the LSS, the LSS equations of motion (without secondary controller) are given by:

$$A_s \ddot{x}_s + B_s \dot{x}_s + C_s x_s = \sum_{i=1}^{\sigma} \gamma_{ti} T_i \quad (15)$$

where $x_s = (a_s^T, q^T)^T$, $A_s = \text{diag. } (I_s, I_{n_q \times n_q})$, $B_s = \text{diag. } (0, D)$, $C_s = \text{diag. } (0, \Lambda)$.

$$\gamma_{ti} = \begin{bmatrix} I_{2 \times 2} \\ \phi_{mi}^T \end{bmatrix}, \quad T_i = \begin{bmatrix} T_{xi} \\ T_{yi} \end{bmatrix} \quad (16)$$

ϕ_{mi} being the $2 \times n_q$ "torque mode-shape matrix" corresponding to location of actuator i . T_{xi} and T_{yi} are the X and Y axis torques.

Collocated Actuators and Sensors. Assuming that σ , two-axis attitude and rate sensors are also located at the same points as the torque actuators, the measured attitude vector α_{mi} and the measured attitude rate vector α_{mri} at location i (ignoring noise) are given by:

$$\alpha_{mi} = \gamma_{ti}^T x_s \quad (17)$$

$$\alpha_{mri} = \dot{\gamma}_{ti}^T x_s \quad (18)$$

Denoting $\Gamma = [\gamma_{t1}, \dots, \gamma_{t\sigma}]$, $T = (T_1^T, \dots, T_{\sigma}^T)^T$, $\alpha_m = [\alpha_{m1}^T, \dots, \alpha_{m\sigma}^T]^T$, $\alpha_{mr} = [\alpha_{mr1}^T, \dots, \alpha_{mr\sigma}^T]^T$, Eqs. (15), (17), and (18) can be written as:

$$A_s \ddot{x}_s + B_s \dot{x}_s + C_s x_s = \Gamma^T T \quad (19)$$

$$\alpha_m = \Gamma^T x_s \quad (20)$$

$$\alpha_{mr} = \dot{\Gamma}^T x_s \quad (21)$$

Consider the control law

$$T = -(G_p \alpha_m + G_r \alpha_{mr}) \quad (22)$$

where G_p and G_r are $2\sigma \times 2\sigma$ positive definite symmetric matrices. For example, a simple control law for controlling the rigid-body attitude would be:

$$T_i = \frac{1}{\sigma} I_s \left[\begin{pmatrix} 2\rho_x \omega_{sx} & 0 \\ 0 & 2\rho_y \omega_{sy} \end{pmatrix} \alpha_{mri} + \begin{pmatrix} \omega_{sx}^2 & 0 \\ 0 & \omega_{sy}^2 \end{pmatrix} \alpha_{mi} \right]$$

for $i = 1, 2, \dots, \sigma$, where ρ_{sk} and ω_{sk} ($k = x, y$) denote the desired rigid-body damping ratio and natural frequency. In this case G_p and G_r will be block-diagonal matrices.

The closed-loop equations become:

$$A_s \ddot{x}_s + (B_s + \Gamma G_r \Gamma^T) \dot{x}_s + (C_s + \Gamma G_p \Gamma^T) x_s = 0 \quad (23)$$

Theorem 2. The system of Eq. (23) is stable in the sense of Lyapunov if $G_p > 0$, $G_r \geq 0$.

Outline of Proof. Consider a Lyapunov function:

$$V(x_s, \dot{x}_s) = x_s^T \bar{C}_s x_s + \dot{x}_s^T A_s \dot{x}_s \quad (24)$$

where $\bar{C}_S = C_S + \Gamma G_P \Gamma^T$. It can be shown that $\bar{C}_S > 0$, and that:

$$\dot{V} = -\dot{x}_S^T \bar{B}_S \dot{x}_S \leq 0 \quad (25)$$

(since $\bar{B}_S = B_S + \Gamma G_r \Gamma^T \geq 0$).

Thus the primary control law using colocated torque actuators and attitude and rate sensors gives a stable closed-loop system. The controller is robust because it is stable regardless of parameter inaccuracies. In addition to controlling rigid-body modes, the "colocated" primary controller also increases damping in some of the structural modes, depending on the locations of the torque actuators. The secondary controller consisting of AMCD's can be added in order to enhance modal damping and improve the overall performance. When the secondary controller is included, it can be shown that the overall closed-loop system is Lyapunov stable if $G_p > 0$, $G_r \geq 0$, $K_p > 0$ and $K_r \geq 0$.

Noncolocated Actuators and Sensors. The stability of the closed-loop system is no longer guaranteed when actuators and sensors of the primary controller are not colocated. This is because of control and observation spillovers [11]. For the noncolocated case, the primary controller design must be accomplished using methods such as truncation [12] and modified truncation (or model error sensitivity suppression (MESS) [13]). When the secondary controller is activated, it can greatly improve the performance of the primary controller. The truncation method merely ignores the presence of residual (uncontrolled) modes in the design process. The effect of control input on selected residual modes is included in the performance function in a quasi-static sense in the model error sensitivity suppression (MESS) method. Of the methods investigated in [12], the MESS method was found to be the most promising for primary controller design with noncolocated actuators and sensors. Only truncation method and MESS method are considered in this paper for the noncolocated actuators/sensors case. As a simple special case, it is assumed in the following analysis that the primary controller controls only rigid-body attitude, without attempting to actively control any structural modes. This assumption is justified to some extent because structural modes will be controlled by the secondary controller. In order to simplify implementation, the primary control law is constrained to require feedback of only the measured attitude and rate (measured attitude and rate includes contributions of rigid-body and structural modes). It should be noted that this special case is included only for the purpose of demonstration and that primary controller design using truncation or MESS methods is not restricted to active control of rigid-body modes only.

MESS method - a special case: Assuming that the primary controller is to be designed to control only rigid-body modes $\alpha_S = [\phi_S, \theta_S]$, and considering the case with a single 2-axis torque actuator, consider the control law given by

$$T = \begin{bmatrix} T_x \\ T_y \end{bmatrix} = I_S \left[\begin{pmatrix} \omega_x^2 & 0 \\ 0 & \omega_y^2 \end{pmatrix} \alpha_{sm} + \begin{pmatrix} \rho_x^2 R_x^{-1} & 0 \\ 0 & \rho_y^2 R_y^{-1} \end{pmatrix} \dot{\omega}_{sm} \right] \quad (26)$$

where ω_i , ρ_i ($i = x, y$) denote the desired rigid-body bandwidth and damping ratio, and α_{sm} , $\dot{\omega}_{sm}$ denote the measured attitude and rate vectors; $R_i = 1/2\omega_i$. If control spillover were absent (i.e., if the actuators could force only rigid-body modes), this control law would minimize the performance function

$$J_O = \int_0^\infty \left\{ \alpha_S^T \begin{bmatrix} \omega_x^4 R_x & 0 \\ 0 & \omega_y^4 R_y \end{bmatrix} \alpha_S + \dot{\alpha}_S^T \begin{bmatrix} \rho_x^2 R_x^{-1} & 0 \\ 0 & \rho_y^2 R_y^{-1} \end{bmatrix} \dot{\alpha}_S \right. \\ \left. + 2\alpha_S^T \begin{bmatrix} R_x \omega_x^2 & 0 \\ 0 & R_y \omega_y^2 \end{bmatrix} T + T^T \begin{bmatrix} R_x & 0 \\ 0 & R_y \end{bmatrix} T \right\} dt \quad (27)$$

This can be verified along the lines of [9]. However, because of flexibility, the control input also forces structural modes. The model error sensitivity suppression method requires augmentation of a quadratic function of the forcing terms corresponding to a few selected structural modes, to the performance function in Eq. (27). If modes k_1, \dots, k_p are selected for augmentation, denoting the mode-shapes (for the k th mode) at the actuator locations by ρ_{xk} , ρ_{yk} , the modified performance function becomes

$$J = J_0 + \sum_{k=k_1}^{k_p} Q_k T^T \begin{bmatrix} \phi_{xk}^2 & \phi_{xk}\phi_{yk} \\ \phi_{xk}\phi_{yk} & \phi_{yk}^2 \end{bmatrix} T \quad (28)$$

where Q_k is a positive weighting coefficient. The effect of addition of this term to the performance function is to modify the control weighting matrix. The optimal control law for this type of performance index requires feedback only of measured attitude and rate. A modified state estimator can be similarly designed for generating estimates of rigid-body attitude and rate.

Use of AMCD's for Primary Attitude Control. The AMCD's used for the secondary controller can be simultaneously used for actuation of the primary attitude controller. Primary attitude control is accomplished by torquing against AMCD momenta. In this dual control mode, however, the relative rotation angles between LSS and AMCD's (i.e., $\alpha_{ai} - \alpha_s$, $i=1,2,\dots,v$) cannot be controlled simultaneously with LSS rigid-body attitude α_s (controllability of AMCD/rigid-body modes is discussed in [14]). This entails that the control law of Eq. (11) for the secondary controller should be redesigned to exclude feedback of $(\alpha_{ai} - \alpha_s)$. However, the rates $(\dot{\alpha}_{ai} - \dot{\alpha}_s)$ must be zero in steady-state, and must be fed back. That is, the position feedback must be redesigned to control only ϵ_i , the motion of AMCD rim centers relative to LSS, and AMCD rim transverse rotation angles are allowed to be nonzero in steady-state. Provided that the relative angles, $(\alpha_{ai} - \alpha_s)$, are sufficiently small (so that the actuator gap limits are not exceeded), the AMCD's can be used in this dual control mode.

The columns of the $2 \times \ell_i$ matrix C_{1i} are given by $(y_{ij}, -x_{ij})^T$, $j=1,2,\dots,\ell_i$. Since the actuators are located along a circle, columns 1 and 2 are linearly independent, and columns 3 through ℓ_i can be expressed as linear combinations of the first two columns. That is, C_{1i} can be expressed as:

$$C_{1i} = C_i [I_2 \mid \Gamma_i] \quad (29)$$

where C_i is the 2×2 matrix formed by the first two columns of C_{1i} , I_2 is the 2×2 identity matrix, and Γ_i is a $2 \times (\ell_i - 2)$ matrix. If K_p is designed as follows:

$$K_p = \text{diag.} \left[\begin{pmatrix} \Gamma_1 \\ -I \end{pmatrix}, \dots, \begin{pmatrix} \Gamma_v \\ -I \end{pmatrix} \right] \tilde{K}_p \text{diag.} \left[\begin{pmatrix} \Gamma_1 \\ -I \end{pmatrix}, \dots, \begin{pmatrix} \Gamma_v \\ -I \end{pmatrix} \right]^T \quad (30)$$

where \tilde{K}_p is a $(\ell - 2v) \times (\ell - 2v)$ positive definite matrix, it can be verified that the resulting coefficient matrix multiplying $(\alpha_{a1}^T - \alpha_s^T, \dots, \alpha_{av}^T - \alpha_s^T)^T$ in Eq. (11) is zero. Defining

$$h = (\epsilon^T, q^T)^T \quad (31)$$

the resulting closed-loop system is the form:

$$\begin{bmatrix} \dot{h} \\ \dot{x} \end{bmatrix} = \begin{bmatrix} 0 & 0 & I \\ \alpha_1 & \alpha_2 & \end{bmatrix} \begin{bmatrix} h \\ x \end{bmatrix} \quad (32)$$

where α_1 , α_2 are appropriately dimensioned matrices.

Theorem 3. The system defined by Eq. (32) is stable in the sense of Lyapunov if $\tilde{K}_p > 0$ and $K_r \geq 0$.

Outline of Proof. The proof is similar to that of Theorem 2 (part a) in [8], except that it is additionally necessary to prove that $C_2 K_p C_2^T > 0$ (positive definite) for the specially structured K_p of Eq. (30). This can be proved by establishing that $z^T C_2 K_p C_2^T z$ can be zero for some $z \neq 0$ if and only if

$$[\Gamma_i^T, -I] C_{2i}^T = 0 \quad (i=1,2,\dots,v) \quad (33)$$

Using the fact that actuators for each AMCD are located along a circle, it can be proved that Eq. (33) cannot hold. Therefore,

$$C_2^T K_p C_2^T > 0$$

This type of secondary controller essentially provides rate feedback for modal damping enhancement. The only function of the position gain is to keep the AMCD rim centers at their nominal positions. Additional force commands can now be superimposed on the electromagnetic actuators in order to produce the desired primary control torque for controlling α_s . Since the AMCD's are small compared to LSS, the effect of control moments generated in this manner would approximate point-torque actuators. If an attitude and a rate sensor is located on the LSS at the nominal position of the center of each AMCD, this configuration would approximate colocated torque actuators and attitude/rate sensors, and should therefore have the associated Lyapunov-stability property. In this configuration, the AMCD's must have sufficiently large momenta in order to exert the magnitude of torque required to achieve the desired rigid-body bandwidth (without exceeding the electromagnetic actuator gap limits). Separate AMCD's may also be used for primary control actuation. The position gains for the rim suspension control system should be structured as discussed above to retain the closed-loop stability properties of the structural modes. For orbital applications it will be necessary to gimbal the AMCD's for primary controller actuation.

4. NUMERICAL RESULTS

For the purpose of demonstration of the primary and secondary controller design methods, a 44-mode finite element model of a 30.48 m x 30.48 m x 2.54 mm, completely free aluminum plate was used. Inherent damping ratios of all the structural modes were assumed to be zero. The AMCD's were chosen to have rims having 1.79 m diameter and 34 kg mass, suspended in four equally spaced electromagnetic actuators, and spinning at 5000 RPM. Secondary controller design was considered first.

Three AMCD's, centered at coordinates (4.44 m -8.26 m), (-12.06 m, -0.635 m) and (14.6 m, -14.6 m) were used for the secondary controller (in the coordinate system with axes parallel to the plate edges and origin at the plate center). Gain matrices K_p and K_r were assumed to be diagonal, with entries k_{pi} , k_{ri} corresponding to the i th AMCD. Keeping position gains constant at $k_{p1} = 146$ N/m, $k_{p2} = 14.6$ N/m, $k_{p3} = 14.6$ N/m, rate gains (k_{ri}) were increased for the three AMCD's, starting with zero rate gains. As shown in the root loci of Figure 2, damping ratios of the structural modes increase, the lowest damping ratio being 0.071 for nominal gains (i.e., position gains as given previously, and rate gains of respectively 5636 N-sec/m, 2050 N-sec/m and 7174 N-sec/m for the three AMCD's). Although only the first seven modes are shown in Figure 2, all modes exhibit similar behavior.

Primary controller design using two-axis torque actuators and attitude/rate sensors was next considered. As discussed in the previous section, the primary controller was to be designed to control only rigid-body attitude, without attempting to actively control any structural modes.

The secondary controller gains (when used) were set at their nominal values given above. Numerical results were obtained using either single torque actuator (2-axis) located at the center of the plate, or three torque actuators placed at the locations of AMCD centers given previously. Both colocated and noncolocated actuators/sensors cases were considered. For the noncolocated case, single torque actuator located at the plate center was used, and the attitude and rate sensors were located at (15.24 m, 0 m). The "evaluation" or "truth model" for the noncolocated case was assumed to consist of rigid-body modes and the first seven structural modes. Numerical results were obtained for the following cases:

1. single primary actuator with noncolocated sensors--truncation method;
2. single primary actuator with noncolocated sensors - MESS method;
3. single primary actuator with colocated sensors; and
4. three distributed primary actuators with colocated sensors.

For all cases, direct feedback of measured attitude and rate was used instead of using a state estimator.

Numerical results for cases 1 through 4 were first obtained without the secondary controller, and then with the secondary controller (K_p and K_r being at their nominal values). The objective was to vary the primary controller position and rate feedback gains (or weighting coefficients Q_k in case of MESS method) in order to get the highest rigid-body closed-loop bandwidth ω_{rb} with the restriction that the rigid-body damping ratio (ρ_{rb}) does not fall below 0.5. Closed-loop damping ratios of the structural modes must also be reasonably high in order to obtain satisfactory shape/vibration control. Figure 3 shows a bar graph of ω_{max} , the maximum rigid-body bandwidth achievable such that $\rho_{rb} \geq 0.5$, and of ρ_{smin} , which represents the smallest closed-loop damping ratio for structural modes.

Since the purpose of these computations was to gain some insight into performance of the methods discussed, formal numerical optimization routines were not used for obtaining ω_{max} ; rather, it was accomplished by varying the parameters mentioned above and observing the trends. When the secondary controller was not used, it was not possible to obtain a stable design for the noncolocated case with either truncation or MESS methods, as

indicated by zero value of ω_{\max} in Figure 3. With the secondary controller included, however, stable designs were obtained for the noncolocated case, with the MESS method causing slight improvement over the truncation method. For the colocated cases, although the closed-loop stability is guaranteed, it is possible to have zero closed-loop damping on some structural modes (with no secondary controller), as indicated by the results for Case 3. In addition, because of interaction of structural modes, the maximum achievable rigid-body closed-loop bandwidth is also limited with this type of control law, although all eigenvalues are guaranteed to be in the closed left-half of the complex plane. The highest ω_{\max} (about 0.05 rad/sec) was obtained using three distributed torque actuators with colocated sensors, when the secondary controller was included. It should be possible to increase it further by using additional AMCD's in the secondary controller. In all the cases considered, addition of secondary controller caused significant improvement. For investigating the use of the same AMCD's in primary and secondary controllers, preliminary numerical results were obtained for the case where attitude and rate sensors were located on LSS at the AMCD center nominal locations. There was very little difference in the damping-enhancement characteristics in spite of using the specially structured K_p matrix. The overall closed-loop system was asymptotically stable even though actuators/sensors in this case are only approximately colocated. However, it will be necessary to have larger total AMCD angular momentum in order to get rigid-body closed-loop bandwidth of the order of 0.05 rad/sec.

5. CONCLUDING REMARKS

A controller design approach for large space structures, which uses several Annular Momentum Control Devices (AMCD's) for modal damping enhancement, and torque actuators (or AMCD's) for primary attitude control, was investigated. The secondary or damping enhancement controller makes the system asymptotically stable under certain relatively simple conditions, regardless of parameter inaccuracies and number of modes in the model. The primary controller using torque actuators and colocated attitude and rate sensors makes the closed-loop system Lyapunov stable. A method for structuring the secondary controller position gain matrix was presented, which permits the use of the same AMCD's for secondary and primary control actuation. Numerical results indicate that a control system consisting of a secondary controller using several AMCD's and a primary controller using several distributed torque actuators (or AMCD's) with colocated attitude and rate sensors, holds significant promise.

6. REFERENCES

1. Joshi, S. M. and Groom, N. J.: Stability Bounds for the Control of Large Space Structures. AIAA J. Guidance and Control, Vol. 2, No. 4, July-August, 1979, pp. 349-351.
2. Balas, M. J.: Direct Velocity Feedback Control of Large Space Structures. AIAA J. Guidance and Control, Vol. 2, No. 3, May-June, 1979, pp. 252-253.
3. Canavin, J. R.: Control Technology for Large Space Structures. AIAA Conference on Large Space Platforms, Los Angeles, California, September, 1978.
4. Aubrun, J. R.; Lyons, M.; Margulies, G.; Arbel, A.; and Gupta, N.: Stability Augmentation for Flexible Space Structures. 18th IEEE Conference on Decision and Control, Ft. Lauderdale, Florida, December, 1979.
5. Anderson, W. W. and Groom, N. J.: The Annular Momentum Control Device (AMCD) and Potential Applications. NASA TN D-7866, March, 1975.
6. Joshi, S. M. and Groom, N. J.: Modal Damping Enhancement in Large Space Structures Using AMCD's. AIAA J. Guidance and Control, Vol. 3, No. 5, September-October, 1980, pp. 477-479.
7. Joshi, S. M. and Groom, N. J.: A Two-Level Controller Design Approach for Large Space Structures, 1980 Joint Automatic Conference, San Francisco, California, August, 1980.
8. Joshi, S. M.: Damping Enhancement and Attitude Control of Large Space Structures. Proceedings of the 19th IEEE Conference on Decision and Control, Albuquerque, New Mexico, December, 1980.
9. Joshi, S. M.: An Asymptotically Stable Damping Enhancement Controller for Large Space Structures. AIAA 2nd Conference on Large Space Platforms, San Diego, California, February 2-4, 1981, (Paper No. AIAA-81-0455).
10. Groom, N. J. and Terray, D. E.: Evaluation of a Laboratory Test Model Annular Momentum Control Device. NASA TP-1142, 1978.
11. Balas, M. J.: Feedback Control of Flexible Systems. IEEE Trans. Automatic Control, Vol. 23, No. 4, August, 1978, pp. 673-679.

12. Joshi, S. M. and Groom, N. J.: Controller Design Approaches for Large Space Structures Using LQG Control Theory. Proceedings of Second VPISU/AIAA Symposium on Dynamics and Control of Large Flexible Spacecraft, Blacksburg, Virginia, June, 1979, pp. 35-50.
13. Sesak, J. R.; Likins, P. W. and Coradetti, T.: Flexible Spacecraft Control by Model Error Sensitivity Suppression (MESS) J. Astronautical Sciences, Vol. 27, No. 2, April-June, 1979, pp. 131-156.
14. Nadkarni, A. A. and Joshi, S. M.: Optimal Maneuvering and Fine-Pointing Control of Large Space Telescope with a New Magnetically Suspended, Single Gimbaled, Momentum Storage Device. Proceedings of the 15th IEEE Conference on Decision and Control, Clearwater Beach, Florida, December 1-3, 1976.

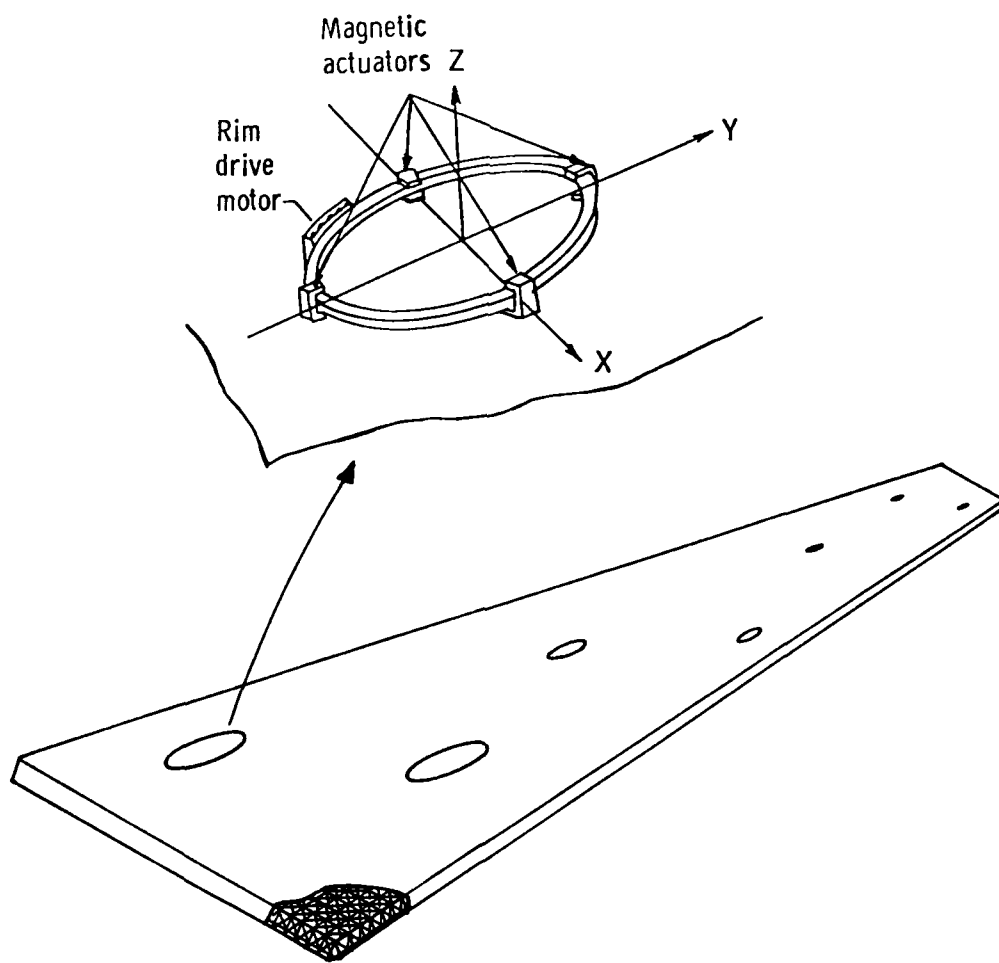


FIGURE 1. AMCD/LSS CONFIGURATION

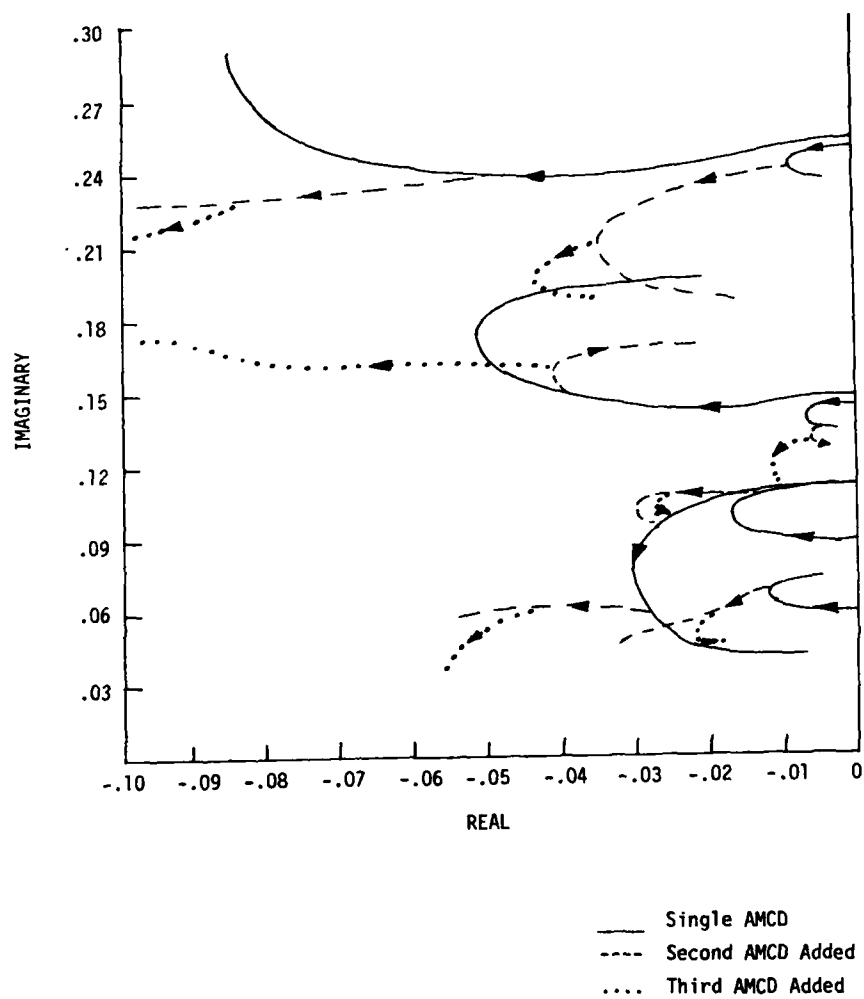
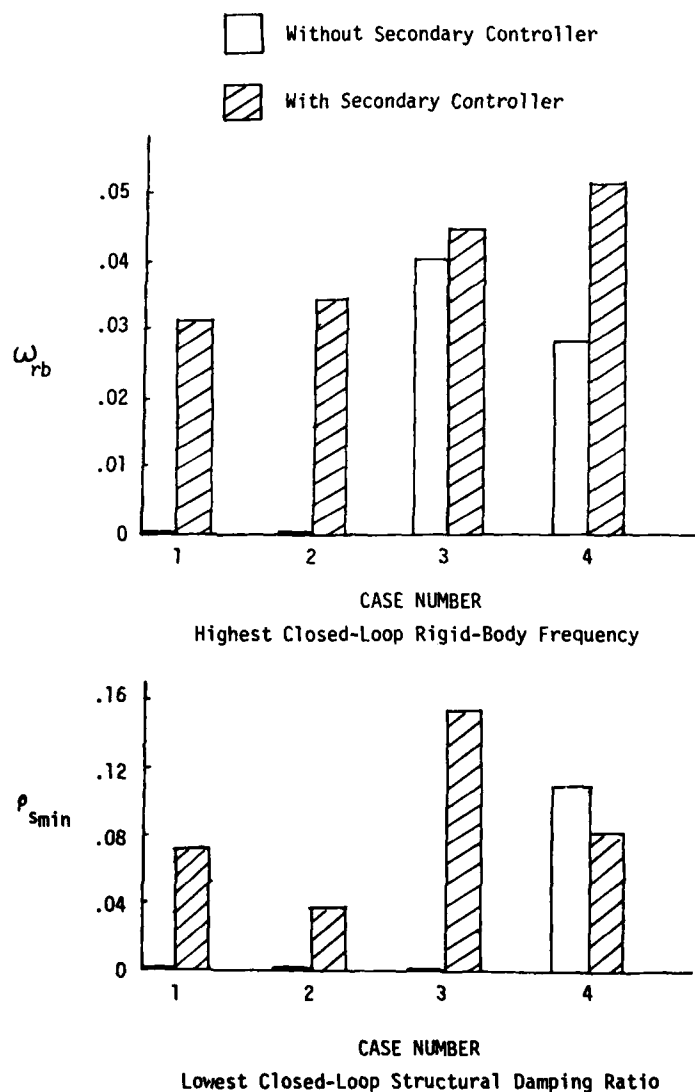


FIGURE 2. SECONDARY CONTROLLER ROOT LOCI



Case 1. Non-colocated primary actuator (single)/sensor - truncation method

Case 2. As above, but modified truncation method

Case 3. Colocated primary actuator (single)/sensor

Case 4. Colocated primary actuators (three)/sensors

FIGURE 3. NUMERICAL RESULTS FOR PRIMARY ATTITUDE CONTROLLER

MODERN SIMULATION TECHNIQUES IN SPACECRAFT DYNAMICS

by

R. Stapf, G. Heimbold, J. Pule
Deutsche Forschungs- und Versuchs alt für
Luft- und Raumfahrt e.V., 8031 Oberpfaffenhofen, F.R.G.

SUMMARY

For investigation of the dynamic behaviour of spacecraft systems, simulations are commonly used in nearly every phase of a mission. In the present paper, three hardware simulation methods are presented:

A pure physical simulation method, which makes extensive use of scaling techniques in order to overcome technical and environmental difficulties is demonstrated by means of two examples.

A hybrid simulation technique is presented, which allows to include the dynamic behaviour of flexible appendages into a physical simulation.

Finally, the possibility of implicating satellite hardware in a computer simulation by use of a three axes flight simulator is pointed out.

1. INTRODUCTION

A widely used method for investigation of the dynamic behaviour of technical systems is the simulation. Typical application fields of simulations in spacecraft dynamics are

- System design and development
- System selection
- System test and qualification
- Ground operation simulation,

each of which imposes its very special requirements to the simulation technique to be used.

Spacecraft dynamics is essentially governed by three items:

- Physical properties of spacecraft (moments of inertia, energy dissipation, flexibility etc.)
- Environmental influences causing disturbance torques
- Attitude control system.

Starting from this, two different types of simulation methods may be characterized: Simulations which include parts of spacecraft hardware and simulations which do not so.

In a computer simulation, spacecraft dynamics, control system, sensors and torquers are modelled mathematically as well as the disturbance torques acting upon the spacecraft. This type of simulation is frequently used in system design and system development, but also in application fields, where hardware simulation seems to be not feasible (e.g. large flexible space structures). Difficulties will appear in computer simulations, if the mathematical models are only imperfect representations of the real components and systems, for example because of the poor knowledge of the physical effects in such a system.

Methods including spacecraft hardware are necessary for system selection, test and qualification. The physical simulation is a method which includes the complete attitude measurement and control system in a physical manner. This means, that control torques from the actuators and the physically simulated disturbance torques act upon the "spacecraft" represented by a three-axes airbearing platform. The attitude of this platform is determined by the original spacecraft sensors relative to the simulated external references.

The purely physical simulation of spacecraft with large flexible appendages seems to be not feasible with reasonable effort. Therefore a hybrid simulation technique is used in this field, which combines the physical airbearing platform simulation with the computer-aided simulation of the flexible parts.

Another hybrid simulation technique combining computer simulation with a three axes servo platform is mainly used for system qualification. The physical properties of the spacecraft, the environmental influences and the actuators of the attitude control system are implemented in a computer and thus can be easily adapted to special mission requirements and manoeuvres, while the optical sensors and the attitude measurement and control electronics are implicated in the simulation as hardware parts.

The following contributions deal only with hardware dedicated simulation techniques. Pure computer simulations are not within the view of this paper.

2. PHYSICAL SIMULATION METHODS IN SPACECRAFT DYNAMICS

Frequently, effects which are not well-known or even unexpected might have a considerable influence on the dynamic behaviour of a spacecraft. A physical simulation will then be a suitable means for finding out those effects and thus enables the system designer to take them into account.

Characteristic features of physical simulations in spacecraft dynamic are:

- A hardware model is used for the performance of spacecraft dynamics
- Almost torque-free conditions of the undisturbed simulator have to be provided
- Control torques and disturbance torques are applied physically to the airbearing table
- Spacecraft attitude measurement and control hardware is used in the simulation
- External attitude references (sun, earth etc.) are simulated by optical simulators.

Physical simulation methods may be applied to spin-stabilized spacecraft as well as to three-axes-stabilized systems [1,2,3]. They can be used for the investigation of single components just as for testing of complete systems.

2.1 Simulation Hardware

Primary facility for physical simulations is a so-called spacecraft-motion-simulator, which is essentially a mounting platform, equipped with a spherical airbearing, so that it can move almost frictionless about all three axes. If the centre of mass of the platform and all mounted equipment is located in the centre of the airbearing sphere, the airbearing table represents a nearly torque-free system [4]. The remaining disturbance torques may be divided into two groups:

a) Internal Disturbance Torques

These disturbance torques originate from the simulator itself. The main contributions are:

- Unbalance torque, which occurs if centre of mass and centre of airbearing sphere do not coincide. The largest amount of disturbance torque is caused by unbalances, mainly because this torque is time-variable. Thermal loads acting on the simulator structure will cause bending of the structure and thus shifting of the centre of mass; the same holds for the depletion of coldgas tanks although these are arranged symmetrically and are carefully adjusted.
- Turbine torque, caused by an angular momentum in the air-flow of the bearing and by imperfections of the bearing itself.
- Anisoelectricity torque, resulting from variable bending of the structure at different inclination angles of the platform.

b) External Disturbance Torques

These are disturbance torques coming from environmental influences:

- Air turbulences, caused by the motion of persons, by convection from the heating etc. This torque may be exceptionally suppressed.
- Magnetic torques, resulting from the interaction of the earth magnetic field with the magnetic dipole moment of the simulator. The magnetic torque can be kept small by using antimagnetic materials and by suitable electrical wiring.

The airbearing table (Fig. 2.1) is equipped with a complete coldgas system consisting of four tanks, tubing, valves and a set of thrusters. It carries a battery assembly as electric power supply and a telemetry/telecommand system. For acquisition manoeuvres an external large angle attitude measurement system is available. Fine attitude measurement is achieved by an opto-electronic system.

The optical simulators used for the simulation of the external optical references are presented in detail in chapter 4.

Fig. 3.10 gives an impression of a typical simulation set-up.

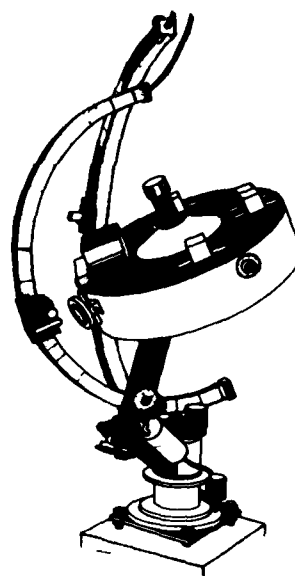


Fig. 2.1 Airbearing Platform

2.2 Simulation Technique

Physical simulations mostly are performed for selection or testing of systems and components. The aim of physical simulations therefore is either the comparison and evaluation of the behaviour of different systems and components or the determination of specific parameters and of the performance of components and complete systems. From this it is clear, that the simulation has to be accomplished in a manner, which allows to derive all the significant parameters with a high confidence level. Furthermore, in a real project it is necessary that there is a well-defined relation between simulation and spacecraft, this means, that the simulation results have to be representative for the spacecraft too. From this point of view, a number of problems arises when performing physical simulations:

Influence of gravity

Due to the influence of gravity the residual disturbance torque level of the airbearing platform is limited to a lower value, which for most spacecraft missions is considerably beyond the expected nominal disturbance torque level. As indicated in chapter 2.1, this is mainly caused by thermal effects, depletion of the coldgas system and anisoclasticity of the platform structure which in any case will cause a time - dependent shift of the centre of mass.

Geometry and dimensions

Normally it is no longer possible, to realize the geometric dimensions and above all the moments of inertia of present spacecraft in the simulation.

Limited simulation time

Battery capacity as well as fuel supply impose severe limitations upon the maximum simulation time.

A problem encountered during the feasibility analysis of a simulation for a geostationary satellite is appropriate to demonstrate the above mentioned difficulties:

An unscaled simulation of a complete orbit should be accomplished, based on the following parameters:

- | | |
|------------------------------------|-----------------------|
| • Maximum moment of inertia | 2700 kgm ² |
| • Nominal disturbance torque level | $\approx 10^{-8}$ Nm |
| • Simulation time | 24 hours |

Consequences for the simulation:

- Diameter of airbearing platform ≈ 4 m
- Weight of airbearing platform > 1000 kg
- Required residual disturbance torque level of the airbearing platform $\approx 10^{-6}$ Nm

These values are equivalent to the requirement that the maximum centre of mass shift of the platform is about 10^{-10} m in 24 hours, which means $1/5000$ of light wavelength. It is obvious that this requirement cannot be fulfilled. As a consequence of this, the necessity rises to scale the parameters, in order to come to realizable orders of magnitude. The scaling method applicable to the problem depends on the actual task and the specific object in view. Generally for each project a new method has to be developed [5].

The parameters which usually need to be scaled depend on the technical and physical properties of the simulation equipment to be used.

In particular these are:

- Moments of inertia
Typical values for the moments of inertia of present application satellites are in the order of $1000 - 3000$ kgm². The realization of this for a simulation would result in the before-mentioned weight and dimensions. The disturbance torques produced by such a facility mainly by inclination - depended elastic bending are by a factor $100 - 1000$ beyond the nominal disturbance torques of such a satellite. In the simulation, a reasonable upper value of the moments of inertia is 150 kgm².
- Disturbance torques
The residual disturbance torque level of airbearing tables with complex payloads over a period of one hour or more is about 10^{-3} Nm if the simulation set-up is very carefully designed. This means, that the nominal disturbance torques to be applied to the platform must be at least in the order of $5 \cdot 10^{-3}$ Nm.
- Control torques
As far as reaction jets are used as actuators in the simulation, the thrust level has to be adapted once to the nominal disturbance torque level and secondly to the laboratory conditions. If the thrust is too low, this will result in a bad reproducibility of actuator pulses. On the other hand, a too high thrust will produce heavy air turbulences and thus induce additional non-deterministic disturbance torques upon the simulator platform.
- Drift angles
Simulations of spacecraft with very high attitude pointing accuracy impose hard requirements to the optical reference simulators. Therefore it may be desirable to scale up the drift angles. Beyond this, it is frequently necessary to perform drift angle scaling as a consequence of the applied scaling method.
- Simulation time
Battery capacity and fuel supply normally require a time limitation. Furthermore, the time-dependent residual disturbance torques recommend a time limitation of the simulation too.

In the following chapters two different methods shall be presented, which have been employed in actual satellite projects.

2.3 Simulation of a Pure Reaction-Jet Attitude Control System

To study system behaviour and to evaluate system performance of a new type of reaction-jet attitude control system, a physical simulation was accomplished [2,6]. In detail, the objectives to be investigated were:

- Fuel consumption
- Number of thruster switchings
- Adaptivity to variable disturbance torques
- Fine pointing capability
- Critical system modes

In that simulation, the drift angle being input to the controller should remain unscaled. The moments of inertia and the thrust of the jets could be changed only by rather small amounts, so that scaling was necessary in order to transfer the results to any spacecraft. The simulation parameters are given in table 1.

Moments of inertia	17 - 35 kgm ²
Control torque	0.23 Nm
Disturbance torque	$\geq 1 \cdot 10^{-4}$ Nm

Table 2.1: Simulation Parameters

2.3.1 Scaling Factor Simulation/Spacecraft

With the before-mentioned parameters and conditions, the dynamics of the simulation is determined. The motion of the spacecraft and of the simulator platform about one axis is given by Eq. (2.1)

$$(2.1) \quad J \cdot \frac{d^2\varphi}{dt^2} = T_d + T_c$$

where J is the moment of inertia, T_d and T_c are disturbance torque and control torque respectively and φ is the drift angle. T_c is non-zero only during short time periods δt when a thruster is fired. Otherwise the motion is given by Eq. (2.2)

$$(2.2) \quad J \frac{d^2\varphi}{dt^2} = T_d$$

In general the following relations will be valid:

$$J_{\text{Sim}} < J^{\text{S/C}} \text{ and } T_d^{\text{Sim}} > T_d^{\text{S/C}}$$

which means, that the motion of the simulator will be faster than that of the spacecraft. Thus a time scaling of the simulation is achieved and the relation between simulation and spacecraft is represented by a time scaling factor.

Integration of Eq. (2.2) yields

$$(2.3) \quad \varphi = \frac{1}{2} \frac{T_d}{J} t^2 + \dot{\varphi}_0 \cdot t + \varphi_0$$

which represents the motion of the simulator between two successive thruster pulses. For a chain of successive pulses, the time course of motion is shown in Figure 2.2.

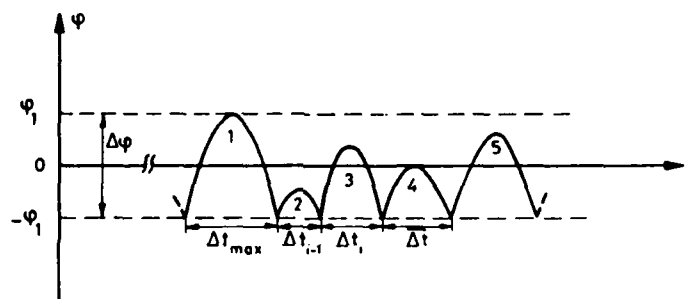


Figure 2.2 Schematic Representation of the Simulator Motion about one Axis

The initial values (at the moment of thruster firing) are:

$$\varphi_0 = -\varphi_1 \text{ (switching level)}$$

$$(\dot{\varphi}_0)_i = \dot{\varphi}_0 \frac{\Delta t_{i-1}}{2} = \frac{T_d}{J} \cdot \frac{\Delta t_{i-1}}{2}$$

($\dot{\varphi}$: angular acceleration due to disturbance torque)

The principle of the system in test is, to control the peak heights of the parabolas such that the peaks are oscillating about zero. The mean time Δt between two pulses (as represented by parabola 4 in Fig. 2.2) can be calculated:

$$(2.4) \quad \Delta t = \sqrt{\frac{4 \cdot J \cdot \Delta \varphi}{T_d}}$$

and from this, the time scaling factor can be determined, which enables transfer of the simulation results to an actual spacecraft mission.

$$(2.5) \quad K = \frac{\Delta t^{\text{Sat}}}{\Delta t^{\text{Sim}}} = \sqrt{\frac{J^{\text{Sat}} \cdot T_d^{\text{Sim}}}{J^{\text{Sim}} \cdot T_d^{\text{Sat}}}}$$

The dynamics of a modern communication satellite ($J = 2500 \text{ kgm}^2$, $T_d = 5 \cdot 10^{-8} \text{ Nm}$) for example will be scaled by a factor $K = 27$ in this simulation.

2.3.2 Scaling Method for Fine Pointing Simulations

Due to the fixed thrust level of the coldgas system and to a system-inherent minimal thruster pulse length of 10 milliseconds, modifications of the scaling method had to be done for the fine pointing simulations. For a correct performance of the attitude control system in test, a mean pulse length $\bar{\delta t}$ considerably beyond the minimal pulse length of 10 msec is necessary. With the parameters given before a limitation for fine pointing of about 0.1 degree results, which however is not a limit of the system itself, but of the simulation method. Therefore it was necessary to modify the simulation method in order to enable simulations with increased pointing accuracy.

Regarding again parabola 4 in Fig. 2.2, the angular rate of the simulator platform after being accelerated by T_d for a time period $\Delta t/2$ is calculated.

$$(2.6) \quad \dot{\phi} = \sqrt{\frac{\Delta\phi \cdot T_d}{J}}$$

With this angular rate, the switching level $-\phi$, is crossed and a mean pulse of length $\bar{\delta t}$ should invert this angular rate $\dot{\phi}$:

$$(2.7) \quad \frac{T_c}{J} \cdot \bar{\delta t} = 2 \sqrt{\frac{\Delta\phi \cdot T_d}{J}},$$

so that

$$(2.8) \quad \bar{\delta t} = \sqrt{\frac{4 \cdot \Delta\phi \cdot J \cdot T_d}{T_c^2}}.$$

Taking the simulation parameters from Tab. 2.1, it can be seen that $\bar{\delta t} = 10$ msec is reached at pointing accuracies of about 0.1 degree.

Therefore, a new scaling technique was applied: Starting from a correct limit cycle whose pulse length is sufficiently separated from the minimal pulse length, the disturbance torque is increased by a factor $n > 1$. Thus it is possible, to simultaneously decrease the deadband-width $\Delta\phi$ (which corresponds to increased pointing accuracy), without decreasing the mean pulse length, according to Eq. (2.9)

$$(2.9) \quad \bar{\delta t}^* = \sqrt{\frac{4 \cdot \frac{\Delta\phi}{n} \cdot J \cdot (T_d \cdot n)}{T_c^2}} = \bar{\delta t}.$$

As a consequence of this, the mean time between two pulses changes again, according to Eq. (2.4)

$$(2.10) \quad \Delta t^* = \frac{\Delta t}{n}$$

so that a total time scaling factor

$$(2.11) \quad C = K \cdot n$$

results. With this technique, pointing accuracies of about 0.001 degree could be obtained. This however represented the utmost capability of this simulation method, because with this time scale factor the time between two pulses is of the same order of magnitude as the pulse lengths. This fact causes an instability of the system behaviour.

Taking again the modern communication satellite as an example, the total time scaling factor is about 2700, which means that five minutes of simulation time correspond to more than 9 days mission time of the spacecraft.

2.4 Simulation of an Attitude Control System with Fixed Momentum Wheel

A very interesting example for an extensive use of scaling methods is the simulation of an attitude control system with a fixed momentum wheel for a geostationary satellite. The attitude control system is essentially a WHECON system and is presented in detail in [7]. The primary simulation task for this project has already been mentioned in chapter 2.2: Unscaled simulation of a complete 24h-orbit. As could be shown it is not possible to accomplish these requirements and scaling technique has to be used for an adequate simulation. Considerations concerning the most critical parameters of the simulation gave as a result, that the residual disturbance torque level of such a complex set-up has to be expected at about 10^{-3} Nm, the moments of inertia should not exceed 150 kgm² and a simulation time of 0.5 to 1 hour would be suitable.

As a consequence of this, nominal disturbance torques of $5 \cdot 10^{-3}$ Nm have to be simulated which can easily be done by a set of coldgas thrusters. Furthermore, time scaling requires, that the orbital angular velocity of the spacecraft ($2\pi/24h$) which is responsible for the kinematic coupling of roll and yaw axis also has to be scaled up, which means that there was a demand for an appropriate simulation technique.

2.4.1 Scaling Method

The desing of a suitable scaling method was governed by four crucial requirements:

- Minimal modifications of the control system
- High reliability of the results
- Transferability of the results to spacecraft
- Angular momentum must remain unscaled.

From these requirements, a fundamental scaling principle for this simulation was deduced: The ratio of the three main components of attitude motion

- nutation (ω_N),
- angular drift due to disturbance torques (ω_D),
- orbital angular velocity (ω_E)

relative to each other should be maintained.

A characteristic value for the normal operation roll-yaw-controller performance is

$$(2.12) \quad \frac{\Delta\phi_N}{\Delta\phi_{DB}} = \frac{\pi}{\Delta\phi_{DB}} \cdot \frac{\omega_D}{\omega_N} = \frac{\pi}{\Delta\phi_{DB}} \cdot \frac{T_d \sqrt{J_X \cdot J_Z}}{H^2},$$

which is the attitude drift due to disturbance torque T_d within half a nutation period related to the deadband-width $\Delta\phi_{DB}$. This quantity is directly related to the stability of the controller and therefore should not be changed in the simulation. So the condition

$$(2.13) \quad \frac{\Delta\phi_N}{\Delta\phi_{DB}} = \text{const.}$$

was taken as a scaling law for the simulation and it will be seen, that the application of the scaling principle derived before implies condition (2.13).

The scaling procedure is now, that primarily a simulation set-up is realized, whose ratios of the moments of inertia are the same as those of the spacecraft. Then the nutation frequency ω_N^* of this set-up is determined:

$$(2.14) \quad \omega_N^* = \frac{H}{\sqrt{J_X \cdot J_Z}}.$$

Comparison of ω_N^* to the nutation frequency ω_N of the spacecraft provides the time scaling factor K . From this the orbital angular rate to be simulated can be calculated:

$$(2.15) \quad \omega_E^* = K \cdot \omega_E.$$

Next, the scaling constant $\Delta\phi_N/\Delta\phi_{DB}$ is calculated from spacecraft data. Taking now the simulated moments of inertia and the simulated disturbance torque, the angle scaling factor C may be determined using Eq. (2.12).

The control torque pulse for removing an attitude offset $\Delta\phi_{DB}$ from the spacecraft is

$$(2.16) \quad T_c \cdot \Delta t = H \cdot \Delta\phi_{DB}.$$

Thus the angle scaling factor C accordingly applies to the control torque pulse.

In the following table, a comparison of spacecraft and simulation data is presented.

	S/C	Simulation
Angular momentum H [Nms]	35	35
Moments of inertia [kg·m ²]		
J_X	2720	100
J_Y	1330	71
J_Z	2140	85
Nutation frequency ω_N [sec ⁻¹]	$1.45 \cdot 10^{-2}$	$3.8 \cdot 10^{-1}$
Time scaling factor K		26.2
Orbital angular rate ω_E [sec ⁻¹]	$7.27 \cdot 10^{-5}$	$1.9 \cdot 10^{-3}$
Disturbance torque T_d [Nm]	10^{-5}	$5 \cdot 10^{-3}$
Drift rate ω_D [sec ⁻¹]	$3 \cdot 10^{-7}$	$1.5 \cdot 10^{-4}$
Deadband $\Delta\phi_{DB}$	0.05	1.0
Scaling constant $\Delta\phi_N/\Delta\phi_{DB}$	$7.1 \cdot 10^{-2}$	$7.1 \cdot 10^{-2}$
Angle scaling factor C		20
Control torque pulse $T_c \cdot \Delta t$ [Nms]	$3 \cdot 10^{-2}$	$6 \cdot 10^{-1}$

Table 2.2: Spacecraft and Simulation Parameters

With this scaling method, only slight modifications of the control system settings have to be made; the motion of the simulator platform is the same as those of the satellite, only modified by two constant factors. In this way, the requirements postulated before are satisfied and a suitable means to overcome the experimental difficulties is available.

2.4.2 Scaled Simulation of Roll/Yaw Coupling

As consequence of the time scaling, the orbital angular rate which provides roll/yaw coupling has to be speeded up by the time scaling factor K . One method to do this is, to amplify the natural gyrocompass effect due to earth rotation by rotating the earth simulator with an appropriate angular rate about an axis parallel to the flywheel rotation axis and passing through the center of the airbearing sphere. The linearized equations of motion for a circular, geostationary orbit (orbital angular rate $\omega_E = \text{const.}$) and small angular motions are

$$\begin{aligned} J_X \ddot{\phi} + \omega_E H \dot{\phi} + H \dot{\psi} &= T_X \\ (2.17) \quad J_Y \ddot{\theta} - \dot{H} &= T_Y \\ J_Z \ddot{\psi} + \omega_E H \dot{\psi} - H \dot{\phi} &= T_Z \end{aligned}$$

(ϕ, θ, ψ Euler angles)

The same equations of motion are valid for the simulation. If an additional angular rate ω_0 is applied, we get the roll and yaw equations of motion as follows:

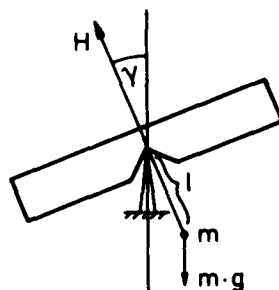
$$\begin{aligned} (2.18) \quad J_X \ddot{\phi} + H \cdot (\omega_0 + \omega_{EV}) \cdot \dot{\phi} + H \cdot \dot{\psi} &= T_X - H \cdot \omega_{EH} \cdot \sin \omega_0 t \\ J_Z \ddot{\psi} + H \cdot (\omega_0 + \omega_{EV}) \cdot \dot{\psi} + H \cdot \dot{\phi} &= T_Z - H \cdot \omega_{EH} \cdot \cos \omega_0 t \end{aligned}$$

where the simulator pitch axis is parallel to the local vertical axis and ω_{EV} and ω_{EH} are the vertical and the horizontal component of the earth angular rate. As can be seen from Eq. (2.18) an additional torque modulated by the orbit angular rate is generated by this method. This torque would act upon the simulator in the same manner as for example the solar pressure disturbance torque acts upon the spacecraft. Thus, this additional torque represents a realistic disturbance torque.

However, a number of problems arises from this simulation method: The required accuracy of the earth simulator rotation is very high (positional accuracy $\pm 0.02^\circ$) and furthermore all other external equipment aligned towards the airbearing table has to be rotated with high accuracy, because the airbearing platform itself rotates with the simulated orbital angular rate. For this reason, an alternative method was selected, to introduce the roll/yaw coupling into the simulation [3,8].

A very simple possibility to get an effect similar to the gyrocompassing effect is to definitely shift the center of mass of the simulator platform, thus generating a torque caused by the gyropendulum effect. Although these two effects are of quite different nature, their mathematical description is very similar as can be seen from Fig. 2.3.

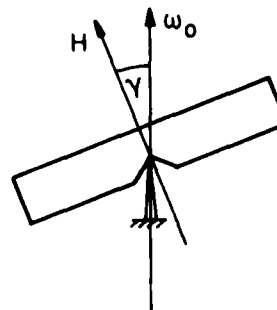
Gyropendulum effect



Reaction torque

$$T = mgl \sin \gamma = p \cdot \sin \gamma$$

Gyrocompassing effect



equivalent torque

$$T = -\omega_0 \times H = \omega_0 H \sin \gamma$$

Fig. 2.3: Gyropendulum effect and Gyrocompassing Effect

Introducing the gyro pendulum effect into the linearized equations of motion 2.17, this yields for roll and yaw axis:

$$(2.19) \quad \begin{aligned} J_X \ddot{\phi} + (\omega_{EV} \cdot H + p) \cdot \dot{\phi} + H \dot{\psi} &= T_X - \omega_{EH} \cdot \sin \delta \\ J_Z \ddot{\psi} + (\omega_{EV} \cdot H + p) \cdot \dot{\psi} + H \dot{\phi} &= T_Z - \omega_{EH} \cdot \cos \delta \end{aligned}$$

where δ is a fixed angle now instead of $\omega_0 \cdot t$ in equation 2.18 because the simulator pitch axis is again parallel to the local vertical axis, but no additional rotation is applied.

If the gyropendulum torque p is adjusted now in a manner, that the artificially increased "angular rate"

$$(2.20) \quad \omega_0 = \omega_{EV} + \frac{p}{H}$$

is equal to $K \cdot \omega_E$ (K = time scaling factor), then the roll/yaw coupling in the scaled simulation is equivalent to the natural roll/yaw coupling in the orbit.

3. HYBRID SIMULATION OF SPACECRAFT WITH FLEXIBLE APPENDAGES

A realistic approach to ground-based attitude control system design verification is three-axis air-bearing testing with actual system hardware mounted on an air-bearing platform which simulates the spacecraft dynamics. In particular this is true for control systems employing angular momentum storage devices (e.g. a Doubled Gimballed Momentum Wheel [3, 9]) which exert internal control torques on the satellite only detectable by the investigation of the motion of the complete system. Air-bearing testing offers the ultimate representation of the system dynamics but provides limited accuracy in dynamic modeling due to the facility disturbance torques and because only rigid body dynamics are available. Flexible structures like solar arrays, antennas etc. are designed for zero-g conditions and cannot be incorporated as hardware in the simulations on earth. On the other hand it is known that for example rotating dissipating systems like flywheels with compliant bearings (grease bearing, magnetic bearing) can significantly change not only the overall rigid body motion [10, 11] but also the relative motion of deformable structures [10]. Therefore it is desirable to include the effects of relative elastic motions of substructures in the simulations. In this chapter a general approach is presented to overcome the limitations of air-bearing testing by augmenting the platform dynamics by either active or passive means.

3.1 Mathematical Modeling and General Considerations

The fundamental objective in this context is extension of the scope of three-axis air-bearing tests to spacecraft configurations for which flexibility is significant. The basic idea of constructing a flexible dynamics simulator [12] is the physical realisation of the principle of internal reaction forces and torques (Newton's Third Law) widely utilized in the theory of multibody systems. That means to investigate the dynamical behaviour of a single body it is sufficient to cut off the connections to all other bodies. The internal loads transferred by the connecting elements like springs, dampers or even fixed mountings may now act on the body like an external excitation.

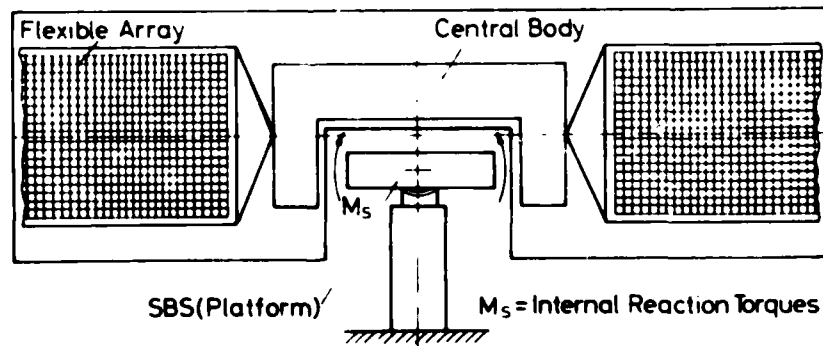


Fig. 3.1: Principle of Internal Reaction Torques

Fig. 3.1 represents this principle in case of a satellite motion simulation using an air-bearing table. The simulator comprises the complete hardware of the ACS (electronics, sensors, actuators) to be tested. All other parts of the system in particular the dynamics of flexible subbodies and the internal reaction torques M_s representing the connection between hardware and software are computer simulated using appropriate mathematical models. By some additional actuators the internal loads M_s are transferred to the air-bearing table like an external excitation. The dynamic response of the platform should be that of a satellite to be simulated driven by the real control actuator torques including errors from the laboratory environment.

The mathematical modeling of spacecraft with flexible subbodies and the utilization of such models in the control theory is well known in literature [13,14,15]. Most of them are based on a formulation technique introduced by Likins which is called "method of hybrid coordinates". It represents the equations of motion in terms of discrete parameters as far as the rigid body motions are concerned while the elastic deformation is described by distributed parameters.

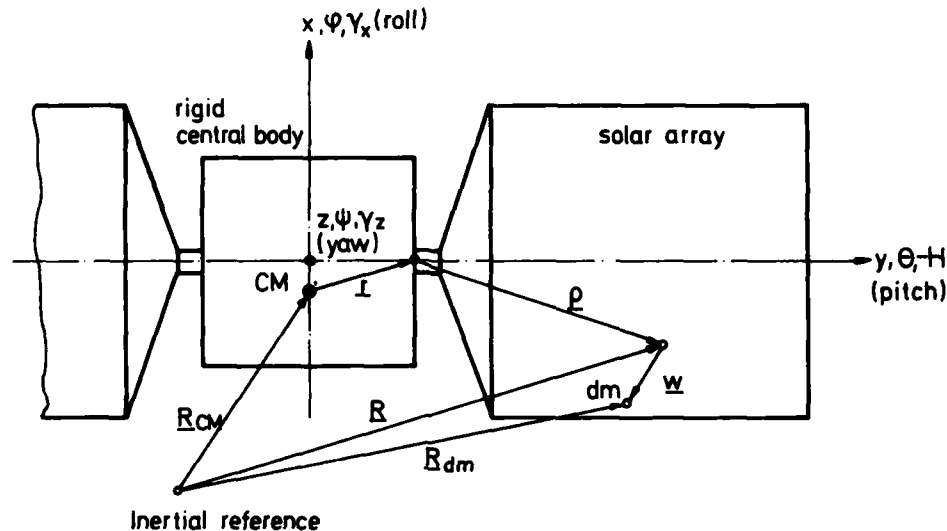


Fig. 3.2: Configuration of a Modern Communication Satellite

A sketch of the configuration of a three axes stabilized modern communication satellite is depicted in Fig. 3.2. It consists of a rigid central body serving as a reference for the antennas, the sensors and the actuators of the attitude control system. Attached to it there are two rotating solar arrays with their axis of rotation coincident with the spacecraft pitch axis (y, θ) being aligned normal to the orbit plane. Usually the arrays are mounted on a shaft to avoid shading of them by the central body or the antennas. The spacecraft yaw axis (z, ψ) points towards the earth center while the roll axis (x, ϕ) is coincident with the flight direction. In case of stabilization by a Double Gimbaled Momentum Wheel the spin axis (H) is normally parallel to the pitch axis the spin rate vector being negative while the gimbal axes are parallel to roll (γ_x) and yaw (γ_z).

A good approach to derive the equations of motion of the system is the usage of Lagrange's formalism

$$(3.1) \quad \frac{d}{dt} \left(\frac{\partial T}{\partial \dot{g}_i} \right) - \frac{\partial T}{\partial g_i} + \frac{\partial V}{\partial g_i} = Q_i$$

where

T = kinetic energy,

V = potential energy,

g_i = generalized coordinates,

Q_i = generalized forces.

The kinetic energy of the system is given by

$$(3.2) \quad T = \frac{1}{2} \int_s \dot{\mathbf{R}}_{dm}^T \dot{\mathbf{R}}_{dm} dm$$

where $[]^T$ denotes the absolute time derivative of the corresponding vectors and $[]^T$ means vector transposed. The mass integral is taken over the whole system. Using $\mathbf{R}_{dm} = \mathbf{R} + \mathbf{w}$ yields

$$(3.3) \quad T = \frac{1}{2} \int_s \dot{\mathbf{R}}^T \dot{\mathbf{R}} dm + \int_s \dot{\mathbf{R}}^T \dot{\mathbf{w}} dm + \frac{1}{2} \int_s \dot{\mathbf{w}}^T \dot{\mathbf{w}} dm$$

In Eq. (3.3) there are three distinguished parts

$$\text{rigid body motion:} \quad T_r = \frac{1}{2} \int_s \dot{\mathbf{R}}^T \dot{\mathbf{R}} dm = \frac{1}{2} m_s \dot{\mathbf{R}}_{CM}^T \dot{\mathbf{R}}_{CM} + \frac{1}{2} \dot{\boldsymbol{\omega}}^T \mathbf{I}_{CM} \dot{\boldsymbol{\omega}}$$

$$\text{elastic deformation:} \quad T_e = \frac{1}{2} \int_p \dot{\mathbf{w}}^T \dot{\mathbf{w}} dm_p$$

$$\text{coupling rigid body/} \\ \text{elastic motion:} \quad T_{re} = \int_p \dot{\mathbf{R}}^T \dot{\mathbf{w}} dm_p$$

Note that since \mathbf{R} incorporates no deformation the integral of T_r can be substituted by the system mass m_s and the matrix of the system moments of inertia \mathbf{I}_{CM} related to the overall

center of mass CM of the undeformed structure and the angular velocities ω (discrete coordinates). The deflection w depends on time and on the spatial coordinates of the solar arrays. So the integrals of T_{re} , T_r may not be resolved and are taken only over the range of the array coordinates ρ (distributed parameters).

Neglecting the influence of gravitation the only source of potential energy is the stiffness of the deformable structures. The corresponding term in Eq. (3.1) can be written

$$(3.4) \quad V = \int_{\rho} w^T \bar{K} w d\rho$$

where \bar{K} is the local stiffness matrix of the appendages. It depends on the spatial coordinates and their spatial derivatives respectively.

To separate the time dependence of the deflection w from the spatial distribution of mass and stiffness, w is resolved in a series of time and space dependent functions

$$(3.5) \quad w = L \cdot q, \quad L = [\phi_1(\rho) \dots \phi_j(\rho) \dots \phi_n(\rho)] \quad , \quad q = [q_1(t) \dots q_j(t) \dots q_n(t)]^T$$

where $\phi_j(\rho)$ are the mode shapes of the deformation and $q_j(t)$ are the corresponding amplitude time functions. These modes are orthogonal and represent the result of a static analysis of the structure, e.g. using finite element techniques. In general they are the solutions of a homogenous system of linear algebraic equations and therefore can be properly normalized.

Substituting $w(t)$ of Eq. (3.4) by Eq. (3.5) yields

$$(3.6) \quad V = q^T K q, \quad K = \int_{\rho} L^T \bar{K} L d\rho$$

where K is the global stiffness matrix of the system. Normalizing the modes to the extent that the mass integral resulting from T_e is given by

$$(3.7) \quad \int_{\rho} \phi_i^T \phi_j d\rho = \begin{cases} 1, & i=j \\ 0, & i \neq j \end{cases} \quad (\text{orthogonality condition})$$

results in a diagonal form of the global stiffness matrix representing the eigenfrequencies ω_i of the deformation

$$(3.8) \quad K = \text{diag} [\omega_i^2], \quad i=1(1)n,$$

while the mass matrix of the elastic motion becomes the unit matrix.

Supposing complete linearity and applying the formalism of Eq. (3.1) to the energy expressions of Eq. (3.3) and Eq. (3.4) respectively the satellite equations of motion can be written

$$(3.9) \quad I\ddot{a} + G\dot{a} + Pa + Ry + \Delta^T \ddot{q} = B\dot{y} + \underline{M}_c + \underline{M}_d \quad (\text{rigid body motion})$$

$$(3.10) \quad \Delta\ddot{a} + \ddot{q} + \text{diag}[d_i]\dot{q} + \text{diag}[\omega_i^2]q = 0 \quad (\text{elastic deformations})$$

where

- I = mass matrix of the rigid body motion,
- Δ = coupling matrix rigid body motion/elastic deformation,
- G, P, R, B = input matrices of a Double Gimballed Momentum Wheel,
- d_i = structural (modal) damping,
- y, \dot{y} = gimbal angles and time derivative respectively,
- \underline{M}_c = additional control forces and torques (e.g. exerted by gas jet thrusters),
- \underline{M}_d = disturbance forces and torques.

The coupling matrix Δ resulting from T_{re} depends on the attachment point r and the general undeflected orientation of the appendages with respect to the central body. Note that the external forces and torques \underline{M}_c , \underline{M}_d act only on the rigid body motion and that rigid body and relative elastic motion couple only through accelerations, i.e. internal dynamic loads. External forces like station keeping thruster forces will not produce torques on the spacecraft but by the coupling Δ may excite the appendage deformations.

In the same way the equations of motion of the air bearing table can be derived

$$(3.11) \quad \underline{I}_t \ddot{a}_t + G\dot{a}_t + Pa_t + Ry_t = B\dot{y}_t + \underline{M}_{c,t} + \underline{M}_{d,t} + \underline{M}_s$$

where the index t indicates table motion and M_s is the vector of the internal reaction torques. The parameters Y_t, \dot{Y}_t and M_c are real physical quantities. Since hardware of the satellite has to be tested, without a control actuator error it is

$$(3.12) \quad \underline{Y} = \underline{Y}_t, \quad \dot{\underline{Y}} = \dot{\underline{Y}}_t, \quad \underline{M}_c = \underline{M}_{c,t}$$

Supposing

$$(3.13) \quad \underline{\ddot{a}} = \underline{\ddot{a}}_t, \quad \underline{\dot{a}} = \underline{\dot{a}}_t, \quad \underline{a} = \underline{a}_t, \quad \underline{M}_d \approx \underline{M}_{d,t}$$

means the platform dynamics are equivalent to that of the real spacecraft to be simulated. From Eq. (3.9) and Eq. (3.11) together with Eq. (3.12) and Eq. (3.13) the internal reaction torques can be computed by

$$(3.14) \quad \underline{M}_s = (\underline{I}_t - \underline{I})\underline{\ddot{a}} - \underline{\Delta}^T \underline{\ddot{q}}.$$

Eq. (3.14) reveals, that \underline{M}_s depends only on the difference of the system mass matrices and that the intersection point need not to be a real physical interface.

Examining Eq. (3.10) and Eq. (3.14) the question may arise, whether it is possible to realize the internal reaction torques by passive means. In this case a configuration which maintains an invariant center of mass is a clear requirement, unless gravitational effects are intentionally employed as an effective spring. One approach which meets this constraint is the torsional pendulum. Consider a single mode with the table representing the central body. One-to-one modeling of a bending mode with an effective bending inertia of about 600 kgm² (a typical value for usual three-axis stabilized communication satellites) requires a pendulum inertia of the same amount. Even if the inertia is scaled downward with 10:1 scaling (at the expense of maintaining on-orbit torque to inertia ratios) the pendulum mass is still excessive. In addition to size and weight, other factors which limit desirability of the passive approach are bearing friction (which will exclude attainment of zero damping) and operational convenience. With any passive configuration parameter changes will result in inertia changes, spring constant changes etc. which will be time consuming and will affect table balance.

Therefore an active configuration is the appropriate answer. Possible candidates for the additional internal reaction torque actuators are coldgas thrusters, reaction wheels and special electro-magnetic actuators. Gas thrusters have the disadvantage of increasing the disturbance torque level in the laboratory and may only be used if the demanded torques are very large. Electro-magnetic actuators, consisting of coils and permanent magnets are the superior concerning torque accuracy but their range of linearity is limited and they permit only very small motions of the air bearing table. So for the actual configurations discussed here, ball bearing reaction wheels have been selected, although there may be difficulties at zero rotation speed due to the sticktion torque effect. The control laws proposed for these actuators are based on two different approaches to the system. They differ by the method how the appendage reaction torques are generated as functions of the table motion. They are called the "model tracking approach" and the "explicit torque approach" and will be discussed in detail in the following paragraphs.

As indicated above a general characteristic of communication satellites is the presence of a rotating solar array with the axis of rotation parallel to the satellite pitch axis. From Fig. (3.1) it is clear that the effective bending inertia about the transverse axes (roll/yaw) is much more significant than about the rotational (pitch) axis. While the roll/yaw modes will be excited by attitude and velocity dependent control forces and torques, primary excitation of the pitch array mode results from the array drive. Although interaction with the attitude control system can occur in each case, the roll and yaw axes usually present the more challenging design problem. It is realistic, therefore, to consider the roll/yaw dynamics as the primary objective of the simulator with pitch as a secondary goal.

3.2 The Model Tracking Approach

The model tracking approach was suggested in 1973 by H.L. Mork and P.C. Wheeler [12]. The block diagram of their "Flexible Dynamics Simulator" is shown in Fig. (3.3).

Here a spacecraft model realized by electronic hardware is driven by a torque signal corresponding to the central body external torques, that means the table external torques without the internal reaction torques resulting from the additional actuators. A comparison is made between the model and table attitude behaviour to generate the model tracking error. It is used to command the actuators and thereby driving the table response to follow the model response. If the error is small, the actuators will be producing the internal reaction torques on the table, that the flexible appendages exert upon the spacecraft. In this case the appendage reaction torques are not explicitly derived.

Utilizing accelerometers for table motion sensors and if there is no momentum wheel ($G, P, R, B = 0$) it is possible to get information about the external disturbance and control torques acting on the table. The tracking error equation can now be written using Eq. (3.14) in its Laplace transformed form

$$(3.15) \quad s^2 \underline{e}(s) = \underline{M}_s - s^2[(\underline{I}^{-1} \underline{I}_t - \underline{E})\underline{a}_t - \underline{I}^{-1} \underline{\Delta}^T \underline{q}]$$

where the model attitude angles are $\underline{a} = \underline{a}_t + \underline{e}$ and \underline{E} is the unit matrix. Suppose there is a small or zero coupling between the rigid body motion and the elastic deformations ($\underline{I}^{-1} \underline{\Delta}^T \approx 0$)

then Eq. (3.15) reduces to the error of the rigid body motion between the simulator and the model.

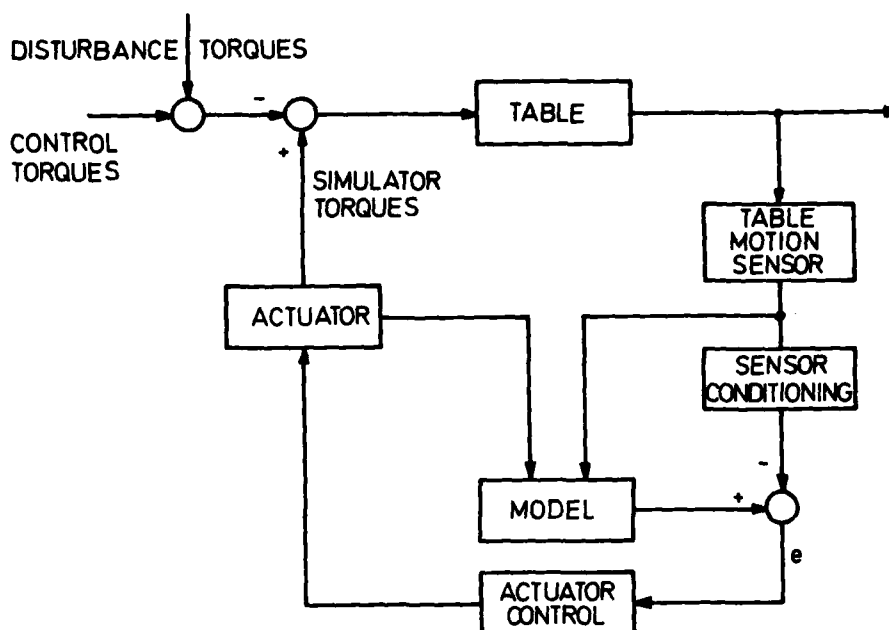


Fig. 3.3: Model Tracking Approach of a Flexible Dynamics Simulator

In case of equal moments of inertia $I_t = I_r$ the coefficient multiplying the sensed table rate is zero and the tracking error, considering only the sensed rate and the rigid body motion will be identically zero. Since the control loop commands the actuators as a function of the tracking error, no internal reaction torques are exerted on the table. This case corresponds to the table inertia representing the total rigid body inertia of the spacecraft and the appendages.

The second case is for $I_t < I_r$, e.g. I_t equal to the moments of inertia of the rigid central body. The coefficient of the sensed table rate is negative resulting in additional reaction torques. The actuators will act to scale down the other applied torques on the table so that the apparent table inertias will appear to have been increased, thereby achieving the total rigid body inertias. In both cases the effects of flexibility are added to the system like additional disturbance torques.

Evaluating and comparing the transfer functions of the simulator and the model for several values of bending frequencies and bending moments of inertia Mork and Wheeler have shown that the dynamic responses for a given configuration are in very close agreement to each other in the frequency range of interest, i.e. the ACS crossover frequency range. This accuracy is achieved by proper selection of the control loop parameters, the characteristic of the table motion sensors and the additional actuators. The effects of nonlinearities inherent in the system like actuator saturation and wheel friction can be kept small.

In [12] no simulations of attitude control systems incorporating a momentum wheel have been investigated. In this case the dynamic response of the air bearing table will be completely changed because now it shows nutational and precessional motions. Although the rigid body motion of the model has the same characteristic, the frequency range is different if the table moments of inertia are not equal to the overall satellite plus appendage moments of inertia. Since the table motion sensor signal now contains not only information about the external torques but also the internal dynamic loads exerted from the wheel on the simulator it may be difficult to achieve stability of the model tracking approach. At the DFVLR in 1978 an alternative simulator concept has been developed [16], based on the direct torque approach, which permits the simulation of wheel attitude control systems with arbitrary rigid body configurations of the air bearing table.

3.3 The Direct Torque Approach

Contrary to the simulation concept discussed before the internal reaction torques will now be synthesized and computed explicitly in a digital computer and exerted upon the air bearing table by additional actuators. No tracking error signal is generated forcing the simulator to follow the computed model output.

3.3.1 Simulation Concept

A sketch of the simulation principle is given in Fig. 3.4:

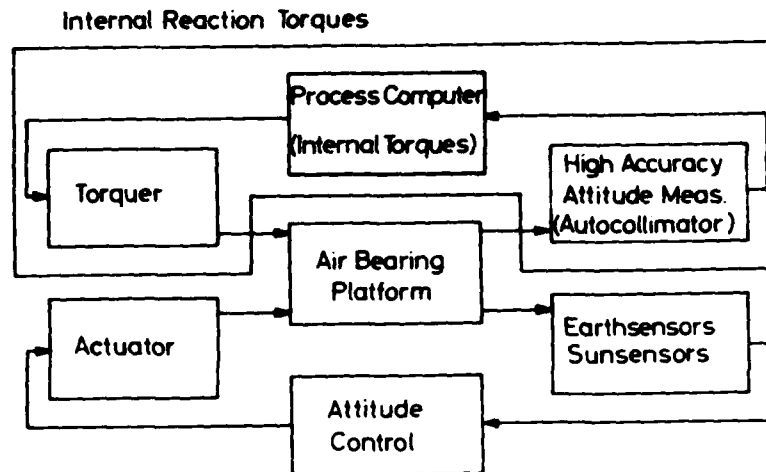


Fig. 3.4: Simulation Principle, Direct Torque Approach

The lower part of Fig. 3.4 comprises the components of the attitude control system to be tested. It consists of earth and sun sensors, the attitude control electronics and the control actuators, represented here by a Double Gimballed Momentum Wheel and coldgas jet thrusters. The upper part comprises the computer simulated part of the system. This simulation needs an additional measurement of the air bearing table attitude angles with very high accuracy using optical sensors. These measurements provide the necessary information about the table motion for a digital computer to integrate the system equations of motion and to evaluate the internal reaction torques. From these torques control commands are derived which are transferred to additional actuators mounted on the table.

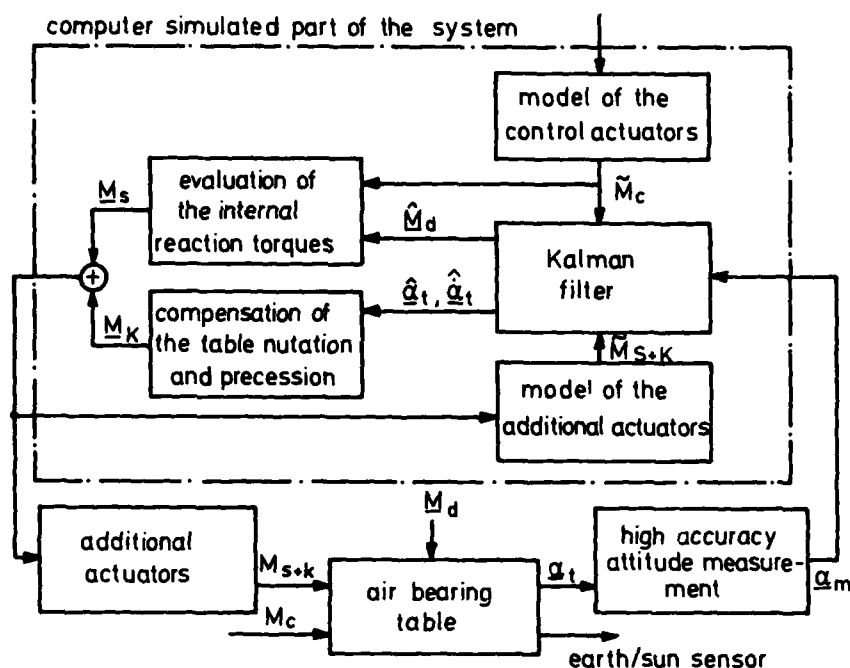
A detailed representation of the computer simulated part is depicted in Fig. 3.5. In general it consists of three subsystems, which shall be discussed below.

The Kalman-filter estimates the external disturbance torques acting on the air bearing table and the table state variables with minimal estimation error variance. The disturbance torques are modeled as two Gauß-Markoff processes of first order. According to the environmental conditions in the laboratory they have a short term and a long term component. Filtering of the attitude measurements is done via a model of the air bearing table/momentum wheel dynamics represented by Eq. (3.11).

The evaluation of the internal reaction torques starts with an integration of the overall system equations of motion, i.e. an evaluation of the satellite motion. The dynamic model of the satellite described by Eq. (3.9), (3.10) is driven by the estimated disturbance torques in addition to the computed torques of the attitude control actuators. Modelling of these control torques is done in the same way as it is necessary for the performance evaluation of the control system. Utilizing Eq. (3.14) with the known model accelerations \ddot{q} and $\ddot{\eta}$ the internal reaction torques can be computed. From the torques M_s a control command is derived, being transferred to a set of reaction wheels as additional actuators on the table. They force the dynamic response of the table to be equal to the motion of the real satellite.

As can be seen from Fig. 3.5 nowhere in the computation a tracking error signal between the table and the model attitude angles is utilized. There is only an explicit realisation of the internal reaction torques. In case of a control actuator error i.e. $M_c \neq M_s$, therefore the dynamic response of the simulator coincides with the dynamic response of the real satellite driven by the incorrect control torque. The difference $\Delta M_c = M_c - M_s$ is estimated by the filter and added to the system as an additional disturbance torque and thereby it is incorporated in the evaluation of the internal reaction torques. The main task of air bearing simulations to detect control actuator failures and to study their influence on the overall system motion is preserved.

The dynamic response of a satellite and also the response of the air bearing table stabilized by a momentum wheel and excited by external disturbance torques is a nutational motion. Its frequency is determined by the nominal value of the angular momentum and in addition depends on the moments of inertia. According to Eq. (3.9) and Eq. (3.11) the wheel angular momentum is equal for the satellite to be simulated and for the platform but usually this is not true for the moments of inertia.



α_t, α_m table attitude angles and measurement resp.
 $\hat{\alpha}_t, \hat{\alpha}_t$ estimated table state variables
 $\underline{M}_d, \hat{M}_d$ actual and estimated disturbance torques
 $\underline{M}_S, \underline{M}_K$ internal reaction torques and compensation torques
 $\underline{M}_C, \tilde{M}_C$ real and modeled attitude control torques
 $\underline{M}_{S+K}, \tilde{M}_{S+K}$ real and modeled torques of the additional actuators

Fig. 3.5: Computer Simulated Part of the System

Performing the simulations according to the concept described so far the result would be a platform motion as shown in Fig. 3.6.

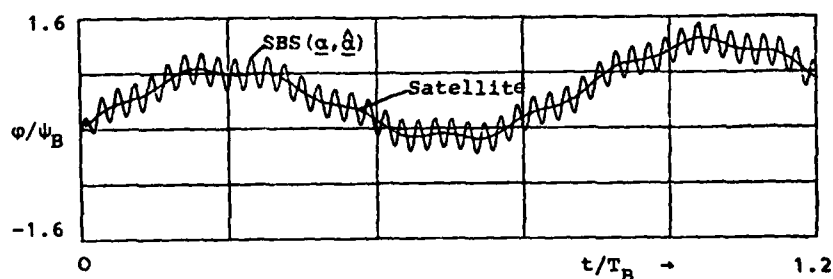


Fig. 3.6: Time Record of the Simulator and Satellite Roll Angle

The response of the air bearing table exhibits two oscillations. The sinoidal motion with the long period represents the dynamics of the satellite with flexible appendages. But in addition there is another short period oscillation due to the nutation frequency of the simulator which in general is not equal to that of the satellite as outlined before. Therefore, in the block diagram of Fig. 3.5 a feedback of the estimated table state variables $\hat{\alpha}_t, \hat{\alpha}_t$ has been introduced called the table nutation and precession compensation according to the following equation

$$j) \quad \dot{M}_k = K_1 \hat{\alpha}_t + K_2 \hat{\alpha}$$

By proper selection of the feedback parameter matrices K_1, K_2 in the interesting frequency range the response of the table will be equal to that of the satellite without any additional resonance.

3.3.2 System Dynamics

The dynamics of the overall system have been investigated in a numerical simulation. The corresponding parameters are listed in Table 3.1:

		satellite	air bearing table
rigid body motion:			
momentum bias	H_n [Nms]	20	20
ratio of moments of inertia	I_{SAT}/I_t [-]	50	
nutaton frequency	ω_n [rad/s]	$3.1 \cdot 10^{-2}$	$9.3 \cdot 10^{-1}$
precession frequency	ω_p [rad/s]	$7.3 \cdot 10^{-5}$	$7.3 \cdot 10^{-3}$
reference angle	ψ_B [rad]		$6.25 \cdot 10^{-3}$
reference period	T_p [s]		253
flexible appendages:			
1. bending frequency/roll	$\omega_{R,1}/\omega_{n,SAT}$	6.05	
2. bending frequency/roll	$\omega_{R,2}/\omega_{n,SAT}$	37.9	
1. bending frequency/yaw	$\omega_{G,1}/\omega_{n,SAT}$	60.5	
2. bending frequency/yaw	$\omega_{G,2}/\omega_{n,SAT}$	379.2	
bandwidth/simulator	ω [rad/s]		0.3
external excitation:			(compensated)
(torque impulse/roll)			
nominal	$M_{d,c} \cdot \Delta t$ [Nms]		0.13
erroneous	$M_{d,c} \cdot \Delta t$ [Nms]	0.117	0.13
reference torque	M_B [Nm]		0.25

Table 3.1: Simulation Parameters

In roll and yaw, two bending modes of the flexible appendages have been considered. According to the ratio of transverse moments of inertia satellite/table of 50 the frequency of the table nutation is much higher than that of the real satellite. Using Eq. (3.16) it is compensated with a simulator corner frequency of 3 rad/s. The corresponding change in the air bearing table response is given by Fig. 3.7 with the transfer function roll torque/roll angular velocity for an example.

The nutational motion was excited by a jet thruster torque impulse about the roll axis. By this external disturbance also the appendage mode with the lowest bending frequency is primarily excited. The results for the roll axis motion are shown in Fig. 3.8. As time base the nutation period of the real satellite has been chosen. Due to the external torque impulse at the first moment the dynamic response of the simulator is faster than that of the real satellite. The corresponding difference in the roll angle plot results from the transient phase in the torque estimation and the discrete computation of the internal reaction torques (Fig. 3.8 a,b,c). After that transient the roll angle estimation and the simulator and satellite roll angle are equal up to a very high degree of accuracy (Fig. 3.8 d). The dynamic behaviour exhibits the satellite nutation disturbed by the relative appendage motion due to the first roll bending mode. The influence of the second bending mode is almost negligible. By proper compensation the disturbance effects due to the nearly undamped simulator eigenfrequencies (ref. to Fig. 3.6) have completely vanished from the system. The dynamic response in yaw not plotted here is in the same order of accuracy.

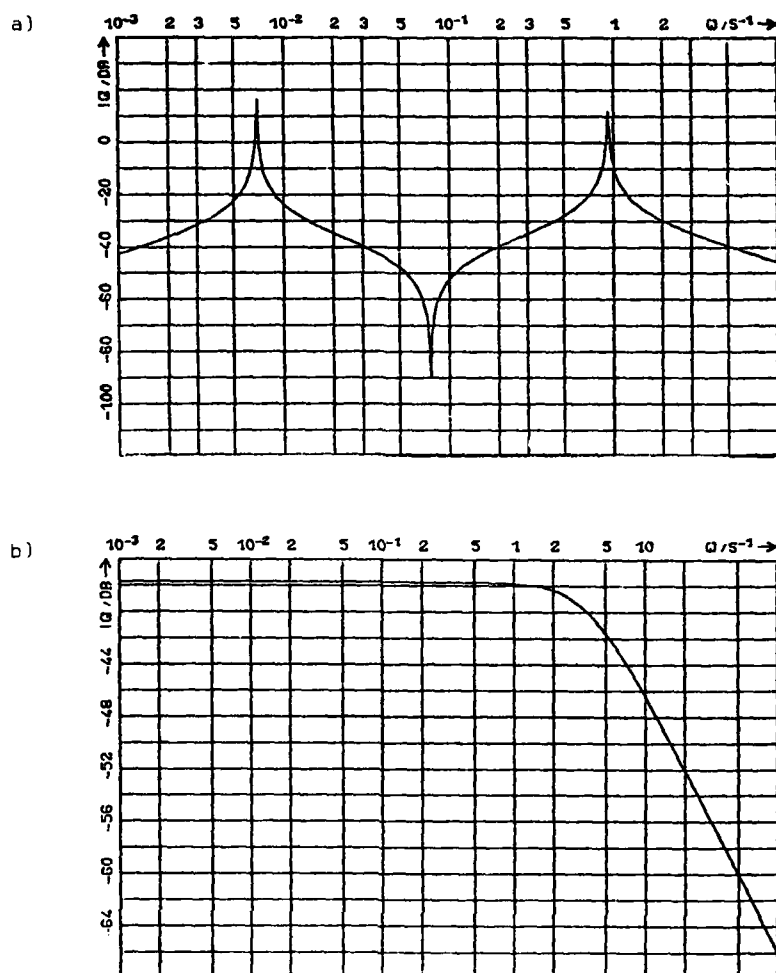


Fig. 3.7: Simulator Transfer Function with Uncompensated (a) and Compensated (b) Eigenfrequencies.

Suppose there is a control actuator error. To investigate the simulator response the assumption is made that the torque impulse ΔM_c exerted by the thruster remains the same as before, while the impulse ΔM_c commanded by the attitude controller is about 10% smaller. From the controller point of view the period of the torque impulse is now 10% too long which is equivalent to an error of the thruster torque. Fig. 3.9 shows the result. The simulator does not follow the commanded torque impulse. Its response is equivalent to the unperturbed case, i.e. in accordance to the physical thruster impulse.

In addition the dynamic response of the air bearing table is still equal to that of the real satellite. This means, the system behaves as if the incorrect torque impulse was acting not only on the simulator but also on the real spacecraft thus offering realistic test conditions by the air bearing simulation. The roll angle time records of Fig. 3.8d (real torque equal to commanded torque) and Fig. 3.9c (real torque as before but with commanded torque 10% smaller) differ only in the transient phase but after the transient they are identical. This dynamic behaviour can be explained by a compensating effect from the torque estimation. The Kalman filter is able to estimate the additional incorrect angular momentum introduced to the system by the thruster. This information is properly resolved as an additional external disturbance torque driving the model of the satellite where it is involved in the computation of the internal reaction torques. Comparing the torque estimation Fig. 3.8a and Fig. 3.9a the filter transient is completely different. In Fig. 3.9a the estimation of the incorrect angular momentum is marked by the dashed area.

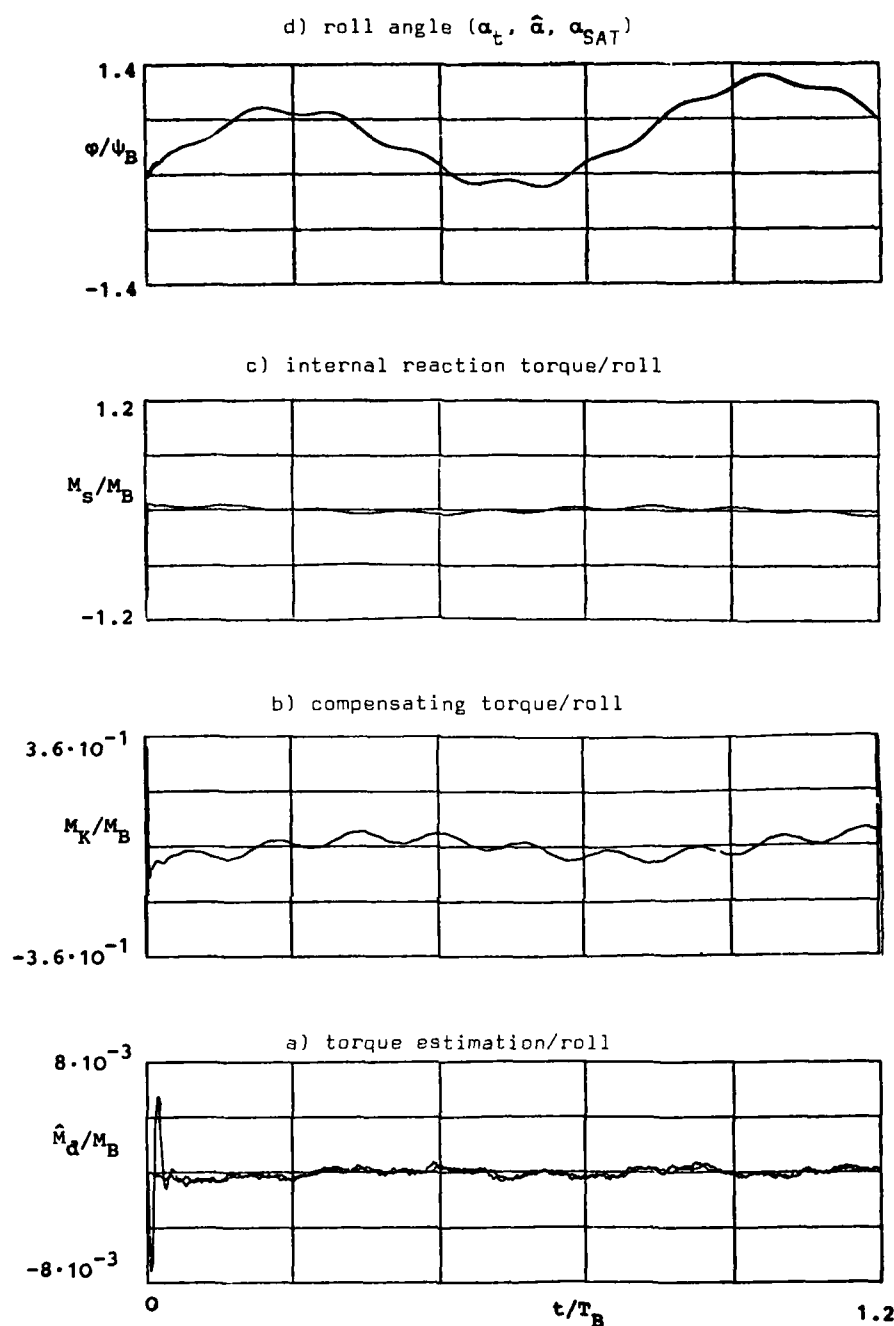


Fig. 3.8: Time Record of the Roll Angle and Corresponding Simulator Torques, Nominal Case

In [12] Mork and Wheeler stated that for lightly or undamped systems stability of the direct torque approach could be difficult to achieve. The system described here is stable in roll and yaw because here the dynamic response of the simulator is dominated by the wheel and that means by changes of the overall angular momentum. The filter is able to estimate these changes and to derive the correct information about the external disturbance torques. But there is no influence of the angular momentum bias in the pitch axis. Here the problem of stability is more significant. Employing the same method as in roll/yaw (i.e. to realise a prescribed transfer function of the simulator by a proper feedback of the estimated table states) and using the filter as a predictor of the disturbance torques also in pitch satisfying stability can be achieved.

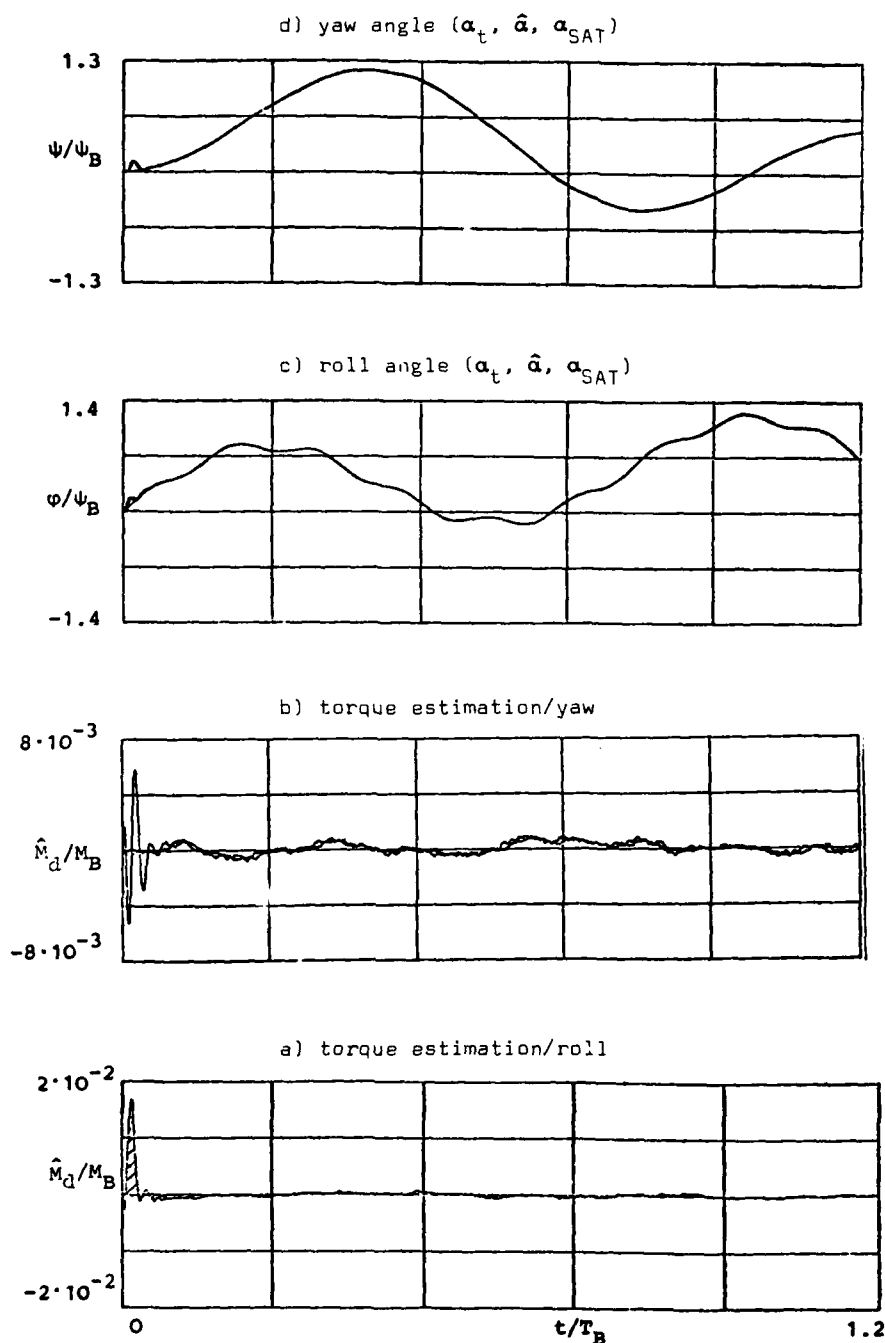


Fig. 3.9: Time Record of the Roll and Yaw Angle and Corresponding Torque Estimation, Erroneous Control Torque

3.3.3 Realisation

The hardware configuration of the complete simulator is presented in Fig. 3.10. The rigid body moments of inertia achievable with this configuration are only about 30 kgm^2 . This explains the large value of the inertia ratio in Tab. 3.1. On the air bearing platform two different sets of momentum wheels manufactured by Teledix, Heidelberg are mounted. A Double Gimbaled Momentum Wheel (DGMW) with a momentum bias of 20 Nms is stabilising the satellite and represents together with cold gas jet thrusters for wheel desaturation the actuators of the control system. In addition a set of three ball bearing wheels with zero momentum bias (reaction wheels) are used for generating the internal reaction torques. They are not driven by direct torque commands but by a speed control loop to minimize the effects of friction torques. Thereby the output of the reaction torque evaluation implemented in a digital processor are wheel speed commands directed to a microprocessor rather than motor torques. The microprocessor serves as a decentral control-

ler of the actual rotation speed.

Data handling between ground and simulator is performed via flexible wires. Due to the additional disturbance torques introduced by the wires this method is only feasible for small angular deflections of the table. For larger attitude angles they must be substituted by a TM/TC-system. The interaction between the processor and the wheel controller depends on the minimum time, required for the computation of the internal reaction torques. It is determined by the number of modes incorporated in the evaluation and by the degree of inter-axis coupling. A typical sampling period for the system described is 150-200 ms. This rate is too slow to get a satisfying operation of the reaction wheels and so the microprocessor has to interpolate and smooth the discrete wheel speed commands.

As mentioned before this active configuration of a flexible dynamics simulator can be adapted to various satellite configurations in a very short time. If there are any changes in the satellite parameters (e.g. larger moments of inertia, modified bending frequencies of the appendages etc.), only the parameters of the internal reaction torque evaluation have to be adapted. Kalman filter, nutation and precession compensation and, most important of all the hardware configuration of the air bearing table needs no changes, since now the eigenfrequencies of the simulator are independent from the actual satellite configuration.



Fig. 3.10: Simulation Hardware, Direct Torque Approach

4. SIMULATION OF SPACECRAFT DYNAMICS BY MEANS OF A THREE-AXES FLIGHT SIMULATOR

The theoretical design of a satellite attitude control system advantageously will be performed by means of analog and/or digital computer simulation techniques. Commonly this means fairly high expenses in case of hardware oriented - e.g. sensors and torquers-investigation.

In order to keep down computer and software extent a simulation method has been developed including a three-axes servo-system.

4.1 Computer Based Simulation with Hardware

This simulation method is based on the mathematical modelling of the spacecraft dynamics and the sensor and torquer transfer functions. The models are programmed in a digital or analog computer. The sensor and torquer hardware is attached to the gimballed mounting platform of the servo-system. The gimbals are driven by hydraulic or electric motors. The motor control signals are produced by the computer charged Euler equations. The computer input data are identified by the sensor output signals that are generated at different platform attitudes and rates by means of reference simulators, e.g. earth simulator and sun simulator. In this way the servo-platform reproduces the rotary motion of the spacecraft, thus the sensors move in the same way with respect to sun and earth as the real satellite does. Figure 4.1 demonstrates the block diagram of the dynamic simulation.

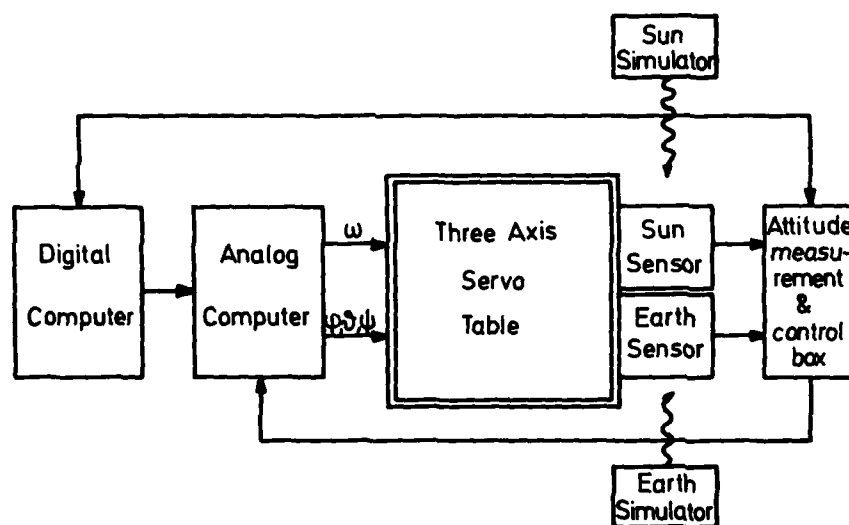


Fig. 4.1: Block Diagram of the Dynamic Simulation

4.2 Dynamic Simulation Facility

4.2.1 Mathematical Fundamentals

The control signals of the dynamic simulation facility corresponding to the Euler angles ϕ , θ , ψ and the angular velocity components ω_i are defined with respect to a labor fixed coordinate system (x_1^l , x_2^l , x_3^l) and must be transformed to the body fixed coordinate system (x_1^b , x_2^b , x_3^b) of the simulation facility. This is established by three consecutive matrix multiplications:

- Notation: 1. x_1 -axis: inner gimbal frame
 x_2 -axis: middle gimbal frame
 x_3 -axis: outer gimbal frame
2. Angular velocity in
- labor fixed (earth fixed) system: ω_i^l
 - body fixed (platform fixed) system: ω_i^b
3. Components of the motor angular velocity:

$$\dot{\Omega} = \begin{pmatrix} \dot{\phi} \\ \dot{\theta} \\ \dot{\psi} \end{pmatrix}$$

(The time differentiations of the Euler angles are identical to the skewed components of the satellite angular velocity.)

The transformation from the x_1^l -system to the outer gimbal frame x_3 is executed by:

$$(4.1) \quad \begin{bmatrix} \omega_{31}^b \\ \omega_{32}^b \\ \omega_{33}^b \end{bmatrix} = \begin{bmatrix} \cos\psi & \sin\psi & 0 \\ -\sin\psi & \cos\psi & 0 \\ 0 & 0 & 1 \end{bmatrix} \cdot \begin{bmatrix} \omega_1^l \\ \omega_2^l \\ \omega_3^l \end{bmatrix} + \begin{bmatrix} 0 \\ 0 \\ \dot{\psi} \end{bmatrix}$$

Neglecting the earth rate: $\omega_i^l = 0$ the matrix equation is reduced to

$$(4.2) \quad \omega_{3i}^b = \omega_{3i} = \begin{bmatrix} 0 \\ 0 \\ \dot{\psi} \end{bmatrix}.$$

The transformation from the outer x_3 to the middle frame x_2 is:

$$(4.3) \quad \begin{bmatrix} \omega_{21} \\ \omega_{22} \\ \omega_{23} \end{bmatrix} = \begin{bmatrix} \cos\theta & 0 & -\sin\theta \\ 0 & 1 & 0 \\ \sin\theta & 0 & \cos\theta \end{bmatrix} \cdot \begin{bmatrix} 0 \\ 0 \\ \dot{\psi} \end{bmatrix} + \begin{bmatrix} 0 \\ \dot{\theta} \\ 0 \end{bmatrix}.$$

That means

$$(4.4a) \quad \begin{aligned} \omega_{21} &= -\sin\theta \cdot \dot{\psi} \\ \omega_{22} &= \dot{\theta} \\ \omega_{23} &= \cos\theta \cdot \dot{\psi} \end{aligned}$$

or

$$(4.4b) \quad \omega_{2i} = \begin{bmatrix} -\sin\theta \cdot \dot{\psi} \\ \dot{\theta} \\ \cos\theta \cdot \dot{\psi} \end{bmatrix}.$$

The next transformation (middle frame x_2 to inner gimbal frame x_1) is

$$(4.5) \quad \begin{bmatrix} \omega_{11} \\ \omega_{12} \\ \omega_{13} \end{bmatrix} = \begin{bmatrix} 1 & 0 & 0 \\ 0 & \cos\varphi \sin\vartheta & \dot{\vartheta} \\ 0 & -\sin\varphi \cos\vartheta & \cos\vartheta \cdot \dot{\psi} \end{bmatrix} \cdot \begin{bmatrix} -\sin\vartheta \cdot \dot{\psi} \\ \dot{\vartheta} \\ \cos\vartheta \cdot \dot{\psi} \end{bmatrix} + \begin{bmatrix} \dot{\varphi} \\ 0 \\ 0 \end{bmatrix} ,$$

that means

$$(4.6a) \quad \begin{aligned} \omega_{11} &= \sin\vartheta \cdot \dot{\psi} + \dot{\varphi} \\ \omega_{12} &= \cos\varphi \cdot \dot{\vartheta} + \sin\varphi \cos\vartheta \cdot \dot{\psi} \\ \omega_{13} &= -\sin\varphi \cdot \dot{\vartheta} + \cos\varphi \cos\vartheta \cdot \dot{\psi} \end{aligned}$$

or

$$(4.6b) \quad \omega_{1i} = \begin{bmatrix} 1 & 0 & -\sin\vartheta \\ 0 & \cos\varphi & \sin\varphi \cos\vartheta \\ 0 & -\sin\varphi & \cos\varphi \cos\vartheta \end{bmatrix} \begin{bmatrix} \dot{\varphi} \\ \dot{\vartheta} \\ \dot{\psi} \end{bmatrix} = \underline{A} \cdot \underline{\dot{\Omega}} .$$

Transposing the matrix \underline{A} yields to

$$(4.7) \quad \begin{aligned} \dot{\varphi} &= \omega_{11} + \sin\varphi \tan\vartheta \cdot \omega_{12} + \cos\varphi \tan\vartheta \omega_{13} , \\ \dot{\vartheta} &= \cos\varphi \cdot \omega_{12} - \sin\varphi \omega_{13} , \\ \dot{\psi} &= \frac{\sin\varphi}{\cos\vartheta} \cdot \omega_{12} + \frac{\cos\varphi}{\cos\vartheta} \omega_{13} . \end{aligned}$$

Figure 4.2 demonstrates this transformation.

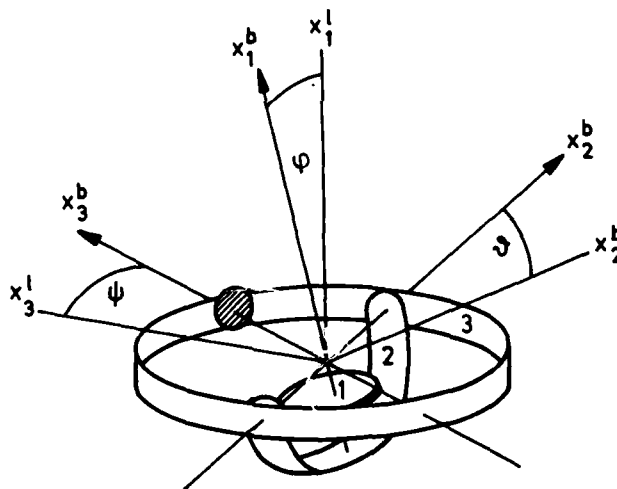


Fig. 4.2: Transformation from labor fixed (1) to simulator fixed (b) coordinates

4.2.2 System Requirements

The purpose of the dynamic simulation facility is the hardware oriented investigation of attitude stabilization systems of earth orbiting satellites in geostationary orbits as well as in low(er) orbits. The different attitude manoeuvres thoroughly determine the specification of the simulator dynamics and control characteristics.

The three gimbal frames physically simulate the angular motion of the satellite. The gimbal torques required are determined by the components of the satellite motions with respect to the simulator kinematics.

The data of the gimbals angular velocities, accelerations and ranges are determined by the corresponding satellite acquisition and operation manoeuvres by means of the above defined transformations.

Table 4.1 summarizes these data in the body fixed (satellite-) coordinates in case of a geostationary satellite. This is taken as a typical reference for specifying the simulator requirements. The kinematic specifications of satellites on lower orbits are commonly within these ranges. In order to meet the manoeuvre characteristics (table 4.1) the simulator has to cover the angular accelerations, velocities and ranges as listed up in table 4.2. Phaseshift and gain of the gimbal control must be specific for the simulation of nutation motions in transfer and operation orbits.

	angular accelerations [rad s ⁻²]			angular velocities [rad s ⁻¹]			angular ranges [degree]		
	x ₁ ^b	x ₂ ^b	x ₃ ^b	x ₁ ^b	x ₂ ^b	x ₃ ^b	x ₁ ^b	x ₂ ^b	x ₃ ^b
Geostationary Orbit									
Earth acquisition	0.01	0.005	0.005	0.05	0.01	0.01	360	± 20	± 20
spin axis control	0	0.005	0.005	0	0.005	0.005	0	± 3	+ 30 to - 90
normal operation	0.01	0.05	0.05	0.01	0.005	0.005	± 4	± 4	± 4
wheel despin	0.006	0.01	0.01	0.01	0.005	0.005	± 4	± 4	± 4
orbit control	0.01	0.05	0.05	0.005	0.005	0.005	± 4	± 4	± 4
Transfer Orbit									
attitude measurement	0	1.4	1.4	12.6	0.1	0.1	360	± 10	± 20
attitude control	0	1.4	1.4	12.6	0.1	0.1	360	± 10	± 20

Table 4.1: Minimum satellite motion characteristics of a geostationary satellite (example: SYMPHONIE)

	Cardan Frame		
	outer	middle	inner
Angular freedom [°]	-120 to +30		continuously
Angular velocity [rad s ⁻¹]			
- min.	3,5 · 10 ⁻⁷	3,5 · 10 ⁻⁷	3,5 · 10 ⁻⁷
- max.	4π	0,1	0,15
Angular acceleration [rad s ⁻²]	0,38	2,15	2,20
Position accuracy [°]		0,1	
Frequency response [at 3 Hz]			
Phase shift [°]		5	
Gain [db]		1	

Table 4.2: Requirements on the dynamic simulation facility

4.2.3 Description of the Simulation Facility

The simulation facility consists of the three axis motion servo-platform and the sun and earth simulators as optical references for the attitude measurement sensors that are attached to the inner gimbal of the motion platform.

The principal item of the three axis motion simulator is the mounting platform that is pivoted on a u-staped middle gimbal frame in order to guarantee free field of view to the optical reference simulators. This frame is fixed to the outer gimbal that is closed upon itself. To gain high angular accelerations of the middle and outer gimbal hydraulic motors are provided for each whilst the inner gimbal, the servo mounting platform is driven continuously by an electric motor for high precision synchronism.

The sun simulator consists of a high pressure xenon radiation source, a circular aperture that is adjusted to the focal plane of the collimation lense. To reduce the constructional length, a deviating mirror is established. Regarding the focal length the diameter of the aperture is such that the simulated sun has an angular aperture of 32 arcmin. The collimation accuracy of the radiation is better than 25 arcsec. The sun simulator is mounted on a suspension facility that is tiltable about the three axis servo table such that the optical axis crosses the intersection of the three gimbal axes.

The thermal irradiance of the earth is simulated by a heated copper plate that is attached to the outer gimbal of the three axis servo table. The center of the plate is adjusted to

the gimbal tilt axis. The diameter of the plate is of about 12,8 cm to simulate the earth diameter of 17.3° at a distance of 36000 km (geostationary orbit). The temperature of the copper plate is controllable in the region of 30°C to about 100°C .

Figure 4.3 depicts the whole assembly of the dynamic simulation facility.

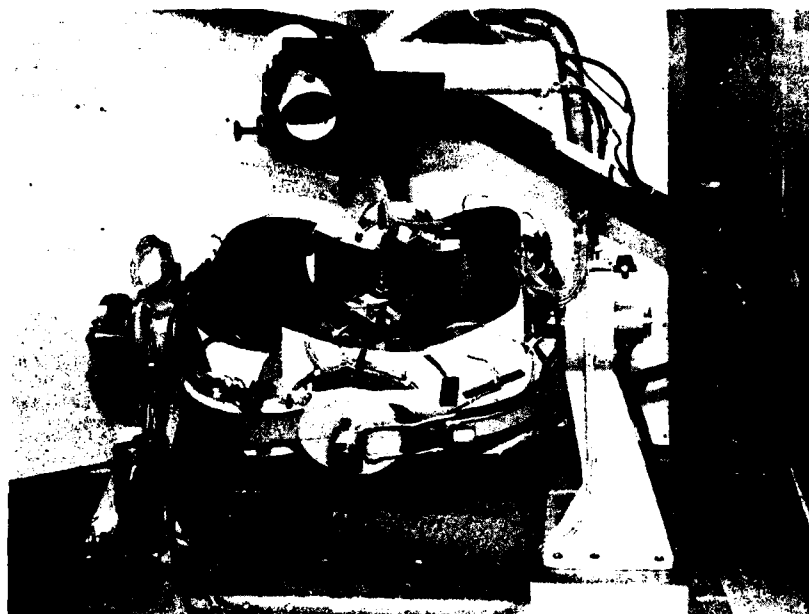


Fig. 4.3: Dynamic simulation facility

4.3 Tasks of the Dynamic Simulation Facility

The dynamic simulation facility of the DFVLR is specified for executing the following tasks:

- system selection
- system tests and qualification
- tests of attitude sensors
- operation simulation.

System Selection

The selection of a suitable attitude stabilization method for defined satellite manoeuvres principally is associated by the following steps:

1. Comparison of different stabilization methods in dynamic tests.
2. Evaluation of the test results with respect to mission requirements.
3. Selection of a preferred stabilization system.

Investigations of attitude stabilization systems advantageously are carried out by means of a dynamic simulation especially in the field of

- long term stability,
- drift characteristics,
- dynamics and
- limit cycle.

Otherwise, i.e. a computer simulation gives no chance of finding system errors. The selection criteria (system architecture, reliability, handling) commonly can be determined in a very simple way by dynamic simulations.

System Tests and Qualification

System tests and system qualification consecute the selection phase. Qualification tests of subsystems and components are closely connected with quantitative measurements of the

hardware-system parameters i.e. pointing accuracies of the attitude measurement sensors, dead band of the control loop etc. The goal of a dynamic simulation within this field is "space qualification".

Tests of Attitude Sensors

Attitude measurement sensors are attached to the mounting platform (inner gimbal) of the three axis table and the kinematics of the satellite is simulated such that the sensors are moved with respect to the optical references (sun and earth simulator). The motion simulation includes all manoeuvres of a satellite mission, i.e. such as nutation damping in the transfer orbit, apogee injection, earth acquisition etc. The dynamic simulation gives informations about the sensor characteristics (dead band, characteristic curve, pointing accuracy, repeatability, field of view) in these manoeuvres.

Operation Simulation

The dynamic simulation facility offers the possibility of simulating the satellite operation and training the ground personal.

This simulation requires all the hardware of an attitude stabilization system as the control electronics and torquers, the transfer functions of that are, besides the satellite dynamics, programmed in an analog or process computer. The attitude measurement system is - as mentioned above - attached to the inner gimbal mounting platform. The operational programmes are implemented in a digital computer. Doing this, the whole stabilization control loop is closed and satellite attitude manoeuvres can be established.

LITERATURE

- [1] Puls, J.
Stapf, R. "Die Dynamik des Aeronomie-Satelliten DIAL im Anschluß an die Abtrennphase", Raumfahrtforschung, Vol. 17, 1973, 221-224
- [2] Stapf, R.
Becker, K. "Simulationstests eines Lageregelungssystems mit gestaffelten Impulsen auf dem Satellitenbewegungssimulator der DFVLR", DFVLR, 1978, BMFT-FB W 78-29
- [3] Hirzinger, G.
Lange, Th. "Direct Digital Attitude Control with a Double Gimballed Momentum Wheel", Proc. of the VII. IFAC Symposium on Automatic Control in Space, 1976
- [4] Rölker, A. "Der Satellitenbewegungssimulator der DFVLR in Oberpfaffenhofen", DFVLR, 1969, DLR-Mitt. 69-20
- [5] Bullok, G.F.
Morell, F.R. "A Scaling Technique for Air-Bearing Simulation of Precision Pointing Systems", 1971, NASA TN D-6197
- [6] Becker, K. "Attitude Control System for Long Time Missions Using Pure Jet Control Torquing with Staggered Pulses", Proc. of the V. IFAC Symposium on Automatic Control in Space, 1973
- [7] Bittner, H.
et al. "The Attitude Determination and Control Subsystem of the INTELSAT V Spacecraft", Proc. of a Conference on "Attitude and Orbit Control Systems", ESA SP-128, 1977
- [8] Lange, Th. "Luftlager-Simulation des Kreiselkompass-Effektes bei einem Satellitenlageregelungssystem mit Schwungrad", DFVLR, 1976, IB 552/76-23
- [9] Schulz, G.
Lange, Th. "Attitude Control of Geostationary Satellites with Double Gimballed Momentum Wheels" AGARDograph "Spacecraft Guidance and Control", 1981
- [10] Heimbold, G.
Lange, Th. "Test on the Magnetic Bearing Momentum Wheel RCPM50 Manufactured by Aerospatiale, France, Final Report", DFVLR, Oberpfaffenhofen, 1980
- [11] Lacombe, J.L.
et al. "Study of OTS2 Inflight Behaviour Nutation Interaction with Momentum Wheel", Matra Espace, ESA CR(P) 1328, 1979
- [12] Mork, H.L.
Wheeler, P.C. "Three-Axis Attitude Control System Air-Bearing Tests with Flexible Dynamics", AIAA Paper, 73-866, 1973

- [13] Likins, P.W.
Fleischer, G.E. "Results of Flexible Spacecraft Attitude Control Studies Utilizing Hybrid Coordinates",
Journal of Spacecraft and Rockets, Vol. 8, No. 3, 1971, 264-273
- [14] Meirovitch, L.
Hale, A.L. "Response of a Dual-Spin Spacecraft with Flexible Appendages via Modal Analysis",
Journal of Spacecraft and Rockets, Vol. 12, No. 7, 1975, 445-448
- [15] --- "Dynamics and Control of Non-Rigid Spacecraft",
Proceedings, ESA SP 117, Frascati, 1976
- [16] Heimbold, G.
Lange, Th.
Schulz, G. "Physikalische Simulation von Satelliten mit Flexiblen Auslegern",
Deutscher Luft- und Raumfahrtkongress, Vortrag-Nr. 78-120, 1978
- [17] Holzach, H.
Puls, J.
Reinel, K. "Dynamische Simulationsanlage für Satellitenlageregelungssysteme",
DFVLR, 1974, BMFT-FB W 74-02

REPORT DOCUMENTATION PAGE			
1. Recipient's Reference	2. Originator's Reference	3. Further Reference	4. Security Classification of Document
	AGARD-AG-260	ISBN 92-835-1408-4	UNCLASSIFIED
5. Originator	Advisory Group for Aerospace Research and Development North Atlantic Treaty Organization 7 rue Ancelle, 92200 Neuilly sur Seine, France		
6. Title	SPACECRAFT POINTING AND POSITION CONTROL		
7. Presented at			
8. Author(s)/Editor(s)	P.Ph. van den Broek and Dr S.Z.Szirmay		9. Date November 1981
10. Author's/Editor's Address	See Flyleaf		11. Pages 264
12. Distribution Statement	This document is distributed in accordance with AGARD policies and regulations, which are outlined on the Outside Back Covers of all AGARD publications.		
13. Keywords/Descriptors	<div style="display: flex; justify-content: space-between;"> <div> Pointing control Position control Orbit determination </div> <div> Dynamic control Factorization methods </div> </div>		
14. Abstract	<p>This AGARDograph addresses recent developments in spacecraft pointing and position control and the state-of-the-art technologies in these areas. The following topics are covered:</p> <p>PART I: Attitude control and instrument pointing ,</p> <p>PART II: Orbit determination and control ,</p> <p>PART III: Flexible satellite control.</p> <p>This AGARDograph was prepared at the request of the Guidance and Control Panel of AGARD.</p>		

<p>AGARDograph No.260 Advisory Group for Aerospace Research and Development, NATO SPACECRAFT POINTING AND POSITION CONTROL Edited by P.Ph. van den Broek and Dr S.Z.Szirmay Published November 1981 264 pages</p> <p>This AGARDograph addresses recent developments in spacecraft pointing and position control and the state-of-the-art technologies in these areas. The following topics are covered: PART I: Attitude control and instrument pointing PART II: Orbit determination and control PART III: Flexible satellite control.</p> <p>P.T.O.</p>	<p>AGARD-AG-260</p> <p>Pointing control Position control Orbit determination Dynamic control Factorization methods</p>	<p>AGARDograph No.260 Advisory Group for Aerospace Research and Development, NATO SPACECRAFT POINTING AND POSITION CONTROL Edited by P.Ph. van den Broek and Dr S.Z.Szirmay Published November 1981 264 pages</p> <p>This AGARDograph addresses recent developments in spacecraft pointing and position control and the state-of-the-art technologies in these areas. The following topics are covered: PART I: Attitude control and instrument pointing PART II: Orbit determination and control PART III: Flexible satellite control.</p> <p>P.T.O.</p>	<p>AGARD-AG-260</p> <p>Pointing control Position control Orbit determination Dynamic control Factorization methods</p>
<p>AGARDograph No.260 Advisory Group for Aerospace Research and Development, NATO SPACECRAFT POINTING AND POSITION CONTROL Edited by P.Ph. van den Broek and Dr S.Z.Szirmay Published November 1981 264 pages</p> <p>This AGARDograph addresses recent developments in spacecraft pointing and position control and the state-of-the-art technologies in these areas. The following topics are covered: PART I: Attitude control and instrument pointing PART II: Orbit determination and control PART III: Flexible satellite control.</p> <p>P.T.O.</p>	<p>AGARD-AG-260</p> <p>Pointing control Position control Orbit determination Dynamic control Factorization methods</p>	<p>AGARDograph No.260 Advisory Group for Aerospace Research and Development, NATO SPACECRAFT POINTING AND POSITION CONTROL Edited by P.Ph. van den Broek and Dr S.Z.Szirmay Published November 1981 264 pages</p> <p>This AGARDograph addresses recent developments in spacecraft pointing and position control and the state-of-the-art technologies in these areas. The following topics are covered: PART I: Attitude control and instrument pointing PART II: Orbit determination and control PART III: Flexible satellite control.</p> <p>P.T.O.</p>	<p>AGARD-AG-260</p> <p>Pointing control Position control Orbit determination Dynamic control Factorization methods</p>

<p>This AGARDograph was prepared at the request of the Guidance and Control Panel of AGARD.</p> <p>ISBN 92-835-1408-4</p>	<p>This AGARDograph was prepared at the request of the Guidance and Control Panel of AGARD.</p> <p>ISBN 92-835-1408-4</p>
<p>This AGARDograph was prepared at the request of the Guidance and Control Panel of AGARD.</p> <p>ISBN 92-835-1408-4</p>	<p>This AGARDograph was prepared at the request of the Guidance and Control Panel of AGARD.</p> <p>ISBN 92-835-1408-4</p>

B337
4

AGARD

NATO OTAN

**7 RUE ANCELLE · 92200 NEUILLY-SUR-SEINE
FRANCE**

Telephone 745.08.10 · Telex 610176

**DISTRIBUTION OF UNCLASSIFIED
AGARD PUBLICATIONS**

AGARD does NOT hold stocks of AGARD publications at the above address for general distribution. Initial distribution of AGARD publications is made to AGARD Member Nations through the following National Distribution Centres. Further copies are sometimes available from these Centres, but if not may be purchased in Microfiche or Photocopy form from the Purchase Agencies listed below.

NATIONAL DISTRIBUTION CENTRES

BELGIUM

Coordonnateur AGARD - VSL
Etat-Major de la Force Aérienne
Quartier Reins Elisabeth
Rue d'Evere, 1140 Bruxelles

CANADA

Defence Science Information Services
Department of National Defence
Ottawa, Ontario K1A 0K2

DENMARK

Danish Defence Research Board
Osterbrogades Kaserne
Copenhagen Ø

FRANCE

O.N.E.R.A. (Direction)
29 Avenue de la Division Leclerc
92320 Châtillon sous Bagneux

GERMANY

Fachinformationszentrum Energie,
Physik, Mathematik GmbH
Kernforschungszentrum
D-7514 Eggenstein-Leopoldsdorfen 2

GREECE

Hellenic Air Force General Staff
Research and Development Directorate
Holargos, Athens

ICELAND

Director of Aviation
c/o Flugrad
Reykjavik

ITALY

Aeronautica Militare
Ufficio del Delegato Nazionale all'AGARD
3, Piazza Adlonner
Roma/EUR

LUXEMBOURG

See Belgium

NETHERLANDS

Netherlands Delegation to AGARD
National Aerospace Laboratory, NLR
P.O. Box 126
2600 A.C. Delft

NORWAY

Norwegian Defence Research Establishment
Main Library
P.O. Box 25
N-2007 Kjeller

PORTUGAL

Direcção do Serviço de Material
da Força Aérea
Rua da Escola Politécnica 42
Lisboa
Attn: AGARD National Delegate

TURKEY

Department of Research and Development (ARKE)
Ministry of National Defence, Ankara

UNITED KINGDOM

Defence Research Information Centre
Station Square House
St. Mary Cray
Orpington, Kent BR5 3RE

UNITED STATES

National Aeronautics and Space Administration (NASA)
Langley Field, Virginia 23365
Attn: Report Distribution and Storage Unit

**THE UNITED STATES NATIONAL DISTRIBUTION CENTRE (NASA) DOES NOT HOLD
STOCKS OF AGARD PUBLICATIONS, AND APPLICATIONS FOR COPIES SHOULD BE MADE
DIRECT TO THE NATIONAL TECHNICAL INFORMATION SERVICE (NTIS) AT THE ADDRESS BELOW.**

PURCHASE AGENCIES

Microfiche or Photocopy

National Technical
Information Service (NTIS)
5285 Port Royal Road
Springfield
Virginia 22161, USA

Microfiche

Space Documentation Service
European Space Agency
18, rue Mario Nikis
75015 Paris, France

Microfiche

Technology Reports
Centre (TRI)
Station Square House
St. Mary Cray
Orpington, Kent BR5 3RE
England

Requests for microfiche or photocopies of AGARD documents should include the AGARD serial number, title, author or editor, and publication date. Requests to NTIS should include the NASA accession report number. Full bibliographical references and abstracts of AGARD publications are given in the following journals:

Scientific and Technical Aerospace Reports (STAR)

published by NASA Scientific and Technical
Information Facility
P.O. Office Box 8757
Baltimore-Washington International Airport
Maryland 21240, USA

Government Reports Announcements (GRA)

published by the National Technical
Information Service, Springfield
Virginia 22161, USA

Printed by Technical Information Administration Ltd
London W14 7-9, London W14 7-9

ISSN 0043-1489-4

DATE
ILME